frontiers | Research Topics

Advanced functional materials for disease diagnosis, drug delivery and tissue repair

Edited by
Liqun Yang and Xianzhi Zhang

Published in
Frontiers in Bioengineering and Biotechnology

ISSN 1664-8714
ISBN 978-2-8325-6249-9
DOI 10.3389/978-2-8325-6249-9

About Frontiers

Frontiers is more than just an open access publisher of scholarly articles: it is a pioneering approach to the world of academia, radically improving the way scholarly research is managed. The grand vision of Frontiers is a world where all people have an equal opportunity to seek, share and generate knowledge. Frontiers provides immediate and permanent online open access to all its publications, but this alone is not enough to realize our grand goals.

Frontiers journal series

The Frontiers journal series is a multi-tier and interdisciplinary set of open-access, online journals, promising a paradigm shift from the current review, selection and dissemination processes in academic publishing. All Frontiers journals are driven by researchers for researchers; therefore, they constitute a service to the scholarly community. At the same time, the *Frontiers journal series* operates on a revolutionary invention, the tiered publishing system, initially addressing specific communities of scholars, and gradually climbing up to broader public understanding, thus serving the interests of the lay society, too.

Dedication to quality

Each Frontiers article is a landmark of the highest quality, thanks to genuinely collaborative interactions between authors and review editors, who include some of the world's best academicians. Research must be certified by peers before entering a stream of knowledge that may eventually reach the public - and shape society; therefore, Frontiers only applies the most rigorous and unbiased reviews. Frontiers revolutionizes research publishing by freely delivering the most outstanding research, evaluated with no bias from both the academic and social point of view. By applying the most advanced information technologies, Frontiers is catapulting scholarly publishing into a new generation.

What are Frontiers Research Topics?

Frontiers Research Topics are very popular trademarks of the *Frontiers journals series*: they are collections of at least ten articles, all centered on a particular subject. With their unique mix of varied contributions from Original Research to Review Articles, Frontiers Research Topics unify the most influential researchers, the latest key findings and historical advances in a hot research area.

Find out more on how to host your own Frontiers Research Topic or contribute to one as an author by contacting the Frontiers editorial office: frontiersin.org/about/contact

Advanced functional materials for disease diagnosis, drug delivery and tissue repair

Topic editors

Liqun Yang — Shengjing Hospital of China Medical University, China

Xianzhi Zhang — Yale University, United States

Citation

Yang, L., Zhang, X., eds. (2025). *Advanced functional materials for disease diagnosis, drug delivery and tissue repair*. Lausanne: Frontiers Media SA. doi: 10.3389/978-2-8325-6249-9

Table of contents

frontiers | Frontiers in Bioengineering and Biotechnology

TYPE Editorial
PUBLISHED 11 April 2025
DOI 10.3389/fbioe.2025.1602628

OPEN ACCESS

EDITED AND REVIEWED BY
Candan Tamerler,
University of Kansas, United States

*CORRESPONDENCE
Liqun Yang,
yangliqun@sj-hospital.org

RECEIVED 30 March 2025
ACCEPTED 04 April 2025
PUBLISHED 11 April 2025

CITATION
Yang L and Zhang X (2025) Editorial: Advanced functional materials for disease diagnosis, drug delivery and tissue repair.
Front. Bioeng. Biotechnol. 13:1602628.
doi: 10.3389/fbioe.2025.1602628

Editorial: Advanced functional materials for disease diagnosis, drug delivery and tissue repair

Liqun Yang[1]* and Xianzhi Zhang[2]

[1]Research Center for Biomedical Materials, Shenyang Key Laboratory of Biomedical Polymers, Engineering Research Center of Ministry of Education for Minimally invasive Gastrointestinal Endoscopic Techniques, Shengjing Hospital of China Medical University, Shenyang, China, [2]Department of Biomedical Engineering, Yale University, New Haven, CT, United States

KEYWORDS

advanced functional materials, disease diagnosis, sensing, imaging, drug delivery, tissue repair

Editorial on the Research Topic
Advanced functional materials for disease diagnosis, drug delivery and tissue repair

In recent years, with the rapid advancement of science and technology, advanced functional materials have demonstrated extensive potential in disease diagnosis, drug delivery, and tissue repair (Shi, 2009; Hu et al., 2020; Fenton et al., 2018; Varanko et al., 2020; Whitaker et al., 2021; Christman, 2019). The current Research Topic, Advanced Functional Materials for Disease Diagnosis, Drug Delivery, and Tissue Repair, focuses on the theoretical breakthroughs and multidimensional applications of these emerging materials, exploring how interdisciplinary collaboration drives medical innovation. By integrating materials science, biotechnology, and clinical needs, these studies provide systematic solutions to complex pathological challenges in modern medicine and lay a solid foundation for precision medicine and regenerative medicine.

In the field of diabetes management, significant progress has been achieved in precision diagnostics and chronic wound repair. Guan et al. reported the integration of intelligent nanosensor technology and biosensors, enabling more efficient and non-invasive dynamic glucose monitoring with significantly enhanced sensitivity and specificity (Guan and Zhang). Moreover, Mills et al. demonstrated that dressings coated with multipotent adult progenitor cells (MAPC) accelerated angiogenesis and anti-inflammatory responses, reducing the healing time of chronic diabetic wounds by 40% (Mills et al.). Additionally, Chen et al. developed a synergistic approach using graphene oxide (GO) alginate hydrogels in combination with platelet-rich plasma (Chen et al.), significantly enhancing collagen synthesis and microvascular growth, offering a promising strategy for the precise treatment of complex and irregular wounds.

In the field of cancer diagnosis and treatment, functional materials are revolutionizing the way malignant tumors are diagnosed and treated. For tumor imaging, Zhou et al. highlighted the use of PL002 bimodal contrast agents for precise localization during glioblastoma surgery, substantially improving the efficiency of tumor removal (Zhou et al.). Na et al. summarized major breakthroughs in the use of metallic nanoparticles and carbon-based materials for cerebrovascular imaging, enhancing the ability to conduct early screening for conditions such as aneurysms and strokes (Na et al.). On the therapeutic

front, Xu et al. reported that metal-based nanomaterials exhibited synergistic effects in photothermal and immunotherapy (Xu et al.), paving a new pathway for precise breast cancer treatment. Zhao et al. investigated the controlled drug-release capabilities of metal-organic frameworks (MOFs) (Zhao et al.), which have now become a critical tool in treating bone tumors. Ren et al. successfully fabricated SPIO/TP53/PLGA nanobubbles with a diameter of approximately 200 nm and, in combination with low-intensity focused ultrasound, achieved targeted delivery of the TP53 gene, significantly promoting the apoptosis of osteosarcoma cells and providing substantial support for gene-targeted therapies of malignant tumors (Ren et al.). Furthermore, Liu et al. developed a novel sonosensitizer, $La_2(WO_4)_3/CuWO_4$ composite material (LC-10), through a two-step hydrothermal method (Liu et al.). When used in a U251 glioblastoma cell model, this composite material inhibited electron-hole (e^-–h^+) recombination and generated stronger oxidative reactive oxygen species (ROS), effectively inducing glioblastoma cell apoptosis.

In the field of chronic wound repair, multifunctional smart materials have shown remarkable therapeutic potential. For infectious chronic wounds, Yang et al. developed CS/PVP composite nanofiber membranes with antimicrobial and antioxidant properties (Yang et al.), which not only enhanced the healing efficiency of acute burn wounds but also improved angiogenesis and re-epithelialization. Dai et al. designed shellac microspheres for the sustained release of nonsteroidal anti-inflammatory drugs (e.g., ketoprofen) (Yang et al.), extending bioactivity for up to 3 weeks and effectively reducing systemic side effects of conventional drugs. Regarding antibacterial applications, Zheng et al. created fluoride-releasing nano-zirconia-based composite coatings with long-term fluoride release, high wear resistance, and mechanical stability (Zheng et al.), representing a groundbreaking advancement for dental restorative materials. Tian et al. further demonstrated that multifunctional smart biomaterials hold significant promise for improving wound healing and preventing infections (Tian and Bian).

Repair and engineering of the nervous system have also benefited from the innovative design of functional materials. In spinal cord injury repair, Zhang et al. developed a dual-phase hydrogel scaffold (DPSH) capable of the controlled co-release of neurotrophic factors and Ang-(1–7) (Zhang et al.), effectively reducing local inflammation, promoting neural stem cell proliferation and differentiation, and significantly enhancing the recovery of motor function. In the urological and skeletal systems, the exploration of functional materials also yielded success. Hu et al. proposed that biodegradable ureteral stents (BUS), incorporating antibacterial coating and drug delivery technologies (Hu et al.), can mitigate infections and complications caused by long-term stent implantation, thereby improving patient safety and comfort. Moreover, Cao et al. fabricated PCL-PEG/CS/AST nanofibers (Cao et al.), which induced osteogenic differentiation of bone marrow mesenchymal stem cells (BMSCs), greatly promoting bone repair and functional reconstruction, providing a powerful tool for precision treatment of complex bone diseases.

In conclusion, advanced functional materials, with their multifunctional integration and precise design capabilities, offer multidimensional solutions to complex diseases. Under the impetus of interdisciplinary collaboration in materials science, biology, medicine, and engineering, these research outcomes have enabled dynamic diagnosis, intelligent drug delivery, and tissue regeneration, paving the way for clinical translation in precision medicine. However, several challenges persist, such as optimizing biocompatibility, controlling production costs, and accelerating regulatory approval processes. Looking forward, artificial intelligence may play a critical role in optimizing material properties and designing drug delivery systems, further accelerating the development of smart medical technologies. With continued research progress, multilayered medical technologies involving precise diagnosis, personalized treatment, and tissue repair will gradually emerge in clinical practice, bringing greater hope to patients worldwide and advancing global health to unprecedented heights.

Author contributions

LY: Writing – original draft, Writing – review and editing. XZ: Writing – review and editing.

Funding

The author(s) declare that financial support was received for the research and/or publication of this article. This research was funded by the Natural Science Foundation of Liaoning Province (2024JH2/102600340) and the support program for excellent young scholars at China Medical University.

Conflict of interest

The authors declare that the research was conducted in the absence of any commercial or financial relationships that could be construed as a potential conflict of interest.

Generative AI statement

The authors declare that no Generative AI was used in the creation of this manuscript.

Publisher's note

References

Christman, K. L. (2019). Biomaterials for tissue repair. *Science* 363 (6425), 340–341. doi:10.1126/science.aar2955

Fenton, O. S., Olafson, K. N., Pillai, P. S., Mitchell, M. J., and Langer, R. (2018). Advances in biomaterials for drug delivery. *Adv. Mater.* 30 (29), 1705328. doi:10.1002/adma.201705328

Hu, X. L., Kwon, N., Yan, K. C., Sedgwick, A. C., Chen, G., He, X., et al. (2020). Bioconjugated advanced materials for targeted disease theranostics. *Adv. Funct. Mater.* 30 (13), 1907906. doi:10.1002/adfm.201907906

Shi, D. (2009). Integrated multifunctional nanosystems for medical diagnosis and treatment. *Adv. Funct. Mater.* 19 (21), 3356–3373. doi:10.1002/adfm.200901539

Varanko, A., Saha, S., and Chilkoti, A. (2020). Recent trends in protein and peptide-based biomaterials for advanced drug delivery. *Adv. drug Deliv. Rev.* 156, 133–187. doi:10.1016/j.addr.2020.08.008

Whitaker, R., Hernaez-Estrada, B., Hernandez, R. M., Santos-Vizcaino, E., and Spiller, K. L. (2021). Immunomodulatory biomaterials for tissue repair. *Chem. Rev.* 121 (18), 11305–11335. doi:10.1021/acs.chemrev.0c00895

frontiers | Frontiers in Bioengineering and Biotechnology

TYPE Original Research
PUBLISHED 22 August 2023
DOI 10.3389/fbioe.2023.1213021

OPEN ACCESS

EDITED BY
Bing Tang,
First Affiliated Hospital of Sun Yat-sen University, China

REVIEWED BY
Guido Moll,
Charité University Medicine Berlin, Germany
Lina R. Nih,
University of California, Los Angeles, United States

*CORRESPONDENCE
S. J. Mills,
stuart.mills@unisa.edu.au

RECEIVED 27 April 2023
ACCEPTED 09 August 2023
PUBLISHED 22 August 2023

CITATION
Mills SJ, Kirby GT, Hofma BR, Smith LE, Statham P, Vaes B, Ting AE, Short R and Cowin AJ (2023), Delivery of multipotent adult progenitor cells via a functionalized plasma polymerized surface accelerates healing of murine diabetic wounds. *Front. Bioeng. Biotechnol.* 11:1213021. doi: 10.3389/fbioe.2023.1213021

Delivery of multipotent adult progenitor cells via a functionalized plasma polymerized surface accelerates healing of murine diabetic wounds

S. J. Mills[1,2]*, G. T. Kirby[1,2], B. R. Hofma[1,2], L. E. Smith[1,2], P. Statham[1,2], B. Vaes[3], A. E. Ting[4], R. Short[5] and A. J. Cowin[1,2]

[1]Future Industries Institute, University of South Australia, Mawson Lakes, SA, Australia, [2]Cooperative Research Centre for Cell Therapy Manufacturing, Adelaide, SA, Australia, [3]ReGenesys BV, Bio-Incubator Leuven, Leuven, Belgium, [4]Athersys Inc., Cleveland, OH, United States, [5]Material Science Institute, Lancaster University, Lancaster, United Kingdom

Introduction: Stem cell therapies have been investigated as potential treatment modalities for chronic wounds however there has been limited success to date. Multipotent Adult Progenitor Cells (MAPCs©) have been identified as having potential as an allogenic stem cell product due to their high population doubling number and their characteristic dampening of T-cell proliferation. This helps to prevent autoimmunity and graft/cell rejection.

Methods: We have developed a dressing, consisting of medical grade silicone coated with a heptylamine plasma polymer, which supports the growth and transfer of MAPCs to skin. To determine if the dressing can deliver functional stem cells into diabetic wounds, they were loaded with MAPCs and then placed over excisional wounds in both normal and diabetic mice.

Results and discussion: Accelerated healing was observed in both the normal and diabetic wounds with wound gape being significantly smaller at day 3 when compared to controls. Wound analysis showed that treatment with the MAPC dressings dampened the inflammatory response with reduced numbers of neutrophils and macrophages observed. Additionally, an increase in pro-angiogenic VEGF and CD31 positive endothelial cells was observed indicating improved new blood vessel formation. The MAPC dressings had no effect on fibrosis with collagen I and III being equally affected in both control and treated wounds. Overall, the functionalized MAPC dressings improve healing responses particularly in diabetic mice with impaired healing responses and therefore, show potential for development as an advanced therapeutic approach for the treatment of chronic diabetic wounds.

KEYWORDS

MAPC, Inflammation, wounds, diabetes, biomaterials, plasma polymerization

1 Introduction

Diabetes is one of the main causes of chronic wounds and the burden of this disease is rapidly increasing (Australia, 2021). There are thought to be around 422 million diabetic people and one in two adults undiagnosed with diabetes worldwide (Australia, 2021; Organisation, 2021). Approximately 15% of diabetic patients will go on to form diabetic foot ulcers and complications from these wounds lead to an occurrence of a major amputation every 30 s (Johannesson et al., 2009) with follow up mortality rates as high as 80%, over the next 5 years (Reiber et al., 2001). Clearly, there is an unmet demand for effective treatments, which improve healing of chronic wounds in diabetic patients.

The use of stem cells as a treatment for a variety of wound types has been around for some time. Mesenchymal Stem Cells (MSCs) are a cell type that have been widely used for this purpose due to their multipotent characteristics enabling them to differentiate into many different cell types including, chondrocytes, adipocytes, tenocytes, and myocytes (Kirby et al., 2015). The majority of studies show that treatment of a wound with MSCs accelerates the rate of wound closure in both normal and diabetic mice (Badiavas and Falanga, 2003; Ichioka et al., 2005; Mansilla et al., 2005; Falanga et al., 2007; Dash et al., 2009; Stoff et al., 2009; Mills et al., 2013; Gao et al., 2014; Huang et al., 2015; Ahangar et al., 2020a; Thomas et al., 2021). This improvement in healing is achieved via increases in vascularization, cellularity and elastin production as well as reduction in scar formation. Isolated human MSCs have been delivered to wounds using a variety of different methods. Badiavas and Falanga (2003) isolated the patients MSCs, via a bone marrow aspirate of the iliac crest. These cells were then administered directly onto a debrided wound site and were also injected intradermally into the wound margins. A remainder of the cells were also cultured, and three additional treatments were administered. This treatment was applied to three patients, all of which had chronic cutaneous ulcerations. The MSC treatment resulted in wound closure, with increased vascularization, in all three patients with no reoccurrence of the wounds after following up 1-2 years later (Badiavas and Falanga, 2003). Falanga et al. (2007) refined their treatment in this later study by isolating the mononuclear cells from the iliac crest, and then culturing them in MSC media. These cells were then characterised before being incorporated into a fibrin spray containing 5 mg/mL fibrinogen and 25 U/mL thrombin. This cell suspension was then sprayed topically onto the surface of acute and chronic human wounds. The acute wounds were shown to heal with some of the MSCs incorporated into the newly formed tissue. The chronic wounds were shown to reduce in wound area with the MSCs again remaining in the wound site. MSCs isolated from mice and applied using the fibrin spray technique were also able to accelerate healing in diabetic mice (Falanga et al., 2007). Ichioka et al. (2005) investigated the use of a collagen matrix to delivery their bone marrow cells (Ichioka et al., 2005). The cells were isolated from the bone marrow of mice and then impregnated into the collagen matrix. The cells using in this study were not passaged or characterised and are more likely a mixed population of stromal cells rather than an enriched population of MSCs. The collagen matrix containing the cells was then placed in a wound created using a skin fold model of healing, which allowed the visualization of new blood vessel growth. Treatment with the bone marrow suspension showed increased vascularization of the murine wounds. This method of treatment was also used for the treatment of a human non-healing ulcer. After treatment there was an induction of granulation tissue formation that led to the eventual closing of the wound (Ichioka et al., 2005). Human MSCs have also been shown to have low immunogenicity and promote healing in incisional wounds in rabbits (Stoff et al., 2009). In this study, 3 cm incisional wounds were created on the dorsum of New Zealand White rabbits. The wounds were sutured and then fluorescently labelled human MSCs were intradermally injected around the wound site. After 7 days the sutures were removed, and the wounds left to heal. The wounds treated with hMSCs were shown to have increased tensile strength and reduced scarring (Stoff et al., 2009).

Other studies with human MSCs and stromal cells also showed that in addition to their beneficial effects on the wound healing process in skin they can also improve healing in other tissues such as the spinal cord and the myocardium (Mansilla et al., 2005; Huang et al., 2010). Their effects are wide ranging and have also shown to alter lipid metabolism during wound healing in diabetic wounds (Gao et al., 2014). However, despite the numerous studies being performed using MSCs, several differences in how the cells are characterized, where they are harvested from, their dosage and method of application has hindered their uptake or application (Kirby et al., 2015). Additionally, the term “MSC” in the literature has also referenced mesenchymal stromal cells, which unlike stem cells are a heterogenous population of different cell types, of which only a small population may be true mesenchymal stem cells. Whilst mesenchymal stem cells can help to repopulate lost cells and tissues the mesenchymal stromal cell population acts more by homing to the wound and secreting factors which are often immunomodulatory in nature (Viswanathan et al., 2019). This confusion and poor characterization has led to an increasing number of treatments with a high degree of variability, which has potentially hindered the approval of MSC treatments available for the treatment of chronic wounds (Moll et al., 2019; Moll et al., 2022).

Given the lack of progress with the development of MSC treatments, other types of stem cells have been investigated. Multipotent adult progenitor cells (MAPCs) are bone-marrow derived non-haematopoietic adherent cells that have been identified as a potential allogenic cell type for the treatment of various conditions (Boozer et al., 2009; Reading et al., 2013; Laing et al., 2020; Carty et al., 2021). They were first described in 2002, by Jiang et al., and were found to have similar characteristics to MSCs in that they could proliferate without senescence and differentiate into the three germ layers to create bone, cartilage, fat, muscle, tendon, endothelium, neurons, glia and hepatocytes (Jiang et al., 2002; Khan and Newsome, 2019).

One advantageous characteristic of MAPCs, not shared by MSCs, is that they can be expanded for over 70 population doublings, unlike MSCs which are limited to around 20–25 doublings. This makes MAPCs much more robust when expanding the population for *in vivo* treatments and for upscaling during manufacturing of a therapeutic (Roobrouck et al., 2011). MSCs and MAPCs have also been shown to be non-immunogenic as they lack the expression of MHC class II and have low expression of MHC class I molecules, as well as costimulatory markers (CD40, CD80, and CD86), and CD45 (Khan and Newsome, 2019).

Interestingly, it has been observed that upon differentiation or exposure to IFNγ, MSCs increase their expression of MHC class I and class II molecules making them susceptible to lysis by natural killer cells (Le Blanc et al., 2003). MAPCs, however, upregulate MHC class I but not class II molecules and they even inhibit host IL-7-dependant effector T-cells proliferation, which may prolong their persistence (Tolar et al., 2006; Jacobs et al., 2013; Reading et al., 2015). This dampening of the immune response and inhibition of T-cell proliferation, brought about by MAPC expression of prostaglandin E2, suggests that potentially MAPCs make an ideal allogenic product and is why they are currently being tested in graft versus host disease, immunomodulation after liver transplant and for cardiac regeneration (Pelacho et al., 2007; Highfill et al., 2009; Jacobs et al., 2013; Soeder et al., 2015).

MAPC actions, *in vivo*, appear not to be limited to immunomodulatory properties but they also have beneficial effects on existing vasculature as well as promoting new vessel growth. This has been observed in a variety of models including islet cell transplantation were significantly increased VEGF expression and vascularization was observed. This resulted in an increased number of islet cells that survived engraftment (Cunha et al., 2017). This improvement in vascularization has also been shown in a model of limb ischaemia where treatment with MAPCs led to improved vascularization and blood flow with improved vascular and skeletal muscle cell growth repairing the ischaemic damage (Aranguren et al., 2008). MAPCs have also been shown, via proteomic analysis, to regulate a wide variety of proteins when stimulated with either IFNγ, LPS or (a tolerogenic CD74 ligand) RTL1000 (Burrows et al., 2013). The functions of these proteins included in processes such as extracellular matrix formation and regulation (MMPs and proteases), angiogenesis and immune regulation of cells such as neutrophils, macrophages and T-cells (Burrows et al., 2013). MAPCs not only possess many of the beneficial traits of their MSC counterparts, when used for the treatment of a wide variety of disorders, but they also have selective advantages over MSCs when being considered for an allogenic therapeutic. The increased number of cells cycles that they can be expanded for mean that MAPCs are more robust when generating the required number of cells for *in vivo* treatment. In addition, their dampening of the immune response means that they can persist within the body to prolong their beneficial effects on the immune response and vascularization process resulting in better treatment outcomes when compared to MSCs.

When developing stem cell products for the treatment of acute and chronic wounds the effects of the mode of delivery and its optimization is often not fully considered. A common method of delivering stem cells is with the cells in suspension (Basiouny et al., 2013), however this is often preceded by enzymatic digestion, which can be detrimental to the cells. Cells are also administered via injection but this technique has been shown to increase rates of apoptosis in the delivered cells (Amer et al., 2015). This has led to interest in producing stem cell therapies which avoid enzymatic digestion and deliver the cells as a sheet (Kirby et al., 2017). We have previously described the manufacture of a functionalized heptylamine surface on a silicone backing, using plasma polymerization, that can transfer MAPCs onto a dermal equivalent *in vitro* (Kirby et al., 2017). This dressing negates the need for any enzymatic digestion prior to use and the functional surface allows the cells to detach and migrate into the wound site (Kirby et al., 2017). The functional effects of MAPCs and this mode of delivery suggests that the functionalized dressings with adherent MAPCs may be beneficial for the treatment of diabetic wounds which have impaired healing.

Here, for the first time, we describe the delivery, and optimization of dosage, of MAPCs using a functionalized dressing for wound healing. Using preclinical wound models in normal and diabetic mice we have shown that MAPC dressings improve healing outcomes through a dampening of the immune response and an increase in angiogenesis. In addition, we also showed that when MAPCs are delivered to the entire surface of the wound via the dressing that healing is accelerated when compared to injecting MAPCs intradermally around the perimeter of the wound.

Material and methods

Chemical and reagents

Primary antibodies NIMP-R14 (sc-59338) and MRP-14 (sc-8114) were from Santa Cruz Biotechnology (United States), collagen I (600-401-103) and collagen III (600-401-105) were from Rockland Immunochemicals Inc. (United States), VEGF (MA1-16626) was from Thermo Fisher Scientific (MA, United States) and CD31 (ab28364) and HNA antibody (ab215396) was from Abcam (Cambridge, UK). All secondary antibodies were Alexa Fluors, goat anti-rat 660 (A21054), donkey anti-goat 594 (A11057) and goat anti-rabbit 488 (A11008) and IgG antibody (02-6502) were from Thermo Fisher Scientific (MA, United States). Streptozotocin (STZ; S0130) and heptylamine were sourced from Sigma-Aldrich (MO, United States). Silicone was obtained from Polymer Systems Technology Ltd. (High Wycombe, UK).

Functionalized dressing manufacture

Dressings were manufactured using a backing substrate of 0.3 mm-thick silicone, which were coated with heptylamine using plasma polymerization and a parallel plate reactor (Figure 1A). A radio frequency power of 13.56 MHz was used along with an initial pressure of 2×10^{-2} mbar. The deposition time was 20 min, and the precursor flow was maintained for a further 10 min. The method and physico-chemical analysis of the polymer produced is more fully described in Kirby et al. (2017) (Kirby et al., 2017).

Cell culture

Human MAPCs were obtained from ReGenesys (Heverlee, Leuven, Belgium), prepared from the bone marrow of a healthy volunteer and cultured under previously described conditions (Boozer et al., 2009). Briefly. MAPCs were expanded on a primed and fibronectin-coated hollow-fibre cartridge of the Quantum cell expansion system (TerumoBCT, NJ, United States), harvested using

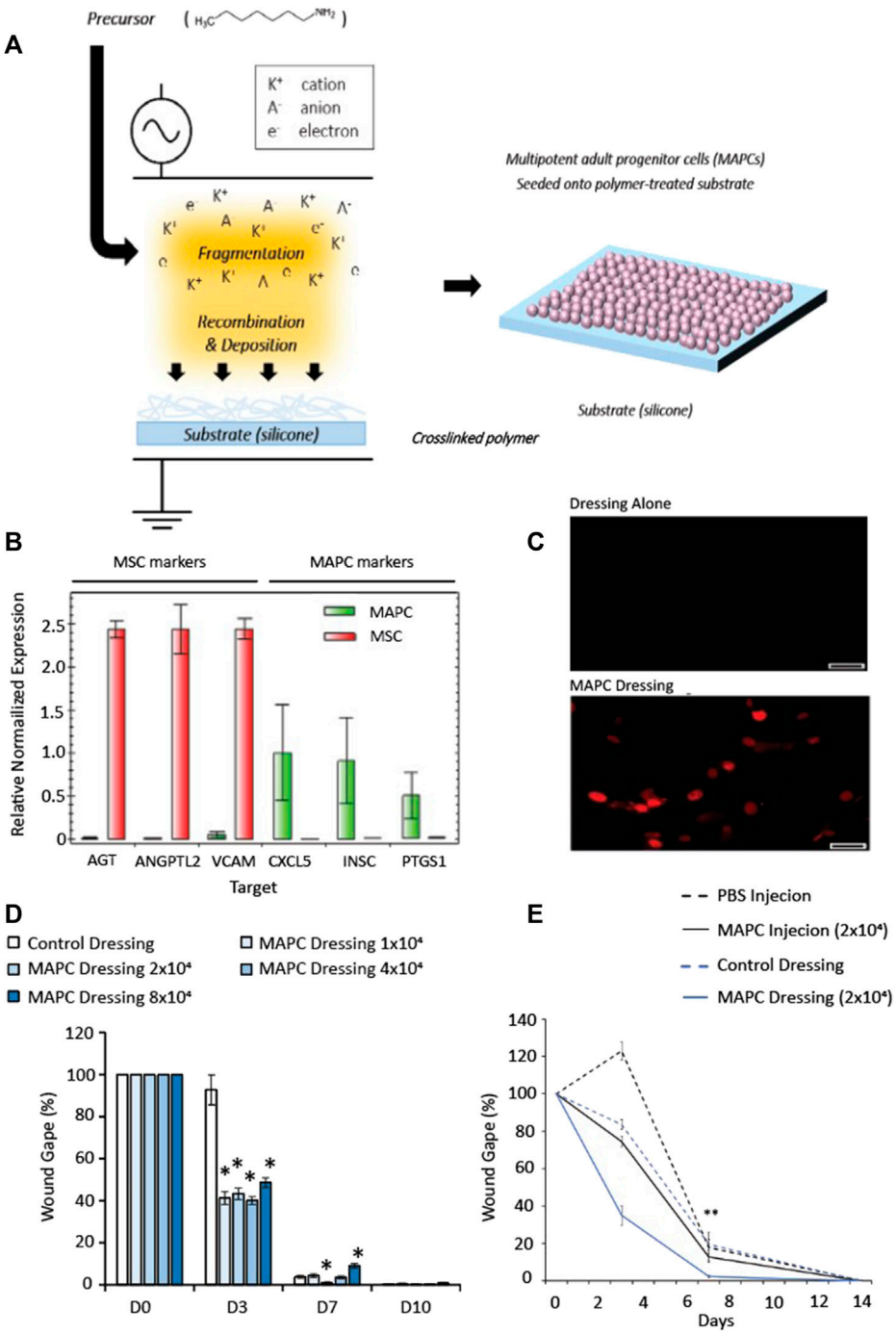

FIGURE 1
Schematic representation showing the fabrication steps for the cell-dressing **(A)**. A radio-frequency plasma polymer process is used to generate a chemically functional polymer onto the silicone dressing (A, left). Multipotent adult progenitor cells are then seeded onto the dressing and allowed to adhere for 24 h (A, right). **(B)** Expression of MAPC and MSC markers of donor matched MAPCs and MSCs to confirm the genotypes of the cells. **(C)** HNA staining of human MAPC cells in mouse wounds in MAPC treated and dressing alone at day 7 (scale bars = 50 μm). **(D)** Dose response of MAPCs in diabetic wounds. **(E)** Comparison of wound gape from diabetic mouse wounds injected at D0 with 2×10^4 MAPC or treated with a dressing seeded with 2×10^4 MAPC. Markers of significance are * = $p \leq 0.05$, and ** = $p \leq 0.01$. The data in **(D,E)** was compared using a one-way ANOVA with a Bonferroni correction.

trypsin/EDTA (Lonza, Basel, Switzerland), cryopreserved and stored in the vapour phase of liquid nitrogen until use. Cells were further expanded on fibronectin-coated plastic tissue culture flasks. Cell cultures were maintained under low oxygen tension in a humidified atmosphere of 5% CO_2. Cells were cultured to sub-confluence in MAPC, low glucose DMEM, culture media (Thermo Fisher

Scientific, MA, United States) supplemented with FBS (Atlas biologicals, CO, United States), MCDB (Sigma-Aldrich, MO, United States), platelet-derived growth factor (R&D Systems, MN, United States), epidermal growth factor (R&D Systems, MN, United States), dexamethasone (Sigma-Aldrich, MO, United States), penicillin/streptomycin (Invitrogen, CA, United States), 2-Phospho-L-ascorbic acid (Sigma-Aldrich, MO, United States), and linoleic acid–albumin (Sigma-Aldrich, MO, United States). Cells were imaged live using phase contrast microscopy and were split when they reach confluence using phosphate buffer saline (PBS, Lonza, Basel, Switzerland) and trypsin-EDTA (Lonza, Basel, Switzerland). Prior to use, cells were washed in PBS and seeded onto the functionalized dressings using a seeding ring, to keep the cells within a defined area. To achieve this a 10 mm seeding ring with an area of 0.8 cm^2 was used and either 1×10^4, 2×10^4, 4×10^4 or 8×10^4 cells were seeded per dressing. After 24 h the seeding ring was removed, and the dressing was ready for use.

mRNA isolation and analysis

Cell expression of MAPC and MSC markers were assessed via mRNA isolation and qRT-PCR as previously described (Kirby et al., 2017). In brief, donor matched MSCs and MAPCs were cultured, and RNA extracted using an AllPrep Protein/RNA Isolation Kit according to the manufacturers protocol (QIAGEN, Germany). The RNA was quantified using a NanoDrop Lite Spectrophotometer (Thermo Fisher Scientific, MA, United States) and the expression of the following markers was assessed via qRT-PCR: AGT, VCAM1, ANGPTL2, VCAM, CXCL4, INSC, and PTGS1. Expression was normalised to the housekeeping gene ATP5B following iScript cDNA synthesis (BioRad, CA, United States) and qPCR on the BioRad CFX Connect using the SsoAdvanced SYBR Green Universal Supermix synthesis (BioRad, CA, United States).

Animal studies

All animal studies were carried out with approval from the Women's and Children's Health Network Animal Ethics Committee (secondary healing model—AE971/4/2018 and diabetic healing model—AE984/6/2017) and carried out in accordance with the Australian code of practice for the care and use of animals. Mice were all eight-to ten-week-old females (BALB/C) sourced from the Animal Resources Centre (Perth, WA, Australia). Mice were acclimatized for 7 days upon arrival and were kept in a 12-h light/dark cycle, in a temperature and humidity-controlled environment. Only female mice were used as there are significant inherent difference in the wound healing mechanism when compared to male mice. It has been reported in the literature that oestrogen can accelerate healing via a dampening of the inflammatory response whilst androgen have the opposing effect (Ashcroft and Mills, 2002; Ashcroft et al., 2003). Studies in male mice will be conducted if the MAPC treatment is successful.

Diabetes induction

10–12-week-old mice were fasted 4 h prior to streptozotocin (STZ) being injected interperitoneally at 50 mg/kg, in citrate buffer pH 4.5 (100 ul), for 5 consecutive days. The mice were then group housed and mushy food was supplied until healthy weights were maintained. Blood glucose levels were tested daily and 1-2 U of insulin was administered as required to maintain the blood glucose levels within the diabetic range of 15–25 mmol/L. Following maintenance for 6 weeks post-STZ injection, only mice within the diabetic range for the entirety of weeks 4–6 were included in the study. Overall, 70% of the mice in this study became diabetic using this method and these were included in the diabetic groups to give $N = 7$. The other 30% of the non-diabetic mice were used for other studies.

Surgical procedures

Groups of healthy and diabetic mice were anaesthetized with inhaled isoflurane. Mice were initially placed in an induction box supplied with at 2 L/min of oxygen and 3% isoflurane. Once under surgical depth anaesthesia the mice were transferred to a nose cone which was supplied with 0.2 L/min oxygen and 2% isoflurane. At this point the dorsum was shaved, depilated with Veet cream and cleaned with 70% ethanol. Two equidistant 6 mm full thickness excisional wounds were created, using a punch biopsy, on the dorsal surface, 1 cm from the base of the skull and 1 cm either side of the midline. Each wound was then covered with a circular 1 cm diameter dressing which was held in place using a 3 cm by 1 cm strip of Tegaderm. Mice were under anaesthetic for an average of 5 min.

MAPC and control treatments

Treatments were either administered as intradermal injections or via the functionalized dressing. For the intradermal injection the treatment consisted of MAPCs in PBS or PBS alone, with a total volume of 100 uLs. 25 μLs of PBS or the cell suspension was injected intradermally 2 mm from the wound margin, at 4 sites equidistant around the wound circumference. The dressings were either the functionalized surface alone or the functionalized surface seeded with MAPCs. Both the wounds on the mice received the same treatment for all studies i.e., either control dressings or inject MAPCs or dressing seeded with MAPCs or PBS injection. The dressings were removed after 72 h, and the wounds left to heal by secondary intention i.e., no sutures or dressings were used after 72 h. $N = 7$ mice per group were used as calculated using a power calculation.

Dose response study

An initial *in vivo* wound healing study was performed to identify the optimal dose of MAPCs that would result in the fastest rate of wound closure. The wounding was carried out as described in the surgical procedures section in diabetic mice and five groups were compared, a control functionalized dressing with no cells and dressing seeded with either 1×10^4, 2×10^4, 4×10^4 or 8×10^4

cells. Macroscopic wound gape measurements were then compared to determine the rate of healing.

Comparison of MAPC delivery

In this study using diabetic mice, MAPCs were delivered to the wound either via intradermal injection or via the functionalized dressing. The controls used were wounds treated with PBS delivered via an intradermal injection or a functionalized dressing with no MAPCs. MAPCs in PBS were initially delivered to the wound surface but the cell suspension was not retained within the wound site due to a lack of viscosity as such it was decided to deliver the cells via intradermal injections.

Acute and diabetic wound healing studies

These studies were carried out as specified in the surgical procedures section and the MAPC dose used was 2×10^4 cells per wound. The two treatment groups were the functionalized dressing seeded with MAPCs or the functionalized dressing alone.

Macroscopic assessment

All wounds were photographed daily, and macroscopic measurements of re-epithelialization, termed wound gape, were measured from these digital images.

Microscopic assessment

Wounds were collected from groups of mice on days 3, 7 and 14 and bisected. Half the wounds were snap frozen in liquid nitrogen and used for molecular analysis and half the wounds were fixed for 24 h in 10% normal buffered formalin before being processed into paraffin and used for histological analysis. 5 µm wound sections cut and mounted onto coated glass slides. Slides were stained with haematoxylin and eosin for microscopic wound measurements including, wound width, wound area and percentage re-epithelialization.

Immunohistochemical staining

5 µm sections on glass slides were placed into xylene before the sections were rehydrate using graded concentrations of ethanol. Antigen retrieval was carried out in 10 mM citrate buffer, pH 6.0, where the sections were heated to 90°C for 10 min. Once cooled the sections were incubated with an appropriate blocking serum for 30 min. Primary antibodies to NIMP-R14, MRP-14, VEGF, CD31, HNA, collagens I and III were diluted 1:100 using PBS and secondary antibodies were diluted 1:200 in PBS. Control staining used an appropriate IgG antibody, which was used in place of the primary antibody. Secondary antibodies were Alexa Fluor, mouse anti-rat 660, mouse anti-goat 594 and mouse anti-rabbit 488. All sections were counterstained with DAPI (4', 6-diamidino-2-phenylindole) at a concentration of 1:5000. Images were captured on Olympus IX83 with a DP80 camera, at ×20 magnification. Analysis and quantification of cells per unit area (mm^2), fluorescent intensity and wound measurements were performed using CellSens software (Olympus, Japan).

Statistical analysis

Statistical significance was calculated using a two-tailed Student's t-test when comparing two groups. A one-way ANOVA was performed, with a Bonferroni correction, for comparison of multiple groups. A p-value of less than 0.05 was considered significant.

Results

Expression of MSC and MAPC panel markers

To confirm the population of cells used were MAPCs, analysis of expression markers for donor matched MSCs and MAPCs was performed. Significantly more expression of MSC markers (AGT, ANGPTL2, and VCAM) were observed in the MSC cells compared to MAPCs, which had little measurable expression (Figure 1B). The expression of the MAPC markers (CXCL5, INSC and PTGS1) had greater expression in the MAPCs when compared to the MSCs, which had little or no expression of these markers (Figure 1B).

Identification of the optimal dose of MAPCs delivered using the functionalized dressings to treat diabetic wounds

Wounded diabetic mice ($n = 7$) were treated with functionalized dressings seeded with: 1×10^4, 2×10^4, 4×10^4, 8×10^4 MAPCs or functionalized dressing (cell-free) alone. Macroscopic images were taken at day 0, day 3, day 7 and day 10 and wounds harvested at day 7 and day 10. To confirm delivery of human MAPCs into the murine wounds, human nuclear antigen (HNA) antibody staining was performed. The presence of human MAPCs was confirmed at day 7 with HNA positive cells observed within the wounds (Figure 1C). Macroscopic wound measurements showed that at day 3 all mice treated with MAPC dressings had smaller wounds when compared to those treated with cell-free control dressings with wound gape being 44.1%–52.7% smaller than the dressing alone depending on the dosage used. At day 7, only wounds treated with the 2×10^4 MAPC dressing remained significantly smaller than wounds with dressing alone ($p = 0.0103$) (Figure 1D). In addition, wounds treated with the highest dose of MAPCs showed delayed healing compared to those treated with the cell-free dressings ($p = 0.0009$). Due to this data all other studies used a dosage of 2×10^4 MAPCs as this was shown to be most effective at promoting wound repair.

MAPCs delivered using functionalized dressings improved healing when compared to injected MAPCs

To determine if injection of MAPCs was as effective as delivery via a functionalized dressing, wounded diabetic mice ($n = 7$) were

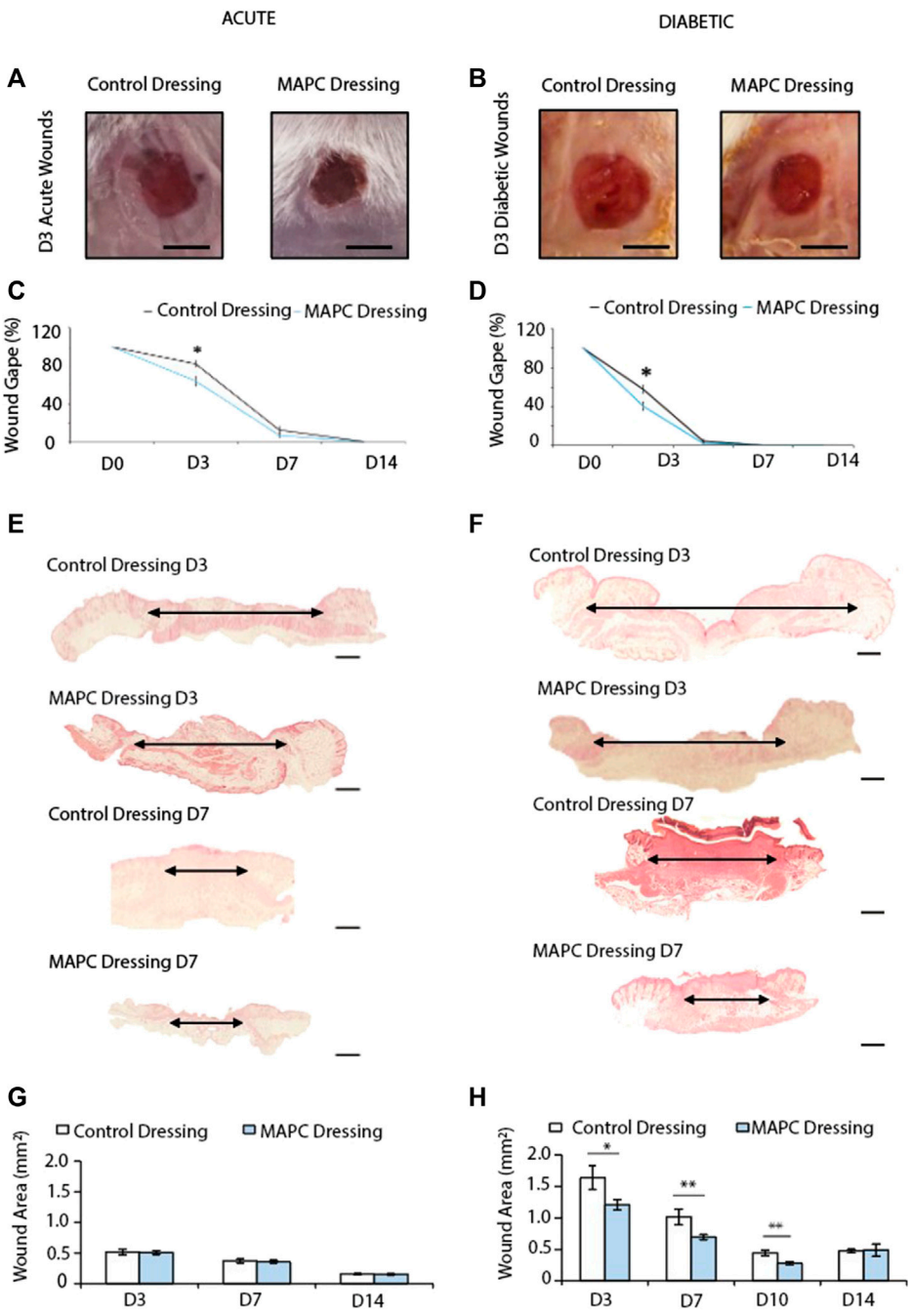

FIGURE 2
Representative images of the macroscopic appearance of the day 3 normal **(A)** and diabetic **(B)** wounds treated with MAPC dressings and control dressings (Scale bars = 2 mm) and the respective macroscopic wound gape measurements **(C,D)**. Histological H&E images of day 3 and day 7 normal **(E)** and diabetic **(F)** wounds treated with MAPC dressings or control dressings (scale bars are 20 μm) and their respective microscopic wound area measurements **(G,H)**. Markers of significance are * = $p \leq 0.05$, and ** = $p \leq 0.01$. Significance was determined using a two tailed student t test.

either treated at day 0 with 2×10^4 MAPC injected intradermally at four sites around the wound margin or a functionalized dressings seeded with 2×10^4 MAPCs. Two control groups of injected PBS or a dressing alone treatment were also included. At day 3, wounds treated with the MAPC dressings (34.9%) had smaller wounds when compared to wounds treated with MAPC injections (74.5%), PBS injections (122%) and dressing alone (83.6%), though this data was not significant. Wounds treated with the MAPC dressings (2.38%) were significantly smaller at day 7 ($p = 0.003$) when compared to wounds directly injected with equivalent numbers of MAPCs (12.76%) or the PBS (17.8%) and dressing alone (19.4%) groups (Figure 1E).

Figure 1E showed a trend to suggest that the wounds treated with injected MAPCs, or the dressing alone were healing at a faster rate than the PBS injected wounds, at day 3. This, however, was not significant when the data was compared by one-way ANOVA. It has

been reported in the literature that plasma polymerized surfaces can promote the proliferation of human keratinocytes, which may explain the perceived reduction in wound area of the wounds treated with the dressing alone, when compared to the PBS group at day 3 (Haddow et al., 2003).

Interestingly, the wounds treated with the MAPC dressing had a wound gape of 34.9% and 2.4%, at day 3 and 7 respectively, whereas the MAPC injected wounds had a wound gape of 74.5% and 12.7%. These observed differences may be because the dressing administration delivered the MAPCs to the entire wound surface whereas the intradermally injected MAPCs were only delivered into the wound margins and had to migrate into the wound site. There are also reports in the literature that show up to 80% of a dose delivered via injection can be non-viable depending on the needle size and flow rate used (Amer et al., 2015). This may also account for the reduction in efficacy seen with the injected MAPCs. As a comparatively low dose of MAPCs was administered to each wound (2×10^4 cells per wound) any loss via injection could significantly impact the effect of the MAPC treatment. In addition to this, it would result in differing doses being delivered to the wound site when comparing the intradermal injection and the dressing delivery system. As such the intradermal injection was not considered a reliable control and only the dressing alone control was used for the remainder of the study.

Delivery of MAPCs improves macroscopic healing in both normal and diabetic wounds

In both normal and diabetic mice, the delivery of MAPCs by the functionalized dressings significantly accelerated macroscopic wound closure at 3 days post-wounding (Figures 2A–D). At day 3, excisional wounds in normal mice treated with MAPC dressings had reduced by 26.9% (Figure 2C). This was significantly smaller ($p = 0.021$) than the 17.9% reduction observed in the control wounds (Figure 2C). This improvement was also seen in diabetic mice treated with the MAPC dressing with wound gape being significantly reduced by 59.8% compared to wounds treated with control dressings which were reduced by 36.3% ($p = 0.001$) (Figure 2D). There were no significant differences seen at day 7 in either the normal or diabetic wounds.

MAPC dressings decrease wound area in diabetic but not normal wounds

When wound area in normal mice was assessed microscopically, no differences were observed at any of the time points between wounds treated with MAPC dressings or control dressings (Figures 2E, G). Diabetic wounds have impaired healing, and the wounds were significantly larger than those in normal healthy mice. When treated with MAPC dressings, a decrease in wound area was observed, in the diabetic mice, of 26% at day 3 (0.43 mm, $p = 0.04$), 31.5% reduction at day 7 (0.32 mm, $p = 0.02$) and 35.9% at day 10 (0.15 mm, $p = 0.002$) when compared to control dressings (Figures 2F, H).

Reduced neutrophil influx in normal and diabetic wounds treated with MAPC dressings

Neutrophils are among the first immune cells to immigrate into the wound site and whilst there were no significant differences observed in the day 3 excisional wounds in normal mice there was a significant reduction ($p = 0.002$) in neutrophilic persistence in the MAPC dressing treated wounds when compared to control wounds at day 7 (Figures 3A, C). In contrast, a significant reduction in neutrophilic influx at day 3 ($p = 0.0008$) was observed in MAPC dressing treated diabetic wounds and persistence at day 7 ($p = 0.006$) was again observed compared to control dressings (Figures 3B, D).

MAPC dressings modulate macrophage influx into normal and diabetic wounds

Excessive macrophage recruitment to the wound site is often linked with a delayed wound healing phenotype (Kirby et al., 2015). In the normal mice wounds, treatment with MAPC dressings significantly reduced the numbers of macrophages at both day 3 ($p = 0.0005$) and day 7 ($p = 0.001$) when compared to control wounds (Figures 3E, G). This reduction in macrophages was also seen at day 3 in the diabetic wounds ($p = 0.003$) but was not maintained at day 7 (Figures 3F, H).

Treatment with MAPC dressings increases blood vessel formation in normal and diabetic wounds

Angiogenesis is key to successful wound healing as without blood vessels the wound tissue and the cells within that tissue are starved of oxygen. This results in hypoxia and delays wound healing (Velazquez, 2007). Two markers of angiogenesis are VEGF and the endothelial cell marker CD31. Treatment of the excisional wounds in normal mice with MAPC dressings showed increased VEGF expression at day 3 ($p = 0.005$) and day 7 ($p = 0.05$) when compared to wounds treated with control dressings (Figures 4A, C). No significant difference was observed in VEGF expression in day 3 diabetic wounds, but increased levels of VEGF expression was observed in the wounds treated with the MAPC dressings at day 7 ($p = 0.036$) when compared to control wounds (Figures 4B, D). In the acute wounds there were significantly more CD31 positive cells in the MAPC treated wounds ($p = 0.02$) when compared to the control wounds (Figures 4E, G), which also reflected the similar expression levels of VEGF in these wounds. There were no significant differences in CD31 expression observed in the acute wound at day 7. In the diabetic wounds there was only a significant difference in CD31 positive cell numbers at day 7 ($p = 0.03$), with more CD31 cells in the MAPC treated wounds (Figures 4F, H). This also reflects the VEGF data which also showed significantly more expression in the MAPC diabetic wounds at day 7.

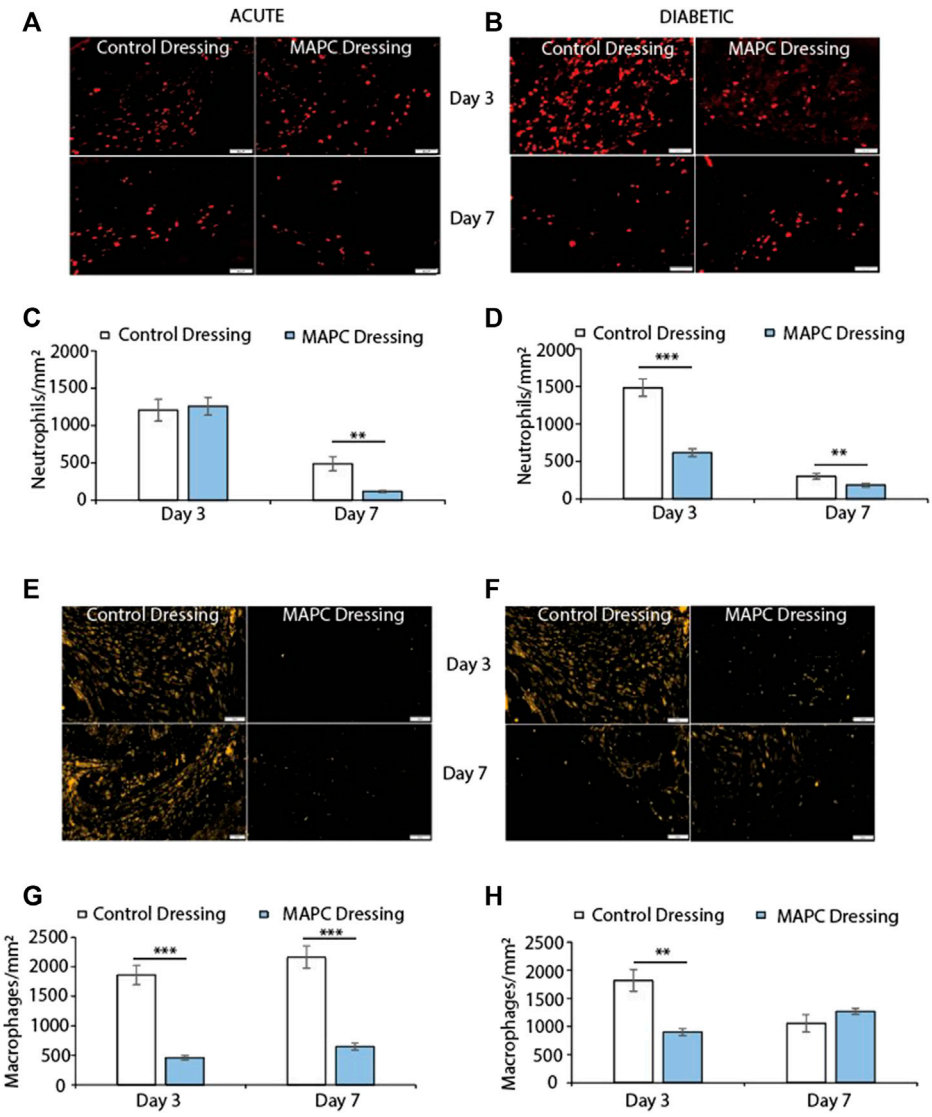

FIGURE 3
Representative images showing NIMP-R14 positive neutrophils at day 3 and day 7 in normal **(A)** and diabetic **(B)** wounds treated with MAPCs dressings or control dressings and their respective positive cell staining counts per mm^2 **(C,D)**. Representative images of the immunohistochemical staining of MRP-14 positive macrophages in day 3 and day 7 normal **(E)** and diabetic wounds **(F)** and their cell counts per mm^2 **(G,H)**. Markers of significance are ** = $p \leq 0.01$ and *** = $p \leq 0.001$ and scale bars are 50 μm. Significance was determined using a two tailed student t test.

MAPC dressings had no effect on collagen deposition in normal and diabetic wounds

Collagen deposition is another key element of the wound healing process. Collagen is initially deposited in the form of collagen III, which is then replaced by collagen I (Kirby et al., 2015). In this study collagen I and III expression were investigated in both normal and diabetic wounds at day 3 and day 7 treated with the MAPC dressings. No significant differences were observed at any of the time points assessed (Figures 5A–H). The ratio of collagen I to collagen III were also considered as this is a marker of wound remodelling but again no significant differences were observed (Figure 5I).

Discussion

In this study we have assessed the effectiveness of delivering MAPCs using a functionalized heptylamine surface on a silicone backing, using plasma polymerization. By manufacturing these MAPC dressings and applying them topically to normal and diabetic murine wounds, we have shown that we can positively influence healing and increase the rate of wound closure. This was achieved with only one application of the cells at the time of wounding, via the dressing, which remained in place for 72 h. In both the normal and diabetic wounds, treatment with the MAPC dressing increased the rate of wound closure. Previous studies have investigated the effects of MAPCs encased in alginate and discovered that when applied *in vitro*

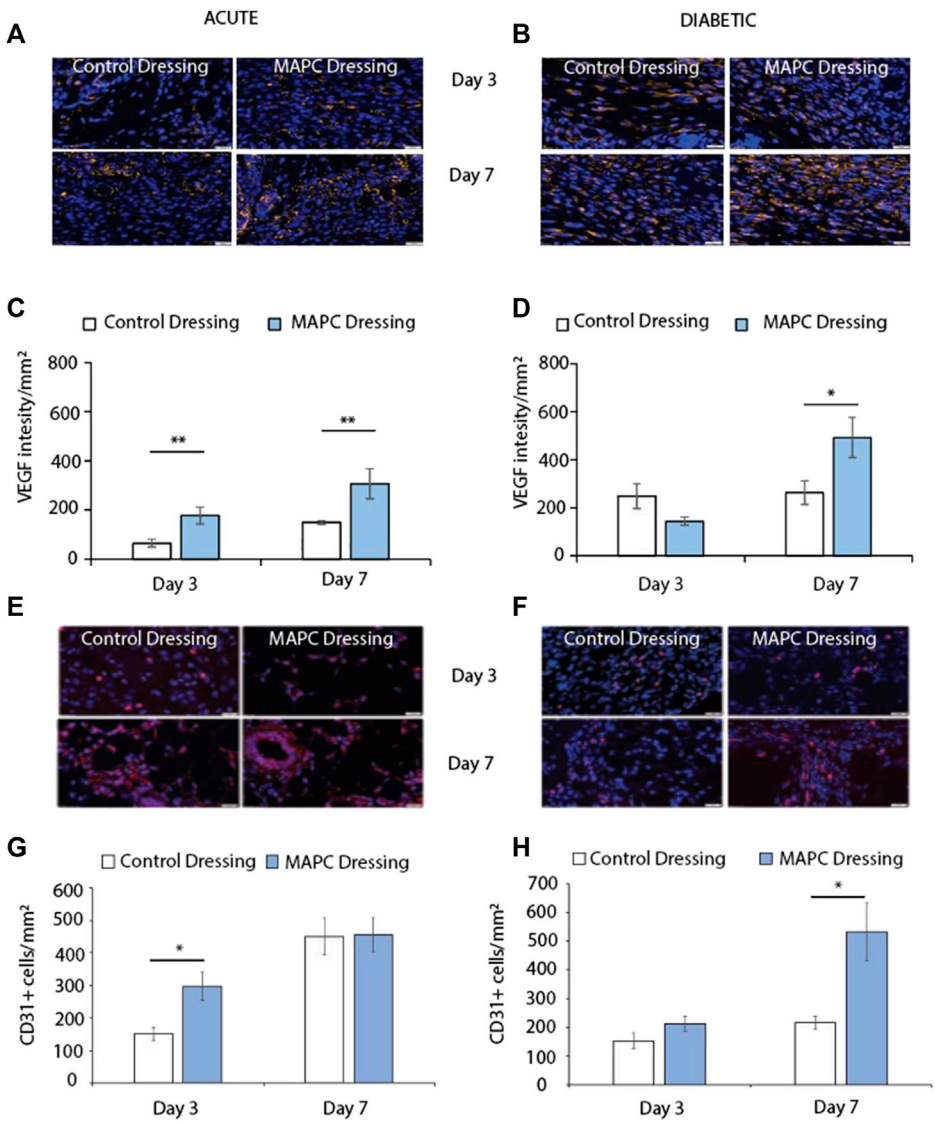

FIGURE 4
Representative images of VEGF staining in normal **(A)** and diabetic **(B)** wounds at day 3 and day 7 treated with MAPCs dressings or control dressings. Graphical representation of the intensity per $mm^2$of the control and treated wounds **(C,D)**. Representative images of the immunohistochemical staining of CD31 positive cells in day 3 and day 7 normal **(E)** and diabetic wounds **(F)** and their cell counts per mm^2 **(G,H)**. Markers of significance are * = $p \leq 0.05$ and ** = $p \leq 0.01$ and scale bars are 50 μm. Significance was determined using a two tailed student t test.

to scratch wounded corneal stromal cells, there was a significant increase in the rate of wound closure (Al-Jaibaji et al., 2018). In another study, a mixture of rodent MAPCs, epidermal stem cells and fibroblasts were injected intravenously and subcutaneously around excisional wounds of nude mice leading to accelerated wound healing rates (Ji et al., 2009). Interestingly, this study also showed that the MAPCs were able to incorporate themselves into the hair follicle bulge in the epidermis, which is a known location of stem cell populations, and were then able to contribute to wound healing in the surrounding skin (Ji et al., 2009). MAPCs have also been shown to improve the vasculature in an ischaemic limb injury model in mice where intramuscular injections of murine MAPCs showed improved muscle regeneration, increased blood flow and improved function of the effected limb. This was compared to treatments with murine MAPC vascular derived progenitors and murine bone marrow cells, which were not as effective (Aranguren et al., 2008). Vaes et al. have shown that MAPCs not only improve the invasion of vessels into a Matrigel plug injected subcutaneously in mice but that when MAPCs were injected intraperitoneally into wounded mice improvements in the vascularization and healing of the wounds was observed (Vaes et al., 2020). MAPCs can improve the vasculature around injected islet cells increasing the number of engrafted islet cells and improving the rate of diabetes reversal in mice (Cunha et al., 2017). In our study the data also showed that there was an improvement in blood vessel formation at day 3 and 7 in the model of normal healing and at day 7 in the diabetic impaired healing model determined by VEGF and CD31 staining. More recently, treatment of excisional wounds with MAPC secretome has been shown to increase the rate of healing by dampening the

10.3389/fbioe.2023.1213021

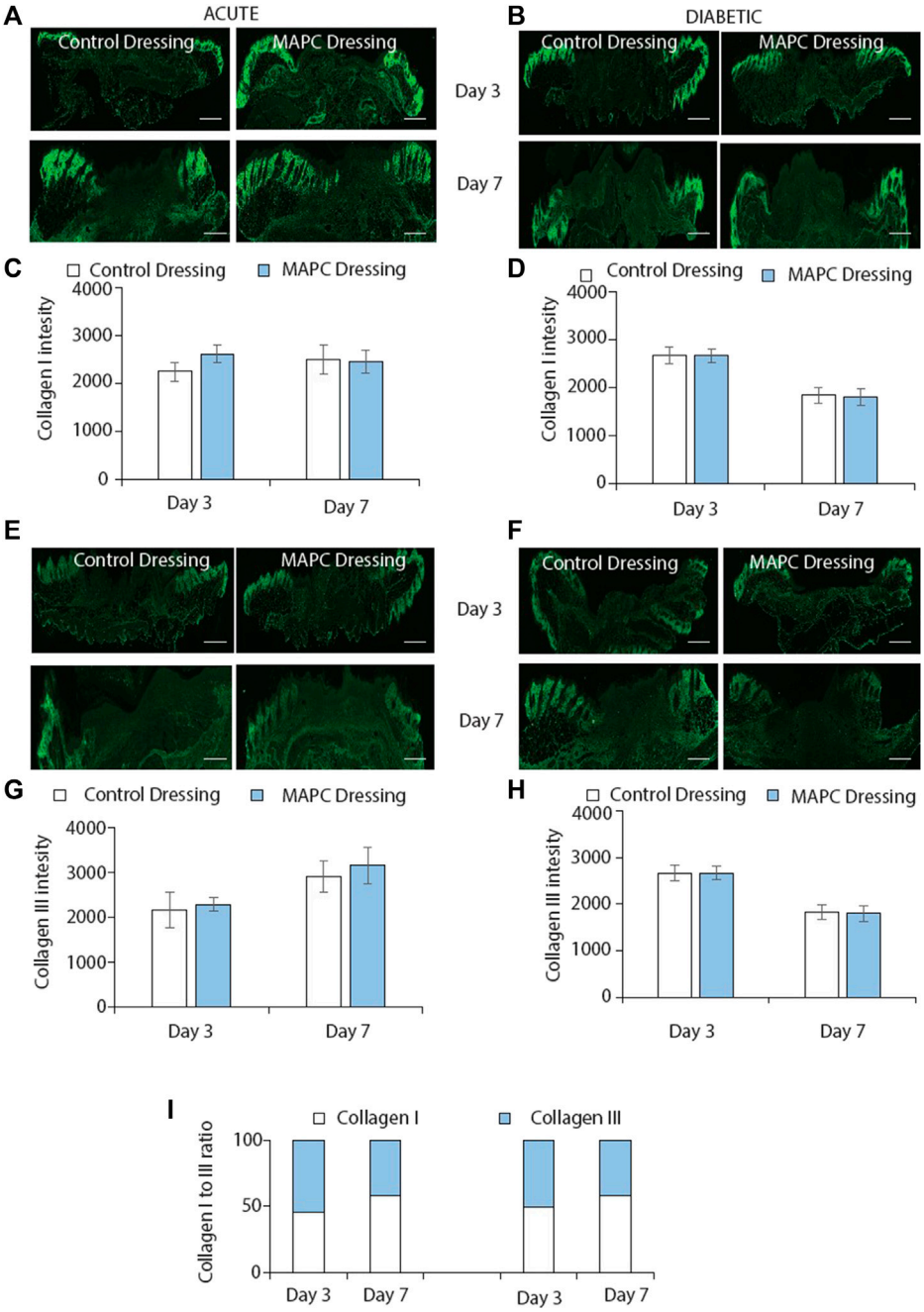

FIGURE 5
Immunofluorescent staining of collagen I in normal **(A)** and diabetic **(B)** wounds at day 3 and day 7 treated with MAPC dressings and control dressings and the graphical representation of the intensity measurements of those wounds **(C,D)**. Collagen III staining of normal **(E)** and diabetic **(F)** wounds at day 3 and day 7 when treated with the MAPC dressings and control dressings and their intensity measurements **(G,H)**. Ratio of collagen I and collagen III staining in normal and diabetic wounds at day 3 and day 7 for MAPC dressing and control dressing treated wounds **(I)**. Scale bars = 500 μm. Significance was determined using a two tailed student t test. *de*.

immune response and increasing angiogenesis (Ahangar et al., 2020b).

MAPCs have a dampening effect on the host immune system, which helps prevent rejection of the MAPCs and autoimmunity (Reading et al., 2015). They achieve this phenomenon by the suppression of T-cell proliferation in conjunction with prostaglandin E2 (PGE2) production. These characteristics make MAPCs prime candidates for allogenic products. In addition to the effects of MAPCs on the regrowth of the vasculature, described by us and others, we have now shown that MAPCs also influence the inflammatory response *in vivo*. Previous studies looking into the effects of MAPCs on the immune response have been *in vitro* and focused on the effect on T-cells to assess their potential as an allogenic product (Burrows et al., 2013; Reading et al., 2013; Reading et al., 2015). These studies show that MAPCs can inhibit the IL-7 dependent T-cell

expansion to prevent autoimmunity and graft rejection. Interestingly, within these studies MAPCs were also shown to inhibit the expression of TNF and IFNγ. Whilst this was only confirmed *in vitro* it does provide an explanation for the effect of MAPCs on neutrophil and macrophage infiltration observed in this *in vivo* study. TNF and IFNγ are two cytokines that are known to increase the recruitment of both neutrophils and macrophages into the wounds site (Zhang, 2007; Ashcroft et al., 2012). With this study we also observed an inhibition of the inflammatory process with a reduction of neutrophil and macrophage numbers seen in the MAPC dressing treated wounds. Prostaglandin E2 (PGE2), which is upregulated by MAPC treatment, has also shown to have some links to the resolution of the inflammatory response (Walker et al., 2012), which further supports the reduction in the inflammatory response seen in this study. Finally, the data showed that there was little effect on collagen deposition within the wound. As accelerated healing is often associated increased scarring, treatment with the MAPC dressings was shown to not only accelerate the rate of healing but that this improvement was not achieved with a poorer cosmetic outcome.

In summary, we have shown that treatment of wounds with the MAPC dressings can accelerate healing in both normal and diabetic mice when compared to cell-free dressings. The MAPC dressings also significantly accelerated healing when compared to MAPC injections into the wound margins. This suggested that delivery of the MAPCs, via the dressing, to the entire wound surface rather than relying on the cells to migrate into the wound site can result in an overall improved rate of healing. The mechanisms by which MAPCs increase the rate of healing was achieved through a dampening of the immune response and an increase in angiogenesis. Overall, this allogenic dressing has the potential to improve the healing of chronic diabetic wounds in patients to help alleviate their suffering and the financial costs to the health services worldwide.

Data availability statement

The datasets presented in this article are not readily available because there are IP restrictions in place for this product and as such the data can not be made available at this time. Requests to access the datasets should be directed to stuart.mills@unisa.edu.au.

Ethics statement

The animal study was reviewed and approved by the Women's and Children's Health Network Animal Ethics Committee.

Author contributions

SM was responsible for writing the manuscript and designing the figures. GK and LS were responsible for manufacturing the dressings and seeding the MAPCs onto the dressings. SM, BH, and PS were responsible for carrying out the *in vivo* work and the analysis of the data from the *in vivo* studies. BV and AT were supervisory and responsible for the supply of the MAPCs. BV, AT, RS, LS, and AC were supervisory and responsible for securing the funding and study design. All authors contributed to the article and approved the submitted version.

Funding

This research was supported by the Cell Therapy Manufacturing Cooperative Research Centre (CTM CRC) through the Australian Government's Cooperative Research Centre Program.

Acknowledgments

We thank our colleagues from Future Industries Institutes, University of South Australia. The authors also acknowledge the facilities and scientific and technical assistance of Microscopy Australia at the University of South Australia, a facility that is funded by the University of South Australia and the State and Federal Governments.

Conflict of interest

AT was employed by the company Athersys Inc.

The remaining authors declare that the research was conducted in the absence of any commercial or financial relationships that could be construed as a potential conflict of interest.

Publisher's note

References

Ahangar, P., Mills, S. J., and Cowin, A. J. (2020a). Mesenchymal stem cell secretome as an emerging cell-free alternative for improving wound repair. *Int. J. Mol. Sci.* 21 (19), 7038. doi:10.3390/ijms21197038

Ahangar, P., Mills, S. J., Smith, L. E., Strudwick, X. L., Ting, A. E., Vaes, B., et al. (2020b). Human multipotent adult progenitor cell-conditioned medium improves wound healing through modulating inflammation and angiogenesis in mice. *Stem Cell Res. Ther.* 11 (1), 299. doi:10.1186/s13287-020-01819-z

Al-Jaibaji, O., Swioklo, S., Gijbels, K., Vaes, B., Figueiredo, F. C., and Connon, C. J. (2018). Alginate encapsulated multipotent adult progenitor cells promote corneal stromal cell activation via release of soluble factors. *PLoS One* 13 (9), e0202118. doi:10.1371/journal.pone.0202118

Amer, M. H., White, L. J., and Shakesheff, K. M. (2015). The effect of injection using narrow-bore needles on mammalian cells: administration and formulation considerations for cell therapies. *J. Pharm. Pharmacol.* 67 (5), 640–650. doi:10.1111/jphp.12362

Aranguren, X. L., McCue, J. D., Hendrickx, B., Zhu, X. H., Du, F., Chen, E., et al. (2008). Multipotent adult progenitor cells sustain function of ischemic limbs in mice. *J. Clin. Invest.* 118 (2), 505–514. doi:10.1172/jci31153

Ashcroft, G. S., Jeong, M. J., Ashworth, J. J., Hardman, M., Jin, W., Moutsopoulos, N., et al. (2012). Tumor necrosis factor-alpha (TNF-alpha) is a therapeutic target for impaired cutaneous wound healing. *Wound Repair Regen.* 20 (1), 38–49. doi:10.1111/j.1524-475x.2011.00748.x

Ashcroft, G. S., and Mills, S. J. (2002). Androgen receptor-mediated inhibition of cutaneous wound healing. *J. Clin. Invest.* 110 (5), 615–624. doi:10.1172/jci0215704

Ashcroft, G. S., Mills, S. J., Lei, K., Gibbons, L., Jeong, M. J., Taniguchi, M., et al. (2003). Estrogen modulates cutaneous wound healing by downregulating macrophage migration inhibitory factor. *J. Clin. Invest.* 111 (9), 1309–1318. doi:10.1172/jci16288

Australia, D. (2021). Diabetes globally. Available at: https://www.diabetesaustralia.com.au/about-diabetes/diabetes-globally/.

Badiavas, E. V., and Falanga, V. (2003). Treatment of chronic wounds with bone marrow-derived cells. *Arch. Dermatol* 139 (4), 510–516. doi:10.1001/archderm.139.4.510

Basiouny, H. S., Salama, N. M., Maadawi, Z. M., and Farag, E. A. (2013). Effect of bone marrow derived mesenchymal stem cells on healing of induced full-thickness skin wounds in albino rat. *Int. J. Stem Cells* 6 (1), 12–25. doi:10.15283/ijsc.2013.6.1.12

Boozer, S., Lehman, N., Lakshmipathy, U., Love, B., Raber, A., Maitra, A., et al. (2009). Global characterization and genomic stability of human MultiStem, A multipotent adult progenitor cell. *J. Stem Cells* 4 (1), 17–28. jsc.2009.4.1.17.

Burrows, G. G., Van't Hof, W., Newell, L. F., Reddy, A., Wilmarth, P. A., David, L. L., et al. (2013). Dissection of the human multipotent adult progenitor cell secretome by proteomic analysis. *Stem Cells Transl. Med.* 2 (10), 745–757. doi:10.5966/sctm.2013-0031

Carty, F., Dunbar, H., Hawthorne, I. J., Ting, A. E., Stubblefield, S. R., Van't Hof, W., et al. (2021). IFN-Γ and PPARδ influence the efficacy and retention of multipotent adult progenitor cells in graft vs host disease. *Stem Cells Transl. Med.* 10 (11), 1561–1574. doi:10.1002/sctm.21-0008

Cunha, J. P., Leuckx, G., Sterkendries, P., Korf, H., Bomfim-Ferreira, G., Overbergh, L., et al. (2017). Human multipotent adult progenitor cells enhance islet function and revascularisation when co-transplanted as a composite pellet in a mouse model of diabetes. *Diabetologia* 60 (1), 134–142. doi:10.1007/s00125-016-4120-3

Dash, N. R., Dash, S. N., Routray, P., Mohapatra, S., and Mohapatra, P. C. (2009). Targeting nonhealing ulcers of lower extremity in human through autologous bone marrow-derived mesenchymal stem cells. *Rejuvenation Res.* 12 (5), 359–366. doi:10.1089/rej.2009.0872

Falanga, V., Iwamoto, S., Chartier, M., Yufit, T., Butmarc, J., Kouttab, N., et al. (2007). Autologous bone marrow-derived cultured mesenchymal stem cells delivered in a fibrin spray accelerate healing in murine and human cutaneous wounds. *Tissue Eng.* 13 (6), 1299–1312. doi:10.1089/ten.2006.0278

Gao, D., Gu, C., Wu, Y., Xie, J., Yao, B., Li, J., et al. (2014). Mesenchymal stromal cells enhance wound healing by ameliorating impaired metabolism in diabetic mice. *Cytotherapy* 16 (11), 1467–1475. doi:10.1016/j.jcyt.2014.05.014

Haddow, D. B., Steele, D. A., Short, R. D., Dawson, R. A., and Macneil, S. (2003). Plasma-polymerized surfaces for culture of human keratinocytes and transfer of cells to an *in vitro* wound-bed model. *J. Biomed. Mater Res. A* 64 (1), 80–87. doi:10.1002/jbm.a.10356

Highfill, S. L., Kelly, R. M., O'Shaughnessy, M. J., Zhou, Q., Xia, L., Panoskaltsis-Mortari, A., et al. (2009). Multipotent adult progenitor cells can suppress graft-versus-host disease via prostaglandin E2 synthesis and only if localized to sites of allopriming. *Blood* 114 (3), 693–701. doi:10.1182/blood-2009-03-213850

Huang, S., Wu, Y., Gao, D., and Fu, X. (2015). Paracrine action of mesenchymal stromal cells delivered by microspheres contributes to cutaneous wound healing and prevents scar formation in mice. *Cytotherapy* 17 (7), 922–931. doi:10.1016/j.jcyt.2015.03.690

Huang, X. P., Sun, Z., Miyagi, Y., McDonald Kinkaid, H., Zhang, L., Weisel, R. D., et al. (2010). Differentiation of allogeneic mesenchymal stem cells induces immunogenicity and limits their long-term benefits for myocardial repair. *Circulation* 122 (23), 2419–2429. doi:10.1161/circulationaha.110.955971

Ichioka, S., Kouraba, S., Sekiya, N., Ohura, N., and Nakatsuka, T. (2005). Bone marrow-impregnated collagen matrix for wound healing: experimental evaluation in a microcirculatory model of angiogenesis, and clinical experience. *Br. J. Plast. Surg.* 58 (8), 1124–1130. doi:10.1016/j.bjps.2005.04.054

Jacobs, S. A., Pinxteren, J., Roobrouck, V. D., Luyckx, A., van't Hof, W., Deans, R., et al. (2013). Human multipotent adult progenitor cells are nonimmunogenic and exert potent immunomodulatory effects on alloreactive T-cell responses. *Cell Transpl.* 22 (10), 1915–1928. doi:10.3727/096368912x657369

Ji, K. H., Xiong, J., Fan, L. X., Hu, K. M., and Liu, H. Q. (2009). Rat marrow-derived multipotent adult progenitor cells differentiate into skin epidermal cells *in vivo*. *J. Dermatol* 36 (7), 403–409. doi:10.1111/j.1346-8138.2009.00666.x

Jiang, Y., Jahagirdar, B. N., Reinhardt, R. L., Schwartz, R. E., Keene, C. D., Ortiz-Gonzalez, X. R., et al. (2002). Pluripotency of mesenchymal stem cells derived from adult marrow. *Nature* 418 (6893), 41–49. doi:10.1038/nature00870

Johannesson, A., Larsson, G. U., Ramstrand, N., Turkiewicz, A., Wirehn, A. B., and Atroshi, I. (2009). Incidence of lower-limb amputation in the diabetic and nondiabetic general population: a 10-year population-based cohort study of initial unilateral and contralateral amputations and reamputations. *Diabetes Care* 32 (2), 275–280. doi:10.2337/dc08-1639

Khan, R. S., and Newsome, P. N. (2019). A comparison of phenotypic and functional properties of mesenchymal stromal cells and multipotent adult progenitor cells. *Front. Immunol.* 10, 1952. doi:10.3389/fimmu.2019.01952

Kirby, G. T., Mills, S. J., Cowin, A. J., and Smith, L. E. (2015). Stem cells for cutaneous wound healing. *Biomed. Res. Int.* 2015, 1–11. doi:10.1155/2015/285869

Kirby, G. T., Mills, S. J., Vandenpoel, L., Pinxteren, J., Ting, A., Short, R. D., et al. (2017). Development of advanced dressings for the delivery of progenitor cells. *ACS Appl. Mater Interfaces* 9 (4), 3445–3454. doi:10.1021/acsami.6b14725

Laing, R. W., Stubblefield, S., Wallace, L., Roobrouck, V. D., Bhogal, R. H., Schlegel, A., et al. (2020). The delivery of multipotent adult progenitor cells to extended criteria human donor livers using normothermic machine perfusion. *Front. Immunol.* 11, 1226. doi:10.3389/fimmu.2020.01226

Le Blanc, K., Tammik, C., Rosendahl, K., Zetterberg, E., and Ringden, O. (2003). HLA expression and immunologic properties of differentiated and undifferentiated mesenchymal stem cells. *Exp. Hematol.* 31 (10), 890–896. doi:10.1016/s0301-472x(03)00110-3

Mansilla, E., Marin, G. H., Sturla, F., Drago, H. E., Gil, M. A., Salas, E., et al. (2005). Human mesenchymal stem cells are tolerized by mice and improve skin and spinal cord injuries. *Transpl. Proc.* 37 (1), 292–294. doi:10.1016/j.transproceed.2005.01.070

Mills, S. J., Cowin, A. J., and Kaur, P. (2013). Pericytes, mesenchymal stem cells and the wound healing process. *Cells* 2 (3), 621–634. doi:10.3390/cells2030621

Moll, G., Ankrum, J. A., Kamhieh-Milz, J., Bieback, K., Ringden, O., Volk, H. D., et al. (2019). Intravascular mesenchymal stromal/stem cell Therapy product diversification: time for new clinical guidelines. *Trends Mol. Med.* 25 (2), 149–163. doi:10.1016/j.molmed.2018.12.006

Moll, G., Ankrum, J. A., Olson, S. D., and Nolta, J. A. (2022). Improved MSC minimal criteria to maximize patient safety: a call to embrace tissue factor and hemocompatibility assessment of MSC products. *Stem Cells Transl. Med.* 11 (1), 2–13. doi:10.1093/stcltm/szab005

Organisation, W. H. (2021). Diabetes. Available at: https://www.who.int/news-room/fact-sheets/detail/diabetes.

Pelacho, B., Nakamura, Y., Zhang, J., Ross, J., Heremans, Y., Nelson-Holte, M., et al. (2007). Multipotent adult progenitor cell transplantation increases vascularity and improves left ventricular function after myocardial infarction. *J. Tissue Eng. Regen. Med.* 1 (1), 51–59. doi:10.1002/term.7

Reading, J. L., Vaes, B., Hull, C., Sabbah, S., Hayday, T., Wang, N. S., et al. (2015). Suppression of IL-7-dependent effector T-cell expansion by multipotent adult progenitor cells and PGE2. *Mol. Ther.* 23 (11), 1783–1793. doi:10.1038/mt.2015.131

Reading, J. L., Yang, J. H., Sabbah, S., Skowera, A., Knight, R. R., Pinxteren, J., et al. (2013). Clinical-grade multipotent adult progenitor cells durably control pathogenic T cell responses in human models of transplantation and autoimmunity. *J. Immunol.* 190 (9), 4542–4552. doi:10.4049/jimmunol.1202710

Reiber, G. E., Smith, D. G., Carter, J., Fotieo, G., Deery, H. G., 2nd, Sangeorzan, J. A., et al. (2001). A comparison of diabetic foot ulcer patients managed in VHA and non-VHA settings. *J. Rehabil. Res. Dev.* 38 (3), 309–317.

Roobrouck, V. D., Clavel, C., Jacobs, S. A., Ulloa-Montoya, F., Crippa, S., Sohni, A., et al. (2011). Differentiation potential of human postnatal mesenchymal stem cells, mesoangioblasts, and multipotent adult progenitor cells reflected in their transcriptome and partially influenced by the culture conditions. *Stem Cells* 29 (5), 871–882. doi:10.1002/stem.633

Soeder, Y., Loss, M., Johnson, C. L., Hutchinson, J. A., Haarer, J., Ahrens, N., et al. (2015). First-in-Human case study: multipotent adult progenitor cells for immunomodulation after liver transplantation. *Stem Cells Transl. Med.* 4 (8), 899–904. doi:10.5966/sctm.2015-0002

Stoff, A., Rivera, A. A., Sanjib Banerjee, N., Moore, S. T., Michael Numnum, T., Espinosa-de-Los-Monteros, A., et al. (2009). Promotion of incisional wound repair by human mesenchymal stem cell transplantation. *Exp. Dermatol* 18 (4), 362–369. doi:10.1111/j.1600-0625.2008.00792.x

Thomas, H. M., Ahangar, P., Fitridge, R., Kirby, G. T. S., Mills, S. J., and Cowin, A. J. (2021). Plasma-polymerized pericyte patches improve healing of murine wounds through increased angiogenesis and reduced inflammation. *Regen. Biomater.* 8 (4), rbab024. doi:10.1093/rb/rbab024

Tolar, J., O'Shaughnessy, M. J., Panoskaltsis-Mortari, A., McElmurry, R. T., Bell, S., Riddle, M., et al. (2006). Host factors that impact the biodistribution and persistence of multipotent adult progenitor cells. *Blood* 107 (10), 4182–4188. doi:10.1182/blood-2005-08-3289

Vaes, B., Van Houtven, E., Caluwe, E., and Luttun, A. (2020). Multipotent adult progenitor cells grown under xenobiotic-free conditions support vascularization during wound healing. *Stem Cell Res. Ther.* 11 (1), 389. doi:10.1186/s13287-020-01912-3

Velazquez, O. C. (2007). Angiogenesis and vasculogenesis: inducing the growth of new blood vessels and wound healing by stimulation of bone marrow-derived progenitor cell mobilization and homing. *J. Vasc. Surg.* 45, A39–A47. doi:10.1016/j.jvs.2007.02.068

Viswanathan, S., Shi, Y., Galipeau, J., Krampera, M., Leblanc, K., Martin, I., et al. (2019). Mesenchymal stem versus stromal cells: international society for cell & gene Therapy (ISCT®) mesenchymal stromal cell committee position statement on nomenclature. *Cytotherapy* 21 (10), 1019–1024. doi:10.1016/j.jcyt.2019.08.002

Walker, N. G., Mistry, A. R., Smith, L. E., Eves, P. C., Tsaknakis, G., Forster, S., et al. (2012). A chemically defined carrier for the delivery of human mesenchymal stem/stromal cells to skin wounds. *Tissue Eng. Part C Methods* 18 (2), 143–155. doi:10.1089/ten.tec.2011.0037

Zhang, J. (2007). Yin and yang interplay of IFN-gamma in inflammation and autoimmune disease. *J. Clin. Invest.* 117 (4), 871–873. doi:10.1172/jci31860

frontiers | Frontiers in Bioengineering and Biotechnology

TYPE Original Research
PUBLISHED 08 February 2024
DOI 10.3389/fbioe.2024.1334087

OPEN ACCESS

EDITED BY
Hasan Uludag,
University of Alberta, Canada

REVIEWED BY
Gwang-Bum Im,
Harvard Medical School, United States
Yan Pang,
Shanghai Jiao Tong University, China

*CORRESPONDENCE
Haitao Wang,
haitaowang_wh@126.com
Guodong Song,
sgd_zxyy@126.com

†These authors have contributed equally to this work

RECEIVED 06 November 2023
ACCEPTED 25 January 2024
PUBLISHED 08 February 2024

CITATION
Chen N, Li M, Yang J, Wang P, Song G and Wang H (2024), Slow-sculpting graphene oxide/alginate gel loaded with platelet-rich plasma to promote wound healing in rats. *Front. Bioeng. Biotechnol.* 12:1334087. doi: 10.3389/fbioe.2024.1334087

Slow-sculpting graphene oxide/alginate gel loaded with platelet-rich plasma to promote wound healing in rats

Ningjie Chen[1,2†], Mengjie Li[3†], Jincun Yang[2], Peng Wang[4], Guodong Song[1,5*] and Haitao Wang[2*]

[1]Shandong University, Jinan, Shandong, China, [2]Department of Burns and Plastic Surgery, Weihai Municipal Hospital, Weihai, China, [3]Binzhou Medical University, Binzhou, Shandong, China, [4]Ministry of Scientific and Technological Innovation, Yantai Hi-tech Industrial Development Zone, Yantai, Shandong, China, [5]Department of Burns and Orthopedic Surgery, Jinan Central Hospital, Jinan, Shandong, China

Wounds, especially chronic wounds, have become an important problem that endangers human health. At present, there are many repair methods, and among them combines materials science and biology is one of the important repair methods. This study explored the preparation method, physicochemical properties, biological activity and safety of Platelet-Rich plasma (PRP)-loaded slow-sculpting graphene oxide (GO)/alginate gel, and applied it to acute full-thickness skin defect wounds in rats to observe its role in wound healing. The results show that the slow-sculpting GO/alginate gel has excellent plasticity and is suitable for a variety of irregularly shaped wounds. At the same time, its porous structure and water content can maintain the activity of platelets and their released growth factors in PRP, thereby promoting wound collagen synthesis and angiogenesis to accelerate wound healing. This indicates that the slow-sculpting GO/alginate gel is an excellent loading material for PRP, and the combination of the two may become one of the methods to promote wound repair.

KEYWORDS

slow-sculpting gel, platelet-rich plasma, wound healing, graphene oxide, alginate gel

Introduction

With the intensification of the aging society and the increase of obese people, the incidence of refractory wounds such as burn/trauma, diabetic ulcers, vascular ulcers and stress injuries has increased year by year and has become a global problem that endangers human health (Collaborators et al., 2017; Dai et al., 2020; Sen, 2021). As a result, the repair and remodeling of wounds has attracted widespread attention in areas such as tissue engineering and clinical medicine (Buechler et al., 2021; Chen et al., 2021; Mascharak et al., 2021). However, wound healing is a dynamic and orderly biological process, and disturbance or interruption of any one stage will cause it to delay or not heal (Gurtner et al., 2008; Reinke and Sorg, 2012; Eming et al., 2021; Konieczny and Naik, 2021). Studies have found that a variety of functional dressings and biological therapies can promote wound healing, but the polymorphism of wounds affects the application of regular shape dressings, and the therapeutic effect of monotherapy is not satisfactory (Frykberg and Banks, 2015; Martinez-Zapata et al., 2016; Tang et al., 2022). Therefore, there is great

potential for combining functional plastic biomaterials with biotherapies to rationally and effectively restore orderly wound healing processes.

Platelet-Rich plasma (PRP) as a biological therapy is rich of growth factors that can be easily produced from blood samples by centrifugation or platelet apheresis, which has been used for increasing frequency for the treatment of acute/chronic wounds (Gentile et al., 2020; Laschke and Menger, 2022). After PRP activation, the α particles in platelets release a variety of growth factors (such as PDGF, VEGF, TGF-β, EGF and FGF, *etc.*), which have the effect of promoting vascular regeneration, collagen synthesis, and involved in a specific biomolecular activity, which in turn plays an important role in acute and chronic wound healing, inflammation and pain treatment (Martinez-Zapata et al., 2016; Harrison et al., 2018; Gentile et al., 2020; Laschke and Menger, 2022). In addition, the formation of fibrin scaffolds after PRP activation can support growth factors in wound sustained release, so its biological effect is also closely related to the density of fibrin (Harrison et al., 2018; Anitua et al., 2019). However, the PRP gel scaffold is similar to the blood clot, showing a loose and porous network structure, its plasticity and adhesion are not enough to meet the needs of the wound surface, especially the chronic refractory wound surface with variable shape and different depths (Hsu et al., 2019; Irmak et al., 2020; Catanzano et al., 2021; Oneto and Etulain, 2021; Zhou et al., 2022). Therefore, through the principle of tissue engineering, loading PRP with functional materials to improve its biological activity is one of the important directions of current exploration (Qiu et al., 2016).

In recent years, sodium alginate, which has been widely used, is an anionic natural polysaccharide extracted from the cell wall and interstitium of algae, because of its gelatinity, biocompatibility and biodegradability and other advantages (Wang et al., 2018; Sanchez-Fernandez et al., 2021). In the field of biomedicine, because it has good water solubility and rich functional groups, it has excellent characteristics of structural improvement and construction of composite materials. In sodium alginate, sodium ions are exchanged with polyvalent metal cations, crosslinked to form hydrogels with good permeability, which has a significant effect on maintaining the activity of cells, enzymes, sensitive drugs, proteins and other substances (Sanchez-Fernandez et al., 2021). So, it is widely studied in the fields of tissue repair materials, biochemical drug-controlled release carriers, cell immune isolation and other tissue engineering (Kumar et al., 2019; Zhu et al., 2020; Liu et al., 2021; Rami et al., 2021; Shiny et al., 2021; Wang et al., 2021; Zhang et al., 2021). Although alginate (Alg) is currently widely used in clinical practice, and one of the most effective dressings, but there are still many deficiencies in clinical application. The shortcomings of the rapid gel process, poor mechanical strength, no biological activity, no antibacterial activity, poor stability, limited adsorption capacity and poor water resistance limit its promotion to a certain extent. Therefore, researchers try to use the composite covalent crosslinking method to modify it to solve this problem, but chemical crosslinking agents may affect its biosecurity, so physical crosslinking or ion crosslinking to improve its performance is safer and more effective, of which carbon materials are more ideal choices.

Carbon materials include graphene, graphene oxide (GO), reduced graphene oxide, carbon nanotubes, *etc.*, of which GO, as a new type of material, can combine its high specific surface area, great thermal stability, special physicochemical properties, good electronic conductivity and amazing mechanical force and other advantages, and play synergistic role with other materials (Liu et al., 2011; Xie et al., 2018). In recent years, GO-based nanocomposites have received more and more attention in many different fields, and various functional combination strategies can effectively improve the performance of GO, and give materials some properties such as sustained release, stability, photocatalytic properties, *etc.* (Wang et al., 2018; Wu et al., 2019; Joshi et al., 2020; Shen et al., 2020; Wang et al., 2020; Olmos and Gonzalez-Benito, 2021). GO surface contains a variety of oxygen-containing functional groups, with richer surface activity, good hydrophilic and biocompatible, which not only play its hydrogel good biocompatibility and moisturizing effect to promote wound healing, but also has antibacterial effect (Wu et al., 2019; Olmos and Gonzalez-Benito, 2021). Therefore, GO is widely used in antibacterial bioassays, cancer treatment, drugs and gene delivery.

In recent years, a number of studies have investigated the utilization of GO- and Alg-conjugated compounds. These compounds exhibit considerably enhanced biomechanical characteristics in comparison to Alg alone, and have been documented to possess exceptional antibacterial efficacy, as well as the ability to promote cell proliferation and facilitate drug delivery (Ciriza et al., 2015; Chen et al., 2016; Wang et al., 2019). According to the literature reviewed above, in the current study, we prepares a slow sculpting GO/Alg gel support PRP for wound repair. It is expected to provide a new idea for the preparation of wound healing materials and the promotion of PRP.

Materials and methods

Preparation of GO/Sodium alginate solution

The GO powder (Shenzhen Guosen Linghang Technology Co., Ltd., China) was dispersed in sterilized distilled water with a concentration of 2 mg/mL, then placed in an ultrasonic washer (Ningbo Xinzhi Biotechnology Co., Ltd., China) in room temperature for uniform dispersion for 2 h to obtain GO dispersion solution. Appropriate amount of sodium alginate powder (Shanghai Aladdin Biochemical Technology Co., Ltd., China) was added into the GO dispersion (3%wt), stirred well and placed at room temperature for later use.

PRP preparation

For PRP preparation, male SD rats with a body weight of 260–280 g were used, after successful anesthesia with a 10% chloral hydrate (Shanghai Macklin Biochemical Co., Ltd., China), peripheral blood was drawn into a centrifuge tube containing 3.2% concentration of sodium citrate anticoagulant (peripheral blood: sodium citrate = 10:1), shaken well. Peripheral platelet concentrations were measured and PRP was prepared by the two-step centrifugation method. Centrifuge machine (Hunan

Xiangyi Laboratory Instrument Development Co., Ltd., China) was used, blood was first centrifugated at 2000 rpm for 15 min at room temperature. By this step, the whole blood was divided into three layers: the upper layer contained most of the platelets and plasma while most of the red blood cells were sedimented in the bottom layer, and the middle layer (buffer layer) contained white blood cells and platelets. The upper layer and surface part of the middle layer were transferred to another sterile centrifuge tube, the transfer process should be gentle to avoid mixing with too many red blood cells. Then perform a second centrifugation at 3,000 rpm for 10 min, after the second spin, upper 2/3 was called poor platelet plasma (PPP), which contained a small number of platelets, and the lower 1/3 was PRP. 2/3 of the PPP was discarded, gently shaken the centrifuge tube to obtain final PRP. This method of PRP preparation obtained a platelet concentration of approximately 6times compared with the baseline concentration.

Go/Alg gel loaded with PRP

The GO/Alg solution and PRP were mixed evenly with the ratio of 1:2, Added an appropriate amount of calcium carbonate powder (Shanghai Aladdin Biochemical Technology Co., Ltd., China) into the solution to insure the mass concentration of calcium carbonate was 4%, after stirring well, added glucono-delta-lactone (GDL) powder (Shanghai Aladdin Biochemical Technology Co., Ltd., China) with a the molar ratio to calcium carbonate 2.65 to the solution, and after rapid stirring, let it stand for later use.

Gel lyophilization and electron microscopy observation

The GO/Alg gel with PRP was mixed and aliquoted into sterile EP tubes, after 1 h of standing at room temperature, the gel sample with a complete appearance and satisfactory strength was placed in the refrigerator at −80°C for 24 h, and then the frozen sample was placed into a vacuum freeze dryer (−88°C, 0.011 kPa, Labconco Co., US) for 24 h to obtain fluffy lyophilized samples. Sharply cut the middle part of the lyophilized sample for vacuum gold spraying, and then observe the microstructure of the gold-plated sample with SEM.

Plasticity, adhesion and mechanical testing

The gel prepared by the above method was put into a 5 mL sterile bottle at room temperature, and gel formation status was observed by inverting the test tub: tilted the tube 10° every 30 s to observe the fluidity of the gel, gel was judged complete formed when no flow was observed for 10 s, and the gelation time was recorded, repeated the process for three times to take the average value (Nair et al., 2007). Different porcine tissues (skin, fat, muscle and bone) were selected to simulate their adhesion to human tissues.

The adhesive properties of the hydrogels were determined using a lap shear test at 25°C. Briefly, the specimens underwent testing using an INSTRON 5565 tensile testing apparatus (manufactured by Instron, Nor-wood, MA, United States) with a velocity of 10 mm/min until two sections of skin tissue were detached. The adhesive strength was calculated based on the maximum modulus of the adhesive area. Uniaxial tensile tests were conducted on GO/Alg, PRP, and GO/Alg/PRP scaffolds to evaluate their mechanical properties according to previous study (do Amaral et al., 2019).

Porosity testing

The porosity was measured by the drainage method. 50 mL of absolute ethanol was added to the container, and a certain mass of sample (M1) which was already dried to the balance weight was put into the container. The container was then vacuumed circularly until no more bubbles overflow in the sample, weighed the mass of the container containing ethanol and the sample (M2). Then the sample filled with ethanol was taken out, and the remaining ethanol and volumetric bottle were weighed (M3). The porosity was calculated according to the following formula: porosity%= (M2-M3-M1)/(M2-M3) ×100%.

Water content testing

The fully gelled hydrogel sample was immersed in PBS solution, after placing in a 37°C incubator for 24 h, removed the excess water on the surface of hydrogel with filter paper and weighed, the mass was recorded as M1. Then the hydrogel was lyophilized in a low-temperature freeze-drying machine for 24 h, and the weight of the solid after lyophilization was recorded as M2. The water content of hydrogel = (M1-M2)/M1×100%.

Platelet fluorescence staining

PKH67 reagent was diluted 250 times through PBS solution and diluent provided in the kit (Beijing Solarbio Science and Technology CO., Ltd., China), and the prepared gel was stained *in situ* with the staining solution fully covered the gel. After standing at room temperature for 1 h, the staining solution was discarded. After fully rinsing the sample with PBS solution for 3 times, the labeling effect of platelet cells in the gel was observed under a fluorescence microscope.

Degradation rate

The materials with the same mass of GO/Alg, PRP and GO/Alg/PRP were respectively weighed into sterile centrifuge tubes, the weighing mass was denoted as W0 and placed at room temperature (25°C, 40–50%RH). Meanwhile, the materials with the same mass of GO/Alg/PRP were placed at (37°C, 40%–50% RH). Samples were taken out and weighed at week 1,2,3,4,5,6,7 and 8, respectively. The mass of each sample was denoted as W1, and the degradation rate of the gel was calculated according to the mass change: degradation rate% = $(W0\text{-}W_1/W_0)$ %. There were 3 samples in each group and the mean value was taken for statistical comparison.

Sustained release test of PDGF

Approximately 1 mL of the freshly prepared PRP and GO/Alg/PRP solution were placed into sterile EP tubes. PRP was activated and gelatinized by hemocoagulase and calcium chloride, GO/Alg/PRP was gelatinized by adding calcium carbonate and GDL. After fully gelatinized, appropriate amount of PBS was added to completely soak the gel. Medium was changed every day; the supernatant was collected and frozen at −80° for testing. The concentration of PDGF in the supernatant was detected by rat ELISA kit (Jiangsu Meimian industrial Co., Ltd., China).

Establishment and grouping of rat wound model

Male rats with a body weight of 260–280 g were anesthetized by intraperitoneal injection of chloral hydrate. The hair on the back of the rats was removed, and then a full-thickness skin wound with a size of 1.5 × 1.5 cm was created on the back of the rats with a scalpel. After modeling, the rats were randomly divided into 4 groups: control group, GO/Alg group (wounds were applied with GO/Alg gel without other active ingredients), PRP group (wounds were applied with homologous rat PRP) and GO/Alg/PRP group (wounds were applied with GO/Alg/PRP gel). Near-infrared irradiation was performed once a day, with 5min each time. On the 0, 3, 5, 10, and 14 days, the wound was photographed with a single-lens reflex camera, and the area of the wound was estimated using ImageJ (NIH Image, Rockville, MD, United States).

All animals were kept in a pathogen-free environment and fed *ad lib*. The procedures for care and use of animals were approved by the Ethics Committee of the Shandong University and Weihai Municipal Hospital (2021075), and all applicable institutional and governmental regulations concerning the ethical use of animals were followed.

Histopathology and immunohistochemistry

On the 14th day of the experiment, the rats were euthanized, and the wound tissues were excised for hematoxylin-eosin (HE), Masson's staining and CD31 immunohistochemical staining. At the same time, the heart, liver, lung and kidney were excised for further HE staining. The tissue specimens were immediately fixed with 4% paraformaldehyde (Shanghai Macklin Biochemical Co., Ltd., China) for 48 h after removal. And then dehydration, embedding and sectioning (Hua Yong, China; Leica, RM2265) were applied for follow-up inspection. The two pathologists quantitatively analyzed collagen and vascular content using ImageJ.

Statistical analysis

SPSS22.0 software was used for data analysis, and data were expressed as mean ± standard deviation (SD). *t*-test and one-way analysis of variance (ANOVA) were used to determine statistical differences.

Results

Preparation and electron microscopy structure of GO/Alg/PRP

The preparation process of GO/Alg/PRP was shown in Figure 1A. Grossly, the general form of GO/Alg/PRP is denser than GO/Alg. Cuts the spray gold, and scans the electron microscopy to observe the microstructure. Under electron microscopy, GO/Alg and GO/Alg/PRP gels have a three-dimensional network structure, and the pore distribution is uniform and the size is relatively consistent, about 100–200 μm, indicating that GO is well dispersed, which helps GO with rich functional groups on the surface to form hydrogen bonds with hydrogels (Figure 1B); The cross-section of the pore wall is protruding, indicating that the connection with the adjacent structure is good, and there is no separation phenomenon (Figure 1B). After PRP is added, it is evenly distributed in the pores of the material, and the fibrin is cross-linked with the pore wall to form a stable three-dimensional structure (Figure 1C), and this more stable three-dimensional structure is more conducive to exerting the biological activity of PRP.

Plasticity and adhesion of GO/Alg/PRP

Figure 2 shows the slow plasticity and injectability of GO/Alg/PRP sols. The test tube inversion method determines the glue forming time, Go/Alg/PRP sol remains in the sol state at room temperature at 1–4 min, and the viscosity gradually increases, becoming a gel for about 5 min (Figures 2A,C), which is more suitable for clinical applications than PRP immediate gels. GO/Alg/PRP gels can be smoothly extruded through a 18G syringe at room temperature, forming specific patterns (Figure 2E), demonstrating their superior injectability.

As can be seen in Figure 2B, both GO/Alg and GO/Alg/PRP can be easily and firmly adhered to different tissues (such as skin, fat and muscle) surfaces at room temperature, while PRP's tissue adhesion is easy to fall off from the above tissues. The adhesion stress results of the GO/Alg/PRP hydrogels indicated that the addition of GO/Alg improves the adhesion properties of the hydrogel (Figure 2D). The area of GO/Alg/PRP was larger than that of PRP group, indicated that the contractility was reduced (Figure 2F). Tensile modulus analysis revealed that PRP gel exhibits very little resistance to tension, while GO/Alg/PRP exhibits stronger resistance to tension compared to PRP and GO/Alg (Figure 2G).

Wet environment constructed by porosity and moisture content of GO/Alg/PRP

As can be seen in Figure 3A, the appearance of GO/Alg and GO/Alg/PRP gels is more complete, mechanical strength is better, while PRP gels are softer and looser. After lyophilization, GO/Alg and GO/Alg/PRP gels are porous and sponge-like structures, with more pores and uniform pore size, good pore integrity, better penetration between pores, and denser than PRP gels.

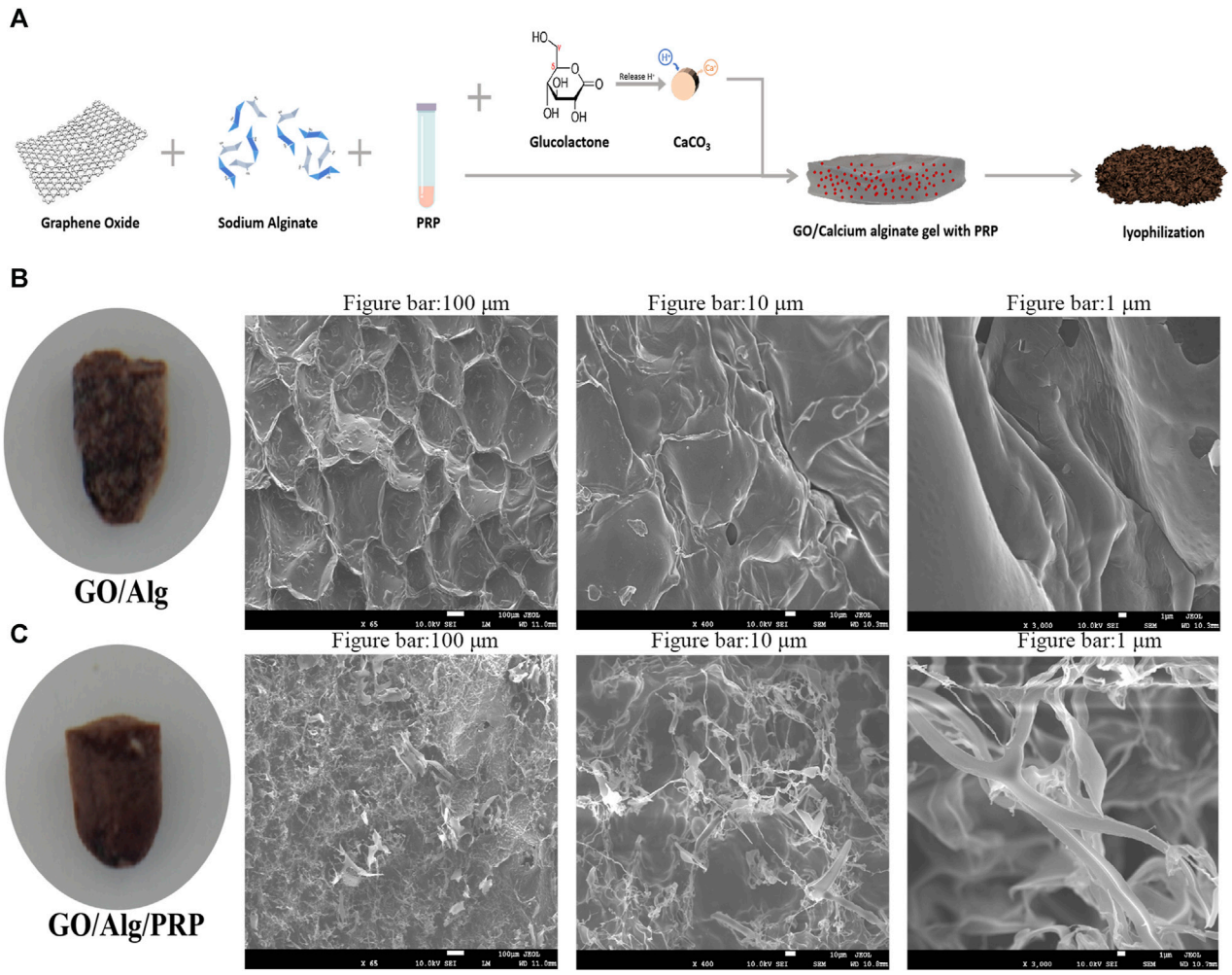

FIGURE 1
Preparation and characterization of the GO/Alg/PRP. Preparation route of the GO/Alg/PRP **(A)**. Gross appearance and SEM image of GO/Alg, GO/Alg/PRP at indicated magnification scale, and their porous structure **(B, C)**.

The use of porous materials to act on the wound surface in order to promote its healing has always been expected by researchers, and porosity is an important factor affecting the load capacity of the material (Yao et al., 2022). Figure 3D showed that the porosity of GO/Alg decreased from (66.67 ± 4.51) % to (56.67 ± 4.51) % after adding PRP. Combined with electron microscopy images, it was found that PRP could be uniformly filled in GO/Alg gel, which further confirmed its loading effect on PRP.

From Figure 3C, it can be seen that the water content of GO/Alg and GO/Alg/PRP hydrogels is significantly higher than that of PRP gels. Immunofluorescence staining of platelets in the gel showed that the platelet aggregation rate in GO/Alg/PRP gel was lower than that in PRP gel, and platelets could flow freely in GO/Alg/PRP gel, as shown in Figure 3B.

Effect of GO/Alg on platelet-derived growth factor controlled release in PRP

At the same time, *in vitro* degradation experiments also found that the degradation of GO/Alg and GO/Alg/PRP gels showed a slow trend, which simulated the wet micro-environment *in vivo* and was conducive to maintaining the activity of platelets and releasing growth factors.

The degradation of GO/Alg/PRP between room temperature (25°C, 40%–50% RH) and body temperature (37°C, 40%–50% RH) was compared, and there was no significant difference in the degradation rate between the two observation time points, but the higher the temperature, the faster the degradation rate (Figure 4A). At the same time, GO/Alg, PRP, and GO/Alg/PRP are stored at room temperature (25°C, 40%–50% RH) under laboratory light for 1–7 weeks for degradation testing. Among them, the PRP group degraded rapidly and was basically completely degraded at 3 weeks; GO/Alg and GO/Alg/PRP degraded slowly, and there was no significant difference in vitro degradation between the two, and the degradation rate remained stable, and it was completely degraded about 7 weeks (Figure 4B).

PDGF, as a representative, plays an important role in wound healing (in collagen prolif-eration, angiogenesis and other aspects), so we choose it as a representative to compare the release kinetics of growth factors between PRP gel and GO/Alg/PRP gel. The PDGF release kinetics in PRP and GO/Alg/PRP was compared using

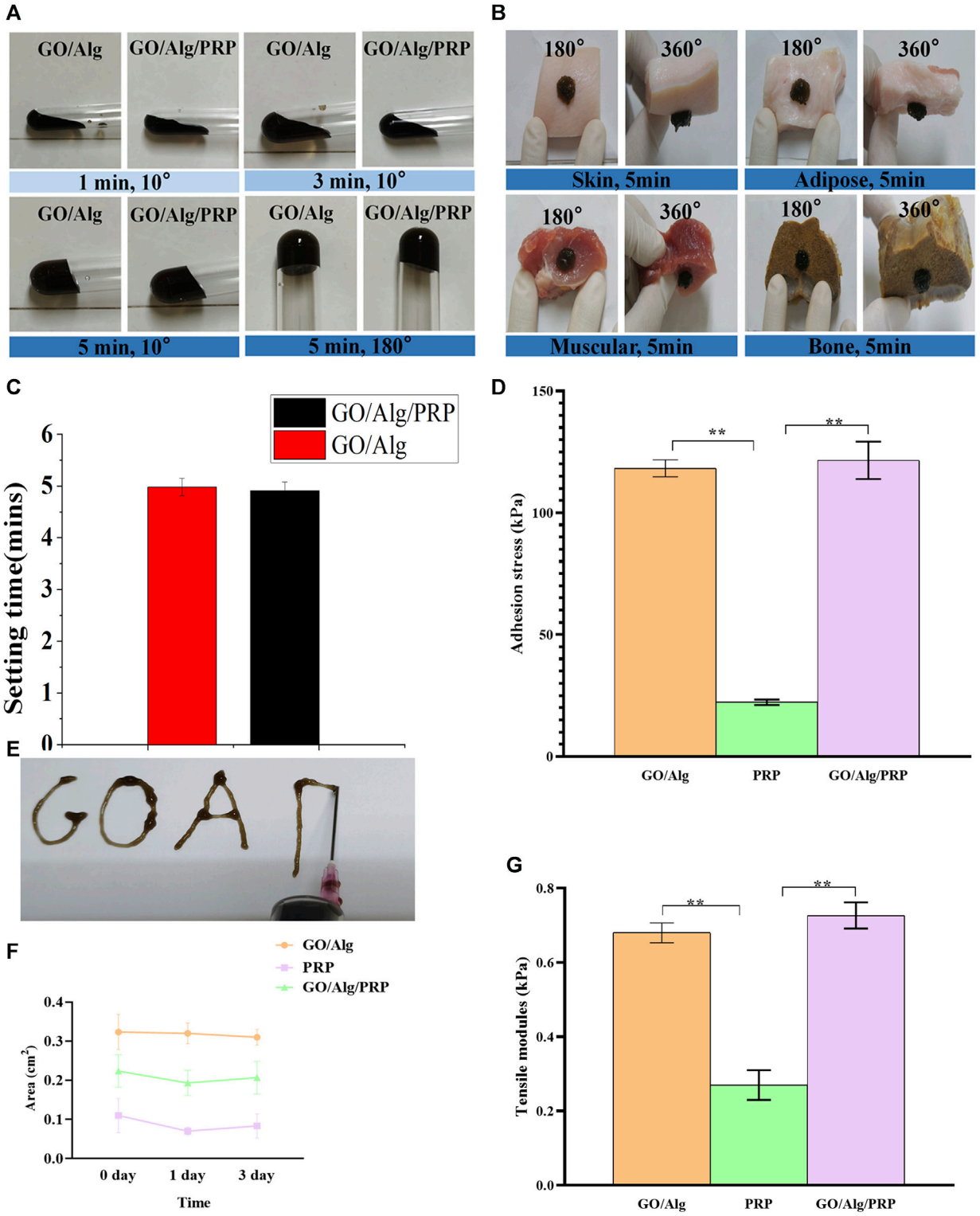

FIGURE 2
Optical photograph of sol-gel transition of GO/Alg/PRP with 10°and 180° change on room temperature **(A)**. The GO/Alg/PRP adhered onto various biological tissues including skin, adipose, muscular and bone **(B)**. The setting time of GO/Alg and GO/Alg/PRP ($p > 0.05$), as shown in **(C)**. The adhension stress of GO/Alg/PRP **(D)**. The injectability of GO/Alg/PRP through the 18G syringe **(E)**. Area **(F)** the results showed that the GO/Alg/PRP acquired a similar shape compared to GO/Alg, as presented in tensile modulus **(G)**.

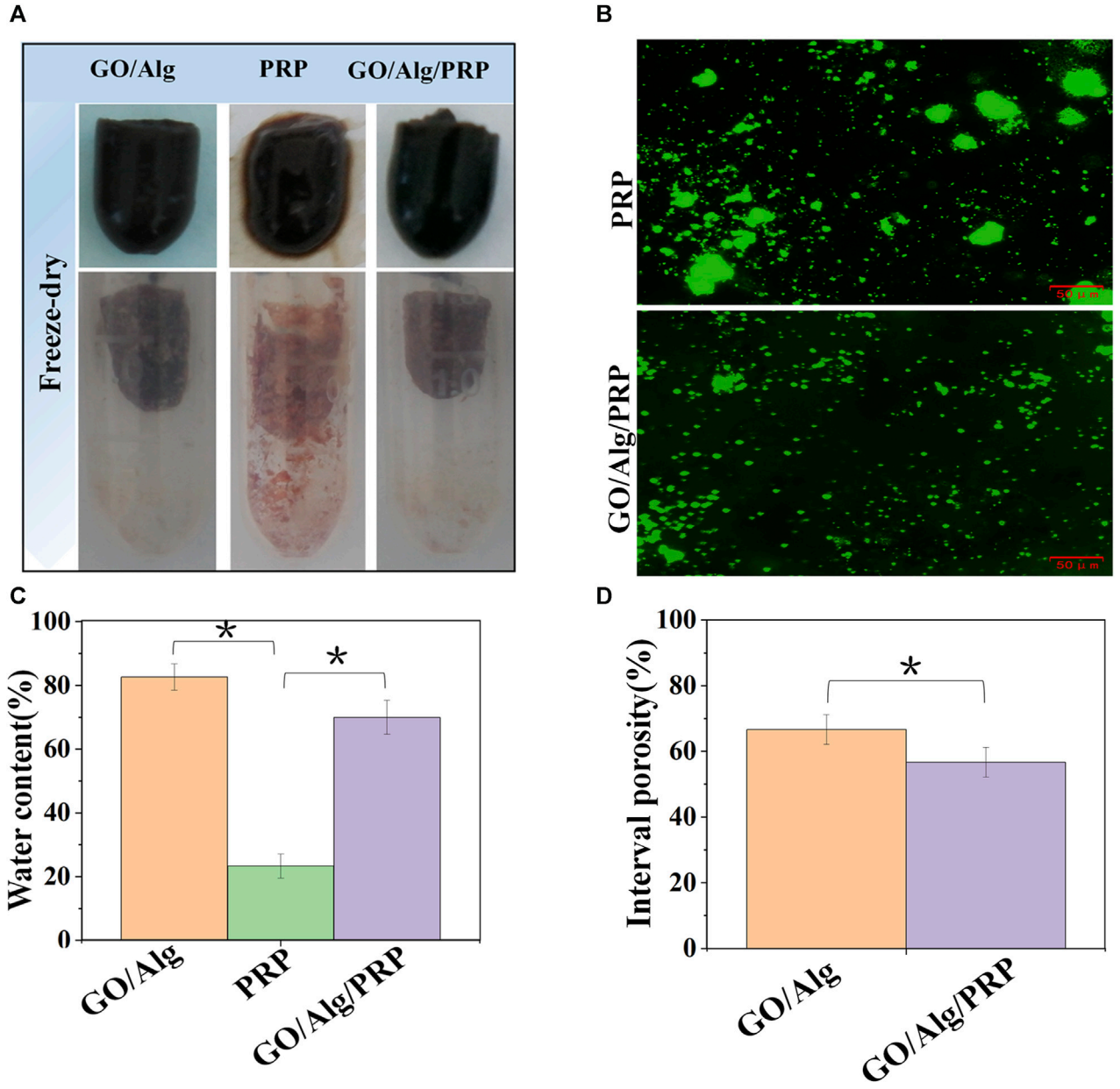

FIGURE 3
Gross appearance of GO/Alg, PRP and GO/Alg/PRP **(A)**. Immuno-fluorescence staining of platelet-rich region in PRP and GO/Alg/PRP **(B)**. Difference of water content in GO/Alg, PRP and GO/Alg/PRP, significantly more water content compared to the PRP group ($^{*}p < 0.05$), as shown in **(C)**. Interval porosity in GO/Alg and GO/Alg/PRP, and difference were observed between GO/Alg and GO/Alg/PRP ($^{*}p < 0.05$), as shown in **(D)**. Data were shown as mean ± SD.

enzyme-linked immunosorbent assay (ELISA). This study found that from day 1 to day 10, the morphology of PRP gel gradually loosened, while GO/Alg/PRP gel was intact and showed no signs of loosening except for a slight reduction in volume. According to the concentration of the standard in the ELISA kit and the absorbance measured, the standard curve was calculated. The standard concentration and the absorbance value correspond well. The standard curve equation is: Y = 0.1533 + 9.9631X. The standard curve equation has a high fitting degree with the standard curve (r = 0.991), see Figure 4C. The results showed that the release concentration of PDGF decreased gradually, and there was no statistical difference between the two on the first, ninth and 10th days. The concentration of PDGF released by GO/Alg/PRP gel was higher than that of PRP gel on the second to eighth days, and there was statistical difference between the two, as shown in Figure 4D.

Wound General View and Healing Rate

The external effects of the three gels were compared by *in vivo* wound experiment. Figure 5A shows the typical wound images of each group on days 0, 3, 5, 10 and 14. From the dynamic changes of

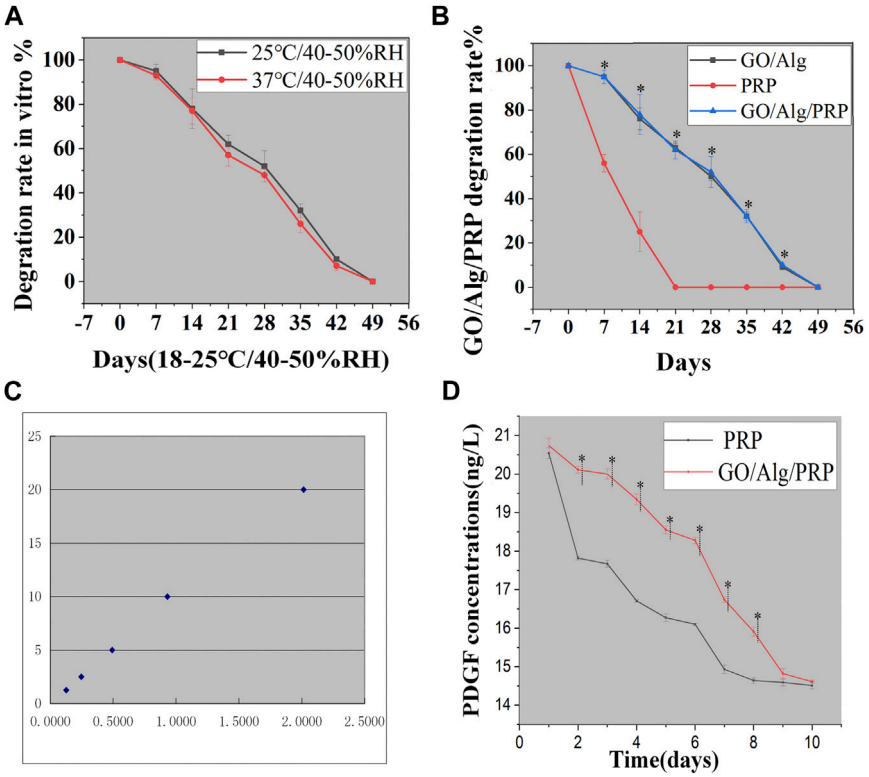

FIGURE 4
GO/Alg/PRP degradation at different temperature has no statistical difference for 7 weeks ($p > 0.05$), as shown in **(A)**. GO/Alg, PRP, and GO/Alg/PRP degradation at room temperature for 1–7 weeks ($^*p < 0.05$, compared to PRP group), as shown in **(B)**. Standard curve **(C)**. PDGF slow release from PRP and GO/Alg/PRP in PBS of 37 °C, and data were shown as mean ± SD ($^*p < 0.05$), as shown in **(D)**.

wound morphology, the wounds of all groups gradually healed with time, and the GO/Alg/PRP group showed the best healing effect. Quantitative analysis of Figure 5B showed that the wound healing rate of PRP group and GO/Alg/PRP group was better than that of control group and GO/Alg group on the third and fifth day with no significant difference in wound healing rate. On the 10th and 14th days, the GO/Alg/PRP group was superior to the other three groups, and the healing speed of GO/Alg/PRP group was faster than the PRP group and the control group.

Wound histology

On day 14 of the experiment, HE staining of wound tissue showed that the GO/Alg/PRP group showed better epithelial regeneration than the control group, GO/Alg group and PRP group (Figure 6A). Masson staining was used to observe collagen formation. Compared with the other three groups, the GO/Alg/PRP group not only increased collagen deposition, but also had dark blue-stained collagen directional arrangement in the tissue, and tissue remodeling was improved (Figures 6B,D). CD31 staining was used to observe angiogenesis. The brown part of the GO/Alg/PRP group was significantly higher than that of the other three groups, indicating that GO/Alg has a role in promoting vascular proliferation in wound repair (Figures 6C,E).

Effects of metabolic rate and vital organs

Through the pathological analysis of important histopathology of the heart, lungs, liver and kidneys, the organ toxicity of GO/Alg and the presence or absence of accumulation *in vivo* were studied. On day 14 of the experiment, the stained sections of vital organs of the heart, lungs, liver and kidneys in each group showed no pathological changes, rejection inflammation, and signs of accumulation *in vivo*, indicating good biosecurity, as shown in Figure 7.

Discussion

The results showed that the slow-sculpting GO/Alg gel has excellent plasticity and is suitable for a variety of irregularly shaped wounds. At the same time, its porous structure and water content can maintain the activity of platelets and their released growth factors in PRP, thereby promoting wound collagen synthesis and angiogenesis to accelerate wound healing.

Wound dressing materials including hydrogels, films, wafers, nanofibers, foams, topical formulations, transdermal patches, sponges and bandages were widely used in clinical. Hydrogels exhibit unique features which make them suitable wound dressings. A certain adhesion between the material and the wound can not only prevent its self-wound surf ace from falling off, but also play a role in shrinking the wound surface and

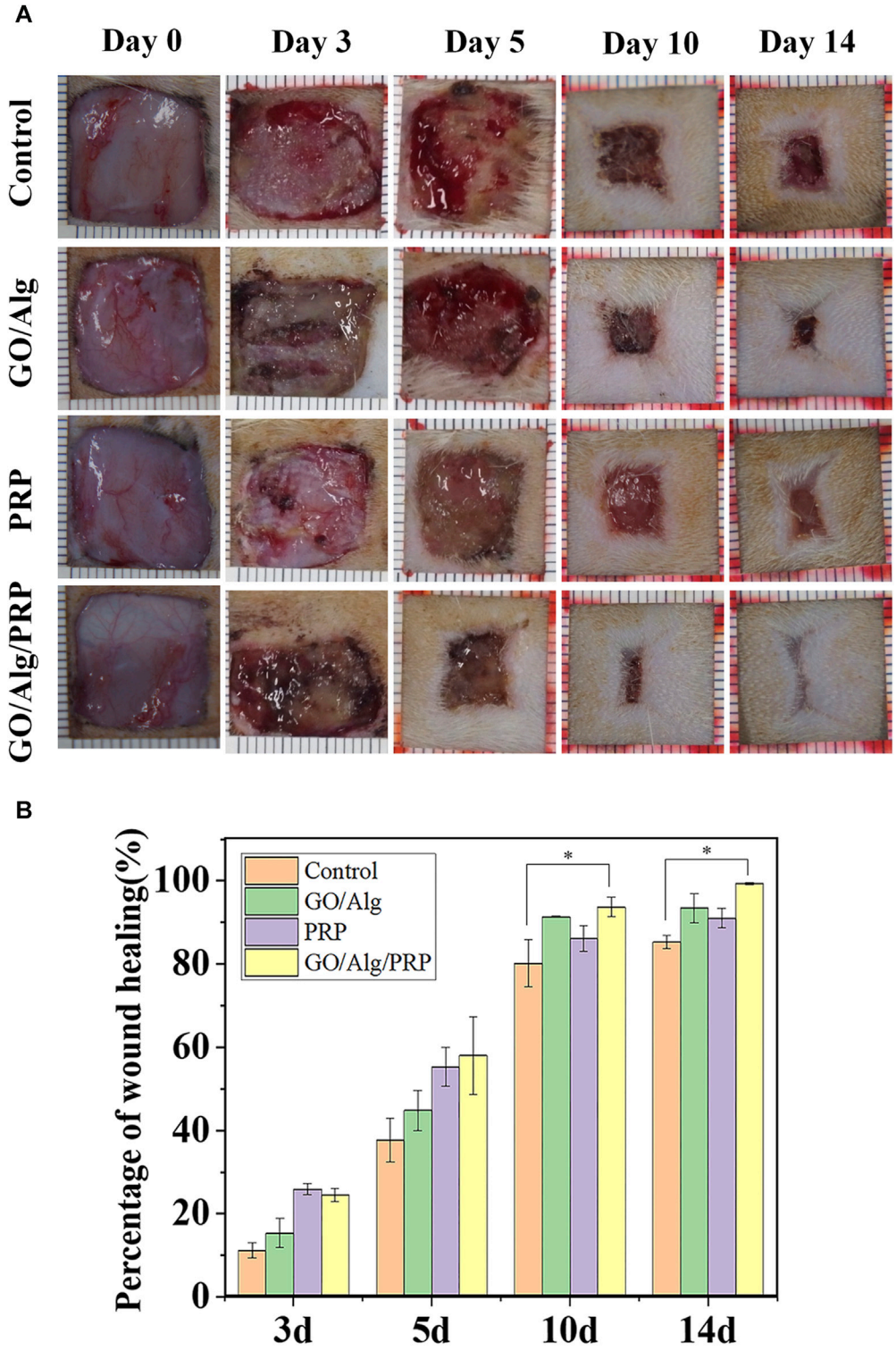

FIGURE 5
Evalution of the different groups on wound healing. Macroscopic full-thickness skin wounds images were recorded during wound healing on day 0, 3, 5, 10, and 14 **(A)**. Percentage of wound healing process **(B)**, and data were shown as mean ± SD, significantly faster wound closure was observed in GO/Alg/PRP, $^{*}p < 0.05$.

promoting wound healing, which is one of the indispensable characteristics of hydrogel as a wound dressing (Li and Wang, 2011; Hu et al., 2018; Blacklow et al., 2019). By incorporating calcium ions as crosslinking agents in sodium alginate hydrogels, their mechanical properties are significantly enhanced, especially in terms of tensile strength (Wang et al., 2022). In order to enhance the plasticity and antioxidant activity of the GO/Alg gel, and then improve the biological activity and mechanical strength of PRP

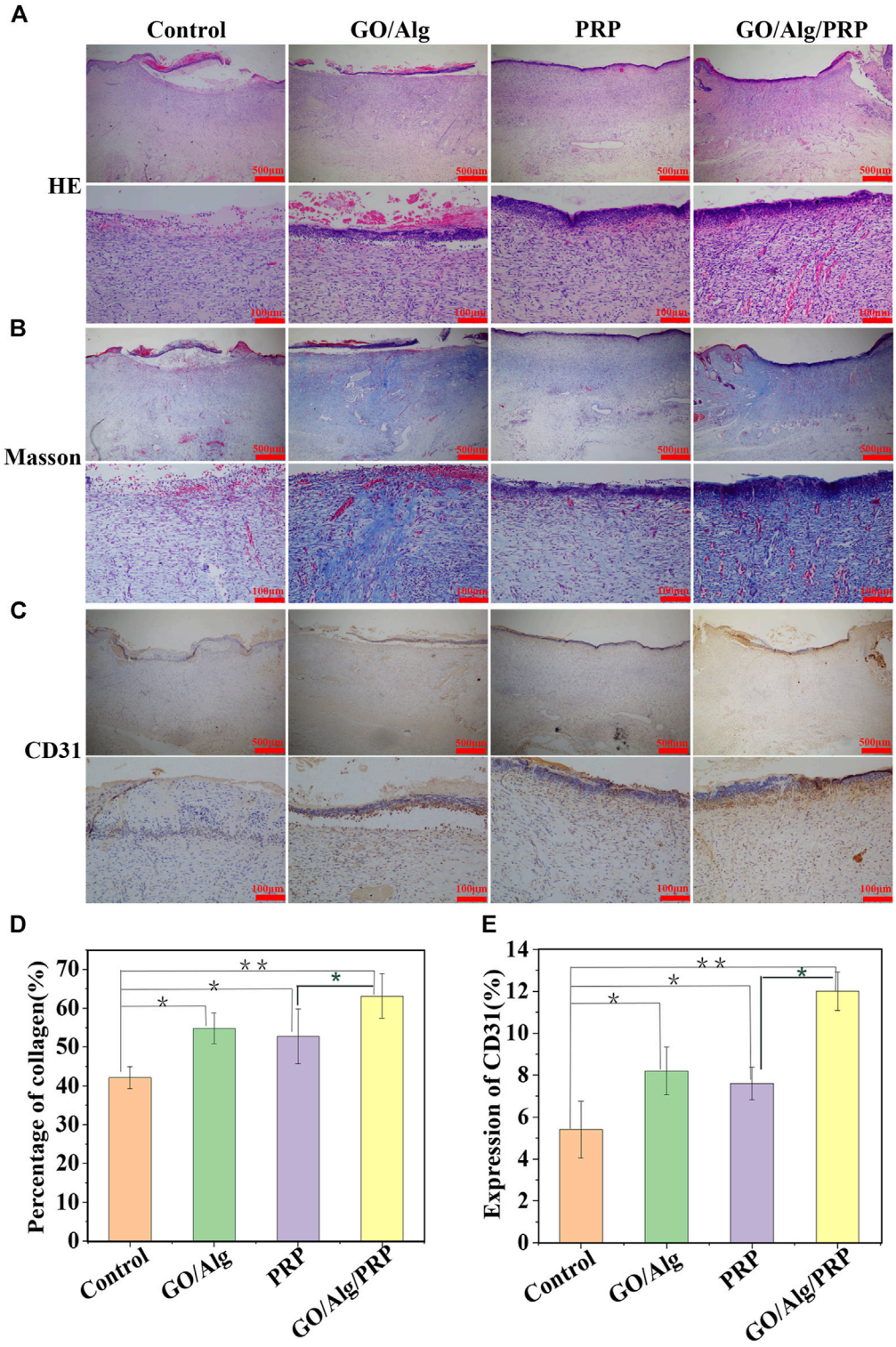

FIGURE 6
Histological appearance and analysis of the control, GO/Alg, PRP and GO/Alg/PRP group on day 14. Transmitted light images of HE-stained **(A)**, Masson's trichrome-stained **(B)** and CD31 immunohistochemical-stained **(C)**. Significantly faster collagen synthesis **(D)** and CD31 **(E)** were observed in GO/Alg/PRP group, bars represent mean ± SD, Signifificances are presented by $^{*}p < 0.05$, $^{**}p < 0.001$.

gel, we use gluconolactone to decompose calcium carbonate and slowly release calcium ions to produce a homogeneous calcium source, and prepares a slow sculpting gel support PRP for wound repair. Consistent with the previous studies, our results showed that the slow-sculpting GO/Alg gel has perfect porosity to act on the wound surface meanwhile the water content can create a moderate wet environment for wound healing. The excellent plasticity is suitable for a variety of irregularly shaped wounds.

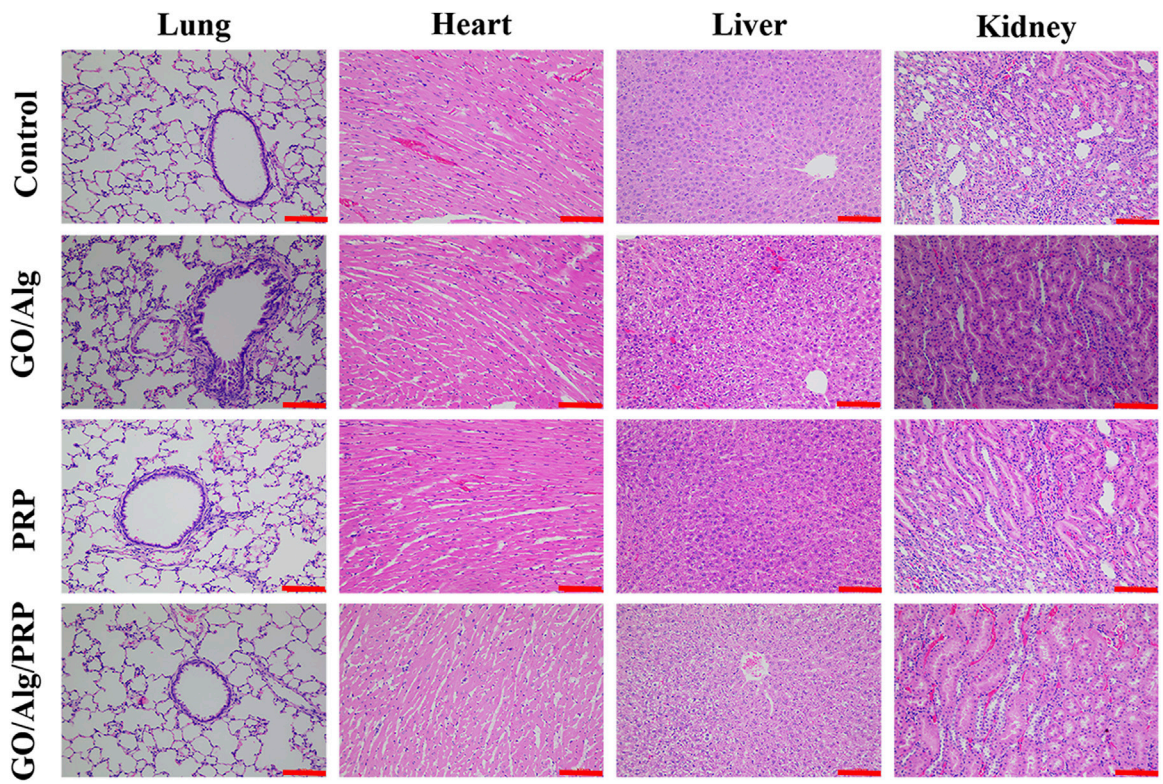

FIGURE 7
Potential organs (including lung, heart, liver and kidney) toxicity of GO/Alg/PRP with HE-stained on day 14. Scale bars are 100 μm.

The growth behavior of active substances on tissue engineering materials directly affects their tissue repair and reconstruction. Therefore, the ideal tissue engineering material must not only have a microenvironment suitable for the active substance, but also have the needs for the active substance to secrete its own extracellular matrix, nutrient infiltration, and metabolite discharge. Studies have shown that primary cells can grow albumin-secreting on three-dimensional structures for more than 6 weeks, and this function is missing during monolayer culture. Therefore, porous scaffold materials with three-dimensional microstructures play an important role in tissue engineering. Platelets in PRP are rapidly activated *in vitro* to release a variety of growth factors such as PDGF, TGF, FGF, VEGF and so on. PDGF, as a representative, plays an important role in wound healing (in collagen proliferation, angiogenesis and other aspects), so we choose it as a representative to compare the release kinetics of growth factors between PRP gel and GO/Alg/PRP gel (Hong et al., 2019; Kim et al., 2020; Laschke and Menger, 2022). Consistent with the previous studies, our study revealed that the concentration of PDGF released by GO/Alg/PRP gel was higher.

As we all know, wound healing is divided into: hemostasis, inflammation, proliferation and remodeling period, and the main risk factors affecting the delay or interruption of its healing can be roughly divided into: local factors (such as infection, hypoxia, re-injury and tissue necrosis, *etc.*), systemic diseases (such as diabetes, malnutrition and immunodeficiency, *etc.*) and pharmaceutical factors (such as the use of steroid drugs) (Martinez-Zapata et al., 2016; Zahn et al., 2017; Anitua et al., 2019; Spater et al., 2020; Laschke and Menger, 2022). In the current study, the external effects of the gels were compared by *in vivo* wound experiment. Based on the previous studies, we established a rat model of full-thickness skin defect on the back and explored the role of each group in wound healing. The wound closure rate was recorded at fixed time points from day 1–14. Wound General View and Healing Rate, HE staining and Masson results of wound tissue showed that the GO/Alg/PRP group showed better epithelial regeneration.

Both cell proliferation and migration are fundamental processes in the context of angiogenesis. Platelet endothelial cell adhesion molecule, commonly referred to as CD31, is a glycoprotein with a molecular weight of 130–140 kD. It belongs to the immunoglobulin (Ig) superfamily. The interactions between endothelial cells mediated by CD31 play a crucial role in angiogenesis. This biological process typically initiates with the proliferation of endothelial cells, which is subsequently followed by migration, adhesion, and differentiation. In the current investigation, a notable increase was observed in the GO/Alg/PRP group. This discovery implies that the sustained release of functional GO/Alg/PRP has the potential to enhance angiogenesis by expediting the proliferation and migration of endothelial cells, thereby preserving the integrity of the vascular system.

The study of GO -based materials for dressings is still in the experimental stage, and clinical applications need to clarify their metabolism and tissue and organ tox-icity. Through the pathological analysis of important histopathology of the heart, lungs, liver and kidneys, the organ toxicity of GO/Alg and the presence or absence of accumulation *in vivo* were studied. In the current study, the stained sections of vital organs of the heart, lungs, liver and kidneys in each group

showed no pathological changes, rejection inflammation, and signs of accumulation *in vivo*, indicating good biosecurity of GO/Alg/PRP.

In summary, our study suggests that GO/Alg/PRP gel exhibits potential in wound repair. Nevertheless, the precise underlying mechanism remains unclear and more investigations are needed to further elucidate and clarify.

Conclusion

The present study indicates that the slow-sculpting GO/Alg gel is an excellent loading material for PRP, and the combination of the two may become one of the methods to promote wound repair.

Data availability statement

The raw data supporting the conclusions of this article will be made available by the authors, without undue reservation.

Ethics statement

The procedures for care and use of animals were approved by the Ethics Committee of the Shandong University and Weihai Municipal Hospital (2021075). The study was conducted in accordance with the local legislation and institutional requirements.

Author contributions

NC: Conceptualization, Data curation, Methodology, Writing–review and editing. ML: Conceptualization, Data curation, Project administration, Writing–review and editing. JY: Investigation, Software, Supervision, Writing–review and editing. PW: Data curation, Methodology, Writing–review and editing. GS: Conceptualization, Data curation, Writing–review and editing. HW: Conceptualization, Data curation, Methodology, Writing–original draft.

Funding

The author(s) declare financial support was received for the research, authorship, and/or publication of this article. This work was supported by grants from Shandong Province Medical and Health Development Plan Project (202104030779), Jinan Clinical Medical Research Center for Burns/Trauma Chronic Wounds (201912010), Jinan Science and Technology Innovation Plan on Medicine and Health (201907080), Science and Technology Development Project of Shandong Province (2013GSF11870). National Clinical Key Specialty, Wang Zhengguo Traumatology Development Foundation "Growth Factor Rejuvenation Program" (SZYZ-TR-15), Shandong Province Medicine Health Science and Technology Development Plan (202004030738).

Acknowledgments

We highly appreciate the warmhearted discussions from Prof Zhou-Weiwei for their critical reading and suggestions on the manuscript.

Conflict of interest

The authors declare that the research was conducted in the absence of any commercial or financial relationships that could be construed as a potential conflict of interest.

Publisher's note

References

Anitua, E., Nurden, P., Prado, R., Nurden, A. T., and Padilla, S. (2019). Autologous fibrin scaffolds: when platelet- and plasma-derived biomolecules meet fibrin. *Biomaterials* 192, 440–460. doi:10.1016/j.biomaterials.2018.11.029

Blacklow, S. O., Li, J., Freedman, B. R., Zeidi, M., Chen, C., and Mooney, D. J. (2019). Bioinspired mechanically active adhesive dressings to accelerate wound closure. *Sci. Adv.* 5 (7), eaaw3963. doi:10.1126/sciadv.aaw3963

Buechler, M. B., Pradhan, R. N., Krishnamurty, A. T., Cox, C., Calviello, A. K., Wang, A. W., et al. (2021). Cross-tissue organization of the fibroblast lineage. *Nature* 593 (7860), 575–579. doi:10.1038/s41586-021-03549-5

Catanzano, O., Quaglia, F., and Boateng, J. S. (2021). Wound dressings as growth factor delivery platforms for chronic wound healing. *Expert Opin. Drug Deliv.* 18 (6), 737–759. doi:10.1080/17425247.2021.1867096

Chen, K., Ling, Y., Cao, C., Li, X., Chen, X., and Wang, X. (2016). Chitosan derivatives/reduced graphene oxide/alginate beads for small-molecule drug delivery. *Mater Sci. Eng. C Mater Biol. Appl.* 69, 1222–1228. doi:10.1016/j.msec.2016.08.036

Chen, L., Zhang, L., Zhang, H., Sun, X., Liu, D., Zhang, J., et al. (2021). Programmable immune activating electrospun fibers for skin regeneration. *Bioact. Mater* 6 (10), 3218–3230. doi:10.1016/j.bioactmat.2021.02.022

Ciriza, J., Saenz del Burgo, L., Virumbrales-Munoz, M., Ochoa, I., Fernandez, L. J., Orive, G., et al. (2015). Graphene oxide increases the viability of C2C12 myoblasts microencapsulated in alginate. *Int. J. Pharm.* 493 (1-2), 260–270. doi:10.1016/j.ijpharm.2015.07.062

Collaborators, GBDO, Afshin, A., Forouzanfar, M. H., Reitsma, M. B., Sur, P., Estep, K., et al. (2017). Health effects of overweight and obesity in 195 countries over 25 years. *N. Engl. J. Med.* 377 (1), 13–27. doi:10.1056/nejmoa1614362

Dai, H., Alsalhe, T. A., Chalghaf, N., Ricco, M., Bragazzi, N. L., and Wu, J. (2020). The global burden of disease attributable to high body mass index in 195 countries and territories, 1990-2017: an analysis of the Global Burden of Disease Study. *PLoS Med.* 17 (7), e1003198. doi:10.1371/journal.pmed.1003198

do Amaral, R., Zayed, N. M. A., Pascu, E. I., Cavanagh, B., Hobbs, C., Santarella, F., et al. (2019). Functionalising collagen-based scaffolds with platelet-rich plasma for enhanced skin wound healing potential. *Front. Bioeng. Biotechnol.* 7, 371. doi:10.3389/fbioe.2019.00371

Eming, S. A., Murray, P. J., and Pearce, E. J. (2021). Metabolic orchestration of the wound healing response. *Cell Metab.* 33 (9), 1726–1743. doi:10.1016/j.cmet.2021.07.017

Frykberg, R. G., and Banks, J. (2015). Challenges in the treatment of chronic wounds. *Adv. Wound Care (New Rochelle)* 4 (9), 560–582. doi:10.1089/wound.2015.0635

Gentile, P., Calabrese, C., De Angelis, B., Dionisi, L., Pizzicannella, J., Kothari, A., et al. (2020). Impact of the different preparation methods to obtain autologous non-activated

platelet-rich plasma (A-PRP) and activated platelet-rich plasma (AA-PRP) in plastic surgery: wound healing and hair regrowth evaluation. *Int. J. Mol. Sci.* 21 (2), 431. doi:10.3390/ijms21020431

Gurtner, G. C., Werner, S., Barrandon, Y., and Longaker, M. T. (2008). Wound repair and regeneration. *Nature* 453 (7193), 314–321. doi:10.1038/nature07039

Harrison, P., Subcommittee on Platelet, P., Andia, I., Burnouf, T., Dohan Ehrenfest, D., Everts, P., et al. (2018). The use of platelets in regenerative medicine and proposal for a new classification system: guidance from the SSC of the ISTH. *J. Thromb. Haemost.* 16 (9), 1895–1900. doi:10.1111/jth.14223

Hong, Y. K., Lee, Y. C., Cheng, T. L., Lai, C. H., Hsu, C. K., Kuo, C. H., et al. (2019). Tumor endothelial marker 1 (TEM1/Endosialin/CD248) enhances wound healing by interacting with platelet-derived growth factor receptors. *J. Invest. Dermatol* 139 (10), 2204–2214.e7. doi:10.1016/j.jid.2019.03.1149

Hsu, J. T., Chen, Y. W., Ho, T. W., Tai, H. C., Wu, J. M., Sun, H. Y., et al. (2019). Chronic wound assessment and infection detection method. *BMC Med. Inf. Decis. Mak.* 19 (1), 99. doi:10.1186/s12911-019-0813-0

Hu, M. S., Borrelli, M. R., Hong, W. X., Malhotra, S., Cheung, A. T. M., Ransom, R. C., et al. (2018). Embryonic skin development and repair. *Organogenesis* 14 (1), 46–63. doi:10.1080/15476278.2017.1421882

Irmak, G., Demirtas, T. T., and Gumusderelioglu, M. (2020). Sustained release of growth factors from photoactivated platelet rich plasma (PRP). *Eur. J. Pharm. Biopharm.* 148, 67–76. doi:10.1016/j.ejpb.2019.11.011

Joshi, S. R., Sharma, A., Kim, G. H., and Jang, J. (2020). Low cost synthesis of reduced graphene oxide using biopolymer for influenza virus sensor. *Mater Sci. Eng. C Mater Biol. Appl.* 108, 110465. doi:10.1016/j.msec.2019.110465

Kim, N., Choi, K. U., Lee, E., Lee, S., Oh, J., Kim, W. K., et al. (2020). Therapeutic effects of platelet derived growth factor overexpressed-mesenchymal stromal cells and sheets in canine skin wound healing model. *Histol. Histopathol.* 35 (7), 751–767. doi:10.14670/HH-18-196

Konieczny, P., and Naik, S. (2021). Healing without scarring. *Science* 372 (6540), 346–347. doi:10.1126/science.abi5770

Kumar, L., Brice, J., Toberer, L., Klein-Seetharaman, J., Knauss, D., and Sarkar, S. K. (2019). Antimicrobial biopolymer formation from sodium alginate and algae extract using aminoglycosides. *PLoS One* 14 (3), e0214411. doi:10.1371/journal.pone.0214411

Laschke, M. W., and Menger, M. D. (2022). The simpler, the better: tissue vascularization using the body's own resources. *Trends Biotechnol.* 40 (3), 281–290. doi:10.1016/j.tibtech.2021.07.002

Li, B., and Wang, J. H. (2011). Fibroblasts and myofibroblasts in wound healing: force generation and measurement. *J. Tissue Viability* 20 (4), 108–120. doi:10.1016/j.jtv.2009.11.004

Liu, C., Qin, W., Wang, Y., Ma, J., Liu, J., Wu, S., et al. (2021). 3D printed gelatin/sodium alginate hydrogel scaffolds doped with nano-attapulgite for bone tissue repair. *Int. J. Nanomedicine* 16, 8417–8432. doi:10.2147/ijn.s339500

Liu, S., Zeng, T. H., Hofmann, M., Burcombe, E., Wei, J., Jiang, R., et al. (2011). Antibacterial activity of graphite, graphite oxide, graphene oxide, and reduced graphene oxide: membrane and oxidative stress. *ACS Nano* 5 (9), 6971–6980. doi:10.1021/nn202451x

Martinez-Zapata, M. J., Marti-Carvajal, A. J., Sola, I., Exposito, J. A., Bolibar, I., Rodriguez, L., et al. (2016). Autologous platelet-rich plasma for treating chronic wounds. *Cochrane Database Syst. Rev.* 2016 (5), CD006899. doi:10.1002/14651858.CD006899.pub2

Mascharak, S., desJardins-Park, H. E., Davitt, M. F., Griffin, M., Borrelli, M. R., Moore, A. L., et al. (2021). Preventing Engrailed-1 activation in fibroblasts yields wound regeneration without scarring. *Science* 372 (6540), eaba2374. doi:10.1126/science.aba2374

Nair, L. S., Starnes, T., Ko, J. W., and Laurencin, C. T. (2007). Development of injectable thermogelling chitosan-inorganic phosphate solutions for biomedical applications. *Biomacromolecules* 8 (12), 3779–3785. doi:10.1021/bm7006967

Olmos, D., and Gonzalez-Benito, J. (2021). Polymeric materials with antibacterial activity: a review. *Polym. (Basel)* 13 (4), 613. doi:10.3390/polym13040613

Oneto, P., and Etulain, J. (2021). PRP in wound healing applications. *Platelets* 32 (2), 189–199. doi:10.1080/09537104.2020.1849605

Qiu, M., Chen, D., Shen, C., Shen, J., Zhao, H., and He, Y. (2016). Platelet-rich plasma-loaded poly(d,l-lactide)-poly(ethylene glycol)-Poly(d,l-lactide) hydrogel dressing promotes full-thickness skin wound healing in a rodent model. *Int. J. Mol. Sci.* 17 (7), 1001. doi:10.3390/ijms17071001

Rami, A., Kazemi-Lomedasht, F., Mirjalili, A., Noofeli, M., Shahcheraghi, F., and Dounighi, N. M. (2021). Outer membrane vesicles of bordetella pertussis encapsulated into sodium alginate nanoparticles as novel vaccine delivery system. *Curr. Pharm. Des.* 27 (42), 4341–4354. doi:10.2174/1381612827666210907154715

Reinke, J. M., and Sorg, H. (2012). Wound repair and regeneration. *Eur. Surg. Res.* 49 (1), 35–43. doi:10.1159/000339613

Sanchez-Fernandez, J. A., Presbitero-Espinosa, G., Pena-Paras, L., Pizana, E. I. R., Galvan, K. P. V., Vopalensky, M., et al. (2021). Characterization of sodium alginate hydrogels reinforced with nanoparticles of hydroxyapatite for biomedical applications. *Polym. (Basel)* 13 (17), 2927. doi:10.3390/polym13172927

Sen, C. K. (2021). Human wound and its burden: updated 2020 compendium of estimates. *Adv. Wound Care (New Rochelle)* 10 (5), 281–292. doi:10.1089/wound.2021.0026

Shen, H., Lin, H., Sun, A. X., Song, S., Wang, B., Yang, Y., et al. (2020). Acceleration of chondrogenic differentiation of human mesenchymal stem cells by sustained growth factor release in 3D graphene oxide incorporated hydrogels. *Acta Biomater.* 105, 44–55. doi:10.1016/j.actbio.2020.01.048

Shiny, P. J., Vimala Devi, M., Felciya, S. J. G., Ramanathan, G., Fardim, P., and Sivagnanam, U. T. (2021). *In vitro* and *in vivo* evaluation of poly-3-hydroxybutyric acid-sodium alginate as a core-shell nanofibrous matrix with arginine and bacitracin-nanoclay complex for dermal reconstruction of excision wound. *Int. J. Biol. Macromol.* 168, 46–58. doi:10.1016/j.ijbiomac.2020.12.025

Spater, T., Tobias, A. L., Menger, M. M., Nickels, R. M., Menger, M. D., and Laschke, M. W. (2020). Biological coating with platelet-rich plasma and adipose tissue-derived microvascular fragments improves the vascularization, biocompatibility and tissue incorporation of porous polyethylene. *Acta Biomater.* 108, 194–206. doi:10.1016/j.actbio.2020.03.018

Tang, N., Zhang, R., Zheng, Y., Wang, J., Khatib, M., Jiang, X., et al. (2022). Highly efficient self-healing multifunctional dressing with antibacterial activity for sutureless wound closure and infected wound monitoring. *Adv. Mater* 34 (3), e2106842. doi:10.1002/adma.202106842

Wang, C., Yokota, T., and Someya, T. (2021). Natural biopolymer-based biocompatible conductors for stretchable bioelectronics. *Chem. Rev.* 121 (4), 2109–2146. doi:10.1021/acs.chemrev.0c00897

Wang, H., Chen, Q., and Zhou, S. (2018). Carbon-based hybrid nanogels: a synergistic nanoplatform for combined biosensing, bioimaging, and responsive drug delivery. *Chem. Soc. Rev.* 47 (11), 4198–4232. doi:10.1039/c7cs00399d

Wang, P., Luo, Z. G., Xiao, Z. G., and Saleh, A. S. M. (2022). Impact of calcium ions and degree of oxidation on the structural, physicochemical, and in-vitro release properties of resveratrol-loaded oxidized gellan gum hydrogel beads. *Int. J. Biol. Macromol.* 196, 54–62. doi:10.1016/j.ijbiomac.2021.12.043

Wang, Y., Lu, Y., Zhang, J., Hu, X., Yang, Z., Guo, Y., et al. (2019). A synergistic antibacterial effect between terbium ions and reduced graphene oxide in a poly(vinyl alcohol)-alginate hydrogel for treating infected chronic wounds. *J. Mater Chem. B* 7 (4), 538–547. doi:10.1039/c8tb02679c

Wang, Y., Sun, G., Gong, Y., Zhang, Y., Liang, X., and Yang, L. (2020). Functionalized folate-modified graphene oxide/PEI siRNA nanocomplexes for targeted ovarian cancer gene therapy. *Nanoscale Res. Lett.* 15 (1), 57. doi:10.1186/s11671-020-3281-7

Wu, K. H., Wang, J. C., Huang, J. Y., Huang, C. Y., Cheng, Y. H., and Liu, N. T. (2019). Preparation and antibacterial effects of Ag/AgCl-doped quaternary ammonium-modified silicate hybrid antibacterial material. *Mater Sci. Eng. C Mater Biol. Appl.* 98, 177–184. doi:10.1016/j.msec.2018.12.142

Xie, X., Mao, C., Liu, X., Tan, L., Cui, Z., Yang, X., et al. (2018). Tuning the bandgap of photo-sensitive polydopamine/Ag(3)PO(4)/graphene oxide coating for rapid, noninvasive disinfection of implants. *ACS Cent. Sci.* 4 (6), 724–738. doi:10.1021/acscentsci.8b00177

Yao, S., Wang, Y., Chi, J., Yu, Y., Zhao, Y., Luo, Y., et al. (2022). Porous MOF microneedle array patch with photothermal responsive nitric oxide delivery for wound healing. *Adv. Sci. (Weinh).* 9 (3), e2103449. doi:10.1002/advs.202103449

Zahn, J., Loibl, M., Sprecher, C., Nerlich, M., Alini, M., Verrier, S., et al. (2017). Platelet-rich plasma as an autologous and proangiogenic cell delivery system. *Mediat. Inflamm.* 2017, 1–14. doi:10.1155/2017/1075975

Zhang, Y., Wang, T., Zhuang, Y., He, T., Wu, X., Su, L., et al. (2021). Sodium alginate hydrogel-mediated cancer immunotherapy for postoperative *in situ* recurrence and metastasis. *ACS Biomater. Sci. Eng.* 7 (12), 5717–5726. doi:10.1021/acsbiomaterials.1c01216

Zhou, R. X., Dong, Y. S., and Zhou, W. B. (2022). Treatment of chronic refractory wound with autologous platelet-rich plasma in a hemophilia A patient after knee joint surgery. *Zhonghua Shao Shang Za Zhi* 38 (4), 369–372. doi:10.3760/cma.j.cn501120-20210202-00045

Zhu, Y., Ma, Z., Kong, L., He, Y., Chan, H. F., and Li, H. (2020). Modulation of macrophages by bioactive glass/sodium alginate hydrogel is crucial in skin regeneration enhancement. *Biomaterials* 256, 120216. doi:10.1016/j.biomaterials.2020.120216

frontiers | Frontiers in Bioengineering and Biotechnology

TYPE Review
PUBLISHED 20 March 2024
DOI 10.3389/fbioe.2024.1373130

OPEN ACCESS

EDITED BY
Junjie Li,
Kyushu University, Japan

REVIEWED BY
Panyue Wen,
University of Science and Technology of China, China
Hailiang Wu,
University of California, San Francisco, United States

*CORRESPONDENCE
Liqun Yang,
yangliqun@cmu.edu.cn,
yanglq@lnszjk.com.cn
Xiancheng Li,
lxc2620@163.com

†These authors have contributed equally to this work

RECEIVED 19 January 2024
ACCEPTED 06 March 2024
PUBLISHED 20 March 2024

CITATION
Hu K, Hou Z, Huang Y, Li X, Li X and Yang L (2024), Recent development and future application of biodegradable ureteral stents. *Front. Bioeng. Biotechnol.* 12:1373130. doi: 10.3389/fbioe.2024.1373130

Recent development and future application of biodegradable ureteral stents

Ke Hu[1,2†], Zhipeng Hou[2†], Yuanbin Huang[1†], Xueying Li[3], Xiancheng Li[1*] and Liqun Yang[2,4*]

[1]Department of Urology, The Second Affiliated Hospital of Dalian Medical University, Dalian, China, [2]Research Center for Biomedical Materials, Engineering Research Center of Ministry of Education for Minimally Invasive Gastrointestinal Endoscopic Techniques, Shengjing Hospital of China Medical University, Shenyang, China, [3]College of Computer Science and Engineering, Dalian Minzu University, Dalian, China, [4]Liaoning Research Institute for Eugenic Birth and Fertility, China Medical University, Shenyang, China

Ureteral stenting is a common clinical procedure for the treatment of upper urinary tract disorders, including conditions such as urinary tract infections, tumors, stones, and inflammation. Maintaining normal renal function by preventing and treating ureteral obstruction is the primary goal of this procedure. However, the use of ureteral stents is associated with adverse effects, including surface crusting, bacterial adhesion, and lower urinary tract symptoms (LUTS) after implantation. Recognizing the need to reduce the complications associated with permanent ureteral stent placement, there is a growing interest among both physicians and patients in the use of biodegradable ureteral stents (BUS). The evolution of stent materials and the exploration of different stent coatings have given these devices different roles tailored to different clinical needs, including anticolithic, antibacterial, antitumor, antinociceptive, and others. This review examines recent advances in BUS within the last 5 years, providing an in-depth analysis of their characteristics and performance. In addition, we present prospective insights into the future applications of BUS in clinical settings.

KEYWORDS

biodegradable ureteral stent, natural polymers, PLGA, PCL, PTMC, biodegradable metals

1 Introduction

Ureteral stents are widely used in the therapeutic management of urological diseases and are one of the most commonly used devices in clinical urology. Playing a crucial role in providing essential support and facilitating urine drainage, ureteral stents are routinely used in various clinical scenarios, including assisting in the treatment of urinary tract stones and alleviating and treating both benign and malignant ureteral obstructions. They are placed preoperatively to aid in intraoperative identification of the ureter, to facilitate expulsion of small residual stones in the upper urinary tract, and to prevent postoperative complications such as ureteral stricture (Lange et al., 2015; Wang et al., 2018).

In 1949, Herdman initially delineated ureteral stents constructed from polyethylene (Herdman, 1949). However, this material does not prevent mechanical obstruction caused by urine settling on the stent tube, which can lead to hydronephrosis. Zimskind et al. (1967) initially delineated *in vivo* silicone ureteral stents (Zimskind et al., 1967). The stent is made up of a straight silicone tube with an open end and a drainage hole on the side. Encrustations

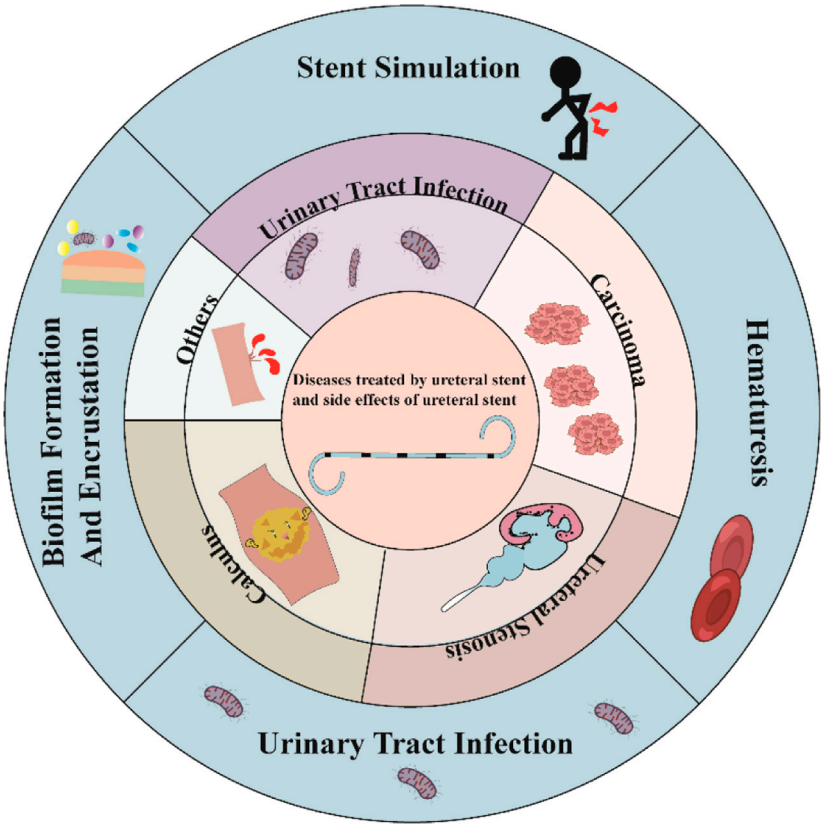

FIGURE 1
Types of diseases treated clinically with ureteral stents and possible complications after stent implantation.

of silicone catheters appear to be less prevalent, albeit with higher stent mobility. In order to enhance stent mobility, Gibbons et al. (1974) employed an acorn-shaped silicone sheath at the distal end of the stent, strategically positioned just within the ureteral orifice, thereby facilitating stent fixation within the ureter (Gibbons et al., 1974). Hepperlen et al. (1978) initially documented the utilization of self-retaining single pigtail stents, featuring a proximal pigtail configuration aimed at mitigating distal displacement, but they still have the potential to migrate to the proximal end, making removal difficult (Hepperlen et al., 1978). In the same year, Finney. (1978) reported that double J tubes, with both distal and proximal ends in a "J" shape, greatly reduced the risk of stent displacement, and are still widely used in clinical diagnosis and treatment (Finney, 1978).

Currently, diseases such as ureteral tumors, ureteral calculus, and ureteral strictures may lead to renal and ureteral hydronephrosis as well as urinary tract infections, often requiring the use of ureteral stents (as shown in Figure 1). Ureteral tumors represent about 2.65% of genitourinary tumors and have a mortality rate of 3%, according to the 2023 United States Cancer Statistics. The number of ureteral tumor patients in the United States is expected to increase by 500 compared to 2020 data, indicating an upward trend (Siegel et al., 2020; Siegel et al., 2023). The incidence of kidney and ureteral calculus ranges between 4% and 20% (Trinchieri, 1996). An examination of adult Americans unveiled that the incidence of kidney and ureteral stones has shown a continuous rise over the years, escalating from 0.6% in 2005 to 0.9% in 2015 (Tundo et al., 2021). Epidemiological data from the United States and Europe indicate a yearly increase in the incidence of sepsis, with an annual increase of 8.7%. It is noteworthy that 8.6%–30.6% of sepsis cases are related to the urinary tract, and the mortality rate can reach 20%–40% (Martin et al., 2003). Therefore, as the incidence of urological diseases continues to rise, the use of ureteral stents is expected to increase accordingly.

Despite the widespread use of ureteral stents, they are associated with diverse complications, the most common of which are infection, crusting on the stent surface, patient discomfort, and hematuria (Xia et al., 2023). At present, the most commonly used stent tube materials are silicone and polyurethane. These materials require a second invasive procedure with cystoscopy for retrieval and are considered permanent. This secondary surgery increases the risk of postoperative complications such as hematuria and ureteral stricture. For pediatric patients, the removal of the stent requires supplementary general anesthesia. Simultaneously, non-biodegradable ureteral stents are associated with stent retention syndrome (Monga et al., 1995). Over time, the presence of a stent in the body increases the risk of urinary tract infection and the rate of surface crust formation (Klis et al., 2009; El-Hayek et al., 2017). In a recent meta-analysis, the early removal of ureteral stents (i.e., within 3 weeks) was found to significantly mitigate the occurrence of urinary tract infections (Wang et al., 2022). Undoubtedly, the combination of the primary disease and the adverse effects

TABLE 1 Comparison of currently used materials for BUS.

BUS materials	Degradation period	Degradation mechanism	Characteristics of BUS	Drawbacks of BUS	References
Alginate	7 days	Benign dissolution	Favorable tissue compatibility	1. Insufficient degradation time	Auge et al. (2002)
				2. Further analysis of human subjects is required	
Alginate	Ureter: 8 days	Even degradation	1. Effective temporary drainage lasting 48 hours	1. 68.2% reported urethral discomfort during the exclusion period	Lingeman et al. (2003a)
	Bladder: 15 days		2. Favorable biocompatibility	2. A 3.4% inadequate degradation rate	
				3. Stent displacement	
Blend of alginate, gelatin, and cold-set jelly	10 days	Even degradation	1. Adjustable *in vitro* degradation rate	1. Rapid *in vivo* degradation rate	Barros et al. (2015a), Barros et al. (2015b), Barros et al. (2016), Barros et al. (2018)
			2. Increased inhibition of bacterial adhesion	2. During *in vivo* degradation, the mechanical performance of BUS decreases	
			3. Uniform degradation		
			4. Effective urine drainage		
			5. High biocompatibility		
			6. Capable of loading ketorolac and anti-tumor drugs		
PLGA (Uriprene™)	First generation: 4–10 weeks	Distal degradation is preferred	1. Distal priority degradation prevents debris from blocking the ureter	1. Sudden disintegration of the material	Hadaschik et al. (2008), Chew et al. (2010), Chew et al. (2013)
	Second generation: 2–10 weeks		2. Excellent drainage performance		
	Third generation:4 weeks				
Poly(ε-caprolactone) (PCL)/poly(lactic-co-glycolic acid) (PLGA) (LA:GA = 80:20)	5% PCL/PLGA:28 days	Block degradation	1. Controllability of mechanical properties	1. Lack of *in vivo* animal implantation experiments	Wang et al. (2015b)
	15% PCL/PLGA:42 days		2. Flexibility of degradation time	2. Mild inflammatory response observed in rabbit bodies	
	25% PCL/PLGA:56 days				
PCL/PLGA	Begins degradation at 4 weeks, completely degrades within 10 weeks	Gradual degradation from the distal to proximal end	1. The function of gradual degradation from distal to proximal	1. Lack of *in vivo* animal implantation experiments	Wang et al. (2015a)
			2. Effective ureteral drainage	2. Acidic degradation products	
			3. favorable biocompatibility		
Mg-Sr-Ag alloy	The stent continuously degrades during the 12-week implantation period	The surface continuously corrodes and degrades	1. Good cell compatibility and blood compatibility	1. The implantation of the scaffold has a mild impact on the bladder function of experimental animals	Tie et al. (2022)
			2. The adjustability of the degradation cycle of the scaffold	2. The degradation products contain Mg(OH)2, which may lead to an increase in pH	

(Continued on following page)

TABLE 1 (*Continued*) Comparison of currently used materials for BUS.

BUS materials	Degradation period	Degradation mechanism	Characteristics of BUS	Drawbacks of BUS	References
			3. Higher antimicrobial activity attributed to the release of silver ions		
			4. The scaffold maintains sufficient structural support during the degradation process		
Biodegradable magnesium alloy wires serve as the scaffold for the stent, surrounded by degradable polyurethane material	The stent rapidly degrades after 2 weeks and completely degrades within 5 weeks	Not mentioned	Good biocompatibility	1. Degradation at 4–5 weeks leads to an increase in artificial urine pH	Jin et al. (2021)
				2. Has not demonstrated a perfect antibacterial effect	

associated with the use of ureteral stents places a significant financial burden on global healthcare systems, presenting substantial challenges to their fiscal resources and long-term sustainability. Researchers are investigating new biomaterials and designs to tackle these issues. Unlike non-degradable ureteral stents, ureteral stents made of biodegradable materials have several advantages, including good biocompatibility that can be broken down into small molecular by-products (Liu et al., 2021), better mechanical properties than currently used polyurethane stents (Antonowicz et al., 2021), the ability of nanoparticles made of biodegradable materials to serve as drug delivery systems (Mehrotra et al., 2023), stent degradability to avoid the risk of second surgery, and the capability to mitigate surface crusting. Biodegradable ureteral stents (BUS) have gained significant attention among scholars due to their potential clinical benefits, making them a promising area of investigation.

The materials used for BUS can be classified into three groups: natural polymers, synthetic polymers, and metallic materials (as shown in Table 1). Regulating the degradation rate and managing the size of degradation fragments are the challenges in the development of biodegradable ureteral stents, which remain in the realm of experimental research. Nevertheless, significant progress has been made in stent design by improving biomaterial properties and biocompatibility. Although still in the experimental research stage, BUS hold promise for future clinical applications. Biodegradable stents have been proposed and shown to be effective in the treatment of benign luminal narrowing in various anatomical structures, including coronary arteries, esophagus, trachea, and others (Saito et al., 2007; Serruys et al., 2010; Zajac et al., 2019).

Interestingly, in addition to their inherent degradability, BUS can exhibit multiple functionalities when integrated with stent coatings and drug-eluting techniques. This versatility positions BUS to achieve different effects in future clinical applications in the field of urology, offering multiple advantages for the treatment of various diseases. Previous research has explored the incorporation of stent coatings and drug-eluting techniques into non-biodegradable stents, laying the foundation for functional features on BUS surfaces (Chew et al., 2006; Kram et al., 2020). Extensive development and study of drug-eluting, degradable stents have been made in the field of cardiovascular disease (El-Hayek et al., 2017; Kutcher, 2018; Liu et al., 2020). Research on the utilization of BUS in the urinary system is limited, causing delays in the development of ureteral stents compared to the cardiovascular field. This paper summarizes the latest developments in the study of BUS over the past 5 years and explores future clinical applications (as shown in Figure 2). Furthermore, we engage in a comprehensive discussion on the merits and drawbacks of BUS in urology. Additionally, we present our unique recommendations for improving BUS to encourage further research and development in clinical practice.

2 Technology applied to the development of BUS

2.1 Biodegradable materials for ureteral applications

2.1.1 Natural polymers

Natural biodegradable materials include alginate, gelatin, silk fibroin, and chitosan. In the early 21st century, Auge et al. reported a temporary ureteral drainage stent based on alginate polymers. Although the stent exhibited a short degradation time in porcine experiments (completely degraded in 7 days), it reassuringly degraded in a benign manner, as confirmed by histologic examination, indicating its safety (Auge et al., 2002). Lingeman et al. patented a BUS based on alginate polymers (Lingeman et al., 2003a). *In vivo* experiments confirmed the effective urinary drainage and excellent biocompatibility of the BUS. However, the stent exhibited an inadequate degradation rate of 3.4%, potentially necessitating secondary surgery for retrieval. A decade ago, Barros et al. utilized alginate, cold-setting gelatin, and their blends with gelatin to produce a naturally sourced polysaccharide-based degradable ureteral stent (Barros et al., 2015b). Subsequently, they developed ketoprofen-eluting BUS and anticancer drug-eluting BUS based on this stent (Barros et al., 2015a; Barros et al., 2016). Despite Barros confirming through *in vitro* experiments that the stent could degrade within 14–60 days, with degradation rates controllable by altering the proportion of biodegradable materials, the *in vivo* degradation rate was excessively rapid (10 days), accompanied by a decline in

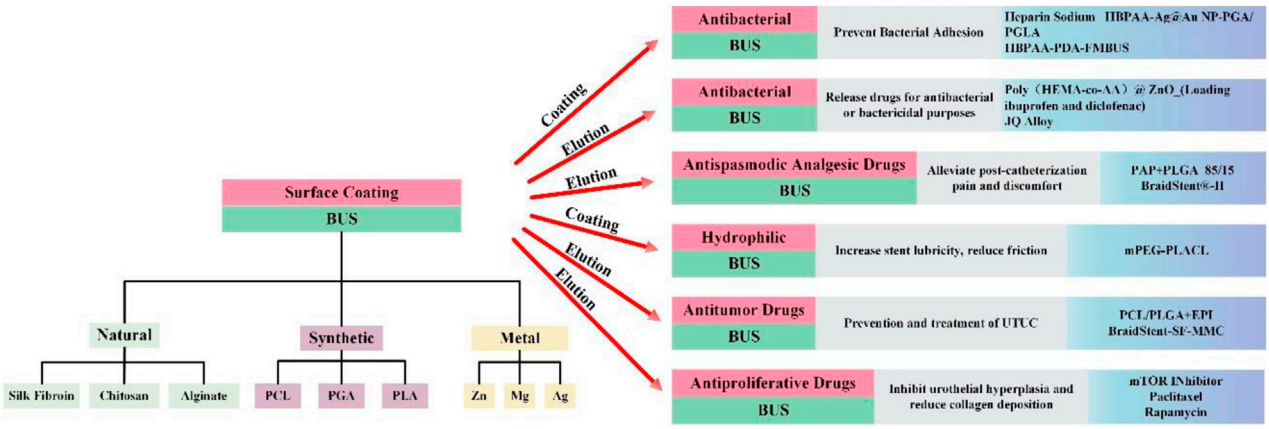

FIGURE 2
The material classification of BUS and the innovation in clinical functions that can be used in the past 5 years.

mechanical performance during the degradation process (Barros et al., 2015a; Barros et al., 2016; Barros et al., 2018). Chitosan and silk fibroin have also been explored by other researchers as surface-degradable coatings for ureteral stents, facilitating drug delivery (Ecevit et al., 2022; Soria et al., 2022).

2.1.2 Synthetic polymers

In the development of ureteral stents, the predominant synthetic biodegradable polymers currently include polycaprolactone (PCL), polyglycolic acid (PGA), and polylactic acid (PLA). The first-generation Uriprene stent was composed of 80% LA and 20% GA. It exhibited the advantage of faster distal degradation than proximal degradation, with degradation beginning at 7 weeks and complete degradation at approximately 10 weeks (Hadaschik et al., 2008). The second-generation Uriprene stent began to degrade at 2 weeks and was completely degraded by 10 weeks, while the third-generation stent degraded uniformly within 4 weeks (Chew et al., 2010). However, Uriprene stents were challenged by uncontrolled degradation, leading to sudden material degradation and transient obstruction in animal experiments (Hadaschik et al., 2008; Chew et al., 2010; Chew et al., 2013). Despite significant advances, various PLGA ureteral stents still have drawbacks such as stiffness, high brittleness, poor shape memory, a lack of inherent stability, and multiple fracture events during the degradation process leading to ureteral obstruction (Wang et al., 2015a). Wang et al. utilized dual-nozzle electrospinning technology to design and manufacture a novel stent with a gradient composition of PCL and PLGA (Wang et al., 2015a). The stent consisted of three segments: proximal (25 wt% PCL), intermediate (15 and 25 wt% PCL), and distal (15 wt% PCL). The varying PCL content provided a gradual degradation function from distal to proximal. This stent began to degrade at week 4 and was completely degraded by week 10, with no ureteral obstruction observed in their animal studies. Despite the acidic nature of the degradation products of the PLGA (Lü et al., 2009), experimental results demonstrated no significant difference in pH values between the two groups compared to the control group (Wang et al., 2015a).

2.1.3 Metals

Compared to polymer-based materials for ureteral stents, metallic materials have greater inherent antimicrobial activity and superior mechanical properties (Fu et al., 2020). The enhanced mechanical performance and prolonged lifespan allow patients to reduce the frequency of ureteral stent replacements, maintaining better luminal patency and preventing complications such as recurrent strictures (Abbasi et al., 2013). However, with the prolonged presence of ureteral stents, the inevitable formation of biofilm on the stent wall and biofilm-associated infections are unavoidable (Akay et al., 2007). Hence, biodegradable metal materials have attracted increasing research interest due to their natural degradation advantages and inherent antimicrobial activity (Lock et al., 2014; Zhang et al., 2020). In recent years, magnesium (Mg) and magnesium alloys, zinc (Zn), and zinc alloys have been investigated for the development of degradable ureteral stents (Nguyen et al., 2018; Fu et al., 2020). In 2021, Tie et al. innovatively developed the Mg-Sr-Ag alloy, combining the exceptional mechanical properties of the Mg-Sr alloy with the pronounced antimicrobial activity of silver (Ag). They validated its biocompatibility and impact on the urological system (Tie et al., 2022). Previously, they had preliminarily confirmed the applicability of the Mg-Sr alloy for the manufacture of biodegradable bone fixation devices and demonstrated the pronounced antibacterial activity of magnesium alloys containing silver in an *in vitro* setting (Tie et al., 2013; Tie et al., 2016).

The innovative biodegradable ureteral stent, synthesized from biodegradable polyurethane and magnesium alloy, represents an innovative endeavor. Jin et al. introduced an innovative degradable stent featuring a surface coating of poly-L-lactic acid (PLLA) and poly (lactic-co-glycolic acid) (PLGA) (Jin et al., 2018). Although this stent demonstrated drainage capabilities similar to those of conventional stents, it exhibited renal hydronephrosis when inserted on the degradable side. After 2 years, by capitalizing on the degradation and antimicrobial properties of magnesium alloy in artificial urine, they innovatively designed a biodegradable ureteral stent composed of biodegradable polyurethane and magnesium

TABLE 2 DDS classification applied to BUS.

Classification of DDS	Advantages	Disadvantages	Application in BUS	参考文献
Traditional DDS (Hot melt extrusion, solvent casting And soak the polymer in a drug solution)	1. The process is simple and easy to make	1. Poor drug control release	1. BraidStent-H® developed by Soria et al., surface-coated heparin for antimicrobial use	Soria et al. (2021b)
	2. Easy for industrial mass production	2. Lack of targeting	2. The BraidStent-SF-MMC developed by Soria et al. is used for the treatment of UTUC	Soria et al. (2023)
		3. Poor water solubility		Edgar and Wang (2017)
		4. Poor sensitivity to drug resistance		
CO_2 Impregnation	1. Facilitates the loading of drugs into a pre-manufactured implant	1. Adequate solubility in CO_2 is imperative for the drug	1. Barros et al. pioneered the utilization of this technique in crafting the ketoprofen-eluting BUS	Barros et al. (2015a)
		2. Both the drug loading rate and drug loading efficiency exhibit suboptimal levels	2. They also used the same method to load paclitaxel and doxorubicin into a BUS based on a natural source polymer for the treatment of UTUC	Barros et al. (2016)
		3. The shape of the stent changed after drug loading		Champeau et al. (2015)
Electrospun Nanofibers	1. High encapsulation efficiency for drug loading	1. The active ingredients are unstable	1. Wang et al. used electrospun nanofibers to develop a PCL/PLGA ureteral stent with adjustable drug release and degradation rates of EPI for UTUC	Wang et al. (2019)
	2. Controlled residence time	2. The initial release of the drug		Luo et al. (2012)
	3. The predictability of the delivery rate of encapsulated drugs	3. Residual solvent quantity		Thakkar and Misra (2017)
	4. Better stability	4. Temporary industrial production difficulties		Zamani et al. (2013)
	5. Satisfactory softness and flexibility			
Nanoparticle-Based Drug Delivery Systems	1. The therapeutic efficacy of loaded drugs can be improved by using active targeting of site-specific delivery and protecting normal cells from damage	1. The majority of nanoparticles remain at the stage of cellular and animal testing	1. Gao et al. developed HBPAA-Ag@Au NPs for antimicrobial use	Gao et al. (2020)
	2. Potentially prolonging the duration of action and reducing toxicity	2. Nanoparticles entering the bloodstream may cause adverse effects		Park (2014)
		3. Low drug loading rate		Ding et al. (2019)
		4. Biodegradable polyester nanoparticles are also complex and costly to manufacture		Wang et al. (2023b)
				Wen et al. (2023)

alloy (Jin et al., 2021). Their research demonstrated negligible cytotoxicity of the degradable stent and excellent biocompatibility. The stent remained nearly intact for the first 2 weeks *in vitro*, followed by rapid degradation and complete degradation within 5 weeks. However, around the 4–5 weeks mark, the stent caused an increase in the pH of the artificial urine, possibly related to the formation of hydroxides from the degradation of the magnesium alloy. The elevated urine pH could promote crystal deposition and lead to incrustation (Tomer et al., 2021). Therefore, further refinement is necessary for the ongoing development of this stent.

2.2 Technology for drug delivery systems in BUS

In the past, the mere application of a drug coating to the stent surface could confer functionality to the stent. However, owing to uncontrolled drug release, the outcomes consistently prove unsatisfactory. Amidst ongoing innovation in drug delivery system (DDS) technology, drug-eluting stents have demonstrated the ability to sustain prolonged and effective drug release. The increased stability of the drug-loading function further enhances the suitability of stents for future clinical applications of BUS.

Numerous drug delivery systems find current applications in the realm of ureteral stents, encompassing traditional DDS methods (such as hot melt extrusion and polymer soaking in drug solutions), CO_2 impregnation, nanofibers, and nanoparticles. We have summarized the representative articles corresponding to DDS for BUS, as shown in Table 2. A comprehensive comprehension of the advantages and disadvantages inherent in diverse DDS, coupled with an insight into the contemporary developmental landscape of DDS, is poised to significantly aid the future evolution and clinical transformation of functional BUS.

2.3 Design for BUS

The current design for ureteral stents involves a bilateral terminal J-shaped tube configuration. While the design of this stent has broad clinical applicability, its use can impede the closure of the ureteral bladder orifice, leading to the occurrence of vesicoureteral reflux (VUR). The stent's distal end has a curling configuration that, combined with the patient's movement, may cause irritation to the kidney or bladder, leading to LUTS such as frequent and urgent urination as well as kidney colic. Various stent designs exist to alleviate bladder irritation and prevent VUR, and some individuals have undertaken summarizations of these designs (Domingues et al., 2022). As far as we know, there is no comprehensive summary available for the enhanced design of the ureter specific to BUS.

Presently, the predominant design employed in BUS remains the double J stent, widely favored for its post-implantation stability and resistance to displacement. The synthetic polymer-based gradient degradable scaffold designed by Wang et al. (Wang et al., 2019), the natural polymer scaffold designed by Barros et al. (Barros et al., 2015a; Barros et al., 2015b; Barros et al., 2016; Barros et al., 2018), and the Uriprene stent designed by Chew et al. (2010, Chew et al. (2013), Chen et al. (2022) all adopted D-J design.

To prevent vesicoureteral reflux caused by the double J-tube structure, Lumiaho et al. developed a biodegradable, self-expanding, self-augmenting spiral scaffold with X-ray visibility using poly (L, D-lactide) material (SR-PLA 96) (Lumiaho et al., 2007). The BUS is a 50 mm long stent that forms a double-helix structure. The self-expanding properties of SR-PLA 96 can effectively secure the bracket in place. *In vivo*, the stent is positioned 2 cm above the ureterovesical junction to protect the integrity of the ureterovesical valve mechanism and reduce the risk of VUR. They then demonstrated through animal experiments that the stent's short ureteral stent design minimizes the use of VUR compared to a double J stent (Lumiaho et al., 2011).

The BraidStent, innovatively devised by Soria et al., boasts a three-part configuration, encompassing a proximal spring coil, a midsection comprising the braidstent, and a distal Nitinol mesh basket for anchoring. The distal end is positioned 2 cm above the ureteral opening to reduce bladder irritation, while the stent prevents ureteral spasms by conforming to the ureteral pathway (Soria et al., 2021b). Nevertheless, the stent deviates from the conventional double J tube design, posing a unique challenge during its implantation for clinicians. Additionally, there is a risk of stent displacement after implantation (Soria et al., 2020).

Wang et al. innovatively engineered a biodegradable mesh ureteral stent tube (Wang Y. C. et al, 2023). The stent length was initially abbreviated by adopting a singular J-shape design. The distal J-shape was eliminated to reduce post-implantation stimulation from the distal coil to the bladder, but this also reduced overall stability. To enhance the stent's stability, the reticulated ureteral stent was expanded and affixed to the ureter using the balloon dilation technique, thereby increasing its overall stability. The *in vitro* experiments demonstrated the stent's commendable biocompatibility. Subsequent *in vivo* experiments substantiated the stent's stability, revealing no instances of displacement post-implantation. However, comprehensive evaluation through animal and clinical trials is still necessary.

Cui et al. (2022) developed a hand-woven PLCL stent and improved the design of the D-J tube to reduce bladder irritation at the distal end of the stent. The distal end of the stent features a singular loop in the J-shaped configuration, which reduces bladder irritation and enhances structural stability.

3 Current clinical development of BUS

The main difference between BUS and conventional ureteral stents is their degradability, which can reduce the side effects of ureteral stents after implantation. Domingues et al. summarize four steps for bringing a ureteral stent to market (Domingues et al., 2022). This statement has significant implications for the marketization of BUS. In this section, we shall summarize the stents that have undergone clinical trials or are poised for imminent clinical trials.

Lingeman et al. conducted a phase I clinical trial on the temporary ureteral drainage stent (TUDS) (Lingeman et al., 2003b). Stent drainage was unimpeded within 48 h of placement, and all stents were removed within 1 month from 18 patients with TUDS placement. Although there were no complications related to TUDS with this stent, experimental errors could not be avoided due to the small sample size of this experiment. Larger prospective studies are needed to confirm the clinical feasibility and safety of this stent.

A Phase II clinical trial was then conducted to increase the sample size. They placed TUDS in 87 patients, 68 of whom showed satisfactory results in draining and degrading (Lingeman et al., 2003a). Despite 17 patients exhibiting stent displacement and 3 patients experiencing stent degradation for a duration exceeding 3 months, a notable 89% of the 80 patients conveyed satisfaction with TUDS. The stent can effectively provide temporary drainage for 48 h, making it particularly suitable for patients who require short-term stent retention after ureteroscopy. However, for patients requiring longer retention after major surgery, TUDS may not be suitable. Displacement and partially undissolved stent fragments after stent implantation require reoperation to resolve, and therefore the stent is not used in clinical practice.

The 2nd and 3rd generation of Uriprene stents developed by Chew et al. showed longer degradation time and a certain degree of degradation controllability in pigs that deserve our attention (Chew et al., 2010). The stent is made by the PLGA. The second generation of scaffolds exhibited characteristics of degradation from the distal to the proximal end due to the varying coating thickness. This feature improved the controllability of scaffold degradation.

Additionally, the 4-week degradation time of the third-generation scaffolds was consistent with the 4-week time required for clinical disease indications. Therefore, we look forward to future clinical trials of this stent. Unfortunately, despite their good mechanical properties before surgery, the mechanical properties of Uriprene stents during *in vivo* degradation have not been demonstrated.

Zhang et al. reported on a poly (lactic-co-glycolic acid) (PLGA)-woven BUS implanted in dogs. The study demonstrated superior mechanical properties of the PLGA-based BUS compared to non-degradable scaffolds *in vivo* (Zhang et al., 2014). However, there were still reports of stent fragments in the renal pelvis and bladder when using the stents developed by Zhang et al. and Chew et al. despite their degradation (Chew et al., 2010; Zhang et al., 2014). Barros et al. developed a natural BUS using a patented technology that combines the injection process with supercritical fluid technology. The scaffold showed good biocompatibility and degradability, with complete degradation in pigs after 10 days (Barros et al., 2018). Although the stent's degradation time is short (10 days), which may limit its clinical application, the combination of supercritical technology and BUS is innovative and has potential for drug loading, giving BUS more functions. However, the formulation of the stent may need further improvement before being applied to clinical trials.

The additional antimicrobial capability of the BraidStent®-H developed by Soria et al. has been shown in pigs to reduce bacterial overgrowth as early as possible, although long-term efficacy needs to be improved (Soria et al., 2021a). The stent had a reasonable degradation time (6 weeks). There was no obstructive debris after stent degradation, and VUR was avoided. The stents provide an important reference for the subsequent animal experiments on the functional development of the scaffolds. It is worth looking forward to the testing of the stent in clinical trials.

4 Future clinical applications of BUS

4.1 Stent encrustation prevention

The incidence of surface stone formation on the ureter is increasing with the prolonged indwelling time of ureteral stents. Encrustation is believed to be a consequence of the development of a urinary conditioning film on the stent's surface. The formation of the conditioning film begins with the adsorption of urinary proteins onto the stent's biocompatible material, usually through electrostatic interactions. Increasing the hydrophilicity of the scaffold surface is a strategy to prevent crusting. Enhancing the hydrophilicity of the stent surface can reduce the friction coefficient of the ureteral stent, thereby preventing scab deposition. Ko et al. explored an innovative anti-encrustation coating comprised of monomethoxy polyethylene glycol (mPEG) and 3,4-dihydroxyphenylalanine, applicable to the modification of the surface of ureteral stents to inhibit biofilm formation and scaling in human urine (Ko et al., 2008). However, advancements in this strategy are restricted to the surface of the ureteral stent. Non-biodegradable ureteral stents still encounter the issue of stent-forgotten syndrome. As a result, the research focus has shifted towards developing an optimal biodegradable ureteral stent with an anti-encrustation coating.

Zhang et al. designed a new biodegradable ureteral stent using methoxy poly (ethylene glycol)-block-poly (L-lactide-ran-ε-caprolactone) (mPEG-PLACL) (Zhang et al., 2021). This is due to the flexibility and high elongation at break of polycaprolactone (PCL), combined with the hydrophilic properties of mPEG's polyether structure, which improve the brittleness and hydrophobicity of poly (L-lactide) (PLA). The combination of mPEG with copolymerized CL and LA products can enhance the hydrophilicity and smoothness of ureteral stents, as well as accelerate their degradation rate. The experimental results suggest that the ureteral stent's increased surface hydrophilicity accelerates its degradation rate. The water absorption rate of MPEG5-PLACL reaches a maximum of 9.69% after 30 days, followed by a slight decrease. MPEG8-PLACL completely degrades after soaking for 10 days, leading to a decline in mechanical strength due to complete degradation. Furthermore, both *in vitro* and *in vivo* experiments demonstrate that mPEG-PLACL exhibits excellent anti-encrustation effects. The *in vivo* experiment showed a 40% diffuse mucosal hyperplasia rate in the mPEG5-PLACL group, compared to the 100% rate in the PLACL control group, indicating better tissue compatibility. This study confirms that a smooth and hydrophilic surface plays a crucial role in preventing encrustation deposition. However, it is important to note that the *in vivo* encrustation experiment was conducted in the bladder of mice, which differs from the physiological peristaltic function and urine flushing environment present in the ureter. Therefore, further experiments are necessary to confirm the feasibility of this stent in the ureter.

4.2 Antibacterial

The bacterial colonization rate of indwelling ureteral stents varies between 42% and 90% (Reid et al., 1992; Kehinde et al., 2004). Both initial contamination during insertion and prolonged indwelling time contribute to the frequent association of stents with urinary tract infections. In a 2021 retrospective analysis, Salari et al. identified positive bacterial cultures from stent specimens as a distinctive risk factor associated with urinary tract infections within 12 months following stent removal (Salari et al., 2021). To reduce bacterial accumulation on stent surfaces, the idea of coating stents and using drug elution has been suggested for biodegradable stents.

ZnO itself possesses intrinsic antibacterial properties (Garino et al., 2019). However, the release of Zn^{2+} has the potential to trigger cytotoxic effects in healthy cells (Dumontel et al., 2017). Therefore, it is necessary to optimize and monitor their release to ensure biocompatibility. Since ZnO has been shown to readily dissolve in aqueous solutions with a pH below 5.5 or in salt-rich solutions, such as phosphates (Laurenti et al., 2019), employing ZnO-based materials in ureteral stents is not just innovative but also presents a multitude of advantages. It is critical to limit the release of Zn^{2+} from ZnO-based ureteral stents and ensure the drug release challenge. Laurenti et al. prepared hydrogels of poly-hydroxyethyl methacrylate (Poly-HEMA) or crosslinked poly (HEMA-co-AA) copolymers using free radical polymerization, combined with zinc oxide (ZnO) microparticles prepared by a hydrothermal method. The composite carried ibuprofen and diclofenac and was studied in

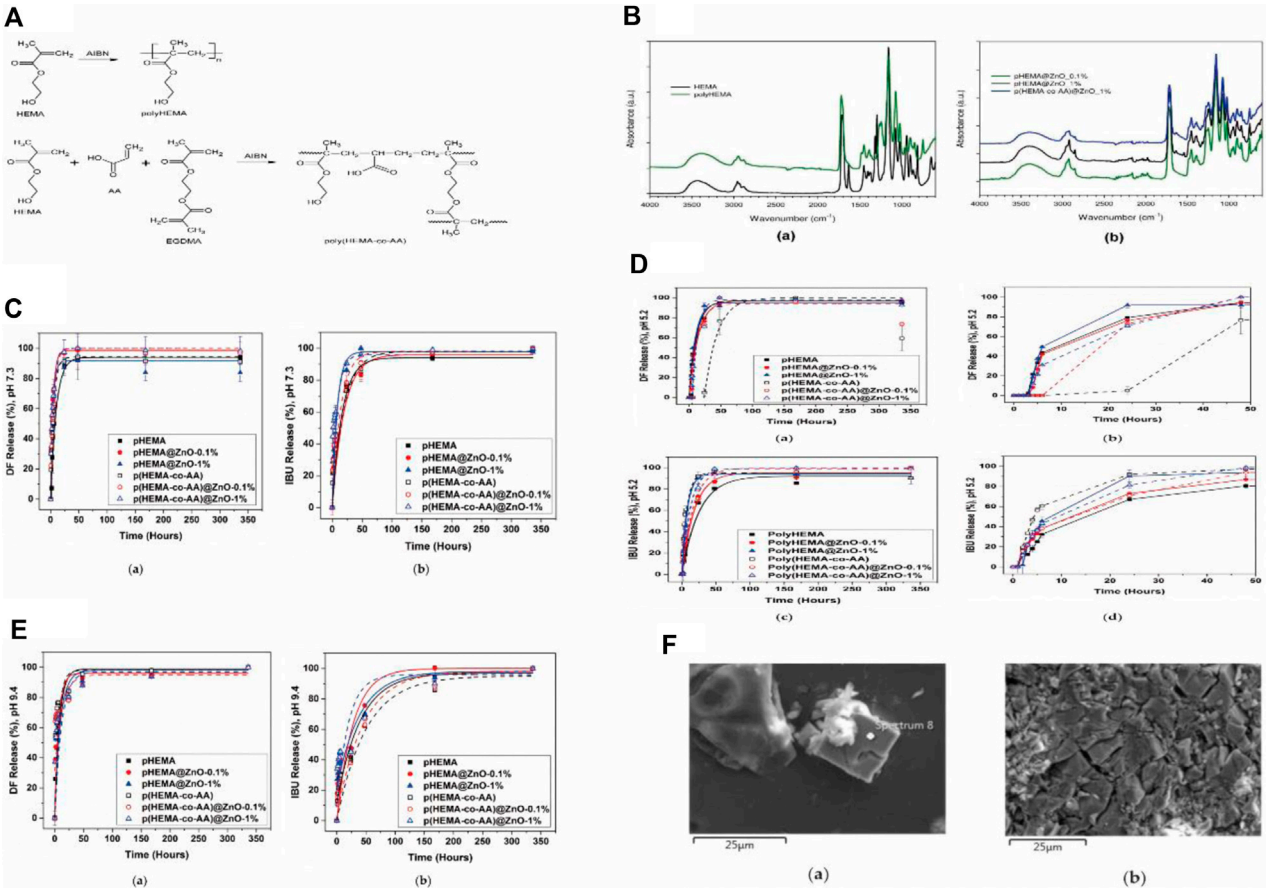

FIGURE 3
(A) The schematic representation of the formation of crosslinked polymers/hydrogel. **(B)** Infrared spectra of HEMA monomer and hydrogels with varying HEMA content, obtained through free radical polymerization, as well as composite samples with different zinc oxide concentrations, were compared. **(C)** Drug release kinetics over time in a simulated physiological urine solution. **(D)** The time-dependent drug release patterns in an acidic simulated urine solution. **(E)** Drug release kinetics over time in an alkaline simulated urine solution. **(F)** FESEM images illustrating the formation of salt deposits and encrustations on the surface of polyHEMA@ZnO after 2 weeks of immersion in artificial urine. Reproduced with permission from ref (Laurenti et al., 2020). CC BY 4.0. Copyright © 2020 by the authors.

artificial urine (AU) (Laurenti et al., 2020). Their experimental results demonstrated that the combination of ZnO particles with poly-HEMA successfully reduced the release of Zn^{2+}, with a decrease of 74.6% and 80.4% in the released Zn^{2+} amount after 3 and 7 days, respectively, compared to pure ZnO particles. This could potentially enhance its cell compatibility. Thermal analysis indicated increased stability of the copolymer as a result of the incorporation of ZnO. Drug release studies conducted In artificial urine under both acidic and alkaline pH conditions, it was demonstrated that the presence of ZnO in the formulation did not adversely affect the hydrogel's capability to store and release anti-inflammatory drugs. Additionally, ZnO microparticles endowed the composite material with supplementary antibacterial characteristics compared to the pure hydrogel. Furthermore, their release studies indicated that poly (HEMA-co-AA)@ZnO_(0.1%) exhibited good stability and optimal release trends, with modest kinetic constants and restricted burst release. The inherent antibacterial activity of this composite material will be further tested in future studies (Refer to Figure 3 for further details).

Heparin sodium, a naturally occurring glycosaminoglycan, is commonly used as an anticoagulant due to its anti-adhesive properties. In theory, this reduces bacterial adhesion on stents and prevents biofilm formation and encrustation (Al-Aown et al., 2010). Soria et al. found that BraidStent®, a type of BUS, was associated with a high bacterial contamination rate, affecting study subjects with a contamination rate as high as 50% (Soria et al., 2020). Consequently, 1 year later, they developed a novel BraidStent®-H, utilizing coating technology to give it a heparin surface coating (Soria et al., 2021b). Their research results demonstrated that BraidStent®-H exhibited a programmable and predictable degradation rate, with 91.7% completely degrading within the intended 6 weeks. Although heparin-coated catheters reduced the initial bacteriuria rate, they did not decrease long-term bacteriuria, and the long-term positive asymptomatic bacteriuria rate remained high. Further research is needed to enhance the antibacterial coating to reduce contamination in BraidStent®-H. Additionally, the impact of changes in urinary pH values on degradation rates and biocompatibility in patients, considering that experimental animals follow a controlled diet, requires further validation upon human application.

Gao et al. (2020) developed a ureteral stent consisting of a poly (ethylene glycol) (PEG)/poly (lactic-co-glycolic acid) (PLGA) fiber

membrane structure with hyperbranched poly (amide-amine) (HBPAA)-terminated silver-coated gold core nanoparticles (Ag@Au NPs). The scaffold's surface gradient degradation, achieved through continuous peeling, provided the stent with self-cleaning attributes and sustained antibacterial functionality, exposing the HBPAA-terminated Ag@Au NPs inside to eliminate adhered bacteria and proteins. Results from their *in vitro* degradation experiments confirmed the scaffold's persistent antimicrobial activity, limited release of Ag and Au elements (6.7%, ~8 μg), coupled with negligible cytotoxicity (L929 cell relative growth rate >80%). In in vivo experiments in pigs, the scaffold exhibited significant absorbable membrane characteristics, reducing inflammation and levels of necrotic cells. No large fragments were noted in the urinary system throughout the degradation process of this scaffold.

Most proteins carry charges and can establish strong adhesive interactions with nonpolar surfaces while demonstrating weak interactions with polar surfaces (Kehinde et al., 2004). By manipulating the material-protein and material-bacteria interface forces, it is possible to enhance repulsive interactions over adhesive attractions. Regarding the material-protein interaction, grafting highly polar polymer coatings with negative or neutral charges onto the scaffold surface can create an anti-protein polar surface. However, due to the lack of antibacterial activity in amphiphilic polymers, they do not prevent biofilm formation caused by bacterial proliferation *in vivo*. At the interface between the material and bacteria, contact-killing surfaces were created by attaching polycationic polymer brushes. However, their antibiofilm properties *in vivo* and durability fell short of expectations. This is due to the fact that host proteins, bacteria, and bacterial fragments are readily drawn by electrostatic forces to engage with positively charged antibacterial surfaces. The resulting biofilm shields the bactericidal moieties, providing a substrate for adjacent thermophilic bacteria, ultimately leading to the loss of surface contact-killing activity. To construct a dual-functional surface simultaneously possessing antibacterial and anti-protein functions, Gao et al. engineered an amino-terminated hyperbranched poly (amidoamine) (HBPAA) with inherent hydrophobicity internally and hydrophilicity externally. This arrangement streamlines the formation of a stronger and denser antibacterial hydrophilic layer (Gao et al., 2021). They further prepared a biomimetic super-hydrophilic patterned (rough) surface through an *in-situ* approach, creating biocompatible polydopamine (PDA) microparticles (MP) on the surface of a biodegradable ureteral stent. They then chemically grafted HBPAA onto the PDA MP, resulting in a highly hydrophilic surface designed for contact-killing. The surface exhibited robust resistance to protein adhesion and achieved synergistic antibacterial and anti-protein adhesion activity. They fabricated the ureteral stent using poly (glycolic acid) (PGA) and poly (lactide-co-glycolide) (GA/LA ratio of 9:1) fibers woven into a structure and converted into a PGA fiber-PGLA membrane structure ureteral stent (FMBUS) through melt processing. Experimental results demonstrated that FMBUS had radial resistance similar to polyurethane ureteral stents (PUUS) used clinically, and no significant decrease in mechanical performance was observed after modification with PDA and HBPAA. Surface charge measurements confirmed that the surface charge of FMBUS could be controlled by adding HBPAA. Results from protein adsorption assessment indicated that increasing amino content could enhance surface hydrophilicity, and the improvement in surface hydrophilicity could provide sufficient repellence to overcome the electrostatic attraction of proteins. *In vitro* and *in vivo* antibacterial experiments proved its effective bacterial inhibition. Cytotoxicity experiments demonstrated that HBPAA-PDA-FMBUS had good biocompatibility. The stent holds great clinical potential for preventing urinary tract infections (UTIs) and stent surface encrustation caused by ureteral stents in the future.

In 2022, Tie et al. fabricated Mg-1.0Sr-0.5Ag (wt.%) alloy (JQ alloy) through semi-solid rheo-extrusion (Tie et al., 2022). Their experimental results demonstrated a 111% increase in ultimate tensile strength for JQ alloy (223.7 MPa) compared to pure magnesium (105.9 MPa). There was a noteworthy improvement in both tensile strength and elongation at the breaking point, ensuring sufficient support performance of the scaffold throughout its entire degradation process. *In vitro* cell compatibility tests indicated that JQ alloy showed comparable cell compatibility and similar blood compatibility to pure magnesium. Pure magnesium has been proven to be a non-toxic implant material (Sun et al., 2019). *In vitro* antibacterial experiments showed that the release of magnesium ions and silver ions from the JQ alloy played a crucial role in its antibacterial effect. The JQ scaffold continuously degraded during the 12-week implantation, reducing the risk of urinary tract obstruction caused by biofilm formation. The reduction in urinary tract obstruction is beneficial for decreasing post-void residual urine volume, which can improve bladder function postoperatively. While this experiment yielded many scientifically significant positive results, additional randomized and prospective multicenter studies, employing diverse animal models, are required to thoroughly showcase the applicability of the alloy. Customization of alloy composition, long-term testing, and comparative studies with different magnesium alloys will be the main directions for future research.

During that very year, Ecevit et al. successfully grafted chitosan (CS) coating polymer chains with three distinct fatty acids (FAs): stearic acid (SA), oleic acid (OA), and linoleic acid (LinA). Afterwards, the CS-FA derivative solution was coated on the surface of a polyurethane (PU) scaffold. This study represents the initial evaluation of these coatings as antibacterial materials on PU-based ureteral stents (Ecevit et al., 2022). The researchers verified the minimal cytotoxicity of the formulated coatings, and the materials exhibited antibacterial potential against various microorganisms. This study provides a new idea for the future use of CS-FA as a surface coating in combination with biodegradable ureteral stents. In order to fully tap the potential of CS-FA as a surface coating for biodegradable ureteral stents, further research and clinical trials are needed.

4.3 Carcinoma treatment and prevention

Urothelial carcinoma can occur in both the upper and lower urinary tracts. The upper tract includes the ureters and the renal pelvis-calyceal system, while the lower tract comprises the urethra and bladder. It is a multifocal disease with a tendency for local recurrence and metastasis. According to the 2023 US cancer

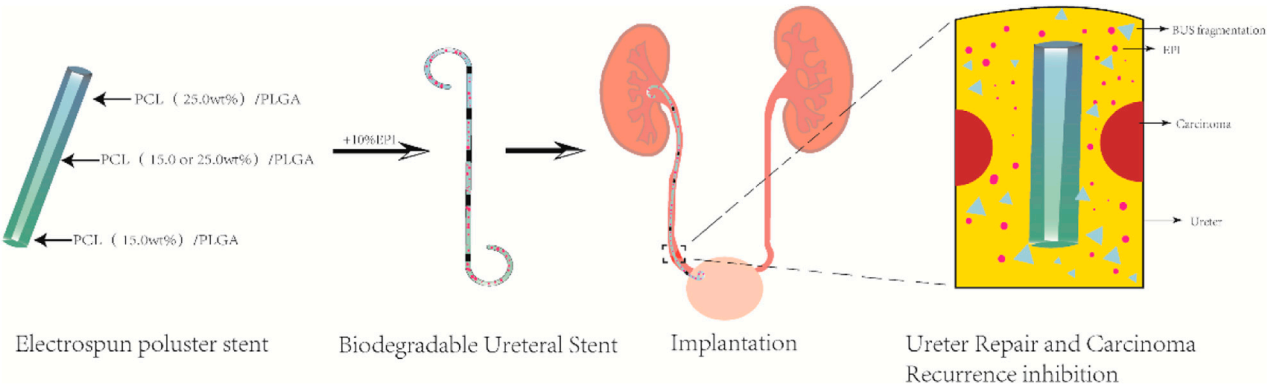

FIGURE 4
Illustration depicting the *in vivo* application of a ureteral stent to prevent the recurrence of upper urinary tract tumors and facilitate ureter repair.

statistics, bladder urothelial carcinoma is the fourth most common cancer in males in terms of incidence and the eighth most common in terms of mortality. Bladder tumors make up 90%–95% of urothelial carcinomas, which are the most common tumors in the urinary tract. In contrast, upper tract urothelial carcinoma (UTUC) is less common, with ureteral tumors accounting for only about 2.65% of urinary system tumors and a mortality rate of 3% (Siegel et al., 2023). UTUC is stratified into low-grade and high-grade risk levels. Low-grade UTUC patients benefit from nephron-sparing surgeries. After the surgery, it is crucial to place a ureteral stent to support the ureter and ensure the smooth flow of urine into the bladder. The most critical postoperative challenge is preventing tumor recurrence and managing the side effects associated with ureteral stent placement. To prevent the recurrence and progression of low-grade UTUC, drug instillation therapies can be used. Adjuvant instillation of mitomycin C (MMC) has shown promise in reducing the likelihood of urothelial recurrence and progression in individuals diagnosed with low-grade UTUC, offering hope for survival without nephroureterectomy (Metcalfe et al., 2017). However, administering intraluminal chemotherapy infusion is challenging due to the washout effect caused by urine produced by the kidneys and the limited storage capacity of the upper urinary tract, in comparison to bladder instillation (Jung et al., 2019). Patients with low-grade UTUC who undergo nephron-sparing surgery may not benefit from adjuvant chemotherapy instillation procedures, resulting in poorer outcomes. Biodegradable ureteral stents loaded with anti-tumor drugs offer a clinical prospect for tumor treatment and prevention by maintaining long-term effective drug concentrations at the lesion site. Furthermore, their self-degradation capability can overcome the drawbacks of traditional ureteral stents.

Wang et al. developed a biodegradable ureteral stent using electrospinning technology for the targeted delivery of anticancer drugs (Wang et al., 2019). Varying concentrations of the anticancer drug epirubicin (EPI) were loaded onto a gradient-degradable PCL/PLGA scaffold with 15.0% and 25.0% PCL, which was designed for treating UTUC (as shown in Figure 4). The various scaffolds displayed different degradation rates and kinetics of EPI release. The experimental results showed that the PCL/PLGA scaffold had the characteristics of sustained and controllable degradation. The degradation rate of the scaffold could be adjusted by modifying the PCL ratio, and reducing the PCL content could accelerate both drug release and degradation rates. The study demonstrated the effectiveness of the scaffold in inhibiting the growth of bladder tumor cells both *in vitro* and *in vivo*. Additionally, the *in vivo* application of all EPI-loaded scaffolds showed no apparent systemic toxicity. The research suggests that using electrospun polyester scaffolds with gradient degradation is a promising approach to support and repair ureteral drainage while preventing the proliferation of residual tumor cells.

Soria et al. developed a coating for the biodegradable ureteral stent BraidStent® using silk fibroin protein. They then loaded two formulations of mitomycin C into the polymer matrix to evaluate the stent's degradation rate, released mitomycin C concentration, and changes in pH and weight (Soria et al., 2022). The BraidStent® was divided into two groups: BraidStent-1, a long-term woven stent containing GlycomerTM 631 (a Biosyn suture produced by Covidien in Minneapolis, Minnesota, USA) and poly (4-hydroxybutyrate-co-hydroxyvalerate) (PGA); and BraidStent-2, a short-term woven stent containing GlycomerTM 631 and PGA. The polymer composition ratio for each stent remained constant during its manufacturing process: GlycomerTM 631 (54%); PGA and poly (4-hydroxybutyrate-co-hydroxyvalerate) (46%). After degradation in AU, BraidStent-2 was chosen because it complies with degradation standards within the first 7–8 weeks and has weaker medium acidification caused by degradation products compared to BraidStent-1. Silk fibroin coating and MMC formulation addition were performed on BraidStent-2. The results confirmed that the silk fibroin protein matrix can coat the biodegradable stent and release mitomycin C for 6–12 h in artificial urine. Furthermore, the BraidStent-SF-MMC exhibited a significantly delayed degradation rate compared to the uncoated biodegradable stent. The degradation time was extended from 6–7 weeks to 13–14 weeks. Although the degradation process caused a significant decrease in pH, it remained within the normal range for humans. The authors proposed that silk fibroin enables processability in multiple forms, including gel, membrane, coating, and stent. In 2023, Soria et al. conducted further evaluation of BraidStent-SF-MMC in a study involving 14 female pigs with single kidneys (Soria et al., 2023). The

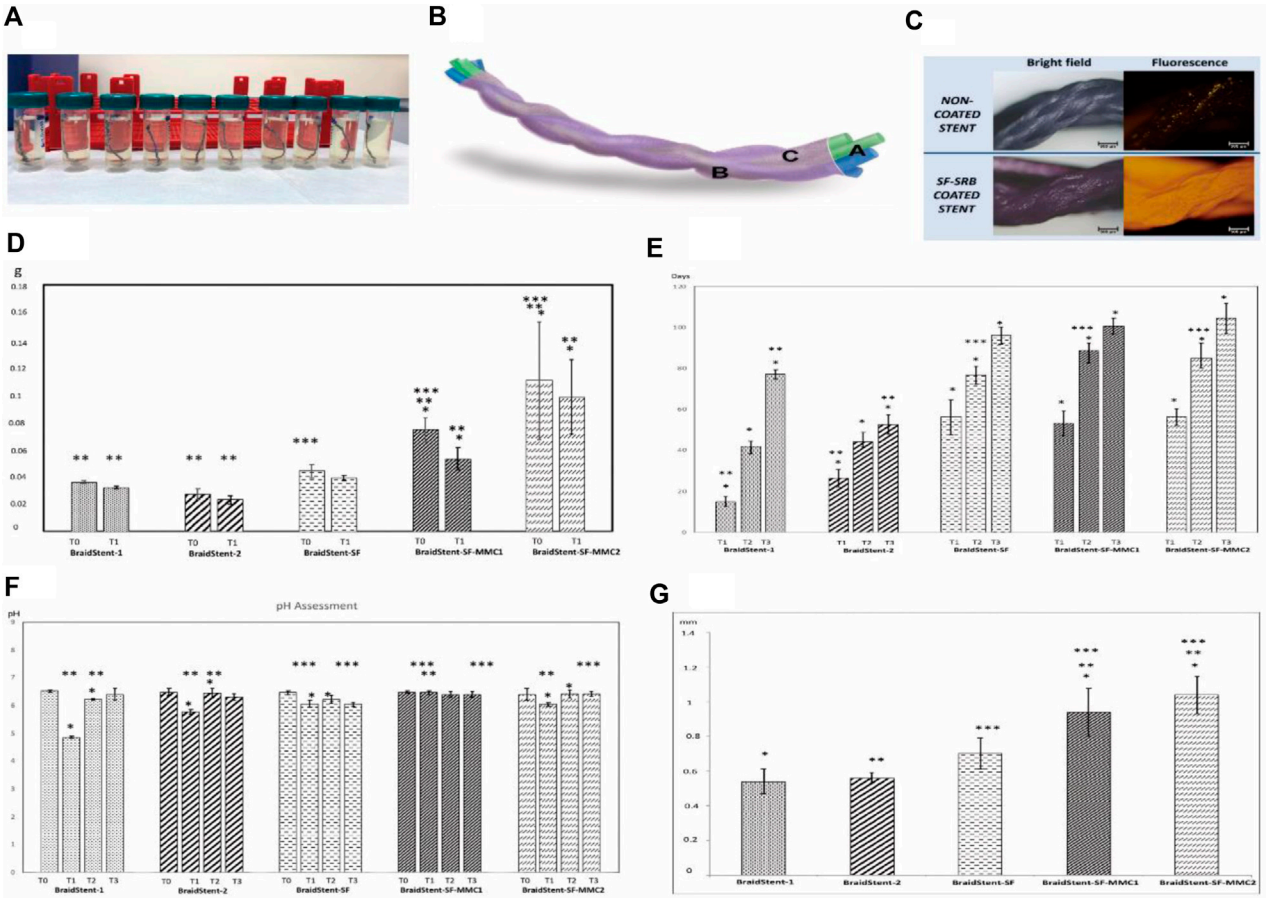

FIGURE 5
(A) Fragments of ureteral stents submerged in artificial urine on the 6th day. **(B)** Illustration of BraidStent-SF-MMC. **(C)** Evaluation of SF coating using SRB fluorescent dye. **(D)** Evaluation of the reduction in weight (in grams) from the initiation of the study (T0) to the commencement of stent degradation (T1). **(E)** Degradation rate assessment (days) **(F)** Assessment of pH throughout the study until complete stent degradation. **(G)** Initial (T0) stent thickness in the experimental groups (in millimeters). Reproduced with permission from ref (Soria et al., 2022). CC BY 4.0. Copyright © 2022 by the authors.

experimental results indicate that the stent was able to release mitomycin within the first 12 h. However, during the first and third weeks, 28.5% and 7.1% of the animals, respectively, experienced the release of obstructive ureteral coating fragments, which may have been caused by a pH < 7.0. Furthermore, a concerning 21% ureteral stricture rate was observed between weeks 4–6. In contrast to the previously mentioned *in vitro* degradation time, the stent completely degraded *in vivo* within 6–7 weeks (Refer to Figure 5 for further details).

4.4 Postoperative discomfort and pain management

Joshi et al. developed and validated the Ureteral Stent Symptom Questionnaire (USSQ). The questionnaire revealed that over 80% of patients with benign conditions who undergo stent implantation experience symptoms of irritative voiding, pain, and discomfort (Joshi et al., 2003). Harper et al. discovered a noteworthy rise in stent-related symptoms among patients on the first day after surgery. However, there was an approximately 50% reduction in pain intensity from postoperative day 1 to day 5, yet the interference caused by pain continued to rise (Harper et al., 2023). Pharmacological intervention is often required to manage lower urinary tract symptoms (LUTS) and stent-induced pain. Treatment options include alpha-1 receptor blockers and antimuscarinic agents such as solifenacin or a combination of solifenacin and tamsulosin (He et al., 2016). To alleviate the pain caused by ureteral smooth muscle contractions resulting from stent implantation, spasmolytic drugs such as papaverine hydrochloride (PAP) are used. This helps to reduce patient discomfort.

Antonowicz et al. (2021) conducted a study on polyurethane ureteral stents coated with poly (lactic-co-glycolic acid) (PLGA) 85/15 containing papaverine hydrochloride (PAP). The research shows that stents coated with PLGA+PAP have better strength properties and a lower dynamic frictional force compared to polyurethane stents, without compromising fluoroscopic visibility (Refer to Figure 6 for further details).

Soon afterwards, they investigated the impact of artificial urine on the physical and chemical properties of PLGA+PAP-coated stent tubes, building upon the foundation of previous studies on the stent tubes (Antonowicz et al., 2022). The study showed that applying PAP coating increased surface hydrophilicity, which could make stent implantation easier. The amount of PAP in the coating

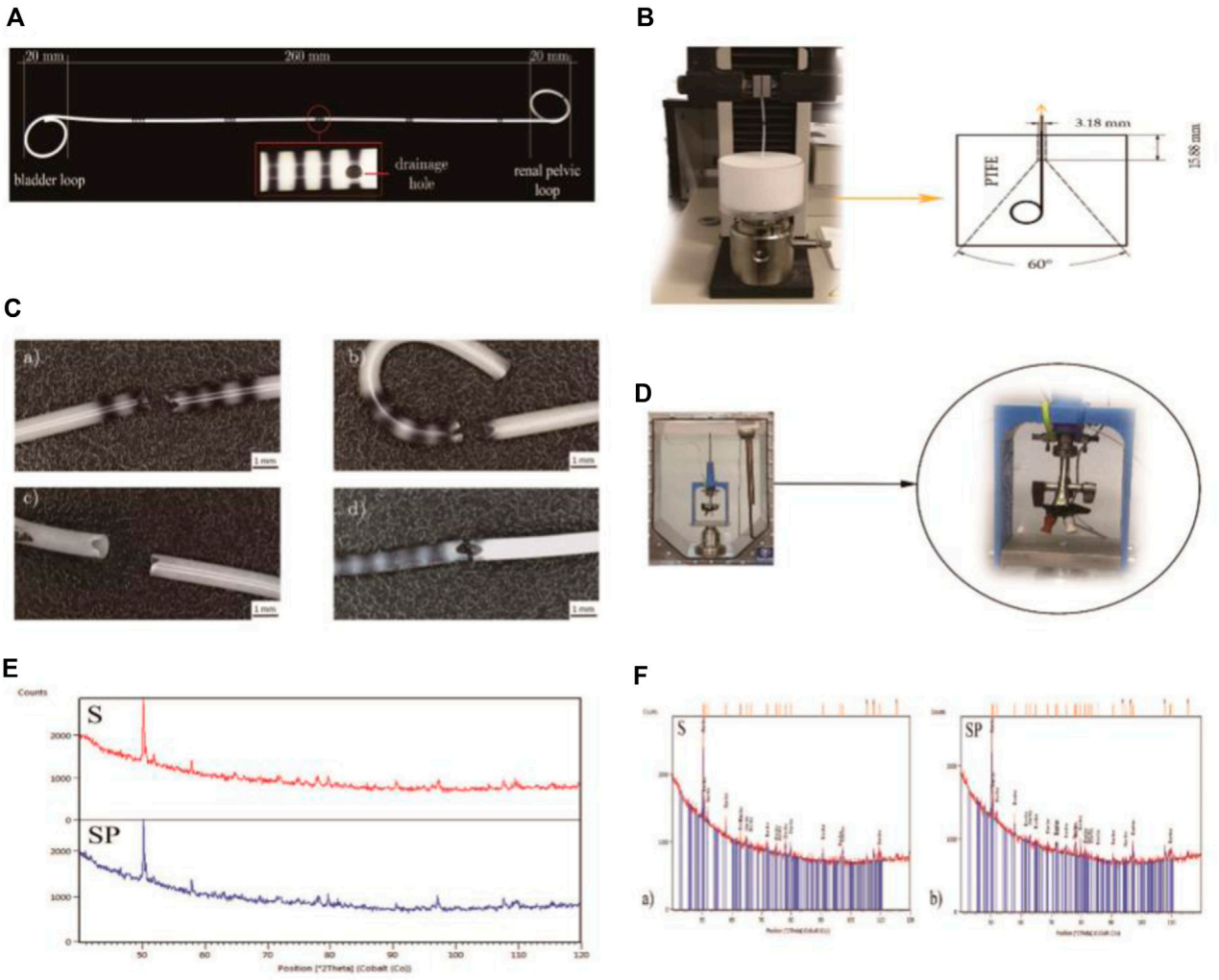

FIGURE 6
(A) Polyurethane Double-J ureteral stents. **(B)** Apparatus for evaluating the retention strength of the distal and proximal ends of ureteral stents. **(C)** Ureteral stents post static tensile testing. **(D)** Experimental setup for conducting dynamic frictional force tests. **(E)** X-ray diffraction (XRD) patterns for the polyurethane stent (S) and the coated stent (SP). **(F)** XRD patterns of the barium sulphate (BaSO4) standard for the ureteral stents. Reproduced with permission from ref (Antonowicz et al., 2021). CC BY 4.0. Copyright © 2021 by the authors.

decreased to 77% on the 10th day and further to 36% after 20 days. The early release of PAP was advantageous as it caused ureteral dilation, reducing patient discomfort. However, stents coated with PLGA+PAP exhibited increased surface roughness, which made them susceptible to the deposition of artificial urine components. Therefore, further refinement is necessary for the developed stents, with a focus on achieving uniform drug distribution, appropriate polymer degradation time, and a smooth, even drug-loaded layer. Additionally, *in vivo* studies are necessary to confirm the effectiveness of the incorporated drug, as the experiments were limited to *in vitro* validation.

In the same year, Soria et al. introduced the BraidStent®-H. Unlike traditional ureteral stents, the distal end of BraidStent®-H is positioned 2 cm above the ureteral orifice, avoiding bladder irritation and the consequent lower urinary tract symptoms (LUTS). The schematic representation of the stent design is illustrated in Figure 7 (Soria et al., 2021b). Existing literature supports the idea that the highest nerve density in the human ureter is located in the distal region (Vernez et al., 2017). Therefore, BraidStent®-H, by expanding along the ureter, can reduce ureteral spasms, consequently minimizing the onset of acute pain. In their study, during the 6-week implantation period, the BraidStent®-H significantly mitigated the side effects associated with conventional stents, as it did not exhibit VUR or induce bladder irritation.

4.5 Prevention and treatment of ureteral stricture

Ureteral strictures are frequently caused by inflammation, stones, trauma, surgical scars, and iatrogenic injuries. Iatrogenic factors account for approximately 75% of cases (Delvecchio et al., 2003). Urothelial cells, like vascular endothelial cells, respond to injuries by inducing excessive proliferation of fibroblasts and smooth muscle cells. This leads to progressive scarring and

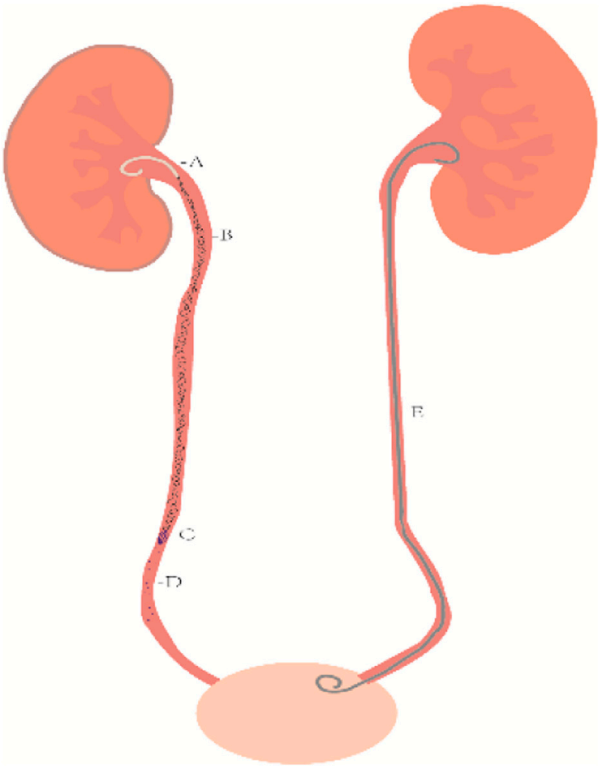

FIGURE 7
Illustration of the upper urinary tract BraidStent®-H. **(A)** proximal pig tail. **(B)** Central portion with a four-line braid. **(C)** Distal anchoring system with a rounded four-line braid. **(D)** Degradation fragments. **(E)** Clinically common non-degradable ureteral stent.

eventual ureteral stricture. Severe strictures can cause obstruction by compressing and deforming ureteral stents. Therefore, the idea of drug-eluting stents with anti-fibrotic properties has been suggested.

The use of biocompatible stents loaded with anti-proliferative drugs, such as paclitaxel, rapamycin, or sunitinib, allows for sustained and controlled drug release to prevent cell proliferation. Research has extensively focused on drug-eluting stents for cardiovascular applications, with studies indicating improved vascular healing with such coatings (Steigerwald et al., 2012). In comparison to cardiovascular stents, drug-loaded biodegradable ureteral stents offer the advantage of partial excretion of drug and polymer fragments through urine after drug release and stent degradation. In 2011, Will et al. (2011) assessed the influence of paclitaxel on the proliferation of ureteral smooth muscle cells and collagen production. The study showed that paclitaxel effectively inhibits smooth muscle cell proliferation and reduces collagen production. Additionally, it was found to be non-toxic to smooth muscle cells.

Kram et al. (2020) investigated the effectiveness of paclitaxel-coated stents in inhibiting tissue proliferation in a rat model. The study involved performing ureteral anastomosis in rats and inserting either coated or uncoated stents. After 28 days, the rats were euthanized, and the ureters were examined histologically and immunohistochemically. The results showed a significant reduction in the proliferation of urothelial cells in animals with paclitaxel-coated stents. However, there were no significant differences in stent patency, migration, or biofilm formation between coated and uncoated stents. The drug released from the stent was limited to the ureter, maintaining its concentration within a non-toxic range. Therefore, their experiments support the idea that coated stents can effectively reduce tissue proliferation in ureteral anastomosis and prevent postoperative stricture formation.

Afterwards, Ho et al. investigated the impact of a drug-eluting biodegradable stent (DE stent) loaded with an mTOR inhibitor (mTORi) on ureteral stricture associated with thermal injury in rabbits (Ho et al., 2021). The DE stent is a recognized device for inhibiting coronary artery restenosis. Their study demonstrated that treatment with a biodegradable stent releasing rapamycin significantly alleviated thermal injury-induced urinary obstruction and reduced the levels of fibrotic proteins.

It is not a mere coincidence that Hu et al. developed a dual-layer drug-eluting ureteral stent with rapamycin loaded onto an optimized 75/25 poly (lactic-co-glycolic acid) (PLGA) and polycaprolactone (PCL) dual-layer polyurethane ureteral stent (Hu et al., 2023). This dual-layer stent prevents the sudden loss of drugs and maintains a sustained delivery time. Their results indicate a significant effect of the drug-eluting stent in inhibiting ureteral scar proliferation compared to the bare stent. Moreover, the dual-layer stent with PCL as the outer layer exhibits a slower release rate of rapamycin than a single-layer PLGA stent. The drug release rate of PLGA/drug/PCL gradually increases over 21 days, providing a consistent inhibitory effect on ureteral stenosis.

The anti-proliferative drug-coated stents, upon future commercialization, are poised to not only prevent postoperative strictures caused by scar formation after reconstructive surgery but also to preclude urothelial proliferation reactions in patients with non-anastomotic ureteral openings. This development not only addresses the risk of postoperative complications in reconstructive surgery but also mitigates urothelial proliferation concerns in patients with yet-to-be-anastomosed ureteral openings.

5 Limitations/shortcomings and strategies for improvement

After years of dedicated research, significant progress has been made in the field of biodegradable ureteral stents (BUS). Many BUS have demonstrated improved performance through continuous efforts for refinement. However, BUS currently still has three major limitations. In the fabrication of scaffolds, it is necessary for researchers to select materials with high biosafety to make BUS. Meanwhile, it is worth exploring how to use processing technology suitable for standardized mass production to produce scaffolds with excellent performance. BUS degradation should be controlled, and degradation debris should not be too large to avoid urinary obstruction. The balance between the ideal degradation time for scaffolds and adequate mechanical properties when degraded remains a challenge. Drug release safety cannot be ignored when developing stents. *In vitro* experiments, the standardization of *in vitro* degradation results may be hampered by the lack of a uniform standard for simulating *in vitro* hydrodynamic conditions and simulating artificial urine to test BUS. Thus, it becomes imperative to develop appropriate standard detection methods to obtain reliable and comparable results, thus contributing to new and

better advances in this area. In terms of *in vivo* experiments, most of the current *in vivo* experiments are mainly based on animal experiments. Clinical experiments are different from animal experiments, and human subjects cannot achieve the same control variables as experimental animals. Human subjects have differences in diet, physique, etc. Therefore, the safety, degradability and functional efficacy of BUS scaffolds still need to be confirmed by clinical trials with a large sample size. Here, we present innovative solutions to address the challenges posed by the development of BUS, which may inspire future BUS development.

5.1 Material innovation

Currently, the predominant scaffolds consist primarily of materials such as PLGA and PLCL. These polymers are mainly bulk degradation modes. An ideal characteristic of this mode is that, under optimal conditions, the mass of the sample remains constant during the initial stages of degradation while the molecular weight continues to decrease. The structure of the sample collapsed, resulting in small fragments. Conversely, the alternative form of degradation is surface corrosion, which initiates from the material's surface and is characterized as "layer-by-layer degradation." The identification of materials possessing surface corrosion properties for constructing BUS could address the issue of sudden support cracking. At the same time, materials whose degradation mode is dominated by surface dissolution during the degradation process are more suitable to be used as drug carriers in the constant rate release drug delivery system (Zhang et al., 2008).

Poly (trimethylene carbonate) (PTMC) has recently gained widespread attention. TMC exhibits unique degradation behaviors, including the production of non-acidic degradation products, resistance to non-enzymatic hydrolysis, and a surface erosion mechanism induced by enzymatic degradation (Fukushima, 2016). Yang et al. synthesized a biodegradable network based on PTMC through the ring-opening polymerization of TMC and CL. The network's glass transition temperature was found to be below physiological temperature (37°C), suggesting its rubbery nature for *in vivo* applications (Yang et al., 2013). It is anticipated that in future development, there will be intensive studies on ureteral stents that are based on the unique degradation properties of PTMC and *in vivo* rubber properties.

The degradation rate of BUS is primarily governed by the choice of the stent's material, allowing for future customization of degradation times based on the selected combination of biodegradable biomaterials and their inherent properties. Yang et al.'s *in vitro* degradation experiments revealed that crosslinking significantly influences degradation behavior. The crosslinked PTMC network is less sensitive and more resistant to lipase degradation, but it exhibits superior shape stability compared to the non-crosslinked PTMC network. Additionally, the degradation of the crosslinked PTMC network is faster in enzymatic degradation than hydrolytic degradation. In in vivo degradation experiments, crosslinking can be adjusted by modulating crosslink density and incorporating CL content to regulate the PTMC degradation rate (Yang et al., 2016). Urine contains amylase and uricase (Stump et al., 1986; Zheng et al., 1991). Therefore, the enzymatic properties of PTMC may have future applications in urology.

Liu et al. prepared a biodegradable elastic PTMC/PLC (80/20) networked ureteral stent (Liu et al., 2021). The *in vitro* degradation experiment of the scaffold demonstrated that the scaffold underwent relatively rapid erosion, facilitated by porcine pancreatic lipase. Surface erosion was observable under SEM, and the scaffold retained adequate tensile strength throughout the degradation process. At the same time, the network is biocompatible. This experiment was lacking in in vivo degradation experiments and clinical trials of this scaffold.

PTMC may become one of the materials for future development in biodegradable ureteral stent (BUS) research, and we are currently conducting research on materials for ureteral stent tubes. Perhaps in the future, copolymers with distinct properties in enzymatic and hydrolytic degradation can be utilized to craft stents with ideal degradation times.

Scaffold surface crusting is a significant issue in clinical stent implantation due to the formation of biofilms composed of bacteria that can cause catheter and scaffold scaling. Current research is primarily focused on slow-release antibiotic coatings, but resistance remains a concern. Biocompatible antifouling coatings, such as novel biomaterials with properties like antimicrobial peptide coatings and brush materials, may be crucial for future BUS development. Yao et al. demonstrated that scaffolds containing antimicrobial peptides exhibit good biocompatibility and inhibit bacterial growth and biofilm formation *in situ*. This ultimately reduces the deposition of struvite and hydroxyapatite crystals, both *in vitro* and *in vivo* (Yao et al., 2022).

Polyvinylpyrrolidone iodine (PVP-I) is a hydrophilic polymer material that can help prevent urinary tract infections. This antibacterial material is not an antibiotic and may significantly reduce the production of drug-resistant bacteria. Khandwekar et al. found that the deposition of struvite and hydroxyapatite, the main components of urinary tract calculus, was significantly reduced on PVP-I modified polyurethanes, especially the reduction of hydroxyapatite calculus (Khandwekar and Doble, 2011). The support exhibits excellent anti-adhesion and anti-scaling properties, as well as remarkable durability. However, the stent has not been extensively studied *in vivo*. Therefore, it is imperative to investigate its effects on animal models and its application to BUS.

The clinical functionality of the stent is primarily manifested by the drug delivery system incorporated into the stent. Nanoparticles made from biodegradable polyester have gained significant attention as a drug delivery system (Cheng and Pun, 2015). Nanoparticles have the advantages of actively targeting and protecting normal cells from damage and improving the therapeutic effect of loaded drugs (Park, 2014).

Owing to the existence of blood vessel barriers, the penetration of nanomaterials into tissues occurs at a slower rate compared to small molecule drugs (Poste et al., 1982). In order to reduce the clearance of the reticuloendothelial system (RES), the development of the cloaking function of the nanocarriers has become a research hotspot. Wen et al. (2023) reviewed the cloaking nanocarriers in detail and proposed the concept of the "pseudo-stealth effect." In future developments, the antifouling or invisibility properties and biocompatibility of the polymer coating of the scaffolds should be

key to future BUS functional development and translational clinical applications.

5.2 Manufacturing process innovation

The innovation in the BUS manufacturing process has the potential to enhance both the physical and chemical properties of the scaffold. 3D-printed stents have the capability to design geometric shapes that are specific to individual patients and possess complexity, thereby achieving optimal mechanical properties. Moreover, it is feasible to 3D-print smart materials endowed with shape memory.

At present, 3D printing has been successfully applied to the manufacture of trachea stents and cardiovascular stents (Zopf et al., 2013; Sousa et al., 2022). Although this technology has been used in the development of non-degradable ureteral stents (Lee et al., 2022), However, there are still few researches on the application of 3D printing technology to BUS production.

Chang et al. (2020) applied 3D printing technology to the production of BUS, and they confirmed that the scaffolds produced by 3D printing technology had suitable mechanical properties and degradation rate.

Through the advancement of 3D printing technology, the biodegradable BUS survival approach emerges as a means to personalize and facilitate the mass production of ureteral stents. The successful integration of this technology with BUS is anticipated to contribute significantly to alleviating patient discomfort.

5.3 Tracking and follow-up capability innovation

In clinical practice, X-rays and computed tomography (CT) are considered the most common and least invasive tools for observing the condition of medical implants in the body (Samuel et al., 2015). Given the challenges of stent breakage and displacement in BUS, the tracking and follow-up capabilities of the stent hold paramount significance. Consequently, the development of BUS with suitable radio-impermeability warrants our attention.

Chang et al. introduced three radiopaque agents into polyglyceryl sebacate acrylate (PGSA), including barium sulfate, bismuth basic carbonate $(BiO)_2CO_3$), and bismuth oxychloride (BiOCl) (Chang et al., 2020). Experimental findings indicate that the mechanical properties of bismuth oxychloride-embedded PGSA (PGSA-BIOCL) at an embedding concentration of 25 wt% surpass those of PGSA-$Baso_4$ and PGSA-$(BiO)_2CO_3$. Furthermore, it demonstrates high linearity in non-transmittance. However, a linear correlation between the transmission linearity and the embedded content cannot be established. *In vitro* experiments reveal that PGSA-BiOCl25wt% exhibits commendable biocompatibility and degradability.

The advancement of materials and technologies amenable to tracking through rapid and non-invasive imaging techniques is poised to play a pivotal role in the initial development and clinical application of BUS. Moreover, the follow-up of various diseases is expected to be facilitated.

6 Future prospects

Since non-degradable stents are still widely used in clinical practice, the complication rate of stents is an issue that clinicians need to weigh, so BUS research is urgently needed for clinical application. The ideal BUS in the future should have: (1) good biocompatibility; (2) moderate mechanical properties to ensure ureteral drainage comfort; (3) complete biodegradation with no obstruction or biological damage caused by degradation products; (4) good ability to prevent migration; (5) diversity of stent functions; (6) good tracking ability. The "ideal" BUS has not yet been produced. The production of stents requires in-depth communication between various disciplines, including but not limited to medicine, materials science, pharmacy, molecular biology, etc.

The controlled degradation time of BUS can be adapted to physicians' different clinical decisions. For example, in cases of malignant tumors, clinicians currently require long-term placement of ureteral stents with periodic replacement, which is inconvenient for both healthcare professionals and patients. In 1 day, BUSs with extended degradation times may address this clinical treatment challenge. Conversely, short-degradation BUS may be more suitable for post-operative patients requiring short-term stent placement.

In addition to the versatile clinical applications for treating diseases with drugs, the surface coatings and drug-eluting capabilities of BUS can also facilitate localized drug delivery. In comparison to systemic administration, local drug delivery offers several advantages, such as reducing drug dosage and minimizing side effects. This may contribute to enhancing treatment efficiency and reducing the harm caused to patients by medications.

The fragments resulting from BUS degradation need to be small enough for easy expulsion from the ureter, avoiding the risk of ureteral obstruction. Simultaneously, the degradation products of BUS should not induce changes in the urinary environment within the human body. In the BUS developed by Jin et al. (2021), an increase in the artificial urine's pH was observed as a consequence of degradation. Hou et al. (2017) demonstrated that cross-linked poly (trimethylene carbonate) networks (PTMC-Ns) offer adjustable degradation rates, enhanced shape stability, and the advantage of producing non-acidic degradation by-products. Perhaps, in the future, the favorable biocompatibility and non-acidic degradation products of PTMC will be utilized in the development of BUS.

In the future, BUS will reduce stent infection, stent crusting, hematuria, pain and other complications caused by stent implantation. It will also reduce the time of stent implantation, reduce the frequency of stent replacement, and prevent stent forgetting. Further exchanges between medicine and other disciplines can promote the progress of human society.

7 Conclusion

This review summarizes the functions, clinical transformation, shortcomings and future prospects of BUS, and puts forward innovative suggestions to solve the related deficiencies. Currently, BUS scaffolds are unable to attain the ideal characteristics primarily due to challenges in controlling degradation time, mechanical

properties, and degradation fragments. Additionally, researchers encounter challenges in achieving the requisite drug release performance for the subsequent follow-up and functionalization of scaffolds. In order to solve the above problems, we believe that innovations need to be made in BUS manufacturing materials, BUS manufacturing processes, selection of BUS coating and development of tracking and follow-up functions, including PTMC as a scaffold material, the application of 3D printing technology, nanoparticle drug delivery and the use of developer. Additionally, the development of functionalities related to stent coatings and drug elution remains a current research focus. At the same time, the interdisciplinary cooperation and learning of biomaterials and medicine are inevitable in the development of BUS in the future, and the in-depth exchanges and communication between clinicians and material science experts will accelerate the development of BUS. In conclusion, BUS holds promising applications in the field of urological surgery.

Author contributions

KH: Writing–original draft. ZH: Writing–original draft. YH: Writing–original draft. XuL: Writing–original draft. XiL: Writing–review and editing. LiY: Writing–review and editing.

Funding

The author(s) declare financial support was received for the research, authorship, and/or publication of this article. This work was supported by the Natural Science Foundation of Liaoning Province (Grant No. 2022-YGJC-69), the support program for excellent young scholars of China Medical University, and the cross-research cooperation project of Dalian Medical University.

Conflict of interest

The authors declare that the research was conducted in the absence of any commercial or financial relationships that could be construed as a potential conflict of interest.

Publisher's note

References

Abbasi, A., Wyre, H. W., and Ogan, K. (2013). Use of full-length metallic stents in malignant ureteral obstruction. *J. Endourology* 27 (5), 640–645. doi:10.1089/end.2012.0448

Akay, A. F., Aflay, U., Gedik, A., Sahin, H., and Bircan, M. K. (2007). Risk factors for lower urinary tract infection and bacterial stent colonization in patients with a double J ureteral stent. *Int. Urology Nephrol.* 39 (1), 95–98. doi:10.1007/s11255-006-9150-1

Al-Aown, A., Kyriazis, I., Kallidonis, P., Kraniotis, P., Rigopoulos, C., Karnabatidis, D., et al. (2010). Ureteral stents: new ideas, new designs. *Ther. Adv. Urology* 2 (2), 85–92. doi:10.1177/1756287210370699

Antonowicz, M., Szewczenko, J., Jaworska, J., Jelonek, K., Joszko, K., Gzik-Zroska, B., et al. (2021). Functional properties of polyurethane ureteral stents with PLGA and papaverine hydrochloride coating. *Int. J. Mol. Sci.* 22 (14), 7705. doi:10.3390/ijms22147705

Antonowicz, M., Szewczenko, J., Kajzer, A., Kajzer, W., Jaworska, J., Jelonek, K., et al. (2022). Assessment of encrustation and physicochemical properties of poly(lactide-glycolide) - papaverine hydrochloride coating on ureteral double-J stents after long-term flow of artificial urine. *J. Biomed. Mater. Res. Part B-applied Biomaterials* 110 (2), 367–381. doi:10.1002/jbm.b.34913

Auge, B. K., Ferraro, R. F., Madenjian, A. R., and Preminger, G. M. (2002). Evaluation of a dissolvable ureteral drainage stent in a Swine model. *J. Urology* 168 (2), 808–812. doi:10.1016/s0022-5347(05)64748-9

Barros, A. A., Browne, S., Oliveira, C., Lima, E., Duarte, A. R., Healy, K. E., et al. (2016). Drug-eluting biodegradable ureteral stent: new approach for urothelial tumors of upper urinary tract cancer. *Int. J. Pharm.* 513 (1-2), 227–237. doi:10.1016/j.ijpharm.2016.08.061

Barros, A. A., Oliveira, C., Reis, R. L., Lima, E., and Duarte, A. R. (2015a). Ketoprofen-eluting biodegradable ureteral stents by CO_2 impregnation: *in vitro* study. *Int. J. Pharm.* 495 (2), 651–659. doi:10.1016/j.ijpharm.2015.08.040

Barros, A. A., Oliveira, C., Ribeiro, A. J., Autorino, R., Reis, R. L., Duarte, A. R. C., et al. (2018). *In vivo* assessment of a novel biodegradable ureteral stent. *World J. Urology* 36 (2), 277–283. doi:10.1007/s00345-017-2124-3

Barros, A. A., Rita, A., Duarte, C., Pires, R. A., Sampaio-Marques, B., Ludovico, P., et al. (2015b). Bioresorbable ureteral stents from natural origin polymers. *J. Biomed. Mater. Res. Part B-applied Biomaterials* 103 (3), 608–617. doi:10.1002/jbm.b.33237

Champeau, M., Thomassin, J. M., Tassaing, T., and Jérôme, C. (2015). Drug loading of polymer implants by supercritical CO_2 assisted impregnation: a review. *J. Control. Release* 209, 248–259. doi:10.1016/j.jconrel.2015.05.002

Chang, C. T., Chen, H. T., Girsang, S. P., Chen, Y. M., Wan, D. H., Shen, S. H., et al. (2020). 3D-printed radiopaque polymer composites for the *in situ* monitoring of biodegradable medical implants. *Appl. Mater. Today* 20, 100771. doi:10.1016/j.apmt.2020.100771

Chen, T., Zhao, X., and Weng, Y. (2022). Self-assembled polylactic acid (PLA): synthesis, properties and biomedical applications. *Front. Chem.* 10, 1107620. doi:10.3389/fchem.2022.1107620

Cheng, J., and Pun, S. H. (2015). Polymeric biomaterials for cancer nanotechnology. *Biomaterials Sci.* 3 (7), 891–893. doi:10.1039/c5bm90025e

Chew, B. H., Cadieux, P. A., Reid, G., and Denstedt, J. D. (2006). *Second prize*: *in-vitro* activity of triclosan-eluting ureteral stents against common bacterial uropathogens. *J. Endourology* 20 (11), 949–958. doi:10.1089/end.2006.20.949

Chew, B. H., Lange, D., Paterson, R. F., Hendlin, K., Monga, M., Clinkscales, K. W., et al. (2010). Next generation biodegradable ureteral stent in a yucatan pig model. *J. Urology* 183 (2), 765–771. doi:10.1016/j.juro.2009.09.073

Chew, B. H., Paterson, R. F., Clinkscales, K. W., Levine, B. S., Shalaby, S. W., and Lange, D. (2013). *In vivo* evaluation of the third generation biodegradable stent: a novel approach to avoiding the forgotten stent syndrome. *J. Urology* 189 (2), 719–725. doi:10.1016/j.juro.2012.08.202

Cui, H. P., Zhang, K., Gao, C. G., Kang, Y. H., and Jiang, H. Y. (2022). Design and characterization of a novel braided biodegradable double-J ureteral stent. *Polym. Adv. Technol.* 33 (8), 2519–2527. doi:10.1002/pat.5706

Delvecchio, F. C., Auge, B. K., Brizuela, R. M., Weizer, A. Z., Silverstein, A. D., Lallas, C. D., et al. (2003). Assessment of stricture formation with the ureteral access sheath. *Urology* 61 (3), 518–522. doi:10.1016/s0090-4295(02)02433-0

Ding, J. X., Feng, X. R., Jiang, Z. Y., Xu, W. G., Guo, H., Zhuang, X. L., et al. (2019). Polymer-Mediated penetration-independent cancer therapy. *Biomacromolecules* 20 (12), 4258–4271. doi:10.1021/acs.biomac.9b01263

Domingues, B., Pacheco, M., de la Cruz, J. E., Carmagnola, I., Teixeira-Santos, R., Laurenti, M., et al. (2022). Future directions for ureteral stent technology: from bench to the market. *Adv. Ther.* 5 (1), 2100158. doi:10.1002/adtp.202100158

Dumontel, B., Canta, M., Engelke, H., Chiodoni, A., Racca, L., Ancona, A., et al. (2017). Enhanced biostability and cellular uptake of zinc oxide nanocrystals shielded with a phospholipid bilayer. *J. Mater. Chem. B* 5 (44), 8799–8813. doi:10.1039/c7tb02229h

Ecevit, K., Silva, E., Rodrigues, L. C., Aroso, I., Barros, A. A., Silva, J. M., et al. (2022). Surface functionalization of ureteral stents-based polyurethane: engineering antibacterial coatings. *Mater. (Basel)* 15 (5), 1676. doi:10.3390/ma15051676

Edgar, J. Y. C., and Wang, H. (2017). Introduction for design of nanoparticle based drug delivery systems. *Curr. Pharm. Des.* 23 (14), 2108–2112. doi:10.2174/1381612822666161025154003

El-Hayek, G., Bangalore, S., Casso Dominguez, A., Devireddy, C., Jaber, W., Kumar, G., et al. (2017). Meta-analysis of randomized clinical trials comparing biodegradable

polymer drug-eluting stent to second-generation durable polymer drug-eluting stents. *JACC-Cardiovascular Interv.* 10 (5), 462–473. doi:10.1016/j.jcin.2016.12.002

Finney, R. P. (1978). Experience with new double J ureteral catheter stent. *J. Urology* 120 (6), 678–681. doi:10.1016/s0022-5347(17)57326-7

Fu, J., Su, Y., Qin, Y. X., Zheng, Y., Wang, Y., and Zhu, D. (2020). Evolution of metallic cardiovascular stent materials: a comparative study among stainless steel, magnesium and zinc. *Biomaterials* 230, 119641. doi:10.1016/j.biomaterials.2019.119641

Fukushima, K. (2016). Poly(trimethylene carbonate)-based polymers engineered for biodegradable functional biomaterials. *Biomaterials Sci.* 4 (1), 9–24. doi:10.1039/c5bm00123d

Gao, L., Liu, X., Xu, M., Sun, G., Xu, S., Zou, T., et al. (2021). Biodegradable anti-biofilm fiber-membrane ureteral stent constructed with a robust biomimetic superhydrophilic polycationic hydration surface exhibiting synergetic antibacterial and antiprotein properties. *Small* 17 (20), 2006815. doi:10.1002/smll.202006815

Gao, L., Wang, Y., Li, Y., Xu, M., Sun, G., Zou, T., et al. (2020). Biomimetic biodegradable Ag@Au nanoparticle-embedded ureteral stent with a constantly renewable contact-killing antimicrobial surface and antibiofilm and extraction-free properties. *Acta Biomater.* 114, 117–132. doi:10.1016/j.actbio.2020.07.025

Garino, N., Sanvitale, P., Dumontel, B., Laurenti, M., Colilla, M., Izquierdo-Barba, I., et al. (2019). Zinc oxide nanocrystals as a nanoantibiotic and osteoinductive agent. *RSC Adv.* 9 (20), 11312–11321. doi:10.1039/c8ra10236h

Gibbons, R. P., Mason, J. T., and Correa, R. J. (1974). Experience with indwelling silicone rubber ureteral catheters. *J. Urology* 111 (5), 594–599. doi:10.1016/s0022-5347(17)60023-5

Hadaschik, B. A., Paterson, R. F., Fazli, L., Clinkscales, K. W., Shalaby, S. W., and Chew, B. H. (2008). Investigation of a novel degradable ureteral stent in a porcine model. *J. Urology* 180 (3), 1161–1166. doi:10.1016/j.juro.2008.05.003

Harper, J. D., Desai, A. C., Maalouf, N. M., Yang, H., Antonelli, J. A., Tasian, G. E., et al. (2023). Risk factors for increased stent-associated symptoms following ureteroscopy for urinary stones: results from STENTS. *J. Urology* 209 (5), 971–980. doi:10.1097/ju.0000000000003183

He, F., Man, L. B., Li, G. Z., and Liu, N. (2016). Efficacy of α-blocker in improving ureteral stent-related symptoms: a meta-analysis of both direct and indirect comparison. *Drug Des. Dev. Ther.* 10, 1783–1793. doi:10.2147/dddt.s103195

Hepperlen, T. W., Mardis, H. K., and Kammandel, H. (1978). Self-retained internal ureteral stents: a new approach. *J. Urology* 119 (6), 731–733. doi:10.1016/s0022-5347(17)57613-2

Herdman, J. P. (1949). Polythene tubing in the experimental surgery of the ureter. *Br. J. Surg.* 37 (145), 105–106. doi:10.1002/bjs.18003714520

Ho, D. R., Su, S. H., Chang, P. J., Lin, W. Y., Huang, Y. C., Lin, J. H., et al. (2021). Biodegradable stent with mTOR inhibitor-eluting reduces progression of ureteral stricture. *Int. J. Mol. Sci.* 22 (11), 5664. doi:10.3390/ijms22115664

Hou, Z., Hu, J., Li, J., Zhang, W., Li, M., Guo, J., et al. (2017). The *in vitro* enzymatic degradation of cross-linked poly(trimethylene carbonate) networks. *Polym. (Basel)* 9 (11), 605. doi:10.3390/polym9110605

Hu, J., Wang, Z., Hu, H., Zhao, J., Li, H., Zhang, X., et al. (2023). *In vitro* and *in vivo* assessment of a bilayered degradable rapamycin-eluting stent for ureteral stricture caused by holmium: YAG laser lithotripsy. *Acta Biomater.* 172, 321–329. doi:10.1016/j.actbio.2023.10.009

Jin, L., Yao, L., Yuan, F., Dai, G., and Xue, B. (2021). Evaluation of a novel biodegradable ureteral stent produced from polyurethane and magnesium alloys. *J. Biomed. Mater. Res. Part B-Applied Biomaterials* 109 (5), 665–672. doi:10.1002/jbm.b.34730

Jin, L., Yao, L., Zhou, Y., Dai, G., Zhang, W., and Xue, B. (2018). Investigation of a novel gradient degradable ureteral stent in a beagle dog model. *J. Biomaterials Appl.* 33 (3), 466–473. doi:10.1177/0885328218792839

Joshi, H. B., Newns, N., Stainthorpe, A., MacDonagh, R. P., Keeley, F. X., Jr., and Timoney, A. G. (2003). Ureteral stent symptom questionnaire: development and validation of a multidimensional quality of life measure. *J. Urology* 169 (3), 1060–1064. doi:10.1097/01.ju.0000049198.53424.1d

Jung, H., Giusti, G., Fajkovic, H., Herrmann, T., Jones, R., Straub, M., et al. (2019). Consultation on UTUC, Stockholm 2018: aspects of treatment. *World J. Urology* 37 (11), 2279–2287. doi:10.1007/s00345-019-02811-w

Kehinde, E. O., Rotimi, V. O., Al-Hunayan, A., Abdul-Halim, H., Boland, F., and Al-Awadi, K. A. (2004). Bacteriology of urinary tract infection associated with indwelling J ureteral stents. *J. Endourology* 18 (9), 891–896. doi:10.1089/end.2004.18.891

Khandwekar, A. P., and Doble, M. (2011). Physicochemical characterisation and biological evaluation of polyvinylpyrrolidone-iodine engineered polyurethane (Tecoflex®). *J. Mater. Science-Materials Med.* 22 (5), 1231–1246. doi:10.1007/s10856-011-4285-8

Klis, R., Korczak-Kozakiewicz, E., Denys, A., Sosnowski, M., and Rozanski, W. (2009). Relationship between urinary tract infection and self-retaining double-J catheter colonization. *J. Endourology* 23 (6), 1015–1019. doi:10.1089/end.2008.0518

Ko, R., Cadieux, P. A., Dalsin, J. L., Lee, B. P., Elwood, C. N., and Razvi, H. (2008). First prize: novel uropathogen-resistant coatings inspired by marine mussels. *J. Endourology* 22 (6), 1153–1160. doi:10.1089/end.2008.0049

Kram, W., Rebl, H., Wyrwa, R., Laube, T., Zimpfer, A., Maruschke, M., et al. (2020). Paclitaxel-coated stents to prevent hyperplastic proliferation of ureteral tissue: from *in vitro* to *in vivo*. *Urolithiasis* 48 (1), 47–56. doi:10.1007/s00240-018-1081-7

Kutcher, M. A. (2018). Biodegradable-polymer drug-eluting stent platforms: the importance of long-term outcomes. *JACC-Cardiovascular Interv.* 11 (10), 1003–1005. doi:10.1016/j.jcin.2018.04.025

Lange, D., Bidnur, S., Hoag, N., and Chew, B. H. (2015). Ureteral stent-associated complications-where we are and where we are going. *Nat. Rev. Urol.* 12 (1), 17–25. doi:10.1038/nrurol.2014.340

Laurenti, M., Grochowicz, M., Dragoni, E., Carofiglio, M., Limongi, T., and Cauda, V. (2020). Biodegradable and drug-eluting inorganic composites based on mesoporous zinc oxide for urinary stent applications. *Mater. (Basel)* 13 (17), 3821. doi:10.3390/ma13173821

Laurenti, M., Lamberti, A., Genchi, G. G., Roppolo, I., Canavese, G., Vitale-Brovarone, C., et al. (2019). Graphene oxide finely tunes the bioactivity and drug delivery of mesoporous ZnO scaffolds. *ACS Appl. Mater. Interfaces* 11 (1), 449–456. doi:10.1021/acsami.8b20728

Lee, J., Sung, J., Jo, J. K., and So, H. (2022). 3D-Printing-Assisted extraluminal anti-reflux diodes for preventing vesicoureteral reflux through double-J stents. *Int. J. Bioprinting* 8 (2), 549. doi:10.18063/ijb.v8i2.549

Lingeman, J. E., Preminger, G. M., Berger, Y., Denstedt, J. D., Goldstone, L., Segura, J. W., et al. (2003a). Use of a temporary ureteral drainage stent after uncomplicated ureteroscopy: results from a phase II clinical trial. *J. Urology* 169 (5), 1682–1688. doi:10.1097/01.ju.0000055600.18515.a1

Lingeman, J. E., Schulsinger, D. A., and Kuo, R. L. (2003b). Phase I trial of a temporary ureteral drainage stent. *J. Endourology* 17 (3), 169–171. doi:10.1089/089277903321618734

Liu, J., Wang, J., Xue, Y. F., Chen, T. T., Huang, D. N., Wang, Y. X., et al. (2020). Biodegradable phosphorylcholine copolymer for cardiovascular stent coating. *J. Mater. Chem. B* 8 (24), 5361–5368. doi:10.1039/d0tb00813c

Liu, X. L., Liu, S., Li, K. Q., Fan, Y. K., Feng, S. M., Peng, L. J., et al. (2021). Preparation and property evaluation of biodegradable elastomeric PTMC/PLCL networks used as ureteral stents. *Colloids Surfaces A-Physicochemical Eng. Aspects* 630, 127550. doi:10.1016/j.colsurfa.2021.127550

Lock, J. Y., Wyatt, E., Upadhyayula, S., Whall, A., Nuñez, V., Vullev, V. I., et al. (2014). Degradation and antibacterial properties of magnesium alloys in artificial urine for potential resorbable ureteral stent applications. *J. Biomed. Mater. Res. Part A* 102 (3), 781–792. doi:10.1002/jbm.a.34741

Lü, J. M., Wang, X., Marin-Muller, C., Wang, H., Lin, P. H., Yao, Q., et al. (2009). Current advances in research and clinical applications of PLGA-based nanotechnology. *Expert Rev. Mol. Diagnostics* 9 (4), 325–341. doi:10.1586/erm.09.15

Lumiaho, J., Heino, A., Aaltomaa, S., Välimaa, T., and Talja, M. (2011). A short biodegradable helical spiral ureteric stent provides better antireflux and drainage properties than a double-J stent. *Scand. J. Urology Nephrol.* 45 (2), 129–133. doi:10.3109/00365599.2010.544673

Lumiaho, J., Heino, A., Kauppinen, T., Talja, M., Alhava, E., Välimaa, T., et al. (2007). Drainage and antireflux characteristics of a biodegradable self-reinforced, self-expanding X-ray-positive poly-L,D-lactide spiral partial ureteral stent: an experimental study. *J. Endourology* 21 (12), 1559–1564. doi:10.1089/end.2005.0085

Luo, C. J., Stoyanov, S. D., Stride, E., Pelan, E., and Edirisinghe, M. (2012). Electrospinning versus fibre production methods: from specifics to technological convergence. *Chem. Soc. Rev.* 41 (13), 4708–4735. doi:10.1039/c2cs35083a

Martin, G. S., Mannino, D. M., Eaton, S., and Moss, M. (2003). The epidemiology of sepsis in the United States from 1979 through 2000. *N. Engl. J. Med.* 348 (16), 1546–1554. doi:10.1056/nejmoa022139

Mehrotra, N., Anees, M., Tiwari, S., Kharbanda, S., and Singh, H. (2023). Polylactic acid based polymeric nanoparticle mediated co-delivery of navitoclax and decitabine for cancer therapy. *Nanomedicine* 47, 102627. doi:10.1016/j.nano.2022.102627

Metcalfe, M., Wagenheim, G., Xiao, L., Papadopoulos, J., Navai, N., Davis, J. W., et al. (2017). Induction and maintenance adjuvant mitomycin C topical therapy for upper tract urothelial carcinoma: tolerability and intermediate term outcomes. *J. Endourology* 31 (9), 946–953. doi:10.1089/end.2016.0871

Monga, M., Klein, E., Castaneda-Zuniga, W. R., and Thomas, R. (1995). The forgotten indwelling ureteral stent: a urological dilemma. *J. urology* 153 (6), 1817–1819. doi:10.1016/s0022-5347(01)67319-1

Nguyen, N. T., Grelling, N., Wetteland, C. L., Rosario, R., and Liu, H. (2018). Antimicrobial activities and mechanisms of magnesium oxide nanoparticles (nMgO) against pathogenic bacteria, yeasts, and biofilms. *Sci. Rep.* 8 (1), 16260. doi:10.1038/s41598-018-34567-5

Park, K. (2014). Controlled drug delivery systems: past forward and future back. *J. Control. Release* 190, 3–8. doi:10.1016/j.jconrel.2014.03.054

Poste, G., Bucana, C., Raz, A., Bugelski, P., Kirsh, R., and Fidler, I. J. (1982). Analysis of the fate of systemically administered liposomes and implications for their use in drug delivery. *Cancer Res.* 42 (4), 1412–1422.

Reid, G., Denstedt, J. D., Kang, Y. S., Lam, D., and Nause, C. (1992). Microbial adhesion and biofilm formation on ureteral stents *in vitro* and *in vivo*. *J. Urology* 148 (5), 1592–1594. doi:10.1016/s0022-5347(17)36976-8

Saito, Y., Tanaka, T., Andoh, A., Minematsu, H., Hata, K., Tsujikawa, T., et al. (2007). Usefulness of biodegradable stents constructed of poly-l-lactic acid monofilaments in patients with benign esophageal stenosis. *World J. Gastroenterology* 13 (29), 3977–3980. doi:10.3748/wjg.v13.i29.3977

Salari, B., Khalid, M., Ivan, S., Ekwenna, O., Petros, F., Saltzman, B., et al. (2021). Urine versus stent cultures and clinical UTIs. *Int. Urology Nephrol.* 53 (11), 2237–2242. doi:10.1007/s11255-021-02964-x

Samuel, R., Girard, E., Chagnon, G., Dejean, S., Favier, D., Coudane, J., et al. (2015). Radiopaque poly (ε-caprolactone) as additive for X-ray imaging of temporary implantable medical devices. *RSC Adv.* 5 (102), 84125–84133. doi:10.1039/c5ra19488a

Serruys, P. W., Onuma, Y., Ormiston, J. A., de Bruyne, B., Regar, E., Dudek, D., et al. (2010). Evaluation of the second generation of a bioresorbable everolimus drug-eluting vascular scaffold for treatment of *de novo* coronary artery stenosis six-month clinical and imaging outcomes. *Circulation* 122 (22), 2301–2312. doi:10.1161/circulationaha.110.970772

Siegel, R. L., Miller, K. D., and Jemal, A. (2020). Cancer statistics, 2020. *A Cancer J. Clin.* 70 (1), 7–30. doi:10.3322/caac.21590

Siegel, R. L., Miller, K. D., Wagle, N. S., and Jemal, A. (2023). Cancer statistics, 2023. *A Cancer J. Clin.* 73 (1), 17–48. doi:10.3322/caac.21763

Soria, F., Aznar-Cervantes, S. D., de la Cruz, J. E., Budia, A., Aranda, J., Caballero, J. P., et al. (2022). Assessment of a coated mitomycin-releasing biodegradable ureteral stent as an adjuvant therapy in upper urothelial carcinoma: a comparative *in vitro* study. *Polym. (Basel)* 14 (15), 3059. doi:10.3390/polym14153059

Soria, F., Delacruz, J. E., Aznar-Cervantes, S. D., Aranda, J., Martínez-Pla, L., Cepeda, M., et al. (2023). Animal model assessment of a new design for a coated mitomycin-eluting biodegradable ureteral stent for intracavitary instillation as an adjuvant therapy in upper urothelial carcinoma. *Minerva Urology Nephrol.* 75 (2), 194–202. doi:10.23736/s2724-6051.23.05152-2

Soria, F., de La Cruz, J. E., Budia, A., Cepeda, M., Álvarez, S., Serrano, Á., et al. (2021a). Iatrogenic ureteral injury treatment with biodegradable antireflux heparin-coated ureteral stent-animal model comparative study. *J. Endourology* 35 (8), 1244–1249. doi:10.1089/end.2020.0591

Soria, F., de la Cruz, J. E., Budia, A., Serrano, A., Galan-Llopis, J. A., and Sanchez-Margallo, F. M. (2020). Experimental assessment of new generation of ureteral stents: biodegradable and antireflux properties. *J. Endourology* 34 (3), 359–365. doi:10.1089/end.2019.0493

Soria, F., de La Cruz, J. E., Fernandez, T., Budia, A., Serrano, Á., and Sanchez-Margallo, F. M. (2021b). Heparin coating in biodegradable ureteral stents does not decrease bacterial colonization-assessment in ureteral stricture endourological treatment in animal model. *Transl. Androl. Urology* 10 (4), 1700–1710. doi:10.21037/tau-21-19

Sousa, A. M., Amaro, A. M., and Piedade, A. P. (2022). 3D printing of polymeric bioresorbable stents: a strategy to improve both cellular compatibility and mechanical properties. *Polym. (Basel)* 14 (6), 1099. doi:10.3390/polym14061099

Steigerwald, K., Ballke, S., Quee, S. C., Byrne, R. A., Vorpahl, M., Vogeser, M., et al. (2012). Vascular healing in drug-eluting stents: differential drug-associated response of limus-eluting stents in a preclinical model of stent implantation. *EuroIntervention* 8 (6), 752–759. doi:10.4244/eijv8i6a115

Stump, D. C., Thienpont, M., and Collen, D. (1986). Purification and characterization of a novel inhibitor of urokinase from human urine. Quantitation and preliminary characterization in plasma. *J. Biol. Chem.* 261 (27), 12759–12766. doi:10.1016/s0021-9258(18)67158-3

Sun, Y., Wu, H., Wang, W., Zan, R., Peng, H., Zhang, S., et al. (2019). Translational status of biomedical Mg devices in China. *Bioact. Mater.* 4, 358–365. doi:10.1016/j.bioactmat.2019.11.001

Thakkar, S., and Misra, M. (2017). Electrospun polymeric nanofibers: new horizons in drug delivery. *Eur. J. Pharm. Sci.* 107, 148–167. doi:10.1016/j.ejps.2017.07.001

Tie, D., Feyerabend, F., Müller, W. D., Schade, R., Liefeith, K., Kainer, K. U., et al. (2013). Antibacterial biodegradable Mg-Ag alloys. *Eur. Cells Mater.* 25, 284–298. doi:10.22203/ecm.v025a20

Tie, D., Guan, R., Liu, H., Cipriano, A., Liu, Y., Wang, Q., et al. (2016). An *in vivo* study on the metabolism and osteogenic activity of bioabsorbable Mg-1Sr alloy. *Acta Biomater.* 29, 455–467. doi:10.1016/j.actbio.2015.11.014

Tie, D., Hort, N., Chen, M., Guan, R., Ulasevich, S., Skorb, E. V., et al. (2022). *In vivo* urinary compatibility of Mg-Sr-Ag alloy in swine model. *Bioact. Mater.* 7, 254–262. doi:10.1016/j.bioactmat.2021.05.046

Tomer, N., Garden, E., Small, A., and Palese, M. (2021). Ureteral stent encrustation: epidemiology, pathophysiology, management and current technology. *J. Urology* 205 (1), 68–77. doi:10.1097/ju.0000000000001343

Trinchieri, A. (1996). Epidemiology of urolithiasis. *Arch. Ital. Di Urol. E Androl.* 68 (4), 203–249.

Tundo, G., Vollstedt, A., Meeks, W., and Pais, V. (2021). Beyond prevalence: annual cumulative incidence of kidney stones in the United States. *J. Urology* 205 (6), 1704–1709. doi:10.1097/ju.0000000000001629

Vernez, S. L., Okhunov, Z., Wikenheiser, J., Khoyilar, C., Dutta, R., Osann, K., et al. (2017). Precise characterization and 3-dimensional reconstruction of the autonomic nerve distribution of the human ureter. *J. Urology* 197 (3), 723–729. doi:10.1016/j.juro.2016.08.118

Wang, J., Wang, G., Shan, H., Wang, X., Wang, C., Zhuang, X., et al. (2019). Gradiently degraded electrospun polyester scaffolds with cytostatic for urothelial carcinoma therapy. *Biomaterials Sci.* 7 (3), 963–974. doi:10.1039/c8bm01317a

Wang, L., Yang, G. G., Xie, H., and Chen, F. (2018). Prospects for the research and application of biodegradable ureteral stents: from bench to bedside. *J. Biomaterials Science-Polymer Ed.* 29 (14), 1657–1666. doi:10.1080/09205063.2018.1498184

Wang, X., Shan, H., Wang, J., Hou, Y., Ding, J., Chen, Q., et al. (2015a). Characterization of nanostructured ureteral stent with gradient degradation in a porcine model. *Int. J. Nanomedicine* 10, 3055–3064. doi:10.2147/ijn.s80810

Wang, X., Zhang, L., Chen, Q., Hou, Y., Hao, Y., Wang, C., et al. (2015b). A nanostructured degradable ureteral stent fabricated by electrospinning for upper urinary tract reconstruction. *J. Nanosci. Nanotechnol.* 15 (12), 9899–9904. doi:10.1166/jnn.2015.10747

Wang, Y. C., Ren, X. H., Ji, C. J., Zhong, D., Wei, X. Y., Zhu, Z., et al. (2023a). A modified biodegradable mesh ureteral stent for treating ureteral stricture disease. *Acta Biomater.* 155, 347–358. doi:10.1016/j.actbio.2022.11.022

Wang, Y. H., Yang, Y., Zhang, H. C., and Wang, Y. (2022). Early removal of ureteral stent after kidney transplant could decrease incidence of urinary tract infection: a systematic review and meta-analysis. *Exp. Clin. Transplant.* 20 (1), 28–34. doi:10.6002/ect.2021.0183

Wang, Z., Xiao, M., Guo, F., Yan, Y., Tian, H., Zhang, Q., et al. (2023b). Biodegradable polyester-based nano drug delivery system in cancer chemotherapy: a review of recent progress (2021-2023). *Front. Bioeng. Biotechnol.* 11, 1295323. doi:10.3389/fbioe.2023.1295323

Wen, P. Y., Ke, W. D., Dirisala, A., Toh, K., Tanaka, M., and Li, J. J. (2023). Stealth and pseudo-stealth nanocarriers. *Adv. Drug Deliv. Rev.* 198, 114895. doi:10.1016/j.addr.2023.114895

Will, T. A., Polcari, A. J., Garcia, J. G., Ouwenga, M. K., Voelzke, B. B., Greisler, H. P., et al. (2011). Paclitaxel inhibits ureteral smooth muscle cell proliferation and collagen production in the absence of cell toxicity. *J. Urology* 185 (1), 335–340. doi:10.1016/j.juro.2010.09.006

Xia, K. G., Shen, X. D., Ang, X., Hou, B. B., Chen, Y., Zhang, K. P., et al. (2023). Surface modification of ureteral stents: development history, classification, function, and future developments. *Expert Rev. Med. Devices* 20 (5), 401–416. doi:10.1080/17434440.2023.2198702

Yang, L., Li, J., Li, M., and Gu, Z. (2016). The *in vitro* and *in vivo* degradation of cross-linked poly(trimethylene carbonate)-based networks. *Polym. (Basel)* 8 (4), 151. doi:10.3390/polym8040151

Yang, L. Q., He, B., Meng, S., Zhang, J. Z., Li, M., Guo, J., et al. (2013). Biodegradable cross-linked poly(trimethylene carbonate) networks for implant applications: synthesis and properties. *Polymer* 54 (11), 2668–2675. doi:10.1016/j.polymer.2013.03.059

Yao, Q., Chen, B., Bai, J., He, W., Chen, X., Geng, D., et al. (2022). Bio-inspired antibacterial coatings on urinary stents for encrustation prevention. *J. Mater. Chem. B* 10 (14), 2584–2596. doi:10.1039/d1tb02318g

Zajac, A., Krysta, M., Kiszka, A., and Górecki, W. (2019). Biodegradable airway stents: novel treatment of airway obstruction in children. *Adv. Clin. Exp. Med.* 28 (7), 961–965. doi:10.17219/acem/94391

Zamani, M., Prabhakaran, M. P., and Ramakrishna, S. (2013). Advances in drug delivery via electrospun and electrosprayed nanomaterials. *Int. J. Nanomedicine* 8, 2997–3017. doi:10.2147/ijn.s43575

Zhang, C., Liao, L. Q., and Gong, S. Q. (2008). Zinc lactate-catalyzed ring-opening polymerization of trimethylene carbonate under microwave irradiation. *J. Appl. Polym. Sci.* 110 (2), 1236–1241. doi:10.1002/app.28651

Zhang, C., Lin, J., Nguyen, N. T., Guo, Y., Xu, C., Seo, C., et al. (2020). Antimicrobial bioresorbable Mg-Zn-Ca alloy for bone repair in a comparison study with Mg-Zn-Sr alloy and pure Mg. *ACS Biomaterials Sci. Eng.* 6 (1), 517–538. doi:10.1021/acsbiomaterials.9b00903

Zhang, M. Q., Zou, T., Huang, Y. C., Shang, Y. F., Yang, G. G., Wang, W. Z., et al. (2014). Braided thin-walled biodegradable ureteral stent: preliminary evaluation in a canine model. *Int. J. Urology* 21 (4), 401–407. doi:10.1111/iju.12297

Zhang, Y., He, J., Chen, H., and Xiong, C. (2021). A new hydrophilic biodegradable ureteral stent restrain encrustation both *in vitro* and *in vivo*. *J. Biomaterials Appl.* 35 (6), 720–731. doi:10.1177/0885328220949376

Zheng, T. L., Schang, T., Soon-Shiong, P., Merideth, N., Lanza, R., and Sutherland, D. E. (1991). Pancreas function index: an early monitor of allograft rejection. *J. Surg. Res.* 50 (1), 24–29. doi:10.1016/0022-4804(91)90005-7

Zimskind, P. D., Fetter, T. R., and Wilkerson, J. L. (1967). Clinical use of long-term indwelling silicone rubber ureteral splints inserted cystoscopically. *J. Urology* 97 (5), 840–844. doi:10.1016/s0022-5347(17)63130-6

Zopf, D. A., Hollister, S. J., Nelson, M. E., Ohye, R. G., and Green, G. E. (2013). Bioresorbable airway splint created with a three-dimensional printer. *N. Engl. J. Med.* 368 (21), 2043–2045. doi:10.1056/nejmc1206319

frontiers | Frontiers in Bioengineering and Biotechnology

TYPE Original Research
PUBLISHED 23 May 2024
DOI 10.3389/fbioe.2024.1397459

OPEN ACCESS

EDITED BY
Liqun Yang,
Shengjing Hospital of China Medical University, China

REVIEWED BY
Sotya Astutiningsih,
University of Indonesia, Indonesia
Glauber Vale,
Federal University of Piauí, Brazil

*CORRESPONDENCE
Qianju Wu,
wuqianju@sjtu.edu.cn
Zhisheng Zhang,
zzshospital@163.com

RECEIVED 07 March 2024
ACCEPTED 29 April 2024
PUBLISHED 23 May 2024

CITATION
Zheng L, Zhang Y, Bai Y, Zhang Z and Wu Q (2024), Study on the mechanical and aging properties of an antibacterial composite resin loaded with fluoride-doped nano-zirconia fillers.
Front. Bioeng. Biotechnol. 12:1397459.
doi: 10.3389/fbioe.2024.1397459

Study on the mechanical and aging properties of an antibacterial composite resin loaded with fluoride-doped nano-zirconia fillers

Liyuan Zheng[1], Yi Zhang[1], Yuming Bai[2], Zhisheng Zhang[1]* and Qianju Wu[1]*

[1]Department of Prosthodontics, Stomatological Hospital of Xiamen Medical College, Xiamen Key Laboratory of Stomatological Disease Diagnosis and Treatment, Xiamen, China, [2]Department of Orthodontics, Stomatological Hospital of Xiamen Medical College, Xiamen Key Laboratory of Stomatological Disease Diagnosis and Treatment, Xiamen, China

Preventing the occurrence of secondary caries serves as one of the significant issues in dental clinic, thus make it indispensable to improving the properties of conventional composite resin (CR) by developing a novel CR. In present study, two groups of experimental CRs loaded with different contents of fluoride-doped nano-zirconia fillers (25 wt% and 50 wt%) were fabricated. The surface topography, mechanical performance, fluoride release, antibacterial effect, aging property and cytotoxicity of the experimental CRs were evaluated subsequently. A uniform distribution of the F-zirconia fillers over the whole surface of resin matrix could be observed. The experimental CRs showed continuous fluoride release within 28 days, which was positively correlated with the content of F-zirconia fillers. Moreover, the amount of fluoride release increased in the acidic buffer. Addition of F-zirconia fillers could improve the color stability, wear resistance and microhardness of the experimental CRs, without reducing the flexure strength. Furtherly, the fluoride ions released continuously from the experimental CRs resulted in effective contact and antibacterial properties, while they showed no cytotoxicity. As a consequence, considerations can be made to employ this new kind of composite resin loaded with fluoride-doped nano-zirconia fillers to meet clinical requirements when the antimicrobial benefits are desired.

KEYWORDS

composite resin, nano-zirconia fillers, fluoride-releasing, antibacterial property, aging test, mechanical performance

1 Introduction

With the enhancement of aesthetic requirements and the development of novel dental materials, tooth-colored materials like composite resins (CRs) have been widely used in dentistry. Due to their strong mechanical properties and good aesthetic characteristics, CRs have gradually become the most commonly used filling and adhesive materials in clinic, surpassing the use of traditional silver amalgam and the glass ionomer cement (GIC) (Pizzolotto and Moraes, 2022; Aldowsari et al., 2023; Maletin et al., 2023). However, the occurrence of secondary caries at the edge of the CR restorations has become the main cause

of secondary filling treatments (Chladek et al., 2023). Furthermore, the secondary filling operations often produce more damage to the hard tissues of teeth, as well as more thermal or chemical stimulus to the dental pulps, which may also lead to the filling failures (Bakhsh et al., 2023). It was reported that the possibility of secondary caries occurring around the CRs was even greater than that using other filling materials such as the GIC or the amalgam (Opdam et al., 2010; Eltahlah et al., 2018). Thus, secondary caries has become an urgent problem in dental clinic. The replacement of CRs has undoubtedly become a heavy burden on the expenditure on health.

Moreover, the polymerization shrinkage occurring in the curing procedure also makes the application of CRs in posterior teeth more stressful, especially in repairing the extensive dental defects (Loguercio et al., 2023). In order to improve the defects of CRs, studies have been conducted to reduce the polymerization shrinkage by improving the filling technique, using the bonding agents in combination (Kaur et al., 2015; Kim et al., 2022; Hosaka et al., 2023). However, the complexity of filling procedure may not only increase the operating time but also improve the technical sensitivity (Shibasaki et al., 2017; Van Ende et al., 2017). Hitherto, there are still no new materials or new technologies that can avoid the microleakage occurring at the edge of the CRs completely. On the other hand, as far as we know that bacterial infection is considered the main cause of secondary caries after restoration, yet the specific cariogenic bacteria and the pathological process are not clear. Thus, adjusting the compositions to develop novel CRs with antibacterial properties has also become one of the research hotspots currently (Stewart and Biostable, 2019).

Back to the early 20th century, the application of fluoride agents had become an important way to maintain oral health (Pollick, 2018). The anti-caries property of fluoride agents is mainly achieved by maintaining a certain concentration of fluoride ions in saliva locally, which forms a mineralization system with calcium ions and phosphate ions together. Calcium fluoride and fluorapatite generated can inhibit the demineralization and promote remineralization process. Furthermore, fluoride can also act on the acid-producing bacteria such as mutans streptococci (S. mutans) directly. While blocking the functions of enzymes related to glycolysis and cellular oxidation, fluoride also inhibits the intake of glucose by the bacteria. Fluoride has been proved to play an excellent anti-caries property in the traditional GIC, and has also been tried to be used in the development of novel antibacterial CRs nowadays (Francois et al., 2020). Since the 1980s, fluoride-containing CRs have been used in the orthodontic adhesives and the fissure sealants, while there were few studies on them as direct filling materials (Ei et al., 2018). But it is worth noting that the release of fluoride ions may result in the porous structure of the material, which will weaken the mechanical properties and wear resistance (Van der Laan et al., 2019).

In recent years, nano-zirconia powders have been applied as inorganic fillers to enhance the mechanical properties of CRs. On the one hand, as one of the commonly used reinforcing materials in biomedicine, zirconia presents excellent strength and biocompatibility. On the other hand, addition of nanoparticles is conducive to increase the aesthetic performance and wear resistance of materials. Furthermore, it was suggested that nanoparticles possess stronger prevention in bacterial adhesion and biofilm formation due to their large surface-volume ratio (Melo et al., 2013). Some commercial CRs products contained nano-zirconia fillers have been used in clinic so far, yet few studies focused on their antibacterial property. Thus, we proposed a hypothesis that combination fluoride with nano-zirconia through a certain way in the fillers of a novel CR would do help to maintain the clinical performance while exerting good fluoride-releasing property. In the early stage of our research, ammonium zirconium hexafluoride was added into zirconium salt as the source of fluoride ions. A kind of high-purity fluoride-doped nano-zirconia particles were synthesized through chemical precipitation and the calcination procedure. A series of experiments were carried out to prove that both the nanoparticles and the novel CR loaded with fluoride-doped nano-zirconia fillers possessed definite release of fluoride ions, and the released ions could inhibit the growth of S. mutans effectively (Zheng et al., 2021).

In the present work, the composition of fillers was optimized furtherly according to the preliminary results. Fluoride release from the experimental CR into media with different pH values were measured to simulate the caries processes. The action mode of antibacterial effect was explored here. Furthermore, thermocycling test were used to simulate the intraoral aging process of the experimental CR. The mechanical performance and cytotoxicity were also evaluated to verify its clinical application prospects.

2 Materials and methods

2.1 Synthesis of the CRs loaded fluoride-doped nano-zirconia fillers

Fluoride-doped nano-zirconia particles were coated with the silane coupling agent KH-570 to improve the interfacial combination between the fillers and resin matrix. The resin matrix consisted of a 70:30 (w/w) bisphenol-A glycidyl dimethacrylate (Bis-GMA) and tri-ethylene glycol dimethacrylate (TEGDMA). The initiator system consisted of 0.5 wt% camphorquinone (CQ) and 1 wt% ethoxylated bisphenol A dimethacrylate (DMAEMA). The experimental CRs were formulated with the resin matrix and varying concentrations of the silaned fillers (25, 50 wt%) through *in situ* dispersion method. The mixtures were filled to Teflon molds and light cured for 40 s on both sides (1200mW/cm2, Elipar S10, 3M Espe, Seefeld, Germany). For comparison, specimens of the pure resin matrix without fillers were also prepared in the same way.

2.2 Field emission scanning electron microscopy

One specimen of each group of the experimental CRs selected and coated with electrically-conductive material. The surface morphology and the dispersion of nanoparticles in CRs were investigated by Field emission scanning electron microscopy (FESEM, MERLIN, ZEISS, Germany).

2.3 Mechanical properties

2.3.1 Flexure strength

Specimens of size 25 mm × 2 mm × 2 mm were prepared in each group (N = 5). Before the test, every specimen was polished

sequentially using #800, #1000, #2000, and #3000 abrasive papers and then stored in the saline solution at 37 °C for 24 h. After drying thoroughly, the specimens were placed on the universal mechanical testing machine (Instron 5566, Instron, United Kingdom) for flexure strength test at a span length of 20 mm and a speed of 0.5 mm/min. At the same time, the fragmentation load was recorded and the flexure strength was calculated according to the formula: $FS = 3Fl/2bh^2$ [Where FS means the flexure strength (unit: MPa), F means the fragmentation load (unit: N), l means the span length, b and h mean the width and height of specimen (unit: mm)].

2.3.2 Wear resistance

Cylindrical specimens with a diameter of 10 mm and a height of 5 mm were prepared (N = 3) and polished sequentially. After stored in the saline solution at 37 °C for 24 h and dried, each specimen was fixed on the mechanical reciprocating friction and wear device (MWF-02, sdbaohang machinery manufacturing co., ltd., China). A Co-Cr stainless steel ball with a diameter of 5 mm was used as the grinding part, and the abradant was prepared by mixing 4:1 (w/w) fluorite powder and water. A 30 N loading force was applied to the specimens during 6000 friction cycles, and the speed of the reciprocating friction movement was 300 rpm/min. The digital micrometer was used to measure the height of specimens before and after the test. Moreover, one specimen was selected randomly to observe the microscopic morphology of the wear surface under SEM.

2.4 Fluoride release

Fluoride release of the experimental CRs into various storage media with different pH values during 28 days was determined using a pH meter (a-AB41PH ZH, OHAUS, China) with fluoride ion selective electrode (F, STISE22, OHAUS, China). Three specimens of each group were eluted in either 2 mL distilled water, 2 mL acidic buffer (20 mM KCl, 154 mM NaCl, 3.6 mM $NaH_2PO_4{\cdot}H_2O$, pH 4.2) or 2 mL neutral buffer (1.9 mM $CaCl_2$, 30mM KCl, HEPES, pH 7.0). All samples were stored in a shaker at 37 °C. The extraction media were collected in the 1st, 3rd, 7th, 14th and 28th days and exchanged by fresh storage media at the time of each measurement. The fluoride ions concentration in the extraction media was measured. Before determination of the samples, the selective electrode was fully activated and calibrated with a series of fluoride standards ranging from 0.001 ppm to 100 ppm.

2.5 Antibacterial property

Streptococcus mutans (S.mutans UA159, Guangdong Microbial Culture Collection Center, China), which was considered as the primary cariogenic bacteria, was used as the experimental strain. The frozen strain was revived and incubated in sterile Brain Heart Infusion broth-agar (BHI-agar, BD, United States) media under anaerobic condition at 37 °C. A single bacteria colony was selected and transferred into fresh BHI media before the experiment. The microplate reader (Elx800, BioTek, United States) was used to regulate and control the absorbance of S. mutans strain at the wavelength of 600 nm.

2.5.1 Colony-forming units (CFUs) counting

Specimens with 8 mm in diameter and 2 mm thick of each group were prepared (N = 3) and sterilized by ultraviolet light for 2 h before the antibacterial test. The specimens of Resin without the experimental fillers were prepared and taken as control group. All specimens were placed in a sterile 48-well plate with 500 uL fresh BHI media and 50 uL of bacterial suspension (1×10^6 CFU/mL). After incubated for 24 h at 37 °C, the bacteria grow and form biofilms on the surface of specimens. Then, the specimens were transferred to another 48-well plate and washed gently with PBS to get rid of the planktonic bacteria. The biofilm formed on the surface of each specimen was collected by shaking and washing with 500 uL fresh BHI media. And the planktonic bacteria in the original 48-well plate were also collected and mixed well. All experimental bacteria suspensions were diluted to 10-5 times and inoculated on BHI-agar plates to count the bacteria colonies. The antibacterial rate (AR) was determined via the following formula: $AR\ (\%) = (C0-C)/C0 \times 100\%$ (Where C0 means the number of colonies in average of the control group, C means the number of colonies in average of the experimental group.)

2.5.2 Metabolic activity test

The metabolic activities of both planktonic bacteria and biofilm were estimated by the Cell Counting Kit-8 assay (CCK-8, Dojindo, Japan). After co-culturing with the experimental CRs for 24 h, the planktonic bacteria and biofilm were collected and transferred to a new 48-well plate by the method as above-mentioned in 2.5.1. 50 uL of CCK-8 liquid was added into each well and incubated for another 2 h in the incubator at 37 °C. Finally, the absorbance at 450 nm was determined by the microplate reader (Elx800, BioTek, United States).

2.6 Aging test

2.6.1 Thermal aging procedure

Specimens with 8 mm in diameter and 2 mm thick of each group were prepared (N = 3) for thermal aging test. No thermal aging status was denoted as time T0. Then the specimens were subjected to 10,000 cycles of thermocycling between 5 °C and 55 °C with a transfer time of 30 s, which was applied to simulate the thermal aging in 1 year. The time at which the 10,000 cycles ended was denoted as T1.

2.6.2 Color change

Color values of the specimens were measured at T0 and T1, respectively, using a tooth color comparator (VITA Easyshade V, VITA Zahnfabrik H. Rauter GmbH and Co. KG, Germany) in 3-point measurement mode. The color comparator was recalibrated before each measurement. After all measurements, average of the CIELab values (L*a*b*) was calculated for each specimen. And the ΔE00 value was calculated with the online color calculator (CIEDE2000 color system, www.colormine.org) to show the color change from before to after the thermo aging procedure.

2.6.3 Microhardness test

The microhardness values of all specimens were measured using a microhardness (Vickers) testing device (Micro Hardness Tester

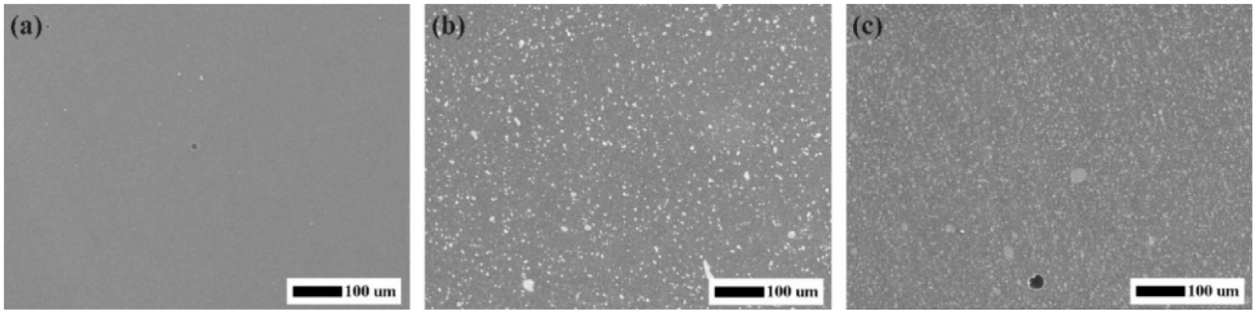

FIGURE 1
SEM micrographs of the experimental composite resins with fluoride-doped nano-zirconia fillers. **(A)** Control group; **(B)** 25 wt% F-zirconia fillers; **(C)** 50 wt% F-zirconia fillers.

HMV-G-FA, SHIMADZU, Japan) at T0 and T1. A load of HV0.1 (980.7 mN) was applied to the surface of each specimen in 3 points selected randomly for 10 s. And averages of the microhardness values before and after thermal aging procedure were calculated.

2.7 Cytotoxicity

Specimens with 8 mm in diameter and 2 mm thick of each group were prepared (N = 5) and sterilized with 75% ethanol for three times. Each specimen was immersed into Dulbecco's modified Eagle's medium (DMEM) high glucose medium (HyClone, United States), which contained 10% fetal bovine serum (Gibco, United States) and 1% pecicillin-streptomycin (EveryGreen, China). Then, the eluates were collected after the incubation at 37 °C for 3 days. A total of human dental pulp cells (HDPs) was seeded per well in a 96-well plate and cultured with DMEM media. After incubated at 37 °C for 24 h, the media was replaced with the eluates of each group. Cells incubated in the pure media without eluates were used as the negative control. The alamar blue kit (Invitrogen, United States) was used for cytotoxicity test according to the manufacturer's instruction. Fluorescence intensities of HDPs at 1, 3, 5 and 7 days in response to the eluates of experimental CRs were measured using the microplate reader.

2.8 Statistical analysis

The data obtained were analyzed with SPSS Statistical software (version 25.0, IBM, Armonk, United States). One-way analysis of variance (ANOVA) and Post hoc analysis for multiple comparisons were performed. $p < 0.05$ was considered as statistically significant.

3 Results

3.1 Field emission scanning electron microscopy

Figure 1 showed the SEM micrographs of the experimental CRs with fluoride-doped nano-zirconia fillers. The micrograph of control group (pure resin matrix) was uniformly dark (Figure 1A), while inorganic fillers presented as gray or white particles distributed uniformly in the resin matrix in the micrographs of experimental CRs (Figures 1B,C). Generally, all the experimental fillers were evenly dispersed in the monomer matrixes and there was only a small minority of agglomeration of fillers.

3.2 Mechanical properties

The result of flexure strength (FS) test was shown in Table 1. It could be seen that the FS of control group was the highest, reaching 88 MPa in average. With the addition of inorganic fillers, the FS of specimens showed no significant decline. Statistical analysis of the result showed that there was no significant difference among the three groups ($p \geq 0.05$). In addition, height loss of the experimental composite resins with fluoride-doped nano-zirconia fillers after the wear resistance test were also presented in Table 1. After the wear resistance test, specimens of the control groups showed a significant height loss of 161 um in average. The height loss decreased to 115 um in average with the addition of 25 wt% F-zirconia fillers, and it furtherly decreased to 60 um in average with the addition of 50 wt % F-zirconia fillers. Statistical results showed that the difference between the group of 50 wt% F-zirconia fillers and the control group was statistically significance ($p < 0.05$).

The morphologies of worn surfaces after the wear resistance test were analyzed via SEM and presented in Figure 2. It could be seen that there were obvious longitudinal wear traces and exfoliative pits on the wear surface of the control group at low magnification (Figure 2A). At high magnification, irregular pits could be found after the outermost layers of resin falling off (Figure 2B). For the group of 25 wt% F-zirconia fillers, horizontal wear traces were observed on the surface, and scattered agglomerated particles were exposed at low magnification (Figure 2C). Further, cracks and small pits appeared after the fillers falling off at high magnification (Figure 2D). Similarly, the wear surface of 50 wt% F-zirconia fillers after wear resistance test was relatively flat and the wear traces were horizontal under low magnification (Figure 2E). Friction striations could be seen at high magnification, a small number of fillers were exposed and scattered, while there were no obvious stripping pits (Figure 2F).

TABLE 1 Flexure strength and height loss after wear resistance test of the experimental composite resin with fluoride-doped nano-zirconia fillers.

Group	Flexure strength (mean ± SD, MPa)	Height loss after wear resistance test (mean ± SD, um)
Control group	88 ± 5.21	161 ± 38.84
25 wt% F-zirconia fillers	82 ± 5.75	115 ± 24.25
50 wt% F-zirconia fillers	85 ± 4.84	60 ± 26.23*

Note: The superscript symbol * means statistical difference compared to the control group ($p < 0.05$).

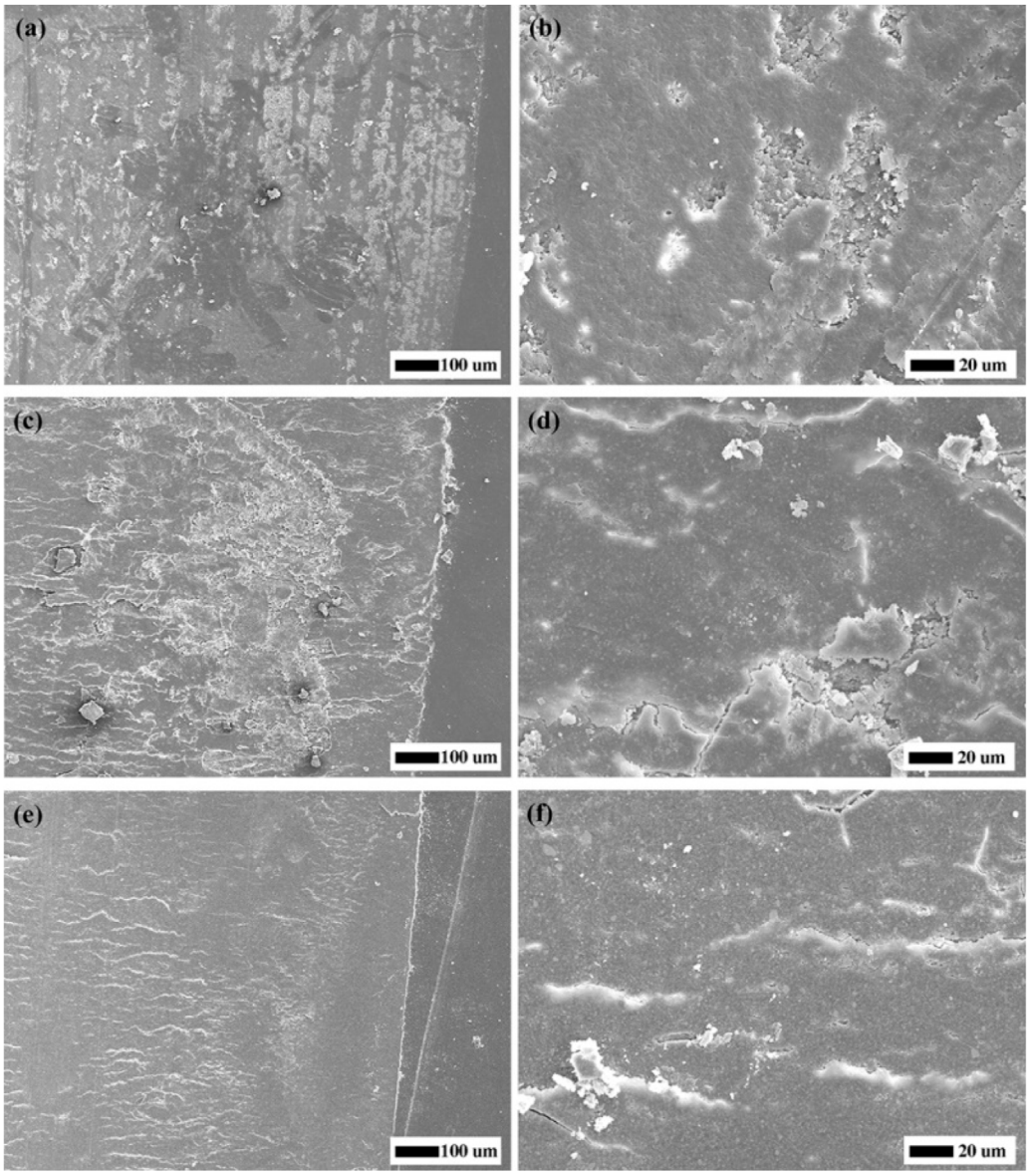

FIGURE 2
SEM micrographs of worn surfaces of the specimens. **(A,B)** Control group; **(C,D)** 25 wt% F-zirconia fillers; **(E,F)** 50 wt% F-zirconia fillers.

TABLE 2 Daily fluoride release (ppm) from the experimental composite resin with fluoride-doped nano-zirconia fillers in different buffers during 28 days.

Time	Groups	Distilled water mean (SD)	Neutral buffer mean (SD)	Acidic buffer mean (SD)
Day 1	25 wt% F-zirconia fillers	1.51 (0.09)	1.51 (0.07)	1.52 (0.20)
	50 wt% F-zirconia fillers	1.77 (0.03)	1.72 (0.06)	1.83 (0.21)
Day 3	25 wt% F-zirconia fillers	1.25 (0.01)	1.25 (0.03)	1.36 (0.13)
	50 wt% F-zirconia fillers	1.53 (0.02)	1.44 (0.04)	1.57 (0.28)
Day 7	25 wt% F-zirconia fillers	1.31 (0.10)	1.25 (0.01)	1.38 (0.12)
	50 wt% F-zirconia fillers	1.43 (0.03)	1.42 (0.02)	1.60 (0.20)
Day 14	25 wt% F-zirconia fillers	0.36 (0.00)	0.36 (0.01)	0.40 (0.05)
	50 wt% F-zirconia fillers	0.47 (0.01)	0.45 (0.02)	0.52 (0.72)
Day 28	25 wt% F-zirconia fillers	0.13 (0.01)	0.10 (0.00)*	0.12 (0.00)*#
	50 wt% F-zirconia fillers	0.15 (0.00)	0.12 (0.01)*	0.16 (0.02)*

Note: The superscript symbol * means statistical difference compared to that in distilled water, # means statistical difference compared to that in the neutral buffer ($p < 0.05$).

TABLE 3 Cumulative fluoride release (ppm) from the experimental composite resin with fluoride-doped nano-zirconia fillers in different buffers at each detection point during 28 days.

Time	Groups	Distilled water mean (SD)	Neutral buffer mean (SD)	Acidic buffer mean (SD)
Day 1	25 wt% F-zirconia fillers	1.51 (0.09)	1.51 (0.07)	1.52 (0.20)
	50 wt% F-zirconia fillers	1.77 (0.03)	1.72 (0.01)	1.83 (0.21)
Day 3	25 wt% F-zirconia fillers	4.01 (0.07)	4.00 (0.09)	4.23 (0.07)*
	50 wt% F-zirconia fillers	4.83 (0.06)	4.60 (0.08)	4.97 (0.49)
Day 7	25 wt% F-zirconia fillers	9.23 (0.34)	8.95 (0.15)	9.75 (0.53)*
	50 wt% F-zirconia fillers	10.55 (0.11)	10.28 (0.08)	11.36 (0.81)*
Day 14	25 wt% F-zirconia fillers	11.75 (0.34)	11.49 (0.18)	12.57 (0.87)
	50 wt% F-zirconia fillers	13.84 (0.15)	13.40 (0.15)	14.98 (1.27)*
Day 28	25 wt% F-zirconia fillers	13.60 (0.44)	12.94 (0.19)	14.18 (0.87)*
	50 wt% F-zirconia fillers	15.90 (0.16)	15.04 (0.05)	17.24 (1.48)*

Note: The superscript symbol * means statistical difference compared to that in distilled water ($p < 0.05$).

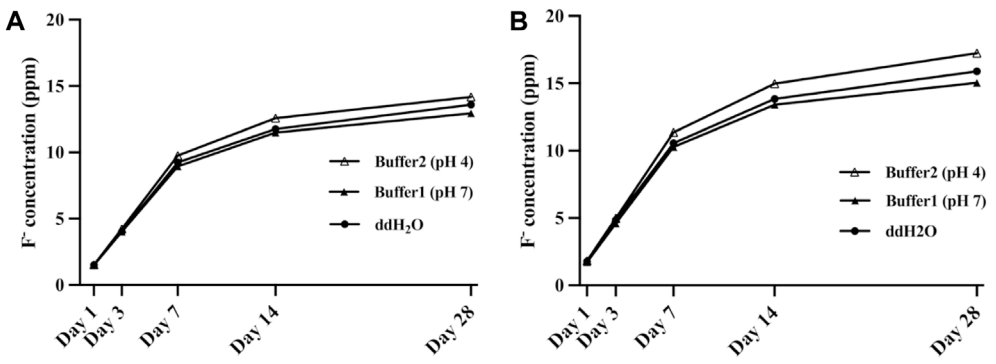

FIGURE 3
Cumulative fluoride release of the experimental composite resin with fluoride-doped nano-zirconia fillers in different buffers within 28 days [**(A)** 25 wt% F-zirconia fillers; **(B)** 50 wt% F-zirconia fillers].

TABLE 4 The antibacterial activities for the biofilm of S.mutans and planktonic bacteria evaluation.

Groups	Biofilm of S.mutans evaluation Log (CFU/mL)	Planktonic bacteria evaluation Log (CFU/mL)
Control group	9.08 ± 0.07	9.05 ± 0.02
25 wt% F-zirconia fillers	8.86 ± 0.05*	8.91 ± 0.01*
50 wt% F-zirconia fillers	8.75 ± 0.04*	8.66 ± 0.03*#

Note: The superscript symbol * means statistically different compared to the control group, # means statistically different compared to the 25 wt% F-zirconia fillers group ($p < 0.05$).

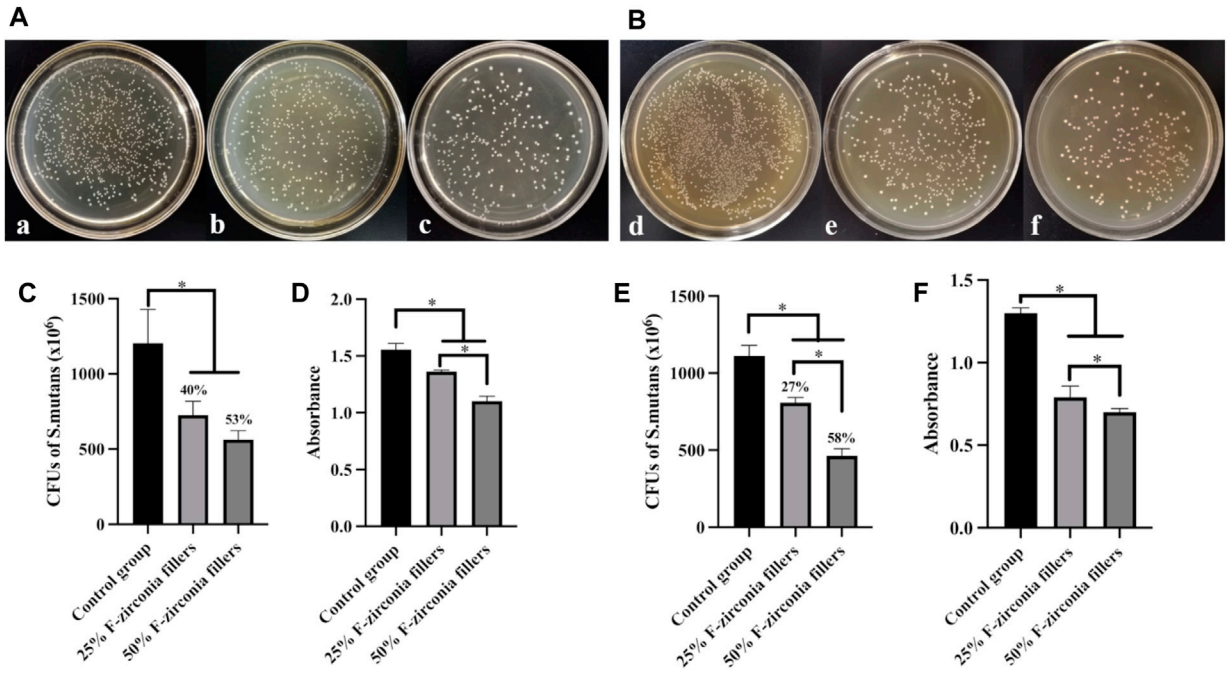

FIGURE 4
The result of antibacterial effect against S. mutans of the experimental composite resin with fluoride-doped nano-zirconia fillers [**(A,C,D)** Antibacterial effect against biofilms of S. mutans; **(B,E,F)** Antibacterial properties against planktonic bacteria; **(A,B)** Images of bacterial colonies; a,d, Control group; b,e, 25 wt% F-zirconia fillers; c,f, 50 wt% F-zirconia fillers; **(C,E)** Number of bacterial colonies (CFUs) and the antibacterial rates (AR); **(D,F)** The CCK-8 test; The symbol * means $p < 0.05$.).

3.3 Fluoride release

Table 2 and Table 3 showed the daily and cumulative amount of fluoride release from the experimental CRs within 28 days, respectively One-way ANOVA test revealed that both the quantity of fillers and time had a statistically significant effect on the amount of fluoride release. In general, the cumulative amount of fluoride released from 50 wt% F-zirconia fillers was significantly higher than that from the group of 25 wt% F-zirconia fillers ($p < 0.05$). Regarding detection of the daily amount, the fluoride release decreased obviously with time. The difference was statistically significant in neutral buffer in every detection point ($p < 0.05$). And the difference between the two groups became more obvious in day 14 and day 28 ($p < 0.05$). However, the pH of media had a little effect on fluoride release. The amount of fluoride release increased in the acidic buffer than that in another two media, but the difference was not statistically different ($p \geq 0.05$). The change trends of cumulative fluoride release could be observed in Figure 3. For both two groups of the experimental CRs, a significant upward trend could be seen in the beginning 7 days, while the upward trend had slowed over the remaining observation period.

3.4 Antibacterial property

Table 4 and Figure 4 showed the antibacterial effects of the experimental CRs against biofilms of S. mutans and the planktonic bacteria. In terms of the contact antibacterial effect against biofilms, the group of 50 wt% F-zirconia fillers showed better antibacterial activity with the antibacterial rate of 53%, followed by the group of 25 wt% F-zirconia fillers (40%), while the difference was not statistically significant ($p \geq 0.05$). In terms of releasing antibacterial effect against the planktonic bacteria, the antibacterial rate improved from 27% to 58% with the increase of F-zirconia fillers, and the difference was statistically significant ($p < 0.05$).

The metabolic activities of S. mutans after culturing with the experimental CRs in the CCK-8 test were also presented in Figures

TABLE 5 ΔE00 during the thermal aging progress of the experimental composite resin with fluoride-doped nano-zirconia fillers.

Group	CIELab value (mean ± SD)			ΔE00 value (mean ± SD)
		T0	T1	
Control group	L*	38.28 ± 3.19	39.67 ± 3.00	1.69 ± 0.35
	a*	−1.04 ± 0.12	−1.24 ± 0.07	
	b*	7.03 ± 0.97	6.04 ± 0.64	
25 wt% F-zirconia fillers	L*	42.30 ± 2.03	43.20 ± 3.18	1.20 ± 0.17γ
	a*	1.52 ± 1.53	1.84 ± 1.98	
	b*	11.83 ± 6.08	12.38 ± 6.79	
50 wt% F-zirconia fillers	L*	45.28 ± 5.23	45.63 ± 5.19	0.78 ± 0.44γ
	a*	1.77 ± 1.18	1.74 ± 1.17	
	b*	11.91 ± 4.58	11.44 ± 4.50	

Note: The superscript symbol γ means statistical difference compared to the control group ($p < 0.05$).

TABLE 6 Microhardness values of the experimental composite resin with fluoride-doped nano-zirconia fillers in different times during the thermal aging test.

Group	Microhardness value (mean ± SD, HV0.1)		
	T0	T1	T0-T1
Control group	18.30 ± 1.25	14.61 ± 0.97	3.69 ± 0.58
25 wt% F-zirconia fillers	48.50 ± 10.49*	44.38 ± 9.31*	4.36 ± 1.83
50 wt% F-zirconia fillers	73.72 ± 5.64*#	71.02 ± 3.56*#	2.69 ± 2.93

Note: The superscript symbol * means statistically different compared to the control group, # means statistically different compared to the 25 wt% F-zirconia fillers group ($p < 0.05$).

4D, F. In general, with the amount of fluoride-doped nano-zirconia fillers increased, the absorbance of bacterial suspension was significantly lower than that of the control group ($p < 0.05$). Furthermore, the differences between two experimental groups observed in antibacterial effects against both biofilms and planktonic bacteria showed statistical significance ($p < 0.05$).

3.5 Aging test

3.5.1 ΔE00 results

The CIELab values of the experimental CRs, which contained the L* (lightness), a* (red-to-green axis) and b* (yellow-to-blue axis) values, were summarized in Table 5. According to the result of one-way ANOVA and multiple comparisons, the control group showed significant differences in CIELab values as compared with another two groups both before and after the thermal aging procedure ($p < 0.05$). The difference of CIELab values between the experimental groups had no statistical significance ($p \geq 0.05$). In addition, comparison of ΔE00 values during the thermal aging progress among three groups was also exhibited in Table 5. The control group had the highest ΔE00 value. ΔE00 values of the experimental groups were significantly lower than that of the control group ($p < 0.05$). And ΔE00 value of the group of 50 wt% F-zirconia fillers was lower than that of the group of 25 wt% F-zirconia fillers, but the difference had no statistical significance ($p \geq 0.05$).

3.5.2 Microhardness

Microhardness values of the experimental CRs before and after the thermal aging process were presented in Table 6. The microhardness of the control group in T0 was 18.30 ± 1.25 HV0.1, while those of the groups of 25 wt% F-zirconia fillers and 50 wt% F-zirconia fillers were 48.50 ± 10.49 HV0.1 and 73.72 ± 5.64 HV0.1, respectively. The microhardness values of all three groups decreased after the thermal aging test (in T1). However, there were no statistically significant differences between the microhardness values of the same group before and after the thermal aging process ($p \geq 0.05$). The statistical results revealed significant differences between the control and experimental groups in both T0 and T1 ($p < 0.05$). In addition, the variation of microhardness values (T0-T1) of each group was also analyzed here. And the difference of the variations among three groups was not statistically significant ($p \geq 0.05$).

3.6 Cytotoxicity

The alamar blue assay was applied in this study to verify the cytotoxicity of the experimental CRs to human dental pulp cells (HDPs). Fluorescence intensities produced by healthy HDPs at 1, 3, 5 and 7 days in response to eluates of the control group or experimental groups were presented in Figure 5. Statistical results with one-way ANOVA analysis revealed that the viabilities of HDPs

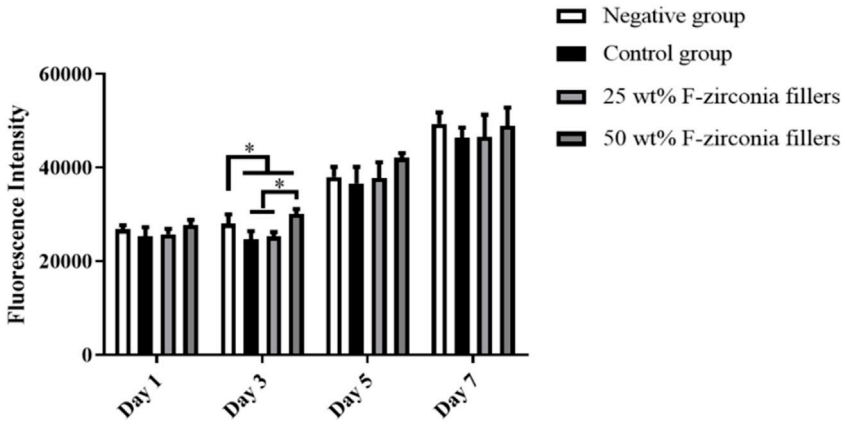

FIGURE 5
Fluorescence intensities of HDPs at 1, 3, 5 and 7 days in response to eluates of the experimental composite resin with fluoride-doped nano-zirconia fillers in the alamar blue assay (The symbol * means $p < 0.05$).

exposed to eluates of each group were not significantly different from that of the negative group ($p \geq 0.05$). But fluorescence intensities of cells exposed to elutes at day 3 were slightly lower than that of the negative group ($p < 0.05$).

4 Discussion

Dental composite resins (CRs) are the most widely used direct restorative materials in clinic because of their high mechanical strength and aesthetic superiority. However, as the traditional CRs has little resistance to bacterial infection, which was considered as the major cause of dental caries, secondary caries might occur adjacent to the CRs restoration margins and shorten their lifespans ultimately. Thus, the development of antibacterial CRs is one of the most important investigations regarding novel dental materials.

The antibacterial action of fluoride agents against cariogenic bacteria has been widely appreciated by previous studies. Fluoride ions in saliva can diffuse into bacterial cells in the form of HF, where they decompose into both hydrogen ions and fluoride ions. This process can not only inhibit the action of enzymes directly but also stimulate more HF to diffuse into the cells (Hamilton, 1977). In addition, the increase of hydrogen ions within the cells can reduce bacterial acid production (Hamilton and Ellwood, 1978). Given the definite antibacterial effect of fluoride agents, various fluoride-releasing restorative materials have emerged and were considered as fluoride reservoirs, which might increase the fluoride level locally (Wiegand et al., 2007; Wei Su et al., 2019). To date, addition of fluoride-containing inorganic fillers was considered as the major method to develop novel fluoride-releasing CRs. Both the soluble salts such as calcium fluoride (CaF2) and the slightly soluble salts like ytterbium fluoride (YbF2) and fluoro-alimino-silicate glasses (FAG) had been applied in previous studies. However, it was reported that most of them showed a "burst release" of fluoride ions and the dissolution of fluoride agents had an adverse effect on the mechanical properties (Van der Laan et al., 2019). It is not hard to spot that those inorganic fluoride agents were added by mixing with other fillers and there were only physical compatibilities among all particles, without chemical combination. Thus, the dissolution of fluoride agents resulted in porous structure of the CRs, which might damage the dense structure of the materials and furtherly declined the strength. It is necessary to improve the chemical structure of inorganic fillers to replace the way of adding fluoride agents directly. Cheng et al. produced a kind of core-shell nanofibers containing sodium fluoride (NaF) and used as fillers of CRs (Cheng et al., 2014). Results showed that fluoride releasing with minor burst release could be achieved, which was quite superior to the case of adding NaF nanocrystals directly. Similarly, a novel LiAl-F layered double hydroxide (LDH) was also developed by Su et al. and was supposed to be a fluoride reservoir filler for CRs (Wei Su et al., 2019). However, this kind of researches were still in the early stage of exploration and were expected to be carried on furtherly.

Although the best way of developing fluoride-releasing CRs has not yet been concluded, the previous studies suggested that it was of necessity to develop a novel CRs with efficient fluoride-releasing effect and proper mechanical properties. Recently, nano-zirconia particles have been used as the reinforcing fillers in dental CRs (Hong et al., 2020). Zirconium salts, which were a kind of raw compositions for the synthesis of zirconia particles, have been proven to exhibit strong chelate formation characteristics. It could form coordination bonds with multiple fluoride ions, forming a highly efficient "fluoride ions receptors" (David et al., 2002). For this reason, zirconium salts were frequently used for fluoride removal in drinking water (Velazquez-Jimenez et al., 2014). Burgess et al. introduced a novel monomer with zirconium fluoride chelate and confirmed it could also be applied to dental resin-based materials (Xu et al., 2006). In our preliminary study, a kind of novel CR loaded with fluoride-doped nano-zirconia (F-zirconia) particles was prepared. The result showed that the major X-ray diffraction (XRD) pattern of fluoride-doped nano-zirconia particles changed from the tetragonal phase to the monoclinic phase with the increase of fluorine content (Zheng et al., 2021). Similarly, in the process of plasma fluorination of yttrium stabilized zirconia, Wolter et al. (2011) observed that the content of oxygen atoms gradually decreased with the increase of fluorine atoms in X-ray photoelectron spectroscopy, which indicated that fluorine atoms might replace oxygen atoms to occupy the spatial position in

zirconium dioxide crystal cells. Hence, based on the uniform distribution of fluorine in the EDS elemental maps, we inferred that the change of XRD pattern was also caused by the substitution of oxygen atoms by fluorine atoms. Fluoride ions could release from the nanoparticles in ddH2O and showed proper antibacterial effect.

Furtherly, the effect of pH values on fluoride release and the action mode of antibacterial activities were explored in the study. In addition, the mechanical performance and aging properties, as well as the cytotoxicity of the experimental CR were also evaluated here.

Previous studies revealed that addition of nano-zirconia fillers could improve the mechanical strength of CRs, but might also reduce the transparency. When the content of nano-zirconia fillers reached 55 wt%, the CRs could not be cured completely through light-curing (Hong et al., 2020). Thus, we prepared two groups of experimental CRs loaded with 25 wt% or 50 wt% F-zirconia fillers, respectively. Figure 1 showed the SEM micrographs of the experimental CRs, and it could be seen that nano-fillers distributed well over the whole surface of resin matrix. Good dispersibility of fillers was attributed to the mechanical strength of CRs (Hata et al., 2022). As presented in Table 1, the three-point bending test showed that the addition of F-zirconia fillers could maintain the flexure strength of experimental CRs. The flexure strengths of all three groups of CRs were >80 MPa, which could meet to the ISO 4049 standard (Goracci et al., 2014). Furtherly, compared to the control group, addition of F-zirconia fillers could significantly improve the wear resistance of experimental CRs. With the increase of F-zirconia fillers, height loss in the surface wear zones decreased significantly and the wear zones were relatively flat (Table 1; Figure 2).

The daily and cumulative amounts of fluoride release from the experimental CRs were presented in Table 2 and Table 3. In general, the two groups of experimental CRs showed continuous fluoride release within 28 days, and the fluoride release was positively correlated with the content of F-zirconia fillers. The significantly higher amounts of fluoride release were observed during the first 7 days. And the daily amounts of fluoride release decreased in day 14 and 28. It was considered that the fluoride ions were dissolved from the surface of specimens in the early stage. Subsequently, a longer time was required for the fluoride ions to diffuse from the inner part of specimens. The trend of fluoride release here was consistent with that in other similar studies (Naoum et al., 2013; Paul et al., 2020). Compared with the traditional GICs, which contained a large amount of fluoro-alimino-silicate glasses fillers, the experimental CRs showed lower fluoride release, relatively. As we all know that GICs had been widely used as dental restorative material in the past because of its excellent fluoride-releasing and anti-cariogenic properties. But studies have reported that GICs exhibited poor mechanical strength and undesirable wear resistance, which was closely related to the dissolution of soluble fillers (Moshaverinia et al., 2024). In fact, the principle of fluoride release from GICs was acid-base reaction in saliva. The reaction was rapid and uncontrolled, which often showed a "burst release" effect and furtherly led to obvious cracks of materials (Thongsri et al., 2024). In contract, the release of fluoride ions in cured CRs was achieved through diffusing outward when water penetration into the gap between the resin matrix and inorganic fillers. We compared the SEM images of the experimental CRs before and after fluoride release examination in the preliminary study (Zheng et al., 2021). And there were no holes or cracks appeared on the surface of the CRs after fluoride release examination. Thus, the release process of fluoride ions did not affect the structure of nano-zirconia particles, so that it did not damage the mechanical properties of the experimental CRs. Moreover, it was reported that only 0.03 ppm–0.07 ppm fluoride ions could be contributed to transform teeth demineralization to the remineralization phase (Ahmed et al., 2015). Moreover, Marquis R.E. suggested that fluoride ions could inhibit oral bacteria when the concentration reached 0.1 mM (Marquis, 1995). Thus, all observations during 28 days were within the expected range.

Meanwhile, the influence of various pH values on the release of fluoride ions from the experimental CRs was also investigated here. It was discussed that fluoride might interfere with the dynamics of dental caries process *in vivo*, so *in vitro* models that could simulated the caries process were recommended to test the effects of fluoride-releasing materials (Serra and Cury, 1992; Cury et al., 2016). One of the most important causes of dental caries is the dissolution of acids produced by cariogenic bacteria (Zhou et al., 2012). And it was reported that the incidence of caries increased significantly when pH value dropped to 4.0–5.5 (Di Lauro et al., 2023). Thus, it is of necessity to verify the fluoride release property of the experimental CRs in acidic media. As shown in Table 3 and Figure 3, it was interesting to find that the amount of fluoride release in the deionized water (ddH_2O) was higher than that in the neutral buffer (pH 7.0). Like in previous studies, ddH_2O was used as an accurate model of fluoride release from dental materials, and a reduced amount of fluoride release could be found when using neutral buffer or artificial saliva (Behrend and Geurtsen, 2001; Harhash et al., 2017). The reason for this was likely to be the multi-ionic environment accelerated the equilibration of fluoride ions. It could also be found that the amount of fluoride release increased in the acidic buffer (pH 4.2) in this study, but the change was not significant. Therefore, the result revealed that intraoral fluoride release from the experimental CRs might be enhanced on restorations or caries surfaces that were eroded by plaque-associated acids.

Among various of bacterial species in the oral environment, S. mutans was proven to play a major role in the formation of plaque biofilms and the development of caries (Sungurtekin-Ekci et al., 2015). Therefore, antibacterial effects of the experimental CRs were investigated against S. mutans biofilms on the surfaces, as well as the planktonic bacteria. The results of antibacterial effect were shown in Table 4 and Figure 4. Compared with the control group, two experimental groups showed obvious decrease of S. mutans colonies in the CFUs counting. Furtherly, the result of CCK-8 assay confirmed that the experimental CRs effectively inhibited the metabolic activities of S. mutans, and the antibacterial effect was enhanced with the increase of fluoride-doped nano-zirconia fillers content. In fact, a previous research suggested that the antibacterial effect of fluoride agents occurred by the diffusion of fluoride ions (Whitford et al., 1977). Nonetheless, the result here indicated that the experimental CRs could inhibit the growth of S. mutans not only by releasing of the fluoride ions in the media but also through direct contact with the biofilms on the surfaces. The large surface-to-volume ratio of nanoparticles on the surfaces of specimens could help to inhibit the bacterial adhesion and biofilm formation (Chladek et al., 2023). Hence, the antibacterial effect of the experimental CRs might be result from the synergistic effect of fluoride ions and the influence of nanoparticles. Moreover, as the CRs wearing out slowly during the chewing movement, more fluoride-doped nano-zirconia fillers shall be exposed to the oral environment and show antibacterial effect continuously.

To date, although CRs exhibit excellent aesthetic effects compared to other restorative materials, the aging of CRs is still inevitable. The aging process can not only lead to discoloration and poor esthetic result, but also affects clinical longevity and is an important cause of restoration failure with CRs (Chen et al., 2024). Thermal changes were thought to exacerbate the aging process, as the intraoral temperature changes constantly in line with breathing and eating. Thermal cycling was the most common approach that applied to simulate the aging of dental materials during temperature fluctuations that occur in the mouth in previous studies (Gale and Darvell, 1999; Tavas et al., 2023). It was carried out at temperatures equivalent to the intraoral temperature, ranging from 5 °C to 55 °C, and 10,000 cycles might be equivalent to 1 year (Gonder and Fidan, 2022). Color change (ΔE00 value) and microhardness of the experimental CRs affected by aging were presented in Table 5 and Table 6. The color stability of restoration materials was important to meet the esthetic demands in dentistry. It was reported that ΔE00 values between 0.8 and 1.8 were considered acceptable for color changes in clinic that could be detected by the human eyes (Paravina et al., 2015). Based on the results in this study, the control group and the experimental groups had the average ΔE00 values of 1.69, 1.20 and 0.78, respectively, which were all within the acceptable range. The control group showed the highest ΔE00 value. The resin matrix, especially the TEGDMA monomer, might be the major reason for color change of the experimental CRs. It was indicated that TEGDMA exhibited high hydrophilicity and interfere with the color stability by allowing more water diffusion (Fidan and Yağci, 2023). Previous research found that the amount and size of inorganic fillers affected the color stability of CRs obviously. On the one hand, CRs loaded with high amounts of fillers showed higher color stability than that loaded with less fillers. On the other hand, addition of nanoparticles could be advantageous to reduce the polymerization shrinkage of CRs by lowering the resin-to-filler ratio significantly (Hamdy, 2021). As a result, addition of the fluoride-doped nano-zirconia fillers with small sizes could reduce the color change of experimental CRs. However, given that the surface roughness is also vital for the esthetic effect of CRs, additional trials are necessary to observe and analysis the changes of microstructure with aging furtherly.

Moreover, it was observed that the microhardness values of all specimens decreased slightly after the thermal aging progress. This might be the result of cracks in the cross-linking of resin structure and the weak bonding between the matrix and fillers. But the variation of microhardness values among three groups was not statistically different.

As we all know, the restorative procedure was usually associated with loss of significant amounts of hard tissues due to caries attack. Application of composite resin following caries removal would contribute to potential adverse effects on the pulp tissue. Jiang et al. (2017) studied the impact of various dentin thicknesses on the cytotoxicity of three commercial restorative materials *in vitro* and showed that one of the materials reached cytotoxic levels when the thickness was at 1 mm. It is of significance to evaluate the cytotoxicity with cells in pulp tissue. As such we chose human dental pulp cells (HDPs) in cell culture here like previous studies (Schneider et al., 2019; Hadjichristou et al., 2020). Statistical results as showed in Figure 5 revealed that the viabilities of HDPs exposed to eluates of the experimental CRs were not significantly different from that of the negative group. Therefore, the experimental CRs developed here showed no significant cytotoxicity and was qualified for application in clinic.

There are still some limitations in this study. Given the anti-caries effects of fluoride ions include both inhibition of the cariogenic bacteria and remineralization of dentin or enamel, additional investigations are indeed required to clarify the remineralization of the novel CRs. In addition, the experimental conditions can not fully simulate the oral environments, which are also affected by the washing process of saliva and the effect of enzymes. Thus, further *in vivo* tests are needed before clinic application.

5 Conclusion

In summary, a novel composite resin loaded with fluoride-doped nano-zirconia fillers was developed successfully. The fluoride ions released continuously from the experimental CRs resulted in effective contact and releasing antibacterial properties. Addition of fluoride-doped nano-zirconia fillers could improve the color stability, wear resistance and microhardness of the experimental CRs, without reducing the flexure strength. Moreover, the novel CRs showed no cytotoxicity to HDPs. Thus, considerations can be made to use this kind of fluoride-releasing composite resin loaded with fluoride-doped nano-zirconia fillers to improve clinical treatment when the antimicrobial benefits are desired.

Data availability statement

The original contributions presented in the study are included in the article/supplementary material, further inquiries can be directed to the corresponding authors.

Author contributions

LZ: Writing–original draft. YZ: Conceptualization, Investigation, Writing–original draft. YB: Writing–original draft, Investigation, Software. ZZ: Writing–review and editing, Investigation, Methodology. QW: Writing–original draft, Conceptualization, Writing–review and editing, Data curation.

Funding

The author(s) declare that financial support was received for the research, authorship, and/or publication of this article. This research was funded by Fujian provincial health technology project, grant number 2021QNB028, 2023GGB07 and 2021GGB037.

Conflict of interest

The authors declare that the research was conducted in the absence of any commercial or financial relationships that could be construed as a potential conflict of interest.

Publisher's note

References

Ahmed, N., et al. (2015). Therapeutic roles of fluoride released from restorative dental materials. *Fluoride*.

Aldowsari, M. K., Alfawzan, F., Alhaidari, A., Alhogail, N., Alshargi, R., Bin Saleh, S., et al. (2023). Comparison of shear bond strength of three types of adhesive materials used in the restoration of permanent molars after treatment with silver diamine fluoride: an *in vitro* study. *Mater. (Basel)* 16 (21), 6831. doi:10.3390/ma16216831

Bakhsh, T. A., Alfaifi, A., Alghamdi, Y., Nassar, M., and Abuljadyel, R. A. (2023). Thermal sensing of photo-activated dental resin composites using infrared thermography. *Polym. (Basel)* 15 (20), 4117. doi:10.3390/polym15204117

Behrend, B., and Geurtsen, W. (2001). Long-term effects of four extraction media on the fluoride release from four polyacid-modified composite resins (compomers) and one resin-modified glass-ionomer cement. *J. Biomed. Mater Res.* 58 (6), 631–637. doi:10.1002/jbm.1062

Chen, S., Zhu, J., Yu, M., Jin, C., and Huang, C. (2024). Effect of aging and bleaching on the color stability and surface roughness of a recently introduced single-shade composite resin. *J. Dent.* 143, 104917. doi:10.1016/j.jdent.2024.104917

Cheng, L., Zhou, X., Zhong, H., Deng, X., Cai, Q., and Yang, X. (2014). NaF-loaded core-shell PAN-PMMA nanofibers as reinforcements for Bis-GMA/TEGDMA restorative resins. *Mater Sci. Eng. C Mater Biol. Appl.* 34, 262–269. doi:10.1016/j.msec.2013.09.020

Chladek, G., Barszczewska-Rybarek, I., Chrószcz-Porębska, M., and Mertas, A. (2023). The effect of quaternary ammonium polyethylenimine nanoparticles on bacterial adherence, cytotoxicity, and physical and mechanical properties of experimental dental composites. *Sci. Rep.* 13 (1), 17497. doi:10.1038/s41598-023-43851-y

Cury, J. A., de Oliveira, B. H., dos Santos, A. P., and Tenuta, L. M. A. (2016). Are fluoride releasing dental materials clinically effective on caries control? *Dent. Mater* 32 (3), 323–333. doi:10.1016/j.dental.2015.12.002

David, A., Kerketta, S., Tanco, M. A. L., Yokoyama, T., and Suzuki, T. M. (2002). Adsorption of fluoride ion on the zirconium(IV) complexes of the chelating resins functionalized with amine-N-acetate ligands. *Sep. Sci. Technol.* 37 (4), 877–894. doi:10.1081/ss-120002221

Di Lauro, A., Di Duca, F., Montuori, P., Dal Piva, A. M. d. O., Tribst, J. P. M., Borges, A. L. S., et al. (2023). Fluoride and calcium release from alkasite and glass ionomer restorative dental materials: *in vitro* study. *J. Funct. Biomater.* 14 (2), 109. doi:10.3390/jfb14020109

Ei, T. Z., Shimada, Y., Nakashima, S., Romero, M. J. R. H., Sumi, Y., and Tagami, J. (2018). Comparison of resin-based and glass ionomer sealants with regard to fluoride-release and anti-demineralization efficacy on adjacent unsealed enamel. *Dent. Mater J.* 37 (1), 104–112. doi:10.4012/dmj.2016-407

Eltahlah, D., Lynch, C. D., Chadwick, B. L., Blum, I. R., and Wilson, N. H. (2018). An update on the reasons for placement and replacement of direct restorations. *J. Dent.* 72, 1–7. doi:10.1016/j.jdent.2018.03.001

Fidan, M., and Yağci, Ö. (2023). Effect of aging and fiber-reinforcement on color stability, translucency, and microhardness of single-shade resin composites versus multi-shade resin composite. *J. Esthet. Restor. Dent.*, 13125. doi:10.1111/jerd.13125

Francois, P., Fouquet, V., Attal, J. P., and Dursun, E. (2020). Commercially available fluoride-releasing restorative materials: a review and a proposal for classification. *Mater. (Basel)* 13 (10), 2313. doi:10.3390/ma13102313

Gale, M. S., and Darvell, B. W. (1999). Thermal cycling procedures for laboratory testing of dental restorations. *J. Dent.* 27 (2), 89–99. doi:10.1016/s0300-5712(98)00037-2

Gonder, H. Y., and Fidan, M. (2022). Effect of different polymerization times on color change, translucency parameter, and surface hardness of bulk-fill resin composites. *Niger. J. Clin. Pract.* 25 (10), 1751–1757. doi:10.4103/njcp.njcp_258_22

Goracci, C., Cadenaro, M., Fontanive, L., Giangrosso, G., Juloski, J., Vichi, A., et al. (2014). Polymerization efficiency and flexural strength of low-stress restorative composites. *Dent. Mater* 30 (6), 688–694. doi:10.1016/j.dental.2014.03.006

Hadjichristou, C., Papachristou, E., Bonovolias, I., and Bakopoulou, A. (2020). Three-dimensional tissue engineering-based Dentin/Pulp tissue analogue as advanced biocompatibility evaluation tool of dental restorative materials. *Dent. Mater* 36 (2), 229–248. doi:10.1016/j.dental.2019.11.013

Hamdy, T. (2021). Polymerization shrinkage in contemporary resin-based dental composites: a Review Article. *Egypt. J. Chem.* 64 (6), 0–3092. doi:10.21608/ejchem.2021.60131.3286

Hamilton, I. R. (1977). Effects of fluoride on enzymatic regulation of bacterial carbohydrate metabolism. *Caries Res.* 11 (Suppl. 1), 262–291. doi:10.1159/000260304

Hamilton, I. R., and Ellwood, D. C. (1978). Effects of fluoride on carbohydrate metabolism by washed cells of Streptococcus mutans grown at various pH values in a chemostat. *Infect. Immun.* 19 (2), 434–442. doi:10.1128/iai.19.2.434-442.1978

Harhash, A. Y., ElSayad, I. I., and Zaghloul, A. G. S. (2017). A comparative *in vitro* study on fluoride release and water sorption of different flowable esthetic restorative materials. *Eur. J. Dent.* 11 (2), 174–179. doi:10.4103/ejd.ejd_228_16

Hata, K., Ikeda, H., Nagamatsu, Y., Masaki, C., Hosokawa, R., and Shimizu, H. (2022). Dental poly(methyl methacrylate)-based resin containing a nanoporous silica filler. *J. Funct. Biomater.* 13 (1), 32. doi:10.3390/jfb13010032

Hong, G., Yang, J., Jin, X., Wu, T., Dai, S., Xie, H., et al. (2020). Mechanical properties of nanohybrid resin composites containing various mass fractions of modified zirconia particles. *Int. J. Nanomedicine* 15, 9891–9907. doi:10.2147/ijn.s283742

Hosaka, K., Tichy, A., Yamauti, M., et al. (2023). Digitally guided direct composite injection technique with a Bi-layer clear mini-index for the management of extensive occlusal caries in a pediatric patient: a case report. *J. Adhes. Dent.* 25 (1), 211–218. doi:10.3290/j.jad.b4515527

Jiang, R. D., Lin, H., Zheng, G., Zhang, X., Du, Q., and Yang, M. (2017). *In vitro* dentin barrier cytotoxicity testing of some dental restorative materials. *J. Dent.* 58, 28–33. doi:10.1016/j.jdent.2017.01.003

Kaur, J., Kapoor, D., Garg, D., Sunil, M. K., Sawhney, A., Malaviya, N., et al. (2015). Evaluation of microleakage of dental composites using bonding agents with different placement techniques: an invitro study. *J. Clin. Diagn Res.* 9 (9), Zc61–Zc64. doi:10.7860/jcdr/2015/14356.6506

Kim, Y. S., Baek, S. H., and Kim, R. J. Y. (2022). Effect of vibration during bulk and incremental filling on adaptation of a bulk-fill composite resin. *Sci. Rep.* 12 (1), 21652. doi:10.1038/s41598-022-26197-9

Loguercio, A. D., Ñaupari-Villasante, R., Gutierrez, M. F., Gonzalez, M. I., Reis, A., and Heintze, S. D. (2023). 5-year clinical performance of posterior bulk-filled resin composite restorations: a double-blind randomized controlled trial. *Dent. Mater* 39 (12), 1159–1168. doi:10.1016/j.dental.2023.10.018

Maletin, A., Knežević, M. J., Koprivica, D. Đ., Veljović, T., Puškar, T., Milekić, B., et al. (2023). Dental resin-based luting materials-review. *Polym. (Basel)* 15 (20), 4156. doi:10.3390/polym15204156

Marquis, R. E. (1995). Antimicrobial actions of fluoride for oral bacteria. *Can. J. Microbiol.* 41 (11), 955–964. doi:10.1139/m95-133

Melo, M. A., Guedes, S. F., Xu, H. H., and Rodrigues, L. K. (2013). Nanotechnology-based restorative materials for dental caries management. *Trends Biotechnol.* 31 (8), 459–467. doi:10.1016/j.tibtech.2013.05.010

Moshaverinia, M., de Almeida Queiroz Ferreira, L., Smidt, G., Shah, K. C., Ansari, S., and Moshaverinia, A. (2024). Evaluation of mechanical, optical, and fluoride-releasing properties of a translucent bulk fill glass hybrid restorative dental material. *J. Esthet. Restor. Dent.* 36 (3), 503–510. doi:10.1111/jerd.13168

Naoum, S., Martin, E., and Ellakwa, A. (2013). Long-term fluoride exchanges at restoration surfaces and effects on surface mechanical properties. *ISRN Dent.* 2013, 1–8. doi:10.1155/2013/579039

Opdam, N. J., Bronkhorst, E. M., Loomans, B. A., and Huysmans, M. C. (2010). 12-year survival of composite vs. amalgam restorations. *J. Dent. Res.* 89 (10), 1063–1067. doi:10.1177/0022034510376071

Paravina, R. D., Ghinea, R., Herrera, L. J., Bona, A. D., Igiel, C., Linninger, M., et al. (2015). Color difference thresholds in dentistry. *J. Esthet. Restor. Dent.* 27 (Suppl. 1), S1–S9. doi:10.1111/jerd.12149

Paul, S., Raina, A., Kour, S., Mishra, S., Bansal, M., and Sengupta, A. (2020). Comparative evaluation of fluoride release and re-release and recharge potential of Zirconomer Improved and Cention. *J. Conserv. Dent.* 23 (4), 402–406. doi:10.4103/jcd.jcd_222_20

Pizzolotto, L., and Moraes, R. R. (2022). Resin composites in posterior teeth: clinical performance and direct restorative techniques. *Dent. J. (Basel)* 10 (12), 222. doi:10.3390/dj10120222

Pollick, H. (2018). The role of fluoride in the prevention of tooth decay. *Pediatr. Clin. North Am.* 65 (5), 923–940. doi:10.1016/j.pcl.2018.05.014

Schneider, T. R., Hakami-Tafreshi, R., Tomasino-Perez, A., Tayebi, L., and Lobner, D. (2019). Effects of dental composite resin monomers on dental pulp cells. *Dent. Mater J.* 38 (4), 579–583. doi:10.4012/dmj.2018-163

Serra, M. C., and Cury, J. A. (1992). The *in vitro* effect of glass-ionomer cement restoration on enamel subjected to a demineralization and remineralization model. *Quintessence Int.* 23 (2), 143–147.

Shibasaki, S., Takamizawa, T., Nojiri, K., Imai, A., Tsujimoto, A., Endo, H., et al. (2017). Polymerization behavior and mechanical properties of high-viscosity bulk fill and low shrinkage resin composites. *Oper. Dent.* 42 (6), E177–E187. doi:10.2341/16-385-l

Stewart, C. A., and Biostable, Y. F. (2019). Biostable, antidegradative and antimicrobial restorative systems based on host-biomaterials and microbial interactions. *Dent. Mater* 35 (1), 36–52. doi:10.1016/j.dental.2018.09.013

Sungurtekin-Ekci, E., Ozdemir-Ozenen, D., Duman, S., Acuner, I. C., and Sandalli, N. (2015). Antibacterial surface properties of various fluoride-releasing restorative materials *in vitro*. *J. Appl. Biomater. Funct. Mater* 13 (2), e169–e173. doi:10.5301/jabfm.5000212

Tavas, B., Celiksoz, O., Tepe, H., Ozaslan, S., and Yaman, B. C. (2023). The effect of whitening toothpastes on the color stability of a smart monochromatic composite resin. *Cureus* 15 (9), e46225. doi:10.7759/cureus.46225

Thongsri, O., Thaitalay, P., Srisuwan, S., Khophai, S., Suksaweang, S., Rojviriya, C., et al. (2024). Enhanced remineralisation ability and antibacterial properties of sol-gel glass ionomer cement modified by fluoride containing strontium-based bioactive glass or strontium-containing fluorapatite. *Dent. Mater* 40, 716–727. doi:10.1016/j.dental.2024.02.014

Van der Laan, H. L., Zajdowicz, S. L., Kuroda, K., Bielajew, B., Davidson, T., Gardinier, J., et al. (2019). Biological and mechanical evaluation of novel prototype dental composites. *J. Dent. Res.* 98 (1), 91–97. doi:10.1177/0022034518795673

Van Ende, A., De Munck, J., Lise, D. P., and Van Meerbeek, B. (2017). Bulk-Fill composites: a review of the current literature. *J. Adhes. Dent.* 19 (2), 95–109. doi:10.3290/j.jad.a38141

Velazquez-Jimenez, L. H., Hurt, R. H., Matos, J., and Rangel-Mendez, J. R. (2014). Zirconium-carbon hybrid sorbent for removal of fluoride from water: oxalic acid mediated Zr(IV) assembly and adsorption mechanism. *Environ. Sci. Technol.* 48 (2), 1166–1174. doi:10.1021/es403929b

Wei Su, L., Lin, D. J., and Yen Uan, J. (2019). Novel dental resin composites containing LiAl-F layered double hydroxide (LDH) filler: fluoride release/recharge, mechanical properties, color change, and cytotoxicity. *Dent. Mater* 35 (5), 663–672. doi:10.1016/j.dental.2019.02.002

Whitford, G. M., Schuster, G. S., Pashley, D. H., and Venkateswarlu, P. (1977). Fluoride uptake by Streptococcus mutans 6715. *Infect. Immun.* 18 (3), 680–687. doi:10.1128/iai.18.3.680-687.1977

Wiegand, A., Buchalla, W., and Attin, T. (2007). Review on fluoride-releasing restorative materials-fluoride release and uptake characteristics, antibacterial activity and influence on caries formation. *Dent. Mater* 23 (3), 343–362. doi:10.1016/j.dental.2006.01.022

Wolter, S. D., Piascik, J. R., and Stoner, B. R. (2011). Characterization of plasma fluorinated zirconia for dental applications by X-ray photoelectron spectroscopy. *Appl. Surf. Sci.* 257 (23), 10177–10182. doi:10.1016/j.apsusc.2011.07.013

Xu, X., Ling, L., Wang, R., and Burgess, J. O. (2006). Formulation and characterization of a novel fluoride-releasing dental composite. *Dent. Mater* 22 (11), 1014–1023. doi:10.1016/j.dental.2005.11.027

Zheng, L., Li, Ke, Ning, C., et al. (2021). Study on antibacterial and fluoride-releasing properties of a novel composite resin with fluorine-doped nano-zirconia fillers. *J. Dent.* 30 (4), 218–224. doi:10.1016/j.jdent.2021.103772

Zhou, S. L., Zhou, J., Watanabe, S., Watanabe, K., Wen, L. Y., and Xuan, K. (2012). *In vitro* study of the effects of fluoride-releasing dental materials on remineralization in an enamel erosion model. *J. Dent.* 40 (3), 255–263. doi:10.1016/j.jdent.2011.12.016

frontiers | Frontiers in Bioengineering and Biotechnology

TYPE Original Research
PUBLISHED 28 June 2024
DOI 10.3389/fbioe.2024.1418903

OPEN ACCESS

EDITED BY
Wei Nie,
Wake Forest Baptist Medical Center,
United States

REVIEWED BY
Dongxu Ke,
Wake Forest University, United States
Tao Ji,
Shenzhen University, China
Xijian Liu,
Shanghai University of Engineering Sciences,
China

*CORRESPONDENCE
Qian Wang,
Drwangqian23@163.com
Nian Zhou,
zhounian_2008@126.com
Zhenming Hu,
spinecenter@163.com

†These authors have contributed equally to this work

RECEIVED 17 April 2024
ACCEPTED 10 June 2024
PUBLISHED 28 June 2024

CITATION
Ren H, Xiang S, Liu A, Wang Q, Zhou N and Hu Z (2024), A noval noninvasive targeted therapy for osteosarcoma: the combination of LIFU and ultrasound-magnetic-mediated SPIO/TP53/PLGA nanobubble.
Front. Bioeng. Biotechnol. 12:1418903.
doi: 10.3389/fbioe.2024.1418903

A noval noninvasive targeted therapy for osteosarcoma: the combination of LIFU and ultrasound-magnetic-mediated SPIO/TP53/PLGA nanobubble

Honglei Ren[1,2†], Shanlin Xiang[1†], Aiguo Liu[1,3,4], Qian Wang[3*], Nian Zhou[1*] and Zhenming Hu[1,5*]

[1]Department of Orthopedic Surgery, The First Affiliated Hospital of Chongqing Medical University, Chongqing, China, [2]Department of Orthopedic Surgery, ChongQing Red Cross Hospital (People's Hospital of JiangBei District), Chongqing, China, [3]Department of Orthopedics, Shanghai Pudong Hospital, Fudan University Pudong Medical Center, Shanghai, China, [4]Department of Orthopedic Surgery, The First Affiliated Hospital of Henan University, Kaifeng, China, [5]Department of Orthopedic Surgery, The University-Town Hospital of Chongqing Medical University, Chongqing, China

Purpose: Osteosarcoma (OS) is the most common type of primary malignant bone tumor. Transducing a functional TP53 gene can effectively inhibit OS cell activity. Poly lactic acid-glycolic acid (PLGA) nanobubbles (NBs) mediated by focused ultrasound (US) can introduce exogenous genes into target cells in animal models, but this technique relies on the passive free diffusion of agents across the body. The inclusion of superparamagnetic iron oxide (SPIO) in microbubbles allows for magnetic-based tissue localization. A low-intensity-focused ultrasound (LIFU) instrument was developed at our institute, and different intensities of LIFU can either disrupt the NBs (RLI-LIFU) or exert cytocidal effects on the target tissues (RHI-LIFU). Based on these data, we performed US-magnetic-mediated TP53-NB destruction and investigated its ability to inhibit OS growth when combined with LIFU both *in vitro* and *in vivo*.

Methods: Several SPIO/TP53/PLGA (STP) NB variants were prepared and characterized. For the *in vitro* experiments, HOS and MG63 cells were randomly assigned into five treatment groups. Cell proliferation and the expression of TP53 were detected by CCK8, qRT-PCR and Western blotting, respectively. *In vivo*, tumor-bearing nude mice were randomly assigned into seven treatment groups. The iron distribution of Perls' Prussian blue-stained tissue sections was determined by optical microscopy. TUNEL-DAPI was performed to examine apoptosis. TP53 expression was detected by qRT-PCR and immunohistochemistry.

Results: SPIO/TP53/PLGA NBs with a particle size of approximately 200 nm were prepared successfully. For *in vitro* experiments, ultrasound-targeted transfection of TP53 overexpression in OS cells and efficient inhibition of OS proliferation have been demonstrated. Furthermore, in a tumor-bearing nude mouse model, RLI-LIFU-magnetic-mediated SPIO/TP53/PLGA NBs

increased the transfection efficiency of the TP53 plasmid, resulting in apoptosis. Adding RHI-LIFU to the treatment regimen significantly increased the apoptosis of OS cells *in vivo*.

Conclusion: Combining LIFU and US-magnetic-mediated SPIO/TP53/PLGA NB destruction is potentially a novel noninvasive and targeted therapy for OS.

KEYWORDS

osteosarcoma, low-intensity-focused ultrasound, nanobubbles, superparamagnetic iron oxide, PLGA

Introduction

Osteosarcoma (OS) is the most common type of primary malignant bone tumor and is characterized by local invasion and distant metastasis. The current clinical treatment modalities for OS include surgical resection of primary tumors and systemic chemotherapy. Research has shown that the application of neoadjuvant chemotherapy increases the tumor-free survival of OS from 1% to 50%–65%. However, resistance of OS cells to chemotherapeutic drugs remains a major limiting factor for current treatment modalities for this disease. Additionally, surgical treatment for OS may cause significant physical trauma. Therefore, a new, less traumatic therapy would be of great significance.

In recent years, gene therapy for OS has emerged as an exciting novel research field. TP53 was found to be the most frequently mutated gene among the tumor suppressor genes, with approximately 60% of human tumors presenting TP53 mutations. Current literature shows that OS exhibits a wide range of gene mutations and molecular alterations. However, apart from mutations in the TP53 and/or retinoblastoma (RB) genes, no novel gene mutations have been identified. Several studies have demonstrated that transfection of a functional copy of the TP53 gene could inhibit the growth of OS cells (Bekeredjian et al., 2007; Chen et al., 2012; Chen et al., 2010).

The introduction of exogenous genes relies on gene vectors, and the stability of the gene will be relatively poor without an optimal gene vector. In recent years, great progress has been made in vector research, and high transfection efficiencies have been shown for viral vectors. However, due to the high immunogenicity of viruses, their application is limited. Nonviral vectors such as liposomes are safe and less toxic compared with viral vectors, but instability and inefficiency remain constraints that cannot be ignored (Chertok et al., 2007; Du et al., 2011; Elzeny et al., 2017; Hida et al., 2011). Therefore, finding a safe, efficient, and targeted gene therapy transfection system has become the focus of researchers.

Poly (lactic-co-glycolic acid) (PLGA) nanobubbles (NBs) are nonviral vectors that offer significant advantages, including slow release, penetration, and 'targeting'. These characteristics make PLGA NBs an ideal choice for drug or gene carriers (Huang et al., 2012; Hynynen et al., 2006; Jiang and Dalby, 2023). However, the "targeting" of this delivery system is still passive and depends on the free diffusion of the medium across the body. Superparamagnetic iron oxide (SPIO, diameter <10 nm) nanoparticles are a type of magnetic nanoparticle that are physically sensitive to external magnetic fields, and magnetic targeting (MT) can be applied to actively enhance the concentration in the target area (Lu et al., 2003; Sirsi et al., 2012). Hence, we hypothesized that the incorporation of SPIO and MT into TP53/PLGA NBs could serve as an effective strategy to augment gene transfection in the targeted area.

Recently, ultrasound (US)-mediated microbubble destruction (UTMD) has undergone rapid development. UTMD has been demonstrated to be a safe and effective method for gene transfection by numerous studies (Sun et al., 2023; Tang et al., 2012; Wells, 2010; Wu et al., 2020). UTMD has been successfully used for gene transfection of the kidney, testis, heart, pancreas, lung, skin, uterus, brain, retina diseases, and spinal cord (Sitta and Howard, 2021; Steiniger et al., 2004; Xenariou et al., 2007). Low-intensity-focused ultrasound (LIFU) can disrupt target nanobubbles at low intensity (referred to as relatively low-intensity mode, RLI mode), whereas at higher intensities (referred to as relatively high-intensity mode, RHI mode), LIFU induces range-controllable cytocidal effects on tissues (Yamaguchi et al., 2011; Yin et al., 2014; Zhong et al., 2012). To the best of our knowledge, few studies have investigated gene therapy for OS through US-magnetic-mediated NB destruction, and direct OS treatment using RHI-mode LIFU has not been reported. Thus, it remains unclear whether US-magnetic-mediated gene transfection in combination with LIFU represents an effective therapeutic strategy for OS.

In this study, we performed US-magnetic-mediated TP53-NB destruction and evaluated its potential to inhibit OS growth when combined with LIFU in both *in vitro* and *in vivo* experiments.

Material and methods

Preparations of SPIO/PLGA-NBs (SP-NBs), TP53/PLGA-NBs (TP-NBs) and SPIO/TP53/PLGA-NBs (STP-NBs)

NBs were freshly prepared prior to use. SPIO nanoparticles (mean diameter = 5 nm, concentration = 25 mg/mL) were purchased from Ocean Nanotech Co., Ltd. The TP53 plasmid was purchased from OriGene Technologies, Inc. and extracted using an endotoxin-free plasmid extract kit (enhanced) (DP120; TIANGEN BIOTECH (BEIJING) Co., Ltd.). PLGA (50:50, molecular weight [MW] = 12,000) was purchased from Polyscitech Co., Ltd. Polyvinyl alcohol (PVA, MW = 30,000-70,000) was purchased from Sigma Co., Ltd.

As reported previously, STP-NBs were prepared by the double-emulsion method. (Kiwada et al., 1986). First, 50 mg PLGA was completely dissolved in 2 mL dichloromethane, 600 μg

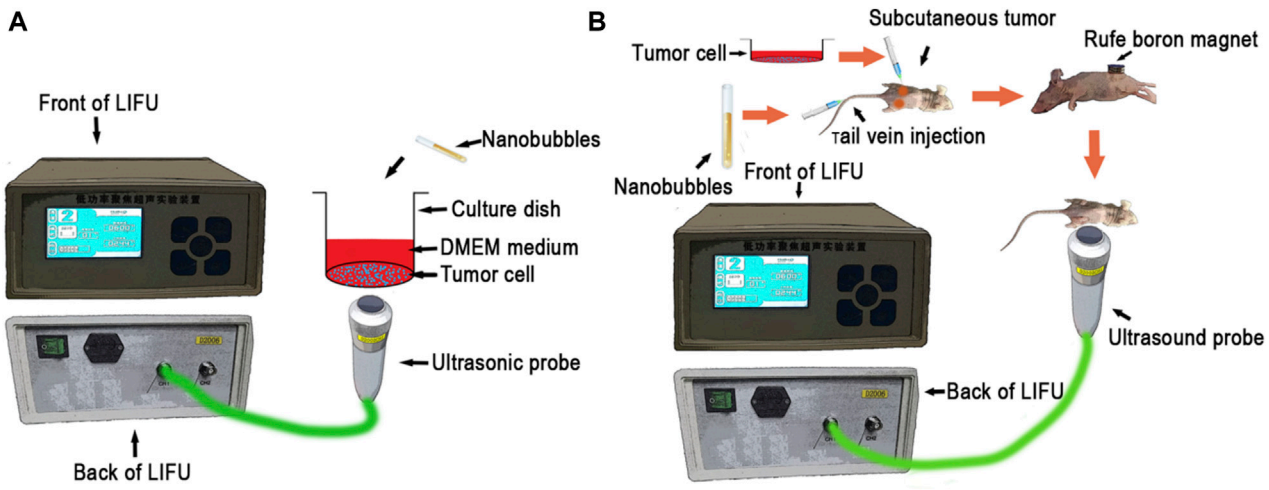

FIGURE 1
(A) Schematic of the *in vitro* experimental setup, **(B)** Schematic of the *in vivo* experimental setup.

TP53 plasmids and 20 μL SPIO were added to the solution. The mixture was emulsified in an ice bath using an ultrasonic processor for 5 min at a power of 175 W. Then, 5 mL cold PVA solution (4% W/V) was added to the initial emulsion, and an ultrasonic processor was used to further emulsify the product in the ice bath with a power of 125 W for 3 min. Then, 10 mL of 1% isopropanol solution was added to the second emulsion. The final solution was stirred with a magnetic agitator for 3 h. The volatilized solution was centrifuged at a low temperature centrifuge at 4°C for 10 min at 10000×g. The precipitate was washed with deionized water, and the supernatant was collected for further detection. The centrifugal washing step was repeated 3 times. Finally, the precipitate after washing was temporarily stored at 4°C for further use. SP-NBs and TP-NBs were similarly prepared without the addition of either TP53 or SPIO.

Characterizations of TP-NBs and STP-NBS

A laser particle size analyzer system (Zeta SIZER, Malvern) was used to analyze the mean diameter, zeta potential, and polydispersity index (PDI) of the samples. Transmission electron microscopy (TEM; Hitachi H-7600) was used to evaluate the shape of the NBs, whereas scanning electron microscopy (SEM; JEOL JSM-7800F) was used to assess the morphological characteristics of the nanoparticles. (Zhao et al., 2015). The iron content of the STP-NBs was determined by the o-phenanthroline method. The encapsulation efficiency of SPIO is calculated as follows: encapsulation efficiency = W1/W2×100%, where W1 is the amount of SPIO in STP-NBs and W2 is the total amount of SPIO used to prepare STP-NBs. (Kiwada et al., 1986; Ting et al., 2012). We compared SPIO encapsulation efficiencies at five SPIO total inputs (0.1, 0.3, 0.5, 0.7 and 0.9 mg). The SPIO encapsulation efficiency test was repeated three times. The gene encapsulation efficiency was determined by an ultraviolet spectrophotometer (Thermo NanoDrop 2000; Thermo Fisher Scientific). The encapsulation efficiency of TP53 is calculated as follows: encapsulation efficiency = (W2-W1/W2 ×100)%, where W1 is the number of genes in the supernatant after centrifugation and W2 is the total amount of TP53 used to prepare STP-NBs. (Zhang et al., 2014; Wang et al., 2019). We compared TP53 encapsulation efficiencies at five TP53 plasmid total inputs (0.1, 0.2, 0.4, 0.8, and 1 mg). The TP53 encapsulation efficiency test was repeated three times. To assess gene release behavior, *in vitro* sonication was performed using an RLI-mode LIFU. The frequency was 0.95 MHz, the power was modulated at a pulse modulation of 300 Hz, and the depth of focus of the probe was 15 mm. The ultrasonic power is 1.5 W and lasts 60 s. STP-NBs (TP-NBs) from 10 mL phosphate buffered saline (PBS) were transferred to dialysis bags (molecular weight cut-off: 10,000 Da) and placed in a 100 mL PBS reservoir after ultrasound. After the appropriate time interval, 1 mL dialysate was taken, and the gene concentration was determined by ultraviolet spectrophotometry. One milliliter of fresh PBS was added to the reservoir to keep the liquid volume constant. The cumulative release ratio of TP53 released was calculated. To investigate the magnetization capacity, STP-NBs were placed under a magnetic field, and the adsorption time was recorded.

In vitro studies on MG63 and HOS osteosarcoma cells

In vitro focused ultrasound (FUS) sonication setup

The MG63 and HOS cell lines used in this study were acquired from Professor Tong-Chuan He (Chongqing Medical University, Chongqing, China). To assess gene release behavior, *in vitro* sonication was performed by using RLI-mode LIFU. The sonication parameters of RLI-mode were set at 1.5 W for 5 min (Figure 1A).

HOS and MG63 cells were randomly assigned into five treatment groups:

1. Control group: 50 μL PBS was added to 24-well plates, and 10 μL PBS was added to 96-well plates.

2. TP53 + SP-NBs group: 25 μL TP53 plasmid (1 μg) and 25 μL SP-NB solution were added to 24-well plates; 5 μL TP53 plasmid (0.2 μg) and 5 μL SP-NB solution were added to 96-well plates.
3. TP53 + US group: 25 μL TP53 plasmid (1 μg) and 25 μL PBS solution were added to 24-well plates, which were then subjected to RLI-mode LIFU irradiation; 5 μL TP53 plasmid (0.2 μg) and 5 μL PBS solution were added to 96-well plates, which were then subjected to RLI-mode LIFU irradiation (Figure 1A).
4. TP-NBs + US group: 50 μL TP-NB (TP53, 1 μg) solution was added to 24-well plates, which were then subjected to RLI-mode LIFU irradiation; 10 μL TP-NB (TP53, 0.2 μg) solution was added to 96-well plates, which were then subjected to RLI-mode LIFU irradiation (Figure 1A).
5. STP-NBs + US group: 50 μL STP-NB (TP53, 1 μg) solution was added to 24-well plates, which were then subjected to RLI-mode LIFU irradiation; 10 μL STP-NB (TP53, 0.2 μg) solution was added to 96-well plates, which were then subjected to RLI-mode LIFU irradiation (Figure 1A).

Cell proliferation assay

The proliferative capacity of cells was detected using a cell counting kit-8 assay (CCK8, MedChemExpress, United States). MG63 and HOS cells were seeded in 96-well plates at a density of 2000 cells/well and cultured for 36 h. Then, the cells were grouped, treated as specified above and cultured for 2 h. After that, the cells were washed three times with PBS and cultured for another 36 h in fresh cell culture medium. Finally, 10 μL CCK8 reagent was added to the wells. After the plates were incubated for 0.5–4 h, cell proliferation was detected by measuring the absorbance at 450 nm with a microplate reader. Cell viability (%) relative to that of the control cells was calculated according to the instructions of the CCK-8 assay. (Livak and Schmittgen, 2001).

Real-time PCR

MG63 and HOS cells were seeded in 24-well plates at a density of 1*105 cells/well and cultured for 36 h. Then, the cells were grouped, treated as specified above and cultured for 2 h. After that, the cells were washed three times with PBS and cultured for another 36 h in fresh cell culture medium. Finally, total RNA was isolated by using TRIzol reagent (TAKARA BIO INC) following the manufacturer's protocols. The PrimeScript™ RT reagent kit was used to reverse transcribe RNA to complementary DNA (cDNA). SYBR Green Super Mixture (TAKARA BIO INC) was used to amplify the resulting cDNA. The P53 primer sequences were as follows: 5′-GCCATCTACAAGCAGTCACAGC-3′ (sense) and 5′- CATCCA AATACTCCACACGCAA-3′ (antisense). The GAPDH primer sequences were as follows: 5′-TCAAGAAGGTGGTGAAGCAGG-3′ (sense) and 5′-AGCGTCAAAGGTGGAGGAGTG-3′ (antisense). The CFX-Connect real-time PCR system (Bio-Rad) was used to conduct qRT-PCR in 96-well plates. The amplification conditions were as follows: 95°C for 3 min, followed by 45 cycles of 95°C for 10 s and 58°C for 30 s. Each qRT-PCR analysis was carried out in triplicate, and the $2^{-\Delta\Delta CT}$ method was used to analyze the data.

Western blotting analysis

MG63 and HOS cells were seeded in 24-well plates at a density of 1*105 cells/well and cultured for 36 h. Then, the cells were grouped, treated as specified above and cultured for another 2 h. After that, the cells were washed three times with PBS and cultured for an additional 36 h in fresh cell culture medium. Finally, proteins were homogenized in lysis buffer and phenylmethanesulfonyl fluoride (Beyotime, China). The bicinchoninic acid assay (Beyotime Institute of Biotechnology, China) was used to determine the protein concentrations. The lysates were centrifuged at a low temperature centrifuge at 4°C for 10 min at 10000×g, and the supernatants were collected and transferred into separate enzyme-free tubes. The same amounts of protein were separated by SDS-PAGE and transferred to a polyvinylidene fluoride (PVDF) membrane. The membranes were blocked in 5% skim milk for 1 h at room temperature and incubated with specific primary antibodies at 4°C overnight. The membranes were sealed in 5% skim milk at room temperature for 1 h and incubated with specific primary antibody (anti-P53, Anffinity, United States; 1:1,000; anti-GAPDH, Anffinity, United States; 1: 10000) overnight at 4°C. After washing with TBST three times, membranes were incubated with the secondary antibodies at room temperature for 1 h. An Immobilon Western Chemiluminescent Kit (NCM Biotech, China) was used to visualize the labeled protein bands. The band density of P53 protein was normalized to GAPDH, and all western blots were quantified using ImageJ software.

In vivo studies on osteosarcoma

In vivo experimental setup

This study was conducted according to the guidelines for the care and use of experimental animals from the National Institutes of Health, and the experimental schemes were approved by the Animal Ethics Committee of Chongqing Medical University (Figure 1B).

HOS cells were digested and collected at 90% density and resuspended in serum-free 1,064 medium to 5×10^7 cells/mL. Each athymic nude mouse (4 weeks old, Beijing HFK Bioscience Corporation, China) was subcutaneously injected with 100 μL cell suspension (approximately 5×10^6 cells). (Lin et al., 2019). To assess gene release behavior, *in vitro* sonication was performed by using LIFU. The sonication parameters of the RLI-mode were 1.5 W for 5 min, and the parameters of the RHI-mode were set as follows: power, 12 W; sound intensity, 19.2 w/cm2 at focus; depth of focus of 1.5 cm. Two weeks after subcutaneous implantation, the tumor-bearing nude mice were randomly assigned into seven treatment groups:

1. Control group: 1 mL NS was injected via the tail vein.
2. TP53 + SP-NBs + MT group: 0.5 mL TP53 plasmid (50 μg) and 0.5 mL SP-NB solution were injected via the tail vein. For animals undergoing the MT procedure, a permanent magnet was placed tightly to the surface skin of the tumor nodules for 30 min.
3. TP53 + US group: 0.5 mL TP53 plasmid (50 μg) solution and 0.5 mL NS were injected via the tail vein and subjected to RLI-mode LIFU irradiation.
4. TP-NBs + MT + US group: 1 mL TP-NB (TP53, 50 μg) solution was injected via the tail vein, and a RuFe boron magnet was

applied tightly to the surface skin of the tumor nodules for 30 min before the mice were subjected to RLI-mode LIFU irradiation (Figure 1B).

5. STP-NBs + US group: A 1 mL STP-NB (TP53, 50 μg) solution was injected via the tail vein, and then the mice were subjected to RLI-mode LIFU irradiation.
6. STP-NBs + US + MT group: A 1 mL STP-NB (TP53, 50 μg) solution was injected via the tail vein, and then a permanent magnet was placed tightly to the surface skin overlaying the tumor nodules for 30 min before the mice were subjected to RLI-mode LIFU irradiation (Figure 1B).
7. STP-NBs + US + MT + LIFU group: A 1 mL STP-NB (TP53, 50 μg) solution was injected via the tail vein, and then a RuFe boron magnet was applied tightly to the surface skin of the tumor nodules for 30 min. Next, the mice were subjected to RLI-mode LIFU irradiation followed by RHI-mode LIFU irradiation for 10 min (Figure 1B).

All mice received their respective drug injections every 24 h, which was continued for 5 days, and tumor nodules were collected 7 days after the last transfection. The retrieved tumor tissues were fixed in 4% paraformaldehyde for 24 h and embedded in paraffin. During the treatment, all nude mice were intraperitoneally injected with pentobarbital for deep anesthesia.

Perls' Prussian blue assay

The iron distribution was determined by examining tissue sections stained with Perls' Prussian blue by light microscopy. (Asano et al., 2006). Briefly, the tissue sections were dewaxed with xylene, rehydrated with reduced ethanol concentration, rinsed with distilled water, and incubated with the staining solution for 20 min. Then, the tissue sections were rinsed with distilled water for 5 min and counterstained with nuclear fast red for 5 min. Prussian blue-positive cells were stained blue. Sections were imaged under a microscope, and the number of positive cells was counted.

TUNEL assay

A terminal deoxynucleotidyl transferase-mediated dUTP-biotin nick end labeling (TUNEL) staining kit was used to analyze OS apoptosis. Briefly, tissue sections were dewaxed in xylene, rehydrated by reducing the concentration of ethanol, washed in distilled water, protease treated, and incubated with TUNEL reactive mixture. Nuclear reverse staining with 4′,6-diamidino-2-phenylindole (DAPI). The nuclei of TUNEL-positive cells were dense and showed green fluorescence, suggesting apoptosis. The sections were imaged by fluorescence microscopy.

Total TP53 expression *in vivo* after transfection

Quantification of gene expression was determined by qRT-PCR as previously described. TP53 protein expression was measured using immunohistochemistry. (Mungarndee et al., 2008). Briefly, tumor tissue sections were incubated at 4°C overnight with a primary antibody and then incubated at room temperature for 1 h with a secondary antibody. The expression of target proteins was observed by using chromogenic DAB substrate. Sections were imaged under a microscope.

Statistical analysis

SPSS 21 software (IBM, Armonk, NY, United States) was used for statistical analysis. All data are presented as the mean ± standard error of the mean of at least three independent samples. The differences among multiple groups were determined by using one-way ANOVA ($p < 0.05$). The differences between two groups at the same time point were analyzed by using Student's t-test. A p-value of less than 0.05 indicated statistical significance.

Results

TP-NBs and STP-NBs were well prepared and with excellent functional characteristics

The TP-NB zeta potential was −6.75 ± 3.06 mV, the mean diameter was 174.7 ± 70.24 nm, and the PDI was 0.195 (Figures 2A, B). The STP-NB zeta potential was −5.92 ± 3.37 mV, the mean diameter was 243.6 ± 46.51 nm, and the PDI was 0.284 (Figures 2C, D). SEM and TEM analysis revealed that TP-NBs and STP-NBs were highly dispersed and had a well-defined spherical morphology, and SPIO was observed in the core of STP-NBs (Figures 2E–H). The o-phenanthroline method was used to measure the SPIO encapsulation efficiency of STP-NBs, and the SPIO encapsulation efficiency decreased with increasing total amount of SPIO. The results revealed that the SPIO content was highest when 0.5 mg of SPIO was used for encapsulation (Figure 2I). The ultraviolet spectrophotometry method was used to measure the TP53 plasmid encapsulation efficiency of TP-NBs and STP-NBs, and when 0.6 mg of TP53 plasmid was used, the TP53 plasmid encapsulation efficiency was highest (Figure 2J). The ultraviolet spectrophotometry method was used to measure the release efficiency of TP53 from TP-NBs and STP-NBs after ultrasonic irradiation. A total of 57.1% of TP53 was released from STP-NBs within 12 h after ultrasonic irradiation; 65.1% of TP53 was released at 48 h after ultrasonic irradiation. Regarding STP-NBs, 52.9% of the loaded TP53 was released from STP-NBs at 12 h after ultrasonic irradiation, and 62.4% was released at 48 h (Figure 2K). In addition, the suspended STP-NBs were attracted by permanent magnet when placed under a magnetic field for 4 min, indicating that STP-NBs have a high magnetization ability (Figure 2L).

Ultrasound-targeted transfection of TP53 in two kinds of OS cell lines and the overexpression of P53, resulting in efficient inhibition of OS cells proliferation *in vitro* studies

The 2 -ΔΔCT method was used to analyze the qRT-PCR data. () TP53 mRNA expression in MG63 cells was significantly higher in the TP-NBs + US and STP-NBs + US groups than in the other

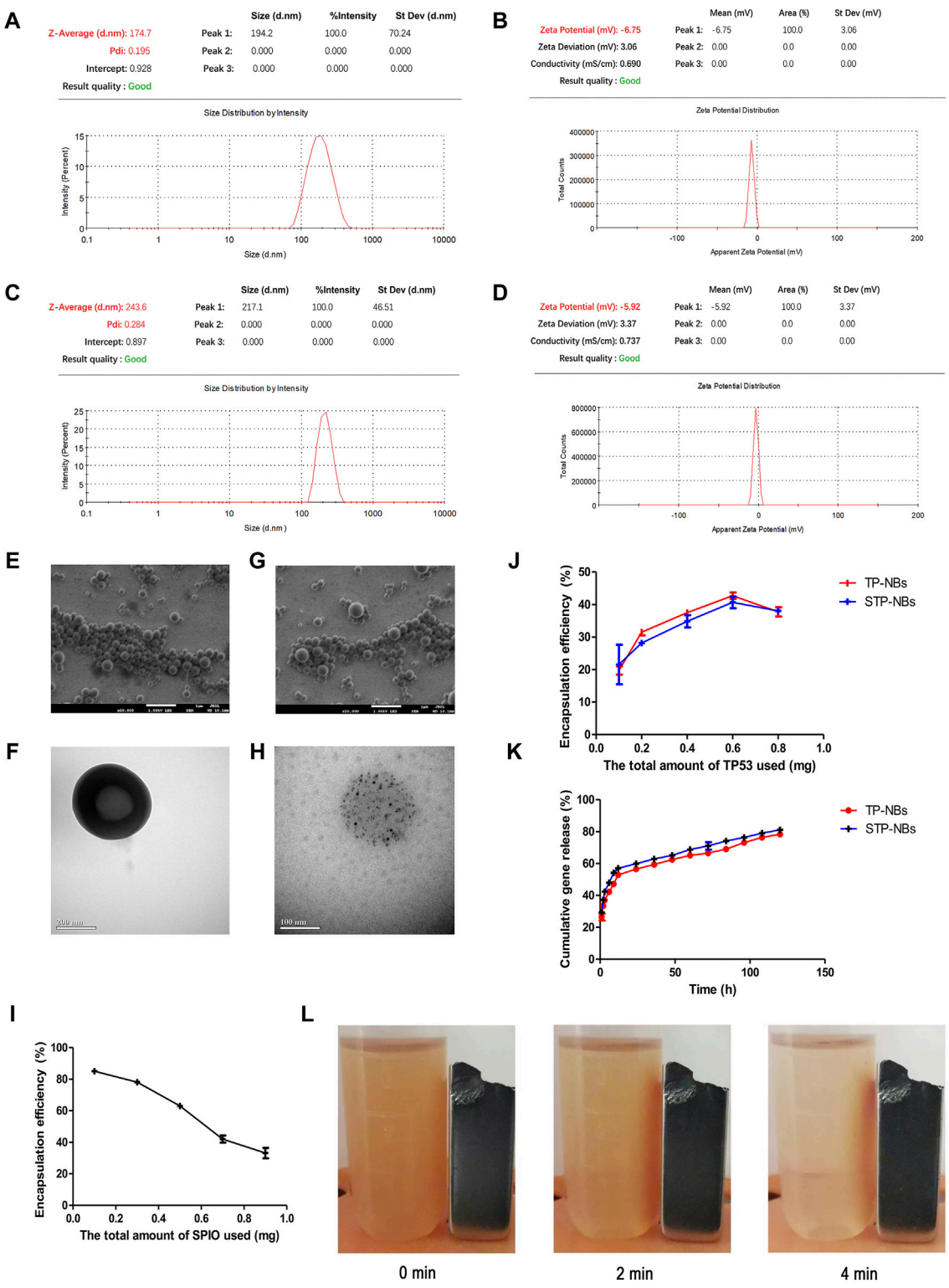

FIGURE 2
Characterization of PP-NBs and SPP-NBS NBs. **(A)** The mean diameter of TP-NBs, **(B)** The zeta potential of TP-NBs, **(C)** The mean diameter of STP-NBs, **(D)** The zeta potential of STP-NBs, **(E)** SEM of TP-NBs, **(F)** TEM of TP-NBs, **(G)** SEM of STP-NBs, **(H)** TEM of STP-NBs, **(I)** SPIO encapsulation efficiency of STP-NBs, **(J)** TP53 plasmid encapsulation efficiency of TP-NBs and STP-NBs, **(K)** Cumulative gene release of TP-NBs and STP-NBs, **(L)** Suspended STP-NBs were attracted to the permanent magnet.

10.3389/fbioe.2024.1418903

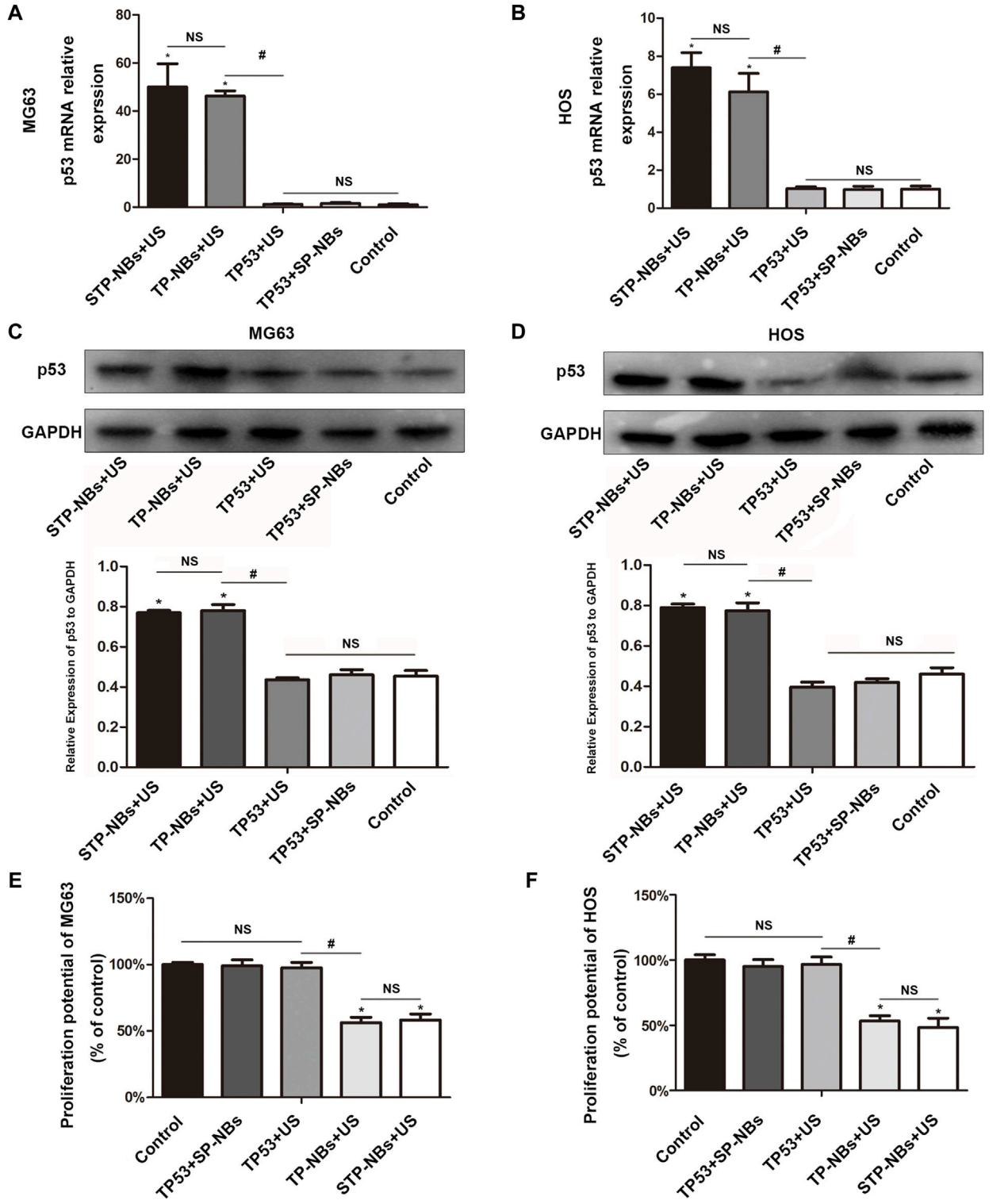

FIGURE 3
(A) qRT-PCR of MG63 cells, **(B)** qRT-PCR of HOS cells, **(C)** WB of MG63 cells, **(D)** WB of HOS cells, **(E)** Proliferation potential of MG63 cells, **(F)** proliferation potential of HOS cells. *, $p < 0.05$, compared with the Control group; NS = no significance; #, $p < 0.05$, compared with the TP53 + US group.

groups at 36 h after transfection ($p < 0.05$) (Figure 3A). Furthermore, the expression patterns were not significantly different between the TP-NBs + US and STP-NBs + US groups. and were also not significantly different between the control group, TP53 + SP-NBs group and TP53 + US group ($p > 0.05$) (Figure 3A). Western blotting (WB) was used to detect TP53 protein expression.

10.3389/fbioe.2024.1418903

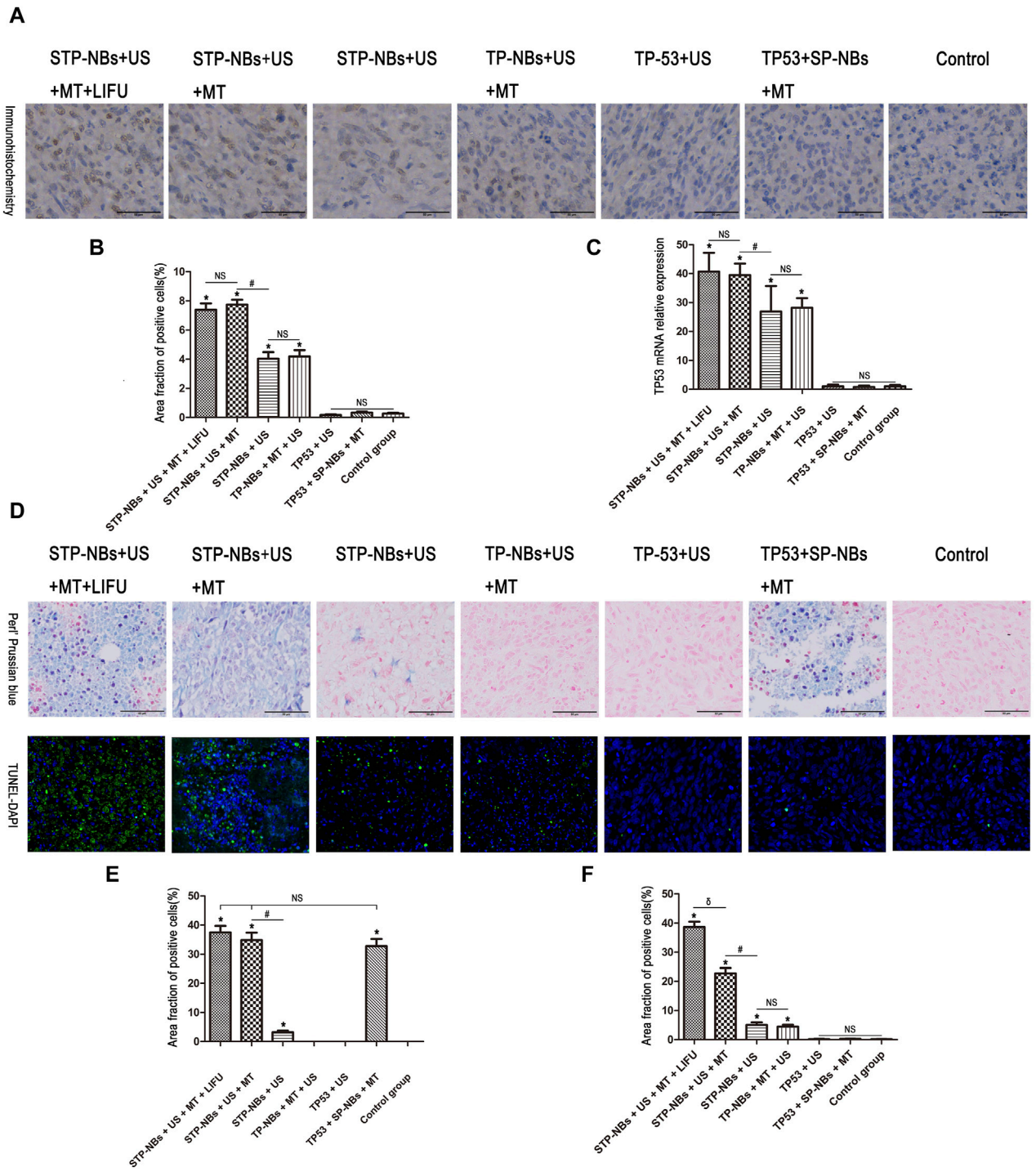

FIGURE 4
(A) Statistical chart of TUNEL-DAPI staining, **(B)** Statistical chart of immunohistochemistry, **(C)** Statistical chart of qRT-PCR. **(D)** Section staining of osteosarcoma tissue for Perls' Prussian blue and the TUNEL assay, **(E)** Statistical chart of Perls' Prussian blue assay, **(F)** Statistical chart of the TUNEL assay. *, $p < 0.05$, compared with the Control group; NS = no significance; #, $p < 0.05$, compared with the STP-NBs group; δ, $p < 0.05$, compared with the STP-NBs + US + MT group.

A double band was observed for each group. TP53 protein expression in MG63 cells 36 h after treatment was highest in the TP-NBs + US and STP-NBs + US groups (Figure 3C). There was no significant difference between the TP-NBs + US and STP-NBs + US groups ($p > 0.05$) and was also not significantly different among the control group, TP53 + SP-NBs group and TP53 + US group ($p > 0.05$) (Figure 3C). Similar results were shown for HOS cells (Figures 3B, D).

The proliferation potential of MG63 cells was detected 36 h after treatment. MG63 cell activity in the TP-NBs + US group and

STP-NBs + US group decreased 36 h compared with the other groups ($p < 0.05$). There was no significant difference in proliferation rates between the TP-NBs + US group and the STP-NBs + US group ($p > 0.05$), and there was also no significant difference among the control group, TP53 + STP-NBs group and TP53 + US group ($p > 0.05$) (Figure 3E). Similar results were shown for HOS cells (Figure 3F). So the proliferation of OS cells was efficiently inhibited by the overexpression of TP53 *in vitro*.

Ultrasound-targeted transfection in magnetic field enhanced the transfection efficiency of the TP53 plasmid in local area, resulting in apoptosis on the osteosarcoma model *in vivo*

TP53 protein expression was detected by immunohistochemistry *in vivo* and showed increases in groups 4, 5, 6 and 7 compared with the other three groups (Figures 4A, B). Groups 6 and 7 showed the highest TP53 protein expression, but there was no significant difference ($p > 0.05$) between the two groups. In addition, there was also no significant difference in TP53 expression between groups 4 and 5($p > 0.05$). Groups 1, 2 and 3 showed the least TP53 protein expression, the values of which were not significantly different among them ($p > 0.05$) (Figures 4A, B). The 2 -ΔΔCT method was used to analyze the qRT-PCR data. TP53 mRNA expression was increased in groups 4, 5, 6 and 7 compared with that in the other three groups (Figure 4C). Groups 6 and 7 showed the highest TP53 mRNA expression, but there was no significant difference ($p > 0.05$) between the two groups, and there was also no significant difference between groups 4 and 5 ($p > 0.05$). Groups 1, 2 and 3 showed the lowest TP53 mRNA expression, which was not significantly different among them ($p > 0.05$) (Figure 4C).

The iron distribution was detected using Perls' Prussian blue assay 7 days after transfection, and the results showed that the iron content was significantly higher in groups 2, 6 and 7 than in the other groups ($p < 0.05$); furthermore, these three groups exhibited no significant differences ($p > 0.05$) (Figures 4D, E). In addition, group 5 showed the highest iron content among all the treatment groups. There was also no significant difference among groups 1, 3, and 4($p > 0.05$) (Figures 4D, E).

The TUNEL assay was used to measure OS apoptosis. The TUNEL-DAPI assay showed significantly increased apoptosis in groups 4, 5, 6 and 7 and significantly higher apoptosis than the other three groups ($p < 0.05$) (Figures 4D, F). Group 7 showed the highest number of TUNEL-negative cells, followed by group 6 ($p < 0.05$). The degree of apoptosis in groups 4 and 5 was not significantly different ($p > 0.05$) (Figures 4D, F). A few TUNEL-negative cells were found in groups 1/2/3 and showed no significance ($p > 0.05$) (Figures 4D, F). So these results demonstrated that ultrasound-targeted transfection in magnetic field enhanced the transfection efficiency of the TP53 plasmid and the overexpression of TP53 in local area, resulting in apoptosis on the osteosarcoma model *in vivo*.

Discussion

Current clinical treatment modalities for OS include surgical resection of primary tumors and systemic chemotherapy. (Panez-Toro et al., 2023). In recent years, the therapeutic use of exogenous genes for treating OS has gained much interest. TP53 is one of the most well-studied tumor suppressor genes. Previous studies have shown that gene transduction of functional TP53 can effectively inhibit OS cell activity. The purpose of gene therapy is to correct abnormal protein expression at the gene level, and the introduction of exogenous TP53 to correct the reduction of TP53 level is a promising OS therapy method. (Tsuchiya et al., 2000; Ganjavi et al., 2006). The mechanism of TP53 is well understood in OS. (Song et al., 2015).

Magnetic nanoparticles could become magnetized and exhibit physical sensitivity to external magnetic fields. Thus, it has been considered to lead to an increase in the local drug concentration at the target site. It was initially used merely for enhancing magnetic resonance imaging in most of the current studies. (Kiwada et al., 1986; Liu et al., 2009; Ting et al., 2012). However, these characteristics signify that magnetic nanoparticles are one kind of most suitable material for gene therapies.

Ultrasound irradiation is an ideal physical gene transfection method to promote extracellular molecules to enter cells. (Feril, 2009). The LIFU device used in this study was developed and patented by our institute. Current studies have indicated that RLI-mode LIFU can destroy target nanobubbles, which not only does not destroy exogenous genes but also improves transfection efficiency; meanwhile, increasing the intensity (RHI-mode) of the LIFU device would exert range-controllable cytocidal effects on tissues. (Xu et al., 2009; Song et al., 2017). To date, limited research on the gene therapy of OS by ultrasound-magnetic-mediated NB destruction has been conducted, and OS treatment using RHI-mode LIFU directly has not been reported.

In an *in vitro* study, the results provide evidence of the successful preparation of STP-NBs. They had a mean diameter of 243.6 ± 46.51 nm, a PDI of 0.284, and a zeta potential of −5.92 ± 3.37 mV. The optimal total input of SPIO and TP53 plasmids was 0.5 mg and 0.6 mg, respectively. The STP-NBs showed good sustained release of genes. In addition, the physical sensitivity of STP-NBs to external magnetic fields has been proven *in vitro*.

In the cell experiments, we loaded STP-NBs with TP53 and administered RLI-mode LIFU to treat MG63 and HOS cells. TP53 protein and mRNA expression in cells were not significantly different between the TP-NBs + US and STP-NBs + US groups. The CCK8 results showed that cell activity was decreased in the TP-NBs + US and STP-NBs + US groups, but there was no significant difference between them. The TP53 + SP-NBs group was not significantly different from the control group for the TP53 + US group. Furthermore, it was also shown that STP-NBs have no cytotoxicity. These results suggest that STP-NBs were able to transfect MG63 cells and HOS cells. The TP53 plasmid was well expressed and inhibited cell proliferation.

In the animal experiments, we used both STP-NBs loaded with TP53 and RHL-mode LIFU to treat tumor-bearing nude mice. The Perls' Prussian blue assay showed that the iron content was significantly higher in groups 2, 6 and 7 than in the other groups, but no significant difference was observed among these three groups. This suggests that STP-NBs can be concentrated in the targeting area in response to external magnetic fields *in vivo*.

The protein and mRNA expression levels of TP53 were increased in groups 4, 5, 6 and 7 compared with the other three groups. Groups 6 and 7 showed the highest TP53 expression, but

there was no significant difference between these two groups; in addition, there was also no significant difference between groups 4 and 5. Groups 1, two and three showed the least TP53 expression, and there was no significant difference between them. These data indicate that STP-NBs were able to mediate TP53 transfection and expression, and the external magnetic field improved the transfection efficiency of STP-NBs *in vivo*.

The TUNEL assay showed significantly increased apoptosis in groups 4, 5, 6 and 7 compared with that of the other three groups. Group 7 showed the highest number of giant, disorganized, TUNEL-negative structures with large clusters of nuclei; group 6 had the next highest map. The degree of apoptosis in groups 4 and 5 was not significantly different. A few TUNEL-negative cells were found in groups 1, 2 and 3, and there was no observed statistical significance. The results demonstrated that following transfection and expression of the TP53 gene, the rate of apoptosis in OS tissue was increased *in vivo*. Meanwhile, this effect further progressed the addition of external magnetic fields and RHI-mode LIFU *in vivo* to our testing ro.

When interpreting these findings, several limitations must be considered. The best guidance method is an external focusing magnetic field located in the center of the tumor body. However, this study was limited by the available equipment, and all magnetic field guidance was generated by the RuFe boron magnet on the surface of the tumor. The strength of the magnetic field in different parts of the tumor was varied. A convergent magnetic field device that can accurately locate the focus will improve future studies of gene therapy. SPIO could enhance magnetic resonance imaging, which could potentially better demonstrate the concentration of nanoparticles in animals. (Fan et al., 2016). Due to equipment limitations, that study could not proceed. Furthermore, the LIFU waves used in this study may have released TP53 into other organs, causing additional biological effects. Previous studies only demonstrated the feasibility of the combination of LIFU and ultrasound-magnetic-mediated Spio-P53-nanobubble destruction at the cell and organism levels. (Elumalai et al., 2024). As a kind of high capacity of reflection biological tissues, less ultrasound energy is able to penetrate the inner portion of the bony tissue. Although high-intensity focused ultrasound (HIFU) experiments have proven that sound attenuation decreases and the sound beam easily passes through because of OS bone destruction, (Wu et al., 2001), the ossifying tumor of the human body needs further study. However, despite these limitations, this does not prevent us from trying some new research methods to treat OS more effectively or to exlpore new method to prepare for surgery.

Conclusion

We used LIFU combined with US-magnetic-mediated SPIO-TP53-NB destruction for OS treatment. Our findings indicate that the destruction of US-magnetic-mediated SPIO/P53/PLGA/NBs facilitates gene transfection and that LIFU combined with the destruction of these NBs may represent a novel, noninvasive and targeted therapy for OS.

Data availability statement

The raw data supporting the conclusion of this article will be made available by the authors, without undue reservation.

Author contributions

HR: Conceptualization, Writing–original draft. SX: Conceptualization, Writing–original draft. AL: Conceptualization, Writing–original draft. QW: Supervision, Writing–original draft. NZ: Supervision, Writing–review and editing. ZH: Supervision, Writing–review and editing.

Funding

The author(s) declare that financial support was received for the research, authorship, and/or publication of this article. This work has been financially supported by the National Natural Science Foundation of China (Nos. 81372003; 82102556). The Science and Technology Development Fund of Shanghai Pudong New Area (Grant No. PKJ2022-Y48), the Outstanding Leaders Training Program of Pudong Hospital affiliated to Fudan University (Grant No. LX202201), Program for the Outstanding Clinical Discipline Project of Shanghai Pudong (Grant No. PWYgy 2021-04), the Project of Key Medical Specialty and Treatment Center of Pudong Hospital of Fudan University (Zdzk 2020-02, Zdzk 2021-01).

Acknowledgments

The authors are grateful to American Journal Experts (AJE) for their help in language editing.

Conflict of interest

The authors declare that the research was conducted in the absence of any commercial or financial relationships that could be construed as a potential conflict of interest.

Publisher's note

References

Asano, Y., Meguro, R., Odagiri, S., Li, C., Iwatsuki, H., and Shoumura, K. (2006). Visualization of non-heme ferric and ferrous iron by highly sensitive non-heme iron histochemistry in the stress-induced acute gastric lesions in the rat. *Histochem Cell Biol.* 125, 515–525. doi:10.1007/s00418-005-0097-6

Bekeredjian, R., Kuecherer, H. F., Kroll, R. D., Katus, H. A., and Hardt, S. E. (2007). Ultrasound-targeted microbubble destruction augments protein delivery into testes. *Urology* 69, 386–389. doi:10.1016/j.urology.2006.12.004

Chen, S., Shimoda, M., Chen, J., Matsumoto, S., and Grayburn, P. A. (2012). Transient overexpression of cyclin D2/CDK4/GLP1 genes induces proliferation and differentiation of adult pancreatic progenitors and mediates islet regeneration. *Cell Cycle* 11, 695–705. doi:10.4161/cc.11.4.19120

Chen, Z. Y., Liang, K., and Qiu, R. X. (2010). Targeted gene delivery in tumor xenografts by the combination of ultrasound-targeted microbubble destruction and polyethylenimine to inhibit survivin gene expression and induce apoptosis. *J. Exp. Clin. Cancer Res.* 29, 152. doi:10.1186/1756-9966-29-152

Chertok, B., David, A. E., Huang, Y., and Yang, V. C. (2007). Glioma selectivity of magnetically targeted nanoparticles: a role of abnormal tumor hydrodynamics. *J. Control Release* 122, 315–323. doi:10.1016/j.jconrel.2007.05.030

Du, J., Shi, Q. S., Sun, Y., Liu, P. F., Zhu, M. J., Du, L. F., et al. (2011). Enhanced delivery of monomethoxypoly(ethylene glycol)-poly(lactic-co-glycolic acid)-poly l-lysine nanoparticles loading platelet-derived growth factor BB small interfering RNA by ultrasound and/or microbubbles to rat retinal pigment epithelium cells. *J. Gene Med.* 13, 312–323. doi:10.1002/jgm.1574

Elumalai, K., Srinivasan, S., and Shanmugam, A. (2024). Review of the efficacy of nanoparticle-based drug delivery systems for cancer treatment. *Biomed. Technol.* 5, 109–122. doi:10.1016/j.bmt.2023.09.001

Elzeny, H., Zhang, F., Ali, E. N., Fathi, H. A., Zhang, S., Li, R., et al. (2017). Polyphosphoester nanoparticles as biodegradable platform for delivery of multiple drugs and siRNA. *Drug Des. Devel Ther.* 22 (11), 483–496. doi:10.2147/DDDT.S128503

Fan, C. H., Cheng, Y. H., Ting, C. Y., Ho, Y. J., Hsu, P. H., Liu, H. L., et al. (2016). Ultrasound/magnetic targeting with SPIO-DOX-Microbubble complex for image-guided drug delivery in brain tumors. *Theranostics* 6, 1542–1556. doi:10.7150/thno.15297

Feril, L. B., Jr (2009). Ultrasound-mediated gene transfection. *Methods Mol. Biol.* 542, 179–194. doi:10.1007/978-1-59745-561-9_10

Ganjavi, H., Gee, M., Narendran, A., Parkinson, N., Krishnamoorthy, M., Freedman, M. H., et al. (2006). Adenovirus-mediated p53 gene therapy in osteosarcoma cell lines: sensitization to cisplatin and doxorubicin. *Cancer Gene Ther.* 13, 415–419. doi:10.1038/sj.cgt.7700909

Hida, K., Lai, S. K., Suk, J. S., Won, S. Y., Boyle, M. P., and Hanes, J. (2011). Common gene therapy viral vectors do not efficiently penetrate sputum from cystic fibrosis patients. *PLoS One* 6, e19919. doi:10.1371/journal.pone.0019919

Huang, Q., Deng, J., Wang, F., Chen, S., Liu, Y., Wang, Z., et al. (2012). Targeted gene delivery to the mouse brain by MRI-guided focused ultrasound-induced blood-brain barrier disruption. *Exp. Neurol.* 233, 350–356. doi:10.1016/j.expneurol.2011.10.027

Hynynen, K., McDannold, N., Vykhodtseva, N., Raymond, S., Weissleder, R., Jolesz, F. A., et al. (2006). Focal disruption of the blood-brain barrier due to 260-kHz ultrasound bursts: a method for molecular imaging and targeted drug delivery. *J. Neurosurg.* 105, 445–454. doi:10.3171/jns.2006.105.3.445

Jiang, Z., and Dalby, P. A. (2023). Challenges in scaling up AAV-based gene therapy manufacturing. *Trends Biotechnol.* 41, 1268–1281. doi:10.1016/j.tibtech.2023.04.002

Kiwada, H., Sato, J., Yamada, S., and Kato, Y. (1986). Feasibility of magnetic liposomes as a targeting device for drugs. *Chem. Pharm. Bull. (Tokyo)* 34, 4253–4258. doi:10.1248/cpb.34.4253

Lin, Y., Lin, Y., Lin, X., Sun, X., and Luo, K. (2019). Combination of PET and CXCR4-targeted peptide molecule agents for noninvasive tumor monitoring. *J. Cancer* 10, 3420–3426. doi:10.7150/jca.31087

Liu, H. L., Hsu, P. H., Chu, P. C., Wai, Y. Y., Chen, J. C., Shen, C. R., et al. (2009). Magnetic resonance imaging enhanced by superparamagnetic iron oxide particles: usefulness for distinguishing between focused ultrasound-induced blood-brain barrier disruption and brain hemorrhage. *J. Magn. Reson Imaging* 29, 31–38. doi:10.1002/jmri.21599

Livak, K. J., and Schmittgen, T. D. (2001). Analysis of relative gene expression data using real-time quantitative PCR and the 2−ΔΔCT method. *Methods* 25, 402–408. doi:10.1006/meth.2001.1262

Lu, Q. L., Liang, H. D., Partridge, T., and Blomley, M. J. (2003). Microbubble ultrasound improves the efficiency of gene transduction in skeletal muscle *in vivo* with reduced tissue damage. *Gene Ther.* 10, 396–405. doi:10.1038/sj.gt.3301913

Mungarndee, S. S., Lundy, R. F. Jr, and Norgren, R. (2008). Expression of Fos during sham sucrose intake in rats with central gustatory lesions. *Am. J. Physiol. Regul. Integr. Comp. Physiol.* 295, R751–R763. doi:10.1152/ajpregu.90344.2008

Panez-Toro, I., Muñoz-García, J., Vargas-Franco, J. W., Renodon-Cornière, A., Heymann, M. F., Lézot, F., et al. (2023). Advances in osteosarcoma. *Curr. Osteoporos. Rep.* 21, 330–343. doi:10.1007/s11914-023-00803-9

Sirsi, S. R., Hernandez, S. L., Zielinski, L., Blomback, H., Koubaa, A., Synder, M., et al. (2012). Polyplex-microbubble hybrids for ultrasound-guided plasmid DNA delivery to solid tumors. *J. Control Release* 157, 224–234. doi:10.1016/j.jconrel.2011.09.071

Sitta, J., and Howard, C. M. (2021). Applications of ultrasound-mediated drug delivery and gene therapy. *Int. J. Mol. Sci.* 22, 11491. doi:10.3390/ijms222111491

Song, R., Tian, K., Wang, W., and Wang, L. (2015). P53 suppresses cell proliferation, metastasis, and angiogenesis of osteosarcoma through inhibition of the PI3K/AKT/mTOR pathway. *Int. J. Surg.* 20, 80–87. doi:10.1016/j.ijsu.2015.04.050

Song, W., Luo, Y., Zhao, Y., Liu, X., Zhao, J., Luo, J., et al. (2017). Magnetic nanobubbles with potential for targeted drug delivery and trimodal imaging in breast cancer: an *in vitro* study. *Nanomedicine (Lond).* 12, 991–1009. doi:10.2217/nnm-2017-0027

Steiniger, S. C., Kreuter, J., Khalansky, A. S., Skidan, I. N., Bobruskin, A. I., Smirnova, Z. S., et al. (2004). Chemotherapy of glioblastoma in rats using doxorubicin-loaded nanoparticles. *Int. J. Cancer* 109, 759–767. doi:10.1002/ijc.20048

Sun, Y., ZhangFang, C. Q., Zhang, W. Q., and Liu, W. (2023). Abnormal signal pathways and tumor heterogeneity in osteosarcoma. *J. Transl. Med.* 21, 99. doi:10.1186/s12967-023-03961-7

Tang, H. L., Wang, Z. G., Li, Q., Ran, H. T., Zheng, Y. Y., Ren, J. L., et al. (2012). Targeted delivery of bone mesenchymal stem cells by ultrasound destruction of microbubbles promotes kidney recovery in acute kidney injury. *Ultrasound Med. Biol.* 38 (4), 661–669. doi:10.1016/j.ultrasmedbio.2012.01.003

Ting, C. Y., Fan, C. H., Liu, H. L., Huang, C. Y., Hsieh, H. Y., Yen, T. C., et al. (2012). Concurrent blood-brain barrier opening and local drug delivery using drug-carrying microbubbles and focused ultrasound for brain glioma treatment. *Biomaterials* 33, 704–712. doi:10.1016/j.biomaterials.2011.09.096

Tsuchiya, H., Mori, Y., Ueda, Y., Okada, G., and Tomita, K. (2000). Sensitization and caffeine potentiation of cisplatin cytotoxicity resulting from introduction of wild-type p53 gene in human osteosarcoma. *Anticancer Res.* 20 (1A), 235–242.

Wang, Y., Yang, L., Chen, T., Liu, X., Guo, Y., Zhu, Q., et al. (2019). A novel lncRNA MCM3AP-AS1 promotes the growth of hepatocellular carcinoma by targeting miR-194-5p/FOXA1 axis. *Mol. Cancer* 18, 28. doi:10.1186/s12943-019-0957-7

Wells, D. J. (2010). Electroporation and ultrasound enhanced non-viral gene delivery *in vitro* and *in vivo*. *Cell Biol. Toxicol.* 26, 21–28. doi:10.1007/s10565-009-9144-8

Wu, F., Chen, W. Z., Bai, J., Zou, J. Z., Wang, Z. L., Zhu, H., et al. (2001). Pathological changes in human malignant carcinoma treated with high-intensity focused ultrasound. *Ultrasound Med. Biol.* 27, 1099–1106. doi:10.1016/s0301-5629(01)00389-1

Wu, Y., Sun, T., Tang, J., Liu, Y., and Li, F. (2020). Ultrasound-targeted microbubble destruction enhances the antitumor efficacy of doxorubicin in a mouse hepatocellular carcinoma model. *Ultrasound Med. Biol.* 46, 679–689. doi:10.1016/j.ultrasmedbio.2019.09.017

Xenariou, S., Griesenbach, U., Liang, H. D., Zhu, J., Farley, R., Somerton, L., et al. (2007). Use of ultrasound to enhance nonviral lung gene transfer *in vivo*. *Gene Ther.* 14, 768–774. doi:10.1038/sj.gt.3302922

Xu, H. X., Lu, M. D., Xie, X. H., Xie, X. Y., Xu, Z. F., Chen, L. D., et al. (2009). Three-dimensional contrast-enhanced ultrasound of the liver: experience of 92 cases. *Ultrasonics* 49, 377–385. doi:10.1016/j.ultras.2008.10.009

Yamaguchi, K., Feril, L. B., Jr, Tachibana, K., Takahashi, A., Matsuo, M., Endo, H., et al. (2011). Ultrasound-mediated interferon β gene transfection inhibits growth of malignant melanoma. *Biochem. Biophys. Res. Commun.* 411, 137–142. doi:10.1016/j.bbrc.2011.06.115

Yin, H., Kanasty, R. L., Eltoukhy, A. A., Vegas, A. J., Dorkin, J. R., and Anderson, D. G. (2014). Non-viral vectors for gene-based therapy. *Nat. Rev. Genet.* 15, 541–555. doi:10.1038/nrg3763

Zhang, X., Zheng, Y., Wang, Z., Huang, S., Chen, Y., Jiang, W., et al. (2014). Methotrexate-loaded PLGA nanobubbles for ultrasound imaging and Synergistic Targeted therapy of residual tumor during HIFU ablation. *Biomaterials* 35, 5148–5161. doi:10.1016/j.biomaterials.2014.02.036

Zhao, Y., Song, W., Wang, D., Ran, H., Wang, R., Yao, Y., et al. (2015). Phase-shifted PFH@PLGA/Fe3O4 nanocapsules for MRI/US imaging and photothermal therapy with near-infrared irradiation. *ACS Appl. Mater Interfaces* 7, 14231–14242. doi:10.1021/acsami.5b01873

Zhong, S., Shu, S., Wang, Z., Luo, J., Zhong, W., Ran, H., et al. (2012). Enhanced homing of mesenchymal stem cells to the ischemic myocardium by ultrasound-targeted microbubble destruction. *Ultrasonics* 52, 281–286. doi:10.1016/j.ultras.2011.08.013

Glossary

CCK8	cell counting kit-8 assay
DAB	diaminobenzidine
DAPI	4′,6-diamidino-2-phenylindole
DMEM	Dulbecco's modified Eagle medium
FBS	fetal bovine serum
FUS	focused ultrasound
HIFU	high-intensity-focused ultrasound
LIFU	low-intensity-focused ultrasound
MT	magnetic targeting
MW	molecular weight
NBs	nanobubbles
NS	normal saline
OS	osteosarcoma
PBS	phosphate-buffered saline
PDI	polydispersity index
PLGA	poly lactic-coglycolic acid
PVA	polyvinyl alcohol
PVDF	polyvinylidene fluoride
qRT-PCR	quantitative reverse transcription polymerase chain reaction
RB	retinoblastoma
RLI-mode	relatively low-intensity mode
RHI-mode	relatively high-intensity mode
SEM	scanning electron microscope
SPIO	superparamagnetic iron oxide
SP-NBs	superparamagnetic iron oxide/poly lactic-co-glycolic acid nanobubbles
STP-NBs	superparamagnetic iron oxide/TP53/poly lactic-co-glycolic acid nanobubbles
TEM	transmission electron microscopy
TP-NBs	TP53/poly lactic-co-glycolic acid nanobubbles
US	ultrasound
UTMD	ultrasound-mediated microbubble destruction
WB	Western blotting

frontiers | Frontiers in Bioengineering and Biotechnology

TYPE Original Research
PUBLISHED 19 July 2024
DOI 10.3389/fbioe.2024.1416659

OPEN ACCESS

EDITED BY
Qianju Wu,
Xiamen Stomatological Hospital, China

REVIEWED BY
Dejian Li,
Fudan University Pudong Medical Center, China
Huihua Yuan,
Nantong University, China
Tonghe Zhu,
Shanghai University of Engineering Sciences, China

*CORRESPONDENCE
Xinyi Dai,
daixy1979@gmail.com
Yi Shen,
shenyi12@sjtu.edu.cn

RECEIVED 12 April 2024
ACCEPTED 27 June 2024
PUBLISHED 19 July 2024

CITATION
Dai X, Nie W, Duan C and Shen Y (2024), Preparation of microspheres with sustained ketoprofen release by electrospray for the treatment of aseptic inflammation. *Front. Bioeng. Biotechnol.* 12:1416659. doi: 10.3389/fbioe.2024.1416659

Preparation of microspheres with sustained ketoprofen release by electrospray for the treatment of aseptic inflammation

Xinyi Dai[1]*, Wei Nie[2], Chuanyou Duan[3] and Yi Shen[4]*

[1]Department of Plastic and Reconstructive Surgery, Shanghai Ninth People's Hospital, School of Medicine, Shanghai Jiao Tong University, Shanghai, China, [2]Wake Forest Institute for Regenerative Medicine, Wake Forest University School of Medicine, Winston-Salem, NC, United States, [3]Luhe People's Hospital, Nanjing, Luhe, China, [4]Bio-ID Center, School of Biomedical Engineering, Shanghai Jiao Tong University, Shanghai, China

The treatment of aseptic inflammation has always been a clinical challenge. At present, non-steroidal drug-loaded microspheres have been widely used in the treatment of aseptic inflammation due to their excellent injectable and sustained release capabilities. In this study, ketoprofen-loaded shellac microspheres (Keto-SLAC) were prepared by electrospray. Alterations of Keto-SLAC morphology was observed in response to changed shellac concentration in ethanol solution through electrospray. Further examination revealed that ketoprofen presented as amorphous solid dispersion in the shellac microspheres. Most importantly, it was also shown that ketoprofen can be slowly released from the shellac matrix for up to 3 weeks. *In vitro* cell experiments verified that the microspheres had favorable cell compatibility. We therefore proposed that the prepared microspheres, being readily available in use in a variety of clinical settings through topical application, have promising therapeutic potential for the treatment of aseptic inflammation.

KEYWORDS

electrospray, ketoprofen, shellac microsphere, aseptic inflammation, drug release

1 Introduction

The treatment of aseptic inflammation is a thorny issue clinically (Tanaka and Kishimoto, 2012; Tarantino et al., 2016). Nonsteroidal Anti-inflammatory Drugs (NSAIDs) are considered to be an ideal drug for the treatment of aseptic inflammation (Zhou et al., 2014). By inhibiting the production of prostaglandin and the activity of cyclooxygenase, it can effectively reduce the symptoms like fever, swelling and pain caused by aseptic inflammation (Shamsudin et al., 2018). Due to its low toxicity and high efficiency, ketoprofen has become a commonly used non-steroidal drug in the treatment of aseptic inflammation caused by arthritis and gout (Yu et al., 2018; Shohin et al., 2012). However, the systemic administration of ketoprofen is associated with some unpredictable toxicity to the liver and heart (Carbone et al., 2013). *In situ* drug delivery has therefore become a preferred route for ketoprofen administration (Stigliani et al., 2013; Basar et al., 2017).

The development of effective methods in materials science for preparing drug-loaded microspheres helps to address these shortcomings. Drug-loaded microspheres are micron or nano-sized spherical particles with drug dispersing in it. Due to the large specific surface area and high drug loading capacity of microsphere, it has been widely used for drug

delivery (Andhariya and Burgess, 2016). As a matter of fact, the injectability of microspheres also allows them to be conveniently delivered to the target site (Targeted drug delivery), which only increases the concentration of the drug in the injection area but avoids unnecessary drug accumulation in other organ, thereby prevents potentially toxic effects of the drug. The common methods for preparing drug-loaded microspheres include emulsification crosslink, emulsification-heating and curing, emulsification-solvent evaporation, spray drying (Mo et al., 2016), emulsification-solvent evaporation method (Baena-Aristizábal et al., 2016) and spray drying method (Fernández-Paz et al., 2020). Although the first two methods may prepare microspheres with relatively ideal particle size distribution, the preparation flow turn out to be more complicated, in which a precise control of parameters (such as temperature, stirring speed, pH value, etc.) is required. Moreover, the use of crosslinking agents with cytotoxicity also reduces the biosafety of microspheres (Cheng et al., 2013). On the contrary, Spray-drying method is commonly adopted to prepare drug-loaded sustained-release microspheres in manufacturing industry. However, the traditional spray drying method often requires very complicated equipment, meanwhile, it also contains high temperature processing step, which will easily destroy chemical structure of bioactive molecules and polymers as drugs (Wei et al., 2020). Therefore, it is necessary to develop a simpler and safer method for the preparation of drug-loaded microspheres.

As a new method of preparing microspheres, electrospray has attracted widespread attention in recent years, as microspheres prepared by this method has wide applications such as drug delivery (Tanhaei et al., 2021), tissue engineering (Xue et al., 2020), composite materials (Xi et al., 2019) chemical sensing (Cho et al., 2020). As a relatively simple method, the main equipment needed for electrostatic spraying are injection pump, high voltage DC power supply and collector. Briefly, The polymer solution is expelled from the pump, and under a high-voltage electric field, it splits into many small droplets. The solvent in the droplet is evaporated and dried at room temperature and at last, microspheres was fall on the receiver. Compared with traditional spray drying technique, electrospray is cost-effective and suitable for most polymers (Zhang et al., 2021). Currently, a variety of polymers have been used for the preparation of electrosprayed microspheres. For example, Richard et al. combined electrostatic spray and thermally induced phase separation technique to prepare porous poly (lactic-co-glycolic) acid (PLGA) (Malik et al., 2016). Also, Tatsuo et al. reported their approach to prepare chitosan/calcium phosphate composite microspheres by electrostatic spray (Yunoki et al., 2014). However, some shortcomings of fabricated microspheres using some of the polymers are obvious: polyester microspheres are prone to produce acidic degradation products that induce inflammatory response of the host (Zhu et al., 2015). The molecular interaction of chitosan is relatively large, and toxic solvents are needed in the electrostatic spraying process (Bilican et al., 2020). Shellac, as a natural polyester with a small molecular weight, has been widely used as matrix material for drug delivery. Particularly, as it is easily soluble in ethanol, shellac turns out to be an ideal material for the preparation of microspheres by mean of electrostatic spray (Wang et al., 2018).

In view of the above, ketoprofen-loaded shellac microspheres (Keto-SLAC) was prepared by electrospray for the treatment of aseptic inflammation. The morphology as well as the physical and chemical properties of the microspheres under different spray parameters was investigated. In addition, the drug release profile and *in vitro* cell compatibility of ketoprofen-loaded microspheres have also been studied to assess its possible application against aseptic inflammation.

2 Materials and methods

2.1 Materials

All chemicals used in the experiment were purchased from Sigma-Aldrich unless stated otherwise. The experimental water was ultrapure water filtered by Mill-pore (the resistivity was 18 MΩ/cm).

2.2 Characterization

The surface morphology of the microspheres was observed by scanning electron microscope (SEM) (JSM 5800, Jeol Ltd., Tokyo, Japan). The thermal analysis of the microspheres is performed by DSC scanning (TA MDSC 2910, TA Instruments 10, United States °C/min, temperature range 20°C–200°C). The structure of the microspheres was further studied by XRD (Riga D/Max-BR, Tokyo, Japan, diffraction angle 4°–50°, 40 mV, and 300 mA).

2.3 Preparation of Keto-SLAC

In order to study the influence of different polymer concentrations on the morphology of microspheres, shellac/ketoprofen solutions of different concentrations were prepared. The ratio of ketoprofen to shellac is maintained at 1:10. Taking 2.5% shellac/ketoprofen as an example, 2.5 g of shellac was dissolved in 10 mL of ethanol. Then 0.25 g of ketoprofen was added. A transparent solution was obtained after 1 h stir (300 rpm) in a water bath at 45°C. The prepared solution was poured into a 5 mL syringe. The 18G flat needle is used as a jet capillary to connect to the positive terminal of the power supply. The aluminum foil connected to the negative electrode used as a receiving plate. The process parameters of electrospray are: the flow rate is 3 mL/h. The distance between the receiving plate and the spinneret is 15 cm and 30 cm respectively. The voltage is 10 kV, the ambient temperature is 25°C, and the ambient humidity is 40% ± 5%. The composition of different concentrations of spray liquid is listed in Table 1.

2.4 *In Vitro* drug release studies

Ketoprofen release test refers to the method published previously (Park et al., 2012). Briefly, 500 mg of Keto-SLAC microspheres were added to the dialysis bag (cut-off molecular weight is 1,000 Mw). The dialysis bag was then immersed in 100 mL of PBS solution and placed on a shaker at 37°C with

TABLE 1 Composition of spinning solution.

Shellac/ ketoprofen solution	The mass ratio of ketoprofen to shellac (wt/wt)	Shellac concentration in ethanol solution (%)
G1	1:10	25
G2	1:10	35
G3	1:10	45
G4	1:10	55
G6	1:10	65

speed at 300 rpm. 1 mL of sustained-release solution was drawn at different time points, and the concentration of ketoprofen was quantified by liquid chromatography (Park et al., 2012). 100 μL of fresh PBS were added to the sustained-release system after each extraction in order to balance the volume of the release solution system.

2.5 Cell culture

NIH 3T3 cells were purchased from ATCC (CRL1658). According to the supplier's instructions, DMEM high glucose medium containing 10% fetal bovine serum (FBS) was used to culture 3T3 cells. Incubation was conducted at 37°C in 5% carbon dioxide. The cells are changed every 2 days during the culture. When 80% confluence is reached, the cells are passaged.

2.6 *In vitro* biocompatibility

The toxicity of microspheres on fibroblasts and cell viability were determined by CCK-8 and LDH tests. In short, NIH 3T3 was seeded in 96-well plates at a density of 4,000 cells/well. After incubating for 12 h, the medium was aspirated and replaced it with fresh medium with various concentrations of Keto-SLAC. The Keto-SLAC solution concentrations at 10, 20, 40, 60, 80, 160, and 320 μg/mL were co-cultured with the cells for 24 and 48 h, respectively. Then CCK-8 and LDH kits were used to detect the cell viability. All tests were performed according to the supplier's instructions, and the cells in the untreated group were expressed as a normalized percentage.

2.7 *In vivo* experiment

All animal experiments were performed according to the protocols approved by the Institutional Animal Care and Use Committee at Shanghai Jiao Tong University (202401131). Wistar rats (male, 125~150 g, 3 weeks old, n = 18) were purchased from Sino-British Sippr/BK Laboratory. Shanghai Animal Co., Ltd., China. All rats were housed under standard laboratory conditions at 25°C. During the experiment, distilled water and commercially available food (Sino-British Sippr/BK Experimental Animal Co., Ltd.) were given freely, and the animals were housed in groups in plastic bottom cages covered with sawdust. The lighting time of the breeding room is 12 h (7:00 a.m. to 7:00 p.m.). All experiments were approved by the Animal Experimentation Ethical Review Committee of Shanghai Jiao Tong University. Experimental arthritis was induced in rats as follows: each rat was injected into the joint with 0.1 mL of CFA containing a mineral oil suspension of *Mycobacterium* butyricum (Sigma Chemical Co.). After 2 weeks of CFA treatment, each rat in the drug test group (6 rats in each group) was given a single dose of prepared ketoprofen suspension,lac-ketoprofen microspheres, and naked lac at the joints according to body weight. Microspheres, dose 20 mg/kg. The control group (n = 6) was injected with the same volume of PBS. After the experiment, the rats were sacrificed, and the joints of the fore and hind limbs were removed for pathological section analysis.

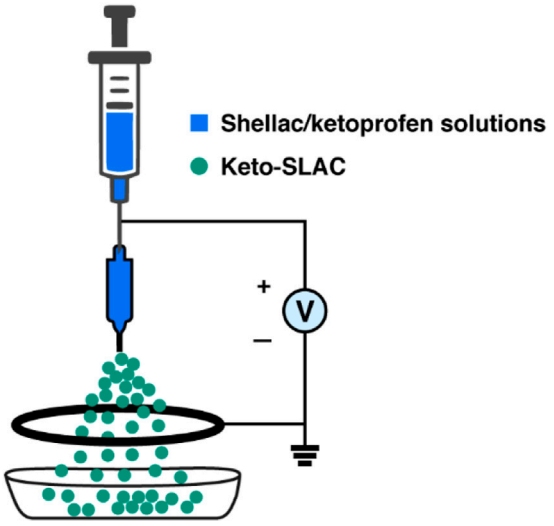

FIGURE 1
Schematic illustration of the electrospray process for Keto-SLAC fabrication.

2.8 Statistical analysis

Origin 9.0 (OriginLab, United States) was used for statistical analysis. Statistical significance was assessed by using one-way or two-way analysis of variance (ANOVA) and Tukey's multiple comparison test. When $p < 0.05$, the data is considered significant. It is represented by *. When $p < 0.01$, it is represented by **. All data are shown as mean ± standard deviation.

3 Results and discussion

3.1 Preparation of Keto-SLAC by electrospray

As was shown in Figure 1, Keto-SLAC microspheres were prepared by electrospray of shellac/ketoprofen solutions of different concentrations with a spray distance of 15 cm. When

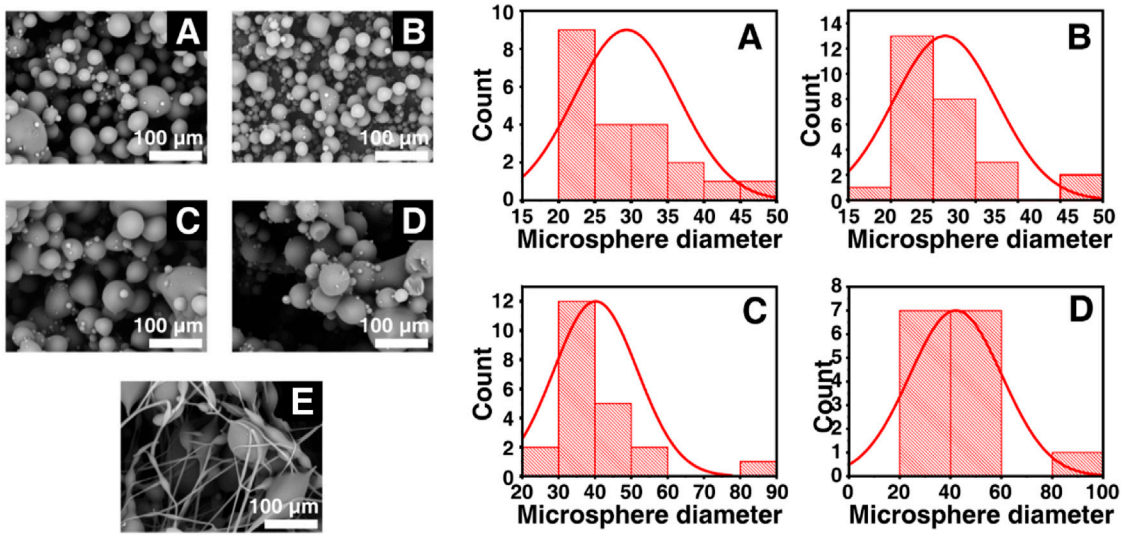

FIGURE 2
Statistical particle sizes distributions (right) of different shellac concentration derived Keto-SLAC based on SEM images (left) with the spray distance in 15 cm. **(A)** 25%, **(B)** 35%, **(C)** 45%, **(D)** 55%, **(E)** 65%.

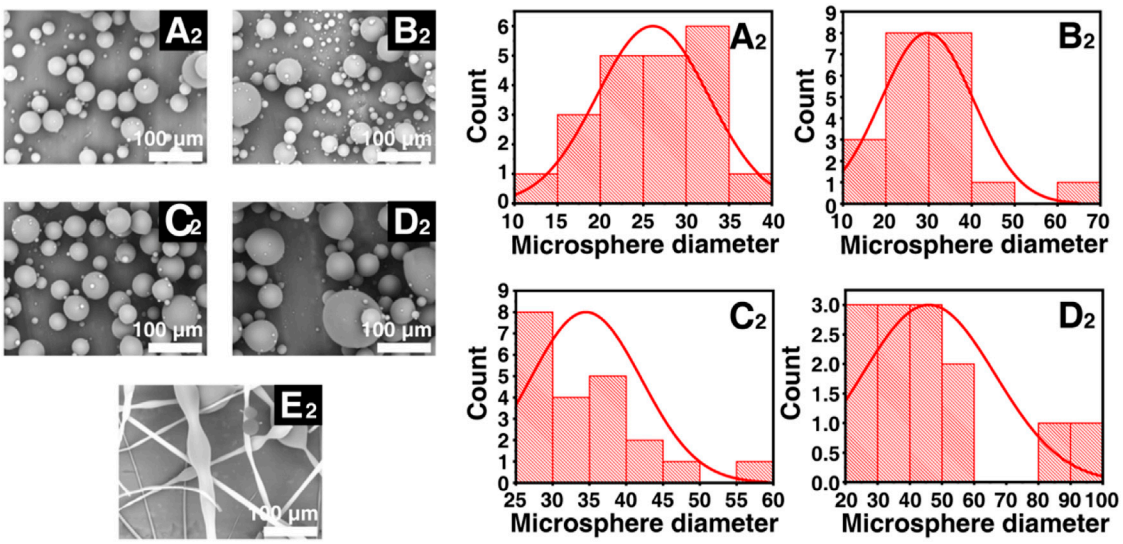

FIGURE 3
Statistical particle sizes distributions (right) of different shellac concentration derived Keto-SLAC based on SEM images (left) with the spray distance in 30 cm. **(A_2)** 25%, **(B_2)** 35%, **(C_2)** 45%, **(D_2)** 55%, **(E_2)** 65%.

the concentration of shellac is 25%–55%, the prepared microspheres have a smooth surface without agglomeration of drug particles and polymers. At the highest shellac concentration (65%), a spindle-like fiber was observed. A zoom-in picture shows the particle size distribution of the microspheres more clearly. The microspheres of all groups displayed a bimodal distribution. Small microspheres are often gathered on or around the surface of larger microspheres (Figure 2).

On the other hand, particle sizes distributions of Keto-SLAC microspheres prepared under the spray distance of 30 cm was also investigated. As was shown in Figure 3, higher concentration of SLAC (65%) also results in spindle-like fiber structure. This suggested that the concentration of shellac is of critical importance for the formation of microspheres. Meanwhile, as the spraying distance increases, the particle size distribution of the microspheres becomes more uniform. It is worth noting that in the 25% drug-loaded shellac microsphere group, the particle size of the microspheres is the most uniform. These results indicated that the optimal parameter to obtain microspheres with uniform size distribution is a receiving distance at 30 cm and a shellac concentration of 25%, which brings about a resultant particle size of 27 μm in average. Therefore, Keto-SLAC microspheres prepared

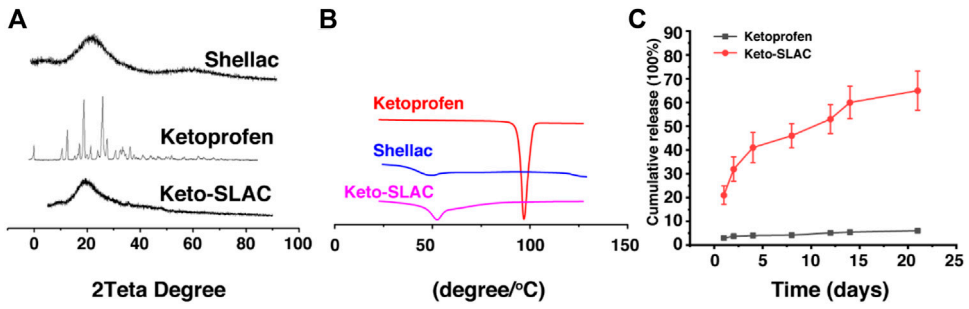

FIGURE 4
Characterization of Keto-SLAC. **(A)** XRD pattern, **(B)** Differential scanning calorimeter, **(C)** Drug release profiles.

under such parameter are used in the follow experiments. The electrospray technique used in this study can be adapted for other drugs by adjusting parameters such as solvent type, polymer concentration, and flow rate to optimize drug encapsulation and release profiles. This method's versatility also allows for the encapsulation of multiple drugs, making it suitable for combination therapies targeting various diseases.

3.2 Characterization of Keto-SLAC

The XRD analysis, shown in Figure 4A, indicated that there was no sharp peak in shellac spectrum, which provided evidence that there was disordered molecule arrangement with in shellac. However, several sharp diffraction peaks was seen in XRD pattern of ketoprofen, which was in consistent with the result from DSC analysis for ketoprofen, indicating an ordered crystal arrangement of ketoprofen molecule. However, crystal peak of ketoprofen disappeared in the diffraction pattern of Keto-SLAC, verifying that ketoprofen had lost its crystal structure and existed in an amorphous state in shellac microspheres. Results from both XRD and DSC provided evidence that ketoprofen had changed its physical state from crystal to amorphous solid dispersion in shellac.

Differential scanning calorimetry (DSC) analysis of the microspheres was shown in Figure 4B. It can be seen that ketoprofen has a very sharp absorption peak at 98.2°C, indicating that ketoprofen exists as an ordered crystal. There is a gentle endothermic peak around 48.3°C of shellac sample, which is the glass transition temperature of shellac. Keto-SLAC has a gentle endothermic peak at 52.6°C, which is slightly deviated from the peak of shellac. This may possibly due to the interaction of shellac and ketoprofen in the composite material. Most importantly, the endothermic peak of ketoprofen at 98.2°C disappeared in the Keto-SLAC sample, indicating that ketoprofen has lost its original crystal form and exists in the microspheres in an amorphous state.

We further examined the release profile of Keto-SLAC *in vitro*, shown in Figure 4C, in which Keto-SLAC exhibited an obvious sustained-release, which is consistent with previous reports on microspheres (DeJulius et al., 2021). From the release curve, the entire drug release lasted about:20 days, in which a relatively fast release was seen in the first 2 days, and then gradually slow down. Probably, the initial rapid release occurred as a result of ketoprofen on the surface of the microspheres. When ketoprofen on the surface of the microspheres has completely unleashed, those in the microsphere is responsible for the slow-down of drug release that gradually reached equilibrium.

3.3 *In vitro* cytocompatibility assay

Cell compatibility of drug-loaded microspheres was examined and shown in Figure 5, where the metabolic activity of cells subjected to Keto-SLAC of different concentrations at different time point (24 and 48 h) was measured. As compared to the untreated cells, no significant difference in cell viability was seen in cells treated with different concentrations of Keto-SLAC (Figures 5A, B). Similarly, after being treated with different concentrations of Keto-SLAC, no significant increase of LDH release was found as compared to those untreated cells, suggesting that Keto-SLAC has favorable cell compatibility and low cytotoxicity (Figures 5C, D). Previous studies have demonstrated the low cytotoxicity and favorable biocompatibility of shellac when used as a matrix material for drug delivery systems. In our study, the cell viability assay (CCK-8) and LDH release assay showed that the Keto-SLAC microspheres had no significant cytotoxic effects on NIH 3T3 cells, even at high concentrations, corroborating these previous findings. This suggests that shellac, as a natural and biodegradable polymer, is a biocompatible and safe material for drug delivery applications.

3.4 Treatment effect of Keto-SLAC *in vivo*

In order to evaluate the pathological changes of the joint, H&E staining was performed after the treatment. Histological results showed that the single-injection ketoprofen treatment group still had obvious inflammatory cell infiltration, pannus formation, cartilage destruction, and synovial hyperplasia (Figure 6). In the ketoprofen microsphere treatment group, intra-articular pannus formation and inflammatory cell infiltration were significantly reduced, but visible cartilage destruction and synovial hyperplasia still existed. AA rats treated with ketoprofen microspheres had significant beneficial effects in inhibiting inflammatory cell infiltration, synovial hyperplasia, cartilage destruction, and pannus formation compared with the ketoprofen group alone. Our results indicate that ketoprofen sustained release from shellac microspheres can reduce pannus formation and significant inflammatory cell infiltration in joints, although it does not prevent cartilage destruction.

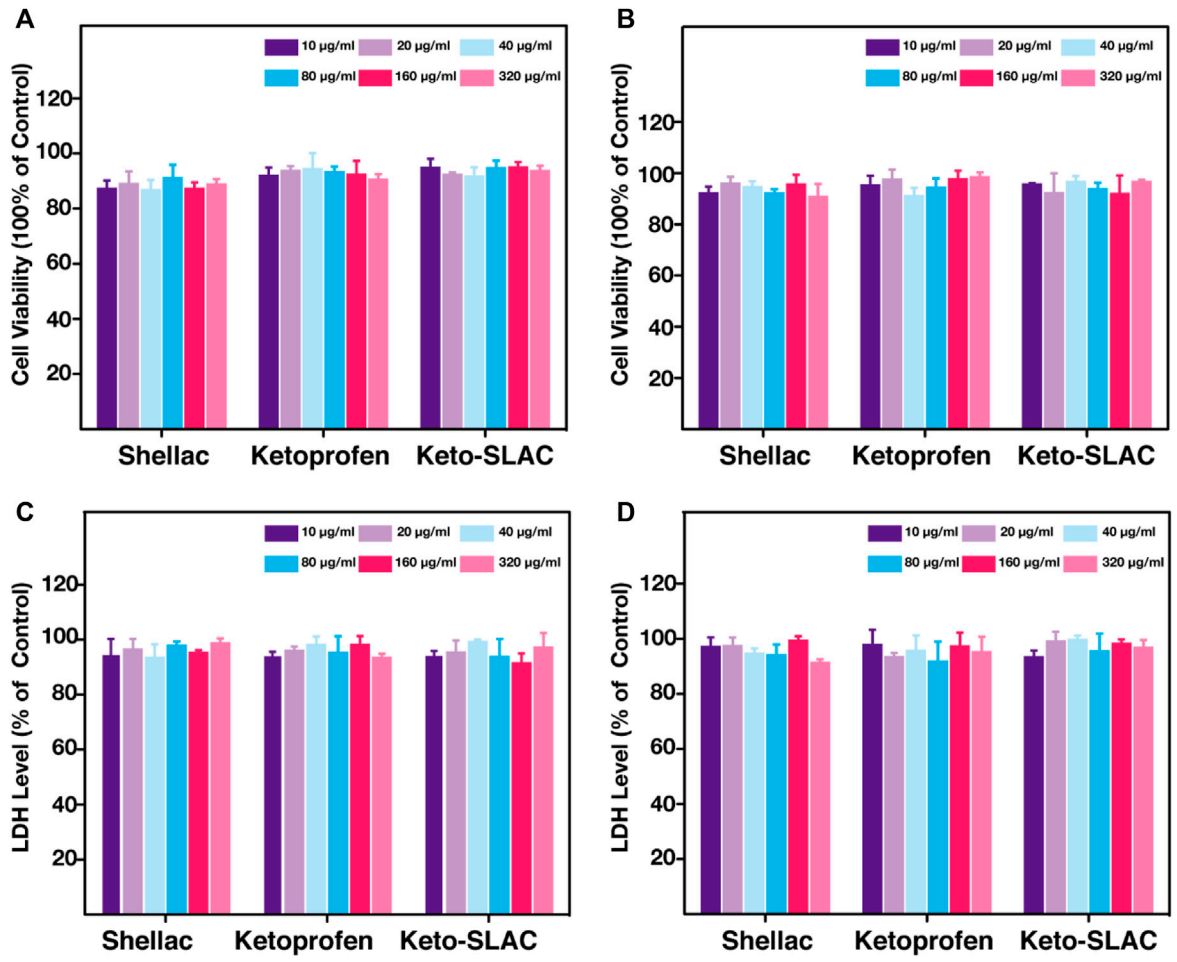

FIGURE 5
CCK-8 analysis of 3T3 cell after treatment of increasing concentration of shellac, ketoprofen and keto-SLAC for 24 h **(A)** and 48 h **(B)**. LDH test of the 3T3 cell with the same treatment as CCK-8 for 24 h **(C)** and 48 h **(D)**. No significant LDH release was found in each group.

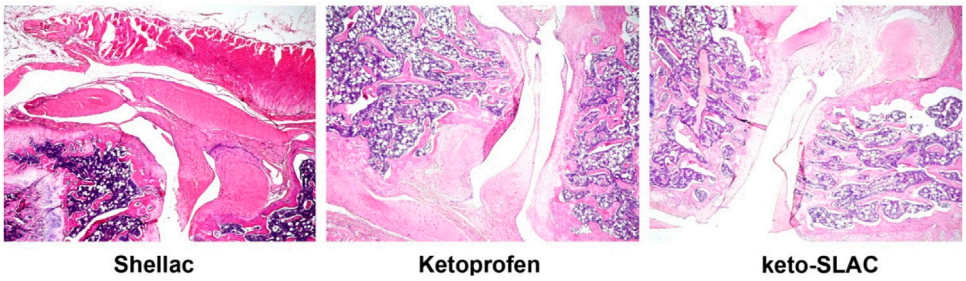

FIGURE 6
Treatment effect of Keto-SLAC on aseptic inflammation induced in a rat model.

4 Conclusion

Ketoprofen-loaded shellac microspheres were successfully prepared by electrospray. Keto-SLAC with more uniform size is obtained by spraying 45% shellac solution at a distance of 30 cm. The DSC analysis revealed that the sharp absorption peak of ketoprofen disappeared in the microspheres. Results from XRD spectroscopy also indicated that the crystal structure of ketoprofen was disrupted as the microspheres formed. The consistent results from DSC and XRD justified the existence of solid dispersion of ketoprofen in shellac. Moreover, *in vitro* release experiments demonstrated that Keto-SLAC can be persistently released for around 20 days. Cell experiments provided evidence that the prepared microspheres had favorable compatibility *in vitro*. In addition to its favorable biological properties, shellac is a

natural and biodegradable polymer, making it an environmentally sustainable choice for pharmaceutical applications. Its use in drug delivery systems aligns with the growing emphasis on reducing environmental impact and promoting sustainability in the pharmaceutical industry. In short, the application of Keto-SLAC microspheres prepared by electrospray may be a promising approach for the treatment of aseptic inflammation. Compared to current commercial drug delivery systems, the electrospray-prepared Keto-SLAC microspheres offer improved control over particle size and drug release profiles. This method also avoids high temperatures and toxic solvents, enhancing drug stability and biocompatibility.

Data availability statement

The original contributions presented in the study are included in the article/Supplementary Material, further inquiries can be directed to the corresponding authors.

Ethics statement

The studies involving human/animal participants were reviewed and approved by the Animal Experimentation Ethical Review Committee of Shanghai Jiao Tong University.

Author contributions

XD: Conceptualization, Investigation, Project administration, Writing–original draft. WN: Methodology, Validation, Visualization, Writing–original draft. CD: Data curation, Software, Validation, Writing–original draft. YS: Conceptualization, Project administration, Supervision, Writing–review and editing.

Funding

The author(s) declare that financial support was received for the research, authorship, and/or publication of this article. This work was supported by the National Natural Science Foundation of China (82072174).

Conflict of interest

The authors declare that the research was conducted in the absence of any commercial or financial relationships that could be construed as a potential conflict of interest.

Publisher's note

All claims expressed in this article are solely those of the authors and do not necessarily represent those of their affiliated organizations, or those of the publisher, the editors and the reviewers. Any product that may be evaluated in this article, or claim that may be made by its manufacturer, is not guaranteed or endorsed by the publisher.

References

Andhariya, J. V., and Burgess, D. J. (2016). Recent advances in testing of microsphere drug delivery systems. *Expert Opin. drug Deliv.* 13 (4), 593–608. doi:10.1517/17425247.2016.1134484

Baena-Aristizábal, C. M., Fessi, H., Elaissari, A., and Mora-Huertas, C. E. (2016). Biodegradable microparticles preparation by double emulsification—solvent extraction method: a Systematic study. *Colloids Surfaces A Physicochem. Eng. Aspects* 492, 213–229. doi:10.1016/j.colsurfa.2015.11.067

Basar, A., Castro, S., Torres-Giner, S., Lagaron, J., and Sasmazel, H. T. (2017). Novel poly (ε-caprolactone)/gelatin wound dressings prepared by emulsion electrospinning with controlled release capacity of Ketoprofen anti-inflammatory drug. *Mater. Sci. Eng. C* 81, 459–468. doi:10.1016/j.msec.2017.08.025

Bilican, I., Pekdemir, S., Onses, M. S., Akyuz, L., Altuner, E. M., Koc-Bilican, B., et al. (2020). Chitosan loses innate beneficial properties after being dissolved in acetic acid: supported by detailed molecular modeling. *ACS Sustain. Chem. Eng.* 8 (49), 18083–18093. doi:10.1021/acssuschemeng.0c06373

Carbone, C., Rende, P., Comberiati, P., Carnovale, D., Mammì, M., and De Sarro, G. (2013). The safety of ketoprofen in different ages. *J. Pharmacol. Pharmacother.* 4 (1_Suppl. l), S99–S103. doi:10.4103/0976-500x.120967

Cheng, N.-C., Estes, B. T., Young, T.-H., and Guilak, F. (2013). Genipin-crosslinked cartilage-derived matrix as a scaffold for human adipose-derived stem cell chondrogenesis. *Tissue Eng. Part A* 19 (3-4), 484–496. doi:10.1089/ten.tea.2012.0384

Cho, H.-J., Choi, S.-J., Kim, N.-H., and Kim, I.-D., Porosity controlled 3D SnO2 spheres via electrostatic spray: selective acetone sensors, Sensors and Actuators B: Chemical, 2020. 304. 127350, doi:10.1016/j.snb.2019.127350

DeJulius, C., Bernardo-Colón, A., Naguib, S., Backstrom, J., Kavanaugh, T., Gupta, M., et al. (2021). Microsphere antioxidant and sustained erythropoietin-R76E release functions cooperate to reduce traumatic optic neuropathy. *J. Control. Release* 329, 762–773. doi:10.1016/j.jconrel.2020.10.010

Fernández-Paz, C., Rojas, S., Salcedo-Abraira, P., Simón-Yarza, T., Remunan-López, C., and Horcajada, P. (2020). Metal–organic framework microsphere formulation for pulmonary administration. *ACS Appl. Mater. interfaces* 12 (23), 25676–25682. doi:10.1021/acsami.0c07356

Malik, S. A., Ng, W. H., Bowen, J., Tang, J., Gomez, A., Kenyon, A. J., et al. (2016). Electrospray synthesis and properties of hierarchically structured PLGA TIPS microspheres for use as controlled release technologies. *J. colloid interface Sci.* 467, 220–229. doi:10.1016/j.jcis.2016.01.021

Mo, F., Lin, B., Lai, F., Xu, C., and Zou, H. (2016). A green modified microsphere of chitosan encapsulating dimethyl fumarate and cross-linked by vanillin and its application for litchi preservation. *Industrial Eng. Chem. Res.* 55 (16), 4490–4498. doi:10.1021/acs.iecr.6b00028

Park, W., Kim, D., Kang, H. C., Bae, Y. H., and Na, K. (2012). Multi-arm histidine copolymer for controlled release of insulin from poly (lactide-co-glycolide) microsphere. *Biomaterials* 33 (34), 8848–8857. doi:10.1016/j.biomaterials.2012.08.042

Shamsudin, Y., Gutiérrez-de-Terán, H., and Åqvist, J. (2018). Molecular mechanisms in the selectivity of nonsteroidal anti-inflammatory drugs. *Biochemistry* 57 (7), 1236–1248. doi:10.1021/acs.biochem.7b01019

Shohin, I. E., Kulinich, J. I., Ramenskaya, G. V., Abrahamsson, B., Kopp, S., Langguth, P., et al. (2012). Biowaiver monographs for immediate-release solid oral dosage forms: ketoprofen. *J. Pharm. Sci.* 101 (10), 3593–3603. doi:10.1002/jps.23233

Stigliani, M., Aquino, R. P., Del Gaudio, P., Mencherini, T., Sansone, F., and Russo, P. (2013). Non-steroidal anti-inflammatory drug for pulmonary administration: design and investigation of ketoprofen lysinate fine dry powders. *Int. J. Pharm.* 448 (1), 198–204. doi:10.1016/j.ijpharm.2013.03.030

Tanaka, T., and Kishimoto, T. (2012). Targeting interleukin-6: all the way to treat autoimmune and inflammatory diseases. *Int. J. Biol. Sci.* 8 (9), 1227–1236. doi:10.7150/ijbs.4666

Tanhaei, A., Mohammadi, M., Hamishehkar, H., and Hamblin, M. R. (2021). Electrospraying as a novel method of particle engineering for drug delivery vehicles. *J. Control. Release* 330, 851–865. doi:10.1016/j.jconrel.2020.10.059

Tarantino, G., Esposito, S., Andreozzi, L., Bracci, B., D'Errico, F., and Rigante, D. (2016). Lung involvement in children with hereditary autoinflammatory disorders. *Int. J. Mol. Sci.* 17 (12), 2111. doi:10.3390/ijms17122111

Wang, K., Wen, H.-F., Yu, D.-G., Yang, Y., and Zhang, D.-F. (2018). Electrosprayed hydrophilic nanocomposites coated with shellac for colon-specific delayed drug delivery. *Mater. Des.* 143, 248–255. doi:10.1016/j.matdes.2018.02.016

Wei, H., Li, W., Chen, H., Wen, X., He, J., and Li, J. (2020). Simultaneous Diels-Alder click reaction and starch hydrogel microsphere production via spray drying. *Carbohydr. Polym.* 241, 116351. doi:10.1016/j.carbpol.2020.116351

Xi, G., Liu, W., Chen, M., Li, Q., Hao, X., Wang, M., et al. (2019). Polysaccharide-based lotus seedpod surface-like porous microsphere with precise and controllable micromorphology for ultrarapid hemostasis. *ACS Appl. Mater. interfaces* 11 (50), 46558–46571. doi:10.1021/acsami.9b17543

Xue, Z., Wang, Z., Huang, J., Wu, W., Chen, M., Hao, X., et al. (2020). Rapid construction of polyetheretherketone (PEEK) biological implants incorporated with brushite (CaHPO4·2H2O) and antibiotics for anti-infection and enhanced osseointegration. *Mater. Sci. Eng. C* 111, 110782. doi:10.1016/j.msec.2020.110782

Yu, C., Zhang, X., Sun, X., Sun, F., Liu, J., Li, X., et al. (2018). Ketoprofen and MicroRNA-124 Co-loaded poly (lactic-co-glycolic acid) microspheres inhibit progression of Adjuvant-induced arthritis in rats. *Int. J. Pharm.* 552 (1-2), 148–153. doi:10.1016/j.ijpharm.2018.09.063

Yunoki, A., Tsuchiya, E., Fukui, Y., Fujii, A., and Maruyama, T. (2014). Preparation of inorganic/organic polymer hybrid microcapsules with high encapsulation efficiency by an electrospray technique. *ACS Appl. Mater. interfaces* 6 (15), 11973–11979. doi:10.1021/am503030c

Zhang, J., Wang, Y., Qu, Q., Lu, T., Li, F., Wang, J., et al. (2021). Preparation of single, heteromorphic microspheres, and their progress for medical applications. *Macromol. Mater. Eng.* 306 (2), 2000593. doi:10.1002/mame.202000593

Zhou, Y., Boudreau, D. M., and Freedman, A. N. (2014). Trends in the use of aspirin and nonsteroidal anti-inflammatory drugs in the general US population. *Pharmacoepidemiol. drug Saf.* 23 (1), 43–50. doi:10.1002/pds.3463

Zhu, H., Yang, F., Tang, B., Li, X.-M., Chu, Y.-N., Liu, Y.-L., et al. (2015). Mesenchymal stem cells attenuated PLGA-induced inflammatory responses by inhibiting host DC maturation and function. *Biomaterials* 53, 688–698. doi:10.1016/j.biomaterials.2015.03.005

frontiers | Frontiers in Bioengineering and Biotechnology

TYPE Original Research
PUBLISHED 05 August 2024
DOI 10.3389/fbioe.2024.1428988

OPEN ACCESS

EDITED BY
Liqun Yang,
Shengjing Hospital of China Medical University, China

REVIEWED BY
Berwin Singh Swami Vetha,
East Carolina University, United States
Jiulong Zhao,
Naval Medical University, China

*CORRESPONDENCE
Min Yang,
yangmin7426@126.com
Ting Zhao,
lyguiwandingdind@163.com

†These authors share first authorship

RECEIVED 07 May 2024
ACCEPTED 19 July 2024
PUBLISHED 05 August 2024

CITATION
Yang Y, Ma S, Li A, Xia G, Li M, Ding C, Sun X, Yan L, Yang M and Zhao T (2024), Antibacterial and antioxidant phlorizin-loaded nanofiber film effectively promotes the healing of burn wounds.
Front. Bioeng. Biotechnol. 12:1428988.
doi: 10.3389/fbioe.2024.1428988

Antibacterial and antioxidant phlorizin-loaded nanofiber film effectively promotes the healing of burn wounds

Ying Yang[1†], Shuang Ma[2†], Anning Li[3], Guofeng Xia[3], Min Li[1], Chuanbo Ding[1,3], Xiaofei Sun[3], Li Yan[3], Min Yang[1,3*] and Ting Zhao[1*]

[1]College of Traditional Chinese Medicine, Jilin Agricultural Science and Technology University, Jilin, China, [2]College of Traditional Chinese Medicine, Jilin Agricultural University, Changchun, China, [3]Jilin Aodong Yanbian Pharmaceutical Co, Ltd., Dunhua, China

Burns usually result in damage and loss of skin forming irregular wound wounds. The lack of skin tissue protection makes the wound site highly vulnerable to bacterial infections, hindering the healing process. However, commonly used wound dressings do not readily provide complete coverage of irregular wounds compared to regular wounds. Therefore, there is an urgent need to prepare a wound dressing with high antimicrobial efficacy for the administration of drugs to irregular wounds. In this study, a chitosan (CS)/polyvinylpyrrolidone (PVP) composite nanofiber membrane (CS/PVP/Phlorizin) loaded with root bark glycosides (Phlorizin) was developed using an electrostatic spinning technique. The incorporation of phlorizin, a natural antioxidant, into the fiber membranes notably boosted their antimicrobial and antioxidant capabilities, along with demonstrating excellent hydrophilic characteristics. *In vitro* cellular experiments showed that CS/PVP/Phlorizin increased Hacat cell viability with the presence of better cytocompatibility. In scald wound healing experiments, Phlorizin-loaded nanofibrous membranes significantly promoted re-epithelialization and angiogenesis at the wound site, and reduced the inflammatory response at the wound site. Therefore, the above results indicate that this nanofiber membrane is expected to be an ideal dressing for burn wounds.

KEYWORDS

chitosan, phlorizin, nanofiber membrane, scalding wound repair, wound dressing

1 Introduction

Skin, as one of the most important organs of a human being (Yan et al., 2020), is not only resistant to damage from external factors, but also a thermoregulator of the human body, and intact skin tissues can maintain the stability of the internal environment of the human body (Ursell et al., 2012; Liao et al., 2015). Whereas, scald injuries, as one of the most serious skin injuries, are showing an increasing trend in incidence globally (Xu et al., 2020). Burns can be classified based on the depth and extent of skin damage: superficial burns affect only the epidermal layer, partial-thickness burns extend into the dermis, and full-thickness burns penetrate both the epidermal and dermal layers (Wang et al., 2018), and full-layer skin injuries completely rupture the epidermal and dermal layers of the skin.

Infection by microorganisms at the burn site contributes to slow recovery of the wound site, increasing the risk of scar formation at the wound site as the healing time increases (Lee et al., 2017). At the same time, scald injuries often result in extremely complicated acute trauma, deformity, disability, or even death, and therefore often cause physical and emotional stress to the scalded patient (Xi et al., 2023). In today's clinical treatment, topical administration at the wound site is usually used. As well as the use of a variety of traditional dressings to cover the scald wound to avoid infection of the wound site (Guo et al., 2022), such as sponges, bandages, and foam, but due to the adhesive effect of the tissue at the wound site, when changing the dressings often bring secondary damage to the patient (Boateng et al., 2008; Ouyang et al., 2024). Therefore, it is urgent to find a method that is more beneficial for the repair of burn wounds. Compared with traditional excipients, nanofiber membranes are not only simple to prepare, versatile, and easy to replace (Khan et al., 2020), but can also absorb wound site exudate, which is beneficial to the exchange of gases at the wound site and prevents bacterial and microbial infections (Lan et al., 2021; Dong et al., 2023). Due to these beneficial qualities, nanofiber membranes are expected to be a valuable dressing for burn wounds.

Chitosan, a natural polymer derived from chitin (Rinaudo, 2006; Song et al., 2018) has garnered significant attention for its use in the preparation of wound dressings due to its exceptional biocompatibility and various beneficial effects such as antibacterial properties, hemostatic abilities, and promotion of cell proliferation (Archana et al., 2013; Zhou et al., 2016). In addition, chitosan has a broader and more efficient antimicrobial activity than other antimicrobial agents, which enhances its biomedical applications. In recent years, chitosan is often used to prepare nanofiber membrane materials, Wei et al. prepared a CS tetragonal composite with effective control of drug release and antibacterial promotion of infected wound repair (Wei et al., 2024). Yin et al. prepared a CS/PLA nanofiber membrane loaded with aloe-emodin, which exhibited high porosity as well as suitable swelling and hydrophobic properties (Yin et al., 2022). Tang et al. prepared a chitosan/sodium cellulose sulfate composite nanofibrous membrane containing silver nanoparticles, which not only existed excellent antimicrobial properties but also significantly shortened the wound repair time (Tang et al. 2022). Referring to the results of existing studies, it was hypothesized that CS-based nanofiber membrane materials have the potential to be excellent wound dressings. However, due to the rapid degradation of CS materials in acidic environments, their use alone does not meet the needs of ideal wound dressings (Wei et al., 2024), so they are often blended with other polymers such as poly (vinyl alcohol) (PVA), poly (vinylpyrrolidone) (PVP), and so on, to improve the performance of nanomaterials and better meet the needs of wound dressings.

Polyvinylpyrrolidone (PVP) is a spinning polymer with excellent fiber membrane formation properties and is often used as a feedstock for making nanofiber membranes (Poonguzhali et al., 2017). Contardi et al. showed that PVP electrostatically spun hydrogels loaded with hydroxycinnamic acid derivatives significantly reduced the inflammatory response at the wound site, thereby promoting wound site healing (Contardi et al. 2021). Phlorizin, a widely available flavonoid, is an important plant-derived dihydrochalcone (Stompor et al., 2019). Dihydrochalcone as a natural antioxidant has received a lot of attention from scientists in recent years (Li et al., 2018). It has been shown that root bark glycosides can regulate the NF-KB signaling pathway to play an antioxidant role, it also has anti-inflammatory, antiviral, antidiabetic, and other functions (Wang et al., 2019; Un et al., 2021). Sun (Sun et al., 2022)et al. demonstrated that SF/PVP nanofiber membranes containing root bark glycosides reduced inflammation at wound sites by decreasing the expression of TNF-α and IL-1β proteins, thus accelerating wound healing. Additionally, Liu et al. (Liu et al., 2021) found that phlorizin increased levels of superoxide dismutase (SOD) and total antioxidant capacity. However, the use of Phlorizin in scald wound repair has not been reported. Therefore, in this paper, root bark glycosides were loaded into CS/PVP nanofiber membranes to investigate their effects on scald wound repair.

As shown in Scheme 1, in this study, chitosan (CS) and polyvinylpyrrolidone (PVP) were used to synthesize blank fiber membranes by electrostatic spinning technique, in addition to loading phlorizin with antioxidant activity into the blank nanofiber membranes (CS/PVP/Phlorizin). The chemical structure and properties of CS/PVP/Phlorizin were also evaluated by various characterization methods, in addition to their antioxidant and antibacterial activities by *in vitro* antioxidant and antibacterial assays. The biosafety of CS/PVP/Phlorizin was evaluated through MTT cytotoxicity and hemocompatibility tests. And finally, the effect of CS/PVP/Phlorizin nanofiber membrane on scald wound repair was investigated. It is expected that CS/PVP/Phlorizin nanofiber membrane with antioxidant and antibacterial properties will provide a new idea for the treatment of burn wound dressing.

2 Experimental section

2.1 Experimental materials

Chitosan (CS) was purchased from Sinopharm Chemical Reagent Co, Ltd. Polyvinylpyrrolidone (PVP, Mn = 1.3 MDa). Phlorizin was purchased from Lemaitan Pharmaceuticals Dexter Biotechnology Company Limited (purity ≥80%). Meibao Scald Cream was purchased from Shantou Meibao Pharmaceutical Co. 2,2-Biazobis (3-ethyl-benzothiazole-6-sulfonic acid) diammonium salt (ABTS) was purchased from McLean Biochemicals Ltd. Protein Antibodies (See Support Information Table 1 for details).

2.2 Preparation of CS/PVP, CS/PVP/Phlorizin, nanofiber membranes

CS/PVP/Phlorizin nanofiber membranes were prepared by first adjusting the concentration of the materials in the preliminary stage. CS, PVP, and Phlorizin powder were dissolved in 90% glacial acetic acid solution at concentrations of 4.4%, 2.1%and 2% to prepare 10 mL of spinning solution, which was stirred continuously for 12 h at 50°C on a magnetic stirrer to achieve complete dissolution and to obtain a homogeneous spinning solution. Finally, through the electrostatic spinning device, spinning is carried out. The distance from the needle to the drum collector was adjusted to 15 cm, the drum speed was 200 r/min, and the voltage was set to

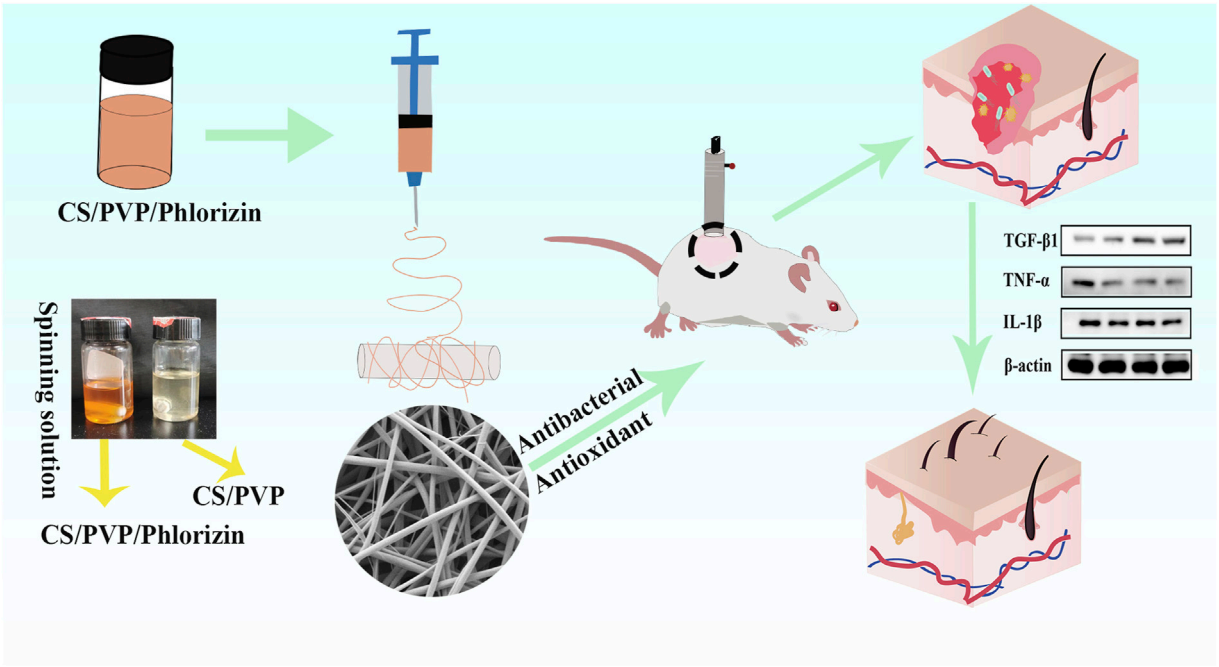

SCHEME 1
Loaded phlorizin nanofiber membrane to promote scald wound healing

TABLE 1 Experimental antibody sources and dilution ratios.

Antibodies	Factory owners
TGF-β1 (DILUTION:1:1000–1:5000)	Proteintech group
IL-1β (DILUTION:1:2000–1:10000)	Proteintech group
TNF-α (DILUTION:1:500–1:2000)	Proteintech group
β-actin (DILUTION:1:5000–1:50000)	Proteintech group
HRP coupled secondary antibodies (SA00001–1 1:2000–1:10000/SA00001-21:2000–1:10000)	Proteintech group

15 KV to obtain the nanofiber membrane, which was vacuum dried overnight (Zhang et al., 2022; Liu et al., 2024). The CS/PVP nanofiber membrane was prepared in the same way as CS/PVP/Phlorizin but without the addition of phlorizin.

2.3 Scanning electron microscopy

The microscopic morphology of CS/PVP, CS/PVP/Phlorizin nanofiber membranes was observed by scanning electron microscopy (ZEISS, EVO/18, Germany). Fixed sample, sprayed with gold, and obtained at an accelerating voltage of 15 kV (Liu et al., 2023). The diameters of 100 fibers were randomly screened in the SEM images, and the calculation of the average diameter of the fiber membrane was performed by ImageJ software.

2.4 Fourier infrared spectroscopy

The infrared spectrograms of the nanofiber membranes were determined in the range of 4,000–500 cm^{-1} using a Fourier infrared spectrometer (FITR, SpectrumTwo, Perkinekmer, United States). To determine the loading of Phlorizin in nanofiber membranes.

2.5 Water contact angle

To assess the hydrophilic and hydrophobic characteristics of CS/PVP and CS/PVP/Phlorizin nanofiber membranes, the two types of nanofiber membranes were prepared as 2-cm-diameter discs, and then the water contact angle of the nanofiber membranes was determined using water contact angle meter (Dataphysics OCA50, Germany). The average contact angle was determined using ImageJ software.

2.6 Water vapor transmission rate

The ideal wound dressing should have an appropriate water vapor transmission rate to control the evaporation of water from the wound site (Xia et al., 2020). Referring to the Li method with slight modification (Li et al., 2024), firstly, 5 mL of distilled water was added to a vial with a mouth area of S. Immediately, the circular nanofiber membrane was placed in the mouth of the vial and weighed and recorded as W_i. They were placed in an incubator at 37°C for 24 h and weighed and recorded as W_t, three times in parallel for each group. The water vapor transmission rate was calculated according to the following equation:

$$WVTR\left(gm^{-2}d^{-1}\right) = (Wi - Wt)/S \quad (1)$$

2.7 Antioxidant effect

A slight modification was made with reference to the existing method. To determine the scavenging effect of CS/PVP and CS/PVP/Phlorizin nanofiber membranes on ABTS free radicals. Configure 7.5 mM of ABTS solution and 2.45 mM of potassium persulfate solution. The reaction was carried out in a 1:1 ratio for 12 h at room temperature. The working solution was diluted at room temperature until its absorbance at 745 nm was 0.7 ± 0.2. Weighing 5 mg of nanofiber membrane was co-incubated with 2 mL of ABTS solution for half an hour, and the group without fiber membrane was used as a blank control group. The ABTS free clearance was calculated according to the following equation (Ma et al., 2024).

$$Removal\ rate\,(\%) = \left(1 - A_s/A_c\right) \times 100\% \quad (2)$$

As is the absorbance of the fiber membrane plus reaction solution, and Ac is the absorbance of the control without the addition of the nanofiber membrane.

2.8 Hemolytic effect

In vitro, the blood safety properties of nanofiber membranes were evaluated using hemolysis of mouse erythrocytes. Mouse erythrocytes were first obtained by centrifugation of fresh mouse blood, and saline was chosen to dilute the erythrocyte suspension to 2%. The CS/PVP and CS/PVP/Phlorizin nanofiber membranes were then cut into equal volume (1 cm × 1 cm) discs. An equal volume of nanofiber membrane was taken and co-incubated with 1 mL of 2% erythrocyte suspension at 37°C for 1 h. The 1% Trion X-100 and PBS groups were selected as positive and negative controls. At the end of the incubation, the supernatant was obtained and its absorbance at 545 nm was determined and calculated according to the following formulae (Lian et al., 2021).

$$Hemolysis\ rate\,(\%) = (A_S - A_P)\Big/\left(A_y - A_p\right) \times 100\% \quad (3)$$

Among them, A_s is the sample group, A_p is the negative control group, and A_y is the positive control group.

2.9 Cytotoxicity

Cytotoxicity of CS/PVP and CS/PVP/Phlorizin membranes was determined using Hacat skin keratinocytes. The CS/PVP, CS/PVP/Phlorizin nanofiber membranes were first sterilized by UV irradiation for 2 h. The sterilized nanofiber membrane was then dissolved in the medium to obtain a drug-loaded medium. Hacat cells in logarithmic growth phase were taken and inoculated at a density of 2×10^4/well in 96-well plates in an incubator at 37°C, 5% CO_2 for 24 h, and then replaced with drug-loaded medium. In the control group, the complete medium was replaced and the culture was continued for 24 h, then 20 μL of MTT solution was added to each well and reacted for 4 h, 150 μL of DMSO was added to each well sequentially, and the absorbance was measured at 490 nm to calculate the cell viability of each group.

2.10 Bacteriostatic effect

Staphylococcus aureus and *Escherichia coli* were selected as model bacteria to evaluate the *in vitro* antimicrobial activity of nanofiber membranes (CS/PVP, CS/PVP/Phlorizin) by colony counting method. Firstly, the nanofiber membrane with a diameter of 1 cm was cut and sterilized by irradiation under UV lamp for 2 h, and the fiber membrane was co-cultivated with the bacterial solution (37°C, 2 h). Absorb 30 μL of the above bacterial solution evenly on solid medium agar plate, without soaking fiber membrane bacterial solution as a control group, and incubate at 37°C for 12–24 h. The bacterial inhibition rate of the nanofiber membrane was calculated according to the following equation (Li et al., 2022).

$$Bacterial\ inhibition\ rate\,(\%) = \frac{N_c - N_s}{N_c} \times 100\% \quad (4)$$

N_c is the control group and N_s is the number of colonies in the sample group.

2.11 *In vivo* scald wound repair

To evaluate the effect of CS/PVP/Phlorizin nanofiber membranes on scald wounds, this paper first creates a scald wound model, which complies with the National Research Council Guide for the Care and Use of Laboratory Animals. In this paper, ICR male mice (25 ± 5 g) were purchased from Changchun Yisi Laboratory Animal Technology Co, mice were first acclimatized for 1 week after rearing. Mice were anesthetized using 4% chloral hydrate and depilatory cream was applied for hair removal. Using the YLS-5Q scalding instrument, a 2.5-cm^2 metal punch was selected, and the temperature was set to 85°C with a pressure of 500 KPa pressed tightly to the hair removal site of the mice for 10 s, to construct a scalding wound (Jieqiong, 2020). Cage hygiene was strictly controlled after molding was completed and an adequate diet was provided. The scalded mice were randomly divided into four groups of 10 mice each, namely, the scald model group, the positive control group, the CS/PVP, and the CS/PVP/Phlorizin groups, with no treatment in the model group, and the other three groups were given daily treatment. Photographs were taken on days 3, 7, 14, and 21 after treatment to observe changes in the wound site, i.e., changes in the color of the wound site, whether it was infected or not, scabbing, and changes in the size of the wound. The wound area was calculated using ImageJ software. The healing rate of the wound area was calculated according to the following formula (Asiri et al., 2021).

$$Wound\ healing\ rate\,(\%) = \frac{S_o - S_t}{S_o} \times 100\% \quad (5)$$

S_o is the initial wound area and S_t is the fixed-time wound area.

2.12 H&E and Masson staining

For further observation of tissue changes and collagen deposition at the wound site. Skin tissues from each group of mice were taken at the fixation time, and after fixation with 4% paraformaldehyde, the residual fixative was removed from the skin tissues using water. Then it was gradient dehydrated with ethanol, cleared with xylene, paraffin embedded, and then cut into 6um sections for H&E and Masson staining.

2.13 Immunohistochemical staining

On day 21 of constructing the scald wounds, skin tissues from the wound site were taken for paraffin embedding, sectioned, and then subjected to immunohistochemical analysis. Firstly, the paraffin sections were deparaffinized and washed with PBS, and 3% BSA was chosen to be closed for half an hour. Then α-SMA, CD31, and VEGF primary antibody were diluted according to the proportion, and incubation was carried out. After incubation for 50 min at room temperature with 2 antibodies corresponding to the primary antibody, the sections were finally stained and observed by microscope.

2.14 Western blot

Skin tissues from the wound site of scalded mice in each group were taken and weighed, and proteins in the skin tissues of each group were extracted by adding RIPA lysate containing PMSF. The protein content in each group of samples was first determined by the BCA method. Sample proteins were electrophoresed through sodium dodecyl sulfate polyacrylamide gel (10%). After waiting for the end of electrophoresis, the membrane was rotated at low temperature for 90 min under the condition of constant voltage 100 V. The PVDF membrane was selected to be closed with 5% skim milk powder for 2 h. The membrane was incubated with the specific primary antibody for 1.5 h. At the end of the incubation, the membrane was washed with TBST 3 times for 10 min each time. Then the membrane was incubated with HPR-labeled secondary antibody for 1 h. The membrane was washed three times in TBST for 10 min each finally, the protein expression level was detected by gel imaging analysis system.

2.15 Statistical analysis

All experimental data were repeated at least three times and expressed as mean ± standard deviation (SD). One-way analysis of variance (ANOVA) was performed using SPSS 22.0 software, and a value of $^*p < 0.05$ indicates a significant difference.

3 Results

3.1 Scanning electron microscopy

The microscopic morphology and diameter of CS/PVP and CS/PVP/Phlorizin nanofiber membranes are shown in Figure 1. As shown in Figure 1A, B it can be observed that the nanofibers in the two types of fibrous membranes exist crosswise and twisted with each other, thus forming a porous three-dimensional structure. Due to this structure, nanofiber membranes are beneficial for the exchange of gases at the wound site as well as the transport of nutrients and the growth and migration of cells at the wound site (Hasani-Sadrabadi et al., 2019). The average diameters of CS/PVP and CS/PVP/Phlorizin were 137.6 ± 35.8 nm and 167.8 ± 45.9 nm, respectively. It was also found that the diameter of the nanofibers increased with the loading of Phlorizin, and at the same time, no non-homogeneous structure was observed on the surface of the nanofibers, indicating that the Phlorizin was fully dissolved in the spinning solution.

3.2 Fourier infrared spectroscopy

The infrared scanning results are shown in Figure 2A. The characteristic peak at 3,374 cm^{-1} corresponds to the O-H tensile vibration. Both CS/PVP and CS/PVP/Phlorizin nanofiber membranes display a characteristic peak of the amide I bond at 1,662 cm^{-1}, associated with C=O stretching vibration. The waveform of the CS/PVP/Phlorizin scaffold amide I bond broadened upon loading of Phlorizin. The CS/PVP/Phlorizin nanofibers exhibited a characteristic C-O peak at 1,035 cm^{-1}, which is the characteristic absorption peak of Phlorizin.

3.3 Water contact angle

Nanofiber membrane materials can quickly absorb excess exudate from the wound site, thus reducing the wound infection rate, while providing a moist microenvironment for the wound site, effectively promoting the proliferation and migration of cells in the wound site thus accelerating the repair of the wound site (Dong and Guo, 2021). In this paper, the hydrophilicity of the surface of the nanofiber membrane was evaluated by determining its water contact angle (He et al., 2016). When the water contact angle of the fiber membrane is less than 90° indicates the existence of good hydrophilicity of the fiber membrane. The results are shown in Figure 2B, and the water contact angles of CS/PVP and CS/PVP/Phlorizin are 78.55° and 61.09°, respectively, indicating the existence of better hydrophilicity of the two materials. Also from the results, it can be seen that the hydrophilicity of the fiber membrane was enhanced after loading phlorizin.

3.4 Water vapor transmission rate

Water vapor transmission rate, as one of the most important evaluation indexes of wound dressings, can reflect the gas transmission rate when nanomaterials are applied to the wound site. Compared with the blank fiber membrane, the transmittance of the nanofiber membrane loaded with phlorizin increased, reaching 2334.28 ± 32.16 $gm^{-2}d^{-1}$. The water vapor transmission rate of the nanofiber membrane was in the range of 2000–2,500 $gm^{-2}d^{-1}$, which meets the water vapor transmission rate requirement for wound healing, and the results are shown in Figure 2C.

3.5 Antioxidant activity

Excess free radicals may lead to cell destruction and DNA damage, which can lead to a number of diseases. Therefore, in this paper, the scavenging effects of CS/PVP, and CS/PVP/Phlorizin on ABTS radicals were determined. The results, as shown in Figure 2D, showed that the clearance of CS/PVP, and CS/PVP/Phlorizin for ABTS was 9.6% ± 2.58% and 90.68% ± 0.05%,

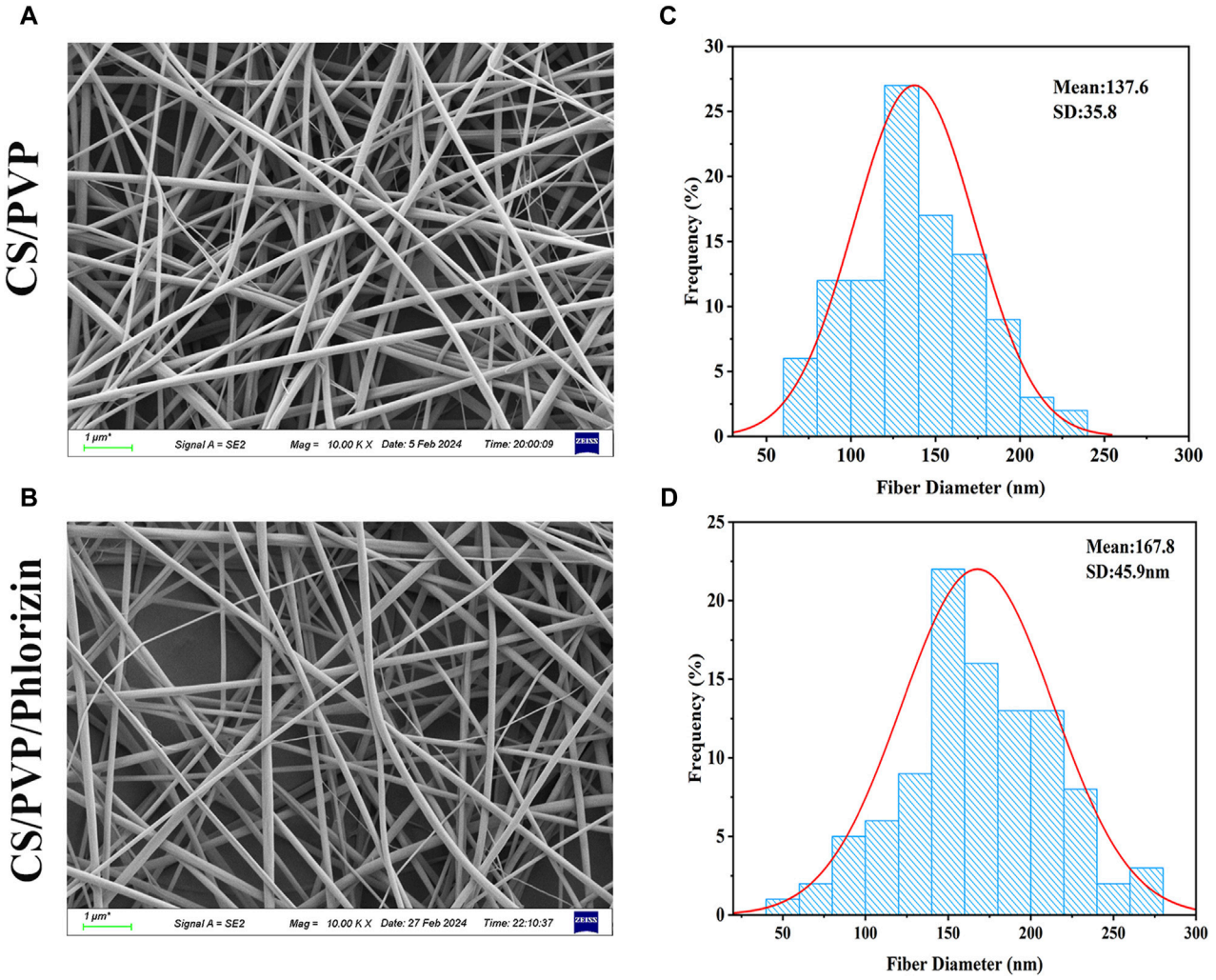

FIGURE 1
SEM image of nanofiber membrane and its nanofiber diameter size. **(A, B)** SEM images of CS/PVP, CS/PVP/Phlorizin nanofiber membranes; **(C, D)** Diameter distribution of CS/PVP, CS/PVP/Phlorizin nanofiber membranes, results were used as mean ± standard deviation.

respectively. The antioxidant activity of the fiber membranes loaded with phlorizin was significantly higher (*$p < 0.05$) compared with that of the blank membranes, which may be attributed to the good antioxidant activity of phlorizin itself.

3.6 Blood compatibility

As shown in Figure 3A, the hemolysis rates of CS/PVP and CS/PVP/Phlorizin nanofiber membranes were 0.056% ± 0.026% and 0.016% ± 0.01%, respectively, and the hemolysis rates of both materials were less than 5%. At the same time, it can be observed that the supernatant of two groups of nanofiber membrane groups is clear and transparent, and there is a significant difference from the red colour of the positive control (*$p < 0.05$). It shows that there is better blood compatibility between the two materials and no hemolysis phenomenon. They meet the basic requirements of safe wound dressing.

3.7 Cytotoxicity analysis

Having good biosafety is a fundamental condition for the application of wound dressings. In this paper, the biosafety properties of the two materials were verified by MTT experiments. Skin keratinocytes (Hacat) were incubated with nanofiber membrane extracts for 24 h and all cell viability was greater than 100%. The results of the statistical analysis are shown in Figure 3B, and there was no significant difference between the two groups. It indicates that the two nanofiber membranes exist better cytocompatibility and can promote the proliferation of Hacat cells.

3.8 Bacteriostatic activity analysis

During the wound healing process, it is highly susceptible to *E. coli* and *S. aureus*, which can cause tissue infection and inflammation to occur at the wound site, resulting in slow healing of the wound site.

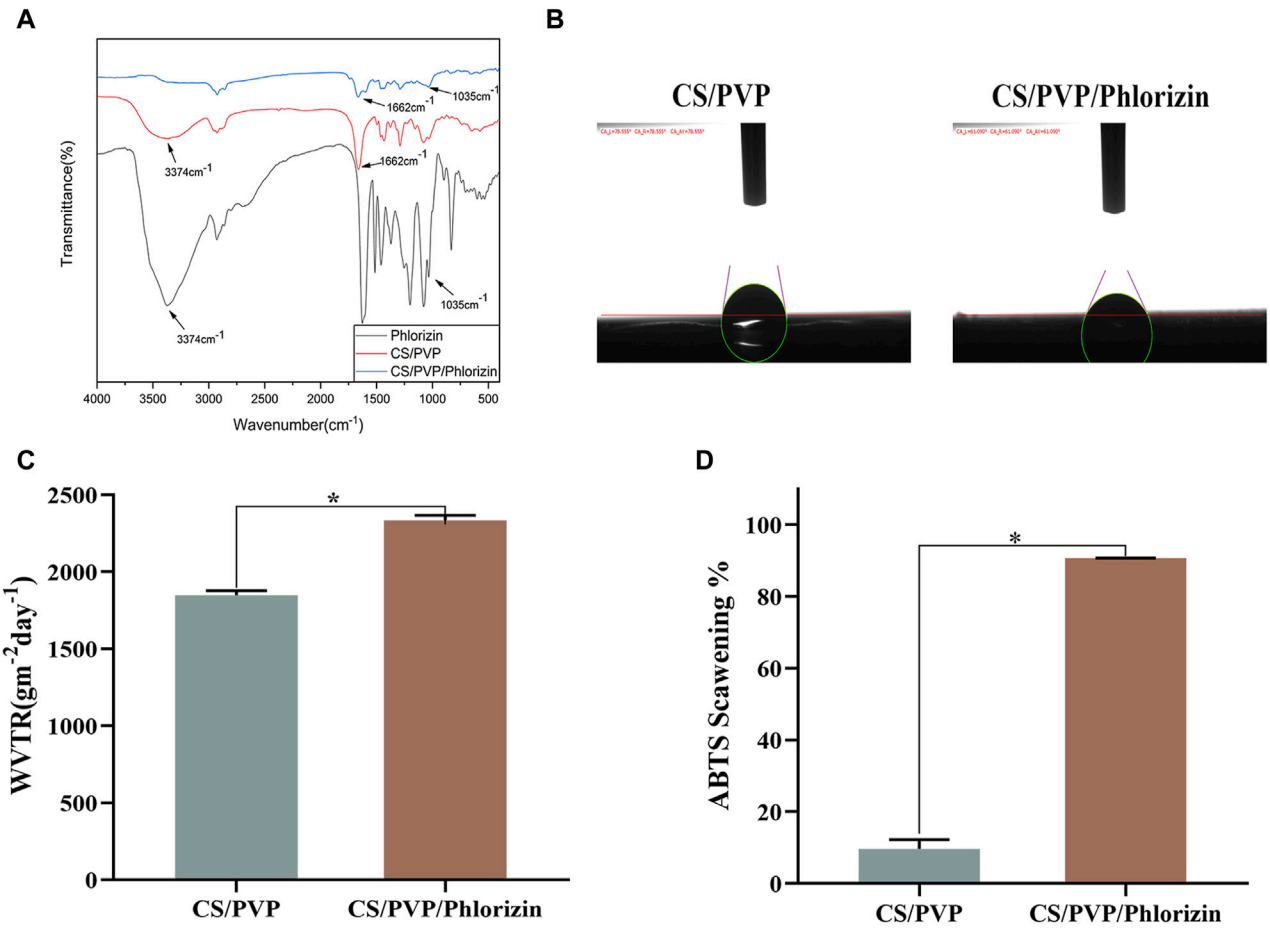

FIGURE 2
(A) Fourier infrared spectra; **(B)** water contact angle; **(C)** water vapor transmission rate; **(D)** ABTS radical scavenging rate.

Therefore, good bacteriostatic activity is necessary for an ideal wound dressing. The results are shown in Figure 3C, CS/PVP and CS/PVP/Phlorizin can significantly reduce the colony count of *E. coli* and *S. aureus*. The results of the quantitative analysis are shown in Figure 3D, E, the inhibition rates of CS/PVP/Phlorizin were 99.5% ± 0.12% and 98.46% ± 0.47% for *S. aureus* and *E. coli*, respectively. The bacterial inhibition rate of nanofiber membranes loaded with Phlorizin was significantly higher ($p^* < 0.05$) compared with that of CS/PVP nanofiber membranes.

3.9 *In vivo* mouse scald wound repair

To investigate the role of nanofiber membrane for the repair of scald wounds. We first successfully constructed deep second-degree scald wounds. Macroscopic observation showed that the skin at the scalded site was wrinkled and yellowish-white, and the skin at the scalded site was hardened when lightly touched, and the pain sensation of the mice was significantly increased. Indicates successful modeling of deep second-degree burns.

The state of the skin at the site of the wound was also observed, and the degree of wound closure was evaluated to assess the healing of the scald wounds in each group, and the results are shown in Figure 4A. On the third day of constructing the scald wounds, the relative enlargement of the wounds in each group may be attributed to the inflammatory response at the wound site that enlarged the wound area, which is consistent with what has been reported. At day 7 of scald wound repair, a thick scab was present on the wound surface in all groups, but partial shedding of the crust was visible in the CS/PVP and CS/PVP/Phlorizin nanofibrous membrane groups. On the 14 days after treatment, the scabs were completely removed from the wound site in the remaining three groups compared to the model group. A smaller wound area existed in the rhizoposide-loaded nanofiber membrane group compared to the CS/PVP nanofiber membrane group. On the last day of wound healing, the wounds of the phlorizin loaded nanofiber membrane group were completely closed, which was significantly different from the wounds of the model group. It indicates that the nanofiber membrane loaded with phlorizin can significantly promote the wound repair of scalded wounds.

3.10 Histopathologic analysis

The efficacy of nanofibrous membranes for scald wound healing was evaluated by hematoxylin eosin staining for

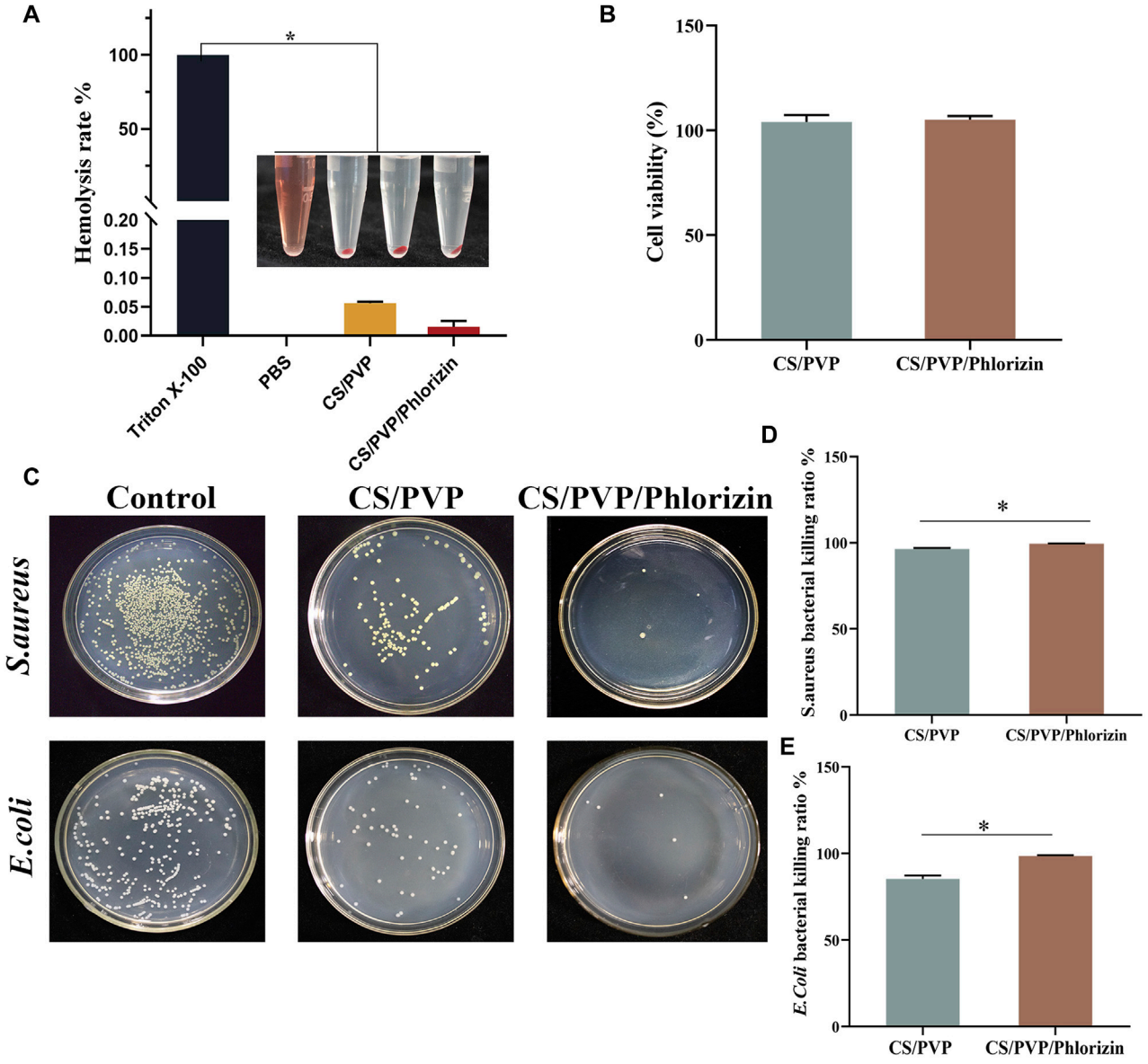

FIGURE 3
(A) Hemocompatibility; **(B)** Cytotoxicity; **(C)** Colony counts of CS/PVP, CS/PVP/Phlorizin nanofiber membranes for *Staphylococcus aureus* and *Escherichia coli*; **(D)** Quantitative graph of the inhibition rate of the nanofiber membranes for *Staphylococcus aureus*; **(E)** Quantitative graph of the inhibition rate of the nanofiber membranes for *Escherichia coli*.

pathological observation of scald wound site tissues in each group. As shown in Figure 5A the epidermal defects and their subdermal blood vessels and tissues were damaged and necrotic tissues were present in all groups of mice as seen on day 3 of wound creation. Indicates successful creation of a deep second-degree burn wound model. At day 21 of wound healing, the positive control and CS/PVP/Phlorizin groups had been completely re-epithelialized compared to the model group. The CS/PVP/Phlorizin group exhibited thicker granulation tissue and angiogenesis. Suggesting that nanofiber membranes loaded with phlorizin can effectively promote scald wound healing. This may be attributed to the excellent antibacterial and antioxidant effects of the nanofiber membrane, which reduces the rate of infection at the wound site and provides a healing-friendly environment for the wound site (Guo et al., 2020).

The collagen expression (blue color) of each group after 21 days of treating the wounds was observed by Masson staining, and the results are shown in Figure 5B. Protein expression of collagen was significantly higher in the other three groups compared to the model group. Compared to the CS/PVP group, CS/PVP/Phlorizin collagen content was increased and collagen fibers were more compactly arranged in bands (Johnson, 2003). In addition, collagen fibers with a tight structure have been reported to be beneficial for ECM formation, thereby accelerating wound healing (Li et al., 2020).

10.3389/fbioe.2024.1428988

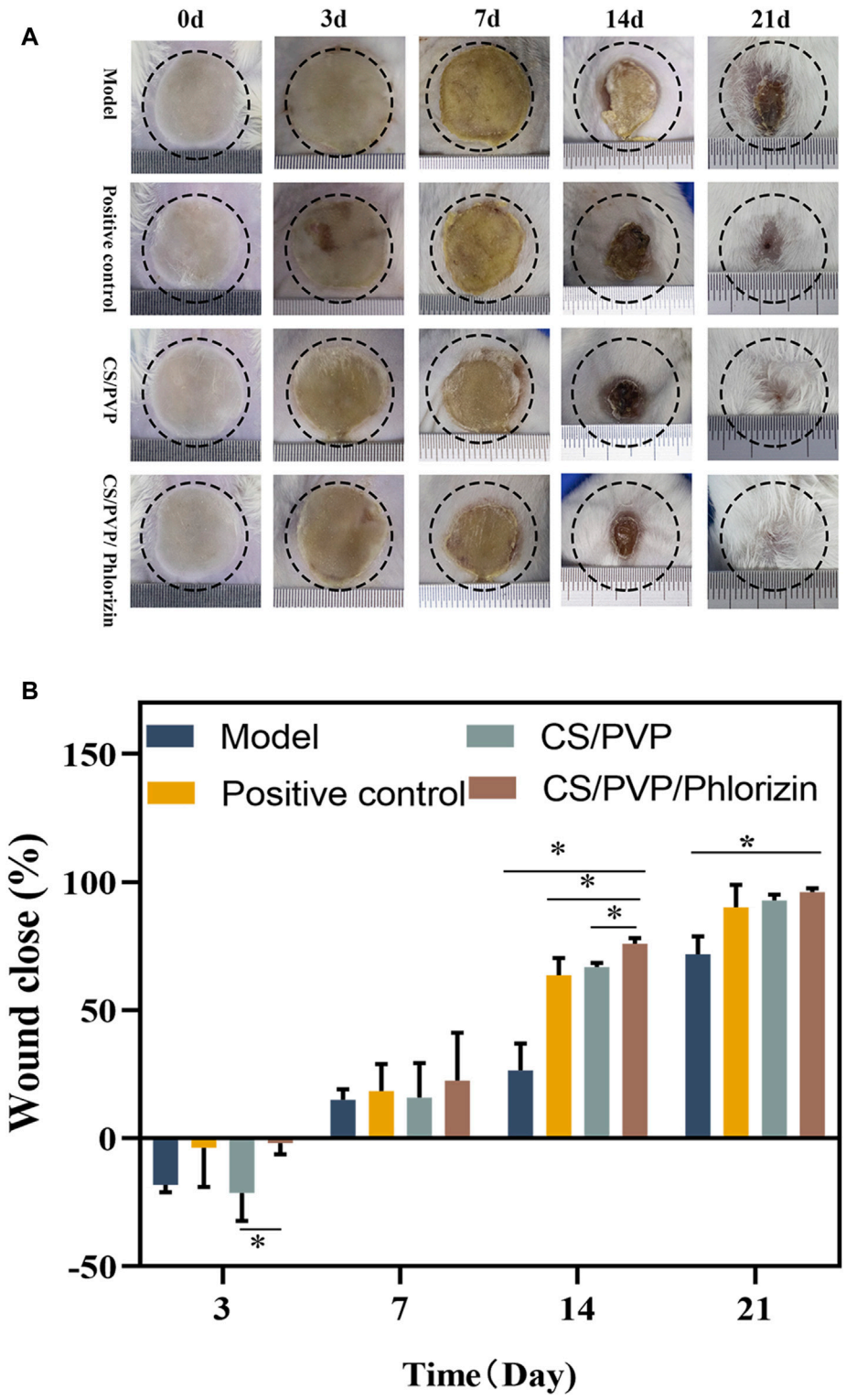

FIGURE 4
(A) Wound status and its size change on days 0, 3, 7, 4, and 21 for Model, Positive control, CS/PVP, and CS/PVP/Phlorizin groups; **(B)** Quantitative plot of wound close rate.

3.11 Immunohistochemical analysis

To further investigate the possible mechanism of CS/PVP/Phlorizin nanofiber membrane to promote the healing of scald wounds, the expression of α-smooth muscle actin (α-SMA), CD31 (early vascular growth factor), and VEGF (vascular endothelial generating factor) was measured at the wound sites of each group. The expression of α-SMA is associated with

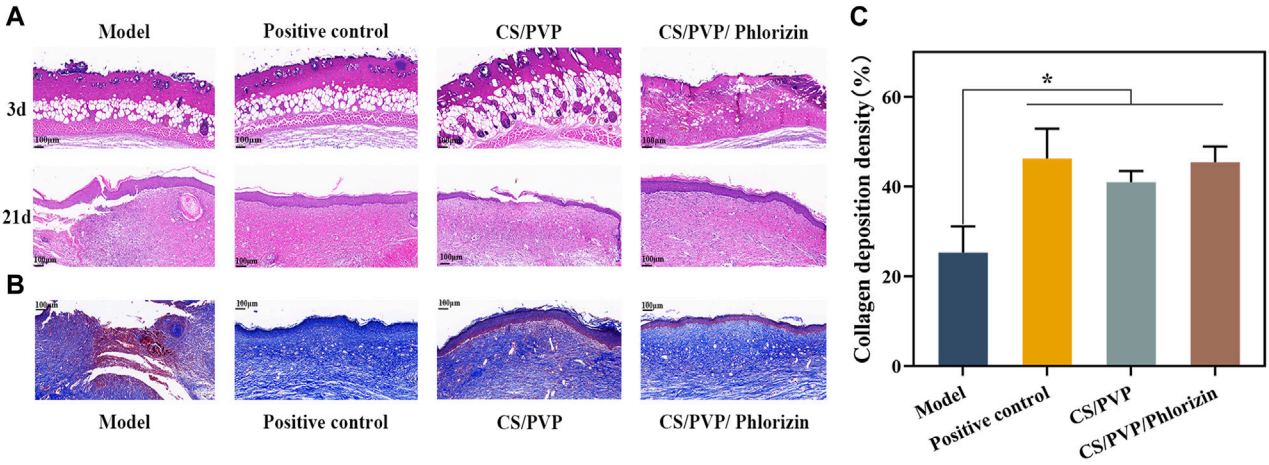

FIGURE 5
(A) H&E staining of Model, Positive control, CS/PVP, and CS/PVP/Phlorizin groups on days 3 and 21; **(B)** Masson staining of each group on day 21; **(C)** collagen deposition statistics of each group.

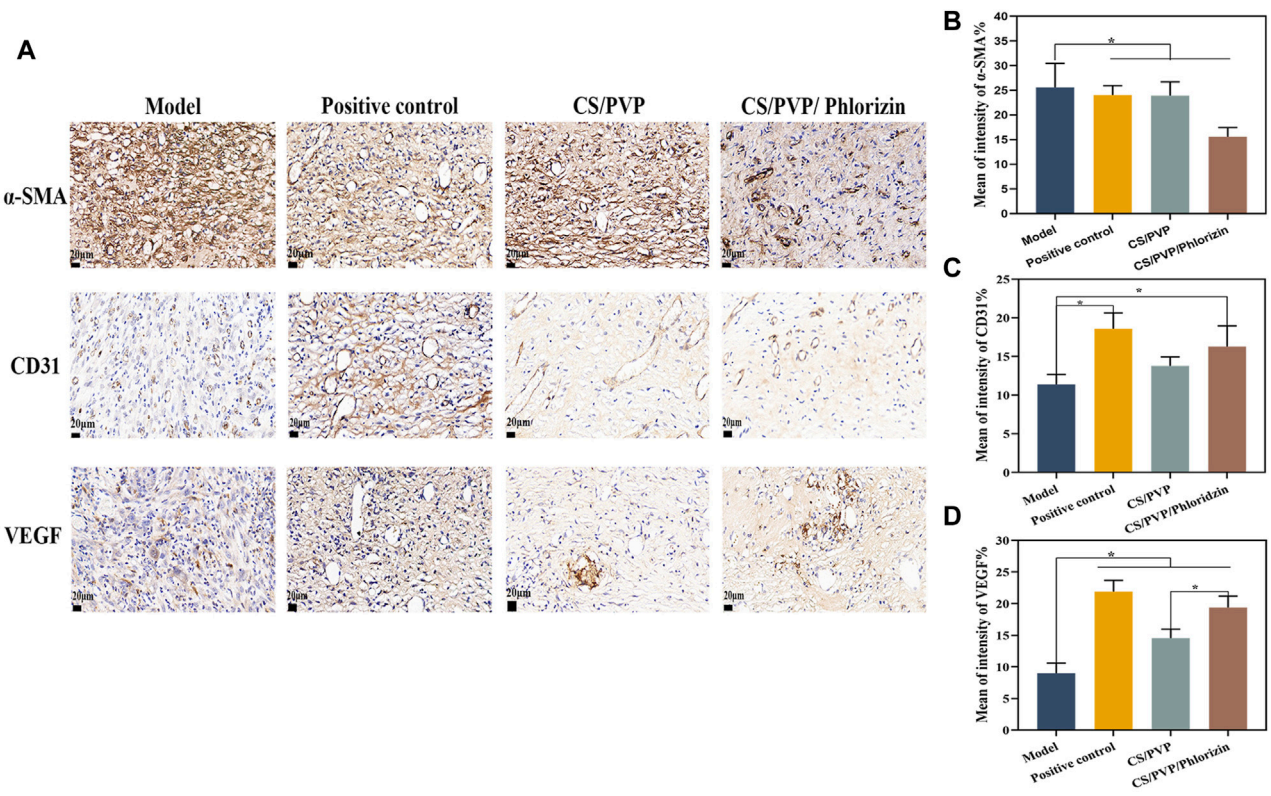

FIGURE 6
(A) Immunohistochemical pictures of α-SMA, CD31, and VEGF in each group; **(B)** Quantitative analysis pictures of α-SMA; **(C)** Quantitative analysis pictures of CD31; **(D)** Quantitative analysis pictures of VEGF.

myofibroblasts, which have a critical role in rapid wound healing, however, rapid contraction at the wound site can lead to scar formation at the wound site (Zonari et al., 2015). The expression of α-SMA was significantly reduced in the CS/PVP/Phlorizin group after 21 days of treatment compared with the model and positive control groups. This result suggests that the nanofiber membrane loaded with phlorizin reduces scar formation at the scald wound site. CD31 and VEGF as vascular growth factors its can respond to the vascular expression at the wound site. Compared to the scald model group, the other three groups showed significantly higher vascular expression (Figure 6A). Higher vascular expression existed in the CS/PVP/Phlorizin group compared to the CS/PVP group, and the

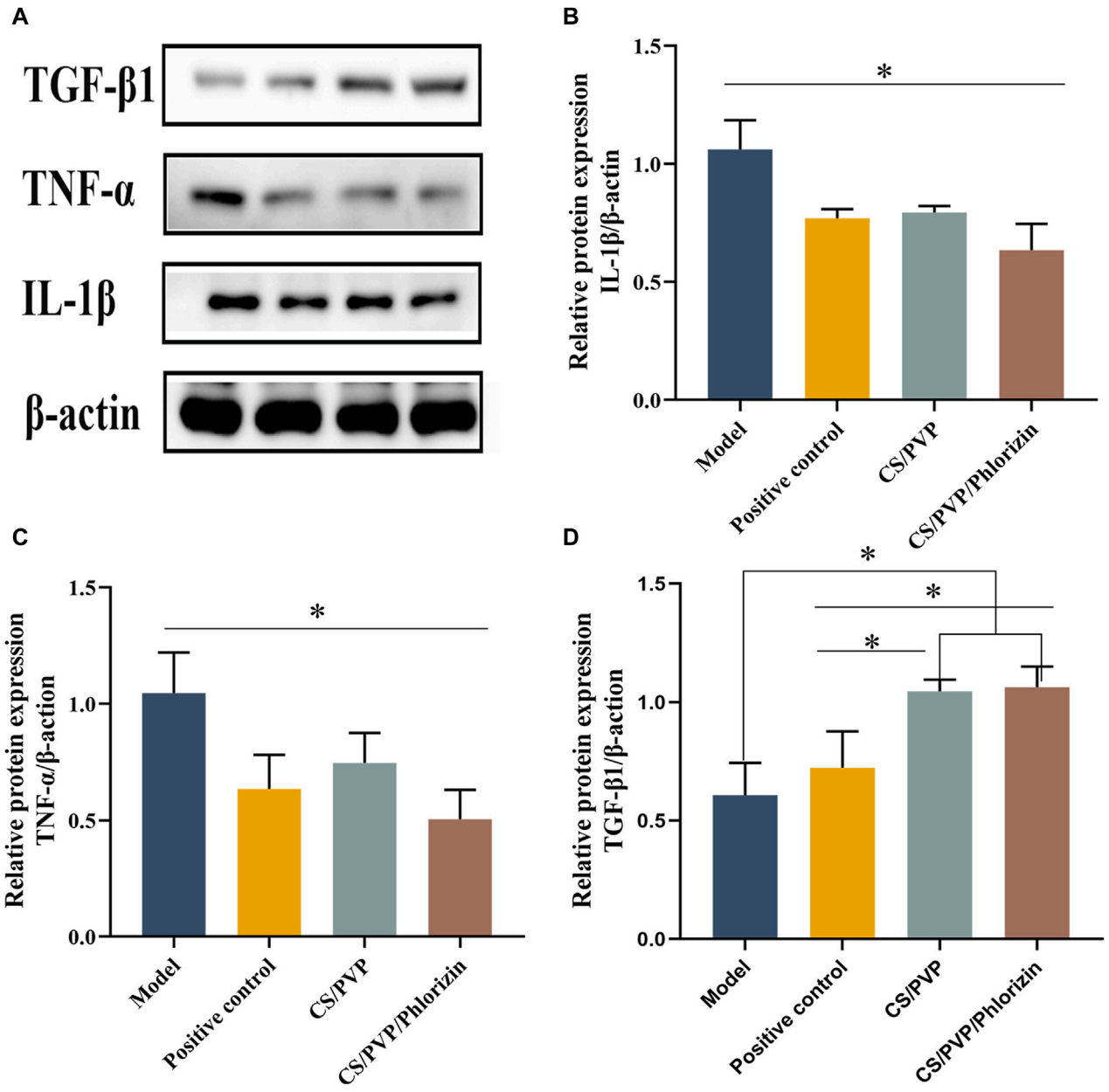

FIGURE 7
(A) Pictures of TGF-β1, TNF-α, and IL-1β protein bands; **(B)** Pictures of quantified gray values of IL-1β protein; **(C)** Pictures of quantified gray values of TNF-α protein; **(D)** Pictures of quantified gray values of TGF-β1 protein.

results suggest that CS/PVP/Phlorizin nanofibrous membranes promote angiogenesis at the wound site and thus promote wound repair.

3.12 Western blot analysis

Following the onset of a burn, a good deal of leachate is present at the site of the burn, which is highly susceptible to infiltration by inflammatory cells, thus causing the onset of an inflammatory response (Liu, 2020). TNF-α and IL-1β, as the most important inflammatory factors in early inflammation, have a great influence on wound healing. There are different effects of different concentrations of TNF-α. Low concentrations of TNF-α activate T and B cells to release antibodies while also promoting phagocytosis by macrophages. However, at high concentrations, it enhances the inflammatory response causing the body to release more inflammatory factors, while causing damage to endothelial cells, contributing to increased vascular permeability and increased wound osmotic fluid thereby impeding wound healing (Peng and Huang, 2004). The results of the expression of TNF-α and IL-1β proteins in each group are shown in Figure 7 BC. TNF-α and IL-1β inflammatory proteins were significantly reduced in the group treated with Phlorizin fiber membrane compared with the scalded model group. The CS/PVP/Phlorizin group exhibited lower expression of inflammatory factors compared to the

positive control group. In addition, we measured the expression of the growth factor TGF-β1 at the wound site in each group, and the results are shown in Figure 7D. CS/PVP and CS/PVP/Phlorizin significantly elevated the expression of TGF-β1 at the wound site compared with the model group.

4 Discussion

Scald wounds often cause large irregular skin defects and injuries, leading to disturbances in the patient's internal environment, imbalance of the immune system, and infections, resulting in slow healing of the scald wounds and even further deepening of the wounds (Sahu et al., 2016). It is crucial to reduce scald wound infections and expedite the healing process for these patients. Research has indicated that incorporating natural actives into wound dressings can enhance wound healing (Li et al., 2022). In this study, we investigated the healing effects of phlorizin loaded into CS/PVP nanofiber membranes on burn wound injuries.

Nanofibrous membranes offer significant advantages in tissue repair due to their unique microstructure, which not only provides a suitable microenvironment for the wound site but also seals the active substances in the membrane to control their release for local delivery (Sun et al., 2022). Hydrophilicity is a necessary condition for the preparation of ideal nanofiber membranes, and it has been reported that nanofiber membranes with good hydrophilicity can rapidly absorb exudate from wound sites to promote wound repair. In this study, loading phlorizin into CS/PVP nanofiber membranes led to a decrease in the water contact angle and an enhancement of the hydrophilicity of the nanofiber membranes, which could be attributed to the increase in the diameter of the sparse nanofibers in the structure of the fiber membranes after loading phlorizin, which is more conducive to the absorption and permeation of water (Ding et al., 2024). At the same time, the CS/PVP/Phlorizin nanofiber membrane showed excellent antioxidant as well as antimicrobial activity, which could effectively inhibit the infection of the wound site and promote the wound healing process (Kumar et al., 2010). In addition, the nanofiber membrane has good blood compatibility and no cytotoxicity to meet the requirements of an ideal wound dressing (Shefa et al., 2017).

The process of scald wound repair involves various factors such as angiogenesis, cell proliferation, migration, and collagen formation at the wound site, all playing crucial roles in the healing process (Pelizzo et al., 2018; Zhang et al., 2019). Collagen, as an extracellular fibrous protein, promotes the formation of intracellular matrix and the repair of damaged cellular structures (Zhan et al., 2019). In the present study Masson staining results showed that CS/PVP/Plorizin nanofibrous membrane significantly promoted the formation of collagen at the wound site, which may be one of the reasons for its accelerated healing of scald wounds.

Growth factors are integral to the wound healing process. CD31 and VEGF, as vascular growth factors, can be evaluated for angiogenesis at the wound site (Torres et al., 2017). It was observed by immunohistochemical staining that the nanofibrous membrane group loaded with root bark glycosides significantly promoted the expression of CD31 and VEGF. Meanwhile, western blot results revealed that the nanofiber membrane not only decreased the expression of inflammatory factors at the wound site but also enhanced the expression of growth factor TGF-β1 and facilitated the accumulation of extracellular matrix, ultimately expediting the healing process of scalded wounds (Zhang et al., 2016; Zubair and Ahmad, 2019).

5 Conclusion

This study successfully loaded the natural antioxidant, phlorizin, into CS/PVP nanofiber membranes, demonstrating remarkable antioxidant, antimicrobial, and biocompatible properties. *In vivo* wound repair experiments revealed that the CS/PVP/Phlorizin nanofiber membrane effectively suppressed inflammatory reactions at the wound site by reducing the expression of inflammatory factors TNF-α and IL-1β. Furthermore, it facilitated blood vessel and collagen formation at the wound site, expediting the healing process of scalded wounds. The porous 3-dimensional mesh structure and hydrophilicity of the nanofiber membrane not only enhance air permeability but also address the challenge of administering drugs to irregular burn wounds. Overall, this innovative nanofiber membrane offers insights for developing new dressing for scald wound treatment.

Data availability statement

The original contributions presented in the study are included in the article/Supplementary Material, further inquiries can be directed to the corresponding authors.

Ethics statement

The animal study was approved by The National Research Council Guide for the Care and Use of Laboratory Animals. The study was conducted in accordance with the local legislation and institutional requirements.

Author contributions

YY: Conceptualization, Methodology, Writing–original draft. SM: Investigation, Visualization, Writing–original draft, AL: Investigation, Software, Visualization, Writing–review and editing. GX: Investigation, Methodology, Software, Visualization, Writing–review and editing. ML: Formal Analysis, Software, Supervision, Writing–review and editing. CD: Investigation, Project administration, Writing–review and editing. XS: Investigation, Project administration, Resources, Writing–review and editing. LY: Formal Analysis, Investigation, Writing–review and editing. MY: Conceptualization, Writing–review and editing. TZ: Funding acquisition, Investigation, Writing–review and editing.

Funding

The author(s) declare that financial support was received for the research, authorship, and/or publication of this article. This work received funding from the Science and Technology Development Plan Project of Jilin Province (YDZJ202301ZYTS135); the Science and Technology Research Project of the Education Department of

Jilin Province (JJKH20240515KJ); the Postdoctoral Foundation of Jilin Agricultural Science and Technology University (Ji Nong Yuan He Zi [2022]744); National Innovative Entrepreneurship Training Program For Undergraduates (GJ202211439027) and the Science and Technology Innovation Development Plan Project of Jilin City (20240103003).

Conflict of interest

Authors AL, GX, CD, XS, LY, and MY were employed by Jilin Aodong Yanbian Pharmaceutical Co, Ltd.

The remaining authors declare that the research was conducted in the absence of any commercial or financial relationships that could be construed as a potential conflict of interest.

Publisher's note

Supplementary material

The Supplementary Material for this article can be found online at: https://www.frontiersin.org/articles/10.3389/fbioe.2024.1428988/full#supplementary-material

References

Archana, D., Dutta, J., and Dutta, P. K. (2013). Evaluation of chitosan nano dressing for wound healing: characterization, *in vitro* and *in vivo* studies. *Int. J. Biol. Macromol.* 57, 193–203. doi:10.1016/j.ijbiomac.2013.03.002

Asiri, A., Saidin, S., Sani, M. H., and Al-Ashwal, R. H. (2021). Epidermal and fibroblast growth factors incorporated polyvinyl alcohol electrospun nanofibers as biological dressing scaffold. *Sci. Rep.* 11 (1), 5634.

Boateng, J. S., Matthews, K. H., Stevens, H. N. E., and Eccleston, G. M. (2008). Wound healing dressings and drug delivery systems: a review. *J. Pharm. Sci.* 97 (8), 2892–2923. doi:10.1002/jps.21210

Contardi, M., Kossyvaki, D., Picone, P., Summa, M., Guo, X., Heredia-Guerrero, J. A., et al. (2021). Electrospun polyvinylpyrrolidone (PVP) hydrogels containing hydroxycinnamic acid derivatives as potential wound dressings. *Chem. Eng. J.* 409, 128144. doi:10.1016/j.cej.2020.128144

Ding, C., Yang, J., Wang, N., Ding, Q., Sun, S., Gao, Y., et al. (2024). Sodium alginate/polyvinyl alcohol nanofibers loaded with Shikonin for diabetic wound healing: *in vivo* and *in vitro* evaluation. *Int. J. Biol. Macromol.* 262, 129937. doi:10.1016/j.ijbiomac.2024.129937

Dong, R., and Guo, B. (2021). Smart wound dressings for wound healing. *Nano Today* 41, 101290. doi:10.1016/j.nantod.2021.101290

Dong, Z., Liu, Q., Han, X., Zhang, X., Wang, X., Hu, C., et al. (2023). Electrospun nanofibrous membranes of recombinant human collagen type III promote cutaneous wound healing. *J. Mat. Chem. B* 11 (27), 6346–6360. doi:10.1039/D3TB00438D

Guo, J., Wang, T., Yan, Z., Ji, D., Li, J., and Pan, H. (2022). Preparation and evaluation of dual drug-loaded nanofiber membranes based on coaxial electrostatic spinning technology. *Int. J. Pharm.* 629, 122410. doi:10.1016/j.ijpharm.2022.122410

Guo, X., Liu, Y., Bera, H., Zhang, H., Chen, Y., Cun, D., et al. (2020). α-Lactalbumin-Based nanofiber dressings improve burn wound healing and reduce scarring. *ACS Appl. Mat. Interfaces.* 12 (41), 45702–45713. doi:10.1021/acsami.0c05175

Hasani-Sadrabadi, M. M., Sarrion, P., Nakatsuka, N., Young, T. D., Taghdiri, N., Ansari, S., et al. (2019). Hierarchically patterned polydopamine-containing membranes for periodontal tissue engineering. *ACS Nano* 13 (4), 3830–3838. doi:10.1021/acsnano.8b09623

He, C., Mighri, F., Guiver, M. D., and Kaliaguine, S. (2016). Tuning surface hydrophilicity/hydrophobicity of hydrocarbon proton exchange membranes (PEMs). *J. Colloid Interface Sci.* 466, 168–177. doi:10.1016/j.jcis.2015.12.023

Jieqiong, L. (2020). *Study on the effect and mechanism of HSK on experimental burns*. Zhejiang University of Technology [D] 2016. doi:10.27463/d.cnki.gzgyu.2016.000069

Johnson, R. L. (2003). Robbins basic pathology. *Arch. Pathol. Lab. Med.* 127 (11), 1532. doi:10.5858/2003-127-1532-RBP

Khan, A. U. R., Huang, K., Jinzhong, Z., Zhu, T., Morsi, Y., Aldalbahi, A., et al. (2020). PLCL/Silk fibroin based antibacterial nano wound dressing encapsulating oregano essential oil: fabrication, characterization and biological evaluation. *Colloids Surfaces B Biointerfaces* 196, 111352. doi:10.1016/j.colsurfb.2020.111352

Kumar, P. S., Abhilash, S., Manzoor, K., Nair, S. V., Tamura, H., and Jayakumar, R. (2010). Preparation and characterization of novel β-chitin/nanosilver composite scaffolds for wound dressing applications. *Carbohydr. Polym.* 80 (3), 761–767. doi:10.1016/j.carbpol.2009.12.024

Lan, X., Liu, Y., Wang, Y., Tian, F., Miao, X., Wang, H., et al. (2021). Coaxial electrospun PVA/PCL nanofibers with dual release of tea polyphenols and ε-poly (L-lysine) as antioxidant and antibacterial wound dressing materials. *Int. J. Pharm.* 601, 120525. doi:10.1016/j.ijpharm.2021.120525

Lee, J., Lee, K., Lee, M., Kim, B., Chinannai, K. S., Hur, H., et al. (2017). Wound healing effects of *Prunus yedoensis* matsumura bark in scalded rats. *Evid.-based Complement. Altern. Med.* 2017, 1–7. doi:10.1155/2017/7812598

Li, A., Li, L., Li, X., Liang, W., Lang, M., Cheng, B., et al. (2022). Antibacterial, antioxidant and anti-inflammatory PLCL/gelatin nanofiber membranes to promote wound healing. *Int. J. Biol. Macromol.* 194, 914–923. doi:10.1016/j.ijbiomac.2021.11.146

Li, F., Ducker, M., Sun, B., Szele, F. G., and Czernuszka, J. T. (2020). Interpenetrating polymer networks of collagen, hyaluronic acid, and chondroitin sulfate as scaffolds for brain tissue engineering. *Acta Biomater.* 112, 122–135. doi:10.1016/j.actbio.2020.05.042

Li, J., Ding, Q., Zha, Y., Xie, J., Li, F., Li, R., et al. (2024). The silk fibroin nanofibrous membrane loaded with polyhexamethyl biguanide for promoting infected wound healing. *Eur. Polym. J.* 202, 112666. doi:10.1016/j.eurpolymj.2023.112666

Li, X., Chen, B., Xie, H., He, Y., Zhong, D., and Chen, D. (2018). Antioxidant structure–activity relationship analysis of five dihydrochalcones. *Molecules* 23, 1162. doi:10.3390/molecules23051162

Lian, J., Ju, G., Cai, X., Cai, Y., Li, C., Ma, S., et al. (2021). Nanofibrous membrane dressings loaded with sodium hydrogen sulfide/endothelial progenitor cells promote wound healing. *Front. Bioeng. Biotechnol.* 9, 657549.

Liao, N., Unnithan, A. R., Joshi, M. K., Tiwari, A. P., Hong, S. T., Park, C., et al. (2015). Electrospun bioactive poly (ε-caprolactone)–cellulose acetate–dextran antibacterial composite mats for wound dressing applications. *Colloids Surfaces A Physicochem. Eng. Aspects* 469, 194–201. doi:10.1016/j.colsurfa.2015.01.022

Liu, S., Chen, Z., Zhang, H., Li, Y., Maierhaba, T., An, J., et al. (2023). Comparison of eugenol and dihydromyricetin loaded nanofibers by electro-blowing spinning for active packaging. *Food Biosci.* 51, 102294. doi:10.1016/j.fbio.2022.102294

Liu, X., Wang, S., Ding, C., Zhao, Y., Zhang, S., Sun, S., et al. (2024). Polyvinylpyrrolidone/chitosan-loaded dihydromyricetin-based nanofiber membrane promotes diabetic wound healing by anti-inflammatory and regulating autophagy-associated protein expression. *Int. J. Biol. Macromol.* 259, 129160. doi:10.1016/j.ijbiomac.2023.129160

Liu, Y., Liu, Y., Guo, Y., Xu, L., and Wang, H. (2021). Phlorizin exerts potent effects against aging induced by d-galactose in mice and PC12 cells. *Food Funct.* 12 (5), 2148–2160. doi:10.1039/D0FO02707C

Ma, S., Ding, Q., Xia, G., Li, A., Li, J., Sun, P., et al. (2024). Multifunctional biomaterial hydrogel loaded with antler blood peptide effectively promotes wound repair. *Biomed. Pharmacother.* 170, 116076. doi:10.1016/j.biopha.2023.116076

Ouyang, Y., Su, X., Zheng, X., Zhang, L., Chen, Z., Yan, Q., et al. (2024). Mussel-inspired "all-in-one" sodium alginate/carboxymethyl chitosan hydrogel patch promotes healing of infected wound. *Int. J. Biol. Macromol.* 261, 129828. doi:10.1016/j.ijbiomac.2024.129828

Pelizzo, G., Avanzini, M. A., Mantelli, M., Croce, S., Maltese, A., Vestri, E., et al. (2018). Granulation tissue-derived mesenchymal stromal cells: a potential application for burn wound healing in pediatric patients. *J. Stem Cells Regen. Med.* 14 (1), 53–58. doi:10.46582/jsrm.1401007

Peng, D. Z., and Huang, W. (2004). Progress of macrophage signal transduction mechanism of uncontrolled inflammatory response after burn injury. *J. Third Mil. Med. Univ.* 23, 2168–2170. doi:10.16016/j.1000-5404.2004.23.034

Poonguzhali, R., Basha, S. K., and Kumari, V. S. (2017). Synthesis and characterization of chitosan-PVP-nanocellulose composites for *in-vitro* wound dressing application. *Int. J. Biol. Macromol.* 105, 111–120. doi:10.1016/j.ijbiomac.2017.07.006

Rinaudo, M. (2006). Chitin and chitosan: properties and applications. *Prog. Polym. Sci.* 31 (7), 603–632. doi:10.1016/j.progpolymsci.2006.06.001

Sahu, S. A., Agrawal, K., and Patel, P. K. (2016). Scald burn, a preventable injury: analysis of 4306 patients from a major tertiary care center. *Burns* 42 (8), 1844–1849. doi:10.1016/j.burns.2016.06.022

Shefa, A. A., Amirian, J., Kang, H. J., Bae, S. H., Jung, H., Choi, H., et al. (2017). *In vitro* and *in vivo* evaluation of effectiveness of a novel TEMPO-oxidized cellulose nanofiber-silk fibroin scaffold in wound healing. *Carbohydr. Polym.* 177, 284–296. doi:10.1016/j.carbpol.2017.08.130

Song, Z., Li, G., Guan, F., and Liu, W. (2018). Application of chitin/chitosan and their derivatives in the papermaking industry. *Polymers* 10, 389. doi:10.3390/polym10040389

Stompor, M., Broda, D., and Bajek-Bil, A. (2019). Dihydrochalcones: methods of acquisition and pharmacological properties—a first systematic review. *Molecules* 24, 4468. doi:10.3390/molecules24244468

Sun, S., Hao, M., Ding, C., Zhang, J., Ding, Q., Zhang, Y., et al. (2022). SF/PVP nanofiber wound dressings loaded with phlorizin: preparation, characterization, *in vivo* and *in vitro* evaluation. *Colloids Surfaces B Biointerfaces* 217, 112692. doi:10.1016/j.colsurfb.2022.112692

Tang, C., Zhao, B., Zhu, J., Lu, X., and Jiang, G. (2022). Preparation and characterization of chitosan/sodium cellulose sulfate/silver nanoparticles composite films for wound dressing. *Mat. Today Commun.* 33, 104192. doi:10.1016/j.mtcomm.2022.104192

Torres, P., Díaz, J., Arce, M., Silva, P., Mendoza, P., Lois, P., et al. (2017). The salivary peptide histatin-1 promotes endothelial cell adhesion, migration, and angiogenesis. *FASEB J.* 31 (11), 4946–4958. doi:10.1096/fj.201700085r

Un, H., Ugan, R. A., Gurbuz, M. A., Bayir, Y., Kahramanlar, A., Kaya, G., et al. (2021). Phloretin and phloridzin guard against cisplatin-induced nephrotoxicity in mice through inhibiting oxidative stress and inflammation. *Life Sci.* 266, 118869. doi:10.1016/j.lfs.2020.118869

Ursell, L. K., Clemente, J. C., Rideout, J. R., Gevers, D., Caporaso, J. G., and Knight, R. (2012). The interpersonal and intrapersonal diversity of human-associated microbiota in key body sites. *J. Allergy Clin. Immunol.* 129 (5), 1204–1208. doi:10.1016/j.jaci.2012.03.010

Wang, H., Sun, Z., Liu, D., Li, X., Rehman, R., Wang, H., et al. (2019). Apple phlorizin attenuates oxidative stress in *Drosophila melanogaster*. *J. Food Biochem.* 43 (3), e12744. doi:10.1111/jfbc.12744

Wang, Y., Beekman, J., Hew, J., Jackson, S., Issler-Fisher, A. C., Parungao, R., et al. (2018). Burn injury: challenges and advances in burn wound healing, infection, pain and scarring. *Adv. Drug Deliv. Rev.* 123, 3–17. doi:10.1016/j.addr.2017.09.018

Wei, W., Wang, M., Liu, Z., Zheng, W., Tremblay, P., and Zhang, T. (2024). An antibacterial nanoclay- and chitosan-based quad composite with controlled drug release for infected skin wound healing. *Carbohydr. Polym.* 324, 121507. doi:10.1016/j.carbpol.2023.121507

Xi, L., Wang, L., Zhang, M., He, C., Yang, X., Pang, Y., et al. (2023). TNF-R1 cellular nanovesicles loaded on the thermosensitive F-127 hydrogel enhance the repair of scalded skin. *ACS Biomater. Sci. Eng.* 9 (10), 5843–5854. doi:10.1021/acsbiomaterials.2c01257

Xia, J., Zhang, H., Yu, F., Pei, Y., and Luo, X. (2020). Superclear, porous cellulose membranes with chitosan-coated nanofibers for visualized cutaneous wound healing dressing. *ACS Appl. Mat. Interfaces.* 12 (21), 24370–24379. doi:10.1021/acsami.0c05604

Xu, X., Che, L., Xu, L., Huang, D., Wu, J., Du, Z., et al. (2020). Green preparation of anti-inflammation an injectable 3D porous hydrogel for speeding up deep second-degree scald wound healing. *RSC Adv.* 10 (59), 36101–36110. doi:10.1039/D0RA04990E

Yan, T., Kong, S., Ouyang, Q., Li, C., Hou, T., Chen, Y., et al. (2020). Chitosan-gentamicin conjugate hydrogel promoting skin scald repair. *Mar. Drugs* 18, 233. doi:10.3390/md18050233

Yin, J., Xu, L., and Ahmed, A. (2022). Batch preparation and characterization of electrospun porous polylactic acid-based nanofiber membranes for antibacterial wound dressing. *Adv. Fiber Mater* 4, 832–844. doi:10.1007/s42765-022-00141-y

Zhan, D., Shen, Y., Zhao, Y., and Meng, F. (2019). Efficacy and safety of basic fibroblast growth factor in the treatment of burns: protocol for a systematic review and meta-analysis of randomized controlled trials. *Med. Baltim.* 98 (14), e15102. doi:10.1097/md.0000000000015102

Zhang, F., Ren, Y., Liu, P., Ren, Y., and Wang, D. (2016). Expression of TGF-β1 and miRNA-145 in patients with diabetic foot ulcers. *Exp. Ther. Med.* 11 (5), 2011–2014. doi:10.3892/etm.2016.3123

Zhang, J., Chen, K., Ding, C., Sun, S., Zheng, Y., Ding, Q., et al. (2022). Fabrication of chitosan/PVP/dihydroquercetin nanocomposite film for *in vitro* and *in vivo* evaluation of wound healing. *Int. J. Biol. Macromol.* 206, 591–604. doi:10.1016/j.ijbiomac.2022.02.110

Zhang, X., Li, X., Zhou, X., Wang, Y., Lai, W., Liu, Y., et al. (2019). The wound healing effect of Callicarpa nudiflora in scalded rats. *Evid.-based Complement. Altern. Med.* 2019, 1–8. doi:10.1155/2019/1860680

Zhou, Z., Yan, D., Cheng, X., Kong, M., Liu, Y., Feng, C., et al. (2016). Biomaterials based on N,N,N-trimethyl chitosan fibers in wound dressing applications. *Int. J. Biol. Macromol.* 89, 471–476. doi:10.1016/j.ijbiomac.2016.02.036

Zonari, A., Martins, T. M. M., Paula, A. C. C., Boeloni, J. N., Novikoff, S., Marques, A. P., et al. (2015). Polyhydroxybutyrate-co-hydroxyvalerate structures loaded with adipose stem cells promote skin healing with reduced scarring. *Acta Biomater.* 17, 170–181. doi:10.1016/j.actbio.2015.01.043

Zubair, M., and Ahmad, J. (2019). Role of growth factors and cytokines in diabetic foot ulcer healing: a detailed review. *Rev. Endocr. Metabolic Disord.* 20, 207–217. doi:10.1007/s11154-019-09492-1

frontiers | Frontiers in Bioengineering and Biotechnology

TYPE Review
PUBLISHED 04 September 2024
DOI 10.3389/fbioe.2024.1448010

OPEN ACCESS

EDITED BY
Wei Nie,
Wake Forest Baptist Medical Center,
United States

REVIEWED BY
Wei Feng,
Shanghai University, China
Niyousha Davari,
University of Tehran, Iran
Tonghe Zhu,
Shanghai University of Engineering Sciences,
China

*CORRESPONDENCE
Daming Dong,
dongdaming0451@sohu.com
Chengqing Yi,
ycq3000@163.com
Dejian Li,
lidejian880820@163.com

†These authors have contributed equally to this work

RECEIVED 12 June 2024
ACCEPTED 27 August 2024
PUBLISHED 04 September 2024

CITATION
Zhao Z, Wang C, Liu A, Bai N, Jiang B, Mao Y, Ying T, Dong D, Yi C and Li D (2024) Multiple applications of metal-organic frameworks (MOFs) in the treatment of orthopedic diseases. *Front. Bioeng. Biotechnol.* 12:1448010. doi: 10.3389/fbioe.2024.1448010

Multiple applications of metal-organic frameworks (MOFs) in the treatment of orthopedic diseases

Ziwen Zhao[1,2†], Chenxu Wang[3†], Aiguo Liu[3†], Ning Bai[4], Bo Jiang[5], Yuanfu Mao[1], Ting Ying[6], Daming Dong[1*], Chengqing Yi[2*] and Dejian Li[2*]

[1]Department of Orthopedics, The First Affiliated Hospital of Harbin Medical University, Harbin, China, [2]Department of Orthopedics, Shanghai Pudong Hospital, Fudan University Pudong Medical Center, Shanghai, China, [3]Department of Orthopedics, The First Affiliated Hospital of Henan University, Kaifeng, China, [4]Department of Gastroenterology, Huaihe Hospital of Henan University, Kaifeng, China, [5]The First Affiliated Hospital of Ningbo University, Ningbo, China, [6]Shanghai YangZhi Rehabilitation Hospital (Shanghai Sunshine Rehabilitation Center), School of Medicine, Tongji University, Shanghai, China

Pharmacologic treatment of orthopedic diseases is a common challenge for clinical orthopedic surgeons, and as an important step in the stepwise treatment of orthopedic diseases, it is often difficult to achieve satisfactory results with existing pharmacologic treatments. Therefore, it is increasingly important to find new ways to effectively improve the treatment pattern of orthopedic diseases as well as to enhance the therapeutic efficacy. It has been found that metal-organic frameworks (MOFs) possess the advantages of high specific surface area, high porosity, chemical stability, tunability of structure and biocompatibility. Therefore, MOFs are expected to improve the conventional traditional treatment modality for bone diseases. This manuscript reviewed the applications of MOFs in the treatment of common clinical bone diseases and look forward to its future development.

KEYWORDS

metal-organic frameworks, MOFs, tumor, osteoporosis, osteoarthritis

1 Introduction

As the foundation of the human body structure, bones have important functions such as supporting the body, protecting organs, supporting movement and blood production. Orthopedic diseases usually accompany people throughout their lives, can occur at different ages. With the aging of the global population and the increase in the popularity of sports, there has been a significant increase in the proportion of orthopedic disorders in the clinical setting. These diseases are often caused by trauma, infection, inflammation, degenerative changes, and oxidative stress, resulting in bone-related diseases such as bone fractures, osteoarthritis, bone tumors, and osteoporosis, which pose a serious threat to human health. However, in the face of the increasing number and complexity of orthopedic diseases, conventional drug therapy has considerable limitations in clinical application, such as the lack of controlled-release properties of drugs, weak targeting ability, and easy degradation of many drugs during the delivery process, resulting in unsatisfactory therapeutic effects, so the conventional drugs in the treatment of orthopedic diseases have entered a bottleneck. Therefore, there is an urgent need to find more efficient and safer drug treatments.

With the development and advancement of nanomedicine, the mechanical, biological and electrochemical properties of nanomaterials have brought many nanomaterials into the field of researchers' vision and achieved good results. Nanomaterials are characterized by ultra-thin thickness and layers of precise chemical functional groups and the thickness of 2D nanomaterials is even as small as 0.34 nm, which is equivalent to the distance between adjacent bases of DNA (Li et al., 2001). Common clinical nanomaterials such as polycaprolactone (PCL), polylactic-co-glycolic acid (PLGA), nanohydroxyapatite (nHA), zirconium oxide nanoparticles (nZr), silicon dioxide nanoparticles (nSi), silver nanoparticles (AgNPs), graphene oxide (GO), MOFs, etc (Bharadwaz and Jayasuriya, 2020). Nanomaterials can be categorized by shape and size. For example, inorganic nanoparticles, organic polymer based nanoparticles and extracellular vesicles belong to zero-dimensional nanomaterials, which can be used for drug delivery (Wang et al., 2021), imaging (Kim et al., 2018) and therapy (Kim et al., 2020; Kwon et al., 2016; Bjorge et al., 2017). GO has been sought after by many researchers in recent years, it always been used as a molecular carrier and an enhancer of cell attachment (Liu et al., 2013; Lee et al., 2011). Its decorated polymer scaffolds can be used for tissue regeneration (Yadid et al., 2019). Among numerous nanomaterials, MOFs stands out in recent years and attracts the attention of doctors and researchers.

In 1995, Yaghi et al. (1995) reported in the journal Nature a coordination compound with a two-dimensional structure synthesized from a rigid organic ligand trimesic acid and transition metal Co., referred to it as MOF. In 2004, Ferey et al. (2004); Ferey et al. (2005) reported two sieve type MOFs with ultra large pore characteristics, MIL-100 and MIL-101. They all have two types of mesoporous cages, with sizes of 25 Å, 29 Å and 29 Å, 34 Å. The specific surface area is as high as 3100 m^2/g and 5900 m^2/g. It can be said that the emergence of these two materials is a milestone in the development history of MOFs. In 2006, Yaghi et al. (Park et al., 2006) synthesized 12 imidazole framework materials with 7 typical topological structures of silica aluminum molecular sieves ZIF-1 to ZIF-12. These materials exhibited superior thermal and chemical stability, among which ZIF-8 and ZIF-11 not only stabilized up to 550°C, but also remained stable in boiling alkaline aqueous solutions and organic solvents. Up to now, MOFs stands out from many other nanomaterials due to its special physicochemical properties and has emerged as one of the most promising nanomaterials for biomedicine. The most common MOFs consist of an infinite lattice formed by metal ions or clusters connected to an organic ligand by strong coordination bonds, and usually exhibit a two or three-dimensional structure (Cao et al., 2021). Due to their unique structures, MOFs have excellent properties for biomedical applications, such as high specific surface area metal (specific surface area in the range of 1,000–10,000 m^2/g), high porosity, chemical stability, structural tunability, and biocompatibility (Furukawa et al., 2013). MOFs release biologically active metal ions and provide inducers to promote osteogenesis and angiogenesis, deliver immune regulatory signal, and eliminate Reactive oxygen species (ROS) to alleviate inflammation. It can also act as drug carriers, photosensitizers and nano enzymes for antimicrobial and antitumor effects, etc. In this paper, we will review MOFs and by discussing the application of various MOFs composites in common orthopedic diseases, aim to guide and inspire for the treatment of bone diseases as well as the creation of efficient nano materials (Figure 1).

Therefore, this article reviews the recent research of MOFs in bone tumors, osteoporosis and osteoarthritis. In addition to summarizing the previous studies of MOFs in orthopedic diseases, the application potential of MOFs in orthopedic diseases was also discussed.

1.1 MOFs in bone tumors

Bone tumors are rare and heterogeneous group of tumors that occur in the skeleton, including many types of malignant and benign tumors, they are one of the major diseases affecting bone health. Among them, osteosarcoma is the most common primary bone tumor and the third most common cancer in the world, it tends to occur more frequently in children and adolescents with rapid bone growth and development. Currently, the treatment of osteosarcoma remains a combination of preoperative neoadjuvant chemotherapy, extensive surgical resection, and postoperative adjuvant chemotherapy. However, even with this treatment modality, tumors recur in 30%–40% of patients and the prognosis for recurrence is poor, with only 23%–29% of patients surviving more than 5 years after second diagnosis (Luetke et al., 2014). Although anticancer drugs can inhibit tumor growth and metastasis throughout the treatment process, chemotherapeutic drugs have the disadvantages of low efficacy, high side effects, and the need for high-dose shock, which leads to huge limitations in the treatment of bone tumor drugs. Therefore, the development of biomaterials with precise and improved anti-tumor capabilities is crucial for bone tumor treatment. MOFs can play a great role by acting as carriers, anti-tumor agents, and drug synergistic systems.

1.1.1 MOFs-mediated chemotherapeutic drug delivery

A novel adriamycin drug delivery system (folic acid/metal organic framework/adriamycin) was developed by taking advantage of the high expression of folate receptors on the surface of tumor cells, this system integrate folic acid and MOFs, which significantly improved the specificity and efficiency of adriamycin delivery (Xu et al., 2020). Ma et al. (2021) utilized the MOFs loading of apelalis to form Apelalis@Au@MOFs, and the mesoporous silica structure was used for the successful loading of the photosensitizer indocyanine green and chemotherapeutic drug cisplatin to form apelalis&cisplatin@Au@ metal-organic framework@mesoporous silica-indocyanine green double-shell nanoparticles (Figure 2). The nanoparticles were able to cluster at the spinal tumor under the effect of targeted peptide and high permeability and long retention effect, which resulted in the precise release of Aperis and cisplatin, achieving effective killing of tumor cells and reducing bone destruction caused by tumor metastasis. Wuttke et al. (Luzuriaga et al., 2019) assemble His-tag-functionalized biomolecules with abundant binding sites on the MOFs, the MOFs-based "self-assembled multifunctional ligand particles" that successfully delivered pro-apoptotic peptides and proteins into cancer cells for therapeutic effects. When MOFs are

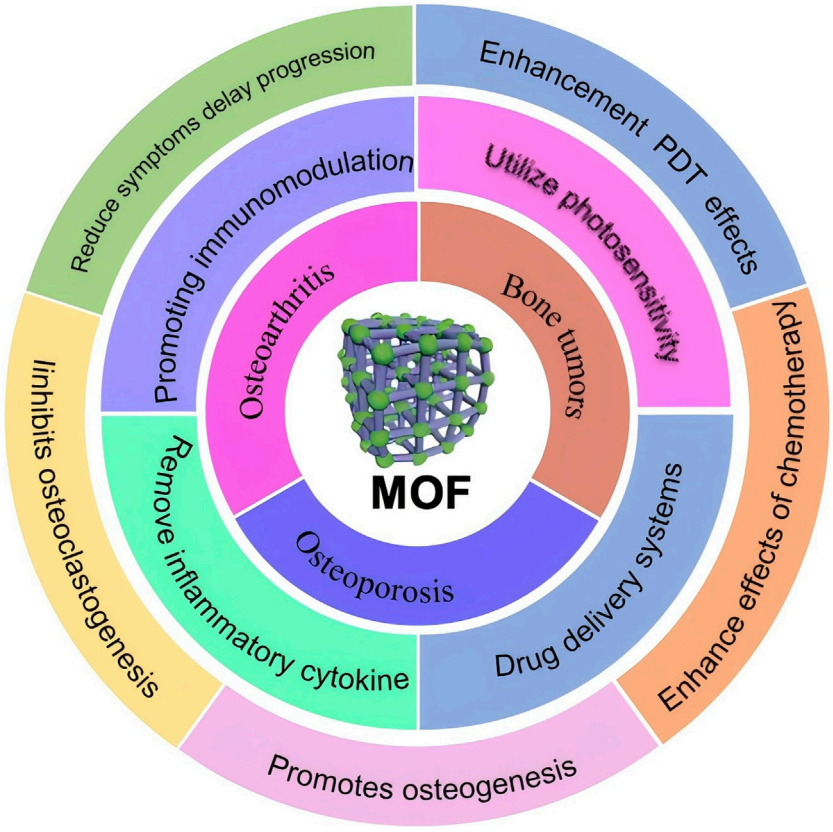

FIGURE 1
Schematic illustration of application of MOF in different orthopaedic diseases in this review.

used to load drugs, the content and specific gravity between different substances can be easily adjusted to optimize synergistic effects and substantially improve therapeutic efficacy. For example, Engelke and Wuttke report differentiated experimental results with different ratios of irinotecan/fluorouracil loaded with liposome-encapsulated MIL-88A (LipMIL-88A) (Zhang et al., 2018). From the above article, it can be found that MOFs have shown great potential in the field of drug delivery. By integrating with different targeting molecules, drugs, and functional components, precise targeting of tumor cells can be achieved, improving therapeutic efficacy and reducing side effects.

1.1.2 MOFs as antitumor agents

MOFs can also be prepared from many functional linkers with antitumor effects and metal ions, and these pairings represent the generation of novel antitumor agents called bioMOFs. Binding between phosphate aptamers and Zr-based nanoscale metal-organic backbones (Zr-NMOFs) and the embedding of the photosensitizer TMPyP4 in the structure of G-quadruplex DNA, the preparation of TMPyP4-G4-Aptamer-NMOFs. This nano system induced 90% target cell death and maintained more than 76% inhibition throughout the entire experimental period of this nano system in the treated group (Wang et al., 2019; Meng et al., 2018). Therefore, by designing functional linkers and MOFs reasonably, the treatment system can have better targeting, reduce damage to normal cells, and improve treatment efficacy.

1.1.3 MOFs in tumor photothermal therapy

MOFs with active lymph nodes can be used for chemo dynamic therapy (CDT), radiotherapy (RT), and catalytic modulation of the tumor microenvironment. In addition, MOFs using photosensitizers, chemotherapeutic agents and peptides as active linkers can be used in photo dynamic therapy (PDT), photothermal therapy (PTT) and chemotherapy (Lu et al., 2018). Therefore, it is important to discover MOFs with intrinsic anti-tumor activity and smart connectivity synergistic system to build anti-tumor platforms (Figure 3) (Gong et al., 2020; Morris et al., 2017). PDT has attracted much attention in recent years as an up-and-coming tool for tumor therapy. Using laser and photosensitizers, MOFs attached with active antitumor agents can produce ROS, which can inhibit the development of cancer cells. Organic photosensitizers are mainly involved in type II PDT, it is a process of converting oxygen into toxic singlet oxygen. The photosensitized portion of MOFs is highly ordered and separated, the molecules are prone to diffusion within the porous structure of MOFs, so MOFs-based photosensitizers can generate a large amount of ROS, which can dramatically increase the therapeutic efficacy of PDT (He et al., 2019). Li, et al. (Liu et al., 2020) have constructed a triphenylphosphine (TPP) functionalized up conversion nanoparticle/pyrrole MOF Janus structure (UCMTs) for near-infrared mediated mitochondria-targeted PDT. Under 808 nm near-infrared irradiation, the mitochondria ROS eruption induced by UCMTs can further trigger the intrinsic apoptotic pathway, enhancing the effect of tumor elimination. This nano

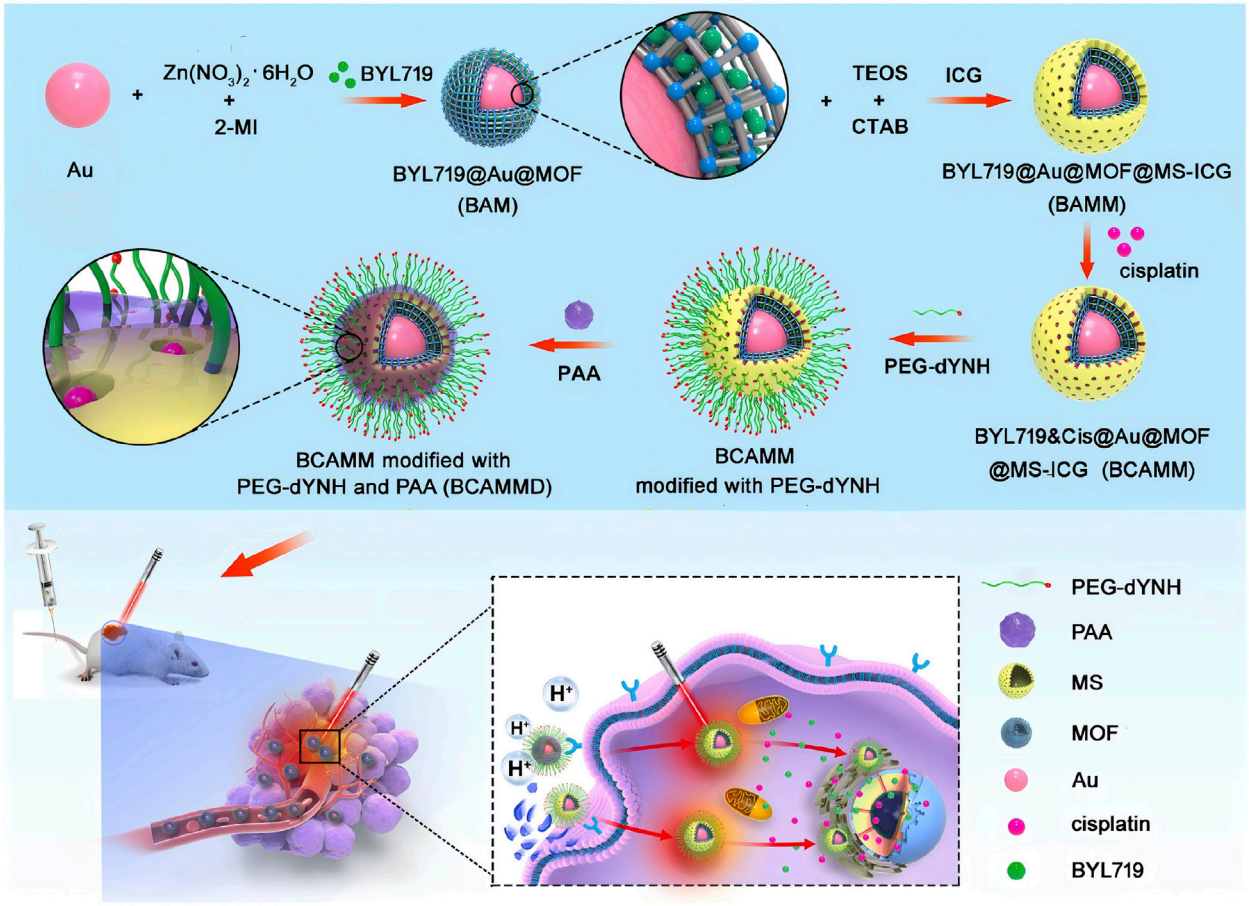

FIGURE 2
Synthesis process scheme of BYL719 cisplatin bilayer nanoparticles (BYL719&Cisplatin@Au@MOF@MS-ICG, BCAMM) modified dYNH targeting peptide and its antitumor mechanism in tumor cells (Ma et al., 2021). Reproduced under the terms of the Copyright Clearance Center (CCC) license. Copyright © 2021 Elsevier.

system enhances the penetration depth of MOFs and the therapeutic effect of photodynamic therapy. Loading the metal organic framework composed of cobalt porphyrin into calcium phosphate bone cement can give it certain photothermal conversion performance, which can target and kill residual tumor cells after osteosarcoma surgery, avoiding tumor recurrence (Deng et al., 2023). DENG et al. (Qu et al., 2021a) developed a core-shell MAZG nanocomposite (mesoporous dopamine/azodiimidazoliumpropane hydrochloride@ZIF-8/Gambogic acid), which was loaded with mesoporous dopamine of azodiimidazoliumpropane hydrochloride in the core. Mesoporous dopamine, and the outer shell consists of ZIF-8 loaded with Gambogic acid, which is encapsulated into the ZIF-8 as an inhibitor specifically targeting heat shock protein 90. The combination of arabinosylcytosine (Ara) and IR820 forms AraIR820, in which the sulfonic acid group of IR820 has a strong interaction with ZIF-8, significantly improving the drug loading efficiency of Ara. After further modification with hyaluronic acid (HA), the final HA/Ara-IR820@ZIF-8 is used for tumor-targeted chemo-photothermal combination therapy, resulting in a tumor inhibition rate of 89%. Therefore, MOFs, as a multifunctional therapeutic platform, combined with various treatment methods such as PTT, CDT and PDT, demonstrate multifaceted intervention capabilities for tumors. This comprehensive treatment strategy can improve treatment effectiveness, reduce side effects, and is expected to become an important direction for future cancer treatment.

1.1.4 MOFs induce ROS production

PDTDEN et al. (Yuan and Zhang, 2017) design porphyrin-zinc-based MOF (ferrocenylbenzoic acid-ZnTCPP) was constructed using the acoustic sensitizer TCPP, which is capable of releasing ROS upon ultrasonic stimulation, and at the same time ferrocenylbenzoic acid can catalytically convert hydrogen peroxide into oxygen, thus avoiding the problem of oxygen deprivation in the tumor microenvironment that may weaken the effect of acoustic power therapy. Li et al. (2024) modified ZIF-90 with zoledronic acid to enable bone targeting. Then the photosensitizer dihydroporphyrin Ce6 was loaded on it to construct Ce6@ZIF-PEG-ZOL (Ce6@ZPZ), which releases ROS under the irradiation of near-infrared light to kill tumor cells through photodynamics, meanwhile synergistically inhibits tumor growth through the Wahlberg effect with the glycolytic agent 2-deoxy-D-glucose to strengthen the effect of photodynamic therapy. Chemodynamic therapy is an emerging method of tumor treatment,

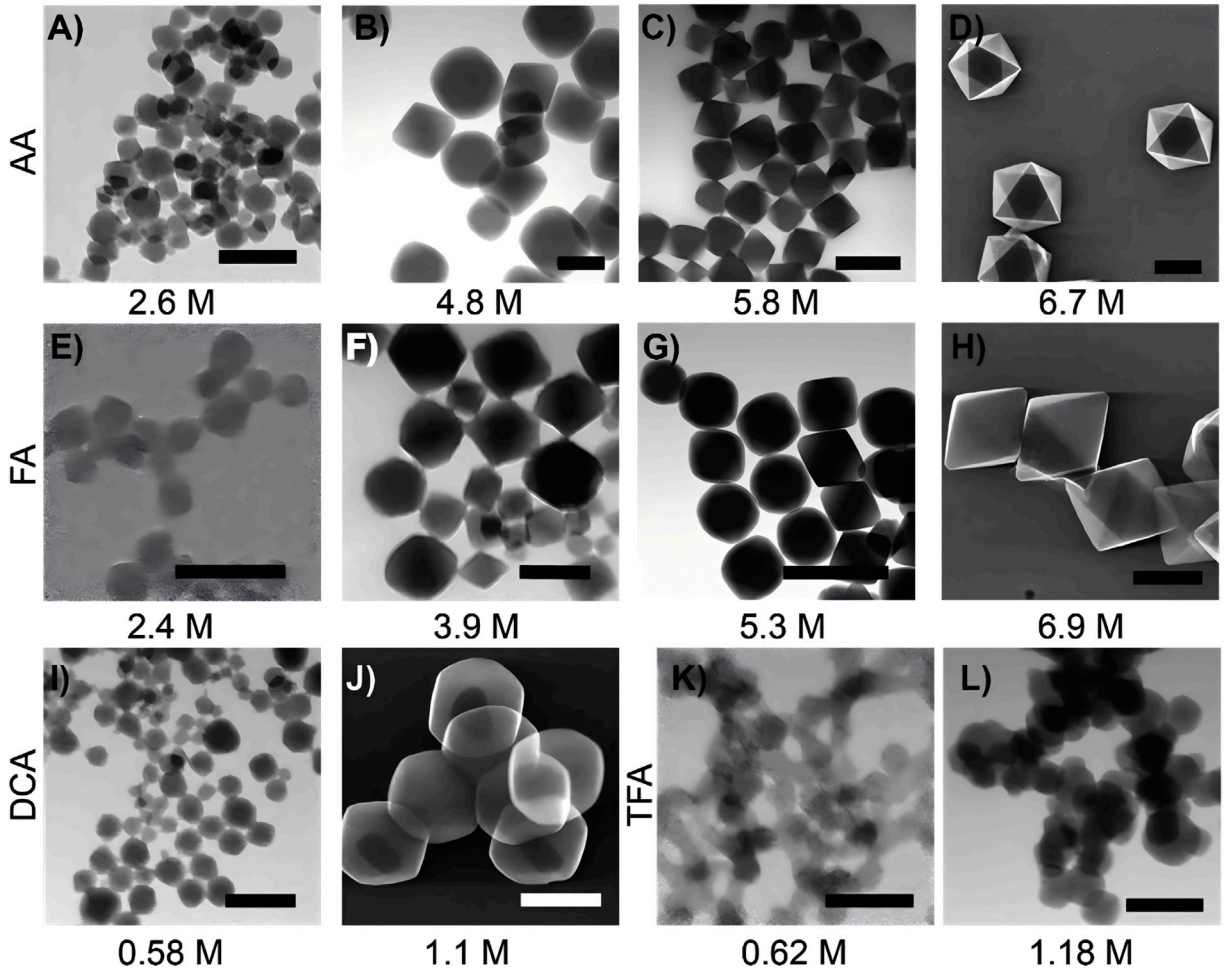

FIGURE 3
Scanning transmission electron microscopy (STEM) images of UiO-66 synthesized using different acid modulators and concentrations are presented as follows. When synthesized with acetic acid, UiO-66 appears as follows: **(A)** at a concentration of 2.6 M, **(B)** at 4.8 M, **(C)** at 5.8 M, and **(D)** at 6.7 M. When synthesized with formic acid, UiO-66 is as follows **(E)** at 2.4 M, **(F)** at 3.9 M, **(G)** at 5.3 M, and **(H)** at 6.9 M. For UiO-66 synthesized with dichloroacetic acid: **(I)** at 0.58 M and **(J)** at 1.1 M. When synthesized with trifluoroacetic acid, UiO-66 is shown as: **(K)** at 0.62 M and **(L)** at 1.18 M. The scale bars are as follows: A = 100 nm, B = 200 nm, C = 500 nm, D = 500 nm, E = 100 nm, F = 100 nm, G = 1,000 nm, H = 1,000 nm, I = 100 nm, J = 500 nm, K = 100 nm, and L = 500 nm (Morris et al., 2017). Reproduced under the terms of the Copyright Clearance Center (CCC) license. Copyright © 2017, American Chemical Society.

and its working principle is mainly based on the Fenton reaction or Fenton-like reaction, in which transition metal ions (Fe^{2+}) convert hydrogen peroxide in the body into ROS to kill cancer cells or inhibit tumor growth. Based on this principle, Wang et al. (2023) constructed a polydopamine-coated iron-based MOF and modified it by a polydopamine coating, combined folic acid bovine serum albumin to achieve the targeting of the tumor site and at the same time function as a contrast agent for magnetic resonance imaging. By loading D-arginine, which can be converted into nitric oxide, glucose oxidase, and block the energy supply of tumor cells, as well as the chemotherapeutic drug tirazamine, a synergistic effect of multiple therapeutic means was achieved (Figure 4). Overall, the understanding and utilization of ROS play a crucial role in tumor therapy. By designing different MOFs systems to regulate changes in ROS, precise killing of tumor cells can be achieved, providing new possibilities for personalized therapy and the implementation of multiple treatment strategies. Future research should further explore the mechanism of ROS in tumor treatment and optimize the design of MOFs to achieve more effective therapeutic effects.

1.1.5 MOFs enhance radiotherapy effects

Radiotherapy is a common method of treating tumors by using ionizing radiation to induce DNA damage, which not only directly damages cancer cells, but also induces the production of reactive oxygen species and the release of tumor-associated antigens to stimulate an immune response, and then induces immunogenic cell death. Osteosarcoma is not sensitive to radiotherapy, and high doses of radiation (up to 80Gy) are often required, which may cause serious adverse effects. MOFs have ultra-small 3D array structure of metal-organic nano framework with loose pores, which is conducive to the scattering of secondary photons and electrons, they can greatly enhance the sensitization effect of high-energy rays. Secondly, the ordered structure of MOFs show large mass

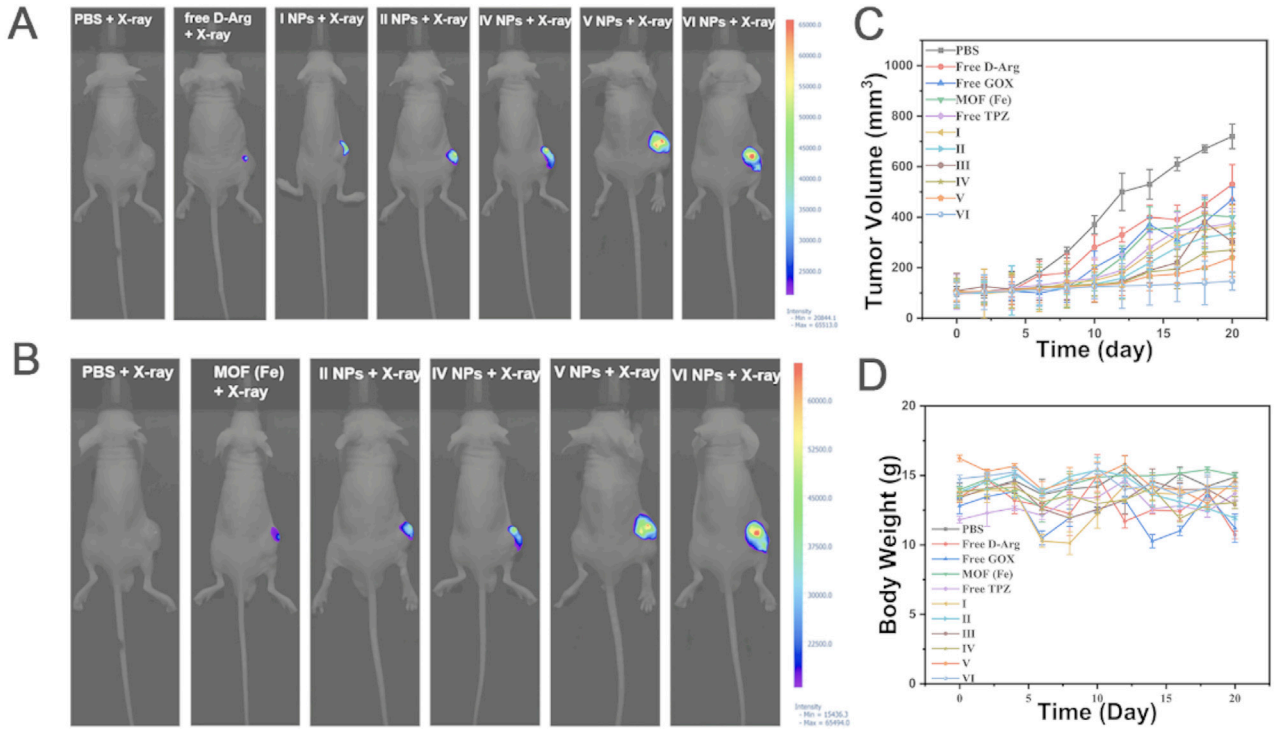

FIGURE 4
The *in vivo* anti-tumor experiment results for 143b tumor-bearing mice are as follows. **(A)** Fluorescence imaging of NO after X-ray irradiation. **(B)** Fluorescence imaging of ROS after X-ray irradiation. **(C)** The average body weight of mice in the 3 weeks following NP treatments and X-ray irradiation is presented (mean ± SD, n = 5). **(D)** Changes in tumor volume in the 3 weeks following NP treatment and X-ray irradiation are shown (mean ± SD, n = 5). MOF (Fe) loaded with D-Arg (I), MOF (Fe) loaded with D-Arg, GOX (II), MOF (Fe) loaded with D-Arg, GOX and TPZ (III), MOF (Fe) loaded with D-Arg, GOX and TPZ, and cloaked with PDA (IV), MOF (Fe) loaded with D-Arg, GOX and TPZ, cloaked with PDA, and grafted with Fe3+(V),MOF (Fe) loaded with D-Arg, GOX and TPZ,cloaked with PDA, and grafted with Fe3+and FA-BSA (VI) (Wang et al., 2023). Reproduced under the terms of the Copyright Clearance Center (CCC) license. Copyright © 2023 Elsevier.

attenuation coefficient and a strong dose-enhancing effect, while the pore structure of the nanometallic organic framework can be used to encapsulate drugs or contrast agents for multimodal imaging-guided synergistic oncology therapy. Du et al. (2021) loaded D-arginine into MIL-100(Fe) nanocarriers, under low-dose X-ray irradiation, nitric oxide released from arginine can downregulate hypoxia-inducible factor 1α to alleviate tumor hypoxia, Fe^{3+} catalyzes the reaction of reactive oxygen species produced by hydrogen peroxide with nitric oxide to generate peroxynitrite anion and other reactive nitrogen species. Therefore, hydroxyapatite@metal-organic framework/D-arginine can effectively inhibit tumor growth and prevent recurrence and lung metastasis of osteosarcoma. Li et al. (2023) developed a TZM radiation sensitizer using tantalum (Ta) and zirconium (Zr) as metal nodes and TCPP as photosensitive ligands. Ta-Zr co doping helps to transfer energy to TCPP, thereby generating singlet oxygen and achieving radiodynamic therapy. TZM induces immunogenic cell death and promotes dendritic cell maturation, also upregulates the expression of programmed cell death protein 1 through the cGAS-STING pathway, thereby triggering a powerful anti-tumor immune response. The impact of radiotherapy on patients has always been a difficult problem for doctors to solve. The advantages of MOF systems, such as enhancing radiation therapy efficacy and inducing immune responses, make radiation therapy safer and more efficient during the treatment process, and provide new ideas and possibilities for radiation therapy.

1.2 MOFs in osteoporosis

Osteoporosis is a serious disease characterized by a persistent decrease in bone mass and destruction of bone structure, leading to fragile bones and an increased risk of fractures. Osteoporosis affects 200 million people worldwide, with a higher prevalence in the elderly and postmenopausal women (Strom et al., 2011). The burden on the population of complications associated with osteoporosis such as fractures, bone defects, and lack of bone growth after defects is enormous, including significant morbidity, reduced quality of life, increased mortality, and substantial healthcare expenditures (Brown et al., 2021; Marrinan et al., 2015; Bliuc et al., 2009). The adult skeleton undergoes bone remodeling to maintain mineral homeostasis and bone quality (Armas and Recker, 2012; Farlay et al., 2019). Bone remodeling consists of resorption by multi-nucleated, myeloid-derived osteoclasts (OCs) followed by formation by mesenchymal-derived osteoblasts (OBs). This coordination of bone remodeling activities is commonly referred to as the coupling of bone resorption to bone formation. With aging and other conditions, such as gonadal

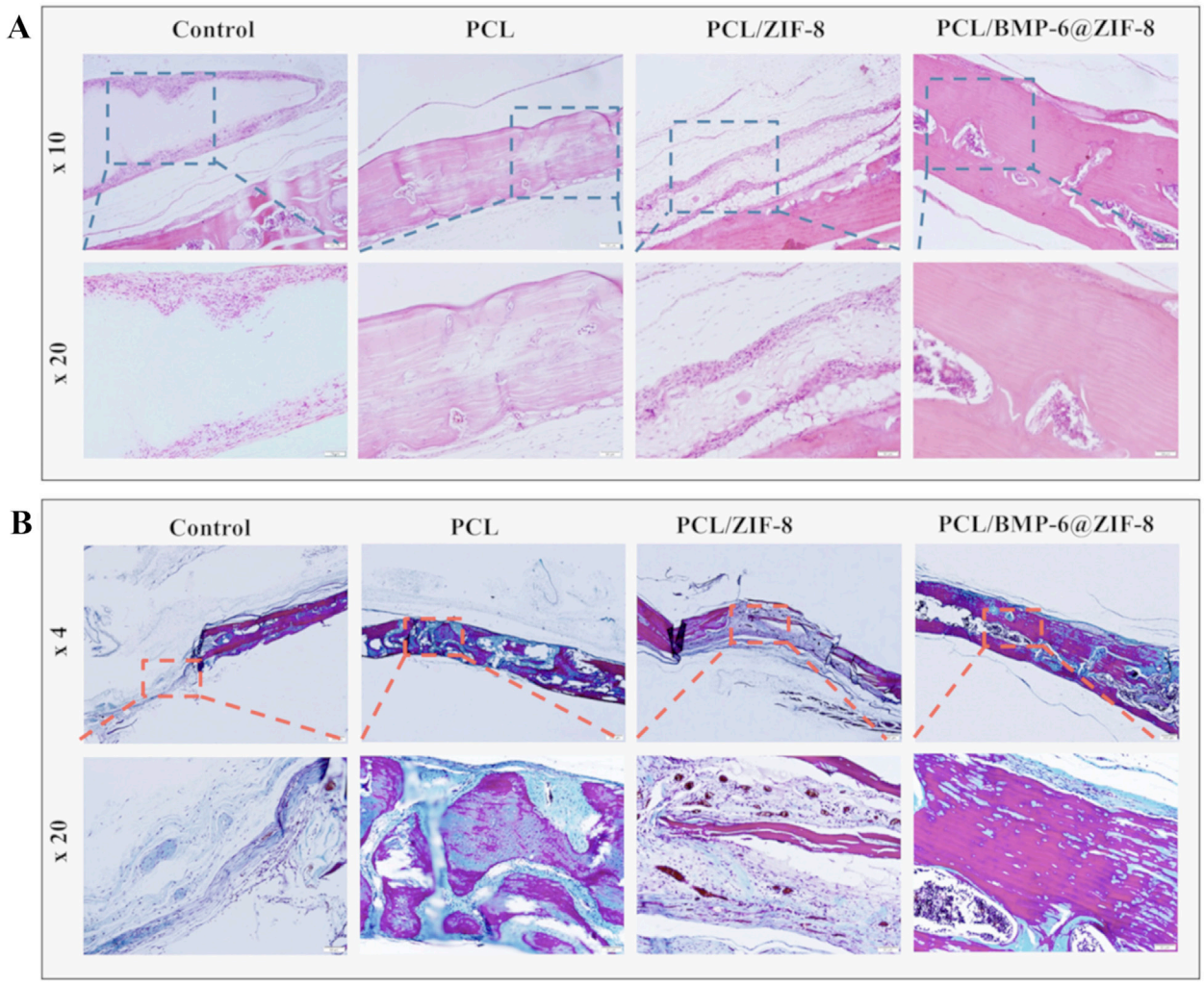

FIGURE 5
After 8 weeks of implantation, H&E staining **(A)** and Masson's trichrome staining **(B)** were carried out on the repaired bone defects (Toprak et al., 2021). Reproduced under the terms of the Copyright Clearance Center (CCC) license. Copyright © 2021 Elsevier.

hormone loss, the rate of resorption exceeds formation resulting in reduced bone mass (Sims and Martin, 2020). In other pathological conditions, resorption occurs independently from subsequent bone formation leading to destructive bone loss (Feng and Mcdonald, 2011). This can result in a reduction in bone mass, deterioration of the microstructure, and an elevated risk of fragility MOFs are able to stimulate the activity of bone mesenchymal stem cells and promote the process of new bone formation and mineralization. Studies have shown that MOFs play a key role in promoting osteoblast growth, inhibiting osteoclasts, and facilitating angiogenesis and bone mineralization, providing novel strategies and ideas for the effective treatment of osteoporosis (Matlinska et al., 2019; Zheng et al., 2020; Dang et al., 2020; Qu et al., 2021b; Dong et al., 2023; Pan et al., 2023; Lin et al., 2024) (Figure 5) (Toprak et al., 2021).

1.2.1 MOFs promote osteogenic gene expression

Proliferation and differentiation of osteoblasts play a key determinant role in the bone repair process. During the early stages of osteogenesis, MOFs promote the osteogenic process by regulating the transcriptional activity of Runx2, a gene central to the osteoblast phenotype (Wang et al., 2024). It was demonstrated that Sr^{2+} loaded on copper 1,3,5- phenylenetricarboxylic acid significantly increased the transcriptional activity and phosphorylation of Runx2, and that a variety of MOFs were effective in promoting the expression of the Runx2 gene (Farasati et al., 2023). Ma et al. (2024) designed alendronate (ALN)-mediated defective MOF sonosensitizer, which can effectively clear Methicillin-resistant *Staphylococcus aureus* (MRSA) infections and promote osteogenic differentiation under differential ultrasonic irradiation. In the presence of zirconium–phosphate coordination, the ALN-mediated porphyrin-based MOF (HN25) with a proper defect has great sonodynamic antibacterial efficiency (98.97%, 15 min) and bone targeting ability. Ren et al. (2022) encapsulation of the SCM in ZIF-8 nanoparticles, which enhances osteogenic fractionation of MSCs and accelerates bone regeneration *in vivo*. The targeting of MOFs nanoparticles represented by SCM/ZIF-8 was demonstrated and their regulatory role on MSCs was confirmed. Many genes associated

with osteogenic *in vivo* differentiation were observed to be upregulated in MSC cultures treated with SCM/ZIF-8, with involvement in the cAMP signal pathway. The efficacy of SCM/ZIF-8 nanoparticles in enhancing bone regeneration was demonstrated in a bone defect model through a series of rigorous experimental procedures. Some researchers found that by utilizing type I collagen, which has its own mechanical support ability and promoting cell attachment, a multifunctional and biodegradable scaffold system was constructed by combining collagen scaffolds with interleukin 4-metal-organic framework @CaP, which provided multiple osteogenic nucleation sites for the bone regeneration multicellular unit and realized functional bone regeneration *in vivo* (Zheng et al., 2020). In the later stages of osteogenesis, bone bridging eggs function by interfering with cell adhesion and migration, while osteocalcin can bind to Ca^{2+}, regulate calcium ion homeostasis, and participate in the bone mineralization process. On the other hand, MOFs increase the expression levels of these proteins through transcription and translation processes, thus promoting osteogenesis (Wang et al., 2023). Chen et al. (2024) successfully prepared bimetallic Mg/Cu-MOF coatings on pure Zn, with the intention of promoting osteogenesis, angiogenesis and antimicrobial activity of Zn substrates. The findings demonstrated that the degradation rate and water stability of the Mg/Cu-MOF coatings could be controlled by adjusting the proportion of Cu. This significantly enhanced modulated the inflammatory response and promoted the vascularization of endothelial cells, while exhibiting excellent antimicrobial activity. Therefore, the high surface area and pore structure of MOFs can be used for effective loading of drugs or growth factors, which can help promote bone cell proliferation and differentiation. They can also be used for anti-inflammatory, antibacterial and other functions, which can help maintain the healthy state of bone tissue.

1.2.2 Osteoclast inhibition by MOFs

A decrease in osteoblasts or an increase in osteoclasts disrupts the structure of bone tissue, greatly increasing the risk of osteoporosis as well as disorders such as osteogenesis imperfecta. Osteoprotegerins are proteins that play a key role in bone metabolism by binding to the ligand of the nuclear transcription factor κB receptor (RANKL) activator, thereby inhibiting osteoclast formation and activity. Antitartrate acid phosphatase is a signature indicator representing osteoclast activity. Therefore, the process of bone resorption can be effectively inhibited by increasing the secretion of osteoprotegerin and decreasing the secretion of anti-tartaric acid phosphatase. The synthesis of a bimetallic metal-organic skeleton (Pt@ZIF-8@La) was achieved by encapsulating metallic platinum (Pt), which exhibits excellent physicochemical and biological properties, in ZIF-8. This was followed by the introduction of lanthanum (La), an osteogenic active element, through ion exchange. This nanoplatform exhibits the functions of efficient ROS scavenging, immunomodulation and promotion of osteogenic differentiation. In addition, Pt@ZIF-8@La has been demonstrated to promote osteogenic mineralization by up-regulating the ratio of osteoprotegerin (OPG)/receptor activator of NF-κB ligand (RANKL). This leads to a synergistic therapeutic effect of immunomodulation, osteogenesis, and alleviates aseptic osteolysis (Pan et al., 2023). Zoledronic acid-functionalized MOFs can be used to combat rheumatoid osteoclasts in rheumatoid arthritis. Osteoclast hyperactivation in arthritis. The ability to block osteoclast binding to bone matrix, thereby interfering with the nuclear transcription factor κB receptor activator ligand/nuclear transcription factor κ receptor activator signaling pathway, inhibits osteoclast differentiation and induces apoptosis of osteoclasts in order to counteract osteoclast-mediated bone resorption (Tao et al., 2023). Pang et al. (2020) design surface modification with the anti-osteoclastic bisphosphonate, zoledronic acid (ZOL), to enable bone-targeted immunostimulatory capabilities cytosine-phosphoguanosine (CpG)-loaded MOF. Functionalized bone-targeted immunostimulatory MOF (BT-isMOF) nanoparticles exhibited strong binding to calcium phosphate and demonstrated specific accumulation in bone tissue *in vivo*. BT-isMOF nanoparticles effectively inhibited osteoclast formation and induced macrophage polarization towards an M1 pro-inflammatory phenotype. Tao et al. (2023) developed ZIF-8@CRIg-CD59@HA@ZA, its achieved bone-targeted delivery and pH-responsive slow release of the complement inhibitor CRIg-CD59. Its surface-mineralized zoledronic acid (ZA) targets the acidic microenvironment of bone in RA, and sustained release of CRIg-CD59 recognizes and prevents the formation of complement membrane attack complexes (MACs) on the surface of healthy cells and significantly inhibits osteoclast-mediated bone resorption. Bone malignancies often cause severe osteoclastic conditions in patients, which are difficult to control or even reverse with conventional treatments. Zou et al. (2022) constructed ICG@Cu2-XSe-ZIF-8 utilized an acidic microenvironment, which allowed ZIF-8 to be cleaved and released large amounts of Cu2-XSe, which could subsequently be degraded to Cu^{+} and Cu^{2+}, triggering a Fenton reaction that induced CDT. What's more, selenium in Cu 2-X Se can regulate selenoproteins and inhibit the production of tumor cells and osteoclasts to reduce the erosion of bone tissue. Moreover, PTT-induced hyperthermia can further enhance the CDT effect in tumors to achieve the synergistic effect of PTT/CDT. Lin et al. (2024) developed an acid-responsive neutralization system with *in vivo* gene editing capability by loading sodium bicarbonate ($NaHCO_3$) and RANKL-CRISPR/Cas9 (RC) plasmid into MOF. It was demonstrated that ZIF8-NaHCO3@Cas9 (ZNC) effectively neutralized the acidic microenvironment and inhibited ROS production. The results demonstrated that nanoparticles loaded with $NaHCO_3$ exhibited a higher transfection efficiency in an acidic environment compared to nanoparticles without this loading. Protection by bi-directionally promoting osteogenesis and inhibiting osteolysis. It takes 3 months for osteoblasts to form new bone, while osteoclasts only take 3 weeks to break a bone fracture. Therefore, in correcting the dynamic balance between osteogenesis and osteoclastogenesis in osteoporosis, inhibition of osteoclastogenesis is particularly crucial. From the above content, it can be concluded that MOFs can effectively inhibit bone resorption, thereby promoting bone tissue regeneration and repair. Therefore, when facing osteoporosis, more attention should be paid to this aspect.

1.2.3 MOFs for angiogenesis

Kusumbe et al. (2014) discovered that capillaries can be classified into H-type and L-type. The number of H-type vessels can be used as a diagnostic indicator of the state of vascular growth and osteogenic capacity, influencing bone metabolism in

many ways, including angiogenesis and abundance. Mi et al. (Leroux et al., 2020) demonstrated that electrical stimulation of the dorsal root ganglion (DRG) at L3 and L4 in rats resulted in the activation of the Ca/CaMKII/CREB signal pathway and action potentials, which directly promoted CGRP synthesis and release and induced osteoporotic fracture healing and H-vessel formation. This breaks the traditional "triadic theory" of bone metabolism and updates it to a new quadratic theory of "peripheral neuroangiogenesis - Osteoclasts - osteogenesis". Kang et al. (2022) utilized human adipose-derived stem cells (hADSCs-exos), Mg and GaMII/CREB signal pathway and action potentials, which directly promoted CGRP synthesis and release and induced osteoporotic fracture healing and H-vessel formation. Using hADSCs-exos, Mg and GA, a unique exosome-functionalized free cell scaffold (PLGA/Exo-Mg-GA MOF) was designed and synthesized. This nano scaffold has the functions of stabilizing bone grafting environment, promoting osteogenic differentiation, angiogenesis and anti-inflammatory ability, and accelerating bone reconstruction. Dang et al. (2020) successfully prepared a nanosheet-structured β-tricalcium phosphate (TCP) (Cu-TCPP-TCP) scaffold by using 3D printing technology in combination with an insitu growth method in a solvothermal system. The excellent photothermal effect of Cu-TCPP nanosheets allows for the modulation of photothermal performance through changes in nanosheet content, ambient humidity, and near-infrared light power density. The nano scaffold was found to be capable of supporting the attachment of human bone marrow stromal cells (HBMSCs) and human umbilical vein endothelial cells (HUVECs). This resulted in the promotion of bone generation in all aspects. The angiogenesis-related genes VE-cadherin and endothelial-type nitric oxide synthase are key vascularization. Qu et al. (2021b) prepared a cobalt-based organometallic framework (Co-TCPP)-modified calcium phosphate bone cement using Co and (4-carboxyphenyl) porphyrin (TCPP), and verified the great potential of Co-TCPP-calcium phosphate bone cement in the treatment of tumor-borne bone defects by up-regulating the content of angiogenesis-related genes, VE-cadherin and endothelial nitric oxide synthase, and by promoting the blood vessel regeneration. In addition, Cu^{2+} also possesses pro-angiogenic activity, while Mg^{2+} has been shown to activate hypoxia-inducible factor 1a after influx into the cell via magnesium transporter protein 1, which stimulates the transcription of vascular endothelial growth factor and induce angiogenesis (Xiang et al., 2023; Xu et al., 2023; Xiao et al., 2021). In addition to the three metal-centered MOFs mentioned above, others can also be used as carriers for loading pro-angiogenic small molecule drugs to promote angiogenesis (Gutowska et al., 2005). These studies reveal the potential of MOFs in promoting angiogenesis and bone tissue regeneration. By regulating the generation of blood vessels and activating signaling pathways, MOFs can affect bone metabolism and promote fracture healing and bone reconstruction processes.

1.2.4 MOFs induced bone mineralization

Bone mineralization is the process by which bone minerals, such as hydroxyapatite, precipitate on an organic collagen scaffold to eventually form a bone matrix. Bone mineralization provides the necessary support and stability for newborn bone tissue and is a critical step in bone repair. Metal ions in MOFs, such as Mg^{2+}, Zn^{2+}, Mn^{2+}, Sr^{2+}, etc., can affect the composition of hydroxyapatite by ion exchange, at the same time, changes in bond lengths induced by ion exchange can lead to deformation of the crystal structure of hydroxyapatite, which in turn affects the process of bone mineralization. In addition, Sr^{2+} has a high affinity for bone tissue, and the Sr-hydroxyapatite-metal-organic framework composite coatings constructed by Zhang et al. (2019). The significantly enhance the early osteogenesis and the integration of bone implants. Meanwhile it projected a good result in alkaline phosphatase activity and bone mineralization. In addition, some MOFs have metal ions with ionic radii close to those of Ca^{2+}, which can also promote phosphate deposition through ion exchange, such as La^{3+}, and it has been demonstrated that the interfacial bonding strength of La-hydroxyapatite coatings is significantly enhanced after doping with La (Lou et al., 2015). From the above content, it can be concluded that metal ions in MOFs play an important role in the process of bone mineralization. It can affect the formation and stability of new bone tissue by regulating ion exchange and crystal structure. This provides new ideas and possibilities for designing and developing new bone repair materials, which are expected to play an important role in fields such as fracture healing and bone defect repair.

1.3 MOFs in osteoarthritis

Osteoarthritis (OA) is estimated to affect 300 million or more people worldwide and is now the leading cause of disability in the elderly. It is often associated with chronic pain, progressive loss of function and a significant reduction in quality of life (James et al., 2018; Cisternas et al., 2016; Nguyen et al., 2014; Hunter et al., 2014; Centers for Disease Control and Prevention, 1995). OA was thought to be a simple degenerative disease characterized by chronic overload and biomechanical impairment of the joints, leading to destruction of articular cartilage and resulting inflammation, followed by stiffness, swelling and loss of function. However, with the deepening of research, scholars have concluded that OA is an extremely complex pathological process composed of inflammatory and metabolic factors. Factors such as trauma, infection, obesity, genetics, metabolic syndrome, atherosclerosis, endocrine system and estrogen abnormalities, and aging (chondrocyte senescence, DNA damage, cartilage matrix aging, oxidative stress, mitochondrial dysfunction, and autophagy) can influence the development of OA (Berenbaum, 2013; Loeser, 2011; Yusuf et al., 2010). Due to the complexity and serious impact of OA, exploring new treatment methods and materials has become an urgent task. MOFs has shown remarkable potential in the treatment of osteoarthritis due to its unique structure and properties.

1.3.1 MOFs for immunomodulation

Macrophages, as key regulators of the inflammatory response and important components of the innate immune system, can be divided into two M1 and M2 subtypes, depending on their function. In the early stages of the inflammatory response, M1 macrophages destroy pathogens by enhancing immune activity, but this pro-inflammatory response inhibits tissue regeneration if it persists for too long. As inflammation progresses, M1-type macrophages convert to M2-type and secrete anti-inflammatory cytokines such

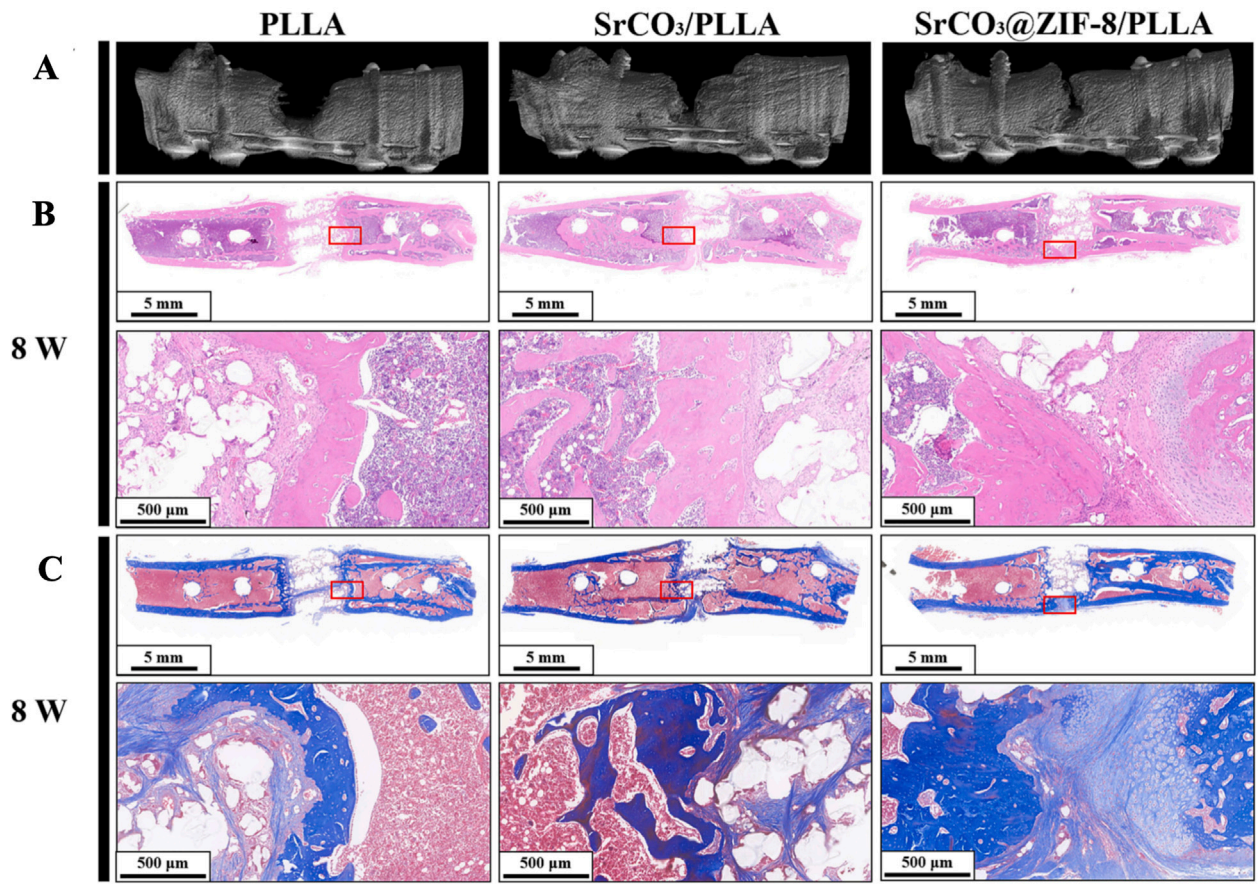

FIGURE 6
After 8 weeks of implanting PLLA, $SrCO_3$/PLLA, and $SrCO_3$@ZIF-8/PLLA scaffolds, the three-dimensional reconstruction images **(A)**, H&E staining **(B)**, and Masson trichrome staining **(C)** of femoral defects are shown (Qian et al., 2024). Reproduced under the terms of the Copyright Clearance Center (CCC) license. Copyright © 2024 Elsevier.

as interleukin 4, interleukin 10, and arginase 1 to alleviate excessive inflammation. Qian et al. (2024) devised a core-shell structure ($SrCO_3$@ZIF-8) that generates ZIF-8 *in-situ* on the surface of $SrCO_3$, and utilized an organic ligand for ZIF-8 with poly (L-lactide) to form a structurally robust composite scaffold (Figure 6). The scaffold not only exhibited excellent mechanical properties, but also promoted the conversion of M0-type macrophages to M2-type macrophages by releasing Sr^{2+} and Zn^{2+}, decreased the expression of tumor necrosis factor, and increased the expression levels of interleukin 10 and arginase1, thereby optimizing the repair microenvironment and significantly promoting the osteogenic differentiation of mouse MSCs. Chen et al. (2022) utilized the immunomodulatory effect of AHT-Ce/Sr metal-organic framework to achieve a decrease in the expression of interleukin 1β and tumor necrosis factor α and an increase in the M2 macrophage-associated marker CD206 in macrophages. Yan et al. (2022) constructed fluorine-doped multifunctional zirconium-based metal-organic skeleton thin films on titanium-based implants. The fluorine-doped zirconium-based metal-organic skeleton stimulated the release of fumaric acid and induced the polarization of macrophages to M2 type. Rheumatoid arthritis (RA), an important component of OA, often exhibits more severe clinical symptoms and rate of progression. Inflammatory infiltration and bone destruction are important pathological features of RA originating from a disturbed ecological niche of macrophages. RA is mediated by the disruption of the barrier function of VSIg4 lined macrophages due to hyperactivation of complement mediating the inflammatory infiltration within the joint. Tao et al. (2023) designed the ZIF8@CRIg-CD59@HA@ZA nanoplatform to address this issue. This recognized and blocked complement membrane attack complex (MAC) on the healthy cell surfaces, reducing the deposition of complement markers and osteoclast inhibition. Moreover, this nanoplatform facilitated the regeneration of VSIg4 synovial macrophages. The successful application of this dual-targeted therapeutic vector indicates that the restoration of the synovial macrophage ecological niche represents an effective therapeutic strategy for RA. So, it can be inferred that MOFs have ability to regulate macrophage activity, inhibit inflammatory factors, promote the release of anti-inflammatory factors, and optimize the repair of the inflammatory microenvironment.

1.3.2 Targeted delivery of anti-inflammatory drugs by MOFs

In terms of arthritis drug therapy, clinical choices are mostly non-steroidal anti-inflammatory drugs (NSAIDs), glucocorticoid,

10.3389/fbioe.2024.1448010

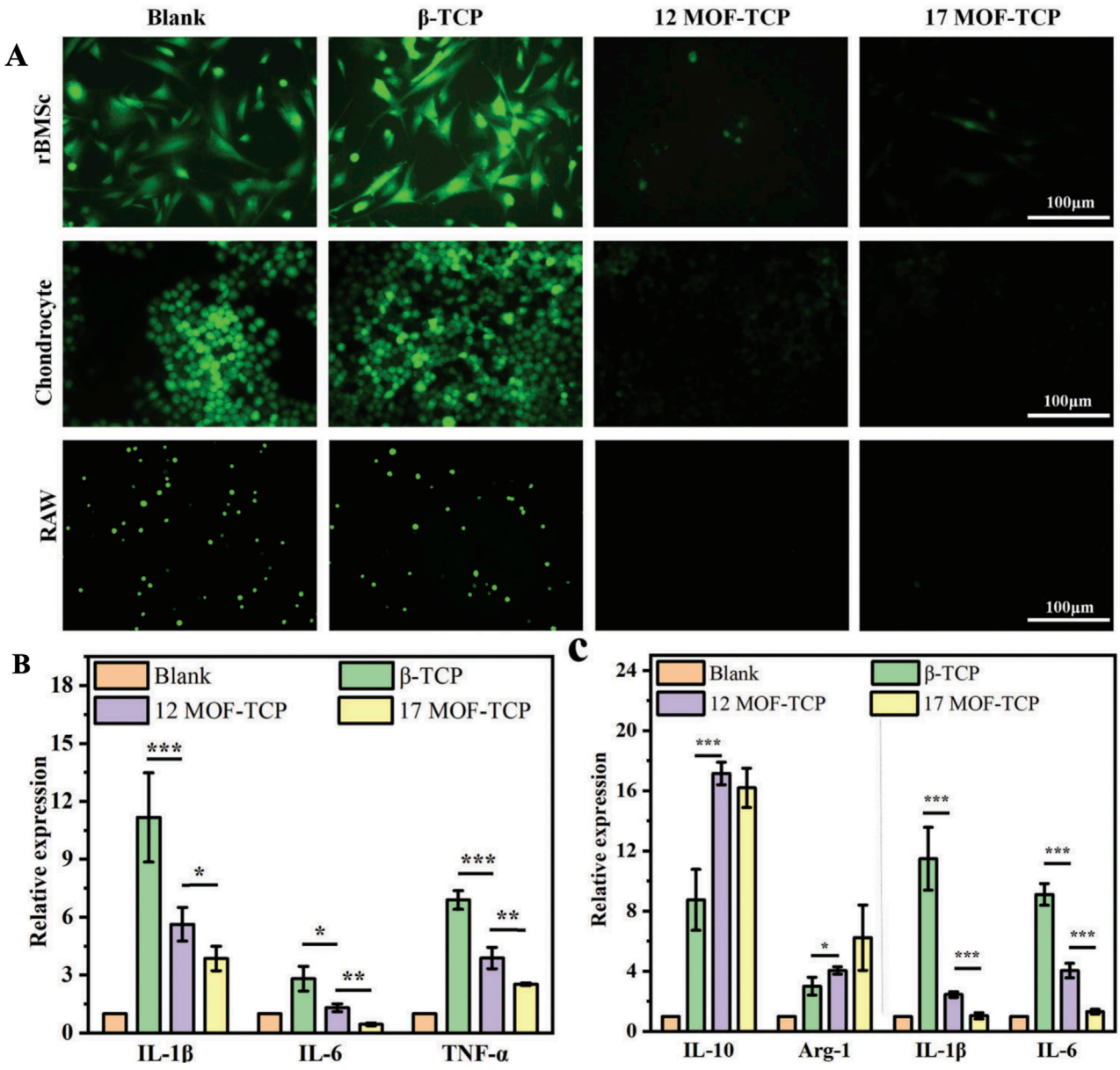

FIGURE 7
The MOF-TCP scaffolds exhibit *in vitro* antioxidative and anti-inflammatory activities. **(A)** The ROS fluorescence staining images are presented for rBMSCs, chondrocytes, and RAW 264.7 cells cultured with scaffolds under H_2O_2 stimulation. **(B)** The expression of proinflammatory genes in chondrocytes is shown (n = 3). **(C)** The expression of anti-inflammatory genes and proinflammatory genes in RAW 264.7 cells. *p < 0.05, **p < 0.01, ***p < 0.001 (Shu et al., 2023). Reproduced under the terms of the Copyright Clearance Center (CCC) license. Copyright © 2023 The Authors. Advanced Science published by Wiley-VCH GmbH. Open access article.

anti-rheumatic drugs (DMARDs), and biologics that control pain and inflammation (Feng and Chen, 2018). However, defects such as poor water solubility, uncontrolled drug release, low cell permeability and early degradation before reaching the target site, and undesirable side effects significantly limit the bioavailability of drugs (Majumder and Minko, 2021). MOFs, as highly efficient drug carriers, have the advantage of being able to accurately control the release of drugs, thanks to the fact that MOFs, in response to signals from an external stimulus, change their own topology. This is mainly because of when the MOFs receives the external stimulus response signal, its topology, size and pore diameter will change, thus realizing the precise control of drug release rate. The large specific surface area of MOFs and the activation and protection of drugs can not only significantly improve the therapeutic efficiency, but also significantly reduce the systemic adverse reactions. For example, loading ketoprofen into Mg metal organic framework significantly reduced the expression of various pain related genes such as cyclooxygenase, significantly upregulated osteoblasts, and downregulated the secretion of pro-inflammatory factors (Ge et al., 2021). Jiang et al. (2023) use ZIF-8 to deliver Neobavaisoflavone (NBIFs), NBIF@ZIF-8 complexes with anti-inflammatory effects were constructed. In addition, MOFs can

not only be used as carriers to carry anti-inflammatory drugs, but also improve the therapeutic efficacy of drugs through on-demand design. Xue et al. (2021) developed a dual drug delivery nanoplatform based on MOFs loaded with rapamycin and bilirubin-mesoporous dobutamine, and at the same time, this system was affixed with a collagen II-targeting peptide on its surface, which resulted in a significant enhancement of the targeting to the cartilage. We can see the potential of MOFs as efficient drug carriers in the treatment of arthritis. MOFs can precisely control drug release, improve therapeutic efficacy and reduce adverse reactions. These nano delivery systems are expected to greatly improve the limitations of existing arthritis drug treatments.

1.3.3 Scavenging of pro-inflammatory cytokines and ROS by MOFs

The main pathological feature of osteoarthritis is the accumulation of excessive pro-inflammatory cytokines and reactive oxygen species at the joints, which can exacerbate bone defects and hinder the regeneration of bone and cartilage tissues. Therefore, the removal of pro-inflammatory factors is a direct and effective therapeutic strategy for osteoarthritis. Shu et al. (2023) has successfully developed a multi-functional scaffold, MOF-TCP, with good biocompatibility and modulation of inflammation by functionalizing βTCP scaffolds with Zn/Co-MOF. This nano scaffold can simultaneously enhance the differentiation of rBMSCs and the maturation of chondrocytes by eliminating ROS-mediated inflammatory microenvironment and protect them from oxidative stress, resulting in good regenerative capacity and regenerative environment for osteochondral bone (Figure 7). The exosome functionalized polylactic acid hydroxyacetic acid copolymer/Mg gallic acid metal organic framework scaffold prepared by Kang et al. (2022). This system significantly reduced the levels of pro-inflammatory cytokine induced nitric oxide synthase, cyclooxygenase-2, and reactive oxygen species by releasing exosomes and gallic acid, effectively suppressing harmful immune responses during osteogenesis. HIF-2α plays a catabolic role in OA, and an increase in HIF-2α exacerbated the chondrocyte response to hypoxia and the expression of catabolic factors, cytokines, chemokines, and MMPs in the synovium (Zhang et al., 2015; Pi et al., 2015; Yang et al., 2010). Since HIF-2α has been shown to be a key pathogenic target during OA progression, downregulation of HIF-2 α expression in locally inflamed joints is important for the treatment of OA cartilage (Pasupneti et al., 2020; Yang et al., 2019). Zhang et al. (2023) constructed an injectable drug co-delivery system by loading MIL-101-NH with Curcumin (CCM) and anti-HIF-2α siRNA (siHIF-2α). In an acidic microenvironment, the release of CCM and siHIF-2α from this scaffold has the potential to alleviate the progression of HIF-2α gene silencing in chondrocytes. This is achieved by a synergistic downregulation of OA-associated catabolic markers and an upregulation of cartilage-specific markers in chondrocytes, resulting in a merit therapeutic effect. The above research demonstrates a novel treatment strategy for osteoarthritis. By using MOFs systems to regulate inflammation, promote cell differentiation and suppress harmful immune responses, these novel scaffolds provide new possibilities for improving treatment outcomes in patients with osteoarthritis. The clearance of pro-inflammatory factors and reactive oxygen species, as well as treatment strategies targeting HIF-2 α, are expected to become important means of treating osteoarthritis in the future.

2 Conclusion and prospect

MOFs exhibit a number of unique advantages compared to other nanomaterials, such as their high specific surface area and drug loading efficiency. This means that MOFs can accommodate more drug molecules in their structure, which improves therapeutic effectiveness. In addition, MOFs exhibit excellent chemical stability, meaning that they are able to maintain their structural and functional integrity in different chemical environments. MOFs also perform well in terms of biosafety, as they do not cause adverse reactions in living organisms, which is essential for clinical applications. Another notable feature is the pH responsiveness of MOFs, which are able to change their structure or release drugs under different pH conditions, enabling precision therapy. In addition to the above advantages, MOFs can also be combined with a variety of other substances to participate in the diagnostic or therapeutic process. For example, they can be combined with specific gases such as hydrogen and nitric oxide to treat the corresponding diseases. These gases can play an important role in the treatment process, such as anti-inflammatory, antioxidant, etc. In addition, MOFs can be combined with gene therapy techniques to serve as high-capacity vectors for the delivery of specific gene segments. This combination opens up new possibilities for gene therapy, allowing gene fragments to be delivered more efficiently into target cells.

Although much has been summarized in the manuscript about the application of MOFs to orthopedic diseases, in reality, the application of MOFs extend far beyond orthopedic diseases. In the medical field, the application prospects of MOFs are very broad, including but not limited to drug delivery, biological imaging, cancer treatment, antibacterial applications, etc. However, MOFs face some challenges before they can be used in the clinic. Researchers need to establish standardized biosafety evaluation criteria to ensure the safety and effectiveness of MOFs *in vivo*. In addition, safety evaluation in animals is needed to further verify the feasibility of its clinical application. In order for MOFs to be widely used in the clinic, researchers also need to develop new methods for making and storing MOFs. These methods should not only reduce production costs, but also ensure the stability and effectiveness of MOFs in clinical applications. In addition, broadening the application scenarios of MOF is also the part we need to focus on. In the future, we should continue to optimize and improve the physical structure and chemical properties of MOFs to achieve its comprehensive application in more fields. Through these efforts, MOFs are expected to become an important nanomaterial in the future, bringing revolutionary changes to the field of medicine.

Author contributions

ZZ: Conceptualization, Data curation, Writing–original draft. CW: Data curation, Formal Analysis, Writing–original draft. AL:

Conceptualization, Data curation, Investigation, Writing–original draft. NB: Conceptualization, Formal Analysis, Software, Writing–review and editing. BJ: Methodology, Software, Writing–review and editing. YM: Conceptualization, Data curation, Writing–review and editing. TY: Methodology, Project administration, Writing–review and editing. DD: Conceptualization, Writing–review and editing. CY: Conceptualization, Supervision, Writing–review and editing. DL: Funding acquisition, Supervision, Writing–review and editing.

Funding

The author(s) declare that financial support was received for the research, authorship, and/or publication of this article. This work has been financially supported by the Health Industry Clinical Research Project of Shanghai Health Commission (Grant No. 20224Y0393), the Young Medical Talents Training Program of Pudong Health Committee of Shanghai (Grant No. PWRq 2021-08), the Science and Technology Development Fund of Shanghai Pudong New Area (Grant No. PKJ2023-Y09), the Outstanding Leaders Training Program of Pudong Hospital affiliated to Fudan University (Grant No. LX202201), the Project of Key Medical Specialty and Treatment Center of Pudong Hospital of Fudan University (Grant No. Tszb2023-05), the Outstanding Clinical Discipline Project of Shanghai Pudong (Grant No. PWYgy2021-04), the Project of Key Medical Specialty and Treatment Center of Pudong Hospital of Fudan University (Zdzk2020-02, Zdzk2021-01).

Conflict of interest

The authors declare that the research was conducted in the absence of any commercial or financial relationships that could be construed as a potential conflict of interest.

Publisher's note

References

Armas, L. A., and Recker, R. R. (2012). Pathophysiology of osteoporosis: new mechanistic insights. *Endocrinol. Metab. Clin. North Am.* 41 (3), 475–486. doi:10.1016/j.ecl.2012.04.006

Berenbaum, F. (2013). Osteoarthritis as an inflammatory disease (osteoarthritis is not osteoarthrosis!). *Osteoarthr. Cartil.* 21 (1), 16–21. doi:10.1016/j.joca.2012.11.012

Bharadwaz, A., and Jayasuriya, A. C. (2020). Recent trends in the application of widely used natural and synthetic polymer nanocomposites in bone tissue regeneration. *Mater Sci. Eng. C Mater Biol. Appl.* 110, 110698. doi:10.1016/j.msec.2020.110698

Bjorge, I. M., Kim, S. Y., Mano, J. F., Kalionis, B., and Chrzanowski, W. (2017). Extracellular vesicles, exosomes and shedding vesicles in regenerative medicine - a new paradigm for tissue repair. *Biomater. Sci.* 6 (1), 60–78. doi:10.1039/c7bm00479f

Bliuc, D., Nguyen, N. D., Milch, V. E., Nguyen, T. V., Eisman, J. A., and Center, J. R. (2009). Mortality risk associated with low-trauma osteoporotic fracture and subsequent fracture in men and women. *JAMA* 301 (5), 513–521. doi:10.1001/jama.2009.50

Brown, J. P., Adachi, J. D., Schemitsch, E., Tarride, J. E., Brown, V., Bell, A., et al. (2021). Mortality in older adults following a fragility fracture: real-world retrospective matched-cohort study in ontario. *BMC Musculoskelet. Disord.* 22 (1), 105. doi:10.1186/s12891-021-03960-z

Cao, G., Yan, J., Ning, X., Zhang, Q., Wu, Q., Bi, L., et al. (2021). Antibacterial and antibiofilm properties of graphene and its derivatives. *Colloids Surf. B Biointerfaces* 200, 111588. doi:10.1016/j.colsurfb.2021.111588

Centers for Disease Control and Prevention (1995). Prevalence and impact of arthritis among women--United States, 1989-1991. *MMWR Morb. Mortal. Wkly. Rep.* 44 (17), 329–334.

Chen, K., Wang, Y., Tang, H., Niu, X., Yang, H., Bai, Y., et al. (2024). Fabrication of a nanoscale magnesium/copper metal–organic framework on zn-based guided bone generation membranes for enhancing osteogenesis, angiogenesis, and bacteriostasis properties. *ACS Appl. Mater Interfaces* 16 (5), 5648–5665. doi:10.1021/acsami.3c16970

Chen, M., Wang, D., Li, M., He, Y., He, T., Chen, M., et al. (2022). Nanocatalytic biofunctional mof coating on titanium implants promotes osteoporotic bone regeneration through cooperative pro-osteoblastogenesis msc reprogramming. *ACS Nano* 16 (9), 15397–15412. doi:10.1021/acsnano.2c07200

Cisternas, M. G., Murphy, L., Sacks, J. J., Solomon, D. H., Pasta, D. J., and Helmick, C. G. (2016). Alternative methods for defining osteoarthritis and the impact on estimating prevalence in a us population-based survey. *Arthritis Care Res. Hob.* 68 (5), 574–580. doi:10.1002/acr.22721

Dang, W., Ma, B., Li, B., Huan, Z., Ma, N., Zhu, H., et al. (2020). 3d printing of metal-organic framework nanosheets-structured scaffolds with tumor therapy and bone construction. *Biofabrication* 12 (2), 025005. doi:10.1088/1758-5090/ab5ae3

Deng, X., Zhao, R., Tang, Y., Ge, Z., Wang, D., Xiong, Z., et al. (2023). Nir laser-activated multifunctional nanocomposites for cascade low-temperature photothermal and oxygen-irrelevant thermodynamic therapy. *Mater Des.* 233, 112206. doi:10.1016/j.matdes.2023.112206

Dong, W., Zhao, S., Wang, Y., Zhou, X., Jiang, J., Dang, J., et al. (2023). Stimuli-responsive metal–organic framework hydrogels endow long carbon fiber reinforced polyetheretherketone with enhanced anti-inflammatory and angiogenesis and osteogenesis. *Mater Des.* 225, 111485. doi:10.1016/j.matdes.2022.111485

Du, C., Zhou, M., Jia, F., Ruan, L., Lu, H., Zhang, J., et al. (2021). D-arginine-loaded metal-organic frameworks nanoparticles sensitize osteosarcoma to radiotherapy. *Biomaterials* 269, 120642. doi:10.1016/j.biomaterials.2020.120642

Farasati, F. B., Naimi-Jamal, M. R., Ahmadi, S., and Rabiee, N. (2023). Enhancing bone tissue engineering with calcium and strontium nanoparticles immobilized on hkust-1. *Alex Eng. J.* 76, 221–235.

Farlay, D., Bala, Y., Rizzo, S., Bare, S., Lappe, J. M., Recker, R., et al. (2019). Bone remodeling and bone matrix quality before and after menopause in healthy women. *Bone* 128, 115030. doi:10.1016/j.bone.2019.08.003

Feng, X., and Chen, Y. (2018). Drug delivery targets and systems for targeted treatment of rheumatoid arthritis. *J. Drug Target* 26 (10), 845–857. doi:10.1080/1061186x.2018.1433680

Feng, X., and Mcdonald, J. M. (2011). Disorders of bone remodeling. *Annu. Rev. Pathol.* 6, 121–145. doi:10.1146/annurev-pathol-011110-130203

Ferey, G., Mellot-Draznieks, C., Serre, C., Millange, F., Dutour, J., Surble, S., et al. (2005). A chromium terephthalate-based solid with unusually large pore volumes and surface area. *Science* 309 (5743), 2040–2042. doi:10.1126/science.1116275

Ferey, G., Serre, C., Mellot-Draznieks, C., Millange, F., Surble, S., Dutour, J., et al. (2004). A hybrid solid with giant pores prepared by a combination of targeted chemistry, simulation, and powder diffraction. *Angew. Chem. Int. Ed. Engl.* 43 (46), 6296–6301. doi:10.1002/anie.200460592

Furukawa, H., Cordova, K. E., O'Keeffe, M., and Yaghi, O. M. (2013). The chemistry and applications of metal-organic frameworks. *Science* 341 (Aug.30 TN.6149), 974. doi:10.1126/science.1230444

Ge, Y., Wang, K., Li, H., Tian, Y., Wu, Y., Lin, Z., et al. (2021). An mg-mofs based multifunctional medicine for the treatment of osteoporotic pain. *Mater. Sci. and Eng. C* 129, 112386. doi:10.1016/j.msec.2021.112386

Gong, T., Li, Y., Lv, B., Wang, H., Liu, Y., Yang, W., et al. (2020). Full-process radiosensitization based on nanoscale metal-organic frameworks. *ACS Nano* 14 (3), 3032–3040. doi:10.1021/acsnano.9b07898

Gutowska, I., Machoy, Z., and Machaliński, B. (2005). The role of bivalent metals in hydroxyapatite structures as revealed by molecular modeling with the hyperchem software. *J. Biomed. Mater. Res. Part A* 75A (4), 788–793. doi:10.1002/jbm.a.30511

He, Z., Dai, Y., Li, X., Guo, D., Liu, Y., Huang, X., et al. (2019). Hybrid nanomedicine fabricated from photosensitizer-terminated metal-organic framework nanoparticles for

photodynamic therapy and hypoxia-activated cascade chemotherapy. *Small* 15 (4), e1804131. doi:10.1002/smll.201804131

Hunter, D. J., Schofield, D., and Callander, E. (2014). The individual and socioeconomic impact of osteoarthritis. *Nat. Rev. Rheumatol.* 10 (7), 437–441. doi:10.1038/nrrheum.2014.44

James, S. L., Abate, D., Abate, K. H., Abay, S. M., Abbafati, C., Abbasi, N., et al. (2018). Global, regional, and national incidence, prevalence, and years lived with disability for 354 diseases and injuries for 195 countries and territories, 1990-2017: a systematic analysis for the global burden of disease study 2017. *Lancet* 392 (10159), 1789–1858. doi:10.1016/s0140-6736(18)32279-7

Jiang, Y., Liao, H., Yan, L., Jiang, S., Zheng, Y., Zhang, X., et al. (2023). A metal–organic framework-incorporated hydrogel for delivery of immunomodulatory neobavaisoflavone to promote cartilage regeneration in osteoarthritis. *ACS Appl. Mater Interfaces* 15 (40), 46598–46612. doi:10.1021/acsami.3c06706

Kang, Y., Xu, C., Meng, L., Dong, X., Qi, M., and Jiang, D. (2022). Exosome-functionalized magnesium-organic framework-based scaffolds with osteogenic, angiogenic and anti-inflammatory properties for accelerated bone regeneration. *Bioact. Mater* 18, 26–41. doi:10.1016/j.bioactmat.2022.02.012

Kim, D., Kim, J., Park, Y. I., Lee, N., and Hyeon, T. (2018). Recent development of inorganic nanoparticles for biomedical imaging. *ACS Cent. Sci.* 4 (3), 324–336. doi:10.1021/acscentsci.7b00574

Kim, S. W., Im, G. B., Kim, Y. J., Kim, Y. H., Lee, T. J., and Bhang, S. H. (2020). Bio-application of inorganic nanomaterials in tissue engineering. *Adv. Exp. Med. Biol.* 1249, 115–130. doi:10.1007/978-981-15-3258-0_8

Kusumbe, A. P., Ramasamy, S. K., and Adams, R. H. (2014). Coupling of angiogenesis and osteogenesis by a specific vessel subtype in bone. *Nature* 507 (7492), 323–328. doi:10.1038/nature13145

Kwon, H. J., Cha, M. Y., Kim, D., Kim, D. K., Soh, M., Shin, K., et al. (2016). Mitochondria-targeting ceria nanoparticles as antioxidants for alzheimer's disease. *ACS Nano* 10 (2), 2860–2870. doi:10.1021/acsnano.5b08045

Lee, W. C., Lim, C. H., Shi, H., Tang, L. A., Wang, Y., Lim, C. T., et al. (2011). Origin of enhanced stem cell growth and differentiation on graphene and graphene oxide. *ACS Nano* 5 (9), 7334–7341. doi:10.1021/nn202190c

Leroux, A., Paiva Dos Santos, B., Leng, J., Oliveira, H., and Amédée, J. (2020). Sensory neurons from dorsal root ganglia regulate endothelial cell function in extracellular matrix remodelling. *Cell Commun. Signal* 18 (1), 162. doi:10.1186/s12964-020-00656-0

Li, J., Stein, D., Mcmullan, C., Branton, D., Aziz, M. J., and Golovchenko, J. A. (2001). Ion-beam sculpting at nanometre length scales. *Nature* 412 (6843), 166–169. doi:10.1038/35084037

Li, T., Gao, M., Wu, Z., Yang, J., Mo, B., Yu, S., et al. (2023). Tantalum-zirconium co-doped metal-organic frameworks sequentially sensitize radio-radiodynamic-immunotherapy for metastatic osteosarcoma. *Adv. Sci. (Weinh)* 10 (10), e2206779. doi:10.1002/advs.202206779

Li, W., Yang, Y., Wang, J., Ge, T., Wan, S., Gui, L., et al. (2024). Establishment of bone-targeted nano-platform and the study of its combination with 2-deoxy-d-glucose enhanced photodynamic therapy to inhibit bone metastasis. *J. Mech. Behav. Biomed. Mater* 150, 106306. doi:10.1016/j.jmbbm.2023.106306

Lin, W., Hu, S., Li, K., Shi, Y., Pan, C., Xu, Z., et al. (2024). Breaking osteoclast-acid vicious cycle to rescue osteoporosis via an acid responsive organic framework-based neutralizing and gene editing platform. *Small Weinheim der Bergstrasse, Ger.* 20 (22), e2307595. doi:10.1002/smll.202307595

Liu, C., Liu, B., Zhao, J., Di, Z., Chen, D., Gu, Z., et al. (2020). Nd(3+) -sensitized upconversion metal-organic frameworks for mitochondria-targeted amplified photodynamic therapy. *Angew. Chem. Int. Ed. Engl.* 59 (7), 2634–2638. doi:10.1002/anie.201911508

Liu, J., Cui, L., and Losic, D. (2013). Graphene and graphene oxide as new nanocarriers for drug delivery applications. *Acta Biomater.* 9 (12), 9243–9257. doi:10.1016/j.actbio.2013.08.016

Loeser, R. F. (2011). Aging and osteoarthritis. *Curr. Opin. Rheumatol.* 23 (5), 492–496. doi:10.1097/bor.0b013e3283494005

Lou, W., Dong, Y., Zhang, H., Jin, Y., Hu, X., Ma, J., et al. (2015). Preparation and characterization of lanthanum-incorporated hydroxyapatite coatings on titanium substrates. *Int. J. Mol. Sci.* 16 (9), 21070–21086. doi:10.3390/ijms160921070

Lu, K., Aung, T., Guo, N., Weichselbaum, R., and Lin, W. (2018). Nanoscale metal-organic frameworks for therapeutic, imaging, and sensing applications. *Adv. Mater* 30 (37), e1707634. doi:10.1002/adma.201707634

Luetke, A., Meyers, P. A., Lewis, I., and Juergens, H. (2014). Osteosarcoma treatment - where do we stand? A state of the art review. *Cancer Treat. Rev.* 40 (4), 523–532. doi:10.1016/j.ctrv.2013.11.006

Luzuriaga, M. A., Welch, R. P., Dharmarwardana, M., Benjamin, C. E., Li, S., Shahrivarkevishahi, A., et al. (2019). Enhanced stability and controlled delivery of mof-encapsulated vaccines and their immunogenic response *in vivo*. *ACS Appl. Mater Interfaces* 11 (10), 9740–9746. doi:10.1021/acsami.8b20504

Ma, L., Cheng, Y., Feng, X., Zhang, X., Lei, J., Wang, H., et al. (2024). A janus-ros healing system promoting infectious bone regeneration via sono-epigenetic modulation. *Adv. Mater. Weinh.* 36 (2), e2307846. doi:10.1002/adma.202307846

Ma, Y., Chen, L., Li, X., Hu, A., Wang, H., Zhou, H., et al. (2021). Rationally integrating peptide-induced targeting and multimodal therapies in a dual-shell theranostic platform for orthotopic metastatic spinal tumors. *Biomaterials* 275, 120917. doi:10.1016/j.biomaterials.2021.120917

Majumder, J., and Minko, T. (2021). Multifunctional and stimuli-responsive nanocarriers for targeted therapeutic delivery. *Expert Opin. Drug Deliv.* 18 (2), 205–227. doi:10.1080/17425247.2021.1828339

Marrinan, S., Pearce, M. S., Jiang, X. Y., Waters, S., and Shanshal, Y. (2015). Admission for osteoporotic pelvic fractures and predictors of length of hospital stay, mortality and loss of independence. *Age Ageing* 44 (2), 258–261. doi:10.1093/ageing/afu123

Matlinska, M. A., Ha, M., Hughton, B., Oliynyk, A. O., Iyer, A. K., Bernard, G. M., et al. (2019). Alkaline earth metal-organic frameworks with tailorable ion release: a path for supporting biomineralization. *ACS Appl. Mater Interfaces* 11 (36), 32739–32745. doi:10.1021/acsami.9b11004

Meng, H. M., Hu, X. X., Kong, G. Z., Yang, C., Fu, T., Li, Z. H., et al. (2018). Aptamer-functionalized nanoscale metal-organic frameworks for targeted photodynamic therapy. *Theranostics* 8 (16), 4332–4344. doi:10.7150/thno.26768

Morris, W., Wang, S., Cho, D., Auyeung, E., Li, P., Farha, O. K., et al. (2017). Role of modulators in controlling the colloidal stability and polydispersity of the uio-66 metal-organic framework. *ACS Appl. Mater Interfaces* 9 (39), 33413–33418. doi:10.1021/acsami.7b01040

Nguyen, N. T. T., Furukawa, H., Gandara, F., Nguyen, H. T., Cordova, K. E., and Yaghi, O. M. (2014). Selective capture of carbon dioxide under humid conditions by hydrophobic chabazite-type zeolitic imidazolate frameworks. *Angew. Chem.* 53 (40), 10645–10648. doi:10.1002/anie.201403980

Pan, H., Miao, X., Deng, J., Pan, C., Cheng, X., and Wang, X. (2023). Bimetallic metal–organic framework for mitigating aseptic osteolysis. *ACS Appl. Mater Interfaces* 15 (4), 4935–4946. doi:10.1021/acsami.2c19449

Pang, Y., Fu, Y., Li, C., Wu, Z., Cao, W., Hu, X., et al. (2020). Metal–organic framework nanoparticles for ameliorating breast cancer-associated osteolysis. *Nano Lett.* 20 (2), 829–840. doi:10.1021/acs.nanolett.9b02916

Park, K. S., Ni, Z., Cote, A. P., Choi, J. Y., Huang, R., Uribe-Romo, F. J., et al. (2006). Exceptional chemical and thermal stability of zeolitic imidazolate frameworks. *Proc. Natl. Acad. Sci. U. S. A.* 103 (27), 10186–10191. doi:10.1073/pnas.0602439103

Pasupneti, S., Tian, W., Tu, A. B., Dahms, P., Granucci, E., Gandjeva, A., et al. (2020). Endothelial HIF-2α as a key endogenous mediator preventing emphysema. *Am. J. Respir. Crit. Care Med.* 202 (7), 983–995. doi:10.1164/rccm.202001-0078oc

Pi, Y., Zhang, X., Shao, Z., Zhao, F., Hu, X., and Ao, Y. (2015). Intra-articular delivery of anti-hif-2α sirna by chondrocyte-homing nanoparticles to prevent cartilage degeneration in arthritic mice. *Gene Ther.* 22 (6), 439–448. doi:10.1038/gt.2015.16

Qian, G., Mao, Y., Shuai, Y., Zeng, Z., Peng, S., and Shuai, C. (2024). Enhancing bone scaffold interfacial reinforcement through *in situ* growth of metal–organic frameworks (mofs) on strontium carbonate: achieving high strength and osteoimmunomodulation. *J. Colloid Interface Sci.* 655, 43–57. doi:10.1016/j.jcis.2023.10.133

Qu, Y., Zhuang, H., Zhang, M., Wang, Y., Zhai, D., Ma, B., et al. (2021a). Bone cements for therapy and regeneration for minimally invasive treatment of neoplastic bone defects. *J. Mater Chem. B* 9 (21), 4355–4364. doi:10.1039/d1tb00703c

Qu, Y., Zhuang, H., Zhang, M., Wang, Y., Zhai, D., Ma, B., et al. (2021b). Bone cements for therapy and regeneration for minimally invasive treatment of neoplastic bone defects. *J. Mater. Chem. B, Mater. Biol. Med.* 9 (21), 4355–4364. doi:10.1039/d1tb00703c

Ren, N., Liang, N., Dong, M., Feng, Z., Meng, L., Sun, C., et al. (2022). Stem cell membrane-encapsulated zeolitic imidazolate framework-8: a targeted nano-platform for osteogenic differentiation. *Small Weinheim der Bergstrasse, Ger.* 18 (26), e2202485. doi:10.1002/smll.202202485

Shu, C., Qin, C., Chen, L., Wang, Y., Shi, Z., Yu, J., et al. (2023). Metal-organic framework functionalized bioceramic scaffolds with antioxidative activity for enhanced osteochondral regeneration. *Adv. Sci. (Weinh)* 10 (13), e2206875. doi:10.1002/advs.202206875

Sims, N. A., and Martin, T. J. (2020). Osteoclasts provide coupling signals to osteoblast lineage cells through multiple mechanisms. *Annu. Rev. Physiol.* 82, 507–529. doi:10.1146/annurev-physiol-021119-034425

Strom, O., Borgstrom, F., Kanis, J. A., Compston, J., Cooper, C., Mccloskey, E. V., et al. (2011). Osteoporosis: burden, health care provision and opportunities in the eu: a report prepared in collaboration with the international osteoporosis foundation (iof) and the european federation of pharmaceutical industry associations (efpia). *Arch. Osteoporos.* 6, 59–155. doi:10.1007/s11657-011-0060-1

Tao, S., Yu, H., You, T., Kong, X., Wei, X., Zheng, Z., et al. (2023). A dual-targeted metal–organic framework based nanoplatform for the treatment of rheumatoid arthritis by restoring the macrophage niche. *ACS Nano* 17 (14), 13917–13937. doi:10.1021/acsnano.3c03828

Toprak, O., Topuz, B., Monsef, Y. A., Oto, C., Orhan, K., and Karakecili, A. (2021). Bmp-6 carrying metal organic framework-embedded in bioresorbable electrospun fibers for enhanced bone regeneration. *Mater Sci. Eng. C Mater Biol. Appl.* 120, 111738. doi:10.1016/j.msec.2020.111738

Wang, B., Chen, H., Peng, S., Li, X., Liu, X., Ren, H., et al. (2023b). Multifunctional magnesium-organic framework doped biodegradable bone cement for antibacterial growth, inflammatory regulation and osteogenic differentiation. *J. Mater. Chem. B, Mater. Biol. Med.* 11 (13), 2872–2885. doi:10.1039/d2tb02705d

Wang, C., Cao, F., Ruan, Y., Jia, X., Zhen, W., and Jiang, X. (2019). Specific generation of singlet oxygen through the russell mechanism in hypoxic tumors and gsh depletion by cu-tcpp nanosheets for cancer therapy. *Angew. Chem. Int. Ed. Engl.* 58 (29), 9846–9850. doi:10.1002/anie.201903981

Wang, H., Chen, S., He, Z., Chen, J., Zhu, Z., Wan, Q., et al. (2024). Synthesis and potential osteogenic applications of wnt3a-loaded zif-8 nanoparticles. *Chin. Chem. Lett.* 35 (3), 108597. doi:10.1016/j.cclet.2023.108597

Wang, J., Chen, D., and Ho, E. A. (2021). Challenges in the development and establishment of exosome-based drug delivery systems. *J. Control Release* 329, 894–906. doi:10.1016/j.jconrel.2020.10.020

Wang, Y., Williams, G. R., Zheng, Y., Guo, H., Chen, S., Ren, R., et al. (2023a). Polydopamine-cloaked fe-based metal organic frameworks enable synergistic multidimensional treatment of osteosarcoma. *J. Colloid Interface Sci.* 651, 76–92. doi:10.1016/j.jcis.2023.07.146

Xiang, J., Zhu, Y., Xie, Y., Chen, H., Zhou, L., Chen, D., et al. (2023). A cu@zif-8 encapsulated antibacterial and angiogenic microneedle array for promoting wound healing. *Nanoscale Adv.* 5 (18), 5102–5114. doi:10.1039/d3na00291h

Xiao, T., Fan, L., Liu, R., Huang, X., Wang, S., Xiao, L., et al. (2021). Fabrication of dexamethasone-loaded dual-metal–organic frameworks on polyetheretherketone implants with bacteriostasis and angiogenesis properties for promoting bone regeneration. *ACS Appl. Mater Interfaces* 13 (43), 50836–50850. doi:10.1021/acsami.1c18088

Xu, C., Kang, Y., Guan, S., Dong, X., Jiang, D., and Qi, M. (2023). Iron-based metal–organic framework as a dual cooperative release system for enhanced vascularization and bone regeneration. *Chin. Chem. Lett.* 34 (5), 107825. doi:10.1016/j.cclet.2022.107825

Xu, W., Lou, Y., Chen, W., and Kang, Y. (2020). Folic acid decorated metal-organic frameworks loaded with doxorubicin for tumor-targeted chemotherapy of osteosarcoma. *Biomed. Tech. Berl.* 65 (2), 229–236. doi:10.1515/bmt-2019-0056

Xue, S., Zhou, X., Sang, W., Wang, C., Lu, H., Xu, Y., et al. (2021). Cartilage-targeting peptide-modified dual-drug delivery nanoplatform with nir laser response for osteoarthritis therapy. *Bioact. Mater* 6 (8), 2372–2389. doi:10.1016/j.bioactmat.2021.01.017

Yadid, M., Feiner, R., and Dvir, T. (2019). Gold nanoparticle-integrated scaffolds for tissue engineering and regenerative medicine. *Nano Lett.* 19 (4), 2198–2206. doi:10.1021/acs.nanolett.9b00472

Yaghi, O. M., Li, G., and Li, H. (1995). Selective binding and removal of guests in a microporous metal–organic framework. *Nature* 378 (6558), 703–706. doi:10.1038/378703a0

Yan, B., Tan, J., Zhang, H., Liu, L., Chen, L., Qiao, Y., et al. (2022). Constructing fluorine-doped zr-mof films on titanium for antibacteria, anti-inflammation, and osteogenesis. **Materials science and engineering**. *C, Mater. Biol. Appl.* 134, 112699. doi:10.1016/j.msec.2022.112699

Yang, Q., Zhou, Y., Cai, P., Fu, W., Wang, J., Wei, Q., et al. (2019). Up-regulated hif-2α contributes to the osteoarthritis development through mediating the primary cilia loss. *Int. Immunopharmacol.* 75, 105762. doi:10.1016/j.intimp.2019.105762

Yang, S., Kim, J., Ryu, J., Oh, H., Chun, C., Kim, B. J., et al. (2010). Hypoxia-inducible factor-2α is a catabolic regulator of osteoarthritic cartilage destruction. *Nat. Med.* 16 (6), 687–693. doi:10.1038/nm.2153

Yuan, Y., and Zhang, Y. (2017). Enhanced biomimic bactericidal surfaces by coating with positively-charged zif nano-dagger arrays. *Nanomedicine (Lond)* 13 (7), 2199–2207. doi:10.1016/j.nano.2017.06.003

Yusuf, E., Nelissen, R. G., Ioan-Facsinay, A., Stojanovic-Susulic, V., Degroot, J., van Osch, G., et al. (2010). Association between weight or body mass index and hand osteoarthritis: a systematic review. *Ann. Rheum. Dis.* 69 (4), 761–765. doi:10.1136/ard.2008.106930

Zhang, F. J., Luo, W., and Lei, G. H. (2015). Role of HIF-1α and HIF-2α in osteoarthritis. *Jt. Bone Spine* 82 (3), 144–147. doi:10.1016/j.jbspin.2014.10.003

Zhang, H., Li, Q., Liu, R., Zhang, X., Li, Z., and Luan, Y. (2018). A versatile prodrug strategy to *in situ* encapsulate drugs in mof nanocarriers: a case of cytarabine-ir820 prodrug encapsulated zif-8 toward chemo-photothermal therapy. *Adv. Funct. Mater* 28 (35). doi:10.1002/adfm.201802830

Zhang, Y., Shen, X., Ma, P., Peng, Z., and Cai, K. (2019). Composite coatings of mg-mof74 and sr-substituted hydroxyapatite on titanium substrates for local antibacterial, anti-osteosarcoma and pro-osteogenesis applications. *Mater Lett.* 241 (C), 18–22. doi:10.1016/j.matlet.2019.01.033

Zhang, Z. J., Hou, Y. K., Chen, M. W., Yu, X. Z., Chen, S. Y., Yue, Y. R., et al. (2023). A pH-responsive metal-organic framework for the co-delivery of HIF-2α siRNA and curcumin for enhanced therapy of osteoarthritis. *J. Nanobiotechnology* 21 (1), 18. doi:10.1186/s12951-022-01758-2

Zheng, Z., Chen, Y., Guo, B., Wang, Y., Liu, W., Sun, J., et al. (2020). Magnesium-organic framework-based stimuli-responsive systems that optimize the bone microenvironment for enhanced bone regeneration. *Chem. Eng. J.* 396, 125241. doi:10.1016/j.cej.2020.125241

Zou, B., Xiong, Z., He, L., and Chen, T. (2022). Reversing breast cancer bone metastasis by metal organic framework-capped nanotherapeutics via suppressing osteoclastogenesis. *Biomaterials* 285, 121549. doi:10.1016/j.biomaterials.2022.121549

frontiers | Frontiers in Bioengineering and Biotechnology

TYPE Original Research
PUBLISHED 21 November 2024
DOI 10.3389/fbioe.2024.1501488

OPEN ACCESS

EDITED BY
Liqun Yang,
Shengjing Hospital of China Medical University, China

REVIEWED BY
Jing Zhao,
Zhejiang University, China
Richard J. A. Moakes,
University of Birmingham, United Kingdom

*CORRESPONDENCE
Shiqing Feng,
shiqingfeng@sdu.edu.cn
Hengxing Zhou,
zhouhengxing@sdu.edu.cn
Na Li,
lina09612@qiluhospital.com

†These authors have contributed equally to this work

RECEIVED 25 September 2024
ACCEPTED 30 October 2024
PUBLISHED 21 November 2024

CITATION
Zhang R, Zhang M, Chen L, Jiang L, Zou C, Li N, Zhou H and Feng S (2024) Dual-phase SilMA hydrogel: a dynamic scaffold for sequential drug release and enhanced spinal cord repair via neural differentiation and immunomodulation. *Front. Bioeng. Biotechnol.* 12:1501488. doi: 10.3389/fbioe.2024.1501488

Dual-phase SilMA hydrogel: a dynamic scaffold for sequential drug release and enhanced spinal cord repair via neural differentiation and immunomodulation

Ruizhi Zhang[1†], Mingzhe Zhang[1,2†], Lu Chen[1†], Linlin Jiang[1], Chenbo Zou[1], Na Li[1*], Hengxing Zhou[1,3*] and Shiqing Feng[1,4*]

[1]Department of Orthopaedics, Qilu Hospital, Shandong University Centre for Orthopaedics, Advanced Medical Research Institute, Cheeloo College of Medicine, Shandong University, Jinan, Shandong, China, [2]The 960th Hospital of the Joint Logistics Support Force of the Chinese People's Liberation Army, Jinan, China, [3]Center for Reproductive Medicine, Shandong University, Jinan, Shandong, China, [4]Department of Orthopaedics, The Second Hospital, Cheeloo College of Medicine, Shandong University, Jinan, Shandong, China

Introduction: Spinal cord injury (SCI) is a severe central nervous system disorder that results in significant sensory, motor, and autonomic dysfunctions. Current surgical techniques and high-dose hormone therapies have not achieved satisfactory clinical outcomes, highlighting the need for innovative therapeutic strategies.

Methods: In this study, we developed a Dual-Phase Silk Fibroin Methacryloyl (SilMA) hydrogel scaffold (DPSH) that incorporates PLGA microspheres encapsulating neurotrophin-3 (NT-3) and angiotensin (1-7) (Ang-(1–7)). The DPSH is designed for temporally controlled release of therapeutic agents to reduce inflammation during the acute phase of SCI and to promote neuronal differentiation and axonal regeneration in later stages.

Results: Comprehensive characterization of the DPSH revealed a highly porous architecture, suitable mechanical properties for spinal cord tissue, and stability unaffected by the incorporation of microspheres and drugs. In vitro studies demonstrated that Ang-(1–7) significantly induced M2 microglia polarization by 1.8-fold ($p < 0.0001$), effectively reducing inflammation. Additionally, NT-3 enhanced neural stem cell differentiation into neurons by 3.6-fold ($p < 0.0001$). In vivo experiments showed that the DPSH group exhibited significantly higher Basso Mouse Scale (BMS) scores ($p < 0.0001$), enhanced motor function, reduced astrocyte scarring by 54% ($p < 0.05$), and improved neuronal survival and regeneration.

Discussion: These findings underscore the therapeutic potential of the DPSH scaffold for SCI repair, presenting a novel strategy to enhance neural recovery through a combination of immunomodulation and neuroprotection.

KEYWORDS

spinal cord injury, SilMA hydrogel, neurotrophin-3, angiotensin-(1–7), immunomodulation, neural differentiation

1 Introduction

Spinal cord injury (SCI) is a severe central nervous system disorder with a poor prognosis, often resulting from traumatic incidents such as traffic accidents or falls from heights. It can also be caused by inflammation or tumors. SCI can lead to significant sensory, motor, or autonomic dysfunctions, drastically reducing patients' quality of life and imposing a heavy economic burden on families and society. In mammals, SCI triggers numerous pathological changes, including blood-brain barrier dysfunction, thrombosis, and neuronal death (Silva et al., 2021; Silva et al., 2014). Currently, clinical treatments for SCI include surgical and pharmacological approaches, but their effectiveness is limited. Surgical treatment cannot fully restore the anatomical structure of the damaged spinal cord and only addresses part of the primary injury, while oral or intravenous medications face challenges crossing the blood-spinal cord barrier to produce significant effects (Sanchez-Dengra et al., 2023; Shultz and Zhong, 2021).

Cell transplantation and *in situ* drug delivery are more effective strategies, providing cellular and nutritional support to the injured area (Lai et al., 2019; Ma et al., 2018). However, due to the lack of connectivity in the damaged region, transplanted cells or drugs struggle to establish cycles, preventing them from exerting their full potential (Sensharma et al., 2017).

SCI progresses through primary and secondary phases. The primary injury results from the initial trauma, causing mechanical disruption of the spinal cord's anatomical continuity, blood-spinal barrier damage, local edema, hemorrhage, ischemia, inflammatory cell infiltration, and axonal demyelination. The secondary injury, triggered by the primary injury, involves continued edema, ischemia, inflammatory cell infiltration, further cell death, and the release of toxic substances (Jin et al., 2021; Zhou et al., 2023). These processes promote the formation of cystic cavities and glial scars, which hinder axonal regeneration and functional recovery (McDonald and Sadowsky, 2002; Ahuja et al., 2017; O'Shea et al., 2017; Sofroniew, 2018).

Microglia, the central nervous system's macrophages, activate in response to SCI, re-leasing chemokines that attract immune cells to the injury site and exacerbate local dam-age. Activated microglia can polarize into M1 (pro-inflammatory) and M2 (anti-inflammatory) phenotypes. M1 microglia secrete TNF-α and IL-6, inducing inflammatory cascades, while M2 microglia secrete IL-10 and IL-4, alleviating inflammation and promoting repair (Orihuela et al., 2016). Currently, it is believed that cell death and scar formation due to an excessive local inflammatory response after spinal cord injury are significant barriers to nerve repair. Therefore, reducing M1 polarization of microglial cells and promoting M2 polarization after the injury to inhibit the local inflammatory response is a crucial research direction in spinal cord injury repair (Okada et al., 2022).

Studies show that anti-inflammatory factors such as IL-4, IL-10, and Ang-(1–7) can reduce inflammatory cell activation and acute inflammatory responses early in SCI, creating a favorable environment for repair (Saraiva and O'Garra, 2010; He et al., 2020; Pan et al., 2021; Gu et al., 2023). Neurotrophic factors like paclitaxel, NT-3, and NT-4 promote neuronal differentiation and axonal regeneration (NGF, 2014; Bao et al., 2022; Yan et al., 2023; Fukuyama et al., 2024). However, endogenous repair mechanisms often fall short due to insufficient recruitment of endogenous neural stem cells and excessive differentiation into astrocytes, forming glial scars that impede repair (Murk et al., 2013; Blanco-Suarez et al., 2017; Zhou et al., 2019; Endo et al., 2022; Hellenbrand et al., 2021).

Hydrogels are a polymer material with a three-dimensional network structure, using water as the dispersion medium, which is both biocompatible and degradable (Yuan et al., 2021). Hydrogel itself can mimic the natural extracellular matrix to fill the damaged area and improve the microenvironment of the damaged area. It can also act as a carrier for seed cells and active factors, helping seed cells to colonize and proliferate, promoting the reconnection of damaged spinal cord tissues, helping to bridge the gap at the injury site and re-establishing nerve conduction, and achieving sustained drug release. In current tissue engineering research for spinal cord injury treatment, hydrogel primarily serves the following roles: First, it provides three-dimensional spatial support for neuronal regeneration and axonal extension, facilitating cell growth, proliferation, and migration, and promoting neural reconstruction (Chedly et al., 2017; Silva et al., 2023); Second, hydrogel acts as a carrier, delivering stem cells to the injury site, thereby reducing cell loss (Peng et al., 2023). Third, hydrogel slowly releases bioactive factors or chemical drugs, ensuring continuous and stable release for improved therapeutic effects (Luo et al., 2021). Additionally, proteins or extracellular matrix components such as hyaluronic acid and filipin proteins, known for their biocompatibility and tissue affinity, and suitability for chemical and structural modifications (Gao et al., 2022), have also been used to synthesize hydrogel scaffolds. Currently, synthetic hydrogel raw materials commonly used in tissue engineering include polyacrylic acid and its derivatives, polyvinyl alcohol, and polyester (Anderson et al., 2018; Ranganathan et al., 2018; Han et al., 2022; Cai et al., 2023; Xiao et al., 2023).

Silk fibroin (SF) derived from processed silkworm silk is a promising biomaterial with excellent degradability, biocompatibility, and high tensile strength (Wen et al., 2016; Hoque et al., 2019). However, its water-insolubility and limited processability can restrict its applications. Methacrylated silk fibroin (SilMA), a modified form of SF, addresses these limitations by offering improved water solubility and the ability to be crosslinked into a gel under UV light. UV crosslinking allows for precise control over the gelation process, enabling tunable mechanical properties and rapid fabrication, making it particularly advantageous for biomedical applications. This approach also facilitates the incorporation of bioactive molecules and cells during gel formation, preserving their functionality. SilMA hydrogels combine the structural benefits of silk fibroin with the functional properties of hydrogel materials, such as controlled degradation and mechanical adaptability, making them a highly versatile and promising option for tissue engineering and regenerative medicine.

This study constructs a Dual-Phase SilMA hydrogel scaffold (DPSH), incorporating PLGA microspheres encapsulating neurotrophin-3 (NT-3) and angiotensin (Silva et al., 2021; Silva et al., 2014; Sanchez-Dengra et al., 2023; Shultz and Zhong, 2021; Lai et al., 2019; Ma et al., 2018; Sensharma et al., 2017) (Ang-(1–7), and neural stem cells. The hydrogel's degradation, in conjunction with PLGA microspheres, enables sequential drug release. Ang-(1–7) is released early to reduce inflammation and protect neurons, followed by the release of neurotrophic factors to promote neuronal differentiation and axonal regeneration. This precise regulation aims to neural function recovery post-SCI, offering a novel therapeutic approach.

2 Materials and methods

2.1 Experimental animals

Experimental animals were purchased from Beijing Viton Lihua Company, 6–8 weeks old C57BL/6J female mice, weighing 18–25 g. All animal procedures were approved by the Ethics Committee of Shandong University (Approval No. ecsbmssdu24019). During the experiment, the mice were housed in the SPF-grade animal room of Shandong University Experimental Animal Center with sufficient feed and water. The mice could freely eat, the temperature was set at 20°C–25°C, and the relative humidity was set at 40%–60%. The feeding and experimental handling process of the mice complied with the "Regulations on the Administration of Laboratory Animals" by the National Science and Technology Com-mission and fully followed the regulations of the Ethics Committee of Shandong University. All operators were trained according to relevant guidelines and regulations.

2.2 Experimental materials

The batch names, brands, and catalog numbers of all materials and reagents used in this study are detailed in Table 1.

TABLE 1 Materials used in the experiment.

Materials	Catalog number	Company name
DMEM	Cat#10566016	Gibco
B-27	Cat#17504044	Gibco
Penicillin-streptomycin	Cat#15140163	Gibco
Stem Pro Accutase	Cat#1110501	Gibco
papain	Cat#G8430	Solarbio
DNAse	Cat#D8071	Solarbio
PBS	Cat#P1022	Solarbio
FBS	Cat#SA101.02	CellMax
DAPI	Cat#C0065	Solarbio
Triton X-100	Cat#T8200	Solarbio
TWEEN-20	Cat#T8220	Solarbio
BSA	Cat#ST023	Beyotime
CCK-8	Cat#C0042	Beyotime
Calcein/Pl	Cat#C2015M	Beyotime
Anti-beta lIl Tubulin antibody	Cat#ab215037	Abcam
GFAP (GAS) Mouse mAb	Cat#3670	CST
SilMA	Cat# EFL-SilMA-001	Engineering For Life
Ang- (1–7)	Cat#12403	Sigma
LPS	Cat#L3024	Sigma
NT-3	Cat#N1905	Sigma

2.3 Preparation of SilMA hydrogel and PLGA microspheres

All SilMA hydrogels used in this study were purchased from Engineering For Life and were prepared for both *in vitro* and *in vivo* experiments through dissolution, filtration for sterilization, and UV cross-linking.

2.3.1 Preparation of SilMA hydrogel

A 0.25% (w/v) initiator solution was prepared by dissolving 0.05 g LAP in 20 mL PBS, heating in a 40°C–50°C water bath for 15 min, and shaking occasionally. An 8% SilMA hydrogel solution was created by weighing the required amount of SilMA, placing it in a centrifuge tube, and adding the initiator solution. The solution was dissolved at room temperature for 30 min, with occasional stirring. The SilMA solution was sterilized using a 0.22 μm sterile needle filter in a clean bench. The SilMA solution was injected into well plates (50 μL/well for 96-well plates, 100 μL/well for 48-well plates, and 300 μL/well for 24-well plates) and was irradiated with a 405 nm light source for 30 s to gel. Culture medium was added to cover the gel, incubated at 37°C for 5 min, then washed and the medium was removed. A cell suspension was added for culturing. For *in vivo* hydrogel scaffolds, the filtered solution was cross-linked with light and trimmed to the appropriate size. To ensure that all hydrogels experienced the same amount of UV energy during crosslinking, a standardized UV exposure protocol was used. Specifically, a uniform UV intensity was applied using a calibrated light source positioned at a fixed distance from the samples, ensuring consistent energy delivery. Additionally, the exposure time was precisely controlled for all samples to maintain consistent crosslinking. This method minimized variability in gelation and mechanical properties, ensuring reproducibility across experiments.

2.3.2 Preparation of PLGA microspheres

5 mg of NT-3 was dissolved in 1 mL deionized water (aqueous phase) and 100 mg of polylactic acid was dissolved in 4 mL dichloromethane and 1 mL acetone (organic phase). The aqueous and organic phases were mixed, then ultrasonicated in an ice bath at 100 W for 1 min to form a uniform dispersion. The mixture was slowly injected into 25 mL of 1% polyvinyl alcohol solution, and sonicated in an ice bath at 200 W for 3 min to form an emulsion. The emulsion was stirred at low speed (400 rpm) for 3–5 h to allow complete dispersion of dichloromethane and acetone. It was frozen and centrifuged at high speed (12000 rpm, 20 min) to separate the PLGA microspheres, which were washed three times with deionized water. The microspheres were freeze-dried, sterilized at 60°C, and stored at 4°C.

2.4 Preparation of DPSH scaffold

Using the same method as for SilMA hydrogel, an 8% hydrogel solution was prepared, dissolved thoroughly, and filtered for sterilization. Then, 10 μg/ml PLGA microspheres containing NT-3 and 5 μg/ml Ang-(1–7) were added to the neural stem cell pellet. The mixture was mixed well and injected into well plates, irradiated with a 405 nm light source for 30 s to gel. The same steps were followed for further processing.

2.5 Characterization of SilMA hydrogel and PLGA microspheres

2.5.1 SilMA hydrogel characterization

The mechanical properties of the hydrogel were measured at 25°C using a HAAKE MARS rheometer, calculating the elastic modulus (G′) and viscous modulus (G″). Mechanical properties were analyzed with a GT TCS-2000 single-column tester. Samples (n = 3) were formed into cylinders of 10 mm diameter and 3 mm height and tested at a 1 mm/min compression speed to determine the Young's modulus from the strain-stress curve slope. For the rheological characterization of the SilMA hydrogel, dynamic rheology experiments were conducted using a HAAKE MARS III photorheometer equipped with a parallel-plate geometry (P20 TiL, 20-mm diameter). Time-sweep oscillatory tests were performed under a 10% strain (in CD mode) with a frequency of 1 Hz and a 0.5 mm gap over 180 s.

2.5.2 PLGA microspheres characterization

The size and morphology of PLGA microspheres were observed under a scanning electron microscope (SEM, Philips XL-30) at a 10 kV acceleration voltage.

2.5.3 *In vitro* drug release

20 mg of each drug-loaded material was weighed, dissolved in 20 mL PBS (Wu et al., 2022), and incubated at 37°C on a constant temperature shaker. At specified intervals (1, 3, 7, 14, 21, 28, 35, 42, 49, and 56 days), the samples were centrifuged at 2000 rpm for 10 min, 1 mL of supernatant was removed, replaced with fresh PBS, and incubation continued. All supernatants were collected and drug content was measured using ELISA kits, plotting the drug release curve over time. This process has the potential to alter the drug concentration and the driving force for release. To ensure accuracy, we factored in both the amount of drug present in the removed PBS and the concentration remaining in the hydrogel. By doing so, we adjusted for any dilution effect caused by the PBS replenishment. This approach allowed us to accurately track the cumulative drug release over time, even as PBS was refreshed. The resulting release profile reflects the actual total drug release, maintaining the integrity of the study despite the replenishment process.

2.6 Cell culture

The water bath was preheated to 37°C. Frozen cells were retrieved from −80°C storage and thawed quickly in the water bath, shaking gently until ice crystals dissolved. The vial was disinfected with 75% alcohol, placed in a sterile workbench, and the cell suspension was transferred to a 10 mL centrifuge tube with 4 mL complete medium. The tube was centrifuged at 1000 rpm for 3 min, the supernatant was removed, and the cells were resuspended in 1 mL complete medium and plated in a 6 cm culture dish with 3 mL complete medium. When cells reached 70%–80% confluence, sterile PBS, trypsin, and complete medium were warmed in a 37°C water bath. The medium was removed, the cells were washed with 1 mL PBS twice, and 1 mL trypsin was added. The cells were incubated until they began to detach. Digestion was stopped with 2 mL complete medium, the cells were collected in a 10 mL centrifuge tube, and centrifuged at 1000 rpm for 3 min. The cells were resuspended in complete medium, replated, and incubated at 37°C, 5% CO2. When cells were in good condition, sterile PBS, trypsin, and complete medium were prepared as described. Cells were detached with trypsin, digestion was stopped, the cells were centrifuged, and resuspended in 900 μL fetal bovine serum and 100 μL DMSO. The suspension was transferred to cryovials, placed in a freezing container, and stored at −80°C.

2.7 Isolation and culture of mouse neural stem cells

Instruments and materials were sterilized, plates were prepared with poly-L-lysine, and all required solutions were readied in a sterile environment. Pregnant mice were euthanized, disinfected in 75% alcohol, and transferred to a sterile workbench. Embryos were extracted, and their heads were placed in pre-cooled high-glucose medium. The cerebral cortex was isolated, removing meninges and other tissues, and transferred to new dishes for mincing. The samples were centrifuged at 1200 rpm for 5 min, resuspended in papain and DNAse, digested at 37°C, and then centrifuged again. The solution was filtered through a 40μm mesh, and the cells were counted. Cells were plated in T75 flasks with proliferation medium, incubated at 37°C, 5% CO_2, and the medium was changed as needed. Cells were passaged when neurospheres grew large and opaque. Finally, cells were plated in differentiation medium with hydrogel scaffolds in Transwell inserts.

2.8 CCK8 assay

Neural stem cells were plated in 96-well plates with varying concentrations of SilMA hydrogel solution. The cells were incubated for 3 days, after which the medium was replaced with medium containing 10% CCK8 reagent. The plates were incubated for 2 h, and absorbance was measured at 450 nm.

2.9 Microglia inflammation induction and staining

BV2 microglial cells were plated on poly-L-lysine-coated 24-well plates, and inflammation was induced using lipopolysaccharide (LPS) to activate the cells. Simultaneously, a Transwell system was used, with a drug-loaded hydrogel placed in the upper chamber and BV2 cells in the lower chamber, to assess the hydrogel's impact on inflammation over 24 h. After 24 h of co-culture with the hydrogel, the BV2 cells were fixed, permeabilized, and blocked. The cells were incubated with primary antibodies (anti-iNOS for M1 macrophages, anti-ARG-1 for M2 macrophages) and then with fluorescently labeled secondary antibodies (488 anti-mouse, 555 anti-rabbit). Finally, the nuclei were stained with DAPI, and the cells were observed under a fluorescence microscope to evaluate the expression of inflammatory markers and the effect of the hydrogel on inflammation.

2.10 Live/dead cell staining

After culturing the cells with 1% SilMA hydrogel for 3 days, the cells were stained with Calcein AM/PI, incubated, and observed under a fluorescence microscope.

2.11 Neural stem cell differentiation and staining

To differentiate neural stem cells with hydrogel scaffolds, a Transwell system was used for a 7-day co-culture. The hydrogel scaffold was placed in the upper chamber, and neural stem cells were placed in the lower chamber, allowing for sustained release of therapeutic agents from the hydrogel while maintaining proximity to the cells. After 7 days of co-culture, the cells were fixed, permeabilized, and blocked. Next, the cells were incubated with primary antibodies (anti-Tuj-1 to identify neurons, anti-GFAP to identify astrocytes) to assess differentiation. Following primary antibody incubation, the cells were treated with appropriate secondary antibodies, their nuclei were stained with DAPI, and they were observed under a fluorescence microscope to evaluate the extent of neural differentiation and astrocyte formation.

2.12 *In vivo* degradation of hydrogel

Mice were acclimated, instruments were sterilized, and subcutaneous implantation of 100 μg hydrogel was performed. Post-surgery, antibiotics were administered, and hydrogel degradation was measured at set intervals.

2.13 Establishment of mouse SCI model

After a 1-week acclimatization period, mice were anesthetized with isoflurane (RWD, R510-22, Guangdong, China) to establish a spinal cord injury model. A longitudinal incision was made over the T10 vertebra, the muscles were gently separated, and the T9-T11 spinal segments were exposed. A complete laminectomy at T10 was performed, followed by a 2 mm complete transection of the spinal cord. Successful model establishment was confirmed, and the incision was sutured in layers.

2.14 Behavioral testing

BMS scores were evaluated using the BMS mouse scale guidelines at pre-SCI, day 1, day 7, and weekly up to 8 weeks post-SCI by three blinded observers. Prior to testing, mice were acclimatized to the testing environment. The open field was surrounded by a trans-parent glass plane, enabling observers to assess hind limb joint movement, weight sup-port, plantar stepping, and coordination. BMS scores ranged from 0 (no ankle movement) to 9 (full recovery) and were recorded to measure hind limb motor function.

2.15 Preparation of frozen sections

Mice were transcardially perfused with pre-cooled PBS until the effluent from the right atrium was clear and the liver appeared pale. Subsequently, pre-cooled 4% para-formaldehyde was perfused, and the spinal cord was harvested. Spinal cord tissues were fixed overnight at 4°C in 4% paraformaldehyde, dehydrated in sucrose solution, embedded in OCT, and sectioned at 10 μm thickness using a cryostat (Leica, CM3050S, Germany). Sections were cut at a thickness of 10 μm to balance tissue detail and structural integrity. The cryostat temperature was set at −20°C to prevent ice crystal formation and tissue damage.

2.16 Immunohistochemical staining

The frozen sections were rinsed with distilled water for 10 min to remove excess embedding medium. A histochemical pen was used to outline the areas for staining. The sections were placed in a humid chamber, and a blocking and permeabilization solution containing 5% BSA and 0.5% Triton X-100 was added. The sections were incubated at room temperature for 1 h to block non-specific antigen sites and permeabilize the cells. After blocking, primary antibodies, including anti-Tuj-1 antibody (1:200), anti-GFAP antibody (1:200), anti-iNOS antibody (1:200), and anti-Arg-1 antibody (1:200), were applied to the sections. The sections were covered with a coverslip and were incubated overnight at 4°C. The next day, the sections were washed three times with TBST solution for 5 min each. Fluorescent secondary antibodies, including 488 anti-mouse antibody (1:400) and 555 anti-rabbit antibody (1:400), were applied to the sections, followed by a 1-h incubation at room temperature in the dark. The sections were washed three times with TBST solution for 5 min each to remove residual secondary antibodies. An appropriate amount of DAPI-containing antifade mounting medium was added to the spinal cord sections. A coverslip was carefully placed on top, ensuring no air bubbles were trapped. The edges of the coverslip were sealed with nail polish. Immunofluorescence staining was observed under a fluorescence microscope, and images were captured for further analysis.

2.17 Hematoxylin and eosin staining

Frozen sections were rinsed with distilled water three times for 5 min each to remove excess embedding medium. The sections were placed in hematoxylin stain for 2 min, then were rinsed under running water until the tissue turned blue. The sections were dipped in 1% hydrochloric acid alcohol for approximately 3 s, then were rinsed under running water for 1 min. The sections were stained with eosin for 3 min, followed by a 1-min rinse under running water. Sequentially, the sections were placed in 80% ethanol, 95% ethanol, and absolute ethanol for 5 min each. The sections were transferred into xylene I and xylene II, each for 5 min. The sections were mounted with neutral resin and observed under a microscope.

2.18 Protein extraction

The lysis buffer, containing RIPA and PMSF in a 1000: 1 ratio, was prepared and kept on ice. The culture medium was discarded, and the cells were rinsed with PBS. Lysis buffer was added to the cells, and they were incubated on ice for 10 min. The cells were scraped into 1.5 mL centrifuge tubes and were sonicated for 1 min. Fresh spinal cord tissue was collected from the injury site and adjacent segments (each 0.5 mm), placed in 1.5 mL centrifuge tubes on ice, lysis buffer was added, and the tissue was homogenized until no visible fragments remained. The lysates were incubated on ice for 10 min. The centrifuge was pre-cooled to 4°C, and the lysates were centrifuged at 12000 rpm for 30 min. The supernatant was transferred to a new tube, and the protein concentration was determined. Loading buffer was added, the solution was heated at 95°C for 10 min to denature the proteins, and the samples were stored at −20°C.

2.19 BCA protein assay

A series of BSA standards with an initial concentration of 5 mg/ml and final concentrations ranging from 0.078125 mg/ml were prepared. Reagent A and reagent B were mixed in a 50: 1 ratio to prepare the BCA working reagent. 20 μL of each standard and protein sample were added to a 96-well plate, followed by 200 μL of BCA working reagent in each well. The mixture was incubated at 37°C for 30–40 min, avoiding light. Absorbance was measured at 562 nm using a microplate reader, and protein concentrations were calculated from the standard curve.

2.20 Western blot analysis

The gel apparatus and glass plates were assembled, filled with water, and checked for leaks. Once confirmed leak-free, the gel preparation was started. SDS-PAGE gels, appropriate for the target protein's molecular weight, were prepared. The separating gel was poured between the glass plates and overlaid with water, then allowed to polymerize for 30–60 min. After removing the water, the stacking gel was added, and the comb was inserted. The gel was allowed to polymerize completely. Frozen protein samples were thawed on ice and loaded into the gel wells along with the protein ladder as a molecular weight marker. The gel was run at 80 V until the samples entered the separating gel, then the voltage was increased to 120 V until the dye front reached the bottom. The gel apparatus was disassembled, and the gel was trimmed. The PVDF membrane was activated in methanol. The transfer sandwich was assembled, and proteins were transferred at 100 V constant voltage. The membrane was blocked with 5% BSA in TBST for 1 h at room temperature to prevent non-specific binding. The membrane was incubated overnight at 4°C with primary antibodies (e.g., anti-β-actin, anti-iNOS, anti-Arg-1, anti-GFAP, anti-Tuj-1, all at 1: 1000 dilution). The membrane was washed three times with TBST and incubated with HRP-conjugated secondary antibodies (goat anti-rabbit IgG or goat anti-mouse IgG, 1:10,000) for 1 h at room temperature. The ECL detection reagent was prepared according to the manufacturer's instructions, applied to the membrane, and the protein bands were visualized using a chemiluminescence imaging system.

2.21 Statistical analysis

All data were analyzed with GraphPad Prism 8.0 (GraphPad Software, USA), and the values are presented as the mean ± standard error of the mean (SEM); each value represents the average of three independent experiments. Statistical significance was deter-mined by the independent sample *t*-test when two groups were being compared, by one-way analysis of variance (ANOVA) followed by Bonferroni *post hoc* analysis for multiple comparisons when three or more groups were being compared. Statistical significance is defined as $P < 0.05$, with * indicating $P < 0.05$, ** indicating $P < 0.01$, *** indicating $P < 0.001$, **** indicating $P < 0.0001$. Non-significant differences are marked as ns.

3 Results and discussion

3.1 Material characterization

The images showing appearance changes before and after hydrogel formation are presented in Figure 1B. To assess whether the structure of SilMA hydrogel is suitable for carrying drugs and cells for spinal cord injury repair, its microstructure was examined using scanning electron microscopy (SEM). The results showed that the SilMA hydrogel exhibits a porous network structure with high porosity (Figure 1C). This structure is capable of carrying drugs, cells, and microspheres, serving as a channel for material exchange within the body and providing the necessary space for injury repair.

Due to the excellent biocompatibility and biodegradability of poly (lactic-co-glycolic acid) (PLGA), PLGA microspheres were used in this study to encapsulate NT-3. This approach prevents the rapid release of NT-3 *in vivo*, ensuring its prolonged presence at the injury site, particularly maintaining high concentrations during the later stages of repair. SEM observations revealed that the microspheres were well-dispersed without aggregation (Figure 1D). Analysis of SEM images using ImageJ software determined that the size and particle size distribution were approximately 200 μm (Figure 1E). This indicates that the microspheres can be evenly distributed within the hydrogel and released gradually as the hydrogel degrades, thereby achieving sustained drug release. These results demonstrate that well-formed NT-3-loaded PLGA microspheres were successfully fabricated for this study.

We also tested the Energy, Intensity, Absorbance, and Swelling rate of the hydrogels, both with and without drug loading. The results showed no significant differences be-tween the drug-loaded hydrogels and the standard SilMA hydrogels (Figures 1F–I). X-ray diffraction (XRD) patterns further confirmed that the diffraction peak positions and intensities remained unchanged across the three hydrogel groups, indicating that the in-corporation of drugs and PLGA microspheres did not alter the protein structure of the SilMA

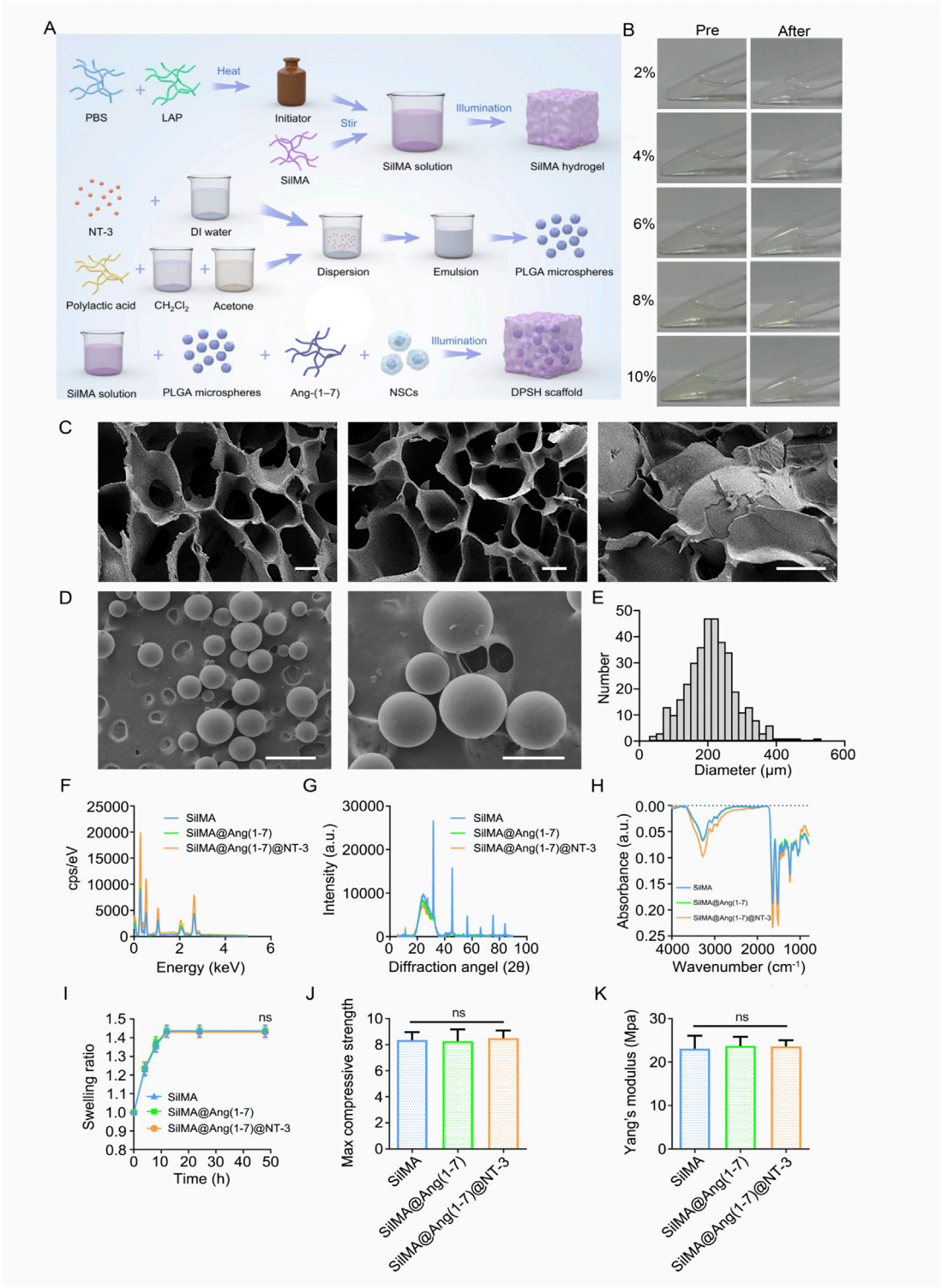

FIGURE 1
Preparation and Characterization of SilMA Hydrogel. **(A)** Schematic diagram of 4-Dimensional SilMA Hydrogel synthesis steps **(B)** Images of SilMA hydrogel before and after formation. **(C)** SEM images of SilMA hydrogel, scale bar = 20 μm. **(D)** SEM images of NT-3 encapsulated PLGA microspheres, scale bars = 500 μm (left) and 200 μm (right). **(E)** Particle size distribution of PLGA microspheres. **(F)** Energy profiles of SilMA hydrogels with different components. **(G)** X-ray diffraction patterns of SilMA hydrogels with different components. **(H)** Absorbance spectra of SilMA hydrogels with different components. **(I)** Swelling rates of SilMA hydrogels with different components. **(J)** Maximum compressive strength of SilMA hydrogels with different components. **(K)** Young's modulus of SilMA hydrogels with different components.

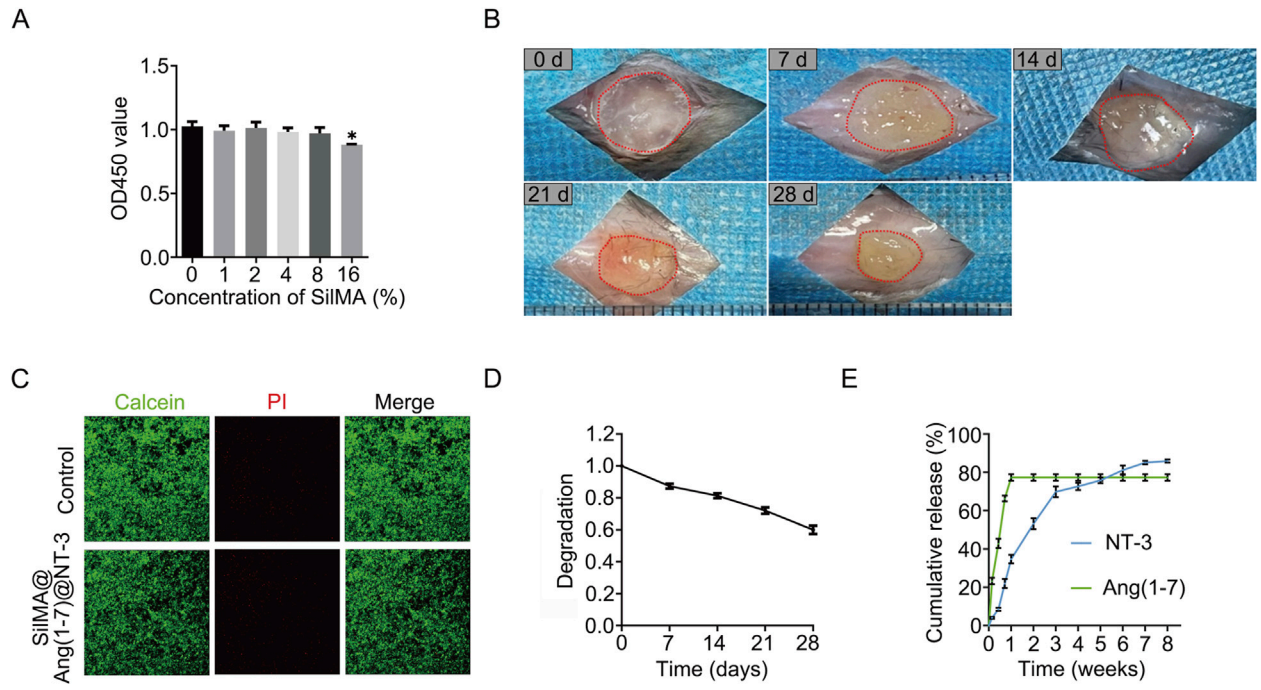

FIGURE 2
Degradation Rate, Sustained Release Capability, and Biocompatibility of SilMA Hydrogels. **(A)** CCK8 assay results of neural stem cells cultured with SilMA hydrogels at different concentrations. **(B)** Degradation images of SilMA hydrogels in mice over the first 4 weeks. **(C)** Live/dead staining results of neural stem cells co-cultured with SilMA hydrogels, scale bar = 100 μm. **(D)** Degradation curve of SilMA hydrogels in mice over the first 4 weeks. **(E)** Drug release curves of SilMA hydrogels loaded with Ang-(1–7) and NT-3 encapsulated in PLGA microspheres.

hydrogels (Figure 1G). Additionally, the Young's modulus and maximum com-pressive strength of the SilMA, SilMA/Ang-(1–7), and SilMA/Ang-(1–7)/NT-3 hydrogels showed no significant differences (Figures 1J,K). This suggests that the addition of drugs and PLGA microspheres does not adversely affect the mechanical properties of the hydrogels. In summary, the 8% concentration of SilMA hydrogel demonstrated the best structural integrity during handling and exhibited optimal mechanical properties suitable for further experimental applications. This concentration was robust enough to support subsequent cellular interactions and drug release studies while also ensuring adequate diffusion of therapeutic agents. Based on these visual observations and practical evaluations, the 8% concentration was chosen for all subsequent experiments, as it provided the right balance between handling ease and experimental consistency, making it ideal for both *in vitro* and *in vivo* settings.

3.2 Biocompatibility and cytotoxicity of SilMA hydrogel

The biocompatibility of a material is a crucial factor influencing its potential applica-tions. The CCK8 assay is a commonly used method for analyzing cell proliferation. To determine whether SilMA affects the proliferation of neural stem cells, the cells were cultured in media containing different concentrations of SilMA under *in vitro* conditions. After 3 days of culture, the CCK8 reagent was added to assess cell proliferation. The results showed that only in the group with a SilMA concentration higher than 16% was the proliferation of neural stem cells inhibited. No statistically significant differences were observed between the lower concentration experimental groups and the control group (Figure 2A). This indicates that SilMA has good biocompatibility and confirms that using an 8% concentration in this study is safe.

Besides the effect on proliferation, it is crucial to assess whether the material causes cytotoxicity, leading to cell death, as this is a critical factor for the success of transplantation. Live/Dead staining is a method used to assess cell viability based on esterase activity and membrane integrity. Commercial kits facilitate this analysis using the dual fluorescence staining method of Calcein-AM (Calcein) and Propidium Iodide (PI). Calcein-AM stains live cells green, while PI stains dead cells red. Similar to the previous method, after 3 and 7 days of culture, no significant cell death was detected, indicating that SilMA has excellent biosafety and does not cause tissue cell death when implanted *in vivo* (Figure 2C).

3.3 Degradation of SilMA hydrogel

During the acute and subacute phases of spinal cord injury, the local environment undergoes significant changes, including severe bleeding, ischemia, and cell necrosis. Hydrogels implanted at the injury site can fill the damaged area and help stop bleeding, thereby reducing secondary damage. However, the degradation rate of the hydrogel is crucial for spinal cord repair. If it degrades too quickly, it will lose its function as a filler; if it degrades too slowly, it can

interfere with normal tissue regeneration and impede repair. To assess the *in vivo* degradation of SilMA hydrogel, it was implanted subcutaneously in mice (n = 3 per group) and observed for 4 weeks. The results showed that the hydrogel gradually degraded over this period, reaching 62% of its original size by the fourth week (Figures 2B, D). This indicates that the SilMA hydrogel can provide long-term support during the spinal cord injury repair process. We initially chose subcutaneous injection for degradation studies due to its simplicity and standardization. However, recognizing that *in-situ* injection at the spinal cord injury site would more accurately represent real conditions, we will adapt this approach in future studies. Furthermore, While the 28-day results clearly showed that the hydrogel underwent significant degradation, leading to the effective release of Ang-(1–7) and achieving our early anti-inflammatory objectives, we recognize the importance of monitoring the hydrogel's performance over a more extended period. Future studies will include longer-term degradation assessments, such as up to 8 weeks, to provide a more comprehensive understanding of the hydrogel's stability and its sustained release profile, especially concerning the prolonged effects of NT-3 on neural regeneration. In general, PLGA degradation can take several weeks to months, providing a sustained release profile for encapsulated agents like NT-3. In our study, although we did not directly measure PLGA degradation rates, similar experiments (Jusu et al., 2020) suggests that PLGA with similar properties to what was used in our system undergoes gradual hydrolysis, which would release NT-3 over an extended period. This slow degradation is essential for ensuring the availability of NT-3 during the later stages of SCI repair, when neuronal differentiation and axonal regeneration are critical for functional recovery. By delivering NT-3 in a controlled and sustained manner, PLGA microspheres help maintain a neurotrophic environment, supporting long-term tissue regeneration.

3.4 Drug release of Ang-(1–7) and NT-3

The local accumulation of endogenous neurotrophic and anti-inflammatory factors is insufficient to mitigate the adverse effects of spinal cord injury, making drug delivery and release a critical aspect of the repair process. The release profiles of the two drugs incorporated into the SilMA hydrogel were assessed using ELISA kits. As shown in Figure 2E, the hydrogel released over 40% of Ang-(1–7) within the first 3 days and nearly all of it within 7 days. This indicates that the SilMA hydrogel has excellent substance ex-change capabilities, enabling a substantial early release of Ang-(1–7) to inhibit local inflammatory responses and improve the inflammatory microenvironment at the injury site. This helps reduce inflammation, protect nerve cells, and create a favorable environment for subsequent neural repair. Due to the encapsulation by PLGA, NT-3 was released slowly and continuously, with approximately 14% still being released between days 28 and 56. This sustained release of neurotrophic factors during the later stages of injury can promote the differentiation of neural stem cells into neurons and axonal regeneration, thereby facilitating the recovery of neural function. We chose PBS for the initial drug release study to maintain reproducibility and control over experimental variables. PBS provides a stable, physiologically relevant environment without introducing external biological factors such as enzymes or proteins, which could complicate the analysis. This allowed us to focus on understanding the fundamental release mechanisms of the drugs within the hydrogel. We acknowledge the limitations of using PBS as the release medium. While PBS is commonly used in in vitro studies for its simplicity and reproducibility, we recognize that it does not fully replicate the complex *in vivo* environment, particularly the oxidative stress and elevated levels of reactive oxygen species (ROS), such as H2O2, present in injury sites like the spinal cord. In future studies, we aim to address this by incorporating conditions that mimic the inflammatory and oxidative stress environments, such as using PBS supplemented with elevated H2O2 levels. Moving forward, we will integrate more physiologically relevant conditions into our experimental setup to enhance the applicability of our findings to clinical settings.

3.5 Ang-(1–7) promotes microglia polarization towards M2 phenotype in vitro

Local inflammatory responses after spinal cord injury are a major cause of cell death during the acute phase. The accumulation of inflammatory cytokines and infiltration of inflammatory cells not only lead to cell death but also contribute to the formation of spinal cord cysts from macrophage death during the subacute and chronic phases, severely hindering injury repair. Additionally, studies have shown that reducing the inflammatory response after spinal cord injury can decrease glial scar formation, promoting axonal re-generation and functional recovery of the spinal cord.

To investigate this, an *in vitro* model was established using lipopolysaccharide (LPS) to induce acute inflammation in mouse microglia (BV2 cells), simulating the acute in-flammatory process. LPS can polarize BV2 cells towards the M1 phenotype. The experimental group consisted of SilMA hydrogel loaded with Ang-(1–7), co-cultured with BV2 cells using Transwell inserts. Immunofluorescence staining and Western blot (WB) analysis were then performed to observe the effect of Ang-(1–7) on microglial polarization.

Immunofluorescence staining results indicated that in an inflammatory environment, the presence of Ang-(1–7) led to fewer M1-polarized microglia and more M2-polarized microglia (Figures 3A–D). In addition, this study examined the expression levels of iNOS and Arg-1 proteins in BV2 cells from different treatment groups. The Western blot (WB) results showed a trend consistent with the immunofluorescence findings. Compared to the LPS group, the Ang-(1–7) group exhibited reduced expression of iNOS, a marker of M1 cells, and increased expression of Arg-1, a marker of M2 cells (Figures 3E–G). This indicates that Ang-(1–7) promotes the polarization of microglia towards the M2 phenotype, which suppresses inflammatory responses and improves the local microenvironment at the injury site.

3.6 NT-3 promotes neural stem cell differentiation into neurons in vitro

The differentiation direction of neural stem cells is a critical factor in spinal cord in-jury repair. The survival and differentiation of neural stem cells determine the extent of neural repair. Neural

10.3389/fbioe.2024.1501488

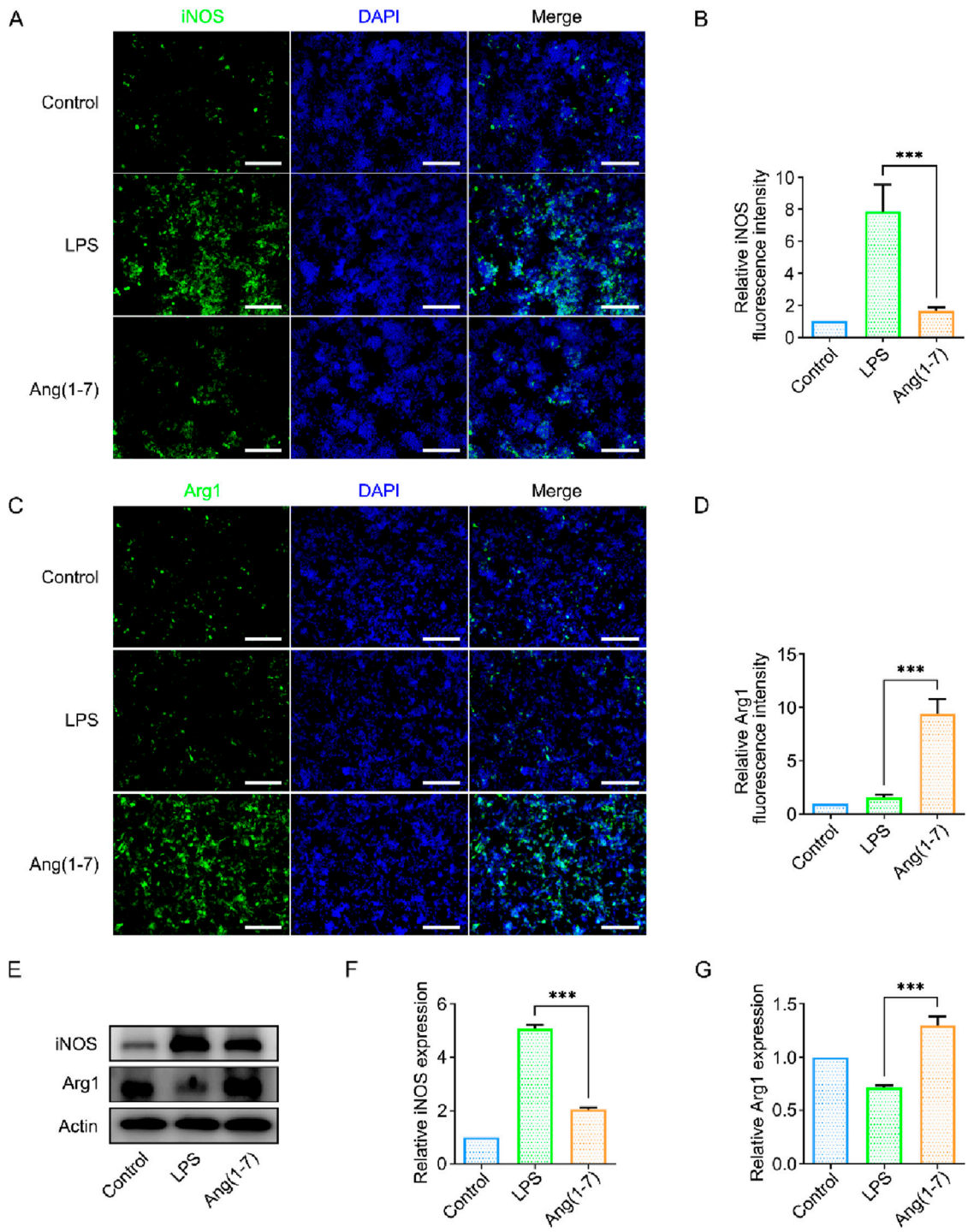

FIGURE 3
Validation of the Effect of Ang-(1–7) on BV2 Cell Polarization *In Vitro*. **(A)** Immunofluorescence images of iNOS (green) in cells from different treatment groups, scale bar = 100 μm. **(B)** Quantification of relative fluorescence intensity of iNOS. **(C)** Immunofluorescence images of Arg1 (green) in cells from different treatment groups, scale bar = 100 μm. **(D)** Quantification of relative fluorescence intensity of Arg1. **(E)** Western blot images of iNOS and Arg1 protein expression in different treatment groups. **(F)** Quantification of iNOS expression levels in different treatment groups. **(G)** Quantification of Arg1 expression levels in different treatment groups.

stem cells have the potential to differentiate into three lineages: astrocytes, neurons, and oligodendrocytes. Among these, astrocytes and neurons are the most important cell types affecting spinal cord injury repair. I In most cases, exogenous neural stem cells predominantly differentiate into astrocytes rather than neurons, both *in vivo* and *in vitro*, which hinders neural function repair. In this study, neural stem cells were co-cultured with NT-3-loaded SilMA hydrogel using Transwell inserts. Neural stem cells cultured

10.3389/fbioe.2024.1501488

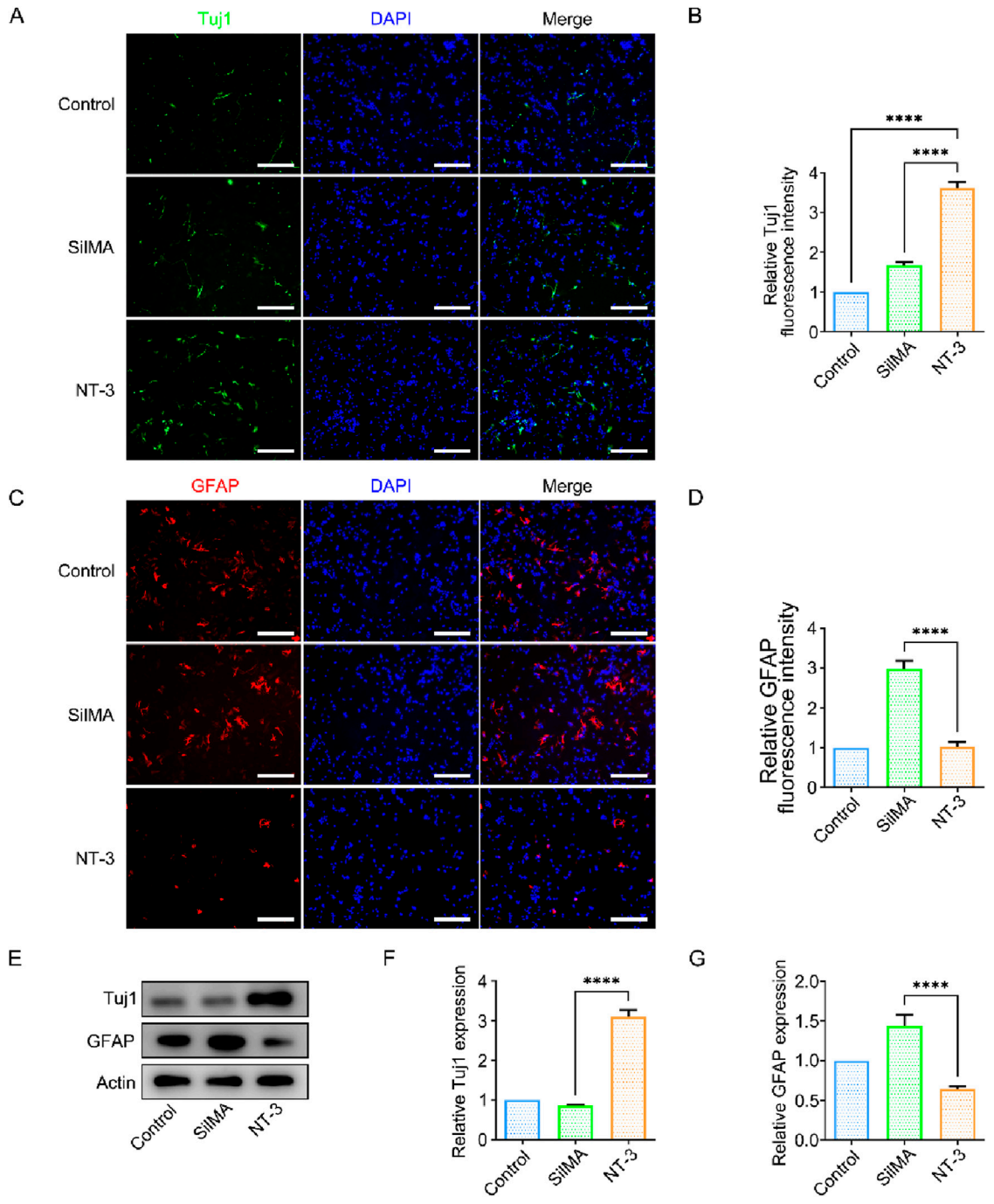

FIGURE 4
Effect of NT-3 on Neural Stem Cell Differentiation. **(A)** Immunofluorescence im-ages of Tuj-1 (green) in cells from different treatment groups, scale bar = 100 μm. **(B)** Quantification of relative fluorescence intensity of Tuj-1. **(C)** Immunofluorescence images of GFAP (red) in cells from different treatment groups, scale bar = 100 μm. **(D)** Quantification of relative fluorescence intensity of GFAP. **(E)** Western blot images of Tuj-1 and GFAP protein expression in different treatment groups. **(F)** Quantification of Tuj-1 expression levels in different treatment groups. **(G)** Quantification of GFAP expression levels in different treatment groups.

without hydrogel were used as the control group. Immunofluorescence staining was performed using the neuron-specific marker β-III tubulin (Tuj-1) and astrocyte-specific marker glial fibrillary acidic protein (GFAP). The results showed a higher proportion of Tuj-1-positive cells and a lower proportion of GFAP-positive cells in the experimental group compared to the control group (Figures 4A–D). This indicates that the NT-3-loaded SilMA hydrogel promotes a higher differentiation rate of neural stem cells into neurons while reducing their differentiation into astrocytes. This suggests that

10.3389/fbioe.2024.1501488

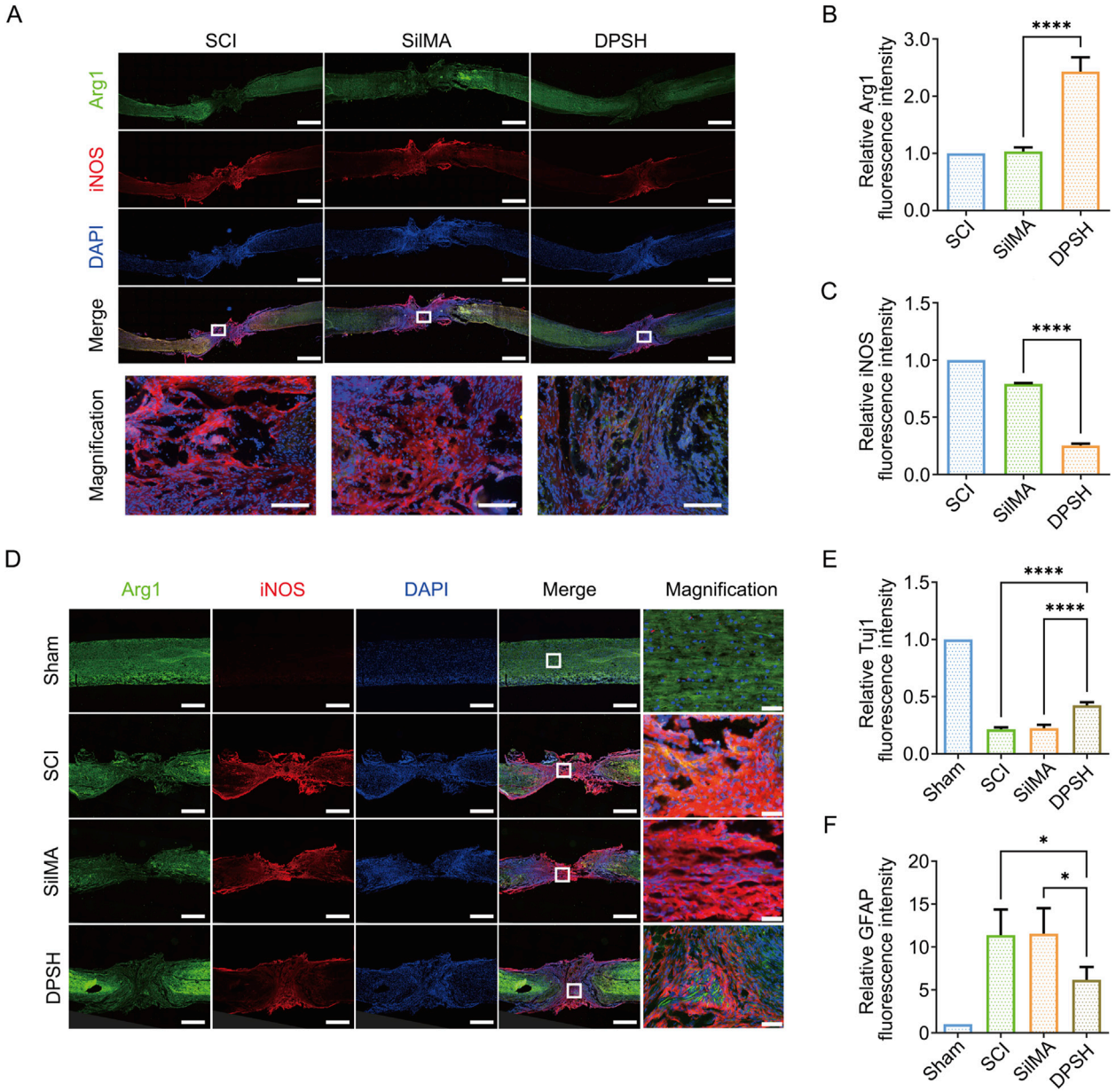

FIGURE 5
Immunofluorescence Staining and Quantitative Analysis of Spinal Cord in Mice 8 Weeks Post-SCI. **(A)** Immunofluorescence staining of Arg-1 (green) and iNOS (red) in the spinal cord of mice from different treatment groups 8 weeks post-SCI, scale bar = 500 μm. **(B)** Quantification of Arg-1 fluorescence intensity in the spinal cord of mice from different treatment groups. **(C)** Quantification of iNOS fluorescence intensity in the spinal cord of mice from different treatment groups. **(D)** Immunofluorescence staining of Tuj-1 (green) and GFAP (red) in the spinal cord of mice from different treatment groups 8 weeks post-SCI, scale bar = 500 μm. **(E)** Quantification of Tuj-1 fluorescence intensity in the spinal cord of mice from different treatment groups. **(F)** Quantification of GFAP fluorescence intensity in the spinal cord of mice from different treatment groups.

NT-3 plays a significant role in directing neural stem cell differentiation towards neurons, which is beneficial for spinal cord injury repair. Furthermore, Western blot analysis was performed to verify the expression of Tuj-1 and GFAP proteins in the cells. The results showed that the expression of Tuj-1 in the NT-3-loaded SilMA hydrogel group was significantly higher than in the control group and the SilMA hydrogel group, while the expression of GFAP was lower (Figures 4E–G). This confirms that NT-3 at the experimental concentration can regulate the differentiation of neural stem cells towards neurons and reduce their differentiation into astrocytes. These findings validate the results obtained from the immunofluorescence experiments.

3.7 Enhanced microglia polarization and neural regeneration with DPSH in vivo

The local inflammatory response after spinal cord injury is a critical factor influencing the repair process. *In vivo* experiments have shown that SilMA hydrogel loaded with Ang-(1–7) promotes the

10.3389/fbioe.2024.1501488

differentiation of microglia into the M2 phenotype, thereby reducing the inflammatory response and creating a favorable microenvironment for spinal cord injury repair. I Immunofluorescence staining of spinal cord tissue cryosections revealed that the proportion of Arg-1-positive cells in the group treated with DPSH loaded with Ang-(1–7) and NT-3 was significantly higher than in the injury group and the SilMA hydrogel group, while the proportion of iNOS-positive cells was significantly lower (Figures

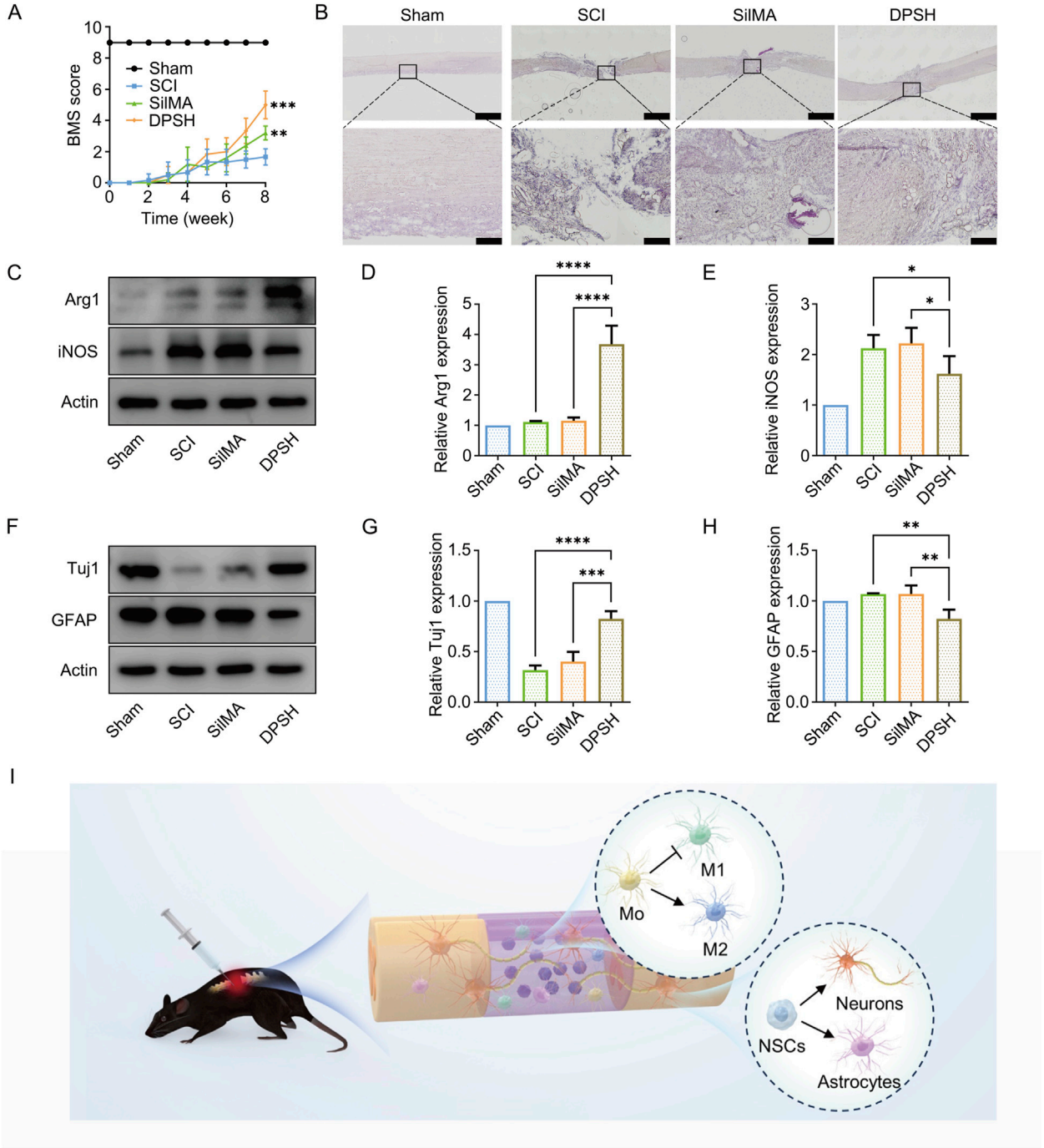

FIGURE 6
Validation of Motor Function and WB Quantitative Analysis in Mice 8 Weeks Post-SCI. **(A)** BMS scores of mice from different groups 8 weeks post-SCI. **(B)** HE staining results of spinal cord in mice from different groups 8 weeks post-SCI. **(C)** Western blot images of Arg-1 and iNOS protein expression in the spinal cord of mice from different treatment groups. **(D)** Quantification of Arg-1 expression in the spinal cord of mice from different treatment groups. **(E)** Quantification of iNOS expression in the spinal cord of mice from different treatment groups. **(F)** Western blot images of Tuj-1 and GFAP protein expression in the spinal cord of mice from different treatment groups. **(G)** Quantification of Tuj-1 expression in the spinal cord of mice from different treatment groups. **(H)** Quantification of GFAP expression in the spinal cord of mice from different treatment groups. **(I)** Schematic diagram of 4-Dimensional SilMA Hydrogel *in vivo* repair of spinal cord injury.

5A–C). This indicates that the DPSH promotes the polarization of microglia to the anti-inflammatory M2 phenotype and reduces M1 polarization at the in-jury site *in vivo*, thereby mitigating the inflammatory response and creating a conducive microenvironment for spinal cord injury repair. These findings suggest that the DPSH not only supports the structural integrity of the spinal cord but also actively modulates the immune environment, promoting better outcomes in spinal cord injury re-pair.

Neurons and synapses are fundamental structures for neural function. The differentiation of neural stem cells into neurons and the regeneration of axons are essential for neural function repair. However, changes in the local microenvironment of spinal cord injury, as well as the differentiation of astrocytes and the formation of glial scars, impede neural regeneration. Reducing scar formation is crucial for spinal cord injury repair and functional recovery. To observe the differentiation of endogenous stem cells and the ultimate outcome of spinal cord injury repair, spinal cord tissue was collected 8 weeks post-injury for protein extraction. Immunofluorescence staining was also performed on spinal cord tissue cryosections, with Tuj-1 staining marking early neurons and GFAP staining marking astrocytes. The results indicate that in the central injury area, the pro-portion of Tuj-1-positive cells in the group treated with DPSH loaded with Ang-(1–7) and NT-3 was higher than in the SCI group and the SilMA hydrogel group, while the proportion of GFAP-positive cells was lower (Figures 5D–F). This suggests that more neurons were regenerated in the DPSH group, demonstrating that NT-3 loaded in the DPSH promotes the differentiation of neural stem cells into neurons rather than astrocytes. This reduction in astrocyte differentiation and subsequent glial scar formation is beneficial for axon regeneration and the establishment of neural networks, leading to the restoration of spinal cord function.

3.8 SilMA hydrogel loaded with Ang-(1–7) and NT-3 PLGA microspheres promotes Motor function recovery in mice

To investigate the effects of hydrogel scaffolds on spinal cord injury repair in mice, the study included a sham surgery control group (sham), a spinal cord transection model group (SCI), a group treated with SilMA hydrogel alone (SilMA), and a group treated with DPSH loaded with Ang-(1–7) and NT-3 in PLGA microspheres (4D-SilMA), with six mice in each group. After establishing the complete spinal cord transection injury model, the mice exhibited complete loss of hindlimb motor function. Over time, varying degrees of recovery were observed across the groups. The Basso Mouse Scale (BMS) was used to assess the recovery of hindlimb motor function on days 1, 7, 14, 21, 28, 35, 42, 49, and 56 post-surgery.

The results showed that on the first day after surgery, all groups of mice exhibited no autonomous hindlimb movement, with a BMS score of 0, indicating successful and stable modeling of the spinal cord transection. By the eighth week post-surgery, the BMS score of the DPSH group loaded with Ang-(1–7) and NT-3 reached 6, significantly higher than the scores of the SCI group and the SilMA hydrogel group (Figure 6A). This suggests that the DPSH scaffold significantly promotes the recovery of motor function following spinal cord injury.

3.9 DPSH promotes spinal cord tissue structure recovery

To investigate the recovery of spinal cord tissue in different groups following injury, hematoxylin and eosin (H&E) staining was performed on spinal cord sections from the mice. The staining results are shown in Figure 6. Sham Group: The spinal cord structure was intact without any defects, with clear boundaries between gray and white matter, abundant neurons, and complete structure. SCI Group: H&E staining revealed that the normal structure of the spinal cord was disrupted, with either incomplete or no connection at the injury site. There were numerous cavities within the spinal cord tissue and a disorganized structure, along with significant scar tissue at the injury site. SilMA Hydro-gel Group: The spinal cord continuity was partially restored with smaller scar tissue compared to the SCI group, but the structure remained disorganized, and many cavities were still present (Figure 6B). DPSH Group: The spinal cord morphology showed significant improvement compared to both the SCI group and the SilMA hydrogel group. The tissue had fewer cavities and inflammatory cells, and the cell arrangement was more orderly. These results indicate that the DPSH loaded with Ang-(1–7) and NT-3 significantly enhances the structural recovery of spinal cord tissue after injury, reducing tissue cavities and inflammation while promoting a more organized cellular structure.

3.10 DPSH modulates immune response and promotes neural differentiation *in vivo*

To validate the effects of DPSH on spinal cord injury repair, protein ex-traction from the injury site was performed for Western blot analysis. Results showed that the expression level of Arg-1 protein in mice treated with DPSH loaded with Ang-(1–7) and NT-3 was significantly higher than in the SCI and SilMA hydrogel groups. Conversely, the expression level of iNOS was significantly lower (Figures 6C–E). This indicates that the DPSH reduces M1 microglia and increases anti-inflammatory M2 microglia at the injury site, supporting the conclusion that it effectively modulates the immune response to promote a favorable environment for spinal cord repair.

Further validation of DPSH's effects on neural stem cell differentiation and spinal cord injury repair was conducted through Western blot analysis. The expression level of Tuj-1 protein in mice treated with DPSH loaded with Ang-(1–7) and NT-3 was significantly higher than in the SCI and SilMA hydrogel groups, while the expression level of GFAP was significantly lower (Figures 6F–H). This trend aligns with immunofluorescence results, confirming that more cells at the injury site differentiated into neurons rather than astrocytes. These findings further support that DPSH promotes neuronal differentiation, reduces astrocyte formation, and aids in spinal cord injury repair and functional recovery.

4 Conclusion

The DPSH scaffold, with sustained-release Ang-(1–7) and NT-3-loaded PLGA microspheres, meets the requirements of a tissue engineering material for SCI treatment. It matches the mechanical properties and microstructure of the spinal cord and exhibits good biocompatibility. The study results indicate that the DPSH can

release Ang-(1–7) to promote microglial M2 polarization, reduce inflammation, aid cell survival and regeneration, and sustain NT-3 release to promote NSC neuronal differentiation, reduce astrocyte differentiation, decrease glial scar formation, and reconstruct neural connections. This facilitates spinal cord function recovery and ultimately restores motor function in SCI mice.

Data availability statement

The original contributions presented in the study are included in the article/supplementary material, further inquiries can be directed to the corresponding authors.

Ethics statement

The animal study was approved by the Ethics Committee of Shandong University (Approval No. ecsbmssdu24019). The study was conducted in accordance with the local legislation and institutional requirements.

Author contributions

RZ: Formal Analysis, Investigation, Resources, Visualization, Writing–original draft. MZ: Formal Analysis, Investigation, Resources, Visualization, Writing–original draft. LC: Formal Analysis, Investigation, Resources, Visualization, Writing–original draft. LJ: Resources, Writing–original draft. CZ: Resources, Writing–original draft. NL: Supervision, Writing–review and editing. HZ: Supervision, Writing–review and editing. SF: Supervision, Writing–review and editing, Conceptualization, Funding acquisition, Project administration.

Funding

The author(s) declare that financial support was received for the research, authorship, and/or publication of this article. The present work was supported by the National Natural Science Foundation of China (Grant number 82220108005), Taishan Scholars Program of Shandong Province-Pandeng Taishan Scholars (tspd20210320), Scientific Research Cooperation Seed Fund of Shandong University (26010287395002), National Natural Science Foundation of China (82372413), the Major Basic Research Project of Shandong Provincial Natural Science Foundation (ZR2024ZD13) and the Taishan Scholars Program of Shandong Province-Young Taishan Scholars (tsqn201909197).

Acknowledgments

We thank Translational Medicine Core Facility of Shandong University for consultation and instrument availability that supported this work.

Conflict of interest

The authors declare that the research was conducted in the absence of any commercial or financial relationships that could be construed as a potential conflict of interest.

Generative AI statement

The author(s) declare that no Generative AI was used in the creation of this manuscript.

Publisher's note

References

Ahuja, C. S., Nori, S., Tetreault, L., Wilson, J., Kwon, B., Harrop, J., et al. (2017). Traumatic spinal cord injury-repair and regeneration. *Neurosurgery* 80 (3), S9–S22. doi:10.1093/neuros/nyw080

Anderson, M. A., O'Shea, T. M., Burda, J. E., Ao, Y., Barlatey, S. L., Bernstein, A. M., et al. (2018). Required growth facilitators propel axon regeneration across complete spinal cord injury. *Nature* 561 (7723), 396-+. doi:10.1038/s41586-018-0467-6

Bao, S.-S., Zhao, C., Chen, H.-W., Feng, T., Guo, X.-J., Xu, M., et al. (2022). NT3 treatment alters spinal cord injury-induced changes in the gray matter volume of rhesus monkey cortex. *Sci. Rep.* 12 (1), 5919. doi:10.1038/s41598-022-09981-5

Blanco-Suarez, E., Caldwell, A. L. M., and Allen, N. J. (2017). Role of astrocyte-synapse interactions in CNS disorders. *J. Physiology-London* 595 (6), 1903–1916. doi:10.1113/jp270988

Cai, M., Chen, L., Wang, T., Liang, Y., Zhao, J., Zhang, X., et al. (2023). Hydrogel scaffolds in the treatment of spinal cord injury: a review. *Front. Neurosci.* 17, 1211066. doi:10.3389/fnins.2023.1211066

Chedly, J., Soares, S., Montembault, A., von Boxberg, Y., Veron-Ravaille, M., Mouffle, C., et al. (2017). Physical chitosan microhydrogels as scaffolds for spinal cord injury restoration and axon regeneration. *Biomaterials* 138, 91–107. doi:10.1016/j.biomaterials.2017.05.024

Endo, F., Kasai, A., Soto, J. S., Yu, X., Qu, Z., Hashimoto, H., et al. (2022). Molecular basis of astrocyte diversity and morphology across the CNS in health and disease. *Science* 378 (6619), eadc9020. doi:10.1126/science.adc9020

Fukuyama, Y., Kubo, M., and Harada, K. (2024). Neurotrophic natural products. *Prog. Chem. Org. Nat. Prod.* 123, 1–473. doi:10.1007/978-3-031-42422-9_1

Gao, X., Cheng, W., Zhang, X., Zhou, Z., Ding, Z., Zhou, X., et al. (2022). Nerve growth factor-laden anisotropic silk nanofiber hydrogels to regulate neuronal/astroglial differentiation for scarless spinal cord repair. *Acs Appl. Mater. & Interfaces* 14 (3), 3701–3715. doi:10.1021/acsami.1c19229

Gu, G., Zhu, B., Ren, J., Song, X., Fan, B., Ding, H., et al. (2023). Ang-(1-7)/MasR axis promotes functional recovery after spinal cord injury by regulating microglia/macrophage polarization. *Cell. Biosci.* 13 (1), 23. doi:10.1186/s13578-023-00967-y

Han, M., Yang, H., Lu, X., Li, Y., Liu, Z., Li, F., et al. (2022). Three-dimensional-cultured MSC-derived exosome-hydrogel hybrid microneedle array patch for spinal cord repair. *Nano Lett.* 22 (15), 6391–6401. doi:10.1021/acs.nanolett.2c02259

He, Y., Gao, Y., Zhang, Q., Zhou, G., Cao, F., and Yao, S. (2020). IL-4 switches microglia/macrophage M1/M2 polarization and alleviates neurological damage by modulating the JAK1/STAT6 pathway following ICH. *Neuroscience* 437, 161–171. doi:10.1016/j.neuroscience.2020.03.008

Hellenbrand, D. J., Quinn, C. M., Piper, Z. J., Morehouse, C. N., Fixel, J. A., and Hanna, A. S. (2021). Inflammation after spinal cord injury: a review of the critical timeline of signaling cues and cellular infiltration. *J. Neuroinflammation* 18 (1), 284. doi:10.1186/s12974-021-02337-2

Hoque, J., Sangaj, N., and Varghese, S. (2019). Stimuli-responsive supramolecular hydrogels and their applications in regenerative medicine. *Macromol. Biosci.* 19 (1), e1800259. doi:10.1002/mabi.201800259

Jin, L.-Y., Li, J., Wang, K.-F., Xia, W.-W., Zhu, Z.-Q., Wang, C.-R., et al. (2021). Blood-spinal cord barrier in spinal cord injury: a review. *J. Neurotrauma* 38 (9), 1203–1224. doi:10.1089/neu.2020.7413

Jusu, S. M., Obayemi, J. D., Salifu, A. A., Nwazojie, C. C., Uzonwanne, V., Odusanya, O. S., et al. (2020). Drug-encapsulated blend of PLGA-PEG microspheres: *in vitro* and *in vivo* study of the effects of localized/targeted drug delivery on the treatment of triple-negative breast cancer. *Sci. Rep.* 10 (1), 14188. doi:10.1038/s41598-020-71129-0

Lai, B.-Q., Che, M.-T., Feng, B., Bai, Y.-R., Li, G., Ma, Y.-H., et al. (2019). Tissue-Engineered neural network graft relays excitatory signal in the completely transected canine spinal cord. *Adv. Sci.* 6 (22), 1901240. doi:10.1002/advs.201901240

Luo, J., Shi, X., Li, L., Tan, Z., Feng, F., Li, J., et al. (2021). An injectable and self-healing hydrogel with controlled release of curcumin to repair spinal cord injury. *Bioact. Mater.* 6 (12), 4816–4829. doi:10.1016/j.bioactmat.2021.05.022

Ma, Y.-H., Zeng, X., Qiu, X.-C., Wei, Q.-S., Che, M.-T., Ding, Y., et al. (2018). Perineurium-like sheath derived from long-term surviving mesenchymal stem cells confers nerve protection to the injured spinal cord. *Biomaterials* 160, 37–55. doi:10.1016/j.biomaterials.2018.01.015

McDonald, J. W., and Sadowsky, C. (2002). Spinal-cord injury. *Lancet* 359 (9304), 417–425. doi:10.1016/s0140-6736(02)07603-1

Murk, K., Suarez, E. M. B., Cockbill, L. M. R., Banks, P., and Hanley, J. G. (2013). The antagonistic modulation of Arp2/3 activity by N-WASP, WAVE2 and PICK1 defines dynamic changes in astrocyte morphology. *J. Cell. Sci.* 126 (17), 3873–3883. doi:10.1242/jcs.125146

Ngf, B. M. (2014). NGF, BDNF, NT3, and NT4. *Handb. Exp. Pharmacol.* 220, 3–15. doi:10.1007/978-3-642-45106-5_1

Okada, T., Muto, E., Yamanaka, T., Uchino, H., and Inazu, M. (2022). Functional expression of choline transporters in microglia and their regulation of microglial M1/M2 polarization. *Int. J. Mol. Sci.* 23 (16), 8924. doi:10.3390/ijms23168924

Orihuela, R., McPherson, C. A., and Harry, G. J. (2016). Microglial M1/M2 polarization and metabolic states. *Br. J. Pharmacol.* 173 (4), 649–665. doi:10.1111/bph.13139

O'Shea, T. M., Burda, J. E., and Sofroniew, M. V. (2017). Cell biology of spinal cord injury and repair. *J. Clin. Investigation* 127 (9), 3265–3276.

Pan, H., Huang, W., Wang, Z., Ren, F., Luo, L., Zhou, J., et al. (2021). The ACE2-ang-(1-7)-mas Axis modulates M1/M2 macrophage polarization to relieve CLP-induced inflammation via TLR4-mediated NF-κb and MAPK pathways. *J. Inflamm. Res.* 14, 2045–2060. doi:10.2147/jir.s307801

Peng, H., Liu, Y., Xiao, F., Zhang, L., Li, W., Wang, B., et al. (2023). Research progress of hydrogels as delivery systems and scaffolds in the treatment of secondary spinal cord injury. *Front. Bioeng. Biotechnol.* 11, 1111882. doi:10.3389/fbioe.2023.1111882

Ranganathan, B., Miller, C., and Sinskey, A. (2018). Biocompatible synthetic and semi-synthetic polymers - a patent analysis. *Pharm. Nanotechnol.* 6 (1), 28–37. doi:10.2174/2211738505666171023152549

Sanchez-Dengra, B., Gonzalez-Alvarez, I., Bermejo, M., and Gonzalez-Alvarez, M. (2023). Access to the CNS: strategies to overcome the BBB. *Int. J. Pharm.* 636, 122759. doi:10.1016/j.ijpharm.2023.122759

Saraiva, M., and O'Garra, A. (2010). The regulation of IL-10 production by immune cells. *Nat. Rev. Immunol.* 10 (3), 170–181. doi:10.1038/nri2711

Sensharma, P., Madhumathi, G., Jayant, R. D., and Jaiswal, A. K. (2017). Biomaterials and cells for neural tissue engineering: current choices. *Mater. Sci. & Eng. C-Materials Biol. Appl.* 77, 1302–1315. doi:10.1016/j.msec.2017.03.264

Shultz, R. B., and Zhong, Y. (2021). Hydrogel-based local drug delivery strategies for spinal cord repair. *Neural Regen. Res.* 16 (2), 247–253. doi:10.4103/1673-5374.290882

Silva, D., Schirmer, L., Pinho, T. S., Atallah, P., Cibrão, J. R., Lima, R., et al. (2023). Sustained release of human adipose tissue stem cell secretome from star-shaped poly(ethylene glycol) glycosaminoglycan hydrogels promotes motor improvements after complete transection in spinal cord injury rat model. *Adv. Healthc. Mater* 12 (17), e2202803. doi:10.1002/adhm.202202803

Silva, D., Sousa, R. A., and Salgado, A. J. (2021). Hydrogels as delivery systems for spinal cord injury regeneration. *Mater. Today Bio* 9, 100093. doi:10.1016/j.mtbio.2021.100093

Silva, N. A., Sousa, N., Reis, R. L., and Salgado, A. J. (2014). From basics to clinical: a comprehensive review on spinal cord injury. *Prog. Neurobiol.* 114, 25–57. doi:10.1016/j.pneurobio.2013.11.002

Sofroniew, M. V. (2018). Dissecting spinal cord regeneration. *Nature* 557 (7705), 343–350. doi:10.1038/s41586-018-0068-4

Wen, Y., Yu, S., Wu, Y., Ju, R., Wang, H., Liu, Y., et al. (2016). Spinal cord injury repair by implantation of structured hyaluronic acid scaffold with PLGA microspheres in the rat. *Cell. Tissue Res.* 364 (1), 17–28. doi:10.1007/s00441-015-2298-1

Wu, X., Huo, Y., Ci, Z., Wang, Y., Xu, W., Bai, B., et al. (2022). Biomimetic porous hydrogel scaffolds enabled vascular ingrowth and osteogenic differentiation for vascularized tissue-engineered bone regeneration. *Appl. Mater. Today* 27, 101478. doi:10.1016/j.apmt.2022.101478

Xiao, L., Xie, P., Ma, J., Shi, K., Dai, Y., Pang, M., et al. (2023). A bioinspired injectable, adhesive, and self-healing hydrogel with dual hybrid network for neural regeneration after spinal cord injury. *Adv. Mater.* 35 (41), e2304896. doi:10.1002/adma.202304896

Yan, Y., Zhang, W., Wu, R., Guan, T., Li, Z., Tu, Q., et al. (2023). Promising application of a novel biomaterial, light chain of silk fibroin combined with NT3, in repairment of rat sciatic nerve defect injury. *Int. J. Biol. Macromol.* 240, 124447. doi:10.1016/j.ijbiomac.2023.124447

Yuan, X., Ding, L., and Deng, D. Y. B. (2021). Research progress of hydrogel combined with mesenchymal stem cells in the treatment of spinal cord injury. *Sheng wu yi xue gong cheng xue za zhi = J. Biomed. Eng. = Shengwu yixue gongchengxue zazhi* 38 (4), 805–811. doi:10.7507/1001-5515.202005055

Zhou, B., Zuo, Y.-X., and Jiang, R.-T. (2019). Astrocyte morphology: diversity, plasticity, and role in neurological diseases. *Cns Neurosci. & Ther.* 25 (6), 665–673. doi:10.1111/cns.13123

Zhou, R., Li, J., Chen, Z., Wang, R., Shen, Y., Zhang, R., et al. (2023). Pathological hemodynamic changes and leukocyte transmigration disrupt the blood-spinal cord barrier after spinal cord injury. *J. Neuroinflammation* 20 (1), 118. doi:10.1186/s12974-023-02787-w

frontiers | Frontiers in Bioengineering and Biotechnology

TYPE Brief Research Report
PUBLISHED 10 January 2025
DOI 10.3389/fbioe.2024.1515043

OPEN ACCESS

EDITED BY
Xianzhi Zhang,
Yale University, United States

REVIEWED BY
Stefano Fedeli,
University of Milan, Italy
Liang Liu,
University of Massachusetts Amherst Amherst, United States, in collaboration with reviewer SF
Hong Kang,
University of Pennsylvania, United States

*CORRESPONDENCE
Wendong Zhu,
wdzhu_chembio@163.com
Xiangfang Peng,
pengxf@fjut.edu.cn
Jian Li,
lijianla2008@foxmail.com

†These authors have contributed equally to this work and share first authorship

RECEIVED 22 October 2024
ACCEPTED 27 December 2024
PUBLISHED 10 January 2025

CITATION
Cao Z, Zhuo H, Zhu W, Peng X and Li J (2025) Rational construction of PCL-PEG/CS/AST nanofiber for bone repair and regeneration. *Front. Bioeng. Biotechnol.* 12:1515043. doi: 10.3389/fbioe.2024.1515043

Rational construction of PCL-PEG/CS/AST nanofiber for bone repair and regeneration

Zhengyu Cao[1†], Hongwu Zhuo[1†], Wendong Zhu[2*], Xiangfang Peng[2*] and Jian Li[1*]

[1]Department of Sports Medicine, The Second Affiliated Hospital of Fujian University of Traditional Chinese Medicine (FJTCM), Fuzhou, China, [2]Key Laboratory of Polymer Materials and Products of Universities in Fujian, Department of Materials Science and Engineering, Fujian University of Technology, Fuzhou, Fujian, China

Humerus greater tuberosity (HGT) avulsion fracture is one of the most common types of proximal humerus fractures. The presence of motion and gap lead to the failure of implants, due to the force pulling from the supraspinatus. In this work, electrospinning technology was applied to fabricate PCL-PEG/CS/AST nanofiber with superior biocompatibility and mechanical property. Furthermore, PCL-PEG/CS/AST nanofiber could promote proliferation and osteogenic differentiation of bone mesenchymal stem cells (BMSCs) *in vitro*. We believe that this work indicates a promising way to promote the union of HGT avulsion fractures by using PCL-PEG/CS/AST nanofiber.

KEYWORDS

electrospinning, nanofiber, humerus, bone, tuberosity

1 Introduction

Bone repair and bone regeneration are crucial task in clinical treatment. The healing of the humerus greater tubercle (HGT) is highly important. As the main attachment point of the rotator cuff, humerus greater tubercle (HGT) plays an important role in maintaining the function of shoulder joint abduction and rotation (Lacheta et al., 2023; Bekmezci et al., 2024). HGT avulsion fractures are among the most common types of proximal humerus fractures, especially in the osteoporosis population, accounting for approximately 20% of proximal humeral fractures (Handoll et al., 2022; Kim et al., 2024b). Arthroscopic suture anchor and locking plate fixation are common methods in the clinical treatment of HGT avulsion fractures, however, surgical treatments still have high failure rates, and adverse events, such as internal fixation failure and fracture displacement often occur (Makaram et al., 2023; Kim et al., 2024b; Tao et al., 2024). Previous studies reported that the suture anchor technique requires adequate bone mineral density to hold the anchor and that the anchors are easily pulled out in patients with severe osteoporosis around the proximal humerus (Lee S. et al., 2021; Kim et al., 2023). In addition, many studies founded that the presence of motion and gaps due to pulling from the supraspinatus, which is known to delay the union of fractures, eventually leaded to failure of internal fixation (Zeng et al., 2021; Handoll et al., 2022). Thus, better approaches for promoting HGT avulsion fracture healing, which are essential for the recovery of shoulder function, are needed for elderly and osteoporotic population.

In recent years, many types of material have been developed and utilized in bone repair and bone regeneration. Among them, nanofiber is an ideal scaffold for therapeutic medicines, with the features of huge aspect ratio, specific surface area, flexibility, and

mechanical strength (Zhu et al., 2021; Cheng et al., 2021; Cheng et al., 2022b; Cheng et al., 2022a). Many polymer nanofibers with excellent biocompatibility have shown outstanding results for prosthetics, including polylactic acid (PLA), polycaprolactone (PCL), polyethylene glycol (PEG) and numerous biomolecules. For example, Kim et al. (2024a) utilized the oxygen plasm to treat PCL nanofibrous scaffold, aiming to improve the hydrophilicity and protein adsorption properties. As the results illustrated the treated PCL nanofiber showed dramatically improved new bone formation behavior (Kim et al., 2024a). As a one of the natural polysaccharides, chitosan owns an unique chemical structure, which attracted enormous interest in controlled drug delivery, gene delivery, cell culture, and tissue engineering. After assisting by bioactivated magnesium-doped hydroxyapatite, electrospun chitosan nanofiber scaffolds simultaneously displayed the great bone mineralization ability (Sedghi et al., 2020). To further improve the effects of bone repair and regeneration, various bioactivated materials are added into the scaffold, including drugs, ceramics, metal-organic frameworks, semiconductor materials (Wang et al., 2019; Liu et al., 2022; Sun et al., 2022; Fan et al., 2024; Makurat-Kasprolewicz et al., 2024). Alendronate sodium ([(4-amino-1-hydroxybutylidene)-bisphosphonate] trihydrate) have the capability inhibit the bone remodeling activity and resorption by interacting with bone matrix to treat osteoporosis and other osteolytic bone diseases (Akyol et al., 2015; Doca et al., 2016). He et al. (2018) chosen Alendronate Sodium modified the collagen type I for bone regeneration, because the Phosphorylated materials could provide the beneficial environment of extracellular matrix. Compared with the treatment of 4 weeks, the new bone formation is apparent after treatment of 8 weeks (He et al., 2018).

In this work, PCL-PEG/CS/AST nanofiber was prepared via electrospinning technology. The fibrous morphology of PCL-PEG/CS/AST nanofiber is beneficial for cell adhesion and proliferation, exhibiting superior biocompatibility. Furthermore, an adhesive-nanofiber membrane based approach was proposed to promote HGT avulsion fracture healing. We hypothesized that PCL-PEG/CS/AST nanofiber membrane could enhance HGT avulsion fracture healing by promoting osteogenesis and reducing the failure rate after surgery. We believe this work provides an universal and simple approach for bone repair and bone regeneration with potential insight.

2 Materials and methods

2.1 Materials and reagent

Polycaprolactone-polyethylene glycol copolymer (PCL-PEG) was synthesized from Ruijiu Technology Co., Ltd. Chitosan (CS, deacetylation degree ≥95%, viscosity: 100–200 Mpa/s), sodium alendronate (AST), hexafluoroisopropyl alcohol (HFIP) were purchased from Shanghai Macklin Biochemical Technology Co., Ltd. Alpha-modified minimal essential medium (α-MEM), penicillin–streptomycin (P/S) and fetal bovine serum (FBS) were purchased from Thermo Fisher Scientific (Scoresby, Vic., Australia). The Cell Counting Kit-8 (CCK-8) was purchased from Bioscience (Shanghai, China). Alkaline Phosphatase (ALP) Assay Kit was purchased from Beyotime (Shanghai, China). Live and Dead™ Viability Assay Kit and rhodamine-conjugated phalloidin were purchased from US Everbright Inc (Suzhou, China). The universal RNA extraction kits and Evo M-MLV RT kits were purchased from Accurate Biotechnology Co., Ltd. (Hunan, China). The primers that used in this study were purchased from Sangon (Shanghai, China). All reagents were used directly without pretreatment.

2.2 Characterizations

The morphologies of PCL-PEG/CS/AST nanofiber membrane was achieved by field emission scanning electron microscope (FE-SEM, Regulus 8100). The chemical structure of PCL-PEG/CS/AST nanofiber membrane was analyzed by Fourier Transform infrared spectroscopy (FTIR, Nicolet IS350). The valence information and surface composition of PCL-PEG/CS/AST nanofiber membranes were analyzed by X-ray photoelectron spectroscopy (XPS, ESCALAB QXi).

2.3 Preparation of PCL-PEG/CS/AST nanofiber membrane

0.2 g of PCL-PEG was added into 4.2 g of HFIP and kept stirring to forming a homogeneous solution. Then, 0.04 g of CS and 0.012 g AST were injected to the above-mentioned solution. Subsquently, the precursor solution was loaded into a syringe with a single stainless steel nozzle for electrospinning. The voltage supply was maintained at 15 kV. Then, the PCL-PEG/CS/AST nanofiber membrane were prepared.

2.4 BMSCs cultivation, BMSCs viability assay and live-dead cell staining

BMSCs were purchased from Shanghai Zhong Qiao Xin Zhou Biotechnology Co., Ltd. BMSCs were cultured in α-MEM complete culture medium for 72 h and the culture medium was changed every 48 h until BMSCs reached 80% confluence. BMSCs were seeded on the surfaces of PCL/PEG, PCL-PEG/ALN, PCL-PEG/CTS and PCL-PEG/ALN/CTS with the density of 5×10^4/well in a 12-well plate, respectively (3 duplicate wells for each sample). The viability of the BMSCs on the surfaces of the four samples was detected on the third and seventh days, respectively, which is according to a related published article. (Zhang et al., 2022). Meanwhile, BMSCs on the samples were fixed and stained according to the live-dead cell staining kit manufacturer's protocol at day third and seventh, respectively. Image J software was used to count the living and dead cells on the surface of nanofiber membranes, respectively.

2.5 Osteogenic differentiation *in vitro*

For quantitative real-time polymerase chain reaction (qRT-PCR) and ALP activity, BMSCs were seeded on each sample as described above and α-MEM complete culture medium was changed

TABLE 1 The sequences of the primers of osteogenic genes.

Gene	Forward primer	Reverse primer
ALP	CCACTATGTCTGGAACCGCA	GGAGAGCGAAGGGTCAGTC
Osteocalcin	GACCATCTTTCTGCTCACTCTGC	ACCTTATTGCCCTCCTGCTTG
GAPDH	AGGAGAGTTTCCTCGTCC	TGAGGTCAATGAAAGGGGTCG

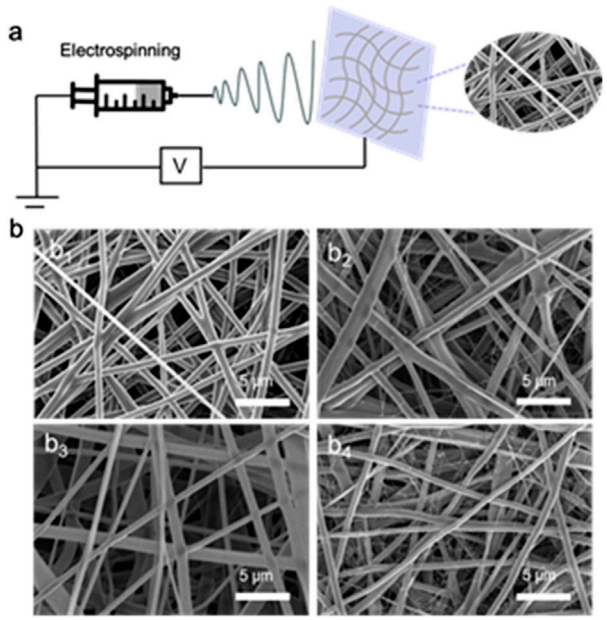

FIGURE 1
(A) Preparation process diagram of PCL-PEG/CS/AST nanofiber; **(B_1)** SEM image of the prepared PCL-PEG nanofiber membrane; **(B_2)** SEM image of the prepared PCL-PEG/CS nanofiber membrane; **(B_3)** SEM image of the prepared PCL-PEG/AST nanofiber membrane; **(B_4)** SEM image of the prepared PCL-PEG/CS/AST nanofiber membrane.

to the osteoblast inducing conditional medium when BMSCs reached 100% confluence. ALP activity of BMSCs was detected according to the manufacturer's protocol after 14 days of osteogenic induction. The absorbance was detected at 405 nm with a microplate reader. The total RNA of BMSCs on the surface of bionanofiber membranes was extracted after 14 days of osteogenic induction via a Universal RNA Extraction Kit, respectively. Then, the total RNA was reverse transcribed into cDNA with an Evo M-MLV RT kit and the data were analyzed by the $2^{-\triangle\triangle CT}$ method. The sequences of the primers of osteogenic genes were shown in Table 1.

2.6 Statistical analysis

In this study, all experiments were repeated at least 3 times. The results were presented as mean ± standard deviation (SD) if the data obeyed normal distribution. GraphPad Prism (version 7, GraphPad Software, San Diego, United States) was used for statistical analysis and statistical graphs. One-way ANOVA with Tukey's post hoc test was used to determine the significant differences among several groups. P values <0.05 were considered to indicate statistically significant differences.

3 Results and discussion

The typical synthesis process of PCL-PEG/CS/AST nanofiber is shown in Figure 1A. The PCL-PEG/CS/AS nanofiber membrane was prepared by electrospinning technology. As shown in Figure $1B_1$, PCL-PEG nanofiber exhibit smooth surface and fibrous morphology, which is suitable for substrate (Figure $1B_1$). Figure $1B_2$ displays the SEM images of PCL-PEG/CS nanofiber, flattening and overlap of nanofiber can be observed, which could be assigned to the presence of chitosan. The SEM images of is PCL-PEG/AST nanofiber reveals the smooth fibrous morphology (Figure $1B_3$). As illustrated in Figure $1B_4$, the morphology of the PCL-PEG/CS/AST nanofiber fiber does not change, indicating that the addition of CS and AST displayed no effect on the morphology of the nanofiber.

The chemical structure and different types of chemical bonds of composites were investigated by FTIR spectroscopy. As shown in Figure 2A, the characteristic peaks at 2,941 cm^{-1} and 2,864 cm^{-1} correspond to the C-H asymmetric and symmetric stretching of the carbonyl group, the characteristic peak at 1726 cm^{-1} is attributed to the stretching movement of C=O, and the characteristic peaks near 1,242 cm^{-1} and 1,178 cm^{-1} prove the formation of COC asymmetric and symmetric stretching, respectively (Deng et al., 2021). Hydrogen bond interactions may occur in PCL-PEG copolymers (Yu et al., 2014), and the peak at 3,370 cm^{-1} confirmed the presence of O-H in the mixture. After the introduction of CS and AST, it is found that the spectrum changes little. However, in the nanofibers containing CS and AST, the peak strength near 1726 cm^{-1} is reduced, illustrating the difference in the amount of C=O in the mixture (Deng et al., 2021), which also indicates that CS and AST are successfully imported. No differences among PCL-PEG (d) and PCL-PEG/CS/AST (a), PCL-PEG/AST (b), and PCL-PEG/CS (c) blends were detected in Figure 2A, which may be due to the low contents of CS and AST in polymer matrix. All FTIR test results prove the successful preparation of PCL-PEG/CS/AST nanofiber membrane.

XPS was applied to further characterize the surface elemental states of PCL-PEG/CS/AST nanofiber (Figures 2B–F). The presence of C, N, and O elements can be clearly calrified in the full spectrum of PCL-PEG/CS/AST. In the fine spectrum of C 1s, it is located at 284.0, 285.4, 288.0 eV, which is corresponded to C-C/C=C, C-C/C-H, hydrocarbons and C=O (Al-Ani et al., 2018; Manakhov et al., 2019; Liu et al., 2020; Yingjun et al., 2023). The fine spectrum d of N 1s can be deconvolved into 398.6 and 399.2 eV, which could be assigned to the presence of N-C and NH_2 (Wang and Liu, 2013;

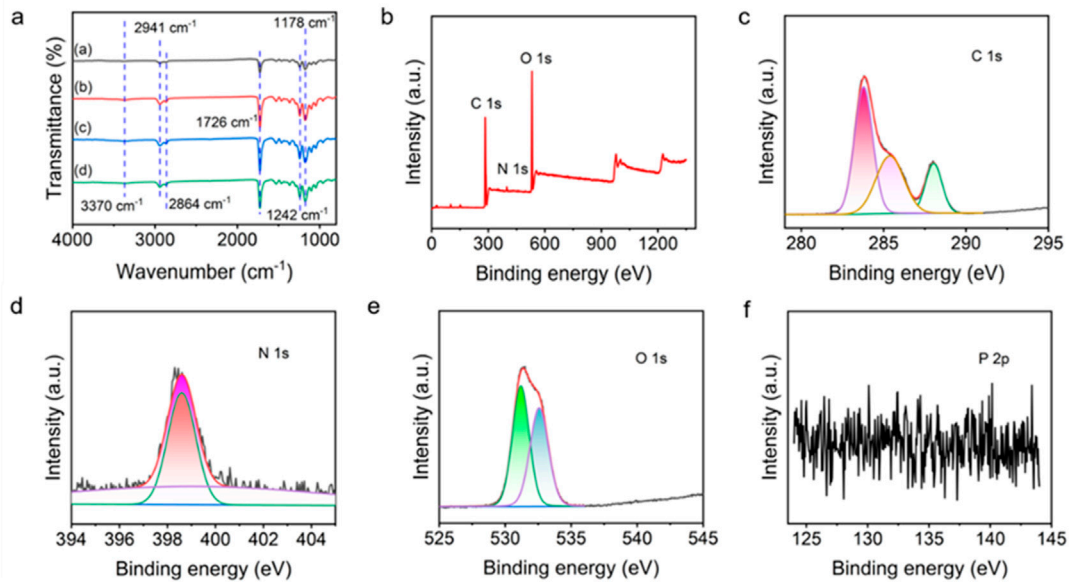

FIGURE 2
(A) FTIR spectra of **(A)** PCL-PEG/CS/AST nanofibers, **(B)** PCL-PEG/AST nanofibers, **(C)** PCL-PEG/CS nanofibers and **(D)** PCL-PEG nanofibers. **(B)**. Full XPS survey of prepared PCL-PEG/CS/AST nanofibers. The fine XPS spectra of the PCL-PEG/CS/AST nanofibers, **(C)** C1s, (**D)** N1s, **(E)** O 1s, and **(F)** P 2p regions.

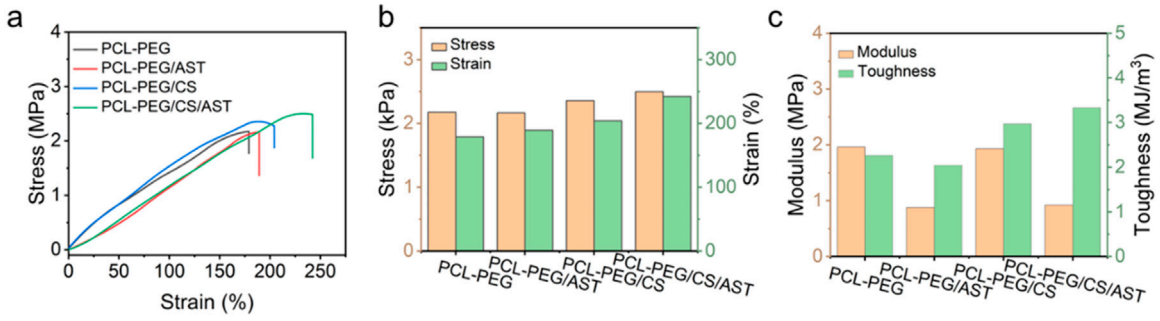

FIGURE 3
(A) Stress–strain curves, histograms of **(B)** stress, strain, **(C)** modulus and toughness of PCL-PEG/CS/AST, PCL-PEG/CS, PCL-PEG/AST and PCL-PEG nanofiber membrance.

Petrović et al., 2022). In the fine spectrum of O 1s, the peaks displayed at 531.2 and 532.6 eV, which is related to C=O and N-C=O in the N-acetylated-glucosamine units (Wang and Liu, 2013; Yingjun et al., 2023). In the full spectrum of PCL-PEG/CS/AST nanofiber and the fine spectrum of P 2p, there are no obvious characteristic peaks related to P was found, which also confirm the trace content of AST in PCL-PEG/CS/AST nanofiber. All XPS test results indicate the successful preparation of PCL-PEG/CS/AST nanofiber membrane.

The mechanical property of PCL-PEG/CS/AST nanofiber membrane was also clarified. As shown in Figure 3, the stress, elongation at break, elastic modulus, and toughness of PCL-PEG/CS/AST nanofiber membrane reach 2.50 MPa, 2,242.33%, 0.92 MPa, and 3.33 kJ/m^3, respectively, proving its favorable mechanical performance. Furthermore, the long-term stability of PCL-PEG/CS/AST nanofiber membrane can be predicted. According to the previous work, Polymer dispersity index (PDI), Zeta potential was applied to verify the long-term stability with satisfactory result in 25°C for 14 days (Wang et al., 2021). Chitosan exhibited the superior stability in varied conditions (high-temperature, high-salt, and long-term storage at 4°C) (Li et al., 2024). Thus, we believe PCL-PEG/CS/AST nanofibers also present the favorable long-term stability.

3.1 Cell viability

In Figure 4A, the proliferation rate of BMSCs on the surface of PCL-PEG/CS nanofiber membrance (0.46 ± 0.01) and PCL-PEG/CS/AST nanofiber membrane (0.55 ± 0.03) was significantly promoted compared with that of the former

10.3389/fbioe.2024.1515043

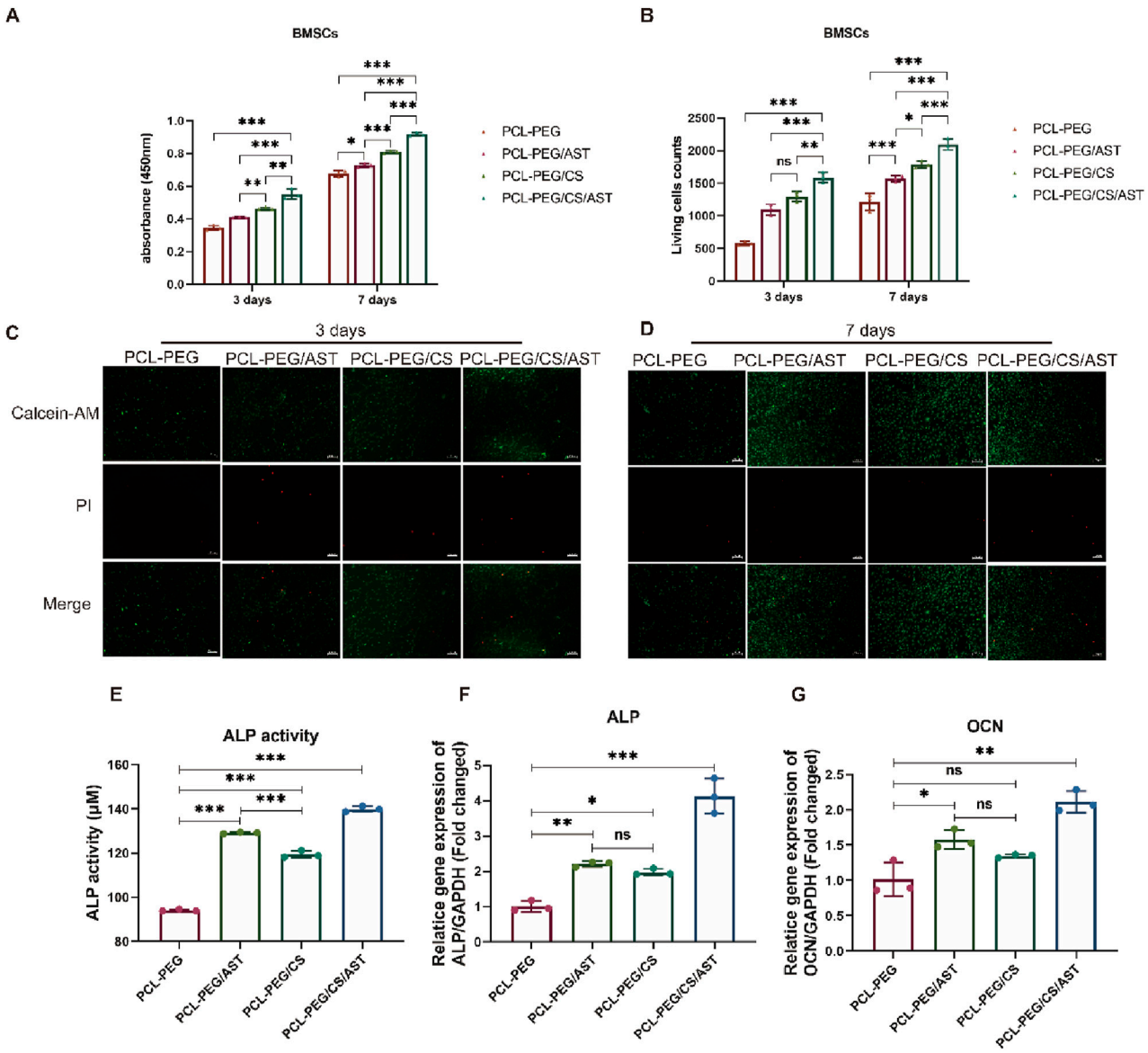

FIGURE 4
(A) The proliferation rate of BMSCs on the surface of each biofilm after inoculation for 3 and 7 days. **(B)** The counts of Living BMSCs on the surface of each biofilm after inoculation for 3 and 7 days. **(C)** The images of living BMSCs and dead BMSCs on the surface of each biofilm after inoculation for 3 days. **(D)** The images of living BMSCs and dead BMSCs on the surface of each biofilm after inoculation for 7 days. **(E)** ALP activity of BMSCs on each biofilm after 14 days of osteogenic induction. **(F)** ALP expression of BMSCs on each biofilm after osteogenic induction for 14 days. **(G)** OCN expression of BMSCs on each biofilm after osteogenic induction for 14 days. *P < 0.05; **P < 0.01; ***P < 0.005; ns, no significant.

2 groups (0.35 ± 0.01, 0.41 ± 0.01, respectively) after inoculation for 3 days (P < 0.05). The result of cell viability test after inoculation for 7 days revealed a similar trend that the proliferation rate of BMSCs on the surface of PCL-PEG/CS nanofiber membrance (0.81 ± 0.01) and PCL-PEG/CS/AST nanofiber membrance (0.92 ± 0.01) was significantly promoted compared with that of the former 2 groups (0.68 ± 0.02, 0.73 ± 0.01, respectively).

In Figures 4B–D, Live BMSCs were dyed green with calcein-AM, dead BMSCs were dyed red with propidium iodide, and few dead BMSCs were observed under the fluorescence microscope in all four groups, the result of live-dead cell staining showed the same trend, the number of living cells (1,589.00 ± 83.50) was the highest on the surface of PCL-PEG/CS/AST nanofiber membrance. The number of living cells on the surface of PCL-PEG/CS nanofiber membrance (1,297.33 ± 78.40) was significantly greater than the former 2 groups (597.33 ± 30.37, 1,098.00 ± 86.09, respectively) (P < 0.05).

Similarly, Cai et al. has constructed a kind of chitosan derivative scaffold, which could promote proliferation and osteogenic differentiation of MSCs via reducing intracellular reactive oxygen species (ROS) (Wang et al., 2020). Another related article has found that chitosan could promote proliferation of tonsil-derived mesenchymal stem cells (TMSCs) via up-regulating cyclin D1 in the G1 phase of the cell cycle (Lee K. E. et al., 2021). In addition, Martín-López et al. reported that different concentration of chitosan could affect the polymer surface topography, which has a direct effect on the growth of cell behavior (Martín-López et al., 2013).

3.2 Osteogenic differentiation of BMSCs *in vitro*

Alkaline phosphatase (ALP) is a kind of exoenzyme of osteoblast, and its expression activity is a very obvious characteristic of osteoblast differentiation and maturation. As shown in Figure 4E, BMSCs on the surface of PCL-PEG/CS/AST nanofiber membrane had a significantly higher level of ALP activity (139.95 ± 1.27) than other 3 groups (94.11 ± 0.48, 129.20 ± 0.33 and 119.47 ± 1.57, respectively) after 14 days of osteogenic induction ($P < 0.05$). As shown in Figures 3F, G, the expression level of osteogenic genes in BMSCs on four kinds of nanofiber membrane, including ALP and Osteocalcin (OCN) were detected via qRT–PCR analysis. Generally, Osteocalcin (OCN) is specifically expressed in osteoblasts and is the most abundant non-collagenous protein in bone, which possess the function of regulating hormone of bone metabolism. The result of ALP gene expression in BMSCs on the surface of PCL-PEG/CS/AST nanofiber membrane (4.13 ± 0.50) had the highest level when compared to the former 3 groups (1.01 ± 0.15, 2.21 ± 0.08 and 1.98 ± 0.09 respectively) ($P < 0.05$), which showed a similar trend as the result of ALP activity. In addition, the expression level of OCN gene in BMSCs on the surface of PCL-PEG/AST (1.58 ± 0.13) and PCL-PEG/CS/AST nanofiber membrane (2.12 ± 0.15) was significantly higher than those on the surface of PCL-PEG and PCL-PEG/CS nanofiber membrane (1.02 ± 0.24, 1.35 ± 0.02 respectively) ($P < 0.05$). Chen et al. obtained similar results; they constructed a kind of ALN-loaded hydrogel scaffold and found that the sustained AST release could indeed promote the expression levels of osteogenic-related genes in BMSCs (Tang et al., 2022). Shi et al. had verified that AST served as an optimal osteo-inductive factor to promote osteogenesis within a certain concentration range *in vitro* (Shi et al., 2009; Chang et al., 2022). In addition, Yoon Shin Park et al. reported that chitosan could enhanced the ability of TMSCs to osteoblasts via enhancing its metabolic rate (Lee K. E. et al., 2021), however, significant upregulation of osteogenic genes may cause several side-effects. One notable consequence is the potential for abnormal hyperplasia of HGT, which is one of the common pathogenies of shoulder impingement syndrome in clinic. What's more, altered bone metabolism, due to osteogenic gene overexpression, may disrupt the delicate balance between bone resorption and formation, which may cause ossification in surrounding soft tissue, such as supraspinatus, infraspinatus and so on.

4 Conclusion

In this work, PCL-PEG/CS/AST nanofiber was fabricated via electrospinning technology, exhibiting fibrous morphology, superior biocompatibility and mechanical performance. Furthermore, PCL-PEG/CS/AST nanofiber could promote proliferation and osteogenic differentiation of bone mesenchymal stem cells (BMSCs) *in vitro*. This work provided an innovative way for promoting the union of HGT avulsion fracture with a promising vision of protecting public health.

Data availability statement

The raw data supporting the conclusions of this article will be made available by the authors, without undue reservation.

Ethics statement

Ethical approval was not required for this study in accordance with the local legislation and institutional requirements because only commercially available established cell lines were used.

Author contributions

ZC: Methodology, Formal Analysis, Writing–original draft. HZ: Methodology, Formal Analysis, Writing–original draft. WZ: Funding acquisition, Formal Analysis, Writing–review and editing, Conceptualization, Methodology, Writing–original draft, Investigation. XP: Funding acquisition, Supervision, Writing–review and editing. JL: Funding acquisition, Supervision, Writing–review and editing.

Funding

The author(s) declare that financial support was received for the research, authorship, and/or publication of this article. This work was supported by research grants from Natural Science Foundation of China (52273032), Natural Science Foundation of Fujian Province (2020J02007, 2022J01839), the Scientific Research Foundation of Fujian University of Technology (GY-Z220184, GY-Z21014, GY-Z17073), Young Teacher Education Research Fund of Fujian, China (JAT220218).

Conflict of interest

The authors declare that the research was conducted in the absence of any commercial or financial relationships that could be construed as a potential conflict of interest.

Generative AI statement

The author(s) declare that no Generative AI was used in the creation of this manuscript.

Publisher's note

References

Akyol, U. K., Sipal, S., Demirci, E., and Gungormus, M. (2015). The influence of low-level laser therapy with alendronate irrigation on healing of bone defects in rats. *Lasers Med. Sci.* 30, 1141–1146. doi:10.1007/s10103-015-1720-y

Al-Ani, A., Boden, A., Al Kobaisi, M., Pingle, H., Wang, P.-Y., and Kingshott, P. (2018). The influence of PEG-thiol derivatives on controlling cellular and bacterial interactions with gold surfaces. *Appl. Surf. Sci.* 462, 980–990. doi:10.1016/j.apsusc.2018.08.136

Bekmezci, T., Çepni, S. K., and Demir, T. (2024). Greater tuberosity medial malposition: does it affect shoulder abductor moment? *Int. Orthop.* 48, 159–167. doi:10.1007/s00264-023-05967-8

Chang, S., Li, C., Xu, N., Wang, J., Jing, Z., Cai, H., et al. (2022). A sustained release of alendronate from an injectable tetra-PEG hydrogel for efficient bone repair. *Front. Bioeng. Biotechnol.* 10, 961227. doi:10.3389/fbioe.2022.961227

Cheng, Y., Zhu, W., Lu, X., and Wang, C. (2021). Recent progress of electrospun nanofibrous materials for electromagnetic interference shielding. *Compos. Commun.* 27, 100823. doi:10.1016/j.coco.2021.100823

Cheng, Y., Zhu, W., Lu, X., and Wang, C. (2022a). Mechanically robust, stretchable, autonomously adhesive, and environmentally tolerant triboelectric electronic skin for self-powered healthcare monitoring and tactile sensing. *Nano Energy* 102, 107636. doi:10.1016/j.nanoen.2022.107636

Cheng, Y., Zhu, W., Lu, X., and Wang, C. (2022b). One-dimensional metallic, magnetic, and dielectric nanomaterials-based composites for electromagnetic wave interference shielding. *Nano Res.* 15, 9595–9613. doi:10.1007/s12274-022-4781-9

Deng, X., Gould, M., and Ali, M. A. (2021). Fabrication and characterisation of melt-extruded chitosan/keratin/PCL/PEG drug-eluting sutures designed for wound healing. *Mater. Sci. Eng. C* 120, 111696. doi:10.1016/j.msec.2020.111696

Doca, S. C., Albu, P., Ceban, I., Anghel, A., Vlase, G., and Vlase, T. (2016). Sodium alendronate used in bone treatment: a complex study on the thermal behavior of the bioactive compound and its binary mixtures with several excipients. *J. Therm. Anal. Calorim.* 126, 189–194. doi:10.1007/s10973-016-5619-z

Fan, Y., Ran, H., Wang, Z., Ning, C., Zhai, J., and Yu, P. (2024). Semiconductive biomaterials for Pathological bone repair and regeneration. *Adv. Funct. Mater.* 34, 2308310. doi:10.1002/adfm.202308310

Handoll, H. H., Elliott, J., Thillemann, T. M., Aluko, P., and Brorson, S. (2022). Interventions for treating proximal humeral fractures in adults. *Cochrane Database Syst. Rev.* 2022. doi:10.1002/14651858.CD000434.pub5

He, Y., Zhu, T., Liu, L., Shi, X., and Lin, Z. (2018). Modifying collagen with alendronate sodium for bone regeneration applications. *RSC Adv.* 8, 16762–16772. doi:10.1039/C8RA01872C

Kim, D., Choi, H., Lee, M.-J., Cho, W. J., Lee, G. W., Seo, Y.-K., et al. (2024a). Oxygen plasma-modified polycaprolactone nanofiber membrane activates the biological function in cell adhesion, proliferation, and migration through the phosphorylation of FAK and ERK1/2, enhancing bone regeneration. *Chem. Eng. J.* 499, 156003. doi:10.1016/j.cej.2024.156003

Kim, D., Lim, J.-R., Yoon, T.-H., Shin, S.-H., and Chun, Y.-M. (2024b). Lateral Wall wntegrity of the greater tuberosity is important for the stability of osteoporotic proximal humeral fractures after plate fixation. *J. Bone Jt. Surg.* 106, 1750–1756. doi:10.2106/JBJS.23.00480

Kim, Y.-J., Ji, J.-H., Park, S.-E., Parikh, D., and Lee, W.-J. (2023). Comparison between arthroscopic suture anchor fixation and open plate fixation in the greater tuberosity fracture of the proximal humerus. *Eur. J. Orthop. Surg. Traumatol.* 34, 621–631. doi:10.1007/s00590-023-03684-x

Lacheta, L., Gao, X., Miles, J. W., Murata, Y., Fukase, N., Utsunomiya, H., et al. (2023). Losartan in iombination with bone carrow mtimulation showed synergistic effects on soad to failure and lendon matrix organization in a tabbit rodel. *Arthrosc. J. Arthrosc. Relat. Surg.* 39, 2408–2419. doi:10.1016/j.arthro.2023.05.020

Lee, K. E., Choi, D. H., Joo, C., Kang, S.-W., Huh, K. M., and Park, Y. S. (2021a). Octanoyl glycol chitosan enhances the proliferation and differentiation of tonsil-derived mesenchymal stem cells. *Carbohydr. Polym.* 264, 117992. doi:10.1016/j.carbpol.2021.117992

Lee, S., Hwang, J.-T., Lee, S.-S., Lee, J.-H., and Kim, T.-Y. (2021b). Greater tuberosity bone mineral density and rotator cuff tear size are mndependent factors issociated with autting-through in arthroscopic suture-cridge rotator cuff repair. *Arthrosc. J. Arthrosc. Relat. Surg.* 37, 2077–2086. doi:10.1016/j.arthro.2021.01.059

Li, Q., Ran, C., Chen, J., Jin, J., He, J., Li, Y., et al. (2024). Chitosan-coated double-loaded liposomes as a promising delivery system for clove essential oil. *J. Food Eng.* 376, 112084. doi:10.1016/j.jfoodeng.2024.112084

Liu, R., Pang, Y., Xiao, T., Zhang, S., Liu, Y., and Min, Y. (2022). Multifunctional PCL composite nanofibers reinforced with lignin and ZIF-8 for the treatment of bone defects. *Int. J. Biol. Macromol.* 218, 1–8. doi:10.1016/j.ijbiomac.2022.06.183

Liu, S., Lai, C., Li, B., Zhang, C., Zhang, M., Huang, D., et al. (2020). Role of radical and non-radical pathway in activating persulfate for degradation of p-nitrophenol by sulfur-doped ordered mesoporous carbon. *Chem. Eng. J.* 384, 123304. doi:10.1016/j.cej.2019.123304

Makaram, N. S., Khan, L. A. K., Jenkins, P. J., and Robinson, C. M. (2023). Functional outcome after nonoperative management of minimally displaced greater tuberosity fractures and predictors of poorer patient experience. *Bone Jt. J.* 105-B, 534–542. doi:10.1302/0301-620X.105B5.BJJ-2022-1142.R1

Makurat-Kasprolewicz, B., Ipakchi, H., Rajaee, P., Ossowska, A., Hejna, A., Farokhi, M., et al. (2024). Green engineered biomaterials for bone repair and regeneration: brinting technologies and fracture analysis. *Chem. Eng. J.* 494, 152703. doi:10.1016/j.cej.2024.152703

Manakhov, A., Permyakova, E. S., Ershov, S., Sheveyko, A., Kovalskii, A., Polčák, J., et al. (2019). Bioactive TiCaPCON-coated PCL nanofibers as a promising material for bone tissue engineering. *Appl. Surf. Sci.* 479, 796–802. doi:10.1016/j.apsusc.2019.02.163

Martín-López, E., Nieto-Díaz, M., and Nieto-Sampedro, M. (2013). Influence of chitosan concentration on cell viability and proliferation *in vitro* by changing pilm topography. *J. Appl. Biomater. Funct. Mater.* 11, 151–158. doi:10.5301/JABFM.2012.10449

Petrović, Ž., Šarić, A., Despotović, I., Katić, J., Peter, R., Petravić, M., et al. (2022). Surface Functionalisation of fental implants with a composite doating of alendronate and cydrolysed collagen: DFT and EIS studies. *Materials* 15, 5127. doi:10.3390/ma15155127

Sedghi, R., Shaabani, A., and Sayyari, N. (2020). Electrospun triazole-based chitosan nanofibers as a novel scaffolds for bone tissue repair and regeneration. *Carbohydr. Polym.* 230, 115707. doi:10.1016/j.carbpol.2019.115707

Shi, X., Wang, Y., Varshney, R. R., Ren, L., Zhang, F., and Wang, D.-A. (2009). *In-vitro* osteogenesis of synovium stem cells induced by controlled release of bisphosphate additives from microspherical mesoporous silica composite. *Biomaterials* 30, 3996–4005. doi:10.1016/j.biomaterials.2009.04.021

Sun, H., Zhang, C., Zhang, B., Song, P., Xu, X., Gui, X., et al. (2022). 3D printed calcium phosphate scaffolds with controlled release of osteogenic drugs for bone regeneration. *Chem. Eng. J.* 427, 130961. doi:10.1016/j.cej.2021.130961

Tang, G., Zhu, L., Wang, W., Zuo, D., Shi, C., Yu, X., et al. (2022). Alendronate-functionalized double network hydrogel scaffolds for effective osteogenesis. *Front. Chem.* 10, 977419. doi:10.3389/fchem.2022.977419

Tao, F., Li, L., Wang, D., Dong, J., Zhou, D., and Song, W. (2024). Comparison study among hhree surgical methods in the treatment of tsolated fractures of the greater tuberosity of the humerus. *Ther. Clin. Risk Manag.* 20, 483–493. doi:10.2147/TCRM.S455379

Wang, D., Luo, F., He, F., Lu, F., Tao, X., Song, K., et al. (2021). Preparation and anti-tumor activity of PEG-PCL polymersomes loaded with curcumol derivative in HepG2 cell line. *J. Drug Deliv. Sci. Technol.* 66, 102782. doi:10.1016/j.jddst.2021.102782

Wang, J., Zhou, L., Sun, Q., Cai, H., and Tan, W.-S. (2020). Porous chitosan derivative scaffolds affect proliferation and osteogenesis of mesenchymal stem cell via reducing intracellular ROS. *Carbohydr. Polym.* 237, 116108. doi:10.1016/j.carbpol.2020.116108

Wang, K., and Liu, Q. (2013). Adsorption of phosphorylated chitosan on mineral surfaces. *Colloids Surf. Physicochem. Eng. Asp.* 436, 656–663. doi:10.1016/j.colsurfa.2013.07.030

Wang, Y., Pan, H., and Chen, X. (2019). The preparation of iollow mesoporous hioglass banoparticles with excellent drug delivery napacity for bone tissue regeneration. *Front. Chem.* 7, 283. doi:10.3389/fchem.2019.00283

Yingjun, M., Shuo, T., Liuyun, J., Yan, Z., and Shengpei, S. (2023). Study on a co-hybrid nano-hydroxyapatite with lignin derivatives and alendronate and the reinforce effect for poly(lactide-co-glycolide). *Int. J. Biol. Macromol.* 253, 126785. doi:10.1016/j.ijbiomac.2023.126785

Yu, H., Jia, Y., Yao, C., and Lu, Y. (2014). PCL/PEG core/sheath fibers with controlled drug release rate fabricated on the basis of a novel combined technique. *Int. J. Pharm.* 469, 17–22. doi:10.1016/j.ijpharm.2014.04.045

Zeng, L.-Q., Chen, Y.-F., Jiang, Y.-W., Zeng, L.-L., Miao, X.-G., and Liang, W.-G. (2021). A new low-profile anatomic locking plate for fixation of comminuted, displaced greater tuberosity fractures of the proximal humerus. *J. Shoulder Elb. Surg.* 30, 1402–1409. doi:10.1016/j.jse.2020.08.036

Zhang, C., Zhong, Z., Sang, W., Ghorbani, F., Ghalandari, B., Mohamadali, M., et al. (2022). The cibenzyl dsoquinoline ilkaloid aerbamine bmeliorates osteoporosis by inhibiting bone resorption. *Front. Endocrinol.* 13, 885507. doi:10.3389/fendo.2022.885507

Zhu, W., Cheng, Y., Wang, C., Pinna, N., and Lu, X. (2021). Transition metal sulfides meet electrospinning: versatile synthesis, distinct properties and prospective applications. *Nanoscale* 13, 9112–9146. doi:10.1039/D1NR01070K

frontiers | Frontiers in Bioengineering and Biotechnology

TYPE Review
PUBLISHED 22 January 2025
DOI 10.3389/fbioe.2024.1456704

OPEN ACCESS

EDITED BY
Liqun Yang,
Shengjing Hospital of China Medical University, China

REVIEWED BY
Yuhai Zhao,
Louisiana State University, United States
Zhipeng Hou,
Shengjing Hospital of China Medical University, China

*CORRESPONDENCE
Zhicheng Yao,
15541955888@163.com

RECEIVED 29 June 2024
ACCEPTED 24 October 2024
PUBLISHED 22 January 2025

CITATION
Na L, Song X, Luo P, Su J and Yao Z (2025) Innovative applications of advanced nanomaterials in cerebrovascular imaging. *Front. Bioeng. Biotechnol.* 12:1456704. doi: 10.3389/fbioe.2024.1456704

Innovative applications of advanced nanomaterials in cerebrovascular imaging

Li Na[1], Xiaofu Song[1], Ping Luo[2], Jingqi Su[2] and Zhicheng Yao[1]*

[1]Department of Neurology, Liaoning Provincial People's Hospital, Shenyang, China, [2]Liaoning Provincial People's Hospital, China Medical University, Shenyang, China

Cerebrovascular imaging is essential for the diagnosis, treatment, and prognosis of cerebrovascular disease, including stroke, aneurysms, and vascular malformations. Conventional imaging techniques such as MRI, CT, DSA and ultrasound have their own strengths and limitations, particularly in terms of resolution, contrast and safety. Recent advances in nanotechnology offer new opportunities for improved cerebrovascular imaging. Nanomaterials, including metallic nanoparticles, magnetic nanoparticles, quantum dots, carbon-based nanomaterials, and polymer nanoparticles, show great potential due to their unique physical, chemical, and biological properties. This review summarizes recent advances in advanced nanomaterials for cerebrovascular imaging and their applications in various imaging techniques, and discusses challenges and future research directions. The aim is to provide valuable insights for researchers to facilitate the development and clinical application of these innovative nanomaterials in cerebrovascular imaging.

KEYWORDS

nanomaterials, cerebrovascular imaging, metal nanoparticles, magnetic nanoparticles, quantum dots, carbon-based nanomaterials, polymer nanoparticles

1 Introduction

Cerebrovascular imaging is crucial for diagnosing, treating, and predicting the course of cerebrovascular diseases (Haller et al., 2018; Hage et al., 2016). Conditions like stroke, aneurysms, and vascular malformations often result in significant morbidity and disability, impacting both patients and society. High-resolution, high-contrast imaging is essential for accurate diagnosis and effective treatment. Current techniques include Magnetic Resonance Imaging (MRI) (Sleight et al., 2021), Computed Tomography (CT) (Abbas and Kumar, 2018), Digital Subtraction Angiography (DSA) (Shaban et al., 2022), and ultrasound (Yan et al., 2019). Each has its advantages and disadvantages. CT is fast and offers high resolution, but it has poor soft tissue contrast and carries radiation risks (Ghekiere et al., 2017). MRI provides excellent soft tissue contrast, but scans take longer and it is sensitive to metal implants (Sammet, 2016). DSA is often considered the gold standard, providing detailed images, but it is invasive, complex, and involves radiation exposure (Orru' et al., 2020). The limitations of these techniques, particularly in resolution, contrast, and safety, motivate researchers to explore and develop more advanced imaging methods for improved diagnosis and treatment of cerebrovascular diseases.

Nanomaterials are materials with at least one dimension in the nanoscale range, approximately 1–100 nm. Due to their minuscule size, they exhibit unique and enhanced properties compared to their bulk counterparts, including increased surface area, quantum effects, and size-dependent optical, electrical, and magnetic behaviors. These

TABLE 1 Representative nanomaterials.

Nanomaterials	Characteristics	Applications	Advantages	Limitations
Metal nanoparticles	Surface Plasmon resonance and optical properties (Kumar et al., 2018)	Cancer treatment, biological imaging, chemical sensing, and drug delivery (Altammar, 2023)	Strong plasma absorption, Biological system imaging, Determine chemical information on metallic nanoscale substrate (Li et al., 2007)	Difficulty in synthesis Particles instability Impurity (Granqvist and Buhrman, 1976)
Magnetic nanoparticles	Superparamagnetic, high magnetic susceptibility, high coercivity, non-toxicity, biocompatibility, low Curie temperature (Yadollahpour and Rashidi, 2015)	Targeted drug delivery, magnetic hyperthermia, contrast agent for magnetic resonance imaging (Yadollahpour and Rashidi, 2015)	Non-toxicity, Biocompatibility, high-level aggregation in the desired tissue, high effective surface areas and lower sedimentation rates	Tendency to aggregate or the poor magnetization, Certain Degree of toxicity (Cardoso et al., 2018)
Quantum dots	Exceptional photochemical and photophysical properties (Reshma and Mohanan, 2019)	Medical diagnostics, drug delivery (Reshma and Mohanan, 2019)	Desirable photon emission properties, advantageous absorption properties (Reshma and Mohanan, 2019)	Unproductive due to antibody binding, Heavy metals present in the core may be toxic to host (Reshma and Mohanan, 2019)
Carbon-based nanoparticles	Electrical conductivity, high strength, structure, electron affinity, and adaptability (Altammar, 2023)	Tissue engineering, drug delivery, imaging, and biosensors (Multifunctional Carbon)	Unique structural dimensions and excellent mechanical, electrical, thermal, optical and chemical properties (Patel et al., 2019)	The toxicity remains a debated issue (Zhang et al., 2014)
Polymer nanoparticles	Biocompatibility, biodegradability (Zielińska et al., 2020)	Molecular imaging, drug delivery, and targeting cancer research (Lu et al., 2011)	Structures can be modified, with intricate definition over their compositions, structures and properties (Elsabahy and Wooley, 2012)	Stability Issues Toxicity Concerns Complex Manufacturing

characteristics make nanomaterials highly versatile and applicable across various fields. Nanotechnology's rapid advancement has created new possibilities in biomedicine (Fakruddin et al., 2012; Campos et al., 2020; Sindhwani and Chan, 2021). Nanomaterials, with their unique physical, chemical, and biological properties, show great promise for bioimaging (Liang et al., 2020; Li et al., 2023; Shen et al., 2022). Their small size, large surface area, diverse surface modification options, and excellent biocompatibility offer advantages over traditional materials. In cerebrovascular imaging, nanomaterials have introduced exciting innovations. For example, metallic nanoparticles, with their strong optical and electrical properties, are ideal contrast agents for optical and electronic imaging (Anderson et al., 2019; Padmanabhan et al., 2016; Srinoi et al., 2018). Magnetic nanoparticles, due to their magnetic behavior, enhance MRI contrast (Jeon et al., 2021; Lin et al., 2020; Zhao Z. et al., 2022). Quantum dots, with tunable spectra and high brightness, are promising for fluorescence imaging (Zhao B. et al., 2022; Wang et al., 2022; Chung et al., 2021). Carbon-based nanomaterials like graphene and carbon nanotubes offer excellent electrical conductivity and mechanical strength, making them suitable for multimodal imaging (Srivastava et al., 2021; Gollavelli et al., 2022). Polymer nanoparticles, with their biocompatibility and degradability, are valuable for molecular imaging and targeted therapy (Ong et al., 2021; Haupt et al., 2020; Yang et al., 2020). These nanomaterials enhance imaging resolution, contrast, and specificity through various mechanisms.

This review systematically analyzes recent advances in nanomaterials for cerebrovascular imaging. It explores their applications across different imaging techniques, evaluating their advantages and disadvantages. It also proposes future research directions. The review focuses on several key nanomaterials (Table 1): metallic nanoparticles, magnetic nanoparticles, quantum dots, carbon-based nanomaterials, and polymer nanoparticles. Their applications in MRI, CT, fluorescence imaging, and multimodal imaging are discussed in detail. Challenges such as biocompatibility, targeting, preparation processes, and ethical considerations are also addressed. This review aims to provide valuable insights for researchers and promote further development and application of advanced nanomaterials in cerebrovascular imaging.

2 Classification and characteristics of advanced nanomaterials

2.1 Metal nanoparticles

Metal nanoparticles, particularly gold and silver nanoparticles, have attracted significant attention for biomedical imaging (Yoon et al., 2015; Dąbrowska-Bouta et al., 2018). Gold nanoparticles, due to their unique optical and electronic properties, are widely used in bioimaging (Si et al., 2021) and techniques like enhanced light scattering (Figure 1). These nanoparticles significantly improve imaging contrast and resolution through surface plasmon resonance (Kim et al., 2019). Their size and shape can be precisely controlled during synthesis to fine-tune their optical properties (Piella et al., 2016). For example, gold nanorods, because of their anisotropic shape, exhibit distinct longitudinal and transverse surface plasmon resonance peaks, enabling signal enhancement across different wavelengths (Zheng et al., 2021; Huang et al., 2009). Furthermore, the gold nanoparticle surface can be chemically modified with various functional groups for targeted delivery and specific molecular recognition.

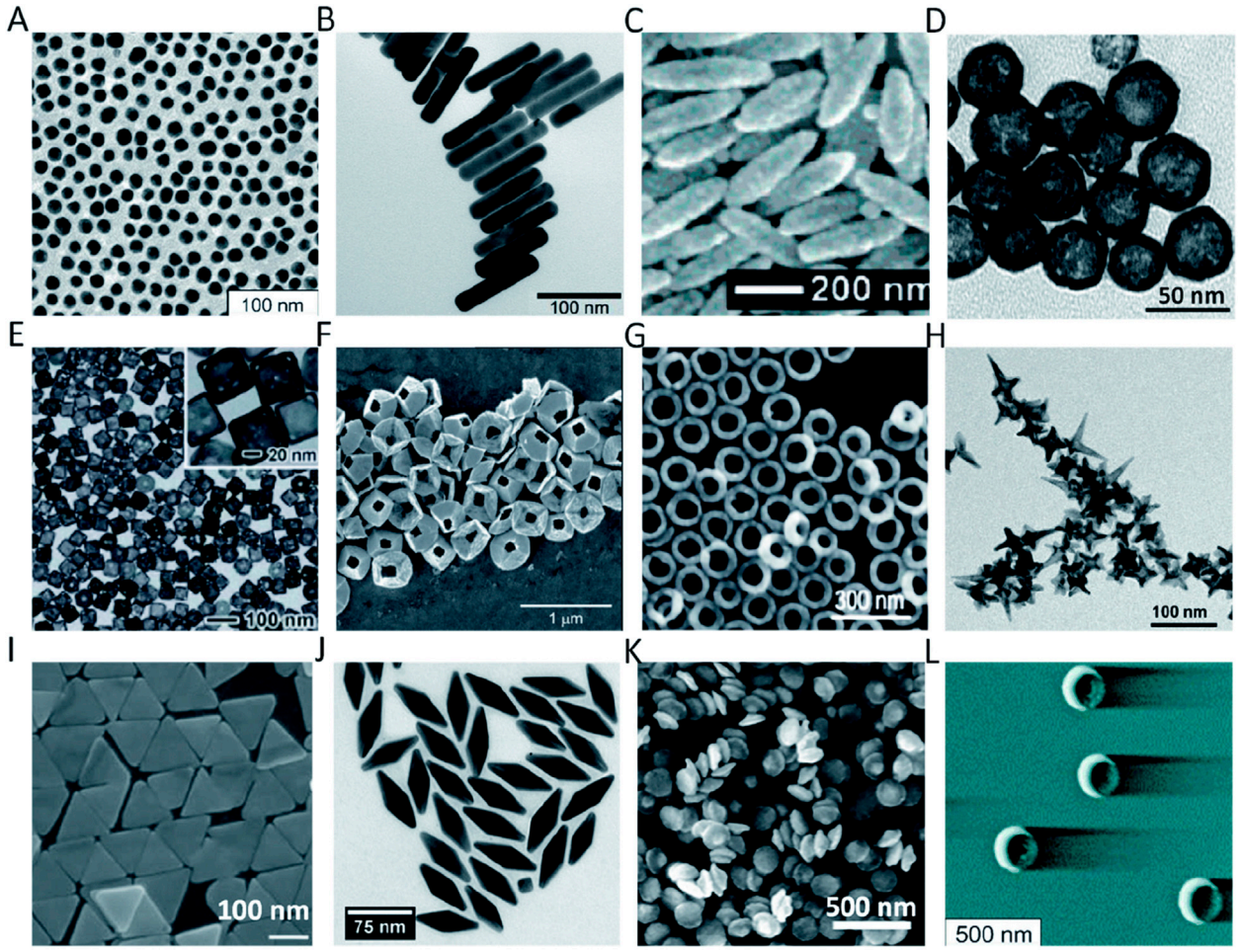

FIGURE 1
Different shapes and sizes of Au nanoparticles in bioimaging: **(A)** AuNS; **(B)** AuNR; **(C)** Au nanorice; **(D)** AuNSh; **(E)** AuNC; **(F)** tipless AuNPy; **(G)** AuNRg; **(H)** AuNSt; **(I)** AuNPr; **(J)** AuNBP; **(K)** AuND; and **(L)** AuNCr. Reproduction with the permission from reference (Si et al., 2021). Copyright © 2021 The Author(s).

Silver nanoparticles, known for their antibacterial properties and excellent optical characteristics (Fahmy et al., 2019; Singh et al., 2015; Balachandran et al., 2013), also hold great promise for biomedical imaging. Like gold nanoparticles, their size and shape can be precisely controlled during synthesis to adjust their optical properties (Shenashen et al., 2014; Pryshchepa et al., 2020; Fahmy et al., 2019). Silver nanoparticles significantly enhance sensitivity and resolution through surface-enhanced Raman scattering (SERS) (Seney et al., 2009; Zhang et al., 2011). SERS not only improves resolution but also provides detailed molecular information, potentially enabling earlier diagnosis of vascular diseases (Joseph et al., 2018).

2.2 Magnetic nanoparticles

Magnetic nanoparticles are widely used in MRI (Du et al., 2019; Yang et al., 2010). These nanoparticles significantly enhance MRI imaging contrast and spatial resolution due to their strong magnetic properties (Figure 2). The core of magnetic nanoparticles is typically composed of magnetic materials, while the outer layer is coated with polymers or other materials to improve their biocompatibility and stability. In addition to enhancing MRI contrast, magnetic nanoparticles can be combined with other imaging techniques to develop multimodal imaging technologies. Such multimodal imaging technologies not only improve imaging sensitivity and specificity but also enable a comprehensive diagnosis of lesions through complementary imaging modes. Moreover, magnetic nanoparticles exhibit excellent magnetic thermal effects, generating local high temperatures under an external alternating magnetic field, thereby being used for hyperthermia of lesions (Prieto and Linares, 2018; Skandalakis et al., 2020). This multifunctional characteristic of magnetic nanoparticles shows great potential in cerebrovascular imaging and treatment.

2.3 Quantum dots

Quantum dots are nanocrystals made of semiconductor materials with unique optical and electronic properties, such as wide excitation spectra, narrow and symmetrical emission spectra, and high optical stability (Agarwal et al., 2023). These properties

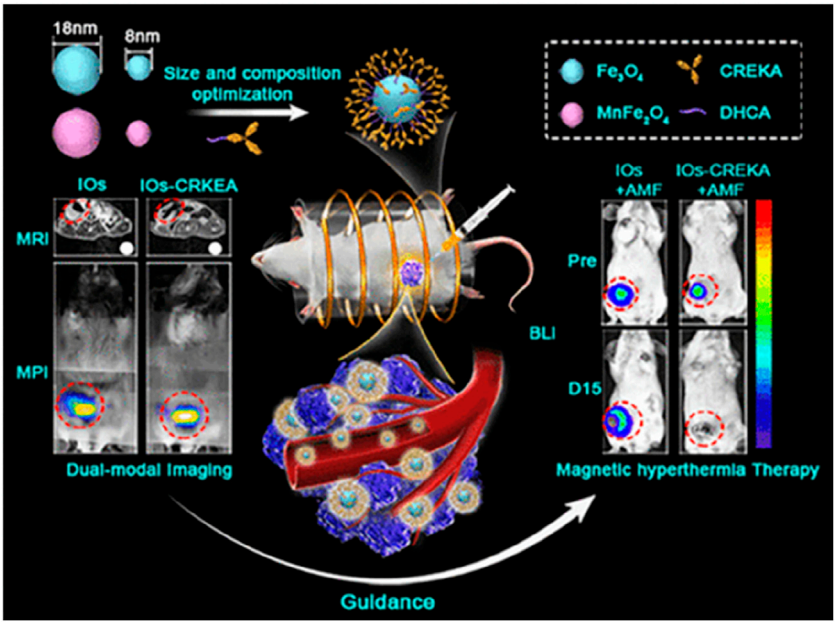

FIGURE 2
CREKA Modified Iron Oxide (IO) NPs for Precision Cancer Imaging and magnetic hyperthermia therapy. Reproduction with the permission from reference (Du et al., 2019). Copyright © 2019 American Chemical Society.

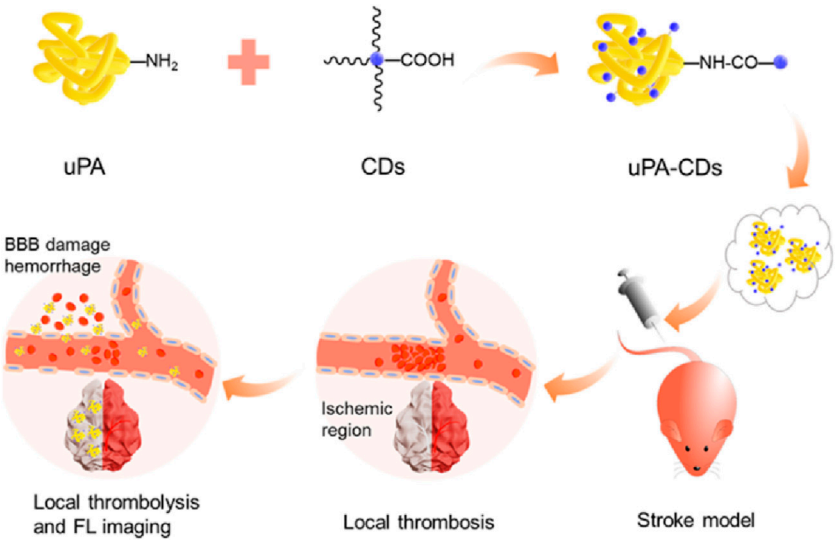

FIGURE 3
Urokinase-type plasminogen activator (uPA)-carbon dot (CD) Nanohybrids for fluorescence (FL) Imaging of Early blood–brain barrier (BBB) injury. Reproduction with the permission of reference (Niu et al., 2020). 2020. Copyright © 2020 American Chemical Society.

give quantum dots great potential in fluorescence imaging. Compared to traditional organic dyes, quantum dots offer higher brightness and longer fluorescence lifetime, enabling higher resolution and sensitivity imaging (Resch-Genger et al., 2008). Quantum dots can also be used for fluorescence imaging (Pandey and Bodas, 2020), where multiple quantum dots are simultaneously excited by different wavelengths of excitation light, displaying the distribution and dynamic changes of multiple biomolecules in the same image. This fluorescence imaging technology can provide rich spatial and temporal information at the molecular level, helping to reveal the complex biological mechanisms of cerebrovascular lesions (Niu et al., 2020) (Figure 3). Additionally, the spectral properties of quantum dots can be adjusted by changing their size and composition (Moreels et al., 2009), achieving fluorescence emission in different wavelength ranges. This flexibility broadens the application of quantum dots in cerebrovascular imaging (Ren

et al., 2021), allowing for the design and optimization of imaging schemes based on specific needs.

2.4 Carbon-based nanomaterials

Carbon-based nanomaterials, such as graphene, carbon nanotubes, and fullerenes, show great potential in bioimaging due to their unique physical and chemical properties (Zhang et al., 2018). Graphene is a two-dimensional material composed of a single layer of carbon atoms with excellent electrical conductivity, mechanical strength, and thermal stability. In biomedical imaging, graphene and its derivatives (such as graphene oxide) can be used for multimodal imaging and photoacoustic imaging (Yang et al., 2012; Toumia et al., 2016) due to their unique optical and electrical properties. Photoacoustic imaging is a method that combines optical and ultrasonic technology, achieving high-resolution deep tissue imaging through the photoacoustic effect generated by laser excitation of graphene. The high thermal conductivity and absorption rate of graphene exhibit excellent signal enhancement effects in photoacoustic imaging, significantly improving the sensitivity and resolution of cerebrovascular imaging.

Carbon nanotubes are nanomaterials with a concentric cylindrical structure made of carbon atoms, exhibiting excellent mechanical properties and electrical conductivity (Manikandan et al., 2021). In cerebrovascular imaging, carbon nanotubes can be used as contrast agents or carriers to enhance imaging signals and target drug delivery (Loh et al., 2018). Additionally, the surface of carbon nanotubes can be functionalized with antibodies, peptides, or drug molecules to achieve targeted imaging and treatment of specific cerebrovascular regions or lesions. This multifunctional characteristic of carbon nanotubes provides a new approach for the diagnosis and treatment of cerebrovascular diseases.

Fullerenes are spherical nanomaterials composed of carbon atoms, possessing unique electronic and optical properties. In biomedical imaging, fullerenes can be used as photosensitizers or contrast agents to enhance imaging signals (Luo et al., 2021). Additionally, fullerenes exhibit excellent photodynamic effects, generating reactive oxygen species to induce cell apoptosis under light irradiation, thus being used for the cancer treatment (Li et al., 2024). This photodynamic therapy combined with imaging technology provides a new treatment approach for cerebrovascular diseases.

2.5 Polymer nanoparticles

Polymer nanoparticles are nanoparticles composed of biodegradable polymers, possessing good biocompatibility and flexibility. Polymer nanoparticles can be loaded with various imaging agents, such as fluorescent dyes, radioactive isotopes, or magnetic nanoparticles, to achieve multimodal imaging (Ong et al., 2021; Yu et al., 2022). Additionally, the surface of polymer nanoparticles can be functionalized with antibodies, peptides, or small molecule drugs to achieve targeted imaging and treatment of specific cerebrovascular regions or lesions (Gao et al., 2022). In addition to their application in imaging, polymer nanoparticles can also be used for drug delivery and gene therapy. For instance, polymer nanoparticles loaded with therapeutic drugs or gene vectors can achieve targeted delivery to cerebrovascular lesion sites (Luo et al., 2020; Zhang et al., 2022), improving treatment efficiency and reducing side effects. This multifunctional characteristic of polymer nanoparticles provides a new approach for the integrated diagnosis and treatment of cerebrovascular diseases.

3 Applications of nanomaterials in different imaging techniques

3.1 Magnetic resonance imaging (MRI)

Magnetic Resonance Imaging (MRI) holds a significant position in cerebrovascular imaging because it provides high-resolution soft tissue contrast without the use of ionizing radiation. Traditional MRI contrast agents are typically gadolinium-based compounds, but their potential nephrotoxicity limits their long-term and high-dose use. Iron oxide-based contrast agents have been investigated as more specific MR imaging agents for central nervous system (CNS) inflammation. Ferumoxtran-10 is a virus-sized nanoparticle, taken up by reactive cells, that allows visualization of the phagocytic components of CNS lesions. Manninger et al. compared Ferumoxtran-10 with standard gadolinium-enhanced MR images in an exploratory trial to assess its potential in the evaluation of CNS lesions with inflammatory aspects (Manninger et al., 2005). In this study, twenty-three patients with different types of intracranial “inflammatory” lesions underwent standard brain MR with and without gadolinium, followed an average of 10 days later by a ferumoxtran-10 scan. Patients were imaged 24 h after infusion of 2.6 mg/kg ferumoxtran-10. All MR images were evaluated subjectively by 4 investigators for a difference in enhancement patterns. The results showed that the ferumoxtran-10 scan showed higher signal intensity, larger area of enhancement, or new enhancing areas compared with gadolinium, indicating that Ferumoxtran-10 showed different enhancement patterns in a variety of CNS lesions with inflammatory components in comparison to gadolinium (Figures 4–6).

Advanced nanomaterials, especially magnetic nanoparticles like USPIO, offer an attractive alternative. USPIO exhibits excellent T2 relaxation effects, which can significantly enhance the contrast of T2-weighted MRI images (Figure 7). These nanoparticles enter the bloodstream through intravenous injection and can target and accumulate at cerebrovascular lesion sites, such as atherosclerotic plaques and tumor vasculature, thereby providing high-resolution cerebrovascular imaging (Buch et al., 2020).

The surface of magnetic nanoparticles can be functionalized to introduce various targeting molecules (such as antibodies, peptides, or small molecule drugs) to enhance their targeting specificity. For example, USPIO modified with anti-angiogenic factor antibodies can specifically bind to the neovasculature of brain tumors (Soliman et al., 2020; Abousalman-Rezvani et al., 2024), enabling precise imaging of lesion sites. In addition to enhancing MRI contrast, magnetic nanoparticles can also be combined with other imaging techniques to develop multimodal imaging probes (Antonelli and Magnani, 2022). By conjugating USPIO with fluorescent dyes or radioactive isotopes, simultaneous imaging with MRI and fluorescence imaging or positron emission tomography (PET) can be achieved, thereby providing more

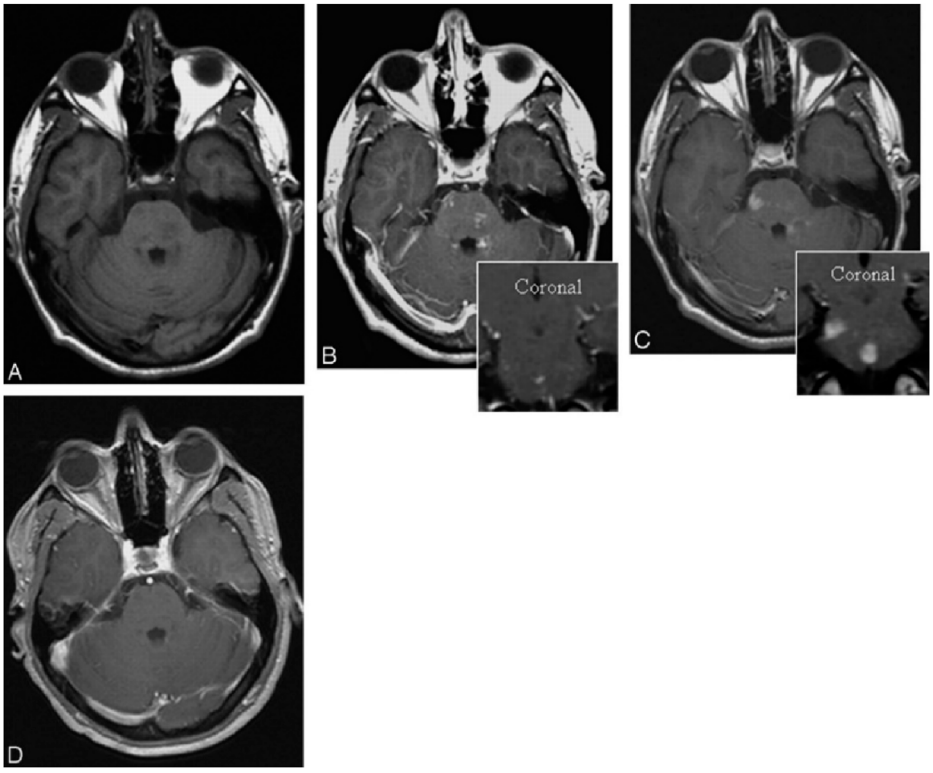

FIGURE 4
Patient with ADEM. Axial T1-weighted images without **(A)** and with **(B)** gadolinium (inset coronal) reveal faint and subtle enhancement in multiple brain stem lesions. Six days later **(C)**, the same site exhibits significant, more pronounced, and larger enhancement with ferumoxtran-10 (inset, coronal). Three months later **(D)**, the lesions no longer show enhancement on T1-weighted images with gadolinium.

comprehensive information on cerebrovascular lesions (Zhang et al., 2023; Yu et al., 2018).

3.2 Computed tomography (CT)

Computed Tomography (CT) is widely used in cerebrovascular imaging, especially in the diagnosis of acute stroke (Mangesius et al., 2021). However, traditional iodine-based contrast agents have limited effectiveness in CT imaging and pose potential nephrotoxicity risks (Zhang P. et al., 2021). Advanced nanomaterials, particularly gold nanoparticles, offer new possibilities for enhancing CT imaging. Gold nanoparticles have a high atomic number and density, which significantly increases X-ray absorption, thereby enhancing CT imaging contrast (Aslan et al., 2020; Asadinezhad et al., 2021). Compared to traditional contrast agents, gold nanoparticles have a longer circulation time in the bloodstream, providing more sustained imaging effects (Owens et al., 2023).

The size and shape of gold nanoparticles can be adjusted during the synthesis process to optimize their performance in CT imaging (Piella et al., 2016). For instance, spherical and rod-shaped gold nanoparticles have different optical and physical properties, making them suitable for various imaging applications (Alam et al., 2022; Bansal et al., 2020). Surface-functionalized gold nanoparticles can achieve targeted imaging of specific cerebrovascular lesion sites through targeting molecules (such as antibodies or peptides). For example, gold nanoparticles modified with anti-platelet-derived growth factor (PDGF) antibodies can target the vasculature of brain tumors, providing high-resolution CT images (Meola et al., 2018).

Besides enhancing CT imaging, gold nanoparticles can also be combined with other imaging modalities to develop multifunctional imaging probes. For example, conjugating gold nanoparticles with fluorescent dyes or magnetic nanoparticles allows for simultaneous CT and fluorescence imaging or MRI (Cheng et al., 2014). This multimodal imaging technology can provide more comprehensive information on lesions, aiding in the improved diagnosis and treatment of cerebrovascular diseases. For instance, the combination of gold nanoparticles and magnetic nanoparticles enables both CT and MRI imaging (Cheng et al., 2014; Sun et al., 2016), offering detailed images of cerebrovascular structures and functions.

Despite the promising prospects of gold nanoparticles in CT imaging, their biosafety and long-term *in vivo* metabolism require further research. Studies have shown that the surface modification of gold nanoparticles can significantly affect their distribution and metabolic pathways in the body. For example, polyethylene glycol (PEG) modification can increase the blood circulation time of gold nanoparticles and reduce their accumulation in the liver and spleen (Kozics et al., 2021), thereby enhancing biosafety. Future research should focus on optimizing the surface modification and functionalization of gold nanoparticles to improve their feasibility and safety in clinical applications.

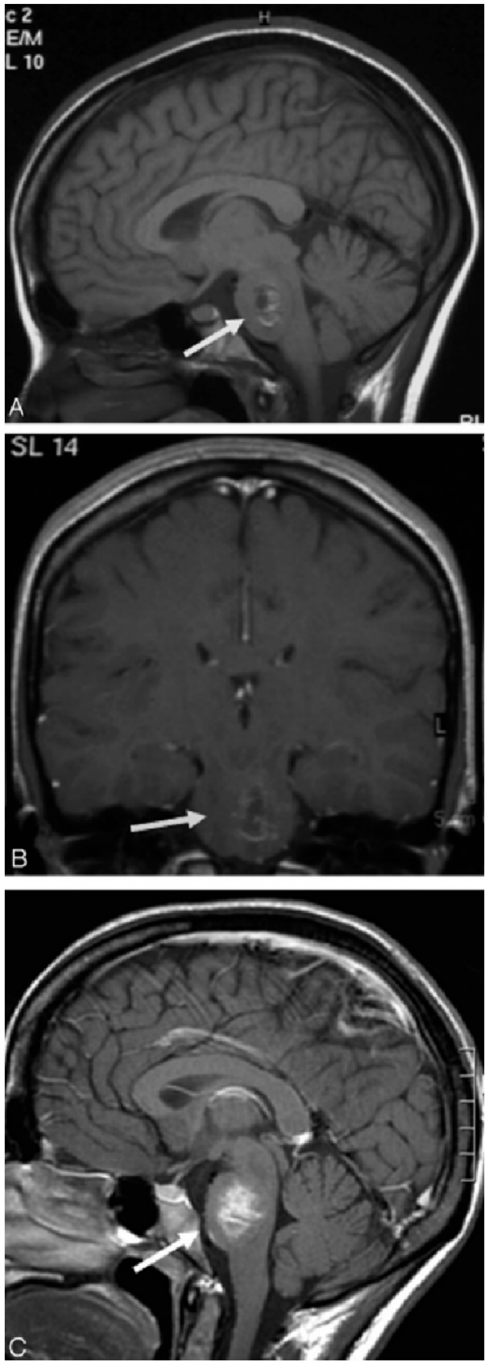

FIGURE 5
Patient with cavernous venous vascular malformation. Sagittal T1-weighted images without gadolinium **(A)** and coronal T1-weighted images with gadolinium **(B)** show no significant enhancement in the left pons lesion. However, 4 days later, T1 MR images **(C)** reveal prominent enhancement of the same lesion with ferumoxtran-10. Reproduction with the permission of reference (Manninger et al., 2005). Copyright ©2005 American Society of Neuroradiology.

3.3 Fluorescence imaging

Fluorescence imaging technology has significant applications in biomedical research and clinical diagnostics, particularly in cerebrovascular imaging (Ren et al., 2021), where it provides high sensitivity and high-resolution real-time imaging (Figure 8). Quantum dots, as an advanced fluorescent probe material, have become a research hotspot in fluorescence imaging due to their unique optical properties and high brightness. Quantum dots have broad excitation and narrow emission spectra, enabling the simultaneous excitation of multiple colors for multicolor imaging (Wang et al., 2020). In cerebrovascular imaging, quantum dots can achieve highly specific imaging of cerebrovascular lesion sites through surface modification with specific targeting molecules. For example, quantum dots conjugated with vascular endothelial growth factor (VEGF) antibodies can target and image areas of neovascularization in the brain (Li et al., 2015), providing strong support for the early diagnosis of brain tumors and strokes. The high optical stability of quantum dots allows them to maintain brightness without fading during prolonged imaging, providing continuous, clear images (Montalti et al., 2015). This is important for dynamically monitoring the progression of cerebrovascular lesions and the effectiveness of treatments. Additionally, the emission spectra of quantum dots can be tuned by adjusting their size and composition (Hu et al., 2015), allowing fluorescence emission over different wavelength ranges and enabling multicolor imaging and multiparameter analysis.

The application of quantum dots in cerebrovascular imaging also includes multimodal imaging (Jing et al., 2014; Swierczewska et al., 2011). By combining quantum dots with magnetic nanoparticles or metal nanoparticles, it is possible to achieve multimodal imaging with fluorescence imaging, magnetic resonance imaging (MRI), and computed tomography (CT). This multimodal imaging technology can provide comprehensive information about lesions, including structural, functional, and molecular-level data, thereby improving diagnostic accuracy and treatment effectiveness. For example, composite probes combining quantum dots and magnetic nanoparticles can switch between fluorescence imaging and MRI (Koole et al., 2009), achieving high-sensitivity, multidimensional imaging of cerebrovascular lesions.

Despite the significant advantages of quantum dots in fluorescence imaging, their biosafety remains a concern. Quantum dots often contain heavy metal elements, such as cadmium and lead, which can cause toxic effects when accumulated in the body. Therefore, developing low-toxicity or non-toxic quantum dot materials, such as carbon quantum dots or silicon quantum dots, is a current research focus. By optimizing the surface modification and functionalization of quantum dots, their biocompatibility and *in vivo* stability can be further enhanced, promoting their development in clinical applications. For instance, coating quantum dots with biocompatible polymer materials can significantly reduce their toxicity and improve their stability and distribution specificity *in vivo*.

3.4 Multimodal imaging

Multimodal imaging technology holds significant importance in cerebrovascular imaging as it combines the advantages of various imaging modalities, providing more comprehensive and detailed information about lesions. Advanced nanomaterials open up new possibilities for the development of multimodal imaging probes. For

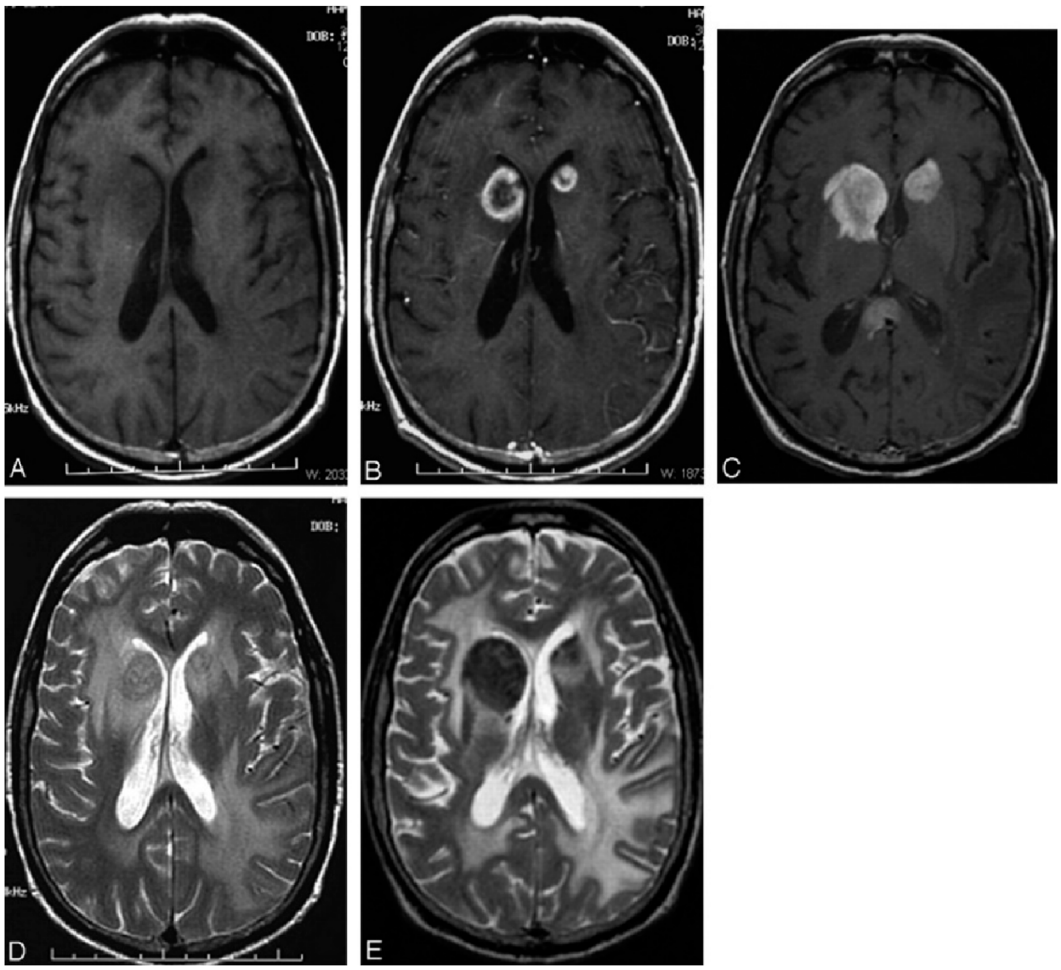

FIGURE 6
Patient with PCNSL. Axial T1-weighted images without gadolinium **(A)** and with gadolinium **(B)** reveal intense ring-enhancing lesions in the head of both caudate nuclei. Fifteen days later, T1-weighted images with ferumoxtran-10 **(C)** demonstrate that the lesions in the caudate head have enlarged and exhibit more intense enhancement. Additionally, another lesion in the splenium of the corpus callosum is visible, showing larger and more intense enhancement compared to the baseline gadolinium image (not shown). T2-weighted images following ferumoxtran-10 administration **(D, E)** display low-intensity changes in both lesions. Reproduction with the permission of reference (Manninger et al., 2005). Copyright ©2005 American Society of Neuroradiology Reproduction with the permission of reference (Manninger et al., 2005). Copyright © 2005 American Society of Neuroradiology.

instance, combining metal nanoparticles with fluorescent dyes, magnetic nanoparticles, or radioactive isotopes can enable the simultaneous application of multiple imaging modes, such as fluorescence imaging, magnetic resonance imaging (MRI), computed tomography (CT), and positron emission tomography (PET) (Huang and Davis, 2011; Burke et al., 2017).

Metal nanoparticles, such as gold and silver nanoparticles, are widely used in multimodal imaging. Gold nanoparticles, with their unique surface plasmon resonance (SPR) properties, can significantly enhance optical imaging contrast. Additionally, their high atomic number makes them excellent at X-ray absorption, thus providing high-contrast CT images. Combining gold nanoparticles with fluorescent dyes allows for simultaneous fluorescence and CT imaging. For example, gold nanoparticles modified with vascular endothelial growth factor (VEGF) antibodies can be used for both fluorescence and CT imaging, providing detailed information about neovascularization in brain tumors (Hariharan et al., 2022).

Magnetic nanoparticles, such as USPIO, also have significant advantages in multimodal imaging. USPIO exhibits excellent T2 relaxation effects, significantly enhancing the contrast of T2-weighted MRI images. By combining USPIO with fluorescent dyes or radioactive isotopes, it is possible to achieve simultaneous MRI and fluorescence imaging or PET imaging (Chen et al., 2016). For instance, composite probes combining USPIO and fluorescent dyes can switch between MRI and fluorescence imaging, providing high-sensitivity, multidimensional imaging of cerebrovascular lesions (Deddens et al., 2012). Moreover, the magnetic hyperthermia effect of USPIO can be used for brain tumor hyperthermia treatment (Israel et al., 2020), offering a non-invasive localized therapy option in addition to imaging.

Carbon-based nanomaterials, such as graphene and carbon nanotubes, also show great potential in multimodal imaging (Yang et al., 2012). Graphene, with its excellent optical, electrical, and mechanical properties, is particularly suitable for photoacoustic

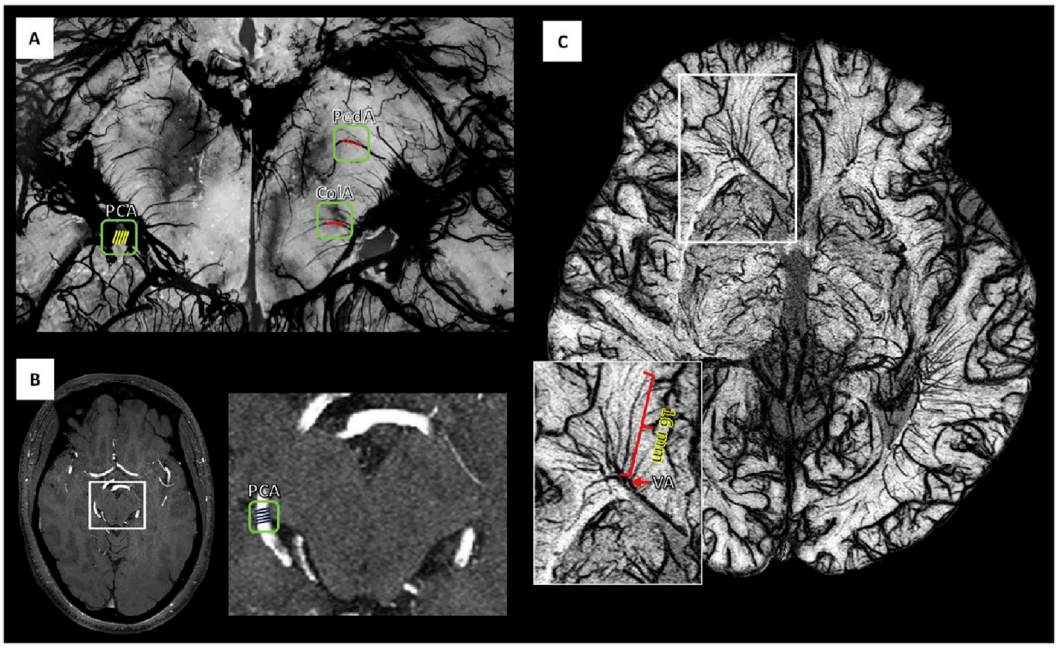

FIGURE 7
Validating the size of the small vessels that were visible after administration of USPIO agent Ferumoxytol **(A)** The ratio of posterior cerebral artery (PCA) to a peduncular artery (PedA) and collicular artery (ColA) was estimated using the histology work by obtaining the vessel diameters at five different locations. **(B)** The true diameter of PCA was obtained from Fe0 short TE magnitude data for all subjects. **(C)** SWIPGAC data (with a zoomed inset of the medullary veins as shown by the white box), focusing on the cerebral white matter vessels. VA = Ventricular angle. Reproduction with the permission of reference (Buch et al., 2020). Copyright © 2020 Elsevier Inc.

imaging (Toumia et al., 2016). Combining graphene with fluorescent dyes or magnetic nanoparticles can achieve multimodal imaging with photoacoustic imaging, fluorescence imaging, and MRI. For example, composite probes combining graphene and magnetic nanoparticles can switch between photoacoustic imaging and MRI, providing high-resolution structural and functional images of cerebrovascular structures (Zhao et al., 2021). Carbon nanotubes, with their unique structure and optical properties, can be utilized to develop multifunctional imaging probes capable of simultaneous fluorescence, photoacoustic, and CT imaging (Thangam et al., 2021). Phillips et al. conducted a human clinical trial involving ultrasmall inorganic hybrid nanoparticles, specifically ^{124}I-cRGDY–PEG–C dot particles, in patients (Phillips et al., 2014). In patient who received an intravenous injection of ^{124}I-cRGDY–PEG–C dots, a well-defined cystic lesion approximately 5 mm in size was observed in the right anterior lobe of the pituitary gland, an area lacking a blood-brain barrier, on axial and sagittal magnetic resonance (MR) images (Figure 9A). Precise co-registration of this tracer-avid focus with multiplanar MRI (Figure 9B) and CT (Figure 9C) images confirmed its location within the interior of the pituitary gland. PET imaging revealed a progressive net accumulation of ^{124}I-cRGDY–PEG–C dot activity at the lesion site (Figure 9D).

Polymer nanoparticles also deserve attention in multimodal imaging applications (Joshi and Joshi, 2022). Polymer nanoparticles have good biocompatibility and degradability, allowing them to carry various imaging probes or drugs for efficient targeted delivery and imaging. For example, polylactic-co-glycolic acid (PLGA) nanoparticles can carry fluorescent dyes, magnetic nanoparticles, or drug molecules for multimodal imaging and targeted therapy (Hashemi et al., 2020; Zhang et al., 2020). By combining PLGA nanoparticles with metal or magnetic nanoparticles, it is possible to develop multimodal imaging probes with fluorescence, MRI, and photoacoustic imaging capabilities (Joshi and Joshi, 2022). This multimodal imaging technology can provide more comprehensive and detailed information about cerebrovascular lesions, thus improving diagnostic accuracy and treatment effectiveness.

The main advantage of multimodal imaging lies in its ability to integrate the benefits of different imaging modalities, providing comprehensive information at structural, functional, and molecular levels. For example, MRI can offer high-resolution soft tissue contrast, CT can provide high-contrast images of bones and blood vessels, fluorescence imaging can deliver highly sensitive molecular information, and PET can offer metabolic and functional data. By combining these imaging modalities, it is possible to obtain more comprehensive information about lesions, thereby improving diagnostic accuracy and treatment outcomes. In brain tumor diagnosis, for instance, multimodal imaging can provide multidimensional information about tumor anatomy, angiogenesis, molecular marker expression, and metabolic activity, offering more comprehensive diagnostic support for clinicians (Overcast et al., 2021).

In summary, the application of advanced nanomaterials in cerebrovascular imaging has broad prospects. By continuously optimizing and improving the synthesis processes and surface modification techniques of nanomaterials, their imaging performance and biosafety can be further enhanced, promoting

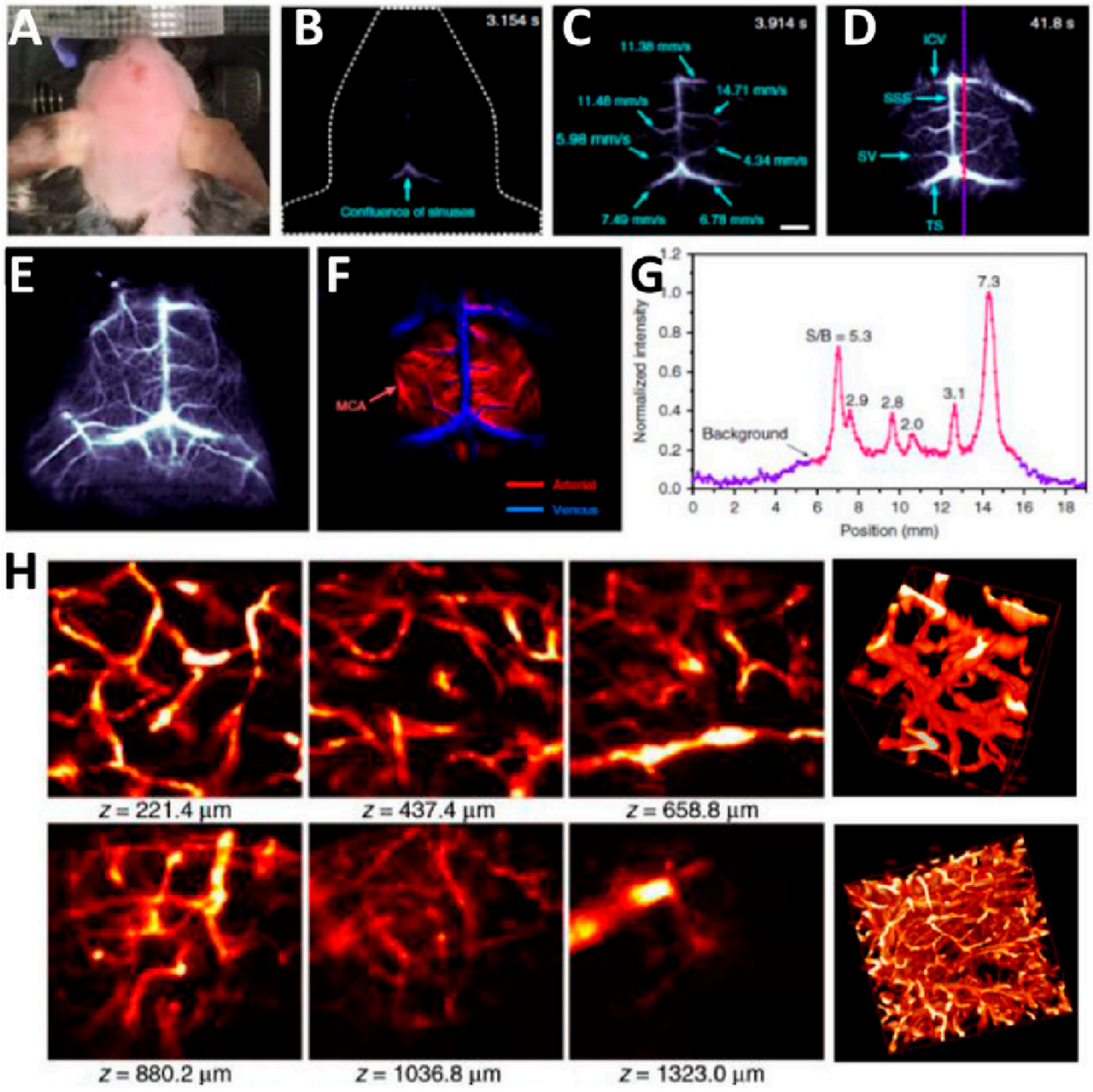

FIGURE 8
(A) Color photograph of a hair-shaved-off C57BL/6 mouse for NIR-IIb fluorescence imaging. **(B–D)** Time-course NIR-IIb brain fluorescence images present the perfusion of rare-earth NPs into various cerebral vessels. **(E, F)** Cerebral vascular image and the corresponding PCA overlaid image F showing arterial (red) and venous (blue) vessels. **(G)** SBR analysis of NIR-IIb cerebrovascular image. **(H)** Small area and 3D reconstruction of vascular confocal images of a mouse brain. Reproduction with the permission of reference (Ren et al., 2021). Copyright © 2021 The Authors.

their translation and application in clinical settings. The use of multimodal imaging technology, particularly in combination with different types of nanomaterials, offers new approaches and methods for the diagnosis and treatment of cerebrovascular diseases. In the future, as nanomaterials and imaging technologies continue to advance, multimodal imaging will play an increasingly important role in cerebrovascular imaging, providing strong support for the early diagnosis and personalized treatment of cerebrovascular diseases.

4 Challenges and future prospects

Despite the significant advantages of nanomaterials in cerebrovascular imaging, there are still many challenges and issues in practical applications. For example, the biosafety, long-term stability, targeting, specificity, large-scale preparation, and clinical translation of nanomaterials require further research and solutions. Therefore, future research should focus on the following aspects.

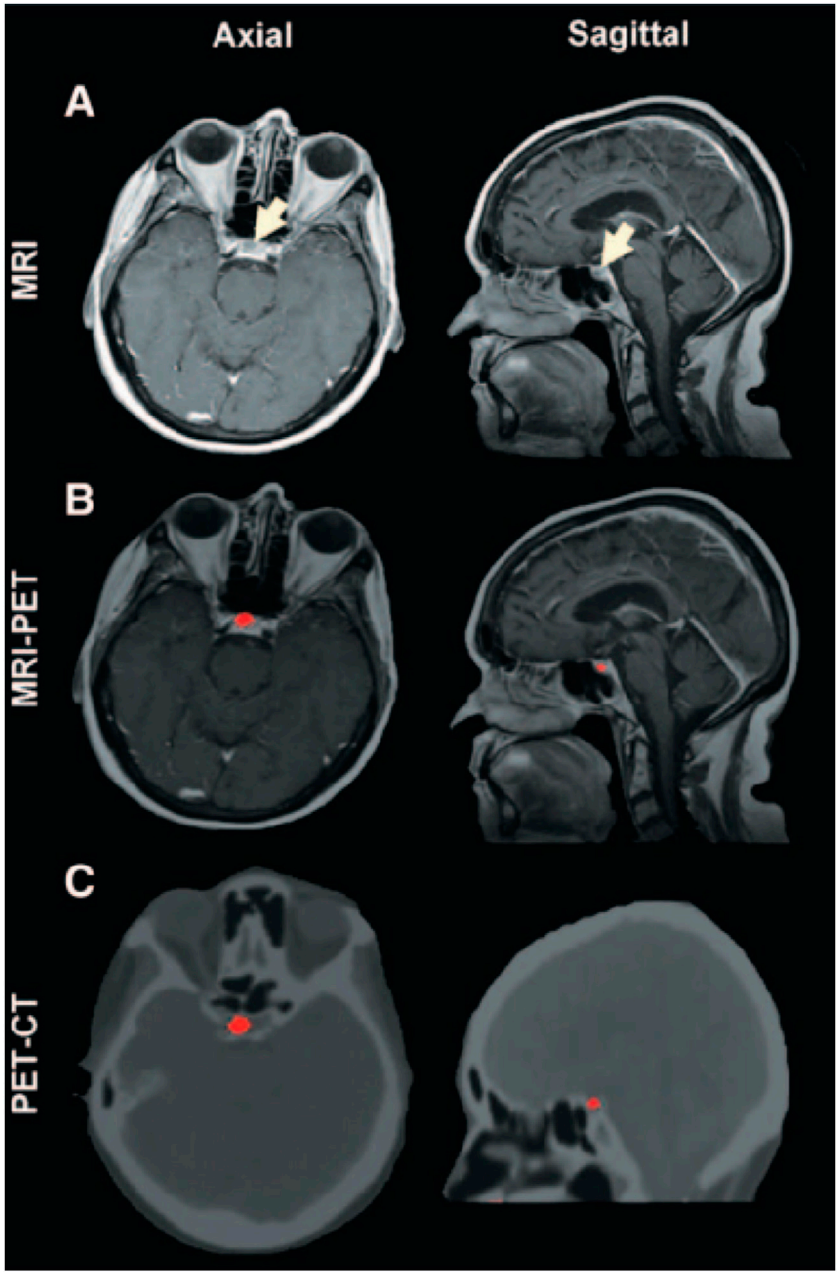

FIGURE 9
Multimodal Imaging of Particle Uptake in a Pituitary Lesion. **(A)** Multiplanar contrast-enhanced MR axial and sagittal images of patient, taken 72 h post-injection, demonstrate a subcentimeter cystic focus (arrows) within the right aspect of the anterior pituitary gland. **(B)** Co-registered axial and sagittal MRI-PET images show increased focal activity (red, 124I-cRGDY–PEG–C dots) localized to the lesion site. **(C)** Axial and sagittal PET-CT images further localize this activity to the right aspect of the sella. Reproduction with the permission of reference (Phillips et al., 2014). Copyright ©2014 American Association for the Advancement of Science.

4.1 Biosafety and long-term stability

A primary challenge for using advanced nanomaterials in cerebrovascular imaging is ensuring their safety. This involves both biocompatibility and minimizing potential toxicity. Nanomaterials have unique properties ideal for imaging, but these same properties can raise safety concerns. Some nanomaterials, like quantum dots and certain metallic nanoparticles, contain potentially toxic elements (e.g., cadmium, lead) (Sengul and Asmatulu, 2020; Sobhanan et al., 2023). These elements can accumulate in the body, harming tissues and organs. Therefore, biocompatibility is crucial for clinical translation. Nanomaterial toxicity is linked to several factors: size, shape, surface chemistry, and functional modifications (Sukhanova et al., 2018; Albanese et al., 2012; Kim et al., 2013). Smaller nanoparticles can more easily cross biological barriers, potentially increasing their biological impact and toxicity (Pandey and Prajapati, 2018; Sani et al., 2021). Functional modifications, such as coating with

polyethylene glycol (PEG), can improve biocompatibility. PEGylation can extend blood circulation time and reduce accumulation in the liver and spleen, minimizing toxic reactions (Fan et al., 2020). Metabolism and excretion pathways are also critical for biosafety. Ideally, nanomaterials should be biodegradable and quickly cleared from the body to prevent long-term accumulation and toxicity. Some polymer-based nanoparticles (e.g., PLGA) show promise in this regard, breaking down into harmless molecules. However, further research is needed to optimize their degradation and metabolic profiles. Researchers are developing strategies to enhance biocompatibility. Surface coating with biocompatible materials (e.g., liposomes, proteins, polysaccharides) can improve stability and reduce toxicity. Liposome-coated gold nanoparticles, for example, show improved blood stability and reduced accumulation in organs (Liang et al., 2017).

In conclusion, while biocompatibility and toxicity are key challenges, ongoing research into surface modifications and other strategies offers promising solutions. Rigorous testing and clinical trials are essential to validate the safety and efficacy of these nanomaterials before widespread use in cerebrovascular imaging.

4.2 Targeting and specificity

Targeting and specificity are crucial for effective cerebrovascular imaging using nanomaterials. These materials must accurately reach and accumulate at the lesion site to generate clear imaging signals. However, the blood-brain barrier (BBB) hinders most nanomaterials from entering brain tissue, limiting their application. Therefore, developing nanomaterials capable of crossing the BBB and targeting cerebrovascular lesions is a key research area (Furtado et al., 2018; Tan et al., 2023; Zhang W. et al., 2021; Gao et al., 2022; Wu et al., 2023). Several strategies enhance targeting. Surface functionalization with ligands (e.g., antibodies, peptides, small molecules) allows nanoparticles to bind specifically to target sites, such as the neovasculature of brain tumors (Winer et al., 2011). Multifunctional molecules can simultaneously provide targeting and imaging capabilities, improving specificity and sensitivity (Rizvi et al., 2021). Leveraging the physicochemical properties of nanomaterials is another approach. Magnetic nanoparticles (e.g., USPIO) can be guided to specific locations using an external magnetic field, improving targeting efficiency and reducing non-specific distribution in healthy tissues, which also lowers potential toxicity (Liu et al., 2021). Nanomaterial size and shape also influence targeting. Non-spherical shapes (e.g., rods, sheets) interact differently with blood vessels compared to spheres, potentially improving accumulation at lesion sites. Precise control over size and shape can optimize *in vivo* distribution and targeting (Annu et al., 2022; Luo et al., 2020).

Despite these advances, challenges remain. The BBB's complexity and individual variability hinder penetration and targeting. The body's complex metabolism and clearance mechanisms can also reduce effectiveness. Future research should explore new targeting strategies and optimize existing technologies to enhance nanomaterial performance in cerebrovascular imaging. This includes further investigation into overcoming the BBB and improving the precision of targeting to specific lesion types within the cerebrovascular system.

4.3 Large-scale preparation and clinical translation

Using nanomaterials for cerebrovascular imaging depends on high-quality materials and scalable production. Optimized preparation processes are essential for consistent material performance. Traditional methods (e.g., chemical precipitation, sol-gel, hydrothermal synthesis, sputtering) (Rafique et al., 2020) can produce high-quality nanomaterials at small scales, but scaling up often presents challenges like low yield, high cost, and complex processes. Newer techniques aim to improve production efficiency and quality. Microfluidic technology (Zhao et al., 2020; Illath et al., 2022), using microscale reactors, allows for precise control over reaction conditions. This leads to greater material uniformity and stability, shorter preparation times, and reduced costs. It also facilitates continuous synthesis of multi-component nanomaterials, enabling the development of multifunctional imaging probes. Self-assembly is another promising technique (Li et al., 2022). By controlling intermolecular forces (e.g., electrostatic, hydrogen bonds, van der Waals), nanomaterials can spontaneously assemble into complex structures. This method is efficient, environmentally friendly, and potentially scalable. It allows for the creation of multilayer nanomaterials capable of carrying multiple imaging probes or drugs for multimodal imaging and targeted therapy (Li et al., 2021).

Despite these advances, large-scale production still faces challenges. Maintaining consistent product quality and reproducibility requires stable process parameters and stringent quality control. Surface modification and functionalization also add complexity. Addressing these challenges requires optimizing process parameters, developing automated equipment, and implementing robust quality control systems. Researchers are exploring new processes and equipment to improve large-scale production. High-pressure homogenizers and ultrasonic dispersers enhance homogenization and dispersion, preventing agglomeration and ensuring product stability. Continuous flow reactors and automated control systems can further increase efficiency and production capacity. Cost-effectiveness and environmental impact are also important considerations. Traditional methods often use large amounts of solvents and energy, creating waste. Developing green, sustainable processes, such as aqueous phase synthesis (using water as a solvent), is crucial for reducing costs and environmental impact.

In summary, efficient preparation and scalable production are critical for translating nanomaterials to clinical cerebrovascular imaging. Optimizing existing methods, developing new technologies and equipment, and prioritizing green chemistry are key areas for future research. These efforts will improve the availability and cost-effectiveness of nanomaterials for clinical use.

4.4 Regulatory and ethical issues

Nanomaterials in cerebrovascular imaging face not only scientific and technical hurdles but also regulatory and ethical challenges. As nanotechnology rapidly advances, governments and international organizations are developing regulations and guidelines to ensure safety, efficacy, and responsible use.

Nanomaterials must meet stringent requirements for clinical trials and commercialization. Regulatory processes for nanomaterials are similar to those for traditional drugs and medical devices, but with added complexities. The unique properties of nanomaterials may require new evaluation standards and approval procedures. Regulatory agencies typically require comprehensive safety and toxicity data to assess potential human health and environmental impacts. Clear standards and guidelines are also needed for material preparation, quality control, and clinical use.

Ethical considerations are equally important. While nanomaterials offer great potential for improved diagnostics and treatment, their long-term effects remain uncertain. Potential risks, such as organ damage or immune responses from long-term accumulation, require careful monitoring and evaluation. Balancing scientific progress with individual rights is also crucial. This includes ensuring informed consent for patients in clinical trials, protecting patient rights, and promoting equitable access to nanomaterial-based technologies. Open discussions among scientists, medical institutions, governments, and the public are essential for developing appropriate guidelines and policies.

In conclusion, addressing regulatory and ethical issues is essential for the successful translation of nanomaterials to cerebrovascular imaging. Establishing robust regulatory frameworks, unified safety standards, and clear ethical guidelines will ensure responsible development and application of these promising technologies. Continued dialogue and collaboration are crucial for maximizing the benefits of nanomaterials while minimizing potential risks.

5 Conclusion

The rapid development of nanotechnology has brought new opportunities to cerebrovascular imaging. Advanced nanomaterials, such as metal nanoparticles, magnetic nanoparticles, quantum dots, carbon-based nanomaterials, and polymer nanoparticles, have shown great potential in improving imaging resolution, contrast, and specificity. These nanomaterials improve imaging sensitivity and specificity through various physical and chemical mechanisms, providing new approaches for the diagnosis and treatment of cerebrovascular diseases. Despite the significant advantages of nanomaterials, there are still many challenges and issues in practical applications, such as biosafety, long-term stability, targeting, specificity, large-scale preparation, and clinical translation. Therefore, future research should focus on addressing these issues to promote the further development and application of advanced nanomaterials in cerebrovascular imaging. Through in-depth discussion of these issues, this review hopes to provide valuable references for researchers in related fields and promote the further development and application of advanced nanomaterials in cerebrovascular imaging.

Author contributions

LN: Writing–original draft, Data curation, Investigation, Methodology. XS: Writing–original draft, Resources. PL: Data curation, Validation, Writing–review and editing. JS: Writing–review and editing, Investigation, Validation. ZY: Writing–review and editing, Conceptualization, Supervision.

Funding

The author(s) declare that financial support was received for the research, authorship, and/or publication of this article. This research was funded by the Support Program for Young and Middle-aged Talents in Science and Technology Innovation in Shenyang (RC210374) and Liaoning Province Science and Technology Research (2023-BSBA-185).

Conflict of interest

The authors declare that the research was conducted in the absence of any commercial or financial relationships that could be construed as a potential conflict of interest.

Publisher's note

References

Abbas, S. G., and Kumar, S. (2018). Importance of computed tomography scan in patients with cerebrovascular accidents. *J. Adv. Med. Dent. Sci. Res.* 6 (11), 48.

Abousalman-Rezvani, Z., Refaat, A., Dehghankelishadi, P., Roghani-Mamaqani, H., Esser, L., and Voelcker, N. H. (2024). Insights into targeted and stimulus-responsive nanocarriers for brain cancer treatment. *Adv. Healthc. Mater.* 13 (12), 2302902. doi:10.1002/adhm.202302902

Agarwal, K., Rai, H., and Mondal, S. (2023). Quantum dots: an overview of synthesis, properties, and applications. *Mater. Res. Express* 10 (6), 062001. doi:10.1088/2053-1591/acda17

Alam, Md. S., Farhad, S. F. U., Tanvir, N. I., Bitu, Md. N. A., Mohammad, M., Mahmuda, H., et al. (2022) "Spherical and rod-shaped gold nanoparticles for surface enhanced Raman spectroscopy," in *2022 4th international conference on sustainable technologies for industry 4.0 (STI)*. IEEE, 1–4.

Albanese, A., Tang, P. S., and Chan, W. C. W. (2012). The effect of nanoparticle size, shape, and surface chemistry on biological systems. *Annu. Rev. Biomed. Eng.* 14, 1–16. doi:10.1146/annurev-bioeng-071811-150124

Altammar, K. A. (2023). A review on nanoparticles: characteristics, synthesis, applications, and challenges. *Front. Microbiol.* 14, 1155622. doi:10.3389/fmicb.2023.1155622

Anderson, D., Anderson, T., and Fahmi, F. (2019). Advances in applications of metal oxide nanomaterials as imaging contrast agents. *Phys. status solidi (a)* 216 (16), 1801008. doi:10.1002/pssa.201801008

Annu, S. A., Qamar, Z., Md, S., Alhakamy, N. A., Baboota, S., and Ali, J. (2022). An insight to brain targeting utilizing polymeric nanoparticles: effective treatment modalities for neurological disorders and brain tumor. *Front. Bioeng. Biotechnol.* 10, 788128. doi:10.3389/fbioe.2022.788128

Antonelli, A., and Magnani, M. (2022). SPIO nanoparticles and magnetic erythrocytes as contrast agents for biomedical and diagnostic applications. *J. magnetism magnetic Mater.* 541, 168520. doi:10.1016/j.jmmm.2021.168520

Asadinezhad, M., Azimian, H., Ghadiri, H., and Khademi, S. (2021). Gold nanoparticle parameters play an essential role as CT imaging contrast agents. *J. Nanostructures* 11 (4), 668–677. doi:10.22052/JNS.2021.04.005

Aslan, N., Ceylan, B., Koç, M. M., and Findik, F. (2020). Metallic nanoparticles as X-Ray computed tomography (CT) contrast agents: a review. *J. Mol. Struct.* 1219, 128599. doi:10.1016/j.molstruc.2020.128599

Balachandran, Y. L., Girija, S., Selvakumar, R., Tongpim, S., Gutleb, A. C., and Suriyanarayanan, S. (2013). Differently environment stable bio-silver nanoparticles: study on their optical enhancing and antibacterial properties. *PLoS One* 8 (10), e77043. doi:10.1371/journal.pone.0077043

Bansal, S. A., Kumar, V., Karimi, J., and Singh, A. P. (2020). Role of gold nanoparticles in advanced biomedical applications. *Nanoscale Adv.* 2 (9), 3764–3787. doi:10.1039/d0na00472c

Buch, S., Wang, Y., Park, M. G., Jella, P. K., Hu, J., Chen, Y., et al. (2020). Subvoxel vascular imaging of the midbrain using USPIO-Enhanced MRI. *Neuroimage* 220, 117106. doi:10.1016/j.neuroimage.2020.117106

Burke, B. P., Cawthorne, C., and Archibald, S. J. (2017). Multimodal nanoparticle imaging agents: design and applications. *Philosophical Trans. R. Soc. A Math. Phys. Eng. Sci.* 375 (2107), 20170261. doi:10.1098/rsta.2017.0261

Campos, E. V. R., Pereira, A. E. S., De Oliveira, J. L., Carvalho, L. B., Guilger-Casagrande, M., de Lima, R., et al. (2020). How can nanotechnology help to combat COVID-19? Opportunities and urgent need. *J. Nanobiotechnology* 18, 125. doi:10.1186/s12951-020-00685-4

Cardoso, V. F., Francesko, A., Ribeiro, C., Bañobre-López, M., Martins, P., and Lanceros-Mendez, S. (2018). Advances in magnetic nanoparticles for biomedical applications. *Adv. Healthc. Mater.* 7 (5), 1700845. doi:10.1002/adhm.201700845

Chen, D., Dougherty, C. A., Yang, D., Wu, H., and Hong, H. (2016). Radioactive nanomaterials for multimodality imaging. *Tomography* 2 (1), 3–16. doi:10.18383/j.tom.2016.00121

Cheng, Y., Morshed, R. A., Auffinger, B., Tobias, A. L., and Lesniak, M. S. (2014). Multifunctional nanoparticles for brain tumor imaging and therapy. *Adv. drug Deliv. Rev.* 66, 42–57. doi:10.1016/j.addr.2013.09.006

Chung, S., Revia, R. A., and Zhang, M. (2021). Graphene quantum dots and their applications in bioimaging, biosensing, and therapy. *Adv. Mater.* 33 (22), 1904362. doi:10.1002/adma.201904362

Dąbrowska-Bouta, B., Sulkowski, G., Frontczak-Baniewicz, M., Skalska, J., Sałek, M., Orzelska-Górka, J., et al. (2018). Ultrastructural and biochemical features of cerebral microvessels of adult rat subjected to a low dose of silver nanoparticles. *Toxicology* 408, 31–38. doi:10.1016/j.tox.2018.06.009

Deddens, L. H., Van Tilborg, G. A. F., Mulder, W. J. M., De Vries, H. E., and Dijkhuizen, R. M. (2012). Imaging neuroinflammation after stroke: current status of cellular and molecular MRI strategies. *Cerebrovasc. Dis.* 33 (4), 392–402. doi:10.1159/000336116

Du, Y., Liu, X., Liang, Q., and Tian, J. (2019). Optimization and design of magnetic ferrite nanoparticles with uniform tumor distribution for highly sensitive MRI/MPI performance and improved magnetic hyperthermia therapy. *Nano Lett.* 19 (6), 3618–3626. doi:10.1021/acs.nanolett.9b00630

Elsabahy, M., and Wooley, K. L. (2012). Design of polymeric nanoparticles for biomedical delivery applications. *Chem. Soc. Rev.* 41 (7), 2545–2561. doi:10.1039/c2cs15327k

Fahmy, H. M., Mosleh, A. M., Abd Elghany, A., Shams-Eldin, E., Abu Serea, E. S., Ali, S. A., et al. (2019). Coated silver nanoparticles: synthesis, cytotoxicity, and optical properties. *RSC Adv.* 9 (35), 20118–20136. doi:10.1039/c9ra02907a

Fakruddin, M., Hossain, Z., and Afroz, H. (2012). Prospects and applications of nanobiotechnology: a medical perspective. *J. nanobiotechnology* 10, 31–38. doi:10.1186/1477-3155-10-31

Fan, Z., Zhu, P., Zhu, Y., Wu, K., Li, C. Y., and Cheng, H. (2020). Engineering long-circulating nanomaterial delivery systems. *Curr. Opin. Biotechnol.* 66, 131–139. doi:10.1016/j.copbio.2020.07.006

Furtado, D., Björnmalm, M., Ayton, S., Bush, A. I., Kempe, K., and Caruso, F. (2018). Overcoming the blood–brain barrier: the role of nanomaterials in treating neurological diseases. *Adv. Mater.* 30 (46), 1801362. doi:10.1002/adma.201801362

Gao, X., Xu, J., Yao, T., Liu, X., Zhang, H., and Zhan, C. (2022). Peptide-decorated nanocarriers penetrating the blood-brain barrier for imaging and therapy of brain diseases. *Adv. drug Deliv. Rev.* 187, 114362. doi:10.1016/j.addr.2022.114362

Ghekiere, O., Salgado, R., Buls, N., Leiner, T., Mancini, I., Vanhoenacker, P., et al. (2017). Image quality in coronary CT angiography: challenges and technical solutions. *Br. J. radiology* 90 (1072), 20160567. doi:10.1259/bjr.20160567

Gollavelli, G., Ghule, A. V., and Ling, Y. C. (2022). Multimodal imaging and phototherapy of cancer and bacterial infection by graphene and related nanocomposites. *Molecules* 27 (17), 5588. doi:10.3390/molecules27175588

Granqvist, C. G., and Buhrman, R. A. (1976). Ultrafine metal particles. *J. Appl. Phys.* 47 (5), 2200–2219. doi:10.1063/1.322870

Hage, Z. A., Alaraj, A., Arnone, G. D., and Charbel, F. T. (2016). Novel imaging approaches to cerebrovascular disease. *Transl. Res.* 175, 54–75. doi:10.1016/j.trsl.2016.03.018

Haller, S., Vernooij, M. W., Kuijer, J. P. A., Larsson, E. M., Jäger, H. R., and Barkhof, F. (2018). Cerebral microbleeds: imaging and clinical significance. *Radiology* 287 (1), 11–28. doi:10.1148/radiol.2018170803

Hariharan, K., Parekh, K., Rani, M., and Mehta, T. (2022) "Development and applications of gold nanoparticles for targeting brain tumors," in *Nanocarriers for drug-targeting brain tumors*. Elsevier, 485–512.

Hashemi, M., Shamshiri, A., Saeedi, M., Tayebi, L., and Yazdian-Robati, R. (2020). Aptamer-conjugated PLGA nanoparticles for delivery and imaging of cancer therapeutic drugs. *Archives Biochem. biophysics* 691, 108485. doi:10.1016/j.abb.2020.108485

Haupt, K., Medina Rangel, P. X., and Bui, B. T. S. (2020). Molecularly imprinted polymers: antibody mimics for bioimaging and therapy. *Chem. Rev.* 120 (17), 9554–9582. doi:10.1021/acs.chemrev.0c00428

Hu, S., Trinchi, A., Atkin, P., and Cole, I. (2015). Tunable photoluminescence across the entire visible spectrum from carbon dots excited by white light. *Angew. Chem. Int. Ed.* 54 (10), 2970–2974. doi:10.1002/anie.201411004

Huang, W. Y., and Davis, J. J. (2011). Multimodality and nanoparticles in medical imaging. *Dalton Trans.* 40 (23), 6087–6103. doi:10.1039/c0dt01656j

Huang, X., Neretina, S., and El-Sayed, M. A. (2009). Gold nanorods: from synthesis and properties to biological and biomedical applications. *Adv. Mater.* 21 (48), 4880–4910. doi:10.1002/adma.200802789

Illath, K., Kar, S., Gupta, P., Shinde, A., Wankhar, S., Tseng, F. G., et al. (2022). Microfluidic nanomaterials: from synthesis to biomedical applications. *Biomaterials* 280, 121247. doi:10.1016/j.biomaterials.2021.121247

Israel, L., Galstyan, A., Holler, E., and Ljubimova, J. Y. (2020). Magnetic iron oxide nanoparticles for imaging, targeting and treatment of primary and metastatic tumors of the brain. *J. Control. Release* 320, 45–62. doi:10.1016/j.jconrel.2020.01.009

Jeon, M., Halbert, M. V., Stephen, Z. R., and Zhang, M. (2021). Iron oxide nanoparticles as T1 contrast agents for magnetic resonance imaging: fundamentals, challenges, applications, and prospectives. *Adv. Mater.* 33 (23), 1906539. doi:10.1002/adma.201906539

Jing, L., Ding, K., Kershaw, S. V., Kempson, I. M., Rogach, A. L., and Gao, M. (2014). Magnetically engineered semiconductor quantum dots as multimodal imaging probes. *Adv. Mater.* 26 (37), 6367–6386. doi:10.1002/adma.201402296

Joseph, M. M., Narayanan, N., Nair, J. B., Karunakaran, V., Ramya, A. N., Sujai, P. T., et al. (2018). Exploring the margins of SERS in practical domain: an emerging diagnostic modality for modern biomedical applications. *Biomaterials* 181, 140–181. doi:10.1016/j.biomaterials.2018.07.045

Joshi, B., and Joshi, A. (2022). Polymeric magnetic nanoparticles: a multitargeting approach for brain tumour therapy and imaging. *Drug Deliv. Transl. Res.* 12, 1588–1604. doi:10.1007/s13346-021-01063-9

Kim, J., Lee, S.-K., Schellingerhout, D., Nahrendorf, M., Kim, K., Kim, J., et al. (2019). Spectroscopic assessment of gold nanoparticle biodistribution using surface plasmon resonance phenomena. *ACS Biomaterials Sci. and Eng.* 5 (12), 6389–6394. doi:10.1021/acsbiomaterials.9b01079

Kim, S. T., Saha, K., Kim, C., and Rotello, V. M. (2013). The role of surface functionality in determining nanoparticle cytotoxicity. *Accounts Chem. Res.* 46 (3), 681–691. doi:10.1021/ar3000647

Koole, R., Mulder, W. J. M., Van Schooneveld, M. M., Strijkers, G. J., Meijerink, A., and Nicolay, K. (2009). Magnetic quantum dots for multimodal imaging. *Wiley Interdiscip. Rev. Nanomedicine Nanobiotechnology* 1 (5), 475–491. doi:10.1002/wnan.14

Kozics, K., Sramkova, M., Kopecka, K., Begerova, P., Manova, A., Krivosikova, Z., et al. (2021). Pharmacokinetics, biodistribution, and biosafety of PEGylated gold nanoparticles *in vivo*. *Nanomaterials* 11 (7), 1702. doi:10.3390/nano11071702

Kumar, H., Venkatesh, N., Bhowmik, H., and Kuila, A. (2018). Metallic nanoparticle: a review. *Biomed. J. Sci. Tech. Res.* 4 (2), 3765–3775. doi:10.26717/bjstr.2018.04.0001011

Li, C., Cao, L., Zhang, Y., Yi, P., Wang, M., Tan, B., et al. (2015). Preoperative detection and intraoperative visualization of brain tumors for more precise surgery: a new dual-modality MRI and NIR nanoprobe. *small* 11 (35), 4517–4525. doi:10.1002/smll.201500997

Li, C., Shuford, K. L., Park, Q. H., Cai, W., Li, Y., Lee, E., et al. (2007). High-yield synthesis of single-crystalline gold nano-octahedra. *Angew. Chemie-International Ed.* 46 (18), 3264–3268. doi:10.1002/anie.200604167

Li, L., Fu, J., Ye, J., Liu, L., Sun, Z., Wang, H., et al. (2024). Developing hypoxia-sensitive system via designing tumor-targeted fullerene-based photosensitizer for multimodal therapy of deep tumor. *Adv. Mater.* 36 (23), 2310875. doi:10.1002/adma.202310875

Li, S., Wei, J., Yao, Q., Song, X., Xie, J., and Yang, H. (2023). Emerging ultrasmall luminescent nanoprobes for *in vivo* bioimaging. *Chem. Soc. Rev.* 52 (5), 1672–1696. doi:10.1039/d2cs00497f

Li, T., Lu, X. M., Zhang, M. R., Hu, K., and Li, Z. (2022). Peptide-based nanomaterials: self-assembly, properties and applications. *Bioact. Mater.* 11, 268–282. doi:10.1016/j.bioactmat.2021.09.029

Li, Z., Fan, Q., and Yin, Y. (2021). Colloidal self-assembly approaches to smart nanostructured materials. *Chem. Rev.* 122 (5), 4976–5067. doi:10.1021/acs.chemrev.1c00482

Liang, G., Wang, H., Shi, H., Wang, H., Zhu, M., Jing, A., et al. (2020). Recent progress in the development of upconversion nanomaterials in bioimaging and disease treatment. *J. Nanobiotechnology* 18, 154. doi:10.1186/s12951-020-00713-3

Liang, R., Xie, J., Li, J., Wang, K., Liu, L., Gao, Y., et al. (2017). Liposomes-coated gold nanocages with antigens and adjuvants targeted delivery to dendritic cells for enhancing antitumor immune response. *Biomaterials* 149, 41–50. doi:10.1016/j.biomaterials.2017.09.029

Lin, Y., Zhang, K., Zhang, R., She, Z., Tan, R., Fan, Y., et al. (2020). Magnetic nanoparticles applied in targeted therapy and magnetic resonance imaging: crucial preparation parameters, indispensable pre-treatments, updated research advancements and future perspectives. *J. Mater. Chem. B* 8 (28), 5973–5991. doi:10.1039/d0tb00552e

Liu, X., Zhang, H., Zhang, T., Wang, Y., Jiao, W., Lu, X., et al. (2021). Magnetic nanomaterials-mediated cancer diagnosis and therapy. *Prog. Biomed. Eng.* 4 (1), 012005. doi:10.1088/2516-1091/ac3111

Loh, K. P., Ho, D., Chiu, G. N. C., Leong, D. T., Pastorin, G., and Chow, E. K. (2018). Clinical applications of carbon nanomaterials in diagnostics and therapy. *Adv. Mater.* 30 (47), 1802368. doi:10.1002/adma.201802368

Lu, X. Y., Wu, D. C., Li, Z. J., and Chen, G. Q. (2011). Polymer nanoparticles. *Prog. Mol. Biol. Transl. Sci.* 104, 299–323. doi:10.1016/b978-0-12-416020-0.00007-3

Luo, Y., Wang, Y., and Fu, J. (2021). Nanomaterials in cerebrovascular disease diagnose and treatment. *Part. and Part. Syst. Charact.* 38 (5), 2000311. doi:10.1002/ppsc.202000311

Luo, Y., Yang, H., Zhou, Y. F., and Hu, B. (2020). Dual and multi-targeted nanoparticles for site-specific brain drug delivery. *J. Control. release* 317, 195–215. doi:10.1016/j.jconrel.2019.11.037

Mangesius, S., Janjic, T., Steiger, R., Haider, L., Rehwald, R., Knoflach, M., et al. (2021). Dual-energy computed tomography in acute ischemic stroke: state-of-the-art. *Eur. Radiol.* 31, 4138–4147. doi:10.1007/s00330-020-07543-9

Manikandan, N., Vp, S. K., Rathis, G., G, R., and T.k, S. (2021). Carbon nanotubes and their properties-The review. *Mater. today Proc.* 47, 4682–4685. doi:10.1016/j.matpr.2021.05.543

Manninger, S. P., Muldoon, L. L., Nesbit, G., Murillo, T., Jacobs, P. M., and Neuwelt, E. A. (2005). An exploratory study of ferumoxtran-10 nanoparticles as a blood-brain barrier imaging agent targeting phagocytic cells in CNS inflammatory lesions. *Am. J. Neuroradiol.* 26 (9), 2290–2300.

Meola, A., Rao, J., Chaudhary, N., Sharma, M., and Chang, S. D. (2018). Gold nanoparticles for brain tumor imaging: a systematic review. *Front. neurology* 9, 328. doi:10.3389/fneur.2018.00328

Montalti, M., Cantelli, A., and Battistelli, G. (2015). Nanodiamonds and silicon quantum dots: ultrastable and biocompatible luminescent nanoprobes for long-term bioimaging. *Chem. Soc. Rev.* 44 (14), 4853–4921. doi:10.1039/c4cs00486h

Moreels, I., Lambert, K., Smeets, D., De Muynck, D., Nollet, T., Martins, J. C., et al. (2009). Size-dependent optical properties of colloidal PbS quantum dots. *ACS nano* 3 (10), 3023–3030. doi:10.1021/nn900863a

Hosseini, S. M., Mohammadnejad, J., Najafi-Taher, R., Beiram Zadeh, Z., Tanhaei, M., Ramakrishna, S., et al. (2024). Multifunctional carbon-based nanoparticles. *Theranostic applications in cancer therapy and diagnosis*

Niu, Y., Tan, H., Li, X., Zhao, L., Xie, Z., Zhang, Y., et al. (2020). Protein–carbon dot nanohybrid-based early blood–brain barrier damage theranostics. *ACS Appl. Mater. and interfaces* 12 (3), 3445–3452. doi:10.1021/acsami.9b19378

Ong, S. Y., Zhang, C., Dong, X., and Yao, S. Q. (2021). Recent advances in polymeric nanoparticles for enhanced fluorescence and photoacoustic imaging. *Angew. Chem. Int. Ed.* 60 (33), 17797–17809. doi:10.1002/anie.202101964

Orru', E., Chung, C. Y., and Hui, F. K. (2020). Cerebral Angiography. In: *Neurointensive Care Unit. Current Clinical Neurology*. Editor S. Nelson and P. Nyquist (Cham: Humana).

Overcast, W. B., Davis, K. M., Ho, C. Y., Hutchins, G. D., Green, M. A., Graner, B. D., et al. (2021). Advanced imaging techniques for neuro-oncologic tumor diagnosis, with an emphasis on PET-MRI imaging of malignant brain tumors. *Curr. Oncol. Rep.* 23, 34–15. doi:10.1007/s11912-021-01020-2

Owens, T. C., Anton, N., and Attia, M. F. (2023). CT and X-ray contrast agents: current clinical challenges and the future of contrast. *Acta Biomater.* 171, 19–36. doi:10.1016/j.actbio.2023.09.027

Padmanabhan, P., Kumar, A., Kumar, S., Chaudhary, R. K., and Gulyás, B. (2016). Nanoparticles in practice for molecular-imaging applications: an overview. *Acta biomater.* 41, 1–16. doi:10.1016/j.actbio.2016.06.003

Pandey, R. K., and Prajapati, V. K. (2018). Molecular and immunological toxic effects of nanoparticles. *Int. J. Biol. Macromol.* 107, 1278–1293. doi:10.1016/j.ijbiomac.2017.09.110

Pandey, S., and Bodas, D. (2020). High-quality quantum dots for multiplexed bioimaging: a critical review. *Adv. Colloid Interface Sci.* 278, 102137. doi:10.1016/j.cis.2020.102137

Patel, K. D., Singh, R. K., and Kim, H. W. (2019). Carbon-based nanomaterials as an emerging platform for theranostics. *Mater. Horizons* 6 (3), 434–469. doi:10.1039/c8mh00966j

Phillips, E., Penate-Medina, O., Zanzonico, P. B., Carvajal, R. D., Mohan, P., Ye, Y., et al. (2014). Clinical translation of an ultrasmall inorganic optical-PET imaging nanoparticle probe. *Sci. Transl. Med.* 6 (260), 260ra149. doi:10.1126/scitranslmed.3009524

Piella, J., Bastus, N. G., and Puntes, V. (2016). Size-controlled synthesis of sub-10-nanometer citrate-stabilized gold nanoparticles and related optical properties. *Chem. Mater.* 28 (4), 1066–1075. doi:10.1021/acs.chemmater.5b04406

Prieto, C., and Linares, I. (2018). Nanoparticles and nanothermia for malignant brain tumors, a suggestion of treatment for further investigations. *Rep. Pract. Oncol. Radiotherapy* 23 (5), 474–480. doi:10.1016/j.rpor.2018.08.001

Pryshchepa, O., Pomastowski, P., and Buszewski, B. (2020). Silver nanoparticles: synthesis, investigation techniques, and properties. *Adv. Colloid Interface Sci.* 284, 102246. doi:10.1016/j.cis.2020.102246

Rafique, M. S., Rafique, M., Tahir, M. B., Hajra, S., Nawaz, T., and Shafiq, F. (2020). *Synthesis methods of nanostructures nanotechnology and photocatalysis for environmental applications*. Elsevier, 45–56.

Ren, F., Jiang, Z., Han, M., Zhang, H., Yun, B., Zhu, H., et al. (2021). NIR-II Fluorescence imaging for cerebrovascular diseases. *View* 2 (6), 20200128. doi:10.1002/viw.20200128

Resch-Genger, U., Grabolle, M., Cavaliere-Jaricot, S., Nitschke, R., and Nann, T. (2008). Quantum dots versus organic dyes as fluorescent labels. *Nat. methods* 5 (9), 763–775. doi:10.1038/nmeth.1248

Reshma, V. G., and Mohanan, P. V. (2019). Quantum dots: applications and safety consequences. *J. Luminescence* 205, 287–298. doi:10.1016/j.jlumin.2018.09.015

Rizvi, S. F. A., Ali, A., Ahmad, M., Mu, S., and Zhang, H. (2021). Multifunctional self-assembled peptide nanoparticles for multimodal imaging-guided enhanced theranostic applications against glioblastoma multiforme. *Nanoscale Adv.* 3 (20), 5959–5967. doi:10.1039/d1na00597a

Sammet, S. (2016). Magnetic resonance safety. *Abdom. Radiol.* 41, 444–451. doi:10.1007/s00261-016-0680-4

Sani, A., Cao, C., and Cui, D. (2021). Toxicity of gold nanoparticles (AuNPs): a review. *Biochem. biophysics Rep.* 26, 100991. doi:10.1016/j.bbrep.2021.100991

Seney, C. S., Gutzman, B. M., and Goddard, R. H. (2009). Correlation of size and surface-enhanced Raman scattering activity of optical and spectroscopic properties for silver nanoparticles. *J. Phys. Chem. C* 113 (1), 74–80. doi:10.1021/jp805698e

Sengul, A. B., and Asmatulu, E. (2020). Toxicity of metal and metal oxide nanoparticles: a review. *Environ. Chem. Lett.* 18 (5), 1659–1683. doi:10.1007/s10311-020-01033-6

Shaban, S., Huasen, B., Haridas, A., Killingsworth, M., Worthington, J., Jabbour, P., et al. (2022). Digital subtraction angiography in cerebrovascular disease: current practice and perspectives on diagnosis, acute treatment and prognosis. *Acta Neurol. Belg.* 122, 763–780. doi:10.1007/s13760-021-01805-z

Shen, C. L., Liu, H. R., Lou, Q., Wang, F., Liu, K. K., Dong, L., et al. (2022). Recent progress of carbon dots in targeted bioimaging and cancer therapy. *Theranostics* 12 (6), 2860–2893. doi:10.7150/thno.70721

Shenashen, M. A., El-Safty, S. A., and Elshehy, E. A. (2014). Synthesis, morphological control, and properties of silver nanoparticles in potential applications. *Part. and Part. Syst. Charact.* 31 (3), 293–316. doi:10.1002/ppsc.201300181

Si, P., Razmi, N., Nur, O., Solanki, S., Pandey, C. M., Gupta, R. K., et al. (2021). Gold nanomaterials for optical biosensing and bioimaging. *Nanoscale Adv.* 3 (10), 2679–2698. doi:10.1039/d0na00961j

Sindhwani, S., and Chan, W. C. W. (2021). Nanotechnology for modern medicine: next step towards clinical translation. *J. Intern. Med.* 290 (3), 486–498. doi:10.1111/joim.13254

Singh, S., Bharti, A., and Meena, V. K. (2015). Green synthesis of multi-shaped silver nanoparticles: optical, morphological and antibacterial properties. *J. Mater. Sci. Mater. Electron.* 26 (6), 3638–3648. doi:10.1007/s10854-015-2881-y

Skandalakis, G. P., Rivera, D. R., Rizea, C. D., Bouras, A., Jesu Raj, J. G., Bozec, D., et al. (2020). Hyperthermia treatment advances for brain tumors. *Int. J. Hyperth.* 37 (2), 3–19. doi:10.1080/02656736.2020.1772512

Sleight, E., Stringer, M. S., Marshall, I., Wardlaw, J. M., and Thrippleton, M. J. (2021). Cerebrovascular reactivity measurement using magnetic resonance imaging: a systematic review. *Front. Physiology* 12, 643468. doi:10.3389/fphys.2021.643468

Sobhanan, J., Rival, J. V., Anas, A., Sidharth Shibu, E., Takano, Y., and Biju, V. (2023). Luminescent quantum dots: synthesis, optical properties, bioimaging and toxicity. *Adv. Drug Deliv. Rev.* 197, 114830. doi:10.1016/j.addr.2023.114830

Soliman, M. A., Guccione, J., Reiter, A. M., Moawad, A. W., Etchison, A., Kamel, S., et al. (2020). Current concepts in multi-modality imaging of solid tumor angiogenesis. *Cancers* 12 (11), 3239. doi:10.3390/cancers12113239

Srinoi, P., Chen, Y. T., Vittur, V., Marquez, M. D., and Lee, T. R. (2018). Bimetallic nanoparticles: enhanced magnetic and optical properties for emerging biological applications. *Appl. Sci.* 8 (7), 1106. doi:10.3390/app8071106

Srivastava, R., Thakur, M., Kumawat, M. K., and Bahadur, R. (2021). Graphene nanomaterials for multi-modal bioimaging and diagnosis of cancer. In: *Next Generation Graphene Nanomaterials for Cancer Theranostic Applications*. Singapore: Springer.

Sukhanova, A., Bozrova, S., Sokolov, P., Berestovoy, M., Karaulov, A., and Nabiev, I. (2018). Dependence of nanoparticle toxicity on their physical and chemical properties. *Nanoscale Res. Lett.* 13, 44–21. doi:10.1186/s11671-018-2457-x

Sun, L., Joh, D. Y., Al-Zaki, A., Stangl, M., Murty, S., Davis, J. J., et al. (2016). Theranostic application of mixed gold and superparamagnetic iron oxide nanoparticle micelles in glioblastoma multiforme. *J. Biomed. Nanotechnol.* 12 (2), 347–356. doi:10.1166/jbn.2016.2173

Swierczewska, M., Lee, S., and Chen, X. (2011). Inorganic nanoparticles for multimodal molecular imaging. *Mol. Imaging* 10 (1), 3–16. doi:10.2310/7290.2011.00001

Tan, Q., Zhao, S., Xu, T., Wang, Q., Zhang, M., Yan, L., et al. (2023). Inorganic nano-drug delivery systems for crossing the blood–brain barrier: advances and challenges. *Coord. Chem. Rev.* 494, 215344. doi:10.1016/j.ccr.2023.215344

Thangam, R., Paulmurugan, R., and Kang, H. (2021). Functionalized nanomaterials as tailored theranostic agents in brain imaging. *Nanomaterials* 12 (1), 18. doi:10.3390/nano12010018

Toumia, Y., Domenici, F., Orlanducci, S., Mura, F., Grishenkov, D., Trochet, P., et al. (2016). Graphene meets microbubbles: a superior contrast agent for photoacoustic imaging. *ACS Appl. Mater. and interfaces* 8 (25), 16465–16475. doi:10.1021/acsami.6b04184

Wang, J., Zheng, J., Yang, Y., Liu, X., Qiu, J., and Tian, Y. (2022). Tunable full-color solid-state fluorescent carbon dots for light emitting diodes. *Carbon* 190, 22–31. doi:10.1016/j.carbon.2022.01.001

Wang, W., Liu, Z., and Lan, X. (2020). Quantum dot-based simultaneous multicolor imaging. *Mol. Imaging Biol.* 22, 820–831. doi:10.1007/s11307-019-01432-4

Winer, J. L., Kim, P. E., Law, M., Liu, C. Y., and Apuzzo, M. L. (2011). Visualizing the future: enhancing neuroimaging with nanotechnology. *World Neurosurg.* 75 (5-6), 626–637. doi:10.1016/j.wneu.2011.02.016

Wu, D., Chen, Q., Chen, X., Han, F., Chen, Z., and Wang, Y. (2023). The blood–brain barrier: structure, regulation, and drug delivery. *Signal Transduct. Target. Ther.* 8 (1), 217. doi:10.1038/s41392-023-01481-w

Yadollahpour, A. L. I., and Rashidi, S. (2015). Magnetic nanoparticles: a review of chemical and physical characteristics important in medical applications. *Orient J. Chem.* 31 (1), 25–30. doi:10.13005/ojc/31.special-issue1.03

Yan, L., Zhou, X., Zheng, Y., Luo, W., Yang, J., Zhou, Y., et al. (2019). Research progress in ultrasound use for the diagnosis and treatment of cerebrovascular diseases. *Clinics* 74, e715. doi:10.6061/clinics/2019/e715

Yang, H., Zhang, C., Shi, X., Hu, H., Du, X., Fang, Y., et al. (2010). Water-soluble superparamagnetic manganese ferrite nanoparticles for magnetic resonance imaging. *Biomaterials* 31 (13), 3667–3673. doi:10.1016/j.biomaterials.2010.01.055

Yang, K., Hu, L., Ma, X., Ye, S., Cheng, L., Shi, X., et al. (2012). Multimodal imaging guided photothermal therapy using functionalized graphene nanosheets anchored with magnetic nanoparticles. *Adv. Mater.* 24 (14), 1868–1872. doi:10.1002/adma.201104964

Yang, Y., Fan, X., Li, L., Yang, Y., Nuernisha, A., Xue, D., et al. (2020). Semiconducting polymer nanoparticles as theranostic system for near-infrared-II fluorescence imaging and photothermal therapy under safe laser fluence. *Acs Nano* 14 (2), 2509–2521. doi:10.1021/acsnano.0c00043

Yoon, H. J., Lee, E. S., Kang, M., Jeong, Y., and Park, J. H. (2015). *In vivo* multi-photon luminescence imaging of cerebral vasculature and blood–brain barrier integrity using gold nanoparticles. *J. Mater. Chem. B* 3 (15), 2935–2938. doi:10.1039/c4tb01759e

Yu, F., Xu, S., Ni, X., Ye, J., Cheng, Y., Wang, P., et al. (2018) "Biomedical applications of functional micro-/nanoimaging probes," in *Advances in functional micro-/nanoimaging probes*, 37–71.

Yu, N., Zhao, L., Cheng, D., Ding, M., Lyu, Y., Zhao, J., et al. (2022). Radioactive organic semiconducting polymer nanoparticles for multimodal cancer theranostics. *J. Colloid Interface Sci.* 619, 219–228. doi:10.1016/j.jcis.2022.03.107

Zhang, K., Xu, H., and Li, K. (2023). *Molecular imaging for early-stage disease diagnosis//visualized medicine: emerging techniques and develo** frontiers*. Singapore: Springer Nature Singapore, 39–58.

Zhang, P., Ma, X., Guo, R., Ye, Z., Fu, H., Fu, N., et al. (2021a). Organic nanoplatforms for iodinated contrast media in CT imaging. *Molecules* 26 (23), 7063. doi:10.3390/molecules26237063

Zhang, S., Zhou, Y., Li, R., Chen, Z., and Fan, X. (2022). Advanced drug delivery system against ischemic stroke. *J. Control. Release* 344, 173–201. doi:10.1016/j.jconrel.2022.02.036

Zhang, W., Mehta, A., Tong, Z., Esser, L., and Voelcker, N. H. (2021b). Development of polymeric nanoparticles for blood–brain barrier transfer—strategies and challenges. *Adv. Sci.* 8 (10), 2003937. doi:10.1002/advs.202003937

Zhang, Y., García-Gabilondo, M., Grayston, A., Feiner, I. V. J., Anton-Sales, I., Loiola, R. A., et al. (2020). PLGA protein nanocarriers with tailor-made fluorescence/MRI/PET imaging modalities. *Nanoscale* 12 (8), 4988–5002. doi:10.1039/c9nr10620k

Zhang, Y., Hong, H., Myklejord, D. V., and Cai, W. (2011). Molecular imaging with SERS-active nanoparticles. *Small* 7 (23), 3261–3269. doi:10.1002/smll.201100597

Zhang, Y., Petibone, D., Xu, Y., Mahmood, M., Karmakar, A., Casciano, D., et al. (2014). Toxicity and efficacy of carbon nanotubes and graphene: the utility of carbon-based nanoparticles in nanomedicine. *Drug metab. Rev.* 46 (2), 232–246. doi:10.3109/03602532.2014.883406

Zhang, Y., Wu, M., Wu, M., Zhu, J., and Zhang, X. (2018). Multifunctional carbon-based nanomaterials: applications in biomolecular imaging and therapy. *Acs Omega* 3 (8), 9126–9145. doi:10.1021/acsomega.8b01071

Zhao, B., Ma, H., Zheng, M., Xu, K., Zou, C., Qu, S., et al. (2022b). Narrow-bandwidth emissive carbon dots: a rising star in the fluorescent material family. *Carbon Energy* 4 (1), 88–114. doi:10.1002/cey2.175

Zhao, W., Yu, X., Peng, S., Luo, Y., Li, J., and Lu, L. (2021). Construction of nanomaterials as contrast agents or probes for glioma imaging. *J. Nanobiotechnology* 19 (1), 125. doi:10.1186/s12951-021-00866-9

Zhao, X., Bian, F., Sun, L., Cai, L., Li, L., and Zhao, Y. (2020). Microfluidic generation of nanomaterials for biomedical applications. *Small* 16 (9), 1901943. doi:10.1002/smll.201901943

Zhao, Z., Li, M., Zeng, J., Huo, L., Liu, K., Wei, R., et al. (2022a). Recent advances in engineering iron oxide nanoparticles for effective magnetic resonance imaging. *Bioact. Mater.* 12, 214–245. doi:10.1016/j.bioactmat.2021.10.014

Zheng, J., Cheng, X., Zhang, H., Bai, X., Ai, R., Shao, L., et al. (2021). Gold nanorods: the most versatile plasmonic nanoparticles. *Chem. Rev.* 121 (21), 13342–13453. doi:10.1021/acs.chemrev.1c00422

Zielińska, A., Carreiró, F., Oliveira, A. M., Neves, A., Pires, B., Venkatesh, D. N., et al. (2020). Polymeric nanoparticles: production, characterization, toxicology and ecotoxicology. *Molecules* 25 (16), 3731. doi:10.3390/molecules25163731

frontiers | Frontiers in Bioengineering and Biotechnology

TYPE Review
PUBLISHED 07 February 2025
DOI 10.3389/fbioe.2025.1550089

OPEN ACCESS

EDITED BY
Liqun Yang,
Shengjing Hospital of China Medical University, China

REVIEWED BY
Dan Li,
Jinzhou Medical University, China
Guanqing Yang,
Chinese Academy of Sciences (CAS), China

*CORRESPONDENCE
Wenhua Feng,
whfeng@symc.edu.cn

†These authors have contributed equally to this work and share first authorship

RECEIVED 22 December 2024
ACCEPTED 20 January 2025
PUBLISHED 07 February 2025

CITATION
Xu Y, Reheman A and Feng W (2025) Recent research progress on metal ions and metal-based nanomaterials in tumor therapy. *Front. Bioeng. Biotechnol.* 13:1550089. doi: 10.3389/fbioe.2025.1550089

Recent research progress on metal ions and metal-based nanomaterials in tumor therapy

Yongcheng Xu[1†], Aikebaier Reheman[2†] and Wenhua Feng[3,4,5*]

[1]The Second School of Clinical Medicine, Shenyang Medical College, Shenyang, China, [2]Fujian Key Laboratory of Toxicant and Drug Toxicology, Medical College, Ningde Normal University, Ningde, Fujian, China, [3]Department of Human Anatomy, School of Basic Medicine, Shenyang Medical College, Shenyang, China, [4]Liaoning Province Key Laboratory for Phenomics of Human Ethnic Specificity and Critical Illness, Shenyang, China, [5]Shenyang Key Laboratory for Phenomics, Shenyang Medical College, Shenyang, China

Tumors, as a disease that seriously threatens human health, have always been a major challenge in the field of medicine. Currently, the main methods of tumor treatment include surgery, radiotherapy, chemotherapy, etc., but these traditional treatment methods often have certain limitations. In addition, tumor recurrence and metastasis are also difficult problems faced in clinical treatment. In this context, the importance of metal-based nanomaterials in tumor therapy is increasingly highlighted. Metal-based nanomaterials possess unique physical, chemical, and biological properties, providing new ideas and methods for tumor treatment. Metal-based nanomaterials can achieve targeted therapy for tumors through various mechanisms, reducing damage to normal tissues; they can also serve as drug carriers, improving the stability and bioavailability of drugs; at the same time, some metal-based nanomaterials also have photothermal, photodynamic, and other characteristics, which can be used for phototherapy of tumors. This review examines the latest advances in the application of metal-based nanomaterials in tumor therapy within past 5 years, and presents prospective insights into the future applications.

KEYWORDS

metal-based nanomaterials, tumor therapy, ferroptosis, calcium overload, cuproptosis, immunotherapy

1 Introduction

There are various essential metal ions in the human body that participate in many important life activities, such as signal pathway activation, enzyme catalysis, and protein composition (Lv et al., 2023). In normal cells, theprecise regulation of ion homeostasis is crucial for cell survival, metabolism, and immunity (Liu et al., 2024). The abnormal distribution or accumulation of certain metal ions can activate cell toxicity-related biochemical reactions and induce cell death. Based on this principle, a new treatment strategy has emerged, namely, metal ion-mediated tumor treatment, which inhibits tumor growth by directly or indirectly regulating the concentration of metal ions within cells (Feng et al., 2023; Sun et al., 2024). In addition, metal ions also play a key role in tumor immune regulation, and the concept of "cancer metal immunotherapy" has been proposed (Wang et al., 2023c). Therefore, an increasing number of compounds with the ability to regulate metal ions (such as curcumin, deferoxamine, disulfiram) have been developed for tumor treatment research (Wu et al., 2020). However, their clinical transformation is hindered by limited specific recognition ability and inadequate ion concentration changes. In recent

years, nanomaterials have made significant progress and development in drug delivery, diagnosis and imaging, treatment, vaccines, and other fields (Wang G. et al., 2023). Various metal ion-regulated nanomaterials have also made great progress in tumor treatment research. They not only optimize the metal ion-based antitumor treatment system but also provide the possibility for the combination of metal ion treatment with other treatment strategies. These characteristics make metal-based nanomaterials show great potential for tumar treatment.

This article will comprehensively summarize the diverse types, intricate mechanisms, and the latest research advancements in the field of metal-based antitumor nanomaterials and offer insights into the anticipated directions of development.

2 Metal ions and tumors

2.1 The role of iron in antitumor therapy

2.1.1 Physicochemical properties, physiological functions of iron and ferroptosis

Iron (symbol: Fe) is the 26th metal element in the periodic table, with valences of Fe^{2+}, Fe^{3+}, and Fe^{6+}, among which Fe^{2+} and Fe^{3+} are the most common and can convert into each other in the human body. Iron is an important essential trace element in the human body, mainly existing in two forms: heme iron and non-heme iron. Heme iron is an important component of hemoglobin in red blood cells and myoglobin in muscle, responsible for oxygen transport in the blood and oxygen storage in the muscle, respectively (Sawicki et al., 2023). Non-heme iron combines with iron-binding proteins, such as ferritin and hemosiderin. In addition to participating in hemoglobin synthesis and oxygen transport, iron also acts as a cofactor for various enzymes involved in many important cellular processes, such as DNA synthesis and repair, electron transfer, and respiration (Powell et al., 2023). The maintenance of iron homeostasis is crucial for the normal life activities of the body.

Inside cells, iron homeostasis is precisely regulated at the transcriptional and translational levels by iron regulatory proteins (IRPs) and iron response elements (IREs) to control iron uptake, storage, and efflux, as well as the management and distribution of iron within cells (Billesbolle et al., 2020). Fe^{2+} is the main active form of iron, participating as a structural or catalytic cofactor in redox reactions. When iron levels surge beyond normal, an abundance of Fe^{2+} can trigger oxidative stress and disrupt the equilibrium of the antioxidant defense system. Excess free radicals, generated through redox reactions, attack the polyunsaturated fatty acids within the cell membrane, thereby triggering a chain reaction of lipid peroxidation, which in turn leads to cell death, a phenomenon designated as ferroptosis. Ferroptosis is a programmed iron ion-dependent cell death mechanism that plays a role in various physiological and pathological processes (Mou et al., 2019; Nguyen et al., 2023). Ferroptosis is mainly caused by the excessive accumulation of intracellular iron ion-dependent reactive oxygen species (ROS) and the weakened elimination of glutathione peroxidase 4 (GPX4), which causes the homeostatic imbalance of ROS generation and degradation. When the cell's own antioxidant capacity is insufficient to remove excessively accumulated lipid ROS, it causes ferroptosis. Iron accumulation and subsequent lipid peroxidation play an important role in mediating the occurrence of ferroptosis. Thus, the various molecules and signals involved in iron metabolism and lipid peroxidation are all critical for regulating iron death. The changes in cell metabolic pathways caused by ferroptosis mainly include inhibited GSH synthesis and LPO accumulates, iron metabolism and ROS metabolic pathway (as shown in Figure 1).

2.1.2 Antitumor mechanisms based on ferroptosis

Iron metabolism disorders are closely related to the occurrence and development of tumors. Since iron is an essential element for cell proliferation and metabolism, the rapid proliferation of tumor cells shows an abnormal demand for iron, so tumor cells promote the accumulation of iron in cells through iron metabolism reprogramming (Yang et al., 2023). Therefore, the iron content in tumor cells is higher than in normal cells. Due to the influence of the tumor microenvironment, tumor cells are more susceptible to ferroptosis inducers than normal cells, creating a fundamental prerequisite to undergo anti-tumor treatment utilizing ferroptosis (Lei et al., 2022). However, the vast majority of iron within tumor cells predominantly exists in the form of non-cytotoxic ferritin. Therefore, targeting ferritin to facilitate the liberation of iron ions or directly modulating the intracellular iron ion concentration are two feasible ferroptosis-based anti-tumor treatment strategies.

In addition, since the concentration of hydrogen peroxide (H_2O_2) in tumor cells is relatively higher than in normal cells, excessive iron ions will undergo the Fenton reaction with H_2O_2 (Huang L. et al., 2023). In the process of this reaction, the interaction between Fe^{2+} and H_2O_2 leads to the production of hydroxyl radicals (·OH), a highly biologically toxic ingredient capable of damaging lipids, proteins, DNA, and other vital cellular components, ultimately leading to the death of tumor cells. Therefore, increasing the concentration of free Fe^{2+} and H_2O_2 within tumor cells at the same time can mediate cell death through the Fenton reaction, which may become one effective anti-tumor strategy based on iron ion.

2.1.3 Iron ion-based anti-tumor nanomedicines

With the in-depth study of ferroptosis and the development of nanotechnology, nanomaterials have been proven to induce ferroptosis more effectively than biological drugs. First, it can break the iron homeostasis both through *ex vivo* delivery mechanisms and endogenous iron utilization pathways, enhancing the elevation of intracellular free iron levels. Currently, various nanodrugs containing Fe^{2+}/Fe^{3+} or capable of delivering Fe^{2+}/Fe^{3+} have been developed for anti-tumor treatment, such as polydopamine (PDA) and amorphous $CaCO_3$ nanoparticles, etc (Han et al., 2022). Iron-bearing nanoparticles can not only release Fe^{2+} in acidic lysosomes but also deliver antitumor medications, such as a chemotherapeutic drug cisplatin, achieving a synergistic antitumor effect (Cheng et al., 2021). Biocompatible iron nanoparticles, Fe_3O_4-NPs, not only promote the production of reactive oxygen species (ROS) but also participate in iron metabolism, leading disruption of intracellular iron balance and induction of ferroptosis. In addition, Fe_3O_4-NPs combined with other technologies, such as photodynamic therapy (PDT), thermal stress, and sonodynamic therapy (SDT), can further induce cellular ferroptosis, thereby

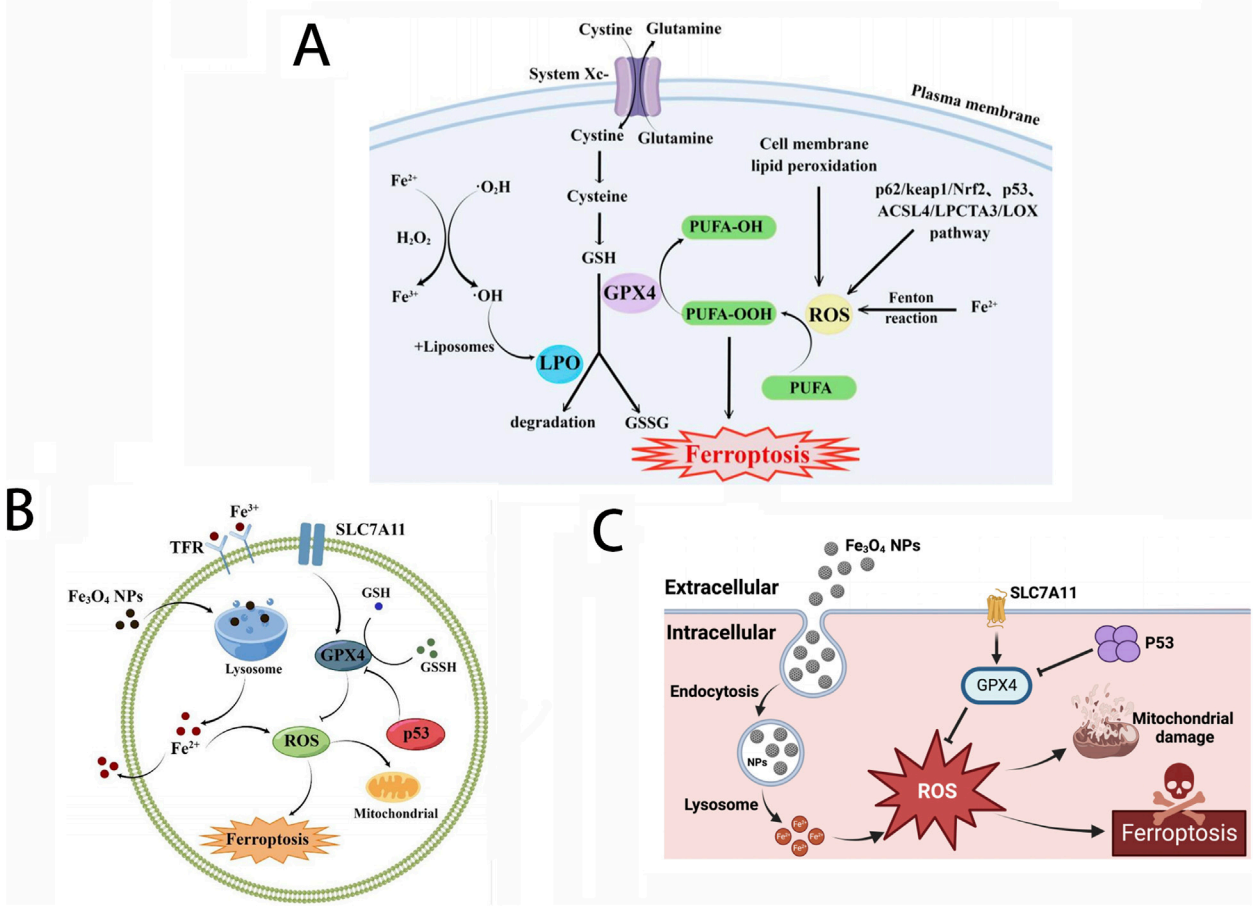

FIGURE 1
(A) Major metabolic pathways of ferroptosis; **(B)** Effect of Fe_3O_4-NPs on cell ferroptosis; **(C)** Mechanism of Fe_3O_4-NP-induced ferroptosis through upregulation of p53. Reproduced with permission from ref (Wang et al., 2023d); CC BY 4.0. Copyright © 2023 by the authors.

enhancing the antitumor effects (Wang et al., 2023d; Yao et al., 2021).

Another method to increase the level of free Fe^{2+} within cells is to target iron-related proteins, among which ferritin degradation is considered an effective approach. A ferritin-hijacking nanoparticle (Ce6-PEG-HKN_{15}) is fabricated, by conjugating the ferritin-homing peptide HKN15 with the photosensitizer chlorin e6 (Ce6) for endogenous ferroptosis without introducing Fenton-reactive metals (Zhu et al., 2022). Since the HKN15 peptide can target ferritin, the photosensitizer chlorin e6 (Ce6) can specifically aggregate around ferritin. Under laser irradiation, the activated Ce6 in these nanoparticles synergizes with the generated ROS to effectively destroy ferritin and release Fe^{2+}. In turn, the released iron partially interacts with intracellular excess H_2O_2 to produce O_2, thereby enhancing photodynamic therapy and further amplifying oxidative stress. Xiong et al. prepared a nano-activator (DAR) which was assembled by doxorubicin (DOX), tannic-acid (TA) and IR820 as a photosensitizer to make full use of endogenous iron stored in endo-lysosome, realizing ferroptosis and its related oxidative stress through artificially intracellular positive feedback loop, providing an innovative solution for the development of antitumor treatment based on ferroptosis-immunotherapy (Xiong et al., 2021).

2.2 The role of calcium in antitumor therapy

2.2.1 Physicochemical properties and physiological functions of calcium

Calcium (symbol: Ca) is a chemical element with an atomic number of 20, and its ionic form is Ca^{2+}. Calcium is the most abundant metal element in the human body and is crucial for the formation of bones and teeth. In the body, calcium exists in three main forms: free calcium, complex calcium, and protein-bound calcium, which can convert into each other. Among them, free calcium is the only physiologically active form. As an indispensable second messenger in cells, calcium ions (Ca^{2+}) participate in the regulation of almost all physiological processes by activating specific target proteins. Due to the importance of Ca^{2+}, its concentration is strictly controlled (Berridge et al., 2000; Carafoli, 2002; Liu et al., 2020; Marchi et al., 2020; Monteith et al., 2017). The concentration of free calcium within cells is only 100 nM, much lower than the extracellular calcium concentration (Bagur and Hajnoczky, 2017). Fluctuations in Ca^{2+} concentration will affect normal calcium signal transmission and thus affect cellular physiological functions. The homeostasis of intracellular Ca^{2+} mainly relies on the orderly cooperation of various Ca^{2+} channels in the cell membrane and organelles (such as the endoplasmic reticulum, mitochondria, and

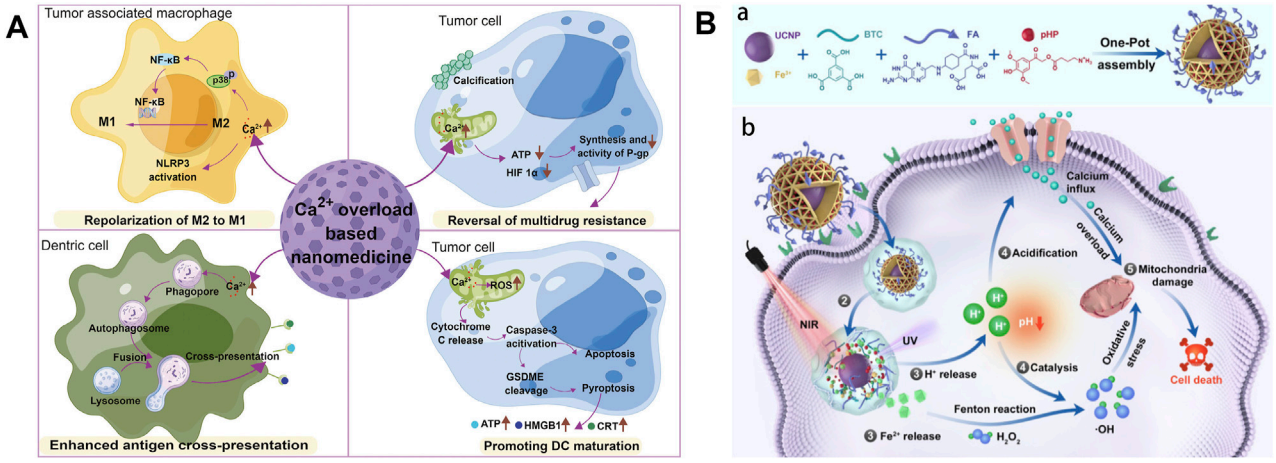

FIGURE 2
(A) Schematic diagram of antitumor mechanisms of Ca^{2+} overload-based nanomedicines. Reproduced with permission from ref (Xu et al., 2024). **(B)** Schematic Illustration of the construction of FMUP nanoagent and the underlying anticancer mechanism. **(a)** Core-shell type FMUP nanoagents with UCNP as the core and photoacid (pHP) encapsulated in the cavity of FA-doped MOFs shell were constructed by one-pot self-assembly. The FMUP nanoagent was synthesized by coordination of carboxyl groups on BTC and FA with Fe^{3+}. The UCNP as the core was located in the shell and simultaneously the pHP was loaded in the pore of the nanoagent. **(b)** Corresponding anticancer mechanism of FMUP nanoagent. ① Active internalization of FMUP in tumor cells helped by FA functionalization. ② Lysosome escape of FMUP induced by the increase of osmotic pressure after NIR light irradiation. ③ Fe^{2+} and H^+ release from FMUP upon NIR light irradiation. ④ Photoacidification of intracellular microenvironment induced calcium influx and therefore calcium overload in the mitochondria and simultaneously generated a key acidic environment for efficient Fenton reactions. The release of Fe^{2+} and photoacidification synergistically reinforced Fenton reactions and therefore produced a large number of ·OH within the close proximity of mitochondria. ⑤ As a result, the calcium overloaded and plentiful ·OH enabled dual damage to mitochondria and further induced cell death. Reproduced with permission from ref (Bao et al., 2021); CC BY 4.0. Copyright © 2023 by the authors.

lysosomes) (Berridge, 2016; Clapham, 2007; Huang et al., 2022). When this homeostatic mechanism is disrupted, excessive intracellular calcium ion concentration may lead to calcium overload, resulting in cell death (Hof et al., 2019).

2.2.2 Antitumor mechanism based on calcium overload

Ca^{2+} is the most abundant metal element and the second messenger in the human body, regulating specific biological functions that involve all aspects of cell life, and closely participate in the formation, proliferation, and migration of tumor cells (Bagur and Hajnoczky, 2017; Wu Y. et al., 2024). The expression of Ca^{2+} signal pathway-related proteins in tumor cells is different from that in normal cells, and the Ca^{2+} signal pathways are related to the pathogenesis of specific tumors such as breast cancer, colon cancer, lung cancer, liver cancer, etc (Jing et al., 2016; Wang et al., 2019; Zhang et al., 2015). Compared to normal cells, tumor cells such as breast cancer, prostate cancer, and melanoma exhibit reduced Ca^{2+} influx mediated by stromal interaction molecules to avoid cell death caused by intracellular Ca^{2+} overload. This mechanism promotes the proliferation of tumor cells (Dubois et al., 2014; Faouzi et al., 2013; Sun et al., 2014). Therefore, tumor cell death caused by calcium overload can be achieved by correcting the abnormal Ca^{2+} signaling pathway or introducing exogenous Ca^{2+} into the cytoplasm via calcium ion carriers (Cao et al., 2024). When a large amount of Ca^{2+} enters the mitochondria, it can inhibit the synthesis and biological activity of drug-resistant proteins, promote the uptake and retention of cells for anticancer drugs. In addition, mitochondrial Ca^{2+} overload can also increase the level of intracellular ROS, causing the release of cytochrome C (Cyt C), thereby activating cysteine protease 3 (caspase-3) and GSDME protein, jointly promoting the occurrence of cell pyroptosis (as shown in Figure 2) (Bao et al., 2021; Xu et al., 2024; Yu et al., 2021). In summary, nanodrugs that can directly introduce $Ca2^{+}$ into cells or organelles can provide new ideas for tumor treatment.

2.2.3 Calcium-based antitumor nanodrugs

With the continuous development of nanotechnology, the functions of nanomaterials are constantly being engineered. The emergence of calcium-based nanocomposites has well solved the problem of low efficiency in directly delivering Ca^{2+} to tumor tissues, greatly expanding the application of Ca^{2+} in the field of tumor treatment (Bai et al., 2022). Calcium-based nanocomposites used in tumor treatment include calcium phosphate (CaP), calcium carbonate ($CaCO_3$), calcium peroxide (CaO_2), etc. (Li et al., 2021; Xu et al., 2018; Zhao et al., 2021; Zheng et al., 2021), which have excellent pH response capabilities and are often used in the design of pH-dependent nanodrug delivery platforms (An et al., 2020). In addition, calcium-based nanocomposites can also target tumor tissues or cells. After internalization, they can degraded under the action of acidic organelles (such as lysosomes), and release a large amount of free Ca^{2+}. This process, when combined with Ca^{2+} influx promoters or Ca^{2+} efflux inhibitors, can further elevate the intracellular Ca^{2+} concentration that consequently induce cell apoptosis due to Ca^{2+} overload (Gao S. et al., 2019). Therefore, calcium-based nanodrugsits are very promising material for antitumor treatment.

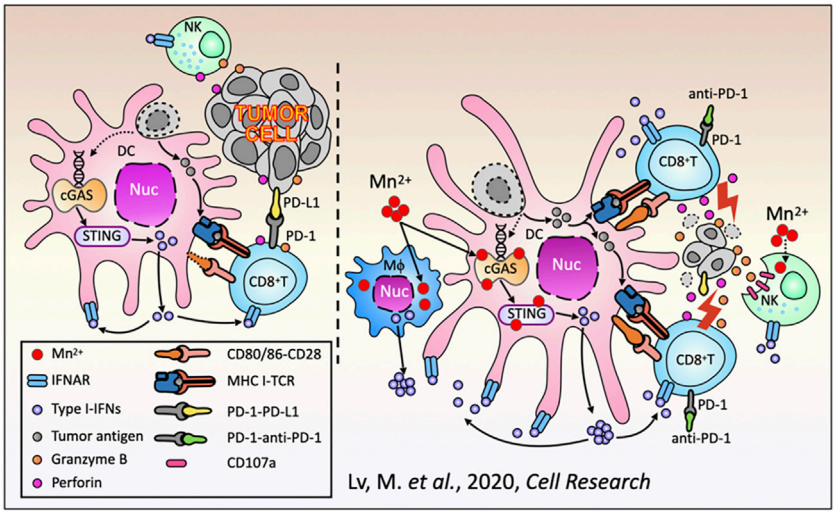

FIGURE 3
Schematic diagram of the antitumor immune responses of Mn^{2+}. Reproduced with permission from ref (Lv et al., 2020); CC BY 4.0. Copyright © 2020 by the authors.

2.3 The role of manganese in antitumor therapy

2.3.1 Physicochemical properties and physiological functions of manganese

Manganese (element symbol: Mn) is a transition element with an atomic number of 25, having various valence states, including Mn^{2+}, Mn^{3+}, Mn^{4+}, Mn^{6+}, and Mn^{7+}. The most common form of manganese found in living tissues is Mn^{2+} and Mn^{3+}. Manganese plays an important role in various physiological processes, including development, energy metabolism, antioxidant defense, and immune function. Manganese acts as a cofactor for various enzymes in the body, such as arginase, manganese superoxide dismutase (MnSOD), and cyclic guanosine monophosphate-adenosine monophosphate synthase (cGAS), etc. (Liu et al., 2022; Zhu et al., 2019). Among them, the cGAS protein is an important DNA sensor that activates the host immune response, and the cGAS-STING signaling pathway plays a crucial role in innate immune responses (Wang et al., 2018). Therefore, manganese is an important immune activator and the level of manganese in cells also needs precise regulation. Manganese efflux pumps and metal transporters ZIP8, ZIP14, and ZnT10 play a key role in this process (Xin et al., 2017). Due to the chemical properties of strong redox capabilities that similarity to iron, manganese can also produce ·OH through a Fenton-like reaction, increasing oxidative stress and producing cytotoxic effects (Ju et al., 2022).

2.3.2 Antitumor mechanism of manganese

Numerous epidemiological investigations have found a significant positive correlation between low manganese and tumor occurrence (Kim, 2010; Tu et al., 2010). The purpose of antitumor manganese nanodrugs is to increase the concentration of intracellular free Mn^{2+}. After nanoparticles are internalized by cells, the release of Mn^{2+} depletes intracellular glutathione (GSH), enabe the sufficient generation of reactive oxygen species (ROS) and effectively kill tumor cells. In addition, Mn^{2+} can also catalyze conversion of cellular H_2O_2 to ·OH through a Fenton-like reaction. It also promotes the decomposition of H_2O_2 to O_2 and continuously catalyzes the conversion of O_2 to cytotoxic $\cdot O^{2-}$ via oxidase-like activity that enhance the therapeutic effects of radiotherapy and starvation therapy (Zhu et al., 2021).

Manganese possesses strong immune activation capabilities. The cGAS-STING signaling pathway plays a crucial role in innate immune responses, where cGAS, as a DNA sensor, can detect double-stranded DNA released into the cytoplasm or extracellularly from damaged tumor cells, triggering an immune response (Wang et al., 2018). As a cofactor for cGAS, Mn^{2+} is a strong activator of the cGAS-STING signaling pathway, which can promote the production of type I interferon (IFN), enhance antigen presentation efficiency, and enhance the differentiation and activation of $CD8^+$ T cells (as shown in Figures 3, 4) (Lv et al., 2020; Sun et al., 2021; Wang et al., 2018). After radiotherapy or chemotherapy, the accumulation of Mn^{2+} and the leakage of nuclear DNA can effectively promote the activation of the cGAS-STING signaling pathway, thereby enhancing the antitumor immunity induced by radiotherapy or chemotherapy (Zhang et al., 2023). Mn^{2+} combined with anti-TGF-β/PD-L1 bispecific antibodies reduces drug resistance by enhancing both innate and adaptive immune pathways. Manganese ion-based "Metalloimmunotherapy" plays a very important role in antitumor treatment.

2.3.3 Manganese ion-based antitumor nanodrugs

As a simple and effective immune stimulant, manganese and its derived nanomaterials have shown significant effects in tumor treatment. Various manganese-based nanomaterials have been widely used as nanocarriers to deliver immunotherapeutic agents, or as immunomodulators to reshape the immunosuppressive tumor microenvironment, or as immune activators to activate the body's immune system directly or indirectly for clinical tumor immunotherapy. Compared with commonly used tumor

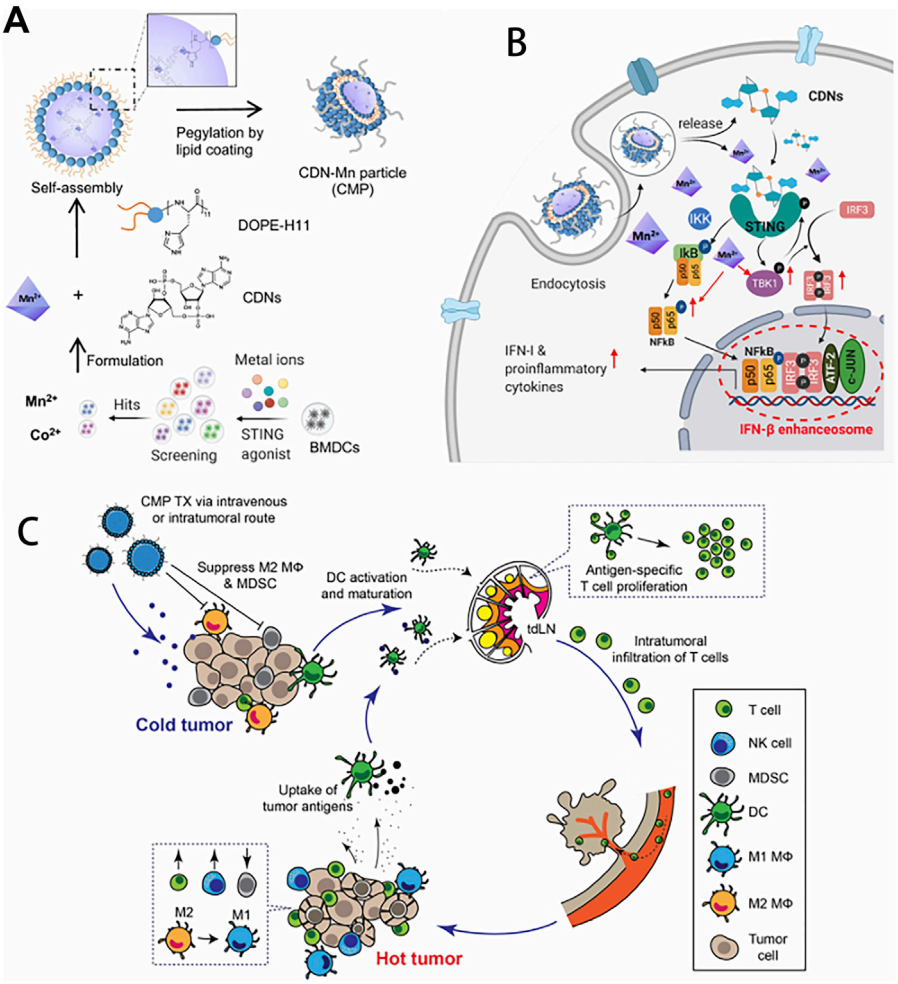

FIGURE 4
Amplifying STING activation with CDN-Manganese particles (CMP) for cancer metalloimmunotherapy. **(A)** CMP is composed of cyclic di-nucleotides (CDNs), Mn^{2+}, DOPE-H11, and a PEG-lipid layer. Mn^{2+} potentiates type-I IFN activities of STING agonists. Mn^{2+} and CDNs self-assemble into coordination polymer. CDN-Mn^{2+} coordination polymer was coated with DOPE-H11 via Mn-histidine coordination to form CDN-Mn@DOPE, followed by PEGylation with PEG-lipid layer, resulting in the formation of CMP. **(B)** CMP boosts STING activation: 1) CMP promotes cellular uptake of CDNs and Mn^{2+}; 2) Mn^{2+} augments CDN induced STING activation via STING-independent TBK1 and p65 phosphorylation, STING dependent IRF3 phosphorylation, and assembly of the IFN-β transcriptional enhanceosome. **(C)** CMP exerts potent anti-tumor efficacy after intratumoral (I.T.) or intravenous (I.V.) administration. CMP reverses immunosuppressive tumor microenvironment while activating T-cells, natural killer (NK) cells, and dendritic cells (DCs). Reproduced with permission from ref (Sun et al., 2021); PDM 1.0. Copyright © 2021 by the authors.

immunotherapies such as tumor vaccines, immune checkpoint blockade therapy, adoptive cell therapy, manganese-based tumor immunotherapy has significant advantages in terms of stability, applicability, convenience, price, etc. In 2020, a research from Peking University showed that manganese ions could effectively synergistically enhance the effects of immune checkpoint inhibitors in various tumor models and significantly reduce the dosage of PD-1 antibodies (Lv et al., 2020). Translating NK cell therapies to treat solid tumors has proven challenging due to the tumor microenvironment (TME). Hypoxia in the TME induces immunosuppression that inhibits the cytotoxic function of NK cells. Thus, reversing hypoxia-induced immunosuppression is critical for effective adoptive NK cell immunotherapy. The particles (PLGA-MnO_2 NPs) were developed by encapsulating MnO_2 NPs into poly (lactic-co-glycolicacid) (PLGA), which can catalyze the degradation of endogenous H_2O_2 to produce oxygen to alleviate tumor hypoxia, resulting in significantly enhanced cytotoxicity of NK cells. This manganese ion-based NPs are promising new tools to improve adoptive NK cell therapy (Murphy et al., 2021). Manganese-based nanomaterials combined with immune activators can synergistically activate the cGAS-STING pathway to enhance antitumor immune effects while reducing the side effects caused by excessive manganese. Chen *et al.* reported a thio-cGAMP-Mn^{2+} nanovaccine, which enhanced the antitumor immune response through direct cytosolic co-delivery of cGAMP and Mn^{2+}. The fixation of cGAMP with Mn^{2+} ions not only improve its stability, but also potentiate the activation of STING pathway. The nanovaccine increased the production of cytokines, and activated $CD8^+$ T cell immunity, and in turn suppressed the primary and distal tumors growth through long-term immune memory and led to long-term survival of poorly immunogenic B16F10 melanoma mice (Chen et al., 2021).

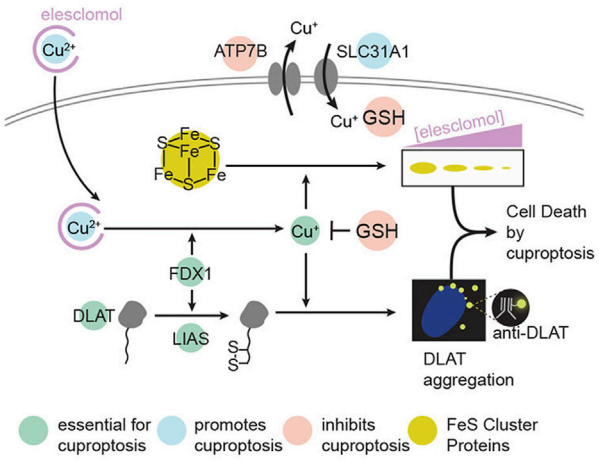

FIGURE 5
Schematic of mechanisms promoting cuproptosis. Reproduced with permission from ref (Tsvetkov et al., 2022), PDM 1.0. Copyright © 2022 by the authors.

2.4 The role of copper in antitumor therapy

2.4.1 Physicochemical properties, physiological functions of copper and cuproptosis

Copper (chemical symbol: Cu) is a transition metal element with redox activity, with an atomic number of 29, and its main valences are Cu^+ and Cu^{2+}. Copper is a very important trace element in the human body, serving as a structural and catalytic cofactor for various enzymes, and is involved in regulating important life processes such as energy metabolism, antioxidation, neurotransmitter synthesis, and iron metabolism (Reznik et al., 2022; Schwarz et al., 2023). When Cu^+ accumulates excessively in cells, it is oxidized by H_2O_2 to produce ·OH, which damages proteins, nucleic acids, and lipids within the cells, and interferes with the synthesis of iron-sulfur cluster proteins. Since iron-sulfur cluster proteins are essential for the activity of many important cellular enzymes, so excessive accumulation of copper in cells can be toxic. Therefore, maintaining copper homeostasis within cells is importantThe body's homeostasis of copper must be precisely regulated by membrane transport systems (Campos et al., 2021). The concentration of copper within cells is strictly controlled by copper transport proteins and copper chaperones. Since only monovalent copper ions Cu^+ are transportable, extracellular Cu^{2+} is often reduced to Cu^+ before entering the cell. Copper transport proteins are responsible for the influx of Cu^+ across the cell membrane, and copper transport enzymes α (ATP7A) and β (ATP7B) are necessary for expelling excess copper from the cell (Ash et al., 2021).

Cuproptosis is a unique type of cell death published in Science recently. The mechanism of cuproptosis is different from other known forms of programmed cell death such as apoptosis, pyroptosis, necrosis, and ferroptosis. By binding to the tricarboxylic acid (TCA) cycle, intracellular copper accumulation triggers the aggregation of mitochondrial lipoylated proteins and the destabilization of Fe-S cluster proteins, which in turn causes a protein toxicity reaction leading to cell death (Tsvetkov et al., 2022) (as shown in Figure 5). Studies have shown that necessary factors for cuproptosis include the presence of glutathione, mitochondrial metabolism of galactose and pyruvate, and glutamine metabolism. Endogenous intracellular glutathione, as a thiol-containing copper chelator, can inhibit cuproptosis (Saporito-Magriñá et al., 2018).

2.4.2 Antitumor mechanisms based on copper homeostasis imbalance

Studies have found that the content of copper in the serum and tissues of patients with various types of tumors is significantly higher than that in normal populations, and is related to tumor staging or progression (Ge et al., 2022). Appropriate high concentrations of copper ions promote tumor cell proliferation, angiogenesis, and metastasis. Both excessively high and excessively low concentrations of copper ions can promote cell death. Therefore, regulating the concentration of intracellular copper ions (copper deficiency and copper overload) has become an attractive new target for tumor treatment. Copper ions participate in the regulation of the structure and activity of copper-related proteins or enzymes, which are crucial for the survival and development of tumors. Copper deficiency can lead to impaired function of copper-binding enzymes and a lack of copper-related proteins, and all processes that lead to cellular copper depletion result in cellular dysfunction (Nyvltova et al., 2022). In addition, copper depletion can lead to energy and nutrient deficiency in cells, as well as increased oxidative stress and mitochondrial membrane rupture, all of which lead to tumor cell apoptosis. Given this, reducing the level of intracellular copper is a promising strategy for tumor treatment.

Furthermore, copper overload is another effective method for killing tumor cells. Copper overload can induce a Fenton-like reaction, mediating cell death. The Cu^+-mediated Fenton-like reaction can proceed at a higher reaction rate over a wider pH range, with a reaction rate about 160 times faster than that of Fe^{2+} (Qiao et al., 2024). Copper overload can also mediate tumor cell death through the cuproptosis pathway. Cells dependent on glycolytic respiration are more sensitive to cuproptosis. With the consumption of glucose and glutathione, Cu^+ binds to the dihydrolipoamide S-acetyltransferase (DLAT) protein more effectively, causing the formation of DLAT oligomers. The aggregation of DLAT oligomers can downregulate Fe-S cluster proteins, thereby leading to cuproptosis of tumor cells (Tsvetkov et al., 2022). Studies have shown that exogenous copper can disrupt redox homeostasis through changes in copper-dependent glutathione, enhancing ferroptosis (Du et al., 2022). In addition, copper ions can also regulate antitumor immune responses. The increase in Cu^{2+} not only promotes dendritic cell maturation but also enhances the antitumor effect mediated by cytotoxic $CD8^+$ T cells (Zhao F. et al., 2023). This new mode of cell death, cuproptosis, also suggests that using copper ion metal carriers to inhibit mitochondrial respiration and kill tumor cells may become a new treatment method.

2.4.3 Copper ion-based antitumor nanodrugs

Copper-based compounds and nanomaterials possess excellent biocompatibility, can selectively target malignant tissues, and have strong permeability and high local retention rates. During the preparation process, their structure, composition, morphology,

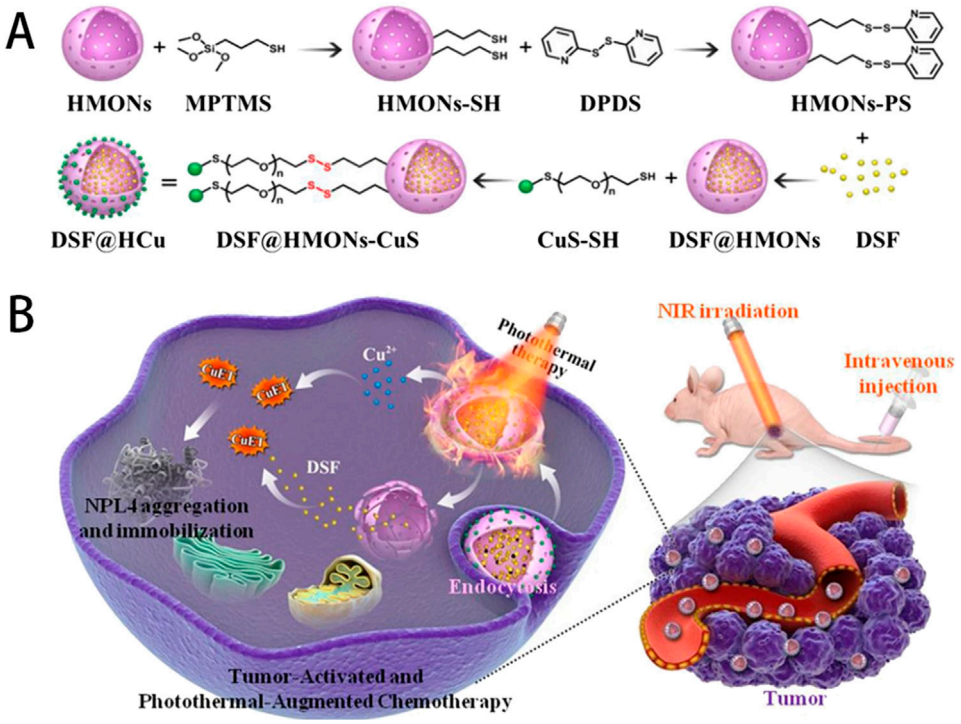

FIGURE 6
(A) Schematic illustration of the stepwise construction of DSF@HCu nanomedicine, and **(B)** NIR photothermal-augmented and in-situCu^{2+} release-activated DSF chemotherapy for the efficient killing of cancer cells and suppression of tumor growth with minimized side effects. Reproduced with permission from ref (Zhang et al., 2021), CC BY 4.0 Copyright © 2021 by the authors.

and size can easier to be controled and adjusted. These advantages make them widely used in tumor imaging and combined tumor therapy (Zhong et al., 2022). Zhang *et al.* utilized hollow mesoporous organosilica nanoparticles to integrate ultrasmall photothermal CuS particles onto the surface of the organosilica and the molecular drug Disulfiram (DSF) inside the mesopores and hollow interiors. The ultrasmall CuS acted as both photothermal agent under near-infrared (NIR) irradiation for photonic tumor hyperthermia and Cu^{2+} self-supplier in an acidic tumor microenvironment to activate the nontoxic DSF drug into a highly toxic diethyldithiocarbamate (DTC)-copper complex for enhanced DSF chemotherapy (as shown in Figure 6), which effectively achieved a remarkable synergistic *in-situ* anticancer outcome with minimal side effects (Zhang et al., 2021).

Chen *et al.* constructed CuS-pgh NMs by encapsulating copper sulfide nanoparticles using polylysine/glucose oxidase/hyaluronic acid shells (Chen et al., 2020), Liu *et al.* constructed a hybrid nanosystem composed of DNAzyme and Cu^{2+} (Liu et al., 2021), in which copper can mediate Fenton-like reactions to generate highly toxic hydroxyl radicals, enhancing thestarvation and chemodynamic tumor suppression effects. Cui *et al.* developed a safe, mitochondria-targeted copper-depleting nanoparticles. These nanoparticles can reduce the oxygen consumption and oxidative phosphorylation of triple-negative breast cancer (TNBC), promote glycolysis metabolism, reduce ATP production, cause mitochondrial membrane potential damage and increased oxidative stress, thereby induce the apoptosis of TNBC (Cui et al., 2021). A kind of nanochelator, Imi-OSi, were reported that can inhibit tumor angiogenesis through copper consumption, and form secondary particles through the phosphate/Cu^{2+} reaction polymerization to block blood vessels (Yang et al., 2019). For starvation-augmented cuproptosis and photodynamic synergistic therapy, a glucose oxidase (GOx)-engineered nonporous copper coordination nanomaterial GOx@[Cu(tz)] was developed. It inhibited 92.4% of tumor growth in athymic mice with bladder tumors, and the systemic toxicity produced was extremely low (Xu WJ. et al., 2022). Chang *et al.* designed a Ce6@AT-PEG-MSN-Pt (CAPMP) nanomotor, consisting of a janus platinum-mesoporous silica core, with acyl thiourea groups (copper chelators) conjugated with polyethylene glycol on the surface, and chlorin e6 (photosensitizer) in the pores, which can spontaneously move in tumor tissues, while performing the enhanced manipulation of the copper level, oxygen level, local temperature, and reactive oxygen species (ROS) level in the tumor microenvironment, to achieve effective tumor treatment (Chang et al., 2022). Nevertheless, copper-based nanomaterials also have their own limitations, and their instability and characteristics of easily oxidized under physiological conditions need to be solved, and the biosafetyneed to be improved (Tsymbal et al., 2022).

2.5 The role of zinc in antitumor therapy

2.5.1 Physicochemical properties and physiological functions of zinc

Zinc (element symbol: Zn) is considered the second most abundant transition metal element in the body, after iron, with an atomic number of 30. Under physiological conditions, zinc exists in the form of divalent cations (Zn^{2+}). Zinc is one of the essential trace elements required by the human body and is a core component

of many proteins, playing the role of a "life gear" in the process of transporting substances and exchanging energy (Kambe et al., 2015). In mammalian cells, there are two forms of zinc: protein-bound zinc and free zinc. The former is used to maintain the catalytic activity and structural stability of metalloenzymes and transcription factors, while the latter acts as a signaling ion to regulate signal transduction (Maret, 2013). Therefore, zinc plays a significant role in many biological processes, including cell division, metabolic regulation, and immune responses. To maintain normal physiological functions, cellular zinc homeostasis is subtly coordinated by a set of zinc homeostasis regulatory proteins, including the Zrt-, Irt-like protein (ZIP) family for zinc influx, the zinc transporter (ZnT) family for zinc efflux, metallothioneins (MTs) for zinc intracellular storage, and metal-response-element-binding transcription factor (MTF)-1 for zinc cytosolic sensing (Colvin et al., 2010).

2.5.2 Antitumor mechanism of zinc ion

It has been confirmed that the imbalance of zinc homeostasis is related to the development, invasion, and metastasis of various tumors (Bendellaa et al., 2024; Wang et al., 2020). Increasing evidence suggests that the elevation of intracellular zinc levels is mainly due to the overexpression of zinc transporters (ZIPs), which may promote the progression of certain specific cancers such as breast and pancreatic cancer. For example, ZIP6, ZIP7, and ZIP10 are highly expressed in breast cancer. Additionally, although zinc itself does not have redox activity, it can indirectly participate in the regulation of redox metabolism by acting as a catalytic or structural cofactor for proteins such as metallothioneins (MTs), copper/zinc superoxide dismutase (Cu/Zn-SOD), and the tumor suppressor protein p53. The balance of zinc homeostasis successfully activates antioxidant defenses, while zinc deficiency can disrupt protein structures and impair protein function, ultimately leading to oxidative stress and causing cell death. Accordingly, zinc chelation therapy mediated by zinc chelators can be used to treat certain types of cancer. Similar to zinc deficiency, zinc overload also has pro-oxidant properties. Excessive intracellular zinc can enter the mitochondria through the mitochondrial Ca^{2+} uniporter (MCU) (Medvedeva and Weiss, 2014), then irreversibly inhibit components of the electron transport chain (ETC.), which may stimulate the production of mitochondrial superoxide anions ($\cdot O_2^-$) and damage mitochondrial function, leading to cell death. Furthermore, zinc overload can promote lysosomal dysfunction caused by increased lysosomal membrane permeability (LMP), which triggers cell death (Yu et al., 2009). Therefore, increasing intracellular zinc concentration is a viable therapeutic strategy to combat cancer.

2.5.3 Zinc ion-based antitumor nanodrugs

Zinc ion-based nanodrugs for cancer treatment can deliver exogenous Zn^{2+} to tumor cells and induce cell death (Yao et al., 2023). PH-responsive zeolitic imidazolate framework-8 (ZIF-8), composed of 2-methylimidazole and Zn^{2+}, can serve as a source of exogenous Zn^{2+} due to its excellent degradation ability (Gao L. et al., 2019). However, the hydrophobicity and relatively large size of ZIF-8 limit its antitumor application. Therefore, Lv *et al.* designed a multifunctional zinc-based nanoplatform, BSArGO@ZIF-8 NS, which can synergize ion interference and photothermal cancer treatment (Lv et al., 2022). BSArGO@ZIF-8 NSs can induce tumor cell apoptosis through intracellular Zn^{2+} overload, and at the same time, induce photothermal effects on cancer cells under (NIR) irradiation, showing higher lethality. In addition, Ding *et al.* synthesized ^{F127}ZIF-8_{CCCP} nanoparticles for efficient cancer immunotherapy (Ding B. et al., 2023). ^{F127}ZIF-8_{CCCP} nanoparticles achieve pH-sensitive Zn^{2+} release in tumor cells, leading to increased intracellular osmotic pressure and production of reactive oxygen species (ROS), which synergize with CCCP to strongly trigger caspase-1/GSDMD-dependent pyroptosis, thereby activating antitumor immunity and inhibiting tumor growth.

In addition to introducing Zn^{2+} exogenously into tumor cells, zinc overload caused by disrupting endogenous zinc homeostasis is another antitumor treatment strategy. Su *et al.* synthesized a series of platinum (IV) -terthiophene complexes for cancer chemotherapeutic immunotherapy (Su et al., 2023). Among these complexes, the cyclometalated platinum (IV) -terthiophene complex (Pt3) showed the best antiproliferative effect on triple-negative breast cancer (MDA-MB-231) cells. Mechanistically, Pt3 can induce DNA damage, disrupt intracellular zinc homeostasis, and disrupt intracellular redox homeostasis, ultimately activating tumor cell pyroptosis through the caspase-1/GSDMD pathway, and can activate antitumor immunity in mice (Riley and Tait, 2020).

In addition to inducing tumor cell death, zinc ions can also activate the cyclic GMP-AMP synthase (cGAS)-stimulator of interferon genes (STING) signaling pathway to enhance the effect of cancer immunotherapy. Therefore, various zinc-containing nanomaterials have been developed for zinc-based tumor immunotherapy. For example, Cen *et al.* prepared a pH-responsive nanocluster (ZnS@BSA) to enhance the immunotherapeutic effect against hepatocellular carcinoma (Cen et al., 2021). Zhang *et al.* reported a Zn^{2+}-doped layered double metal hydroxide (Zn-LDH) to trigger a strong metal immunotherapy against solid tumors (Zhang et al., 2022). Ding *et al.* constructed a zinc-based metal-organic framework vaccine (ZPM@OVA-CpG) that controllably releases Zn^{2+}, providing a promising strategy to improve the effect of immunotherapy (Ding B. et al., 2023). Zhao *et al.* prepared a pH-responsive and photoactive nanoparticle (ALA&Dz@ZIF-PEG) to enhance the effect of photodynamic immunotherapy (Zhao X. et al., 2023).

3 Metal-based antitumor nanoplatforms and multiionic combined interference therapy

Metal ion therapy, as an emerging tumor treatment method, has shown the potential to overcome the resistance of traditional chemotherapy drugs (Urbano-Gamez et al., 2024), In recent years, research on metal-ion-based nanomaterials and platforms has been emerging continuously (Table 1).

Metal nanomaterials are forming a drug-free nanoplatform, in which metal ions are gradually replacing traditional drugs as part of the construction of nanomaterials (Chuang et al., 2023; Lei et al., 2023; Li et al., 2024; Naletova et al., 2023). These nanoparticles can specifically deliver metal ions to tumor cells, thereby reducing damage to normal tissues, improving treatment effects, and reducing side effects. In addition, nanoparticles can also enhance

TABLE 1 Typical metal ions-based nanomaterial for tumor therapy in recent years.

Therapy strategy	Delivered metal ions	Nanomaterials	Size (nm)	Surface modification	Response	Applications of the metal ions	References
Ferroptosis	Fe^{3+}	SPFeN	28 ± 4	PEG	808-nm NIR light	Generating ·OH by Fenton reaction, and achieving LPO	He et al. (2020a)
	Fe^{2+}	PGFCaCO3-PEG	~500	PEG	pH	The same as above	Han et al. (2022)
		Fe-ZnO_2@HA (FZOH)	~220	-	pH	Generating highly ·OH, inducing both ferroptosis and pyroptosis	Lu et al. (2024b)
	Fe^{3+} and Fe^{2+}	Fe^{2+}/Fe^{2+} loaded liposome (LPOgener)	94.6 ± 0.8	-	-	Generating ·OH by Fenton reaction, and achieving LPO	He et al. (2020b)
		Fe_3O_4-SAS@PLT	268.9 ± 8.9	Platelet membranes	-	The same as above	Jiang et al. (2020)
		Pt-FMO	~90	-	pH	The same as above	Cheng et al. (2021)
		Ce6-PEG-HKN	~410	PEG	laser irradiation	Synergistic effect of PDT and ferroptosis	Zhu et al. (2022)
		nano-activator (DAR) assembled by doxorubicin (DOX), tannic-acid (TA) and IR820	73.33 ± 4.95	-	laser irradiation	Promote ferroptosis and immunogenic cell death (ICD)	Xiong et al. (2021)
		USPBNPs@ MCSNs (UPM)	~200	-	pH	Generating ·OH by Fenton reaction, and achieving LPO	Zhao et al. (2024)
Calcium overload	Ca^{2+}	CaO_2@DOX@ZIF-67	mean diameter of 200	-	pH	Suppling O_2 and H_2O_2, producing highly toxic ·OH through a Fenton-like reaction, resulting in improved chemodynamic therapy	Gao et al. (2019b)
		PEGCaCUR + US	~140	PEG	pH, ultrasound	Binding to FDX1, inducing oligomerization of lipoylated DLAT, and mediating ROS-induced cell apoptosis as well	Zheng et al. (2021)
		M@$CaCO_3$@KAE	~100	Cancer cell membrane	-	Inducing mitochondrial damage, causing cytoskeleton collapse and oxidative stress, leading to apoptosis	Li et al. (2021)
		BSO-TCPP-Fe@CaCO3-PEG NPs	125.2 ± 7.7	PEG	pH, ultrasound	The same as above	Dong et al. (2020a)
		CaO_2@ZIF-Fe/ Ce6@PEG	~110	PEG	H+, 660 nm light	The same as above	Shen et al. (2021)
		ZnPP@PAA-CaS NPs	122 ± 11	-	pH	Signaling transduction cascades to amplify the regulatory activity of chemical messengers and mediate antitumor immunotherapy	Zhao et al. (2021)
		CaO2@Cu-LA	80–100	CaO_2	pH	Increasing ·OH radicals and NO molecules, disrupting the DNA structure and energy supply within tumor cells	Wang et al. (2024)

(Continued on following page)

TABLE 1 (*Continued*) Typical metal ions-based nanomaterial for tumor therapy in recent years.

Therapy strategy	Delivered metal ions	Nanomaterials	Size (nm)	Surface modification	Response	Applications of the metal ions	References
Immunotherapy	Mn^{2+}	MnO@mSiO-iRGD NPS	132 ± 7	iRGD	pH	Mn^{2+}-induced cGAS-STING pathway-activated immunotherapy	(Sun et al., 2022)
		amorphous porous Mn_2P (APMP) NPs	~180	Lipid layer	pH	The same as above	Hou et al. (2020)
		Mn-cGAMP nanovaccine	168 ± 20	-	-	The same as above	Chen et al. (2021)
		PLGA-MnO_2NPs	116	PLGA	-	Reducing hypoxia and abundance of immunosuppressive metabolites, increasing NK cell activity	Murphy et al. (2021)
Cuproptosis	Cu^{2+}	Perflourocarbon-/Ce6-loaded Cu@ZIF-8 (SonoCu)	~100	Macrophage membrane	pH, ultrasound	Binding to FDX1, inducing oligomerization of lipoylated DLAT	Chen et al. (2023)
		Elesclomol/Cu coencapsulated polymer nanoparticles	62.8	An amphiphilic biodegradable polymer (PHPM)	ROS	The same as above	Guo et al. (2023)
		H-ferritin-Cu-regorafenib Nanoplatform	15.5	H-ferritin	pH	Inducing cuproptosis, resulting in a synergistical effect with regorafenib-mediated lethal autophagy	Jia et al. (2023)
		CuET-CuO@BSA	40.38 ± 0.17	BSA	ROS	Triggering ROS generation through Fenton-like reaction, inducing cuproptosis, enhancing the therapeutic effect of CuET	Wu et al. (2024a)
		ES@Cu(II)-MOF NPs	152.7	PEG	pH	Generating toxic ·OH and consuming endogenous GSH, triggering cuproptosis, triggering robust ICD, combing with an anti-PD-L1, achieving excellent antitumor effects	Lu et al. (2024a)
	Cu^{+}	GOx@[Cu(tz)]	234	-	-	Binding to FDX1, inducing oligomerization of lipoylated DLAT	Xu et al. (2022a)
Zinc overload	Zn^{2+}	BSArGO@ZIF-8 NSs	~800	BSA	808-nm NIR light	increase of reactive oxygen species (ROS), initiating mitochondrial apoptotic, mediated ion-interference and photothermal combined therapy	Lv et al. (2022)
		^{F127}ZIF-8_{CCCP}	180	Pluronic F127	NIR irradiation	leading to increased intracellular osmotic pressure and production of reactive oxygen species (ROS)	Ding et al. (2023a)
		ZnS@BSA	≈100	BSA	-	activating cGAS/STING signals, leading to an improved immunotherapy efficacy	Cen et al. (2021)
		Zn-LDH	10	-	-	triggering a strong metal immunotherapy against solid tumors	Zhang et al. (2022)

(Continued on following page)

TABLE 1 (*Continued*) Typical metal ions-based nanomaterial for tumor therapy in recent years.

Therapy strategy	Delivered metal ions	Nanomaterials	Size (nm)	Surface modification	Response	Applications of the metal ions	References
		ZPM@OVA-CpG	148	-	pH	stimulating cGAS-STING, improving the effect of immunotherapy	Ding et al. (2023b)
		ALA&Dz@ZIF-PEG	~60	-	-	leading to the damage, releasing of mtDNA and activating the innate immune response	Zhao et al. (2023b)
Chemodynamic therapy	$Fe2^{+}$	DOX/GA-Fe@ $CaCO_3$-PEG	~109.2	PEG	pH	Achieving CDT and subsequently reducing DOX efflux by retarding ATP production	Dong et al. (2020b)
	Cu^{2+}	MoS_2-CuO@BSA heteronanocomposites	~130	BSA	808-nm NIR light	Generating ·OH by Fenton reaction	Jiang et al. (2021)
	Cu^{+}	Cu_2O@$CaCO_3$NCs	~100	HA	pH, H2S, 1,064-nm NIR-II light	The same as above	Chang et al. (2020)
	Mn^{2+}	mPEG-b-PHEP@ ZnxMn1-xS (PPIR780-ZMS)	~150	mPEG-b-PHEP	808-nm light	The same as above	Li et al. (2022)
	Cu^{2+}	Hollow mesoporous organosilica NPs DSF@HCu	98.4	Organosilica	near-infrared (NIR) irradiation	Combination of photonic tumor hyperthermia with *in-situ* Cu^{2+}-activated highly toxic diethyldithiocarbamate (DTC)	Zhang et al. (2021)
	Fe^{3+} and Fe^{2+}	Semiconducting polymer nanocomposites ($SPFeN_{OC}$)	42.1	Surface camouflaging of Hybrid cell membranes of cancer cells and osteoclasts	Ultrasound Irradiation	Mediating CDT by producing ·OH in tumor microenvironment and Enabling SDT by generating $^1O_2$	Zhang et al. (2024)
Pyroptosis	Fe^{3+}	DOPC-coated MIL-100(Fe)	~250	-	pH	Inducing cell pyroptosis, Potential immunotherapy	Ploetz et al. (2020)
synergistic PDT/ CT/CDT therapy	Ca^{2+}	CaO_2@DOX@ZIF@ASQ	625	CaO_2	pH	Generating both ROS and O_2,attenuating the hypoxic condition and potentiates PDT/CT/CDT synergistic cancer therapy	Yu et al. (2024)

the solubility, stability, and biocompatibility of metal ions through their surface modification and functionalization, further optimizing the application of metal ion therapy. Additionally, the nanoplatform is capable of delivering multiple components simultaneously, achieving synergistic effects of different therapeutic mechanisms. Metal ions in combination with other treatment strategies can be used to design new synergistic anti-tumor regimens, improving tumor treatment outcomes, and reducing the potential toxicity of drugs to normal tissues. Additionally, strategies that modulate the homeostasis of multiple metals have shown promising anti-tumor effects. Recently, there has been considerable research on regulating the homeostasis of various metals for cancer treatment. For instance, Shen *et al.* reported a pH-responsive nanoplatform (CaO_2@ZIF-Fe/Ce6@PEG) that simultaneously causes overload of iron and calcium within tumor cells, providing a robust self-supplied ROS pathway to further enhance the efficacy of CDT/PDT (Shen et al., 2021). Xu *et al.* constructed a novel copper/iron mixed hollow nanoplatform (DOX@Fe/CuTHHaMOF) to disrupt intracellular copper/iron metabolism and amplify intracellular oxidative stress, which effectively suppresses tumor growth through synergistic copper apoptosis/iron apoptosis/apoptosis (Xu Y. et al., 2022). Zheng *et al.* developed a Ca^{2+}/Mn^{2+} ion reservoir (PEGCaMnUA) to increase intracellular oxidative stress, enhancing the effect of ion interference therapy (IIT) (Zheng et al., 2023). Deng *et al.* prepared a Ca&Mn dual-ion mixed nanostimulator (CMS) to simultaneously activate iron apoptosis and innate immunity, providing a new strategy for effective immunotherapy against triple-negative breast cancer (TNBC) (Deng et al., 2024). Huang *et al.* constructed a Mn/Zn dual-metal nanoplatform (PMZH) to activate the cGAS-STING signaling pathway and ROS-mediated tumor cell death, achieving enhanced tumor immunotherapy (Huang Y. et al., 2023). Wang *et al.* prepared a carrier-free nanodrug (Mn-ZnO_2 nanoparticles) for delivering zinc-manganese dual ions for the treatment of p53-mutated tumors (Wang J. et al., 2023). In summary, these strategies based on disrupting the homeostasis of multiple metals within cells will provide innovation for cancer treatment. These strategies are expected to address the issue of multiple drug resistance in

tumors. In conclusion, combining the advantages of nanotechnology, metal ions have emerged as a new strategy for anticancer therapy.

4 Advantages of metal-based nanomaterials

Metal-based nanomaterials have been proven to have tremendous potential as targeted drug delivery systems, imaging agents, and therapeutics. Due to their unique advantages, metal nanomaterials have broad application prospects and significant research value in numerous fields. Compared to other types of nanomaterials, metal-based antitumor nanomaterials have the following advantages. First and foremost, metal-based nanomaterials can release a large amount of specific metal ions in the tumor microenvironment, thereby disrupting the metal ion balance required for cellular function. Therefore, metal-based nanomaterials hold great promise for enhancing the imbalance of metal homeostasis in cancer cells. Currently, metal-based nanomaterials under study either through metal chelation or metal overload lead to the disruption of metal homeostasis in cancer cells, ultimately resulting in cell death through various means such as apoptosis, pyroptosis, ferroptosis, cuproptosis, et al. Secondly, due to their small size and high surface area-to-volume ratio, metal nanomaterials exhibit unique physical, chemical, and optical properties, such as strong near-infrared absorption, magnetothermal effects, and the ability to easily accumulate, separate, or undergo targeted movement and localization. These properties enable metal nanomaterials to play a unique role in tumor diagnosis and treatment. For example, gold nanomaterials can rapidly heat up under laser irradiation through the photothermal conversion effect, thereby killing tumor cells and achieving photothermal therapy (Khoobchandani et al., 2020). Magnetic nanomaterials, on the other hand, can indirectly kill tumor cells through the magnetothermal effect, showing good antitumor effects. Furthermore, metal nanomaterials have a high surface area and abundant active sites, which can serve as carriers for anticancer drugs, enhancing the uptake of drugs by cancer cells and improving the efficacy of cancer treatment while reducing the dosage of antitumor drugs. Surface modification of metal nanomaterials can also further enhance their biocompatibility and safety, reducing their potential systemic side effects. Additionally, metal nanomaterials have shown great potential in tumor immunotherapy. For instance, by preparing ultra-small metal-organic nanomaterials, it is possible to achieve sufficient accumulation at the tumor site and rapid renal clearance, enhancing treatment efficacy and greatly reducing long-term toxicity caused by body retention. At the same time, by concentrating multiple functional drug molecules on a single metal nanoplatform, the preparation of multifunctional integrated nanohybrid materials is expected to achieve multimodal synergistic tumor treatment, improving cancer treatment efficiency and imaging resolution. In summary, metal-based antitumor nanomaterials, due to their unique physicochemical properties, high surface area-to-volume ratio, and abundant active sites, as well as their multifunctionality, tunability, and ability to interact with cellular processes, make them attractive candidates for targeted cancer therapy. They have a unique role in tumor diagnosis and treatment and show a broad application prospect.

5 Clinical trials of metal nanomaterials for tumor treatment

Magnetic iron oxide nanoparticles are the earliest metal nanoscale agents applied clinically. They were initially used to treat clinical iron deficiency anemia, with a clinical history dating back to 1930, accumulating valuable data on safety and side effects. In the early 21st century, there was evidence that systemic exposure to iron oxide nanoparticles could induce anti-cancer immune effects. By directly injecting biocompatible iron oxide nanoparticles into tumors and then stimulating them with alternating magnetic fields to generate heat, i.e., using magnetic nanoparticles (Nano-Cancer® therapy) for intratumoral hyperthermia, tumor growth could be suppressed. Given this mechanism, this method was used clinically in the treatment of glioblastoma and prostate cancer about 20 years ago (Johannsen et al., 2007a; Johannsen et al., 2007b; Maier-Hauff et al., 2007). Subsequently, researches on magnetic iron oxide nanoparticles in tumor treatment has become more in-depth, with new formulations continuously emerging and complex mechanisms of action being revealed (Savitsky and Yu, 2019; Soetaert et al., 2020). For example, Nanotherm™ (EU) is used for the clinical treatment of recurrent neuroblastoma (Maier-Hauff et al., 2011). Zanganeh et al. revealed the hidden intrinsic therapeutic effects of iron oxide nanoparticle compounds ferumoxytol (an FDA-approved drug) on tumors (Zanganeh et al., 2016). After mixing ferumoxytol with tumor cells and co-injecting them into mice, compared to tumor cells not injected with ferumoxytol, the growth rate of the tumor was significantly slowed down. Furthermore, they demonstrated that systemic exposure to ferumoxytol in T cell-deficient mice, followed by intravenous injection of small cell lung cancer (SCLC) cells, could prevent liver metastasis. They concluded that the intrinsic therapeutic effect of ferumoxytol on cancer growth comes from the polarization of macrophages to a pro-inflammatory M1 phenotype. In other words, they showed that the innate immune cells in the experimental model tumor microenvironment respond to iron oxide nanoparticles, responsible for the anti-tumor immune effect, rather than T cells. In summary, iron oxide nanoparticles are truly effective agents for hyperthermia and immunotherapy for cancer.

Additionally, there are reports of clinical trials using gold nanoparticles as precious metals for breast cancer patients. The Nano Swarna Bhasma (NSB) Nano-Ayurvedic medicine-gold nanoparticles-based drug was developed using proprietary combinations of gold nanoparticles and phytochemicals through innovative green nanotechnology for human metastatic breast cancer patients. Patients treated with the NSB drug capsules along with the "standard of care treatment" (group B) exhibited 100% clinical benefits when compared to patients in the treatment group A, thus indicating the tremendous clinical benefits of NSB drug in adjuvant therapy (Khoobchandani et al., 2020). The results also indicate that Nano Swarna Bhasma can be safely used as a valuable adjuvant therapeutic agent to reduce the adverse effects of routine chemotherapeutic agents while providing measurable

therapeutic efficacy in treating breast and other forms of human cancers.

6 Limitations and challenges in clinical translation of metal nanomaterials for tumor treatment

Although metal nanomaterials show great potential for tumor treatment at present, they still have many limitations. Firstly, although many anti-tumor mechanisms of metal ion based nanodrugs have been reported, but most of them have only been validated in cell lines. Therefore, further research on these mechanisms in more organoid and animal models is necessary to deeply elucidate the anti-tumor mechanisms and effects of metal ion-based nanodrugs. However, the lack of animal models that can accurately simulate human tumor conditions is one of the recognized deficiencies in the field, leading to a weak correlation between preclinical studies and clinical trial results. For this reason, researchers are trying to establish organoids from patients, which are innovative screening devices as close as possible to the *in vivo* environment. The established platform takes into account tumor angiogenesis and the 3D microenvironment, so as to select the best anti-tumor therapy for patients through the screening device, and collect lymphocytes from the patient's blood to test the effectiveness of immunotherapy. Secondly, there are a series of biological barriers in the body, and if nanocarriers cannot efficiently pass through them, they will also limit the therapeutic effect; interactions between nanomaterials and biological entities in the blood can alter the physicochemical characteristics and stability of nanodrugs, hindering the specific binding of targeting molecules to receptors; most nanoparticles are taken up and cleared by macrophages in the liver or spleen after entering the body, preventing their further delivery to tumor tissues. Therefore, this also poses higher requirements for the design and development of clinical drugs. Lastly, the biological safety of nanomedicines *in vivo* remains the greatest challenge for their clinical application. Currently, most excellent studies have only examined the short-term toxicity of nanomedicines and the corresponding structural damage to major organs, lacking experiments on the long-term toxicity of metal nanomedicines. Therefore, it is necessary to conduct comprehensive studies on their absorption, biodistribution, metabolism, excretion, clearance, long-term tissue accumulation, chronic toxicity, and dose-dependent toxicity before clinical translation. In fact, metal nanomaterials for multimodal combination therapy have shown advantages of synergistic enhanced therapeutic effects and low cytotoxicity. By selecting metal ions with high biocompatibility (e.g., Ca^{2+}, $Fe^{2+/3+}$, Zn^{2+}, etc.) and endogenous bioactive molecules as ligands, toxicity can be effectively prevented (Lai et al., 2021; Simon-Yarza et al., 2018). The additional cargo that may be loaded also needs to be considered, as they may pose a threat to the organism. In addition, there is an increasing need for extensive and in-depth research into the degradation mechanisms and pathways of metal nanomaterials *in vivo*.

Additionally, the synergistic and antagonistic effects among carriers used in cancer treatment, the metal nanoparticles embedded within them, and the complexes containing these metal ions remain unknown. Knowledge of the chemical interactions between metal nanoparticles and these metal ion complexes is still limited. There is currently no answer to the question of whether it is possible to precisely control the release of metal ions from the nanoparticle surface while increasing the biocompatibility of the materials and maximizing their anticancer activity. The properties of organic-inorganic systems, ligand substitution on the surface of metal nanoparticles, and the behavior of maintaining complex stability in the presence of biofluids also remain unexplored.

The clinical translation of metal ion-based nanodrugs for tumor treatment still faces some challenges. Although the valuable experience of intravenous injection of iron oxide nanoparticles for the treatment of anemia is a guide, clinical product iterations have also been carried out in subsequent studies to gain relevant knowledge and sufficient experience. However, nearly a century and the rich clinical experience gained from "three generations" of successful iron oxide nanoparticle formulations have not led to substantial progress in the field of metal nanoparticle anti-tumor drugs as expected. Even with such a long clinical history, new discoveries of complex biological interactions with iron oxide nanoparticles still indicate that our understanding of the complexity of cancer is insufficient. The interactions between nanoparticles and biological systems remain unknown, and incorporating these interactions into the design and function of cancer nanomedicine has greater potential than focusing solely on their engineering design. Cancer is a family of complex diseases, with considerable heterogeneity between subsets, within subsets of the same disease, and within individual patients (Tomasetti and Vogelstein, 2015). The tumor microenvironment is heterogeneous, dynamic, and complex, so each nanoparticle formulation must be evaluated in the context of a wide range of biological scenarios. In addition, preclinical data is not a universally reliable indicator of clinical benefit. Data suggest that more caution is needed when selecting preclinical animal models and that preclinical results need to be carefully assessed.

The historical reality of cancer treatment research and development is that most product concepts fail to translate into clinical applications. The development of small molecule cancer therapeutics has not yet overcome the challenges posed by tumor metastasis, which increases the need for rigorous clinical validation of preclinical data. Metal nanoparticles have great potential for anti-tumor effects, but they must also be modified and designed under the premise of a clear understanding of the specific disease context and interaction with host immune biology, and require the adoption of different research perspectives and multidisciplinary collaboration to achieve efficient therapeutic outcomes.

7 Conclusion and perspectives

In this review, we summarize the mechanisms of metal ions ($Fe^{2+/3+}$, Ca^{2+}, Mn^{2+}, Cu^{2+} and Zn^{2+}) in anti-tumor therapy, and the nanodrugs developed based on these ions over the past 5 years. We analyze the challenges faced by the clinical translation of current metal-based anti-tumor nanomaterials and their future application prospects, and propose suggestions to address related defects. With the proposal and elucidation of concepts such as ferroptosis and cuproptosis, research on metal ion-based anti-tumor nanomaterials has emerged, becoming a new research hotspot. Metal-based anti-tumor drugs can not only cause cell death individually by inducing

intracellular ion imbalances but can also enhance the effects of other anti-tumor therapies such as chemotherapy, radiotherapy, photothermal therapy, and photodynamic therapy. They play a role in comprehensive tumor treatment and achieve synergistic effects of different treatment mechanisms, and demonstrate significant potential. However, many obstacles need to be addressed in various aspects such as the selection of model drugs, the development of preclinical research models, drug safety *in vivo*, and patient screening in clinical research *et al.* The continuous development of new nanomaterial manufacturing processes and standardized procedures, as well as new experimental technologies such as organoid culture systems, will further promote the development of metal nanodrugs in the field of anti-tumor therapy.

With in-depth research on the mechanisms of cancer pathogenesis and the action of metal-based drugs, the design of metal nanodrugs will become more precise and efficient. The application of new strategies and technologies will further promote the development of metal nanodrugs in the field of anti-tumor therapy, and the application of metal nanodrugs in the field of anti-tumor therapy will become more extensive and profound.

Author contributions

YX: Data curation, Investigation, Writing–original draft. AR: Writing–original draft. WF: Writing–review and editing.

Funding

The author(s) declare that no financial support was received for the research, authorship, and/or publication of this article.

Conflict of interest

The authors declare that the research was conducted in the absence of any commercial or financial relationships that could be construed as a potential conflict of interest.

Generative AI statement

The author(s) declare that no Generative AI was used in the creation of this manuscript.

Publisher's note

References

An, J., Zhang, K., Wang, B., Wu, S., Wang, Y., Zhang, H., et al. (2020). Nanoenabled disruption of multiple barriers in antigen cross-presentation of dendritic cells via calcium interference for enhanced chemo-immunotherapy. *ACS Nano* 14, 7639–7650. doi:10.1021/acsnano.0c03881

Ash, D., Sudhahar, V., Youn, S. W., Okur, M. N., Das, A., O'Bryan, J. P., et al. (2021). The P-type ATPase transporter ATP7A promotes angiogenesis by limiting autophagic degradation of VEGFR2. *Nat. Commun.* 12, 3091. doi:10.1038/s41467-021-23408-1

Bagur, R., and Hajnoczky, G. (2017). Intracellular Ca(2+) sensing: its role in calcium homeostasis and signaling. *Mol. Cell* 66, 780–788. doi:10.1016/j.molcel.2017.05.028

Bai, S., Lan, Y., Fu, S., Cheng, H., Lu, Z., and Liu, G. (2022). Connecting calcium-based nanomaterials and cancer: from diagnosis to therapy. *Nanomicro Lett.* 14, 145. doi:10.1007/s40820-022-00894-6

Bao, W., Liu, M., Meng, J., Liu, S., Wang, S., Jia, R., et al. (2021). MOFs-based nanoagent enables dual mitochondrial damage in synergistic antitumor therapy via oxidative stress and calcium overload. *Nat. Commun.* 12, 6399. doi:10.1038/s41467-021-26655-4

Bendellaa, M., Lelievre, P., Coll, J. L., Sancey, L., Deniaud, A., and Busser, B. (2024). Roles of zinc in cancers: from altered metabolism to therapeutic applications. *Int. J. Cancer* 154, 7–20. doi:10.1002/ijc.34679

Berridge, M. J. (2016). The inositol trisphosphate/calcium signaling pathway in health and disease. *Physiol. Rev.* 96, 1261–1296. doi:10.1152/physrev.00006.2016

Berridge, M. J., Lipp, P., and Bootman, M. D. (2000). The versatility and universality of calcium signalling. *Nat. Rev. Mol. Cell Biol.* 1, 11–21. doi:10.1038/35036035

Billesbolle, C. B., Azumaya, C. M., Kretsch, R. C., Powers, A. S., Gonen, S., Schneider, S., et al. (2020). Structure of hepcidin-bound ferroportin reveals iron homeostatic mechanisms. *Nature* 586, 807–811. doi:10.1038/s41586-020-2668-z

Campos, O. A., Attar, N., Cheng, C., Vogelauer, M., Mallipeddi, N. V., Schmollinger, S., et al. (2021). A pathogenic role for histone H3 copper reductase activity in a yeast model of Friedreich's ataxia. *Sci. Adv.* 7, eabj9889. doi:10.1126/sciadv.abj9889

Cao, Z., Yang, X., Yang, W., Chen, F., Jiang, W., Zhan, S., et al. (2024). Modulation of dendritic cell function via nanoparticle-induced cytosolic calcium changes. *ACS Nano* 18, 7618–7632. doi:10.1021/acsnano.4c00550

Carafoli, E. (2002). Calcium signaling: a tale for all seasons. *Proc. Natl. Acad. Sci. U. S. A.* 99, 1115–1122. doi:10.1073/pnas.032427999

Cen, D., Ge, Q., Xie, C., Zheng, Q., Guo, J., Zhang, Y., et al. (2021). ZnS@BSA nanoclusters potentiate efficacy of cancer immunotherapy. *Adv. Mater* 33, e2104037. doi:10.1002/adma.202104037

Chang, M., Hou, Z., Jin, D., Zhou, J., Wang, M., Wang, M., et al. (2020). Colorectal tumor microenvironment-activated bio-decomposable and metabolizable Cu(2) O@CaCO(3) nanocomposites for synergistic oncotherapy. *Adv. Mater* 32, e2004647. doi:10.1002/adma.202004647

Chang, X., Zhu, M., Tang, X., Yu, X., Liu, F., Chen, L., et al. (2022). Enhanced manipulation of tumor microenvironments by nanomotor for synergistic therapy of malignant tumor. *Biomaterials* 290, 121853. doi:10.1016/j.biomaterials.2022.121853

Chen, C., Tong, Y., Zheng, Y., Shi, Y., Chen, Z., Li, J., et al. (2021). Cytosolic delivery of thiolated Mn-cGAMP nanovaccine to enhance the antitumor immune responses. *Small* 17, e2006970. doi:10.1002/smll.202006970

Chen, K., Zhou, A., Zhou, X., Liu, Y., Xu, Y., and Ning, X. (2023). An intelligent cell-derived nanorobot bridges synergistic crosstalk between sonodynamic therapy and cuproptosis to promote cancer treatment. *Nano Lett.* 23, 3038–3047. doi:10.1021/acs.nanolett.3c00434

Chen, Q., Zheng, Z., He, X., Rong, S., Qin, Y., Peng, X., et al. (2020). A tumor-targeted theranostic nanomedicine with strong absorption in the NIR-II biowindow for image-guided multi-gradient therapy. *J. Mater Chem. B* 8, 9492–9501. doi:10.1039/d0tb01915a

Cheng, J., Zhu, Y., Xing, X., Xiao, J., Chen, H., Zhang, H., et al. (2021). Manganese-deposited iron oxide promotes tumor-responsive ferroptosis that synergizes the apoptosis of cisplatin. *Theranostics* 11, 5418–5429. doi:10.7150/thno.53346

Chuang, Y. C., Wu, P. H., Shen, Y. A., Kuo, C. C., Wang, W. J., Chen, Y. C., et al. (2023). Recent advances in metal-based NanoEnhancers for particle therapy. *Nanomater. (Basel)* 13, 1011. doi:10.3390/nano13061011

Clapham, D. E. (2007). Calcium signaling. *Cell* 131, 1047–1058. doi:10.1016/j.cell.2007.11.028

Colvin, R. A., Holmes, W. R., Fontaine, C. P., and Maret, W. (2010). Cytosolic zinc buffering and muffling: their role in intracellular zinc homeostasis. *Metallomics* 2, 306–317. doi:10.1039/b926662c

Cui, L., Gouw, A. M., LaGory, E. L., Guo, S., Attarwala, N., Tang, Y., et al. (2021). Mitochondrial copper depletion suppresses triple-negative breast cancer in mice. *Nat. Biotechnol.* 39, 357–367. doi:10.1038/s41587-020-0707-9

Deng, X., Liu, T., Zhu, Y., Chen, J., Song, Z., Shi, Z., et al. (2024). Ca and Mn dual-ion hybrid nanostimulator boosting anti-tumor immunity via ferroptosis and innate immunity awakening. *Bioact. Mater* 33, 483–496. doi:10.1016/j.bioactmat.2023.11.017

Ding, B., Chen, H., Tan, J., Meng, Q., Zheng, P., Ma, P., et al. (2023a). ZIF-8 nanoparticles evoke pyroptosis for high-efficiency cancer immunotherapy. *Angew. Chem. Int. Ed. Engl.* 62, e202215307. doi:10.1002/anie.202215307

Ding, L., Liang, M., Li, Y., Zeng, M., Liu, M., Ma, W., et al. (2023b). Zinc-organometallic framework vaccine controlled-release Zn(2+) regulates tumor extracellular matrix degradation potentiate efficacy of immunotherapy. *Adv. Sci. (Weinh)* 10, e2302967. doi:10.1002/advs.202302967

Dong, Z., Feng, L., Hao, Y., Li, Q., Chen, M., Yang, Z., et al. (2020a). Synthesis of CaCO3-based nanomedicine for enhanced sonodynamic therapy via amplification of tumor oxidative stress. *Nano Res.* 6, 1391–1407. doi:10.1007/s12274-020-2972-9

Dong, Z., Hao, Y., Li, Q., Yang, Z., Zhu, Y., Liu, Z., et al. (2020b). Metal-polyphenol-network coated CaCO3 as pH-responsive nanocarriers to enable effective intratumoral penetration and reversal of multidrug resistance for augmented cancer treatments. *Nano Res.* 13, 3057–3067. doi:10.1007/s12274-020-2972-9

Du, Y., Zhang, R., Yang, J., Liu, S., Zhou, J., Zhao, R., et al. (2022). A "Closed-Loop" therapeutic strategy based on mutually reinforced ferroptosis and immunotherapy. *Adv. Funct. Mater* 32, 2111784. doi:10.1002/adfm.202111784

Dubois, C., Vanden Abeele, F., Lehen'kyi, V., Gkika, D., Guarmit, B., Lepage, G., et al. (2014). Remodeling of channel-forming ORAI proteins determines an oncogenic switch in prostate cancer. *Cancer Cell* 26, 19–32. doi:10.1016/j.ccr.2014.04.025

Faouzi, M., Kischel, P., Hague, F., Ahidouch, A., Benzerdjeb, N., Sevestre, H., et al. (2013). ORAI3 silencing alters cell proliferation and cell cycle progression via c-myc pathway in breast cancer cells. *Biochim. Biophys. Acta* 1833, 752–760. doi:10.1016/j.bbamcr.2012.12.009

Feng, Z., Chen, G., Zhong, M., Lin, L., Mai, Z., Tang, Y., et al. (2023). An acid-responsive MOF nanomedicine for augmented anti-tumor immunotherapy via a metal ion interference-mediated pyroptotic pathway. *Biomaterials* 302, 122333. doi:10.1016/j.biomaterials.2023.122333

Gao, L., Chen, Q., Gong, T., Liu, J., and Li, C. (2019a). Recent advancement of imidazolate framework (ZIF-8) based nanoformulations for synergistic tumor therapy. *Nanoscale* 11, 21030–21045. doi:10.1039/c9nr06558j

Gao, S., Jin, Y., Ge, K., Li, Z., Liu, H., Dai, X., et al. (2019b). Self-supply of O(2) and H(2)O(2) by a nanocatalytic medicine to enhance combined chemo/chemodynamic therapy. *Adv. Sci. (Weinh)* 6, 1902137. doi:10.1002/advs.201902137

Ge, E. J., Bush, A. I., Casini, A., Cobine, P. A., Cross, J. R., DeNicola, G. M., et al. (2022). Connecting copper and cancer: from transition metal signalling to metalloplasia. *Nat. Rev. Cancer* 22, 102–113. doi:10.1038/s41568-021-00417-2

Guo, B., Yang, F., Zhang, L., Zhao, Q., Wang, W., Yin, L., et al. (2023). Cuproptosis induced by ROS responsive nanoparticles with elesclomol and copper combined with αpd-L1 for enhanced cancer immunotherapy. *Adv. Mater* 35, e2212267. doi:10.1002/adma.202212267

Han, Y., Dong, Z., Wang, C., Li, Q., Hao, Y., Yang, Z., et al. (2022). Ferrous ions doped calcium carbonate nanoparticles potentiate chemotherapy by inducing ferroptosis. *J. Control Release* 348, 346–356. doi:10.1016/j.jconrel.2022.06.002

He, S., Jiang, Y., Li, J., and Pu, K. (2020a). Semiconducting polycomplex nanoparticles for photothermal ferrotherapy of cancer. *Angew. Chem. Int. Ed. Engl.* 59, 10633–10638. doi:10.1002/anie.202003004

He, Y. J., Liu, X. Y., Xing, L., Wan, X., Chang, X., and Jiang, H. L. (2020b). Fenton reaction-independent ferroptosis therapy via glutathione and iron redox couple sequentially triggered lipid peroxide generator. *Biomaterials* 241, 119911. doi:10.1016/j.biomaterials.2020.119911

Hof, T., Chaigne, S., Recalde, A., Salle, L., Brette, F., and Guinamard, R. (2019). Transient receptor potential channels in cardiac health and disease. *Nat. Rev. Cardiol.* 16, 344–360. doi:10.1038/s41569-018-0145-2

Hou, L., Tian, C., Yan, Y., Zhang, L., Zhang, H., and Zhang, Z. (2020). Manganese-based nanoactivator optimizes cancer immunotherapy via enhancing innate immunity. *ACS Nano* 14, 3927–3940. doi:10.1021/acsnano.9b06111

Huang, L., Zhu, J., Xiong, W., Feng, J., Yang, J., Lu, X., et al. (2023a). Tumor-generated reactive oxygen species storm for high-performance ferroptosis therapy. *ACS Nano* 17, 11492–11506. doi:10.1021/acsnano.3c01369

Huang, T., Zhou, J., and Wang, J. (2022). Calcium and calcium-related proteins in endometrial cancer: opportunities for pharmacological intervention. *Int. J. Biol. Sci.* 18, 1065–1078. doi:10.7150/ijbs.68591

Huang, Y., Qin, G., Cui, T. T., Zhao, C. Q., Ren, J. S., and Xg, Q. (2023b). A bimetallic nanoplatform for STING activation and CRISPR/Cas mediated depletion of the methionine transporter in cancer cells restores anti-tumor immune responses. *Nat. Commun.* 14, 4647. doi:10.1038/s41467-023-40345-3

Jia, W., Tian, H., Jiang, J., Zhou, L., Li, L., Luo, M., et al. (2023). Brain-targeted HFn-Cu-rego nanoplatform for site-specific delivery and manipulation of autophagy and cuproptosis in glioblastoma. *Small* 19, e2205354. doi:10.1002/smll.202205354

Jiang, F., Ding, B., Liang, S., Zhao, Y., Cheng, Z., Xing, B., et al. (2021). Intelligent MoS(2)-CuO heterostructures with multiplexed imaging and remarkably enhanced antitumor efficacy via synergetic photothermal therapy/chemodynamic therapy/immunotherapy. *Biomaterials* 268, 120545. doi:10.1016/j.biomaterials.2020.120545

Jiang, Q., Wang, K., Zhang, X., Ouyang, B., Liu, H., Pang, Z., et al. (2020). Platelet membrane-camouflaged magnetic nanoparticles for ferroptosis-enhanced cancer immunotherapy. *Small* 16, e2001704. doi:10.1002/smll.202001704

Jing, Z., Sui, X., Yao, J., Xie, J., Jiang, L., Zhou, Y., et al. (2016). SKF-96365 activates cytoprotective autophagy to delay apoptosis in colorectal cancer cells through inhibition of the calcium/CaMKIIγ/AKT-mediated pathway. *Cancer Lett.* 372, 226–238. doi:10.1016/j.canlet.2016.01.006

Johannsen, M., Gneveckow, U., Taymoorian, K., Thiesen, B., Waldofner, N., Scholz, R., et al. (2007a). Morbidity and quality of life during thermotherapy using magnetic nanoparticles in locally recurrent prostate cancer: results of a prospective phase I trial. *Int. J. Hyperth.* 23, 315–323. doi:10.1080/02656730601175479

Johannsen, M., Gneveckow, U., Thiesen, B., Taymoorian, K., Cho, C. H., Waldofner, N., et al. (2007b). Thermotherapy of prostate cancer using magnetic nanoparticles: feasibility, imaging, and three-dimensional temperature distribution. *Eur. Urol.* 52, 1653–1662. doi:10.1016/j.eururo.2006.11.023

Ju, C., Zhang, Z., Deng, J., Miao, C., Wang, Z., Wallrad, L., et al. (2022). Ca(2+)-dependent successive phosphorylation of vacuolar transporter MTP8 by CBL2/3-CIPK3/9/26 and CPK5 is critical for manganese homeostasis in Arabidopsis. *Mol. Plant* 15, 419–437. doi:10.1016/j.molp.2021.11.012

Kambe, T., Tsuji, T., Hashimoto, A., and Itsumura, N. (2015). The physiological, biochemical, and molecular roles of zinc transporters in zinc homeostasis and metabolism. *Physiol. Rev.* 95, 749–784. doi:10.1152/physrev.00035.2014

Khoobchandani, M., Katti, K. K., Karikachery, A. R., Thipe, V. C., Srisrimal, D., Dhurvas Mohandoss, D. K., et al. (2020). New approaches in breast cancer therapy through green nanotechnology and nano-ayurvedic medicine - pre-clinical and pilot human clinical investigations. *Int. J. Nanomedicine* 15, 181–197. doi:10.2147/IJN.S219042

Kim, A. (2010). Modulation of MnSOD in cancer: epidemiological and experimental evidences. *Toxicol. Res.* 26, 83–93. doi:10.5487/TR.2010.26.2.083

Lai, X., Jiang, H., and Wang, X. (2021). Biodegradable metal organic frameworks for multimodal imaging and targeting theranostics. *Biosens. (Basel)* 11, 299. doi:10.3390/bios11090299

Lei, G., Zhuang, L., and Gan, B. (2022). Targeting ferroptosis as a vulnerability in cancer. *Nat. Rev. Cancer* 22, 381–396. doi:10.1038/s41568-022-00459-0

Lei, H., Pei, Z., Jiang, C., and Cheng, L. (2023). Recent progress of metal-based nanomaterials with anti-tumor biological effects for enhanced cancer therapy. *Explor. (Beijing)* 3, 20220001. doi:10.1002/EXP.20220001

Li, Y., Wang, Y., Zhao, L., Stenzel, M. H., and Jiang, Y. (2024). Metal ion interference therapy: metal-based nanomaterial-mediated mechanisms and strategies to boost intracellular "ion overload" for cancer treatment. *Mater Horiz.* 11, 4275–4310. doi:10.1039/d4mh00470a

Li, Y., Zhou, S., Song, H., Yu, T., Zheng, X., and Chu, Q. (2021). CaCO(3) nanoparticles incorporated with KAE to enable amplified calcium overload cancer therapy. *Biomaterials* 277, 121080. doi:10.1016/j.biomaterials.2021.121080

Li, Z., Chu, Z., Yang, J., Qian, H., Xu, J., Chen, B., et al. (2022). Immunogenic cell death augmented by manganese zinc sulfide nanoparticles for metastatic melanoma immunotherapy. *ACS Nano* 16, 15471–15483. doi:10.1021/acsnano.2c08013

Liu, C., Chen, Y., Zhao, J., Wang, Y., Shao, Y., Gu, Z., et al. (2021). Self-assembly of copper-DNAzyme nanohybrids for dual-catalytic tumor therapy. *Angew. Chem. Int. Ed. Engl.* 60, 14324–14328. doi:10.1002/anie.202101744

Liu, H., Yi, P., Zhao, W., Wu, Y., Acher, F., Pin, J. P., et al. (2020). Illuminating the allosteric modulation of the calcium-sensing receptor. *Proc. Natl. Acad. Sci. U. S. A.* 117, 21711–21722. doi:10.1073/pnas.1922231117

Liu, M., Sun, X., Chen, B., Dai, R., Xi, Z., and Xu, H. (2022). Insights into manganese superoxide dismutase and human diseases. *Int. J. Mol. Sci.* 23, 15893. doi:10.3390/ijms232415893

Liu, Z. Y., Liu, Z. Y., Lin, L. C., Song, K., Tu, B., Zhang, Y., et al. (2024). Redox homeostasis in cardiac fibrosis: focus on metal ion metabolism. *Redox Biol.* 71, 103109. doi:10.1016/j.redox.2024.103109

Lu, X., Deng, W., Wang, S., Zhao, S., Zhu, B., Bai, B., et al. (2024a). PEGylated Elesclomol@Cu(II)-based Metal–organic framework with effective nanozyme performance and cuproptosis induction efficacy for enhanced PD-L1-based immunotherapy. *Mater Today Bio* 29, 101317. doi:10.1016/j.mtbio.2024.101317

Lu, Y., Chen, Y., Hou, G., Lei, H., Liu, L., Huang, X., et al. (2024b). Zinc-iron bimetallic peroxides modulate the tumor stromal microenvironment and enhance cell immunogenicity for enhanced breast cancer immunotherapy therapy. *ACS Nano* 18, 10542–10556. doi:10.1021/acsnano.3c12615

Lv, C., Kang, W., Liu, S., Yang, P., Nishina, Y., Ge, S., et al. (2022). Growth of ZIF-8 nanoparticles *in situ* on graphene oxide nanosheets: a multifunctional nanoplatform for combined ion-interference and photothermal therapy. *ACS Nano* 16, 11428–11443. doi:10.1021/acsnano.2c05532

Lv, M., Chen, M., Zhang, R., Zhang, W., Wang, C., Zhang, Y., et al. (2020). Manganese is critical for antitumor immune responses via cGAS-STING and improves the efficacy of clinical immunotherapy. *Cell Res.* 30, 966–979. doi:10.1038/s41422-020-00395-4

Lv, X., Huang, J., Min, J., Wang, H., Xu, Y., Zhang, Z., et al. (2023). Multi-signaling pathway activation by pH responsive manganese particles for enhanced vaccination. *J. Control Release* 357, 109–119. doi:10.1016/j.jconrel.2023.01.078

Maier-Hauff, K., Rothe, R., Scholz, R., Gneveckow, U., Wust, P., Thiesen, B., et al. (2007). Intracranial thermotherapy using magnetic nanoparticles combined with external beam radiotherapy: results of a feasibility study on patients with glioblastoma multiforme. *J. Neurooncol* 81, 53–60. doi:10.1007/s11060-006-9195-0

Maier-Hauff, K., Ulrich, F., Nestler, D., Niehoff, H., Wust, P., Thiesen, B., et al. (2011). Efficacy and safety of intratumoral thermotherapy using magnetic iron-oxide nanoparticles combined with external beam radiotherapy on patients with recurrent glioblastoma multiforme. *J. Neurooncol* 103, 317–324. doi:10.1007/s11060-010-0389-0

Marchi, S., Giorgi, C., Galluzzi, L., and Pinton, P. (2020). Ca(2+) fluxes and cancer. *Mol. Cell* 78, 1055–1069. doi:10.1016/j.molcel.2020.04.017

Maret, W. (2013). Zinc biochemistry: from a single zinc enzyme to a key element of life. *Adv. Nutr.* 4, 82–91. doi:10.3945/an.112.003038

Medvedeva, Y. V., and Weiss, J. H. (2014). Intramitochondrial Zn2+ accumulation via the Ca2+ uniporter contributes to acute ischemic neurodegeneration. *Neurobiol. Dis.* 68, 137–144. doi:10.1016/j.nbd.2014.04.011

Monteith, G. R., Prevarskaya, N., and Roberts-Thomson, S. J. (2017). The calcium-cancer signalling nexus. *Nat. Rev. Cancer* 17, 373–380. doi:10.1038/nrc.2017.18

Mou, Y., Wang, J., Wu, J., He, D., Zhang, C., Duan, C., et al. (2019). Ferroptosis, a new form of cell death: opportunities and challenges in cancer. *J. Hematol. Oncol.* 12, 34. doi:10.1186/s13045-019-0720-y

Murphy, D. A., Cheng, H., Yang, T., Yan, X., and Adjei, I. M. (2021). Reversing hypoxia with PLGA-encapsulated manganese dioxide nanoparticles improves natural killer cell response to tumor spheroids. *Mol. Pharm.* 18, 2935–2946. doi:10.1021/acs.molpharmaceut.1c00085

Naletova, I., Tomasello, B., Attanasio, F., and Pleshkan, V. V. (2023). Prospects for the use of metal-based nanoparticles as adjuvants for local cancer immunotherapy. *Pharmaceutics* 15, 1346. doi:10.3390/pharmaceutics15051346

Nguyen, N. T., Kim, J., Le, X. T., Lee, W. T., Lee, E. S., Oh, K. T., et al. (2023). Amplified fenton-based oxidative stress utilizing ultraviolet upconversion luminescence-fueled nanoreactors for apoptosis-strengthened ferroptosis anticancer therapy. *ACS Nano* 17, 382–401. doi:10.1021/acsnano.2c08706

Nyvltova, E., Dietz, J. V., Seravalli, J., Khalimonchuk, O., and Barrientos, A. (2022). Coordination of metal center biogenesis in human cytochrome c oxidase. *Nat. Commun.* 13, 3615. doi:10.1038/s41467-022-31413-1

Ploetz, E., Zimpel, A., Cauda, V., Bauer, D., Lamb, D. C., Haisch, C., et al. (2020). Metal-organic framework nanoparticles induce pyroptosis in cells controlled by the extracellular pH. *Adv. Mater* 32, e1907267. doi:10.1002/adma.201907267

Powell, M. M., Rao, G., Britt, R. D., and Rittle, J. (2023). Enzymatic hydroxylation of aliphatic C-H bonds by a Mn/Fe cofactor. *J. Am. Chem. Soc.* 145, 16526–16537. doi:10.1021/jacs.3c03419

Qiao, L., Zhu, G., Jiang, T., Qian, Y., Sun, Q., Zhao, G., et al. (2024). Self-destructive copper carriers induce pyroptosis and cuproptosis for efficient tumor immunotherapy against dormant and recurrent tumors. *Adv. Mater* 36, e2308241. doi:10.1002/adma.202308241

Reznik, N., Gallo, A. D., Rush, K. W., Javitt, G., Fridmann-Sirkis, Y., Ilani, T., et al. (2022). Intestinal mucin is a chaperone of multivalent copper. *Cell* 185, 4206–4215.e11. doi:10.1016/j.cell.2022.09.021

Riley, J. S., and Tait, S. W. (2020). Mitochondrial DNA in inflammation and immunity. *EMBO Rep.* 21, e49799. doi:10.15252/embr.201949799

Saporito-Magriñá, C., Musacco-Sebio, R., Andrieux, G., Kook, L., Orrego, M., Tuttolomondo, M., et al. (2018). Copper-induced cell death and the protective role of glutathione: the implication of impaired protein folding rather than oxidative stress. *Metallomics Integr. biometal Sci.* 10, 1743–1754. doi:10.1039/c8mt00182k

Savitsky, K., and Yu, X. (2019). Combined strategies for tumor immunotherapy with nanoparticles. *Clin. Transl. Oncol.* 21, 1441–1449. doi:10.1007/s12094-019-02081-3

Sawicki, K. T., De Jesus, A., and Ardehali, H. (2023). Iron metabolism in cardiovascular disease: physiology, mechanisms, and therapeutic targets. *Circ. Res.* 132, 379–396. doi:10.1161/CIRCRESAHA.122.321667

Schwarz, M., Meyer, C. E., Loser, A., Lossow, K., Hackler, J., Ott, C., et al. (2023). Excessive copper impairs intrahepatocyte trafficking and secretion of selenoprotein P. *Nat. Commun.* 14, 3479. doi:10.1038/s41467-023-39245-3

Shen, J., Yu, H., Shu, Y., Ma, M., and Chen, H. (2021). A robust ROS generation strategy for enhanced chemodynamic/photodynamic therapy via H2O2/O2 self-supply and Ca2+ overloading. *Adv. Funct. Mater* 31. doi:10.1002/adfm.202106106

Simon-Yarza, T., Mielcarek, A., Couvreur, P., and Serre, C. (2018). Nanoparticles of metal-organic frameworks: on the road to *in vivo* efficacy in biomedicine. *Adv. Mater* 30, e1707365. doi:10.1002/adma.201707365

Soetaert, F., Korangath, P., Serantes, D., Fiering, S., and Ivkov, R. (2020). Cancer therapy with iron oxide nanoparticles: agents of thermal and immune therapies. *Adv. Drug Deliv. Rev.* 163-164, 65–83. doi:10.1016/j.addr.2020.06.025

Su, X., Liu, B., Wang, W. J., Peng, K., Liang, B. B., Zheng, Y., et al. (2023). Disruption of zinc homeostasis by a novel platinum(IV)-Terthiophene complex for antitumor immunity. *Angew. Chem. Int. Ed. Engl.* 62, e202216917. doi:10.1002/anie.202216917

Sun, J., Lu, F., He, H., Shen, J., Messina, J., Mathew, R., et al. (2014). STIM1-and Orai1-mediated Ca(2+) oscillation orchestrates invadopodium formation and melanoma invasion. *J. Cell Biol.* 207, 535–548. doi:10.1083/jcb.201407082

Sun, L., Gao, H., Wang, H., Zhou, J., Ji, X., Jiao, Y., et al. (2024). Nanoscale metal-organic frameworks-mediated degradation of mutant p53 proteins and activation of cGAS-STING pathway for enhanced cancer immunotherapy. *Adv. Sci. (Weinh)* 11, e2307278. doi:10.1002/advs.202307278

Sun, X., Zhang, Y., Li, J., Park, K. S., Han, K., Zhou, X., et al. (2021). Amplifying STING activation by cyclic dinucleotide-manganese particles for local and systemic cancer metalloimmunotherapy. *Nat. Nanotechnol.* 16, 1260–1270. doi:10.1038/s41565-021-00962-9

Sun, Z., Wang, Z., Wang, T., Wang, J., Zhang, H., Li, Z., et al. (2022). Biodegradable MnO-based nanoparticles with engineering surface for tumor therapy: simultaneous fenton-like ion delivery and immune activation. *ACS Nano* 16, 11862–11875. doi:10.1021/acsnano.2c00969

Tomasetti, C., and Vogelstein, B. (2015). Variation in cancer risk among tissues can be explained by the number of stem cell divisions. *Science* 347, 78–81. doi:10.1126/science.1260825

Tsvetkov, P., Coy, S., Petrova, B., Dreishpoon, M., Verma, A., Abdusamad, M., et al. (2022). Copper induces cell death by targeting lipoylated TCA cycle proteins. *Science* 375, 1254–1261. doi:10.1126/science.abf0529

Tsymbal, S., Li, G., Agadzhanian, N., Sun, Y., Zhang, J., Dukhinova, M., et al. (2022). Recent advances in copper-based organic complexes and nanoparticles for tumor theranostics. *Molecules* 27, 7066. doi:10.3390/molecules27207066

Tu, H. K., Pan, K. F., Zhang, Y., Li, W. Q., Zhang, L., Ma, J. L., et al. (2010). Manganese superoxide dismutase polymorphism and risk of gastric lesions, and its effects on chemoprevention in a Chinese population. *Cancer Epidemiol. Biomarkers Prev.* 19, 1089–1097. doi:10.1158/1055-9965.EPI-09-1174

Urbano-Gamez, J. D., Guzzi, C., Bernal, M., Solivera, J., Martinez-Zubiaurre, I., Caro, C., et al. (2024). Tumor versus tumor cell targeting in metal-based nanoparticles for cancer theranostics. *Int. J. Mol. Sci.* 25, 5213. doi:10.3390/ijms25105213

Wang, C., Guan, Y., Lv, M., Zhang, R., Guo, Z., Wei, X., et al. (2018). Manganese increases the sensitivity of the cGAS-STING pathway for double-stranded DNA and is required for the host defense against DNA viruses. *Immunity* 48, 675–687.e7. doi:10.1016/j.immuni.2018.03.017

Wang, G., Jiang, Y., Xu, J., Shen, J., Lin, T., Chen, J., et al. (2023a). Unraveling the plasma protein corona by ultrasonic cavitation augments active-transporting of liposome in solid tumor. *Adv. Mater* 35, e2207271. doi:10.1002/adma.202207271

Wang, J., Qu, C., Shao, X., Song, G., Sun, J., Shi, D., et al. (2023b). Carrier-free nanoprodrug for p53-mutated tumor therapy via concurrent delivery of zinc-manganese dual ions and ROS. *Bioact. Mater* 20, 404–417. doi:10.1016/j.bioactmat.2022.06.005

Wang, J., Zhao, H., Xu, Z., and Cheng, X. (2020). Zinc dysregulation in cancers and its potential as a therapeutic target. *Cancer Biol. Med.* 17, 612–625. doi:10.20892/j.issn.2095-3941.2020.0106

Wang, L., Ge, K., Duan, J., Du, X., Zhou, G., Ma, L., et al. (2024). A double-gain theranostic nanoplatform based on self-supplying H(2)O(2) nanocomposites for synergistic chemodynamic/gas therapy. *J. Colloid Interface Sci.* 654, 774–784. doi:10.1016/j.jcis.2023.10.092

Wang, W., Yu, S., Huang, S., Deng, R., Ding, Y., Wu, Y., et al. (2019). A complex role for calcium signaling in colorectal cancer development and progression. *Mol. Cancer Res.* 17, 2145–2153. doi:10.1158/1541-7786.MCR-19-0429

Wang, Y., Gong, F., Han, Z., Lei, H., Zhou, Y., Cheng, S., et al. (2023c). Oxygen-deficient molybdenum oxide nanosensitizers for ultrasound-enhanced cancer metalloimmunotherapy. *Angew. Chem. Int. Ed. Engl.* 62, e202215467. doi:10.1002/anie.202215467

Wang, Y., Wu, X., Bao, X., and Mou, X. (2023d). Progress in the mechanism of the effect of Fe(3)O(4) nanomaterials on ferroptosis in tumor cells. *Molecules* 28, 4562. doi:10.3390/molecules28114562

Wu, W., Yu, L., Pu, Y., Yao, H., Chen, Y., and Shi, J. (2020). Copper-enriched prussian blue nanomedicine for *in situ* disulfiram toxification and photothermal antitumor amplification. *Adv. Mater* 32, e2000542. doi:10.1002/adma.202000542

Wu, X., Wu, Q., Hou, M., Jiang, Y., Li, M., Jia, G., et al. (2024a). Regenerating chemotherapeutics through copper-based nanomedicine: disrupting protein homeostasis for enhanced tumor therapy. *Adv. Healthc. Mater* 13, e2401954. doi:10.1002/adhm.202401954

Wu, Y., Sun, B., Tang, Y., Shen, A., Lin, Y., Zhao, X., et al. (2024b). Bone targeted nano-drug and nano-delivery. *Bone Res.* 12, 51. doi:10.1038/s41413-024-00356-2

Xin, Y., Gao, H., Wang, J., Qiang, Y., Imam, M. U., Li, Y., et al. (2017). Manganese transporter Slc39a14 deficiency revealed its key role in maintaining manganese homeostasis in mice. *Cell Discov.* 3, 17025. doi:10.1038/celldisc.2017.25

Xiong, H., Wang, C., Wang, Z., Lu, H., and Yao, J. (2021). Self-assembled nano-activator constructed ferroptosis-immunotherapy through hijacking endogenous iron to intracellular positive feedback loop. *J. Control Release* 332, 539–552. doi:10.1016/j.jconrel.2021.03.007

Xu, L., Peng, M., Gao, T., Wang, D., Lian, X., Sun, H., et al. (2024). Nanoenabled intracellular metal ion homeostasis regulation for tumor therapy. *Adv. Sci. (Weinh)* 11, e2306203. doi:10.1002/advs.202306203

Xu, L., Tong, G., Song, Q., Zhu, C., Zhang, H., Shi, J., et al. (2018). Enhanced intracellular Ca(2+) nanogenerator for tumor-specific synergistic therapy via disruption of mitochondrial Ca(2+) homeostasis and photothermal therapy. *ACS Nano* 12, 6806–6818. doi:10.1021/acsnano.8b02034

Xu, W. J., Qian, J. M., Hou, G. H., Wang, T. B., Wang, J. L., Wang, Y. P., et al. (2022a). A hollow amorphous bimetal organic framework for synergistic cuproptosis/ferroptosis/apoptosis anticancer therapy via disrupting intracellular redox homeostasis and copper/iron metabolisms. *Adv. Funct. Mater.* 32, 20222205013. doi:10.1002/adfm.202205013

Xu, Y., Liu, S. Y., Zeng, L., Ma, H., Zhang, Y., Yang, H., et al. (2022b). An enzyme-engineered nonporous copper(I) coordination polymer nanoplatform for cuproptosis-based synergistic cancer therapy. *Adv. Mater* 34, e2204733. doi:10.1002/adma.202204733

Yang, H., Yao, X., Liu, Y., Shen, X., Li, M., and Luo, Z. (2023). Ferroptosis nanomedicine: clinical challenges and opportunities for modulating tumor metabolic and immunological landscape. *ACS Nano* 17, 15328–15353. doi:10.1021/acsnano.3c04632

Yang, Y., Tang, J., Zhang, M., Gu, Z., Song, H., Yang, Y., et al. (2019). Responsively aggregatable sub-6 nm nanochelators induce simultaneous antiangiogenesis and vascular obstruction for enhanced tumor vasculature targeted therapy. *Nano Lett.* 19, 7750–7759. doi:10.1021/acs.nanolett.9b02691

Yao, J., Zhang, A., Qiu, Y., Li, Z., Wu, X., Li, Z., et al. (2023). Navigating zinc-involved nanomedicine in oncotherapy. *Nanoscale* 15, 4261–4276. doi:10.1039/d2nr06857e

Yao, X., Xie, R., Cao, Y., Tang, J., Men, Y., Peng, H., et al. (2021). Simvastatin induced ferroptosis for triple-negative breast cancer therapy. *J. Nanobiotechnology* 19, 311. doi:10.1186/s12951-021-01058-1

Yu, B., Liu, M., Jiang, L., Xu, C., Hu, H., Huang, T., et al. (2024). Aggregation-induced emission photosensitizer-engineered anticancer nanomedicine for synergistic chemo/chemodynamic/photodynamic therapy. *Adv. Healthc. Mater* 13, e2303643. doi:10.1002/adhm.202303643

Yu, H., Zhou, Y., Lind, S. E., and Ding, W. Q. (2009). Clioquinol targets zinc to lysosomes in human cancer cells. *Biochem. J.* 417, 133–139. doi:10.1042/BJ20081421

Yu, P., Zhang, X., Liu, N., Tang, L., Peng, C., and Chen, X. (2021). Pyroptosis: mechanisms and diseases. *Signal Transduct. Target Ther.* 6, 128. doi:10.1038/s41392-021-00507-5

Zanganeh, S., Hutter, G., Spitler, R., Lenkov, O., Mahmoudi, M., Shaw, A., et al. (2016). Iron oxide nanoparticles inhibit tumour growth by inducing pro-inflammatory macrophage polarization in tumour tissues. *Nat. Nanotechnol.* 11, 986–994. doi:10.1038/nnano.2016.168

Zhang, H., Song, F., Dong, C., Yu, L., Chang, C., and Chen, Y. (2021). Co-delivery of nanoparticle and molecular drug by hollow mesoporous organosilica for tumor-activated and photothermal-augmented chemotherapy of breast cancer. *J. Nanobiotechnology* 19, 290. doi:10.1186/s12951-021-01025-w

Zhang, K., Qi, C., and Cai, K. (2023). Manganese-based tumor immunotherapy. *Adv. Mater* 35, e2205409. doi:10.1002/adma.202205409

Zhang, L., Zhao, J., Hu, X., Wang, C., Jia, Y., Zhu, C., et al. (2022). A peritumorally injected immunomodulating adjuvant elicits robust and safe metalloimmunotherapy against solid tumors. *Adv. Mater* 34, e2206915. doi:10.1002/adma.202206915

Zhang, Y., Wang, Y., Zhu, A., Yu, N., Xia, J., and Li, J. (2024). Dual-targeting biomimetic semiconducting polymer nanocomposites for amplified theranostics of bone metastasis. *Angew. Chem. Int. Ed. Engl.* 63, e202310252. doi:10.1002/anie.202310252

Zhang, Z., Liu, X., Feng, B., Liu, N., Wu, Q., Han, Y., et al. (2015). STIM1, a direct target of microRNA-185, promotes tumor metastasis and is associated with poor prognosis in colorectal cancer. *Oncogene* 34, 4808–4820. doi:10.1038/onc.2014.404

Zhao, F., Liang, L., Wang, H., Wang, C., Su, D., Ying, Y., et al. (2023a). H2S-activated ion-interference therapy: a novel tumor targeted therapy based on copper-overload-mediated cuproptosis and pyroptosis. *Adv. Funct. Mater* 33, 2300941. doi:10.1002/adfm.202300941

Zhao, H., Wang, L., Zeng, K., Li, J., Chen, W., and Liu, Y. N. (2021). Nanomessenger-mediated signaling cascade for antitumor immunotherapy. *ACS Nano* 15, 13188–13199. doi:10.1021/acsnano.1c02765

Zhao, X., Cheng, H., Wang, Q., Nie, W., Yang, Y., Yang, X., et al. (2023b). Regulating photosensitizer metabolism with DNAzyme-loaded nanoparticles for amplified mitochondria-targeting photodynamic immunotherapy. *ACS Nano* 17, 13746–13759. doi:10.1021/acsnano.3c03308

Zhao, X., Leng, D., Wang, H., Jin, H., Wu, Y., Qin, Z., et al. (2024). An acid-responsive iron-based nanocomposite for OSCC treatment. *J. Dent. Res.* 103, 612–621. doi:10.1177/00220345241238154

Zheng, P., Ding, B., Jiang, Z., Xu, W., Li, G., Ding, J., et al. (2021). Ultrasound-augmented mitochondrial calcium ion overload by calcium nanomodulator to induce immunogenic cell death. *Nano Lett.* 21, 2088–2093. doi:10.1021/acs.nanolett.0c04778

Zheng, P., Ding, B., Zhu, G., Lin, J., and Li, C. (2023). Usnea acid-incorporated Ca(2+)/Mn(2+) ions reservoirs for elevated ion-interference therapy through synergetic biocatalysis and osmolarity imbalance. *Small* 19, e2300370. doi:10.1002/smll.202300370

Zhong, X., Dai, X., Wang, Y., Wang, H., Qian, H., and Wang, X. (2022). Copper-based nanomaterials for cancer theranostics. *Wiley Interdiscip. Rev. Nanomed Nanobiotechnol* 14, e1797. doi:10.1002/wnan.1797

Zhu, L., You, Y., Zhu, M., Song, Y., Zhang, J., Hu, J., et al. (2022). Ferritin-hijacking nanoparticles spatiotemporally directing endogenous ferroptosis for synergistic anticancer therapy. *Adv. Mater* 34, e2207174. doi:10.1002/adma.202207174

Zhu, Y., Wang, W., Cheng, J., Qu, Y., Dai, Y., Liu, M., et al. (2021). Stimuli-responsive manganese single-atom nanozyme for tumor therapy via integrated cascade reactions. *Angew. Chem. Int. Ed. Engl.* 60, 9480–9488. doi:10.1002/anie.202017152

Zhu, Y., Zou, X., Dean, A. E., Brien, J. O., Gao, Y., Tran, E. L., et al. (2019). Lysine 68 acetylation directs MnSOD as a tetrameric detoxification complex versus a monomeric tumor promoter. *Nat. Commun.* 10, 2399. doi:10.1038/s41467-019-10352-4

frontiers | Frontiers in Bioengineering and Biotechnology

TYPE Review
PUBLISHED 17 February 2025
DOI 10.3389/fbioe.2025.1535588

OPEN ACCESS

EDITED BY
Liqun Yang,
Shengjing Hospital of China Medical University, China

REVIEWED BY
Zhanfei Li,
Huazhong University of Science and Technology, China
Yunen Liu,
Shenyang Medical College, China

*CORRESPONDENCE
Wei Bian,
nkyb666@126.com

RECEIVED 27 November 2024
ACCEPTED 20 January 2025
PUBLISHED 17 February 2025

CITATION
Tian S and Bian W (2025) Advanced biomaterials in pressure ulcer prevention and care: from basic research to clinical practice.
Front. Bioeng. Biotechnol. 13:1535588.
doi: 10.3389/fbioe.2025.1535588

Advanced biomaterials in pressure ulcer prevention and care: from basic research to clinical practice

Shaoqiang Tian[1] and Wei Bian[2]*

[1]Department of Emergency Medicine, The First People's Hospital of Shenyang, Shenyang, China, [2]Department of Neurosurgery, The First People's Hospital of Shenyang, Shenyang, China

Pressure ulcers are a common and serious medical condition. Conventional treatment methods often fall short in addressing the complexities of prevention and care. This paper provides a comprehensive review of recent advancements in advanced biomaterials for pressure ulcer management, emphasizing their potential to overcome these limitations. The study highlights the roles of biomaterials in enhancing wound healing, preventing infections, and accelerating recovery. Specific focus is placed on the innovation and application of multi-functional composite materials, intelligent systems, and personalized solutions. Future research should prioritize interdisciplinary collaboration to facilitate the clinical translation of these materials, providing more effective and tailored treatment approaches. These advancements aim to improve the quality of life and health outcomes for patients by offering more reliable, efficient, and patient-specific therapeutic options.

KEYWORDS

pressure ulcers, hydrogels, alginate, chitosan, PLGA, polyurethane

Highlights

- This review summarizes recent progress in advanced biomaterials for pressure ulcer prevention and treatment, from research to clinical use.
- Multi-functional and intelligent biomaterials hold great promise for improving wound healing and infection prevention.
- Future research highlights the need for interdisciplinary collaboration and personalized strategies to advance clinical applications.

1 Introduction

Pressure ulcers (PUs), also known as pressure sores or bedsores, are areas of tissue damage caused by prolonged pressure on bony parts of the body like the sacrum, hips, heels, and elbows (Mervis and Phillips, 2019). This pressure restricts blood flow, leading to tissue oxygen loss, ischemia, and eventually, necrosis. While constant pressure is the main cause, other factors like shear forces and friction also play significant roles in PU development (Blackburn et al., 2020). PUs are a major healthcare issue, especially among the elderly (Wei et al., 2021), people with limited mobility (Sprigle et al., 2020), and those confined to bed for long periods (Deng et al., 2024). In China, a meta-analysis found the incidence of PUs

among the elderly to be 12.77% (Hu et al., 2020). This highlights the widespread nature of the problem and the differences in prevention and treatment practices across care settings. Globally, the incidence of PUs is increasing due to aging populations and the growing prevalence of chronic illnesses. This trend significantly impacts both patients' quality of life and healthcare systems. PUs cause intense pain and discomfort, severely affecting patients' daily lives and mental health (Qian et al., 2024). The long healing process often leads to frustration, helplessness, and at times, depression. Infections are another serious risk (Malone and Schultz, 2022), which can threaten patients' lives (Hajhosseini et al., 2020). For bedridden individuals, PUs further reduce mobility and independence, worsening their overall quality of life. The economic impact of PUs on healthcare is considerable. Treatment often requires specialized care, advanced wound dressings, and equipment like negative pressure wound therapy. Severe cases involving infection or significant tissue damage may need surgery, increasing costs even more. In the United States, annual PU-related expenses run into billions of dollars. PUs also lengthen hospital stays and raise readmission rates, adding further strain to healthcare systems.

Conventional treatments for pressure ulcers (PUs) include pressure relief (e.g., repositioning and specialized support surfaces), wound dressings, and pharmacological interventions (BoykoTatiana et al., 2018). While these methods can reduce pain and help prevent infection, they often involve long treatment durations, limited effectiveness, and low cure rates. Pressure relief is essential but difficult to fully implement for patients with prolonged immobility, which limits its overall success. Traditional moist dressings, though helpful, carry a risk of infection and may not effectively promote tissue regeneration. Pharmacological treatments can manage symptoms and relieve pain, but their impact on wound healing is often slow, with the added concern of potential drug resistance. These limitations highlight the challenges of current PU management strategies in clinical practice, making it difficult to achieve complete wound resolution. The need for more advanced and effective materials and methods for PU prevention and treatment is clear. Recent research points to the potential of biomedical materials as a promising solution for improving PU outcomes. Innovations in biomaterials have introduced new approaches for managing these challenging wounds. For example, biomaterials can accelerate wound healing, prevent infections, and enhance both the speed and quality of tissue regeneration (Deng et al., 2022; Nguyen et al., 2023). Using biocompatible and pro-regenerative biomaterials is emerging as a highly effective strategy for improving PU treatment outcomes. Studies show that incorporating biomaterials into PU treatment protocols significantly enhances efficacy compared to conventional methods. These materials not only promote faster short-term healing but also provide long-term benefits, reducing treatment costs and improving patients' quality of life (Pan et al., 2023).

This review will explore the role and potential of biomaterials in PU treatment. We will examine the efficacy and advantages of various biomaterials based on recent research and discuss future directions for their development and application in PU prevention and treatment. Our goal is to provide clinicians with evidence-based, effective treatment options and offer valuable insights for future research and clinical practice in this critical area of wound care.

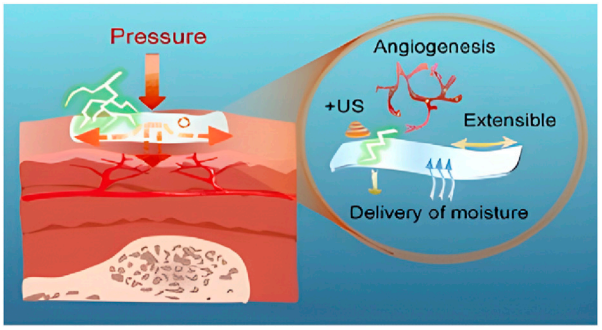

FIGURE 1
Hydrogel for Prophylaxis and Early Treatment of Pressure Injuries/Pressure Ulcers. Reproduced with permission from Li et al. (2022). Copyright © 2022 The Authors.

2 Classification of advanced biomaterials for pressure ulcer prevention and care

2.1 Hydrogels

Hydrogels are a class of biomaterials widely used in biomedicine due to their high water content, softness, and breathability (Cascone and Lamberti, 2020). These unique properties make hydrogels particularly effective for applications such as pressure ulcer (PU) management, wound healing, and drug delivery (Li et al., 2022).

The most defining feature of hydrogels is their high water content, which results from their three-dimensional network structure. This structure allows hydrogels to absorb and retain large amounts of water, creating a moist environment that is essential for cell growth and tissue regeneration during wound healing. Their hydrophilic nature helps accelerate the repair process by maintaining optimal conditions for cell migration and proliferation. The softness and elasticity of hydrogels further enhance their benefits, allowing them to conform closely to the wound bed. This adaptability ensures personalized care for wounds of different shapes and sizes while providing a more comfortable healing experience. Their soft texture also minimizes irritation and friction on healthy surrounding tissues, reducing pain and improving patient comfort. Another key advantage of hydrogels is their excellent breathability, which allows air and water vapor to pass through. This feature prevents bacterial growth, ensures proper oxygen supply, and manages moisture levels, helping to avoid complications caused by excess fluid or temperature fluctuations. Improved breathability not only supports faster wound healing but also increases comfort and wearability for patients. In addition to these physical and functional properties, hydrogels exhibit strong biocompatibility, meaning they rarely cause allergic reactions or skin irritation (Cascone and Lamberti, 2020). This makes them a safe choice for various clinical applications, including wound healing, burn care, and skincare. Their compatibility with biological tissues further underscores their effectiveness in promoting tissue repair and regeneration. By combining these advantageous properties, hydrogels represent a significant advancement in PU

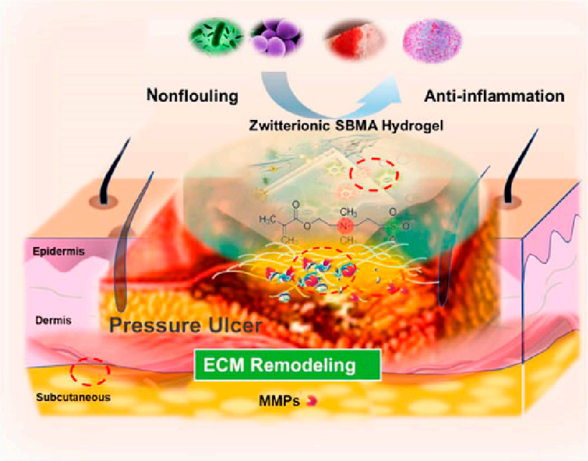

FIGURE 2
Hydrogel Activates Autophagy to Promote Extracellular Matrix Remodeling for Improved Pressure Ulcer Healing. Reproduced with permission from Li et al. (2021). Copyright © 2021 The Authors.

management and other biomedical fields, offering a versatile and patient-friendly solution.

The use of hydrogels as pressure ulcer (PU) dressings offers several key benefits, including wound hydration, pressure relief, and enhanced healing (Figures 1, 2). Studies have shown that hydrogel dressings significantly improve PU management by maintaining a moist wound environment, which prevents desiccation and supports cell growth and tissue regeneration. This moist environment not only reduces healing time but also creates optimal conditions for wound repair. Hydrogel dressings also help alleviate pressure on the affected area. Their softness and elasticity allow them to conform to the wound's contours, effectively distributing pressure and minimizing further tissue damage. By reducing friction and shear forces, they help prevent additional breakdown of surrounding tissues. In addition, the biocompatibility of hydrogels ensures close adherence to the wound surface, creating an ideal environment for healing. Their hydrating properties stimulate tissue regeneration and repair, accelerating the healing process and improving overall treatment outcomes. These combined advantages make hydrogel dressings a valuable tool in PU management.

In conclusion, hydrogel dressings are a highly effective and versatile option for managing pressure ulcers. Their ability to maintain a moist wound environment, relieve pressure, and support tissue regeneration has made them a valuable tool in clinical practice. By creating optimal conditions for healing, hydrogel dressings can accelerate recovery, improve treatment outcomes, and enhance the quality of life for patients with pressure ulcers.

2.2 Nanomaterials

Nanomaterials are increasingly being used in medicine, with nano-silver and nano-zinc oxide standing out for their strong antibacterial properties (Du, 2024). These materials exhibit broad-spectrum activity against bacteria, viruses, and fungi, making them valuable components in medical devices, wound dressings, antimicrobial coatings, and similar products.

Nano-silver's high surface area-to-volume ratio enhances its reactivity, allowing it to release silver ions that disrupt bacterial cell walls and membranes, ultimately causing bacterial death (Du, 2024). This mechanism provides effective antimicrobial activity, including against drug-resistant strains. Nano-silver also targets viral outer membranes and genetic material, preventing replication and spread. These properties make it essential for infection control in medical devices, personal protective equipment, and other healthcare tools. Additionally, nano-silver's antifungal activity helps combat mold and fungal infections, broadening its utility in clinical and environmental applications. Nano-zinc oxide, known for its photocatalytic properties (Chopra, 2022), produces reactive oxygen species when exposed to ultraviolet (UV) light. These reactive molecules effectively eliminate bacteria and viruses, making nano-zinc oxide valuable for applications such as environmental remediation and water purification. In sunscreen products, it provides physical UV protection while also delivering antibacterial benefits, reducing the risk of skin infections caused by sun exposure. Furthermore, nano-zinc oxide's anti-inflammatory properties help soothe skin irritation and promote wound healing, making it an ideal component in wound dressings and topical ointments.

Studies have shown that pressure ulcer (PU) dressings containing nano-silver or nano-zinc oxide can accelerate wound healing, reduce infection risk (Figure 3), and improve overall treatment outcomes (Pollini et al., 2024; Rybka et al., 2022). The antibacterial and anti-inflammatory properties of these nanomaterials play a key role in promoting tissue repair and regeneration. Additionally, dressings incorporating nanomaterials offer favorable features such as conformability, absorbency, and breathability, which help maintain optimal wound moisture and create an ideal healing environment. These dressings are also easy to apply and comfortable for patients, further enhancing their practicality in clinical use.

While the benefits of nanomaterials in PU dressings are well-documented, ongoing research is focused on evaluating potential side effects and long-term safety. Current evidence indicates that, when used at appropriate concentrations, these nanomaterials do not pose significant risks. Overall, the integration of nanomaterials into PU dressings provides substantial advantages, including faster healing, reduced infection rates, and improved treatment outcomes. As rigorous studies continue to validate their efficacy and safety, nanomaterial-based PU dressings are becoming increasingly accepted in clinical practice, offering more effective treatment options for patients.

2.3 Extracellular matrix (ECM)

The extracellular matrix (ECM) is a complex and dynamic network that surrounds cells, consisting of structural proteins, polysaccharides, and bioactive molecules (Karamanos et al., 2021). Its key components include collagen, fibronectin, and elastin, which provide structural and mechanical support; polysaccharides such as sulfated glycosaminoglycans and

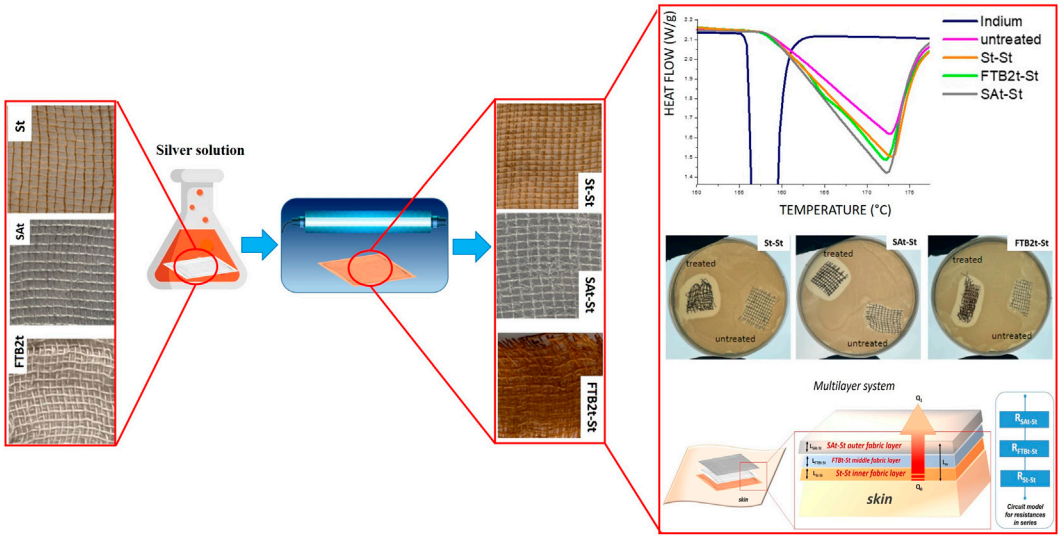

FIGURE 3
Nanotechnological Antibacterial Wound Dressings for Pressure Ulcer Prevention. Reproduced with permission from Pollini et al. (2024). Copyright © 2024 The Authors.

hyaluronic acid, which contribute to hydration and matrix organization; and bioactive molecules like growth factors and cell adhesion molecules, which regulate cell behavior and tissue function. Together, these elements create a supportive framework and transmit essential biochemical and mechanical signals critical for maintaining tissue integrity and cellular activities.

The extracellular matrix (ECM) performs a wide array of functions essential for tissue health and stability. It provides structural support to tissues, facilitates cell adhesion and migration, regulates cell signaling pathways, influences cell morphology and polarization, and maintains tissue homeostasis. By mediating interactions between cells and their microenvironment, the ECM supports cell survival and function, playing a critical role in tissue repair, regeneration, and stability. Understanding ECM composition and function is fundamental for advancing tissue engineering, disease treatment, and related fields. In tissue engineering, the ECM is particularly important for the development of skin substitutes, offering innovative solutions for pressure ulcer (PU) prevention and treatment (Sheikholeslam et al., 2018). ECM-based biomaterials mimic the structure and biological functions of native skin, creating an ideal environment for wound repair. Studies demonstrate that ECM-based skin substitutes can significantly accelerate PU healing by serving as a structural scaffold for cells and delivering a rich array of growth factors and signaling molecules. These elements stimulate cell migration and proliferation, promoting tissue reconstruction (Diller and Tabor, 2022). Additionally, the ECM enhances the wound microenvironment by maintaining a moist environment that prevents desiccation and infection. Antimicrobial components such as sulfated glycosaminoglycans inhibit bacterial growth, while the ECM's ability to regulate wound pH creates conditions conducive to healing. Moreover, angiogenic factors like vascular endothelial growth factor (VEGF) and fibroblast growth factor (FGF) promote angiogenesis, improving blood supply to the wound and ensuring the delivery of nutrients and oxygen critical for tissue repair. ECM-based skin substitutes also play a preventative role in high-risk populations. By acting as a protective barrier, they reduce friction and shear forces over vulnerable areas, effectively lowering the risk of PU development. The combination of these properties makes ECM-based biomaterials highly versatile and effective in wound care.

In summary, ECM-based skin substitutes show immense potential for transforming PU prevention and treatment. Their ability to replicate native skin functions and enhance wound healing offers promising opportunities for clinical practice. Continued research and optimization are crucial to fully harness their benefits and further improve outcomes in PU management.

2.4 Smart biomaterials

Recent advances in smart materials, particularly temperature-sensitive and pH-sensitive types, have unlocked new possibilities for pressure ulcer (PU) monitoring and treatment (Tang et al., 2024; Mu et al., 2024). Temperature-sensitive materials can reversibly alter their physical and chemical properties, such as volume, shape, and wettability, in response to temperature fluctuations. This behavior is driven by their phase transition near a critical temperature, known as the lower critical solution temperature (LCST), which is triggered by the interaction of their hydrophilic and hydrophobic groups (Kotsuchibashi, 2020; Khutoryanskiy and Georgiou, 2018). Similarly, pH-sensitive materials respond to changes in proton concentration, modulating properties like solubility and ionization state. These characteristics make pH-sensitive materials highly adaptable to varying microenvironments, particularly in wounds where pH levels can fluctuate significantly (Ofridam et al., 2021). The intelligent and dynamic behavior of both temperature-sensitive and pH-sensitive materials makes them highly promising for biomedical applications, including advanced wound care and PU management.

Research has shown that skin temperature at pressure ulcer (PU) sites is significantly elevated, making temperature-sensitive materials valuable tools for monitoring PU development and progression in real time. Flexible sensor pads integrating multiple sensors can continuously and non-invasively track PU-related vital signs, providing critical data for early prevention (Kaewjamnong and Hongwitayakorn, 2021). For instance, Gillard et al. explored the relationship between temperature and blood flow in PU detection, demonstrating how temperature sensors can improve early diagnosis by continuously monitoring changes in pressure and temperature (Gillard et al., 2023). Similarly, pH-sensitive materials offer significant potential for assessing PU status. PU wounds often exhibit pH variations, and pH-sensitive materials can act as colorimetric indicators, providing visual feedback on wound conditions. Advanced pH-sensing fabric sensors, based on flexible wearable technology, can continuously monitor wound pH fluctuations, offering clinicians valuable real-time data for wound assessment (Du and Ciou, 2019). Additionally, pH-sensitive hydrogels can respond to these changes by modulating the release of antimicrobials or growth factors, creating a favorable wound environment and accelerating PU healing (Haidari et al., 2021).

The evidence highlights the transformative potential of smart materials, such as temperature- and pH-sensitive technologies, in advancing PU monitoring and treatment. These materials enable real-time tracking of PU development, support early prevention strategies, and enhance clinical assessment. Furthermore, by tailoring their properties, they can actively promote wound healing and improve patient outcomes. Future research aimed at optimizing the performance of these materials, alongside advancements in flexible electronics and wearable sensing technologies, holds great promise for addressing the complex challenges of PU management.

3 Innovative applications of biomaterials in pressure ulcer prevention and care

PUs are a common issue in patients with prolonged immobility. To address this, researchers and medical device manufacturers have developed smart mattresses and seat cushions that utilize advanced biomaterials and sensor technologies. These intelligent products monitor pressure distribution and adjust cushioning properties in real time to achieve balanced pressure dispersion, providing relief and effectively preventing PUs. Smart mattresses incorporate pressure-sensitive sensors, adjustable hardness materials, and breathable materials to optimize patient care. Pressure-sensitive sensors accurately measure tissue pressure and transmit data to a control system for analysis (Silva et al., 2021; Yang et al., 2021). This data enables the dynamic adjustment of mattress firmness using adjustable hardness materials, which provide targeted support and pressure relief where needed (Kumagai et al., 2019). Additionally, breathable materials enhance the skin microenvironment by promoting air circulation and reducing moisture buildup, key factors in PU prevention (Das and Baker, 2016). By continuously monitoring pressure fluctuations and responding in real time, smart mattresses and seat cushions not only prevent the formation of PUs but also mitigate their progression. The integration of biomaterials and sensor technologies in these devices represents a significant advancement in PU management, offering innovative solutions for improving patient outcomes (Memari et al., 2021; Yang et al., 2024; Ghosh et al., 2024).

Similarly, smart seat cushions are designed for patients who sit for extended periods, focusing on reducing pressure on the sacral area to prevent nerve damage and pressure ulcers (Hepburn et al., 2017). Key biomaterials used in these cushions include shape memory foam, pressure-relief contour designs, and position-sensing sensors. Shape memory foam conforms to the patient's body contours, evenly distributing pressure and providing optimal support (Kumar et al., 2019). Contour designs help minimize sacral pressure and reduce skin friction, while position-sensing sensors continuously monitor sitting posture and pressure distribution. These sensors enable real-time structural adjustments, enhancing support and adaptability. Together, these features make smart seat cushions highly effective in preventing sacral pressure ulcers and improving patient comfort and quality of life. In conclusion, the integration of biomaterials into smart mattresses and seat cushions represents an innovative approach to pressure ulcer prevention and treatment. These intelligent devices provide real-time monitoring and pressure redistribution, significantly reducing the risk of pressure injuries caused by prolonged immobility. As biomaterial technology continues to advance, smart mattresses and cushions are becoming indispensable clinical tools. Additionally, specialized garments and wearable devices incorporating biomaterials further enhance PU prevention by providing targeted pressure relief and skin protection for patients confined to prolonged bed rest or sitting (Salgueiro-Oliveira et al., 2023; Barboza et al., 2022).

The integration of sensor technology with biomaterials marks a significant advancement in the development of intelligent medical devices for pressure ulcer (PU) prevention and treatment. These devices continuously monitor pressure distribution, movement, and skin health to assess and mitigate the risks of PU formation. Sensors track pressure levels, posture changes, and activity, while also collecting data on skin health indicators such as temperature, humidity, and pressure. This comprehensive monitoring enables dynamic adjustments in material hardness and shape based on real-time feedback, ensuring optimal pressure relief and support. By tracking patient movement, these devices can quickly detect periods of prolonged immobility and prompt necessary positional adjustments. Skin health monitoring provides immediate feedback on critical factors like temperature and humidity, enabling early interventions to prevent tissue damage. Additionally, continuous data recording and analysis support the creation of personalized PU prevention plans tailored to individual patient needs. This innovative approach allows for more precise and proactive care, significantly reducing the risk of pressure ulcers and enhancing patient quality of life. As sensor and biomaterial technologies continue to advance, these intelligent medical devices have the potential to transform healthcare by improving outcomes for patients at risk of PUs. Such innovations represent a crucial step toward more effective, personalized, and technology-driven medical care.

4 Advanced biomaterials as wound dressings for pressure ulcer prevention and care

The preceding section provided a general classification of advanced biomaterials for pressure ulcer prevention, highlighting

categories such as hydrogels, nanomaterials, ECMs, and smart biomaterials. Building on this framework, this section will explore specific biomaterials, focusing on their applications in wound dressings. Key examples include alginate and chitosan, which demonstrate significant potential in PU prevention and care. This transition from a broad overview to specific case studies aims to illustrate the practical implementation of these biomaterials in enhancing wound management strategies.

4.1 Alginate

Alginate wound dressings have proven to be highly effective and widely used in the clinical management of pressure ulcers (Hill et al., 2022; Dong et al., 2024; Ausili et al., 2013). As a biodegradable material, alginate offers excellent biocompatibility, minimizing secondary damage and pain for patients with chronic wounds (Hurtado et al., 2022; Sahoo and Biswal, 2021). Its superior absorptive capacity efficiently manages wound exudate, creating a dry and clean environment that reduces infection risk and supports healing (Zhang and Zhao, 2020; Barros et al., 2021). These qualities make alginate dressings particularly well-suited for pressure ulcer treatment. In addition to their absorptive properties, alginate dressings exhibit antimicrobial and anti-inflammatory effects, combating infection, reducing inflammation, and promoting faster wound healing (Varaprasad et al., 2020; Huang et al., 2022). Their conformable nature allows them to be tailored to the wound's specific shape and size, ensuring optimal coverage and protection while preventing bacterial ingress (Op't Veld et al., 2020). The ease of application and removal simplifies dressing changes, reducing discomfort for patients and lightening the workload for healthcare providers. Clinically, alginate wound dressings not only alleviate pressure on vulnerable areas but also promote healing, making them an indispensable tool for both the prevention and treatment of pressure ulcers. Their combination of effectiveness, patient comfort, and convenience has made them a preferred choice among healthcare providers and patients alike.

Several commercially available products utilize alginate for effective pressure ulcer management. Purilon® (Coloplast) is a gel containing sodium carboxymethyl cellulose and calcium alginate, specifically designed for necrotic and sloughy wounds. It promotes debridement and hydration, creating an optimal wound environment for healing (Wang et al., 2023; Dong et al., 2020). Askina Calgitrol Ag (B Braun Hospicare Ltd.) is an advanced alginate silver dressing with a bi-layer design. It combines an exudate-absorbing polyurethane foam layer with a contact layer made of an alginate matrix embedded with silver ions. In a moist environment, the silver ions are gradually released, leveraging their antimicrobial properties. This dressing also benefits from the high absorptive capacity of calcium alginate and polyurethane foam, making it suitable for treating pressure ulcers ranging from grade I to IV, with demonstrated clinical efficacy (Ricci et al., 2008; Addison et al., 2005). Another example, Urgosorb™, combines calcium alginate fibers with hydrocolloid technology to address sloughy and granulating wounds with moderate to high exudate levels. This unique composition helps effectively manage exudate while supporting wound healing (Stevens and Chaloner, 2005).

The clinical effectiveness of alginate dressings in pressure ulcer management has been well-documented. Belmin et al. (2002) conducted a study comparing a sequential strategy using calcium alginate followed by hydrocolloid dressings to hydrocolloid dressings alone in treating grade III or IV pressure ulcers. In this study, 110 elderly patients were randomized to either the sequential approach (calcium alginate dressing [UrgoSorb] for 4 weeks followed by a hydrocolloid dressing [Algoplaque] for another 4 weeks) or the control group (hydrocolloid dressing [Duoderm E] for the full 8 weeks). Pressure ulcer surface area was measured weekly, with primary endpoints including the mean absolute surface area reduction (SAR) over 8 weeks and the proportion of patients achieving at least a 40% reduction (SAR40). Patients in the sequential group showed significantly better outcomes, with 68.4% versus 22.6% ($p < 0.0001$) achieving SAR40 at 4 weeks, and 75.4% versus 58.5% ($p < 0.0001$) by 8 weeks, compared to the control group. These results suggest that the sequential use of calcium alginate and hydrocolloid dressings promotes faster healing in grade III or IV pressure ulcers compared to hydrocolloid monotherapy. A similar study on spina bifida patients evaluated the sequential use of calcium alginate and foam dressings. Significant improvements in wound healing were observed, with the mean ulcer surface area reducing from 12.5 ± 7.5 cm^2 at baseline to 3.7 ± 5.2 cm^2 at 12 weeks ($p < 0.001$). Additionally, 75% of patients achieved a 50% reduction in surface area by the end of the study (Ausili et al., 2013). Together, these findings highlight the potential of sequential strategies incorporating calcium alginate dressings to enhance pressure ulcer treatment outcomes across different patient groups.

However, a review by Dumville et al. (2015) concluded that current evidence does not definitively support the superiority of alginate dressings over other dressings, topical treatments, or interventions for healing pressure ulcers. Importantly, the trials included in this review were often small, short-term, and susceptible to bias, resulting in low or very low quality evidence. Therefore, larger, more robust studies with longer follow-up periods are needed to definitively establish the efficacy of alginate dressings in pressure ulcer management.

4.2 Collagen

Collagen-based wound dressings have shown great potential and are widely used in managing pressure ulcers (Graumlich et al., 2003). These dressings offer a comprehensive approach to wound care by combining biocompatibility, healing promotion, antimicrobial activity, and flexibility.

Collagen's natural biocompatibility (Liao et al., 2023a) makes these dressings suitable for a wide range of patients, especially those who are bedridden and require long-term care. As a biological material that closely resembles human tissue components (Nimni and Harkness, 2018), collagen supports cell growth and regeneration, which are essential for effective wound healing. Collagen dressings promote healing at all stages (Sharma et al., 2022), from blood clotting and cell migration to tissue regeneration. By maintaining a moist wound environment, they encourage skin cell growth, accelerate healing, and reduce recovery time. This also helps minimize the risk of complications. The antimicrobial properties of collagen dressings (Liao et al., 2023b; Neacsu et al.,

TABLE 1 Commercially available collagen dressings for the treatment of pressure ulcers.

Brand	Company	Composition
Catrix®	Lescarden Inc	Fine white powder (bovine cartilage)
Collieva™	CollMed Laboratories	Bovine collagen (Type I)
DermaCol™	DermaRite Industries, LLC	Type I bovine collagen powder/sheet
Fibracol®	Systagenix	90% collagen and 10% alginate
Promogran™	Systagenix	55% collagen (bovine), 45% oxidized regenerated cellulose (ORC)
Promogran Prisma®	Systagenix	44% oxidized regenerated cellulose, 55% collagen and 1% silver-ORC
Primatrix®	Integra life sciences	Fetal bovine dermis
Biostep™ Ag	Smith and Nephew, Inc	A silver collagen matrix dressing with calcium alginate and ethylenediaminetetraacetic acid

2021) play a key role in keeping the wound bed clean and reducing the risk of infection. This is particularly important for patients who are immunocompromised or at high risk of infection. Finally, collagen dressings are highly conformable (Zhao et al., 2020), meaning they can easily adapt to the size and shape of the wound. This ensures optimal coverage and protection, further reducing the risk of infection and promoting efficient healing. Their customized fit also helps prevent the development of new pressure ulcers and minimizes surface infections that could delay recovery.

Collagen dressings are widely available for treating pressure ulcers, as shown in Table 1. Clinical studies suggest that these dressings accelerate wound healing, reduce infection risks, and improve the quality of life for patients with pressure ulcers.

In a randomized controlled trial, Graumlich et al. compared collagen injections (Type I collagen, Medifil, Kollagen, BioCore, Topeka, KS) with hydrocolloid therapy (DuoDerm, ConvaTec, Princeton, NJ) in 65 patients with stage II or III pressure ulcers (Graumlich et al., 2003). Thirty-five patients received daily collagen injections, while 30 received hydrocolloid dressings twice weekly. The primary outcome was the rate of complete healing within 8 weeks, while secondary outcomes included time to healing and the daily healed ulcer area. Results showed similar healing rates in both groups after 8 weeks, with mean healing times of 5 weeks for collagen and 6 weeks for hydrocolloids. Both groups also had comparable daily healed areas (6 mm^2/day). The study concluded that collagen and hydrocolloid therapies are equally effective for treating pressure ulcers.

Another randomized, controlled pilot study conducted at RWTH University Hospital in Aachen compared collagen and foam dressings for stagnating pressure ulcers (Piatkowski et al., 2012). Ten patients were enrolled, with five receiving a foam dressing (Suprasorb P; Lohmann and Rauscher) (Group A) and five receiving a collagen dressing (Suprasorb C; Lohmann and Rauscher) covered by the same foam dressing (Group B). The study found that wound fluid from Group B (collagen + foam) significantly improved angiogenesis ($p < 0.05$) compared to Group A (foam only). Group B also showed faster and greater increases in TIMP-1 and TIMP-2 levels, along with a quicker and more pronounced decline in MMP-2, MMP-9 ($p < 0.04$), and elastase levels. These findings indicate a more rapid reduction in inflammation. While both groups experienced healing, Group B demonstrated faster progress, highlighting the therapeutic benefits of collagen dressings for pressure ulcers.

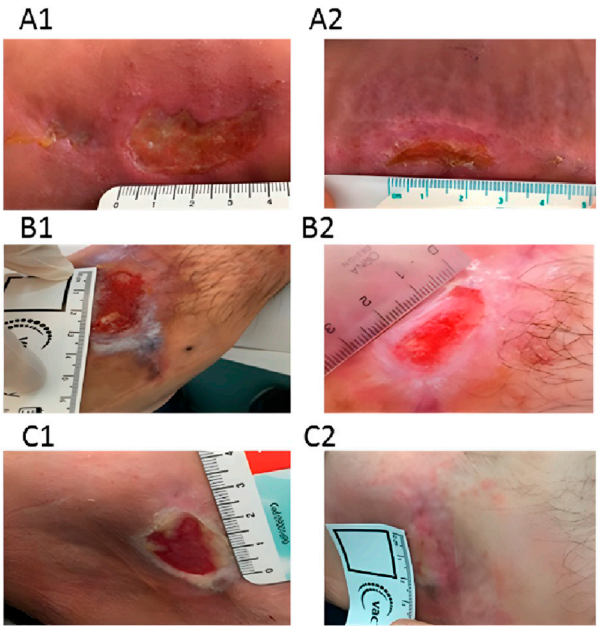

FIGURE 4
The images illustrate the condition of pressure ulcers prior to treatment **(A1, B1, C1)** and following a 30-day course of chitosan gel therapy **(A2, B2, C2)**. Reproduced with permission from Campani et al. (2018). Copyright © 2018 The Authors.

4.3 Chitosan

Chitosan is highly biodegradable, leaving no residue in the body and minimizing the risk of secondary damage or patient discomfort (Wang et al., 2020). Its natural origin ensures excellent biocompatibility with human tissues, making it suitable for a wide range of patients (Tang et al., 2023). Chitosan wound dressings also have strong antimicrobial properties. They inhibit the growth of pathogens, reduce the risk of infection, and accelerate

the healing process (Matica et al., 2019; Moeini et al., 2020). This antimicrobial effect is especially valuable for pressure ulcer patients, as it helps prevent secondary infections and improves overall outcomes. In addition, chitosan dressings maintain a moist environment that supports tissue regeneration (Liu et al., 2018). By stimulating cell growth and repair around the wound, they speed up healing, shorten recovery time, improve outcomes, and reduce complications.

The clinical benefits of chitosan dressings for pressure ulcers are well-documented (Campani et al., 2018). In a pilot study, Campani et al. used chitosan gel to treat pressure ulcers and reported significant reductions in lesion size. Healing was observed in 90% of participants (Campani et al., 2018) (Figure 4). The study also emphasized the cost-effectiveness of the gel, which was prepared at minimal expense in the hospital pharmacy's sterile area, significantly lowering patient care costs.

A multicenter, prospective, randomized, open-label clinical study at three Chinese medical centers compared the safety and efficacy of Next-Generation KA01 chitosan wound dressings with standard gauze (T.V. Gauze) for non-healing chronic wounds, including pressure ulcers, vascular ulcers, diabetic foot ulcers, and minimally infected or at-risk wounds (Mo et al., 2015). Ninety patients participated (45 per group). After 4 weeks, the chitosan group showed significantly greater wound size reduction (65.97% ± 4.48%) compared to the control group (39.95% ± 4.48%). Pain levels were also significantly lower in the chitosan group (1.12 ± 0.23) versus the control group (2.30 ± 0.23). These results suggest that next-generation chitosan dressings enhance wound healing by promoting re-epithelialization and reducing pain.

Another study assessed the efficacy of chitosan-based hydrocolloid dressings in 80 patients with chronic refractory wounds, including pressure ulcers (Liu and Shen, 2022). Patients were randomized into two groups: one treated with chitosan-based hydrocolloid dressings (40 patients) and the other with inert saline gauze (40 patients). After 3 weeks, the chitosan group showed significantly better wound healing, reduced pain levels, and fewer symptoms of itching compared to the control group ($P < 0.05$). Wound area reductions and overall healing efficiency were also significantly higher in the chitosan group. Additionally, dressing changes were less frequent, and total treatment costs were lower in the chitosan group ($P < 0.05$), further supporting its potential as an effective and economical option for pressure ulcer care. These findings are consistent with a separate randomized controlled trial conducted in Iran, which also confirmed the efficacy of chitosan dressings in treating pressure ulcers (Kordestani et al., 2008).

4.4 Poly (lactic-co-glycolic acid)

Poly (lactic-co-glycolic acid) (PLGA) is a biodegradable polymer that serves as a safe and effective dressing for pressure ulcers, thanks to its excellent biocompatibility, controlled release properties, and biodegradability (Chereddy et al., 2016). The composition and molecular weight of PLGA can be tailored to regulate drug release, ensuring consistent and effective therapy for pressure ulcer patients and improving treatment outcomes (Jiang et al., 2021; Choipang et al., 2018; Liu et al., 2020). By incorporating antimicrobial agents and growth factors, PLGA dressings can effectively prevent infections and promote wound healing, offering innovative solutions for pressure ulcer management (Choipang et al., 2018; Liu et al., 2020; Catanzano et al., 2021; Park et al., 2017). Its biodegradability allows PLGA to break down gradually into lactic acid and glycine, which are naturally metabolized by the body. This prevents secondary injuries, reduces adverse effects, and enhances patient comfort and safety. Moreover, PLGA dressings provide excellent mechanical properties and adaptability. They can be customized to fit various wound sizes and shapes, offering superior protection, reducing infection risk, and promoting faster healing.

4.5 Polyurethane

Polyurethane wound dressings have shown significant advantages and progress in pressure ulcer care. As a novel material, polyurethane offers excellent biocompatibility, high absorbency, superior elasticity, and adjustable physicochemical properties (Cui et al., 2023), making it an effective solution for treating pressure ulcers. The biocompatibility of polyurethane ensures its safety for a wide range of patients, including those with allergies to other dressing materials, addressing the need for personalized care. Its exceptional absorbency manages wound exudate efficiently, maintaining optimal moisture levels for cell growth and healing (Samatya Yılmaz and Aytac, 2023). By retaining moisture without peeling or drying out, polyurethane dressings protect wounds and reduce discomfort caused by frequent dressing changes, a critical factor in managing pressure ulcers. Polyurethane's elasticity allows the dressings to conform to changing wound shapes, minimizing mechanical irritation and reducing the risk of further ulcer development (Wang et al., 2024; Abdullah et al., 2023; Pongmuksuwan and Harnnarongchai, 2022). This feature benefits both active and bedridden patients by improving comfort and reducing the likelihood of complications. Additionally, the adaptable physicochemical properties of polyurethane can be tailored to specific needs. Modifying its composition and structure enables adjustments in breathability, hydrophilicity, and degradability, addressing various pressure ulcer scenarios (Sikdar et al., 2022). These features position polyurethane as a promising material for future advancements in pressure ulcer treatment.

Clinical trials strongly support the efficacy of polyurethane wound dressings for managing and preventing pressure ulcers. Dutra et al. investigated the performance of transparent polyurethane film (PF) compared to hydrocolloid dressings (HD) in preventing pressure ulcers (Dutra et al., 2015). In a study with 160 patients, the PF group required significantly fewer dressing changes, especially in the sacral region, suggesting superior performance of polyurethane films. Further research highlighted the lower per-change cost of polyurethane films compared to hydrocolloid dressings (Dutra et al., 2016), enhancing their cost-effectiveness. Additionally, transparent polyurethane films have been shown to effectively prevent heel pressure ulcers (Souza et al., 2013). Polyurethane foam dressings are also widely used for treating pressure ulcers. A randomized controlled trial compared a novel polyurethane foam to standard foam in negative pressure wound therapy. The novel

foam was equally effective but easier to remove, with less fragmentation and residue left in wounds (Wagstaff et al., 2014). It also prevented inward margin growth, reducing trauma during dressing changes and minimizing bleeding from granulation tissue. These findings confirm the safety and biocompatibility of the novel polyurethane foam, supported by earlier animal studies (Greenwood et al., 2010; Greenwood and Dearman, 2012). Furthermore, trials have demonstrated the efficacy of polyurethane foam dressings in preventing sacral pressure ulcers in elderly hip fracture patients (Forni et al., 2018; Forni et al., 2022).

In conclusion, polyurethane wound dressings offer significant advantages in pressure ulcer care. Their biocompatibility, absorbency, elasticity, and adjustable physicochemical properties provide effective and comfortable solutions for patients. Clinical validation demonstrates the progress made in pressure ulcer treatment using polyurethane dressings, contributing to improved patient quality of life. Continued advancements in medical technology promise an even greater role for polyurethane wound dressings in pressure ulcer care.

5 Challenges and prospects

Advanced biomaterials hold great promise for preventing and treating pressure ulcers, but several challenges must still be addressed. First, biocompatibility is crucial. Patient responses can vary, sometimes leading to immune or toxic reactions. To ensure safety, thorough biocompatibility testing—both *in vitro* and in vivo—is essential. Using natural biomaterials, modifying surfaces, and adopting other biocompatible strategies can help reduce these risks. Another challenge is optimizing mechanical properties. Biomaterials need to be strong yet flexible enough to provide proper support and protect wounds. Achieving this balance requires fine-tuning material composition, structure, and fiber alignment, or using composite materials designed for these purposes. Controlling degradation rates is also critical. If a material breaks down too quickly, the wound may lose protection. If it degrades too slowly, healing may be delayed. Adjustments to material composition, microstructure, and degradation mechanisms can help ensure materials degrade at the right pace and integrate seamlessly with surrounding tissues. Cost-effective production is another major factor. To make these materials more accessible, manufacturing must be efficient and affordable. Advances in automation, mass production, and novel synthesis methods will be key to lowering costs without compromising quality. Finally, clinical translation and regulatory approval remain significant hurdles. Moving from lab research to real-world applications requires rigorous clinical trials and navigating complex regulatory processes. Success in this area depends on careful trial design, interdisciplinary collaboration, and close cooperation with regulatory agencies. By overcoming these challenges, advanced biomaterials can see wider use in pressure ulcer care. This will lead to more effective treatments and better outcomes for patients. With ongoing innovation and experience, these materials will continue to evolve, playing an even greater role in improving medical care.

Future research in this field will focus on multifunctional composites, smart materials, and personalized treatments to address current challenges and improve effectiveness. Multifunctional composites are designed to combine multiple properties into a single material. These properties include antimicrobial activity, healing promotion, and monitoring capabilities. Such materials can prevent infections, speed up healing, and track progress in real time, offering a comprehensive solution for pressure ulcer care. Smart materials will focus on responsiveness and controlled drug delivery. These materials can change their properties in response to environmental factors or specific stimuli. Controlled release systems will allow precise delivery of drugs or therapeutic substances, paving the way for more targeted and effective treatments. Personalized treatments will adapt care to the unique needs of each patient. By tailoring biomaterial selection and treatment plans to individual characteristics, these strategies will ensure more precise and effective outcomes. By combining these approaches, future research aims to create comprehensive and personalized solutions for pressure ulcer prevention and treatment. Continued innovation and collaboration across disciplines will further enhance the role of advanced biomaterials, improving patient outcomes and quality of life.

6 Conclusion

Advancements in biomaterials for pressure ulcer prevention and treatment bring new hope and opportunities for patients. Ongoing research and innovation hold the potential to transform pressure ulcer care, enabling more effective treatment strategies, better patient outcomes, and an enhanced quality of life. To achieve these breakthroughs, prioritizing the development of novel biomaterials and fostering interdisciplinary collaboration will be essential. This focus will accelerate the clinical translation of these technologies, ultimately improving medical care and treatment experiences for individuals affected by pressure ulcers.

Author contributions

ST: Conceptualization, Data curation, Methodology, Writing–original draft. WB: Conceptualization, Resources, Supervision, Writing–review and editing.

Funding

The author(s) declare that no financial support was received for the research, authorship, and/or publication of this article.

Conflict of interest

The authors declare that the research was conducted in the absence of any commercial or financial relationships that could be construed as a potential conflict of interest.

Generative AI statement

The author(s) declare that no Generative AI was used in the creation of this manuscript.

Publisher's note

References

Abdullah, M., Ramtani, S., and Yagoubi, N. (2023). Mechanical properties of polyurethane foam for potential application in the prevention and treatment of pressure ulcers. *Results Eng.* 19, 101237. doi:10.1016/j.rineng.2023.101237

Addison, D., Rennison, T. J., and Del Bono, M. (2005). The antimicrobial properties of a silver alginate dressing for moderate to heavily exuding, wounds: 688. *J. Wound Ostomy Cont. Nurs.* 32, S28. doi:10.1097/00152192-200505002-00092

Ausili, E., Paolucci, V., Triarico, S., Maestrini, C., Murolo, D., Focarelli, B., et al. (2013). Treatment of pressure sores in spina bifida patients with calcium alginate and foam dressings. *Eur. Rev. Med. Pharmacol. Sci.* 17 (12), 1642–1647.

Barboza, R., Arruda, L. M., Carvalho, M. A., Fangueiro, R., Salgueiro, A., Parreira, P., et al. (2022). Required attributes of a smart clothing for pressure ulcers prevention. *J. Biomimetics, Biomaterials Biomed. Eng.* 57, 27–36. doi:10.4028/p-09elmg

Barros, N. R., Ahadian, S., Tebon, P., Rudge, M. V. C., Barbosa, A. M. P., and Herculano, R. D. (2021). Highly absorptive dressing composed of natural latex loaded with alginate for exudate control and healing of diabetic wounds. *Mater. Sci. Eng. C* 119, 111589. doi:10.1016/j.msec.2020.111589

Belmin, J., Meaume, S., Rabus, M. T., Bohbot, S., and For The Investigators of the Sequential Treatment of the Eld, (2002). Sequential treatment with calcium alginate dressings and hydrocolloid dressings accelerates pressure ulcer healing in older subjects: a multicenter randomized trial of sequential versus nonsequential treatment with hydrocolloid dressings alone. *J. Am. Geriatrics Soc.* 50 (2), 269–274. doi:10.1046/j.1532-5415.2002.50058.x

Blackburn, J., Ousey, K., Taylor, L., Moore, B., Patton, D., Moore, Z., et al. (2020). The relationship between common risk factors and the pathology of pressure ulcer development: a systematic review. *J. wound care* 29 (Suppl. 3), S4–S12. doi:10.12968/jowc.2020.29.sup3.s4

BoykoTatiana, V., LongakerMichael, T., and YangGeorge, P. (2018). Review of the current management of pressure ulcers. *Adv. wound care* 7, 57–67. doi:10.1089/wound.2016.0697

Campani, V., Pagnozzi, E., Mataro, I., Mayol, L., Perna, A., D'Urso, F., et al. (2018). Chitosan gel to treat pressure ulcers: a clinical pilot study. *Pharmaceutics* 10 (1), 15. doi:10.3390/pharmaceutics10010015

Cascone, S., and Lamberti, G. (2020). Hydrogel-based commercial products for biomedical applications: a review. *Int. J. Pharm.* 573, 118803. doi:10.1016/j.ijpharm.2019.118803

Catanzano, O., Quaglia, F., and Boateng, J. S. (2021). Wound dressings as growth factor delivery platforms for chronic wound healing. *Expert Opin. drug Deliv.* 18 (6), 737–759. doi:10.1080/17425247.2021.1867096

Chereddy, K. K., Vandermeulen, G., and Préat, V. (2016). PLGA based drug delivery systems: promising carriers for wound healing activity. *Wound Repair Regen.* 24 (2), 223–236. doi:10.1111/wrr.12404

Choipang, C., Chuysinuan, P., Suwantong, O., Ekabutr, P., and Supaphol, P. (2018). Hydrogel wound dressings loaded with PLGA/ciprofloxacin hydrochloride nanoparticles for use on pressure ulcers. *J. Drug Deliv. Sci. Technol.* 47, 106–114. doi:10.1016/j.jddst.2018.06.025

Chopra, L. (2022). Photocatalytic activity of zinc oxide for dye and drug degradation: a review. *Mater. Today Proc.* 52, 1653–1656. doi:10.1016/j.matpr.2021.11.283

Cui, M., Chai, Z., Lu, Y., Zhu, J., and Chen, J. (2023). Developments of polyurethane in biomedical applications: a review. *Resour. Chem. Mater.* 2, 262–276. doi:10.1016/j.recm.2023.07.004

Das, S., and Baker, A. B. (2016). Biomaterials and nanotherapeutics for enhancing skin wound healing. *Front. Bioeng. Biotechnol.* 4, 82. doi:10.3389/fbioe.2016.00082

Deng, G. L., Lei, Y. L., Tan, H., Geng, B., and Liu, Z. (2024). RETRACTED: effects of predictive nursing interventions on pressure ulcer in elderly bedridden patients. *Int. Wound J.* 21 (3), e14690. doi:10.1111/iwj.14690

Deng, X., Gould, M., and Ali, M. A. (2022). A review of current advancements for wound healing: biomaterial applications and medical devices. *J. Biomed. Mater. Res. Part B Appl. Biomaterials* 110 (11), 2542–2573. doi:10.1002/jbm.b.35086

Diller, R. B., and Tabor, A. J. (2022). The role of the extracellular matrix (ECM) in wound healing: a review. *Biomimetics* 7 (3), 87. doi:10.3390/biomimetics7030087

Dong, D., Cheng, Z., Zhang, J., Gu, Z., Han, Z., Hou, W., et al. (2024). Using polycaprolactone and sodium alginate to prepare self-pumping/super-absorbent/transportable drug dressings for stage 3–4 pressure ulcer treatment. *Int. J. Biol. Macromol.* 278, 134711. doi:10.1016/j.ijbiomac.2024.134711

Dong, Y., Zheng, Y., Zhang, K., Yao, Y., Wang, L., Li, X., et al. (2020). Electrospun nanofibrous materials for wound healing. *Adv. Fiber Mater.* 2, 212–227. doi:10.1007/s42765-020-00034-y

Du, J. (2024). The mechanism and application of some nano-antibacterial agents. *Eng. Technol.* 91, 316–321. doi:10.54097/jzrh3z40

Du, Y. C., and Ciou, W. S. (2019). A sensor gauze with multi-channel moisture and ph monitoring for chronic wound care. *IEEE Access* 7, 29185–29192. doi:10.1109/access.2019.2901061

Dumville, J. C., Keogh, S. J., Liu, Z., Stubbs, N., Walker, R. M., and Fortnam, M. (2015). Alginate dressings for treating pressure ulcers. *Cochrane Database Syst. Rev.* 133 (5), 455. doi:10.1590/1516-3180.20151335t2

Dutra, R. A. A., Salomé, G. M., Alves, J. R., Pereira, V., Miranda, F., Vallim, V., et al. (2015). Using transparent polyurethane film and hydrocolloid dressings to prevent pressure ulcers. *J. wound care* 24 (6), 268–275. doi:10.12968/jowc.2015.24.6.268

Dutra, R. A. A., Salomé, G. M., Leal, L. M. F., Alves, M., Moura, J., Silva, A., et al. (2016). Cost comparison of pressure ulcer preventive dressings: hydrocolloid dressing versus transparent polyurethane film. *J. wound care* 25 (11), 635–640. doi:10.12968/jowc.2016.25.11.635

Forni, C., D'Alessandro, F., Gallerani, P., Genco, R., Bolzon, A., Bombino, C., et al. (2018). Effectiveness of using a new polyurethane foam multi-layer dressing in the sacral area to prevent the onset of pressure ulcer in the elderly with hip fractures: a pragmatic randomised controlled trial. *Int. wound J.* 15 (3), 383–390. doi:10.1111/iwj.12875

Forni, C., Gazineo, D., Allegrini, E., Bolgeo, T., Brugnolli, A., Canzan, F., et al. (2022). Effectiveness of a multi-layer silicone-adhesive polyurethane foam dressing as prevention for sacral pressure ulcers in at-risk in-patients: randomized controlled trial. *Int. J. Nurs. Stud.* 127, 104172. doi:10.1016/j.ijnurstu.2022.104172

Ghosh, P., Vachana, M. N., Pavish, S. R., S R, P., Pereira, P., C J, T., et al. (2024). Advances in technology-driven strategies for preventing and managing bedsores: a comprehensive review. *Archives Gerontology Geriatrics Plus* 1 (3), 100029. doi:10.1016/j.aggp.2024.100029

Gillard, N., Coignard, P., Kerdraon, J., and Allegre, W. (2023) "Early detection of pressure ulcers: considering dynamic phenomena and temperature[C]," in *2023 international conference on computational science and computational intelligence (CSCI)*. IEEE, 1503–1506.

Graumlich, J. F., Blough, L. S., McLaughlin, R. G., Milbrandt, J. C., Calderon, C. L., Agha, S. A., et al. (2003). Healing pressure ulcers with collagen or hydrocolloid: a randomized, controlled trial. *J. Am. Geriatrics Soc.* 51 (2), 147–154. doi:10.1046/j.1532-5415.2003.51051.x

Greenwood, J. E., Li, A., Dearman, B. L., and Moore, T. G. (2012). Comparison of a sealed, polymer foam biodegradable temporizing matrix against Integra® dermal regeneration template in a porcine wound model. *J. burn care and Res.* 33 (1), 163–173. doi:10.1097/bcr.0b013e318233fac1

Greenwood, J. E., Li, A., Dearman, B. L., Moore, T. G., et al. (2010). Evaluation of NovoSorb novel biodegradable polymer for the generation of a dermal matrix part 2: *in-vivo* studies. *Wound Pract. and Res. J. Aust. Wound Manag. Assoc.* 18 (1). doi:10.3316/informit.984479703765490

Haidari, H., Kopecki, Z., Sutton, A. T., Garg, S., Cowin, A. J., and Vasilev, K. (2021). pH-responsive "smart" hydrogel for controlled delivery of silver nanoparticles to infected wounds. *Antibiotics* 10 (1), 49. doi:10.3390/antibiotics10010049

Hajhosseini, B., Longaker, M. T., and Gurtner, G. C. (2020). Pressure injury. *Ann. Surg.* 271 (4), 671–679. doi:10.1097/sla.0000000000003567

Hepburn, C. D., Anand, S. C., and Wood, C. (2017). Recent advances in three-dimensional pressure relieving cushions for the prevention of pressure ulcers. *J. Text. Inst.* 108 (11), 1940–1948. doi:10.1080/00405000.2017.1301019

Hill, J. E., Edney, S., Hamer, O., Williams, A., and Harris, C. (2022). Interventions for the treatment and prevention of pressure ulcers. *Br. J. community Nurs.* 27 (Suppl. 6), S28–S36. doi:10.12968/bjcn.2022.27.sup6.s28

Hu, Y.-Z., Wang, L., Cao, Z.-D., and Wang, Y. (2020). The incidence of pressure ulcer in the elderly in China between 2009 and 2019: a meta-analysis. *Med. Data Min.* 3 (3), 110–118. doi:10.53388/mdm2020093002

Huang, C., Dong, L., Zhao, B., Lu, Y., Huang, S., Yuan, Z., et al. (2022). Anti-inflammatory hydrogel dressings and skin wound healing. *Clin. Transl. Med.* 12 (11), e1094. doi:10.1002/ctm2.1094

Hurtado, A., Aljabali, A. A. A., Mishra, V., Tambuwala, M. M., and Serrano-Aroca, Á. (2022). Alginate: enhancement strategies for advanced applications. *Int. J. Mol. Sci.* 23 (9), 4486. doi:10.3390/ijms23094486

Jiang, W., Zhang, J., Zhang, X., Fan, C., and Huang, J. (2021). VAP-PLGA microspheres (VAP-PLGA) promote adipose-derived stem cells (ADSCs)-induced wound healing in chronic skin ulcers in mice via PI3K/Akt/HIF-1α pathway. *Bioengineered* 12 (2), 10264–10284. doi:10.1080/21655979.2021.1990193

Kaewjamnong, S., and Hongwitayakorn, A. (2021). Evaluation of a commodity force sensor for building a low-cost bedsore prevention mat. Science. *Eng. Health Stud.* 15, 21020003.

Karamanos, N. K., Theocharis, A. D., Piperigkou, Z., Manou, D., Passi, A., Skandalis, S. S., et al. (2021). A guide to the composition and functions of the extracellular matrix. *FEBS J.* 288 (24), 6850–6912. doi:10.1111/febs.15776

Khutoryanskiy, V., and Georgiou, T. (2018). *Temperature-responsive polymers*. Wiley.

Kordestani, S., Shahrezaee, M., Tahmasebi, M. N., Hajimahmodi, H., Ghasemali, D. H., and Abyaneh, M. (2008). A randomised controlled trial on the effectiveness of an advanced wound dressing used in Iran. *J. wound care* 17 (7), 323–327. doi:10.12968/jowc.2008.17.7.30525

Kotsuchibashi, Y. (2020). Recent advances in multi-temperature-responsive polymeric materials. *Polym. J.* 52 (7), 681–689. doi:10.1038/s41428-020-0330-0

Kumagai, A., Ohno, N., Miyati, T., Okuwa, M., Nakatani, T., Sanada, H., et al. (2019). Investigation of effects of urethane foam mattress hardness on skin and soft tissue deformation in the prone position using magnetic resonance imaging. *J. tissue viability* 28 (1), 14–20. doi:10.1016/j.jtv.2018.10.007

Kumar, B., Noor, N., Thakur, S., Pan, N., Narayana, H., Yan, S. c., et al. (2019). Shape memory polyurethane-based smart polymer substrates for physiologically responsive, dynamic pressure (re) distribution. *ACS omega* 4 (13), 15348–15358. doi:10.1021/acsomega.9b01167

Li, Y., Fu, R., Guan, Y., Zhang, Z., Yang, F., Xiao, C., et al. (2022). Piezoelectric hydrogel for prophylaxis and early treatment of pressure injuries/pressure ulcers. *ACS Biomaterials Sci. and Eng.* 8 (7), 3078–3086. doi:10.1021/acsbiomaterials.2c00448

Li, Y., Jiang, S., Song, L., Yao, Z., Zhang, J., Wang, K., et al. (2021). Zwitterionic hydrogel activates autophagy to promote extracellular matrix remodeling for improved pressure ulcer healing. *Front. Bioeng. Biotechnol.* 9, 740863. doi:10.3389/fbioe.2021.740863

Liao, W., Yang, D., Xu, Z., Zhao, L., Mu, C., Li, D., et al. (2023a). Antibacterial collagen-based nanocomposite dressings for promoting infected wound healing. *Adv. Healthc. Mater.* 12 (15), 2203054. doi:10.1002/adhm.202203054

Liao, W., Yang, D., Xu, Z., Zhao, L., Mu, C., Li, D., et al. (2023b). Antibacterial collagen-based nanocomposite dressings for promoting infected wound healing. *Adv. Healthc. Mater.* 12 (15), 2203054. doi:10.1002/adhm.202203054

Liu, H., Wang, C., Li, C., Qin, Y., Wang, Z., Yang, F., et al. (2018). A functional chitosan-based hydrogel as a wound dressing and drug delivery system in the treatment of wound healing. *RSC Adv.* 8 (14), 7533–7549. doi:10.1039/c7ra13510f

Liu, J., and Shen, H. (2022). Clinical efficacy of chitosan-based hydrocolloid dressing in the treatment of chronic refractory wounds. *Int. Wound J.* 19 (8), 2012–2018. doi:10.1111/iwj.13801

Liu, P., Yang, X., Han, J., Zhao, M., Guo, J., Si, R., et al. (2020). Tazarotene-loaded PLGA nanoparticles potentiate deep tissue pressure injury healing via VEGF-Notch signaling. *Mater. Sci. Eng. C* 114, 111027. doi:10.1016/j.msec.2020.111027

Malone, M., and Schultz, G. (2022). Challenges in the diagnosis and management of wound infection. *Br. J. Dermatology* 187 (2), 159–166. doi:10.1111/bjd.21612

Matica, M. A., Aachmann, F. L., Tøndervik, A., Sletta, H., and Ostafe, V. (2019). Chitosan as a wound dressing starting material: antimicrobial properties and mode of action. *Int. J. Mol. Sci.* 20 (23), 5889. doi:10.3390/ijms20235889

Memari, A., Golpaygani, A. T., Hassani, K., and Hoseinzadeh, M. S. (2021). Design and construction of a smart mattress for monitoring bedsore ulcer prevention in sedentary patients. *J. Clin. Eng.* 46 (1), 22–29. doi:10.1097/jce.0000000000000444

Mervis, J. S., and Phillips, T. J. (2019). Pressure ulcers: pathophysiology, epidemiology, risk factors, and presentation. *J. Am. Acad. Dermatology* 81 (4), 881–890. doi:10.1016/j.jaad.2018.12.069

Mo, X., Cen, J., Gibson, E., Wang, R., and Percival, S. L. (2015). An open multicenter comparative randomized clinical study on chitosan. *Wound Repair Regen.* 23 (4), 518–524. doi:10.1111/wrr.12298

Moeini, A., Pedram, P., Makvandi, P., Malinconico, M., and Gomez d'Ayala, G. (2020). Wound healing and antimicrobial effect of active secondary metabolites in chitosan-based wound dressings: a review. *Carbohydr. Polym.* 233, 115839. doi:10.1016/j.carbpol.2020.115839

Mu, Y., Cheng, J., Shi, W., Yang, W., Qiao, F., Wang, S., et al. (2024). Crosstalk-free hybrid integrated multimodal sensor for human temperature, humidity, and pressure monitoring. *Cell Rep. Phys. Sci.* 5, 102223. doi:10.1016/j.xcrp.2024.102223

Neacsu, I. A., Leau, S. A., Marin, S., Holban, A. M., Vasile, B. S., Nicoara, A. I., et al. (2021). Collagen-carboxymethylcellulose biocomposite wound-dressings with antimicrobial activity. *Materials* 14 (5), 1153. doi:10.3390/ma14051153

Nguyen, H. M., Le, T. T. N., Nguyen, A. T., Thien Le, H. N., and Pham, T. T. (2023). Biomedical materials for wound dressing: recent advances and applications. *RSC Adv.* 13 (8), 5509–5528. doi:10.1039/d2ra07673j

Nimni, M. E., and Harkness, R. D. (2018). *Molecular structure and functions of collagen//Collagen*. New York: CRC Press, 1–78.

Ofridam, F., Tarhini, M., Lebaz, N., Gagnière, É., Mangin, D., and Elaissari, A. (2021). pH-sensitive polymers: classification and some fine potential applications. *Polym. Adv. Technol.* 32 (4), 1455–1484. doi:10.1002/pat.5230

Op't Veld, R. C., Walboomers, X. F., Jansen, J. A., and Wagener, F. A. (2020). Design considerations for hydrogel wound dressings: strategic and molecular advances. *Tissue Eng. Part B Rev.* 26 (3), 230–248. doi:10.1089/ten.teb.2019.0281

Pan, Y., Yang, D., Zhou, M., Liu, Y., Pan, J., Wu, Y., et al. (2023). Advance in topical biomaterials and mechanisms for the intervention of pressure injury. *Iscience* 26 (6), 106956. doi:10.1016/j.isci.2023.106956

Park, J. W., Hwang, S. R., and Yoon, I. S. (2017). Advanced growth factor delivery systems in wound management and skin regeneration. *Molecules* 22 (8), 1259. doi:10.3390/molecules22081259

Piatkowski, A., Ulrich, D., Seidel, D., Abel, M., Pallua, N., and Andriessen, A. (2012). Randomised, controlled pilot to compare collagen and foam in stagnating pressure ulcers. *J. wound care* 21 (10), 505–511. doi:10.12968/jowc.2012.21.10.505

Pollini, M., Striani, R., Paladini, F., Kiani, A., Acocella, M. R., and Esposito Corcione, C. (2024). Nanotechnological antibacterial and conductive wound dressings for pressure ulcer prevention. *Nanomaterials* 14 (15), 1309. doi:10.3390/nano14151309

Pongmuksuwan, P., and Harnnarongchai, W. (2022). Synthesis and characterization of soft polyurethane for pressure ulcer prevention. *Polym. Test.* 112, 107634. doi:10.1016/j.polymertesting.2022.107634

Qian, L., Yan, S., Ting, S. T., Han, Z. M., and Qi, T. (2024). Complications and psychological impact of pressure ulcers on patients and caregivers. *Int. Wound J.* 21 (4), e14836. doi:10.1111/iwj.14836

Ricci, E., Pittarello, M., Cassino, R., Moffa, M., Ferrero, S., Gonella, M., et al. (2008). AskinaCalgitrol Ag®: clinical use of an advanced ionic silver dressing. *Acta Vulnologica* 5, 105–111.

Rybka, M., Mazurek, Ł., and Konop, M. (2022). Beneficial effect of wound dressings containing silver and silver nanoparticles in wound healing—from experimental studies to clinical practice. *Life* 13 (1), 69. doi:10.3390/life13010069

Sahoo, D. R., and Biswal, T. (2021). Alginate and its application to tissue engineering. *SN Appl. Sci.* 3 (1), 30. doi:10.1007/s42452-020-04096-w

Salgueiro-Oliveira, A., Rêgo, A. S., Santos-Costa, P., Bernardes, R. A., Filipe, L., Sousa, L. B., et al. (2023). Design of innovative clothing for pressure injury prevention: end-user evaluation in a mixed-methods study. *Int. J. Environ. Res. Public Health* 20 (18), 6773. doi:10.3390/ijerph20186773

Samatya Yılmaz, S., and Aytac, A. (2023). The highly absorbent polyurethane/polylactic acid blend electrospun tissue scaffold for dermal wound dressing. *Polym. Bull.* 80 (12), 12787–12813. doi:10.1007/s00289-022-04633-0

Sharma, S., Rai, V. K., Narang, R. K., and Markandeywar, T. S. (2022). Collagen-based formulations for wound healing: a literature review. *Life Sci.* 290, 120096. doi:10.1016/j.lfs.2021.120096

Sheikholeslam, M., Wright, M. E. E., Jeschke, M. G., and Amini-Nik, S. (2018). Biomaterials for skin substitutes. *Adv. Healthc. Mater.* 7 (5), 1700897. doi:10.1002/adhm.201700897

Sikdar, P., Dip, T. M., Dhar, A. K., Bhattacharjee, M., Hoque, M. S., and Ali, S. B. (2022). Polyurethane (PU) based multifunctional materials: emerging paradigm for functional textiles, smart, and biomedical applications. *J. Appl. Polym. Sci.* 139 (38), e52832. doi:10.1002/app.52832

Silva, A., Metrôlho, J., Ribeiro, F., Fidalgo, F., Santos, O., and Dionisio, R. (2021). A review of intelligent sensor-based systems for pressure ulcer prevention. *Computers* 11 (1), 6. doi:10.3390/computers11010006

Souza, T. S., Danski, M. T. R., Johann, D. A., De Lazzari, L. S. M., and Mingorance, P. (2013). Prevenção de úlceras por pressão no calcanhar com filme transparente de poliuretano. *Acta Paul. Enferm.* 26, 345–352. doi:10.1590/s0103-21002013000400008

Sprigle, S., McNair, D., and Sonenblum, S. (2020). Pressure ulcer risk factors in persons with mobility-related disabilities. *Adv. Skin and Wound Care* 33 (3), 146–154. doi:10.1097/01.asw.0000653152.36482.7d

Stevens, J., and Chaloner, D. (2005). Urgosorb (TM) dressing: management of acute and chronic wounds. *Br. J. Nurs.* 14 (Suppl. 3), S22–S28. doi:10.12968/bjon.2005.14.sup3.18607

Tang, J., Zhang, P., Liu, Y., Hou, D., Chen, Y., Cheng, L., et al. (2024). Revolutionizing pressure ulcer regeneration: unleashing the potential of extracellular matrix-derived temperature-sensitive injectable antioxidant hydrogel for superior stem cell therapy. *Biomaterials* 314, 122880. doi:10.1016/j.biomaterials.2024.122880

Tang, W., Wang, J., Hou, H., Li, Y., Fu, J., et al. (2023). Review: application of chitosan and its derivatives in medical materials. *Int. J. Biol. Macromol.* 240, 124398. doi:10.1016/j.ijbiomac.2023.124398

Varaprasad, K., Jayaramudu, T., Kanikireddy, V., Toro, C., and Sadiku, E. R. (2020). Alginate-based composite materials for wound dressing application: a mini review. *Carbohydr. Polym.* 236, 116025. doi:10.1016/j.carbpol.2020.116025

Wagstaff, M. J. D., Driver, S., Coghlan, P., and Greenwood, J. E. (2014). A randomized, controlled trial of negative pressure wound therapy of pressure ulcers via a novel polyurethane foam. *Wound Repair Regen.* 22 (2), 205–211. doi:10.1111/wrr.12146

Wang, H., Li, T., Li, J., Zhao, R., Ding, A., and Xu, F. J. (2024). Structural engineering of polyurethanes for biomedical applications. *Prog. Polym. Sci.* 151, 101803. doi:10.1016/j.progpolymsci.2024.101803

Wang, S., Wu, W. Y., Yeo, J. C. C., Soo, X. Y. D., Thitsartarn, W., Liu, S., et al. (2023). Responsive hydrogel dressings for intelligent wound management. *BMEMat* 1 (2), e12021. doi:10.1002/bmm2.12021

Wang, W., Xue, C., and Mao, X. (2020). Chitosan: structural modification, biological activity and application. *Int. J. Biol. Macromol.* 164, 4532–4546. doi:10.1016/j.ijbiomac.2020.09.042

Wei, M., Yang, D., Chen, L., Wu, L., Jiang, Q., Niu, N., et al. (2021). The prevalence and prevention of pressure ulcers: a multicenter study of nine nursing homes in eastern China. *J. Tissue Viability* 30 (1), 133–136. doi:10.1016/j.jtv.2020.07.005

Yang, F., Chen, H., Shan, Y., Che, L., Tang, Q., and Hu, F. (2024). Preventing postoperative moderate-and high-risk pressure injuries with artificial intelligence-powered smart decompression mattress on in middle-aged and elderly patients: a retrospective cohort analysis. *Br. J. Hosp. Med.* 85 (8), 1–13. doi:10.12968/hmed.2024.0112

Yang, L., Wang, H., Yuan, W., Li, Y., Gao, P., Tiwari, N., et al. (2021). Wearable pressure sensors based on MXene/tissue papers for wireless human health monitoring. *ACS Appl. Mater. and Interfaces* 13 (50), 60531–60543. doi:10.1021/acsami.1c22001

Zhang, M., and Zhao, X. (2020). Alginate hydrogel dressings for advanced wound management. *Int. J. Biol. Macromol.* 162, 1414–1428. doi:10.1016/j.ijbiomac.2020.07.311

Zhao, X., Liang, Y., Huang, Y., He, J., Han, Y., and Guo, B. (2020). Physical double-network hydrogel adhesives with rapid shape adaptability, fast self-healing, antioxidant and NIR/pH stimulus-responsiveness for multidrug-resistant bacterial infection and removable wound dressing. *Adv. Funct. Mater.* 30 (17), 1910748. doi:10.1002/adfm.201910748

frontiers | Frontiers in Bioengineering and Biotechnology

TYPE Review
PUBLISHED 07 March 2025
DOI 10.3389/fbioe.2025.1547343

OPEN ACCESS

EDITED BY
Xianzhi Zhang,
Yale University, United States

REVIEWED BY
Mahboubeh Nabavinia,
The Research Institute at Nationwide Children's Hospital, United States
Raj Hazra,
North Dakota State University, United States

*CORRESPONDENCE
Liang Zhang,
rtjpxzl@symc.edu.cn

RECEIVED 18 December 2024
ACCEPTED 30 January 2025
PUBLISHED 07 March 2025

CITATION
Guan W and Zhang L (2025) Applications and prospects of biomaterials in diabetes management.
Front. Bioeng. Biotechnol. 13:1547343.
doi: 10.3389/fbioe.2025.1547343

Applications and prospects of biomaterials in diabetes management

Wenhe Guan[1] and Liang Zhang[2]*

[1]Department of Pediatrics, Shengjing Hospital of China Medical University, Shenyang, Liaoning, China, [2]Department of Human Anatomy, School of Basic Medicine, Shenyang Medical College, Shenyang, Liaoning, China

Diabetes is a widespread metabolic disorder that presents considerable challenges in its management. Recent advancements in biomaterial research have shed light on innovative approaches for the treatment of diabetes. This review examines the role of biomaterials in diabetes diagnosis and treatment, as well as their application in managing diabetic wounds. By evaluating recent research developments alongside future obstacles, the review highlights the promising potential of biomaterials in diabetes care, underscoring their importance in enhancing patient outcomes and refining treatment methodologies.

KEYWORDS

biomaterials, diabetes, insulin delivery, tissue engineering, biosensors

1 Introduction

Diabetes mellitus is a chronic disease marked by prolonged hyperglycemia, which arises from defects in insulin secretion, insulin action, or a combination of both (American Diabetes Association, 2014; Chaudhury et al., 2017; Defronzo, 2009). The primary types of diabetes include Type 1 diabetes mellitus (T1DM) and Type 2 diabetes mellitus (T2DM). T1DM is mainly an autoimmune condition leading to the destruction of insulin-producing beta cells in the pancreas (Khaiz et al., 2025; Nyaga et al., 2018a; Nyaga et al., 2018b). In contrast, T2DM is often linked to insulin resistance, influenced by lifestyle factors and genetic predispositions (Dariya et al., 2019; Ghasemi and Norouzirad, 2019; Memon et al., 2022). The incidence of diabetes worldwide has been on a steady rise, resulting in significant public health implications, particularly as demographic trends lean towards aging populations and lifestyle changes, including increased obesity rates (Cano-Ibanez and Bueno-Cavanillas, 2024). The International Diabetes Federation reported that approximately 537 million adults were diagnosed with diabetes in 2021, with projections indicating a rise to 783 million individuals by 2045 (Klangjareonchai et al., 2021).

Conventional diabetes management approaches include pharmacological treatments such as insulin and oral hypoglycemic agents, as well as lifestyle changes encompassing diet and exercise (Deng et al., 2018). Nonetheless, achieving optimal glycemic control remains a challenge for numerous patients, often due to factors like medication adherence, the complexity of treatment protocols, and the psychosocial burdens associated with the disease (Al-Qerem et al., 2022; Summers-Gibson, 2021). These challenges highlight the urgent need for innovative strategies in diabetes management (Kalra et al., 2022).

In recent times, the application of biomaterials has surfaced as a promising pathway for the enhancement of diabetes treatment and management (Aldahish et al., 2024; Emad et al.,

2024; Nemati et al., 2023). This review seeks to investigate the diverse applications of biomaterials within the realm of diabetes management, addressing their potential to mitigate the limitations of existing treatment methodologies while improving the quality of life for individuals with diabetes. The evolving role of biomaterials in diabetes management marks a significant advancement in addressing the complexities inherent to this chronic condition (Iqbal et al., 2023).

2 Diagnosis of diabetes using biomaterial-mediated strategies

Biosensors have become essential instruments across various domains, particularly in healthcare. Within this sector, they provide rapid and precise monitoring of biological parameters (Kim et al., 2019; Li et al., 2023; Yoon et al., 2020). These sensors possess the capability to detect specific biological markers molecules, delivering crucial real-time information essential for the diagnosis, management, and prevention of diseases (Kong et al., 2024; Xing et al., 2024).

Conventional diagnostic approaches for diabetes, which largely rely on fasting plasma glucose (FPG), oral glucose tolerance tests (OGTT), and hemoglobin A1c (HbA1c) assessments, exhibit several shortcomings. These techniques are susceptible to various influences, such as stress, illness, and inconsistencies in laboratory procedures, which may result in misdiagnosis or delays in diagnosis (Young et al., 2023). For instance, HbA1c levels may not provide an accurate representation of glycemic control in specific populations, including those with hemoglobinopathies or individuals who have recently received blood transfusions (Bhatti et al., 2024). Traditional glucose testing methods, primarily based on blood glucose meters, encounter numerous challenges that hinder patient adherence and effective diabetes management. Ahmadian et al. conducted a comprehensive review of current technologies, comparing the benefits and drawbacks of both invasive and non-invasive glucose monitoring techniques (Ahmadian et al., 2023). Many of these methods necessitate finger-pricking, which can be painful and inconvenient, resulting in many patients opting to forgo regular testing (Burge, 2001). Furthermore, the precision of blood glucose meters can be influenced by several factors, including user error, calibration discrepancies, and environmental conditions, leading to variable readings (Tankasala and Linnes, 2019). Additionally, conventional testing methods typically offer only a snapshot of glucose levels at a single moment, failing to account for fluctuations that occur throughout the day. The psychological strain associated with diabetes management, including the stress from frequent monitoring and apprehension regarding complications, highlights the demand for reliable and minimally invasive glucose testing methods (Xie et al., 2023).

The significance of glucose monitoring sensors in diabetes management cannot be overstated. Recent advancements in biosensor technology have facilitated the development of non-invasive and continuous glucose monitoring systems that enhance patient adherence and improve health outcomes (Dua et al., 2024; Hina and Saadeh, 2020; Teymourian et al., 2020). The integration of biosensors with mobile technology and data analytics platforms has further increased their utility, allowing for continuous monitoring and remote health management (Arun et al., 2024; Bent et al., 2020).

2.1 Detection by sensors composed of nanomaterials in conjunction with Raman spectroscopy

Biomedical nanomaterials, particularly those engineered for glucose sensing, have demonstrated promising advancements in improving the sensitivity and specificity of diabetes diagnostics. For example, electrospun nanofibers have emerged as a novel category of functional nanocomposites exhibiting remarkable biosensing capabilities (Du et al., 2022). The incorporation of nanomaterials, such as gold nanoparticles and carbon nanotubes, has further enhanced the efficacy of biosensors, enabled the simultaneous detection of multiple analytes and accelerated response times (Nisar et al., 2024; Otero and Magner, 2020; Putzbach and Ronkainen, 2013). Moreover, when combined with organometallic compounds, these nanomaterials can significantly augment the performance of Raman spectroscopy, allowing for the detection of subtle spectral variations related to diabetes biomarkers. This synergistic approach not only improves detection sensitivity but also extends the range of potential applications in clinical diagnostics (Jagannathan et al., 2023).

The high surface area of these nanomaterials promotes increased loading of recognition elements, leading to enhanced detection capabilities. Enhanced performance of biosensors has been documented (Mousavi et al., 2022). Furthermore, nanomaterials can be tailored to respond to specific stimuli, facilitating the creation of intelligent biosensors capable of real-time monitoring of physiological variations (Scandurra et al., 2023). Recent innovations utilizing DNA nanostructures have demonstrated significant potential in biosensing applications, where they can be engineered for the selective binding of target molecules, thus improving detection specificity (Mohammad, 2024). Ongoing investigations in this field continue to reveal novel opportunities for the application of nanomaterials in biosensing, which may lead to the development of groundbreaking diagnostic tools for clinical use.

Raman spectroscopy operates on the principle of inelastic scattering of monochromatic light, typically emitted by a laser. When light interacts with the vibrations of molecules, it can scatter with a shift in energy that corresponds to the vibrational modes of those molecules. This characteristic renders Raman spectroscopy a versatile instrument for both qualitative and quantitative analyses across various applications, including the identification of biomarkers for diseases such as diabetes (Xie et al., 2023). A prominent example of this technique's efficacy is its application in measuring urinary albumin levels, a critical biomarker for diabetic kidney disease. Research has illustrated that Raman spectroscopy can effectively identify specific spectral peaks linked to albumin concentrations in urine samples from individuals diagnosed with type 2 diabetes, indicating its potential for non-invasive monitoring of renal complications related to diabetes (Flores-Guerrero et al., 2020). Moreover, Raman spectroscopy has been employed to investigate retinal

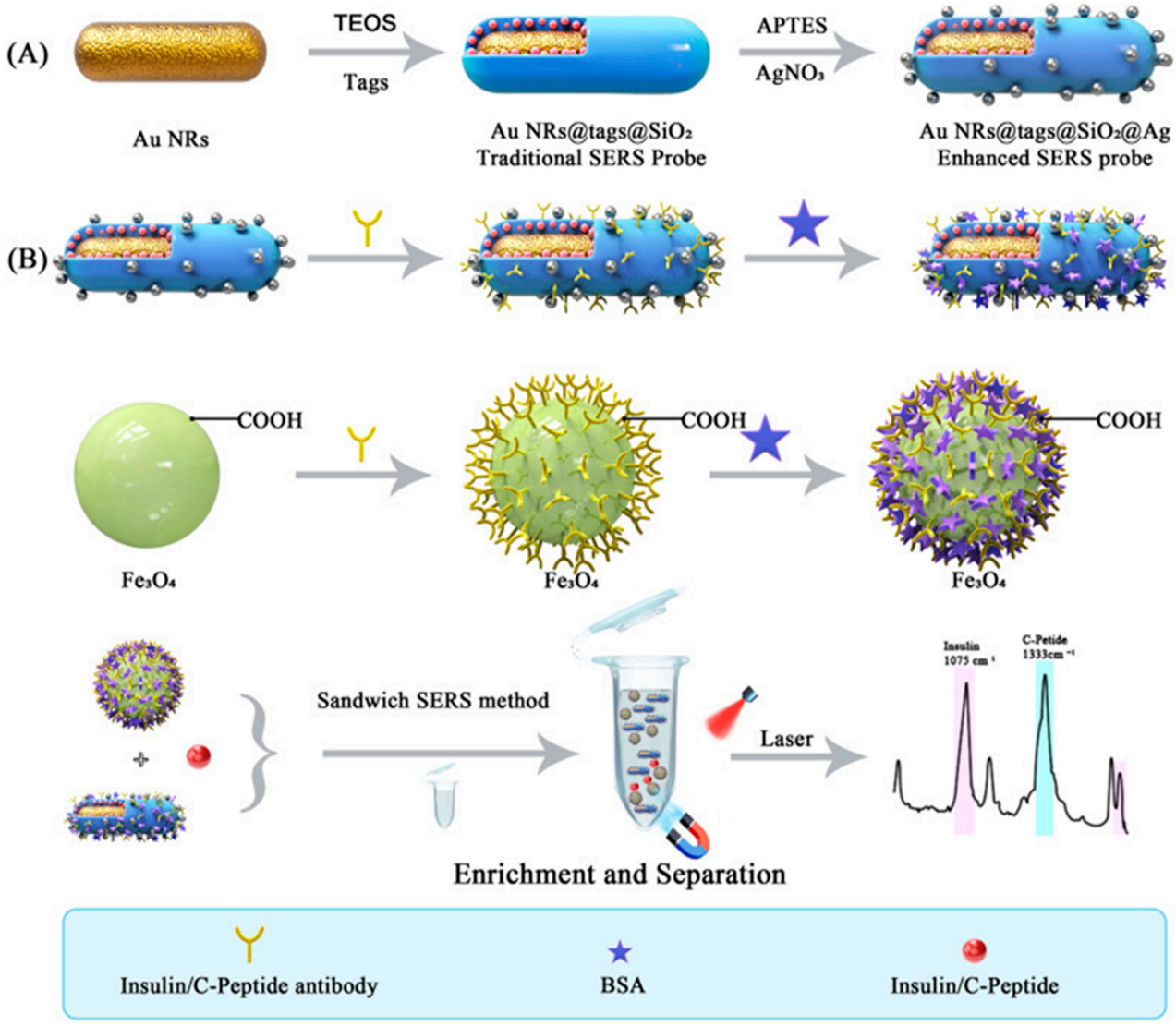

FIGURE 1
Depicts the schematic representation of **(A)** the synthesis of the SERS probe and **(B)** the SERS-based immunoassay utilized for the detection of insulin antibodies and C-peptide antibodies. Reproduced with permission from Zhang et al. (2024b).

tissue for early indicators of diabetic retinopathy, offering insights into the biochemical alterations occurring in the retina due to prolonged hyperglycemia. The capacity of this technique to distinguish between healthy and diseased tissues through spectral analysis renders it an invaluable tool for early diagnosis and timely intervention in diabetic patients (Chen et al., 2021). Furthermore, advancements in machine learning algorithms applied to Raman spectral data have bolstered the precision of diabetes detection, highlighting the technology's potential to transform diabetes management and enhance patient outcomes (Chen et al., 2024e).

The amalgamation of biomedical nanomaterials with Raman spectroscopy presents numerous advantages while also posing significant challenges (Oliveira et al., 2022). A primary advantage of this integration lies in the enhancement of diagnostic accuracy and sensitivity. For instance, a core-shell structure of Au nanorods@ Raman tags@SiO2@Ag nanocomposite has been synthesized and employed for the surface-enhanced Raman scattering (SERS) detection of insulin and C-peptide in trace serum (Zhang et al., 2024b). This is illustrated in Figure 1.

2.2 Detection via gas sensors composed of biomedical metal oxides

Exhalation detection technology has attracted notable interest due to its non-invasive and convenient nature, particularly in the regulation of glucose levels, which is essential for managing conditions such as diabetes. In breath analysis, glucose is often detected indirectly through its metabolic byproducts, including acetone, which is produced during the metabolism of fatty acids when glucose levels are diminished (Galassetti et al., 2005; Hwang et al., 2021; Li et al., 2015). The well-established relationship between breath acetone and blood

TABLE 1 Overview of gas sensors utilizing biomedical metal-oxides for acetone detection in 2024.

Composition of biomaterials	Advantage	Application	References
α-Fe_2O_3-multiwalled carbon nanotube (MWCNT) nanocomposite	detect acetone in exhaled breath under high humidity	diabetes detection	Ansari et al. (2024)
a K/Sn-Co_3O_4 porous microsphere	without the removing water vapor from exhaled breath	diabetes detection	Na et al. (2024)
porous 2D WO_3 nanosheets	1. The rapid diffusion and adsorption of acetone molecules 2. Higher charge activity and adsorption capacity	diabetes detection	Guan et al. (2025)
biofluorometric acetone gas sensor (bio-sniffer) using secondary alcohol dehydrogenase	Sub-ppbv Level Sensitivity (quantitative characteristics in the concentration range of 0.5–1,000 ppbv)	continuous measurement of acetone gas released through the skin	Iitani et al. (2024)
16 wt% N-CQDs/WO_3 sensor	1. Real-time acetone detection 2. Portable human-exhaled gas sensors	diabetes detection	Ni et al. (2024)
Al/CuO:Ni nanostructured thin films	enhances the sensitivity and selectivity of acetone sensors for practical applications as breath detectors in biomedical diagnostics	1. Diabetes detection 2. Ensuring industrial safety by preventing adverse health and environmental impacts of acetone exposure	Litra et al. (2024)
bimetallic PtAu-decorated SnO_2 nanospheres (PtAu/SnO_2)	1. Superior sensitivity to acetone of 0.166–100 ppm at 300°C 2. Remarkable gas response, rapid response and recovery times, strong linear correlation, excellent repeatability, long-term stability, and satisfactory selectivity at 300°C	the early diagnosis and screening of diabetes	Zhu et al. (2024)
ZIF-67-derived oxide cage/nanofiber Co_3O_4/In_2O_3 heterostructure	1. Abundant reversible active adsorption/reaction sites alongside a type-I heterojunction 2.ultrasensitive response to acetone concentrations ranging from 954 to 50 ppm at 300°C 3. A low detection limit of 18.8 ppb, a swift response time of just 4 s, commendable selectivity and repeatability, acceptable resistance to humidity interference, and sustained long-term stability	environmental monitoring and the early diagnosis of diabetes	Wu et al. (2024)
bimetallic Au@Pt core-shell nanospheres (BNSs) functionalized-electrospun $ZnFe_2O_4$ nanofibers (ZFO NFs)	Compared to pure NFs-650 analogue, the ZFO NFs/BNSs-2 sensor exhibits a stronger mean response (3.32 vs. 1.84), quicker response/recovery speeds (33 s/28 s vs. 54 s/42 s), and lower operating temperature (188°C vs. 273°C) toward 0.5 ppm acetone	potential for diabetes diagnosis in individual healthcare settings	Zhao et al. (2024a)
$Gd_2Zr_2O_7$ solid electrolyte and $CoSb_2O_6$ sensing electrode	1. A low detection limit of 10 ppb, enabling linear detection for acetone in an extremely wide range of 10 ppb–100 ppm 2. Excellent selectivity, repeatability, and stability	diagnosis and monitoring of diabetic ketosis	Jiang et al. (2024)
Porous Co(3)O(4) nanofoam	1. A low detection limit of 0.05 ppm and a high sensitivity of −56 mV/decade in the acetone concentration range of 1–20 ppm 2. Outstanding repeatability, acceptable selectivity, effective resistance to O2 and humidity, and long-term stability during continuous measurements over a duration exceeding 30 days	distinguish between healthy individuals and patients with diabetic ketosis	Hao et al. (2024b)

glucose levels provides a foundation for the development of sensors capable of measuring glucose levels via breath analysis (Kalidoss and Umapathy, 2019; Righettoni et al., 2013; Tanda et al., 2014). The accurate and prompt identification of acetone is vital for maintaining safety in industrial production and for the clinical assessment of diabetes. Consequently, the advancement of high-performance acetone sensors has become increasingly significant (Guan et al., 2025) (Table 1). Analyzing breath can facilitate real-time observation of metabolic alterations, enabling timely interventions to avert conditions such as hyperglycemia or hypoglycemia (Xie et al., 2023). Moreover, breath testing is characterized by its convenience and discretion, which enhances patient adherence and promotes ongoing monitoring during daily activities (Vajhadin et al., 2021).

However, environmental factors substantially influence the detection of glucose and its metabolites in exhaled breath, impacting both the collection and analytical processes. Elements such as humidity and the presence of competing volatile compounds

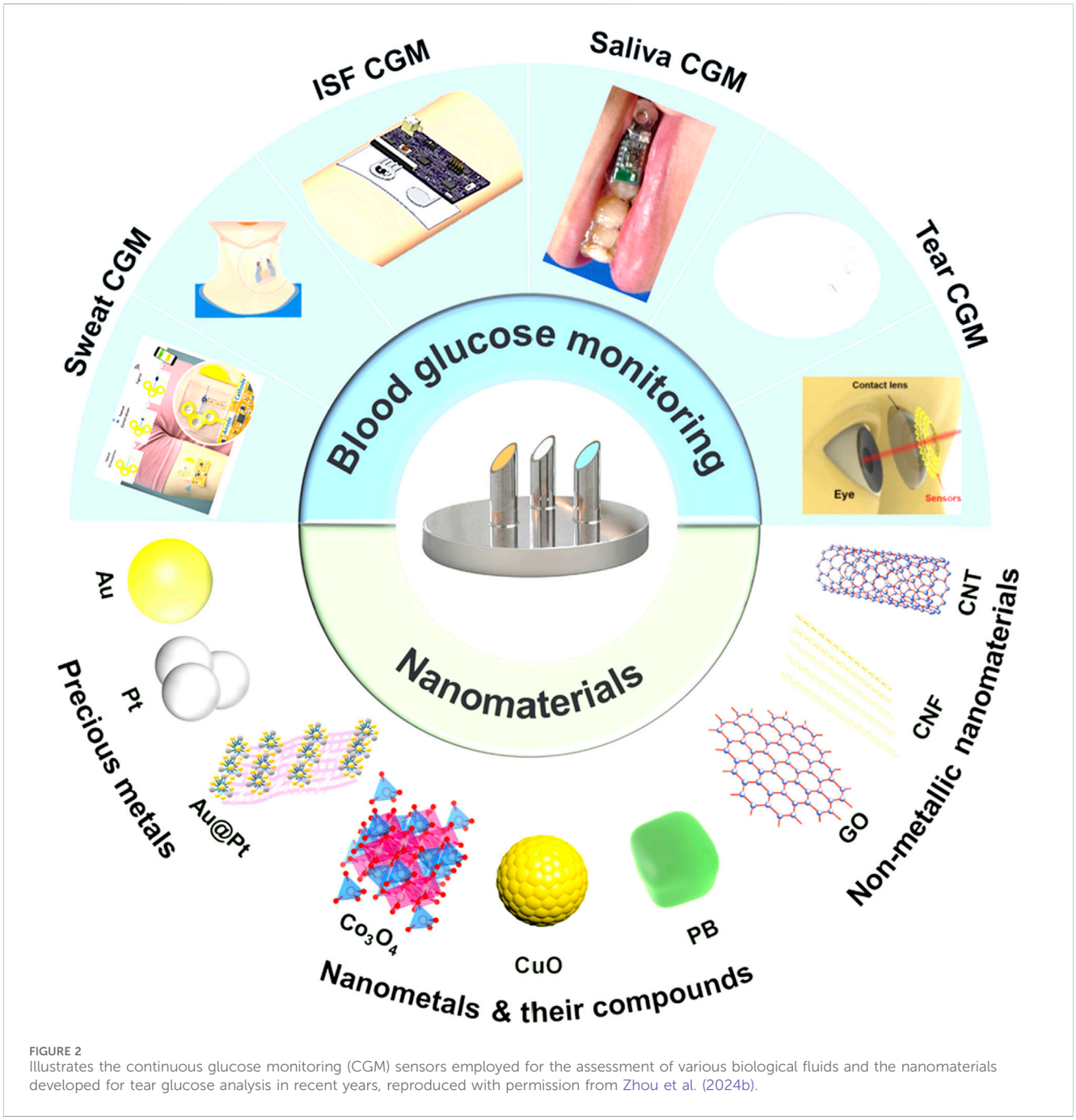

FIGURE 2
Illustrates the continuous glucose monitoring (CGM) sensors employed for the assessment of various biological fluids and the nanomaterials developed for tear glucose analysis in recent years, reproduced with permission from Zhou et al. (2024b).

can hinder gas sensor performance (Esteves et al., 2022; Xie et al., 2018). Therefore, it is essential to optimize the operating conditions of sensors to mitigate these environmental effects. Zhou et al. developed a self-designed condensation device for exhaled breath, which allowed for the condensation and collection of human exhaled breath, enabling the analysis of glucose in the collected condensate via ion chromatography using a pulsed amperometric instrument (Zhou et al., 2022). For instance, custom-built exhaled breath collection devices that regulate temperature and humidity have demonstrated potential for enhancing the reproducibility of glucose measurements in breath samples (Desai et al., 2025). A noninvasive blood glucose detection apparatus that utilizes acetone sensing in exhaled breath employs an α-Fe2O3-multiwalled carbon nanotube (MWCNT) nanocomposite to accurately measure acetone levels, even in high humidity conditions (Ansari et al., 2024). Furthermore, the incorporation of nanostructured materials and composite sensors has been shown to improve sensitivity and selectivity, enabling more precise glucose detection in the presence of interfering substances found in exhaled breath (K et al., 2025). Notably, an ultrasensitive acetone gas sensor based on a K/Sn-Co3O4 porous microsphere can accurately differentiate between diabetic patients and healthy individuals based on variations in acetone concentrations without the need to eliminate water vapor from exhaled breath, highlighting its substantial potential for diabetes diagnosis (Na et al., 2024).

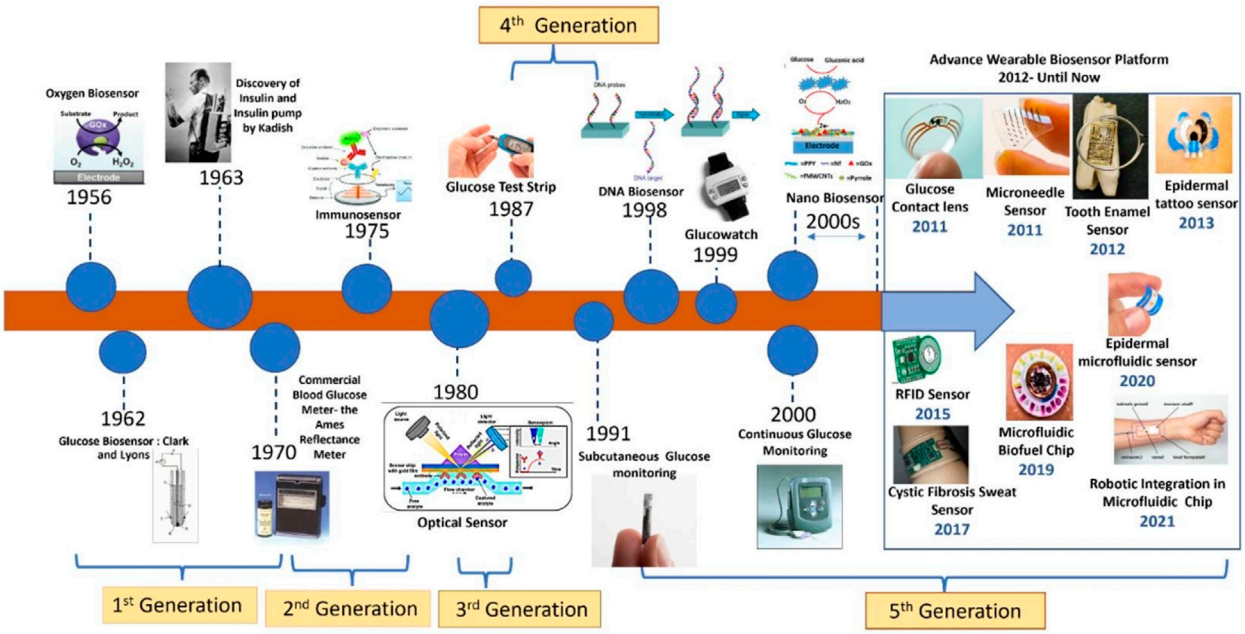

FIGURE 3
Depicts the historical progression of biosensor development for wearable technology up to 2021, reproduced with permission from Zafar et al. (2022).

2.3 Detected by wearable sensors made of biomaterials

Wearable sensors made from biomaterials designed for sweat glucose detection have garnered significant interest due to their capacity for continuous monitoring without the discomfort of finger-prick tests. Zhou et al. conducted a thorough review of the principles and advancements in electrochemical glucose sensors, compiling findings on various innovative nanomaterials suitable for continuous glucose monitoring (CGM) (Zhou et al., 2024b). The work illustrated the applications and construction strategies of diverse nanomaterials, including precious metals, nanometals, their compounds, and nonmetallic nanomaterials. Figure 2 in their study encapsulates these insights on CGM technology, while Figure 3 traces the evolution of biosensor development for wearables up to 2021.

These sensors utilize cutting-edge materials and designs to enhance sensitivity and selectivity, thereby enabling precise real-time glucose detection (Dervisevic et al., 2022; Zafar et al., 2022; Zhou et al., 2023). The hyaluronate (HA)-modified Au@Pt bimetallic electrodes have been validated through animal trials for their capacity to provide long-term, accurate, and robust CGMs in smart contact lenses, paving the way for continuous blood glucose monitoring (Han et al., 2023). In 2023, Zhang et al. summarized the metallic nanomaterials employed in wearable non-invasive glucose sensors, encompassing zero-dimensional (0D), one-dimensional (1D), and two-dimensional (2D) monometallic nanomaterials, as well as bimetallic configurations (Zhang et al., 2023b). In addition, Govindaraj et al. provided a thorough summary of various categories of non-enzymatic glucose sensor materials, which encompass composites, non-precious transition metals along with their respective metal oxides and hydroxides, precious metals and their alloys, carbon-based materials, conducting polymers, metal-organic framework (MOF)-based electrocatalysts, as well as glucose sensors designed for wearable devices (Govindaraj et al., 2023). Furthermore, enzyme-free nanoparticle-based glucose sensors signify a noteworthy advancement, presenting a more straightforward and cost-efficient alternative for glucose monitoring (Boucheta et al., 2024). Additionally, microfluidic devices have been engineered to assess the performance of these sensors, thereby ensuring their reliability in clinical environments (Yunos et al., 2021). Zhang et al. introduced a handheld biosensor capable of detecting acetone through fluorescence, utilizing the enzymatic reaction of secondary alcohol dehydrogenase (S-ADH) in conjunction with β-nicotinamide adenine dinucleotide (NADH, λex = 340 nm, λem = 490 nm). This device, characterized by its portability and high sensitivity and selectivity, is anticipated to see extensive application in clinical diagnostics as well as in the realm of wearable biochemical sensors in the forthcoming years (Zhang G. et al., 2025). As advancements in these technologies continue, they hold the potential to revolutionize diabetes management, enabling patients to achieve optimal glucose levels with enhanced convenience.

3 Treatment of diabetes through biomaterial-mediated strategies

Insulin plays a pivotal role in the management of diabetes, necessitating effective delivery mechanisms. The utilization of biomaterials, known for their exceptional biocompatibility,

TABLE 2 The advantages of various insulin drug delivery vectors.

Vector		Preparation method	Advantage	Treatment object	Treatment stage	References
Microneedle		3D printing and mold-based methods	penetrates the outer layer of the skin without reaching the nerve endings, facilitating sustained insulin release	T1DM, T2DM, and in some cases, used when traditional injection methods cause excessive pain or skin damage in diabetic patients	Initial treatment stage to establish stable insulin delivery, or when patients have difficulties with traditional injection methods	Jin et al. (2018), Xu et al. (2024), Zhao et al. (2024b) Razzaghi et al. (2024) Chen et al. (2019), Lin et al. (2025a), Lin et al. (2025b), Wang et al. (2020)
ASMNs@PVP-INS		antimicrobial sponge MNs (ASMNs@PVP-INS) modified with polyvinylpyrrolidone (PVP)	excellent mechanical strength, effectively maintaining glucose control without inducing hypoglycemia, no significant toxicity to mice	T1DM, T2DM	Not mentioned	Zhang et al. (2025b)
insulin transmitter		ultrasound, microjet method	encapsulation rate >80%, good stability, strong deformation and good transdermal performance	T1DM, T2DM, especially suitable for patients who are reluctant to use injection methods and have relatively good skin conditions	Any stage of diabetes treatment where non-invasive insulin delivery is preferred	Jarosinski et al. (2021)
biodegradable polymer material	Chitosan and its derivatives	emulsification-chemical crosslinking method, spray drying, solvent volatilization method, etc	good biocompatibility, degradability, film-forming or spheroidal properties	T1DM, T2DM, and can be used in diabetic wound healing scenarios	Drug delivery stage in diabetes treatment, and applied in wound care for diabetic patients	Abozaid et al. (2023), Lupascu et al. (2024), Mohamed et al. (2021), Morcol et al. (2004) Ali and Lehmussaari (2006) Baek et al. (2012) Blagden et al. (2007) Aldahish et al. (2024), Ali et al. (2009)
	silk fibroin			T1DM, T2DM, may have potential in long-term insulin storage and delivery due to its unique properties	Potentially used in the stage of developing long - acting insulin formulations	
	polylactose			T1DM, T2DM, might be suitable for patients with specific metabolic requirements	May be involved in the formulation of certain sustained - release insulin products	
	Hydroxyapatite			T1DM, T2DM, can be used in combination with insulin for bone - related diabetes complications	Treatment stage for diabetic patients with bone - related problems	
INS-NPs		ionotropic pre-gelation followed by polyelectrolyte complexation technique	Strengthen drug stability and improve bioavailability; achieve targeted drug release to reduce the toxic and side effects of drugs on the body; control the amount of drug release to make the effect of drugs in the body more obvious	T1DM, T2DM, especially useful when precise control of insulin release is needed	Advanced treatment stage where more refined insulin delivery is required	Kassem et al. (2017)
Chitosan/cyclodextrin nanoparticles		Ionic gel technology	Stable for at least 4 h at simulated intestinal fluid pH 6.8 and 37° C	T1DM, T2DM, beneficial for oral insulin delivery attempts	Exploratory stage of developing oral insulin delivery systems	Krauland and Alonso (2007)
Methocel-lipid hybrid nanocarriers		Methocel was added to solid lipid nanoparticles (SLN) to form	Good biocompatibility, low cytotoxicity, good drug protection, and good interaction with cells, while overcoming its key limitations in effectively encapsulating peptides	T1DM, T2DM, applicable when enhancing the interaction between insulin and cells is necessary	Treatment stage focused on improving the efficacy of insulin at the cellular level	Boushra et al. (2016)

(Continued on following page)

TABLE 2 (*Continued*) The advantages of various insulin drug delivery vectors.

Vector	Preparation method	Advantage	Treatment object	Treatment stage	References
6-O-vinyl sebacic acid-D-galactopyranosyl ester block 3-acrylamide phenylboric acid p (OVNG-b-AAPBA)	block copolymer	With optimal molecular weight and thermal stability, the prepared nanoparticles can be used in drug delivery systems. The prepared nanoparticles have good morphology and their safety has been verified by MTT and chronic animal toxicology tests. The drug loading rate and encapsulation efficiency increase with the increase of AAPBA content in the polymer, which can effectively maintain blood sugar in diabetic mice for 96 h	T1DM, T2DM, effective in maintaining stable blood sugar levels over an extended period	Treatment stage aiming for long - term blood sugar control	Zhong et al. (2020)
chitosan nanoparticle/poly (vinyl alcohol) (PVA) hybrid HGs (CPHGs)	PVA and chitosan nanoparticles (CNPs) are cross-linked with a glucose-responsive formylphenylboronic acid (FPBA)-based cross-linker *in situ*	in vitro drug release assay reveals size-dependent glucose-responsive drug release from the CPHGs under physiological conditions	T1DM	T1DM rat model and in vitro	Ali et al. (2023)

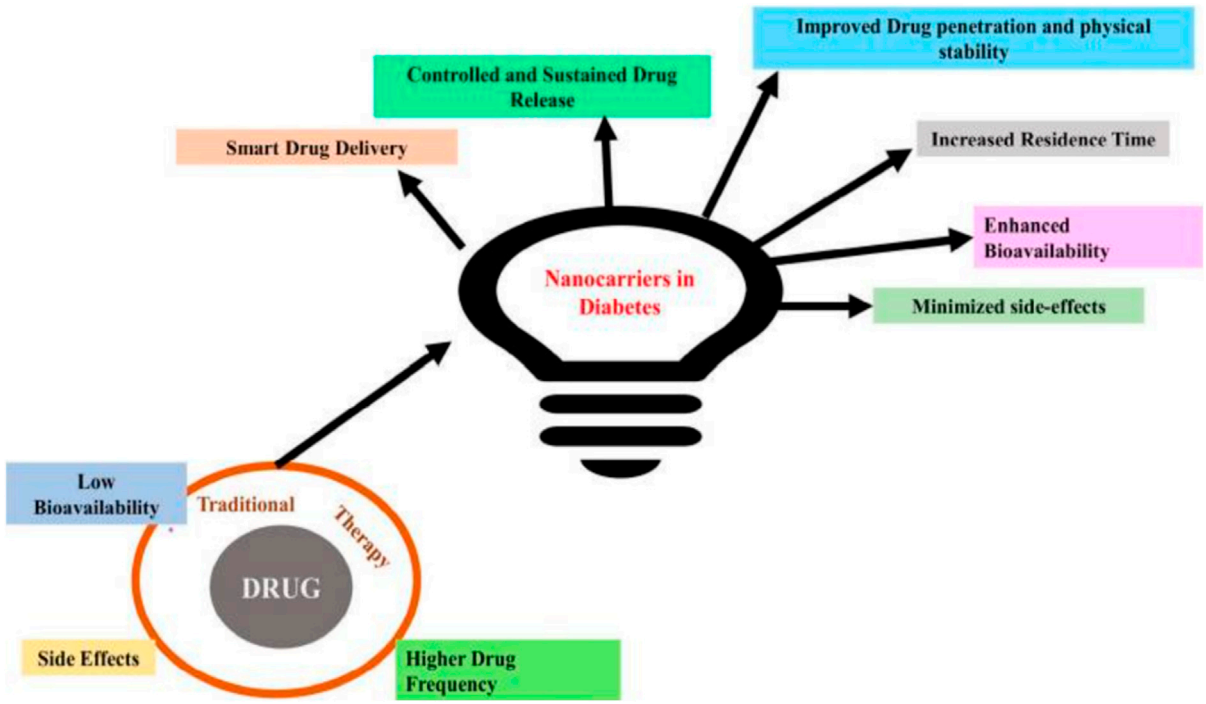

FIGURE 4
Demonstrates the various advantages of employing nanotechnology in diabetes management compared to traditional treatment methodologies. Reproduced with permission from Sarkhel et al. (2024).

degradability, and distinctive functional properties, is essential in this context. Such materials significantly enhance insulin stability, modulate its release kinetics, and facilitate targeted delivery, thereby offering a safer and more efficient therapeutic option for individuals with diabetes. Novel biomaterial carriers can transport antidiabetic drugs to address different types of diabetes (Table 2).

3.1 Delivery via nanoparticles

Insulin is indispensable for managing T1DM and is often required in numerous instances of T2DM. The engineered characteristics of nanoparticles, such as toxicity control, stability, and drug release mechanisms, allow for the delivery of higher drug concentrations to targeted sites (Zaric et al., 2019). The capacity of nanoparticle systems to improve insulin delivery through targeted and controlled release mechanisms has attracted significant attention (Cheng et al., 2021; Karimi et al., 2016; Zhang et al., 2022). Nanocarriers present an innovative strategy by offering advantages such as enhanced drug stability and absorption, targeted delivery to specific tissues or cells, controlled or stimuli-responsive drug release, increased bioavailability, minimized side effects, and improved patient compliance (Figure 4). Sarkhel et al. have encapsulated the diverse applications of nanomaterials in diabetes management, emphasizing the distinctive attributes of nano-based drug delivery systems and intelligent drug delivery techniques (Sarkhel et al., 2024). These nanoparticles can be customized to react to physiological conditions, such as fluctuating glucose levels, thereby permitting a more personalized approach to insulin administration (Karimi et al., 2016; Sharmah et al., 2024). MSN-based nanocomposites have been used to deliver therapeutic molecules like insulin, GLP-1, exenatide, DPP-4 inhibitor and plasmid-containing GLP-1 genes for managing diabetes mellitus for the last decade (Sarkar et al., 2023). For instance, innovative systems have emerged that leverage glucose-responsive nanoparticles to release insulin during hyperglycemic episodes, thereby effectively imitating the pancreas's physiological insulin secretion mechanism (Jeong et al., 2022; Volpatti et al., 2021).

Moreover, the inclusion of biocompatible materials in the formulation of nanoparticles ensures safety and efficacy in clinical applications (Tutty et al., 2022). Research has illustrated that nanoparticles can successfully encapsulate insulin, providing protection against degradation within the gastrointestinal tract during oral administration (Ren et al., 2023). This pioneering strategy not only enhances the stability of insulin but also promotes its absorption, yielding improved glycemic control in diabetic individuals. The integration of nanoparticles into insulin delivery systems indicates substantial potential for the development of more effective and patient-friendly diabetes treatments.

3.2 Delivery via transplantation of tissue-engineered islets

Tissue engineering has emerged as a groundbreaking technique in diabetes management, particularly in addressing the complications associated with the disease (Kaviani and Azarpira, 2016; Woo et al., 2023). This interdisciplinary domain merges biological, mechanical, and engineering principles to restore or enhance the functionality of damaged tissues and organs. Considering the increasing prevalence of diabetes and its complications, innovative strategies such as tissue engineering provide promising avenues for regeneration and repair, particularly in pancreatic and cellular contexts. Advancements within this field possess the potential to significantly enhance patient outcomes and offer alternatives to traditional therapies like insulin administration and organ transplantation.

3.2.1 Pancreatic tissue engineering

The domain of pancreatic tissue engineering is primarily focused on the creation of functional pancreatic tissues or bioartificial organs designed to restore insulin secretion in diabetic patients (Figure 5). Recent investigations have underscored the encouraging role of decellularized pancreatic scaffolds, which maintain the extracellular matrix (ECM) architecture and critical biochemical signals necessary for cell attachment and functionality. The application of decellularized pig pancreas has shown promise in establishing an optimal environment for insulin-producing cells, thereby addressing the impairment of beta-cell function in T1DM (Hao L. et al., 2024; Lim et al., 2023). Research indicates that these bioengineered tissues can effectively replicate the intrinsic architecture of the pancreas, which may enhance both the survival rates and functionality of transplanted islet cells (Lim et al., 2023). Furthermore, advancements in 3D bioprinting technology have enabled the fabrication of complex pancreatic structures, thereby improved vascularization and facilitating the delivery of essential nutrients required for maintaining cell viability (Soetedjo et al., 2021). Additionally, the incorporation of bioactive materials, such as silver nanoparticles, has demonstrated improved biocompatibility of these scaffolds, further supporting their clinical application (Qiu et al., 2022). In summary, pancreatic tissue engineering holds significant promise in the advancement of regenerative therapies for diabetes.

Cell transplantation, particularly the transplantation of islet cells, remains a fundamental aspect of T1DM management, with the primary objective of reinstating endogenous insulin production (Loretelli et al., 2020; Ramesh et al., 2013). However, barriers such as a limited supply of donors and the risk of immune rejection have hindered broader implementation. Recent advancements in tissue engineering have introduced innovative strategies aimed at enhancing the success rates of cell transplantation. For example, the application of interconnected toroidal hydrogels for islet encapsulation has proven effective in protecting transplanted cells from immune attacks. While still facilitating nutrient exchange (Ernst et al., 2019).

Additionally, the engineering of pluripotent stem cells into insulin-producing cells stands as a groundbreaking approach to generate a continual supply of functional cells for transplantation (Carvalho et al., 2022; Kasputis et al., 2018; Pagliuca et al., 2014). Further research has examined the potential of regulatory T cells that have been modified with insulin-specific chimeric antigen receptors to promote tolerance and reduce the risk of rejection during islet transplantation (Azad et al., 2024). These advancements

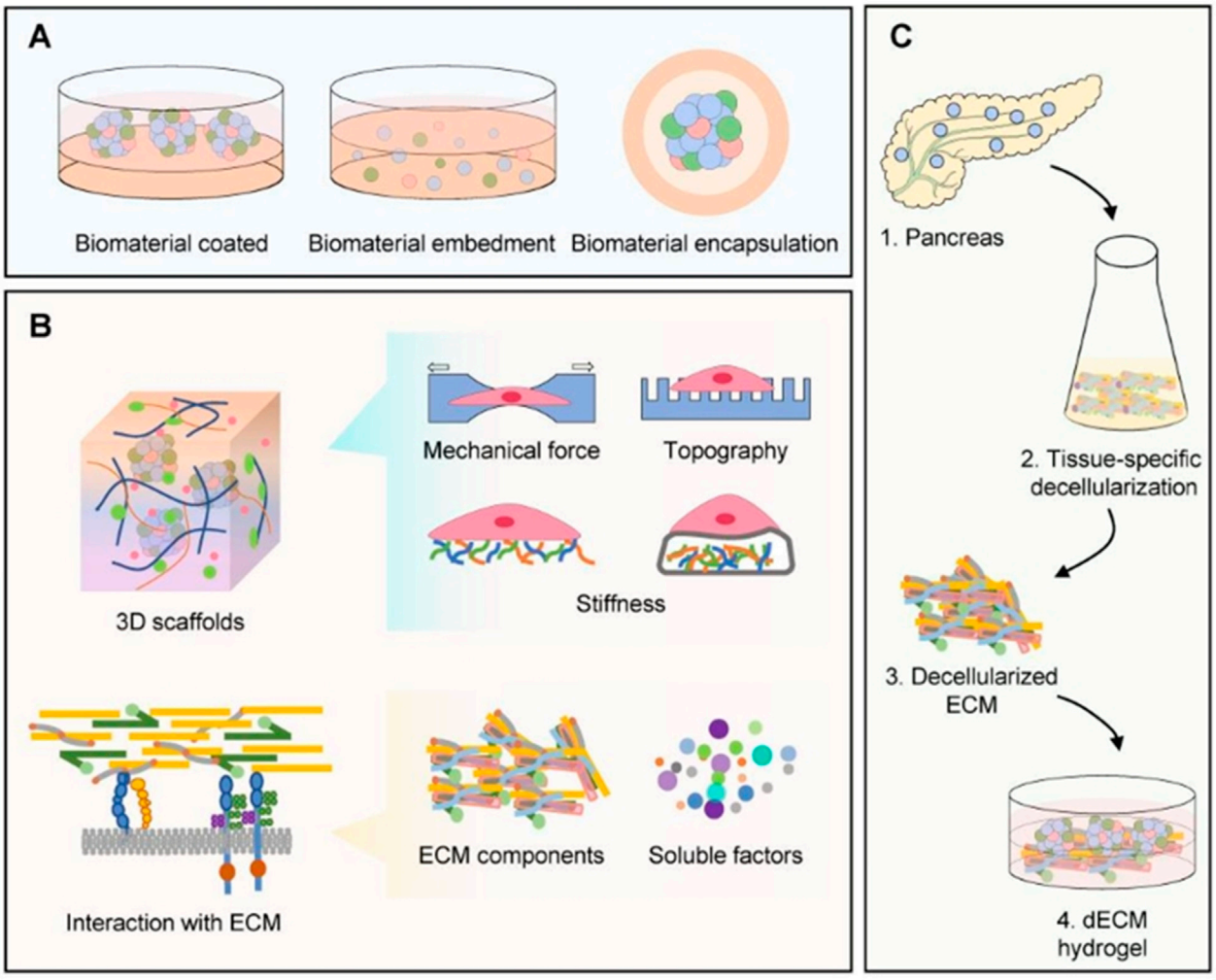

FIGURE 5
Illustrates a diagrammatic representation highlighting the application of materials in human islet organoids. **(A)** Applications of materials for production of human islet organoids, including strategies such as biomaterial coating, embedding, and encapsulation, plays a critical role in the advancement of diabetes treatments. **(B)** Biomaterials serve as three-dimensional scaffolds that replicate the native interactions with the extracellular matrix (ECM) essential for the generation of islet organoids. These scaffolds provide key factors such as mechanical forces, topographical features, stiffness, and signaling from ECM components and soluble factors. **(C)** The manufacturing process of decellularized ECM (dECM) materials is highlighted. This content is reproduced with permission from Jiang et al. (2022).

in cell transplantation methodologies, when integrated with the principles of tissue engineering, hold the promise of significantly enhancing both the effectiveness and accessibility of diabetes treatments.

3.2.2 Development of biomaterial scaffolds

The fabrication of biomaterial scaffolds constitutes a crucial aspect of tissue engineering within the framework of diabetes therapy, as they provide vital structural support for cellular growth and tissue regeneration. These scaffolds emulate the ECM and promote a three-dimensional structure that is conducive to cell proliferation, differentiation, and development. They may also be employed in the management of diabetic wounds, a common complication associated with diabetes (Tallapaneni et al., 2021). Scaffolds can be categorized into two main types based on their origin: natural and synthetic polymer-based scaffolds.

3.2.2.1 Natural biomaterial scaffolds

Natural biomaterials have garnered substantial interest in the field of tissue engineering because of their intrinsic biocompatibility and their capacity to facilitate cellular activities that are crucial for tissue regeneration (Bagheri et al., 2020; Mei et al., 2023). These materials, sourced from biological origins, include collagen, gelatine, chitosan, and alginate, which replicate the ECM of native tissues, thus fostering cellular interactions and enhancing healing processes (Naranda et al., 2021; Sonmezer et al., 2023). This is illustrated in Figure 6. For instance, collagen scaffolds are particularly recognized for their excellent properties regarding cell adhesion and biodegradability, rendering them suitable for applications in wound healing and regenerative medicine (Chu et al., 2018; Larijani et al., 2024). Chitosan, a natural polysaccharide, exhibits remarkable biocompatibility, biodegradability, and antimicrobial capabilities, positioning it as a promising candidate for wound healing and tissue engineering applications (Wang J. et al., 2024).

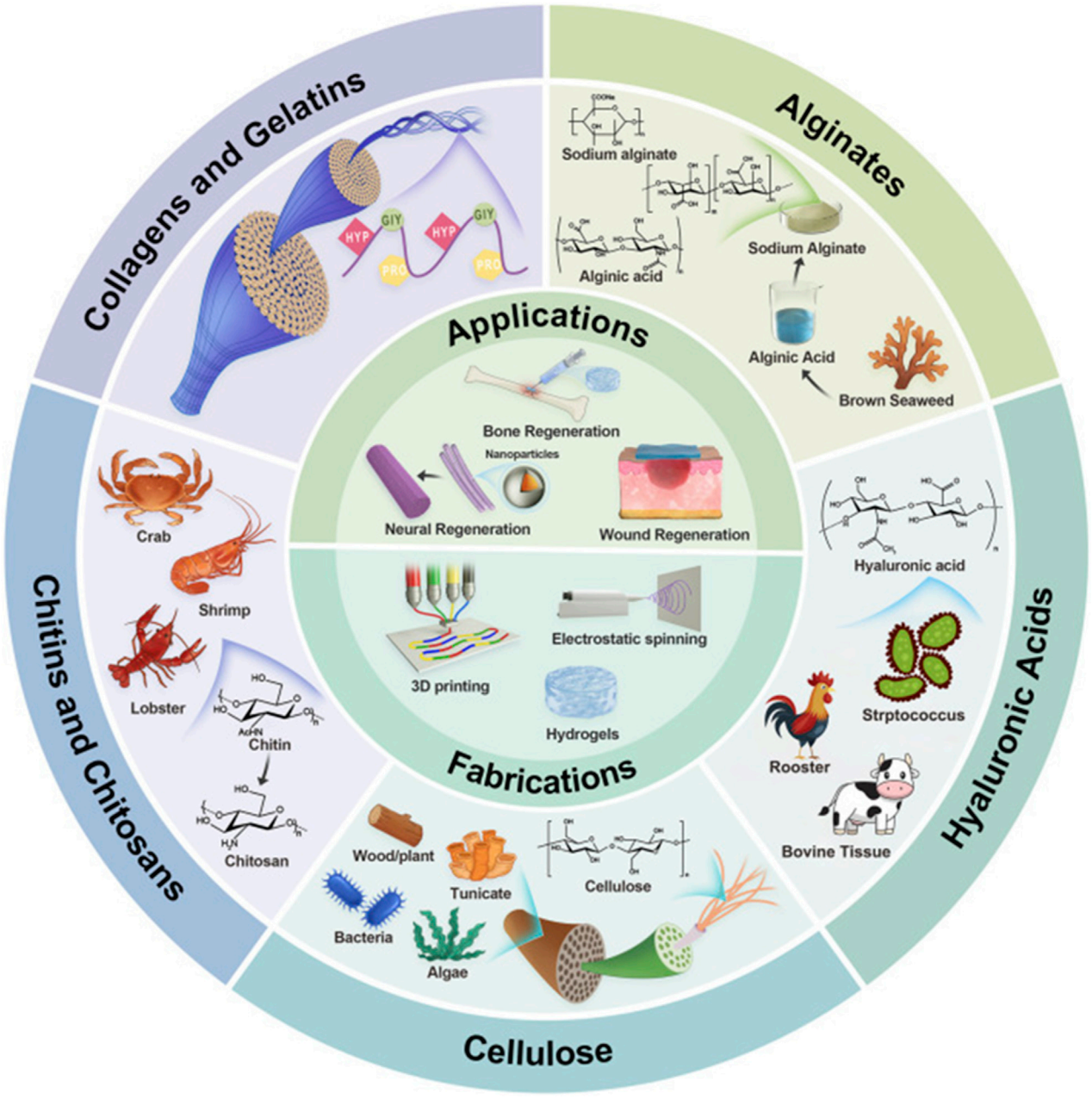

FIGURE 6
Illustrative schematic of naturally derived polymers:origin, structures, fabrications, and applications. Reproduced with permission from Hu et al. (2024a).

Moreover, the incorporation of bioactive molecules, such as growth factors and peptides, into natural materials can significantly enhance their regenerative capacity, leading to improved results in tissue repair and regeneration (Ravoor et al., 2021). Additionally, natural scaffolds can undergo modifications to improve their mechanical strength and degradation rates, thus allowing for customization tailored to specific applications. The inherent bioactive characteristics of natural biomaterials are further validated by their capacity to promote angiogenesis and facilitate tissue integration, both of which are essential for achieving favourable outcomes in tissue engineering (Goonoo, 2022).

The degradation behavior of these natural materials serves as a pivotal aspect concerning their application in biomedical contexts, significantly affecting their longevity, biocompatibility, and overall efficacy in tissue regeneration (Hu T. et al., 2024). Generally, natural materials are preferred due to their ability to undergo in vivo degradation, which permits a gradual replacement by newly synthesized tissue. Specifically, chitosan-based hydrogels have demonstrated a degradation process primarily governed by hydrolytic mechanisms, with degradation rates that can be modulated by varying the degree of crosslinking and the molecular weight (Lv et al., 2023). This characteristic proves particularly beneficial in scenarios such as drug delivery, where

the establishment of controlled release profiles is vital for achieving therapeutic effectiveness.

The degradation byproducts of natural materials are frequently non-toxic and can be metabolically processed by the body, thereby minimizing the likelihood of adverse reactions (Xu et al., 2022). The capacity to engineer natural materials with specific degradation kinetics enhances their applicability across a range of uses, including bone regeneration, where it is optimal for scaffolds to degrade in synchrony with the formation of new bone (Koh et al., 2022). In summary, the degradation characteristics of natural materials not only contribute to their biocompatibility but also are integral to their functionality and efficacy in the field of regenerative medicine.

3.2.2.2 Synthetic biomaterial scaffolds

Synthetic biomaterials, such as polycaprolactone (PCL), polylactic acid (PLA), and polyvinyl alcohol (PVA), have been engineered to address certain limitations associated with their natural counterparts (Deng et al., 2022). Research indicates that PCL scaffolds can effectively support the proliferation of mesenchymal stem cells and promote wound healing in models of diabetes (Abdollahi et al., 2024b). These synthetic materials provide customizable mechanical properties, controllable degradation rates, and can be fabricated into various forms, including fibers, films, and hydrogels (Lim et al., 2023; Li et al., 2020). This flexibility enables the optimization of material properties to better align with the mechanical characteristics of natural tissues, which is critical for applications involving implants and wound dressings. Investigations have shown that by adjusting the cross-linking density and the composition of the polymer network, researchers can develop hydrogels with tailored mechanical properties that are conducive to enhancing cell adhesion and proliferation in tissue engineering (Huang et al., 2023).

The adaptability of synthetic biomaterials facilitates the integration of bioactive agents, including growth factors or therapeutic drugs, allowing for their controlled release to foster healing and tissue regeneration (Guo et al., 2022b). Furthermore, the incorporation of nanomaterials into synthetic polymers has significantly improved their mechanical attributes, yielding materials that not only exhibit enhanced strength and durability but also demonstrate bioactivity that supports healing and integration with surrounding tissues (Abdollahi et al., 2024b). The integration of conductive materials within scaffolds has been explored to enhance the functional capacity of engineered tissues through improved electrical signalling, which is particularly important for insulin secretion in pancreatic cells (Wang and Jin, 2024). Moreover, advancements in three-dimensional printing technologies have facilitated the creation of intricate scaffold architectures that accurately replicate the structure of native tissues, thereby further augmenting the effectiveness of these biomaterials. The enhancement of integration and functionality in biomaterials has been highlighted by (Metwally et al., 2023). The adaptability of these mechanical properties is crucial for the effective incorporation of synthetic materials in clinical applications, as it enables the design of substances capable of enduring physiological stresses while supporting biological activities.

By amalgamating various functionalities within a single biomaterial, researchers are equipped to tackle diverse therapeutic challenges simultaneously. Such biomaterials can facilitate the controlled release of therapeutic agents, thereby promoting localized healing and reducing systemic side effects (Heidari et al., 2023). Additionally, these multifunctional materials can embed antibacterial characteristics to mitigate infections, which commonly arise in chronic wounds (Renuka et al., 2022).

Despite the considerable benefits offered by synthetic materials, significant concerns regarding their degradation and biocompatibility persist as critical hurdles in their utilization. For instance, materials engineered for temporary implants must degrade in synchronization with tissue healing to prevent complications linked to either premature breakdown or prolonged presence in the organism (Li et al., 2022). Moreover, ensuring the biocompatibility of synthetic materials is vital, as those that provoke adverse immune responses can incite chronic inflammation and result in implant failure (Ciatti et al., 2024; Kzhyshkowska et al., 2015). Recent progress has concentrated on the creation of biodegradable polymers that preserve their mechanical strength while systematically decomposing into non-toxic byproducts (Guo et al., 2022b). Addressing these concerns surrounding degradation and biocompatibility is essential for the successful transition of synthetic materials from laboratory settings to clinical implementations, guaranteeing that they offer safe and effective solutions for patients.

3.3 Delivery by transdermal delivery

Microneedle technology has emerged as a groundbreaking approach for insulin delivery, providing a minimally invasive alternative to conventional injection techniques (Bigham et al., 2025; Hong et al., 2022; Zong et al., 2022). The mechanism of insulin release from microneedles is depicted in Figure 7. These micro-scaled needles, which typically range in length from 25 to 1,000 μm (Figure 8), can penetrate the outer layer of the skin while circumventing nerve endings, thus minimizing discomfort and pain for patients (Chen et al., 2019; Luo et al., 2023; Wang et al., 2020). Recent advancements in the manufacturing technologies for microneedles, including 3D printing and mold-based methods, have enabled the creation of arrays capable of delivering precise dosages of insulin (Razzaghi et al., 2024). Evidence suggests that these microneedle arrays achieve bioavailability levels that are comparable to those obtained from traditional subcutaneous injections while significantly enhancing patient adherence due to their ease of use and reduced pain perception (Li et al., 2022; Queiroz et al., 2020). Furthermore, the incorporation of biodegradable materials in microneedle design has allowed for sustained insulin release, presenting a viable solution for long-term diabetes management (Chakraborty et al., 2023; Rajput et al., 2021). A nanoparticle-loaded microneedle (MN) patch, designed for transdermal drug delivery, aims to achieve blood glucose control and reactive oxygen species (ROS) scavenging for the synergistic treatment of diabetic nephropathy, thereby enhancing the efficiency of transdermal drug delivery while extending the duration of insulin action (Zheng et al., 2025). In summary,

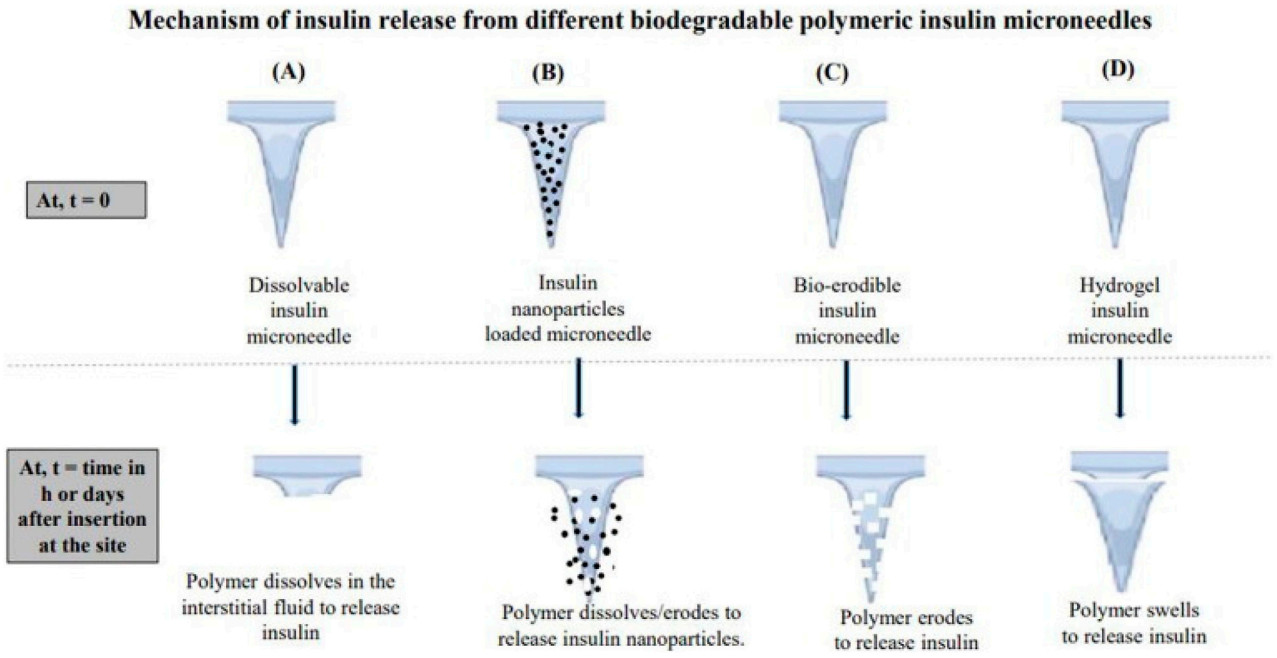

FIGURE 7
Mechanism of insulin release from the microneedles. **(A)** shows a soluble insulin microneedle that releases insulin through polymer dissolution. **(B)** shows a microneedle loaded with insulin nanoparticles, and insulin is released through the biodegradation of the shell or matrix. **(C)** shows a biodegradable insulin microneedle, and insulin is released after enzymatic hydrolysis. **(D)** shows a hydrogel insulin microneedle that continuously releases insulin after entering the dermis. Reproduced with permission from Starlin et al. (2024).

microneedle technology stands as a promising strategy for advancing insulin delivery systems and subsequently enhancing the quality of life for individuals with diabetes.

3.4 Smart delivery systems for diabetes management and treatment

The Smart delivery systems represent the cutting edge of insulin administration technology, merging innovative biomaterials with responsive mechanisms to develop dynamic delivery platforms. These systems are engineered to release insulin in a controlled manner, guided by real-time blood glucose monitoring, thereby providing a customized approach to managing T1DM (Condren et al., 2019; Latham, 2019; Moser et al., 2025; Renard, 2023). For example, hydrogels that expand or contract in response to changes in glucose concentrations have been developed, enabling on-demand insulin release as required (Ali et al., 2022; Annicchiarico et al., 2024). Furthermore, the incorporation of wearable technology within these smart delivery systems facilitates continuous glucose monitoring, which allows for automatic insulin administration in reaction to fluctuations in glucose levels (Renzu et al., 2024). This heightened level of responsiveness not only improves glycemic control but also reduces the risk of hypoglycemia, a prevalent issue in diabetes management. As research progresses, the potential for intelligent delivery systems to transform insulin therapy becomes increasingly evident, paving the way for more effective and user-friendly diabetes care solutions.

4 The role of biomaterials in diabetic wound healing

Current practices in managing diabetic wounds are based on four essential principles: (1) debridement, (2) infection control, (3) offloading, and (4) revascularization (Hu et al., 2022). In the context of diabetic wounds, particularly foot ulcers, the primary factor contributing to delayed healing is the diminished synthesis of collagen. This reduction adversely affects the solubility of the extracellular matrix (ECM) and provokes an exaggerated inflammatory response (Nirenjen et al., 2023). The inflammatory phase is marked by the secretion of pro-inflammatory cytokines such as IL-1, IL-6, and TNF-α. The subsequent proliferative phase is characterized by impaired angiogenesis and vasculogenesis, whereas in the remodeling phase, an increase in matrix metalloproteinases (MMPs) results in further degradation of the ECM, thereby exacerbating the challenges associated with wound healing (Figure 9). These factors present considerable hurdles for clinical management. Although traditional dressings have historically been essential in wound care, their effectiveness in treating diabetic wounds is significantly limited (Saco et al., 2016; Wang et al., 2024).

4.1 Limitations of traditional dressings for diabetic wound treatment

Diabetic wounds exhibit a complex pathophysiological profile that includes impaired angiogenesis, a weakened immune response, and an increased vulnerability to infections (Rodriguez-Rodriguez

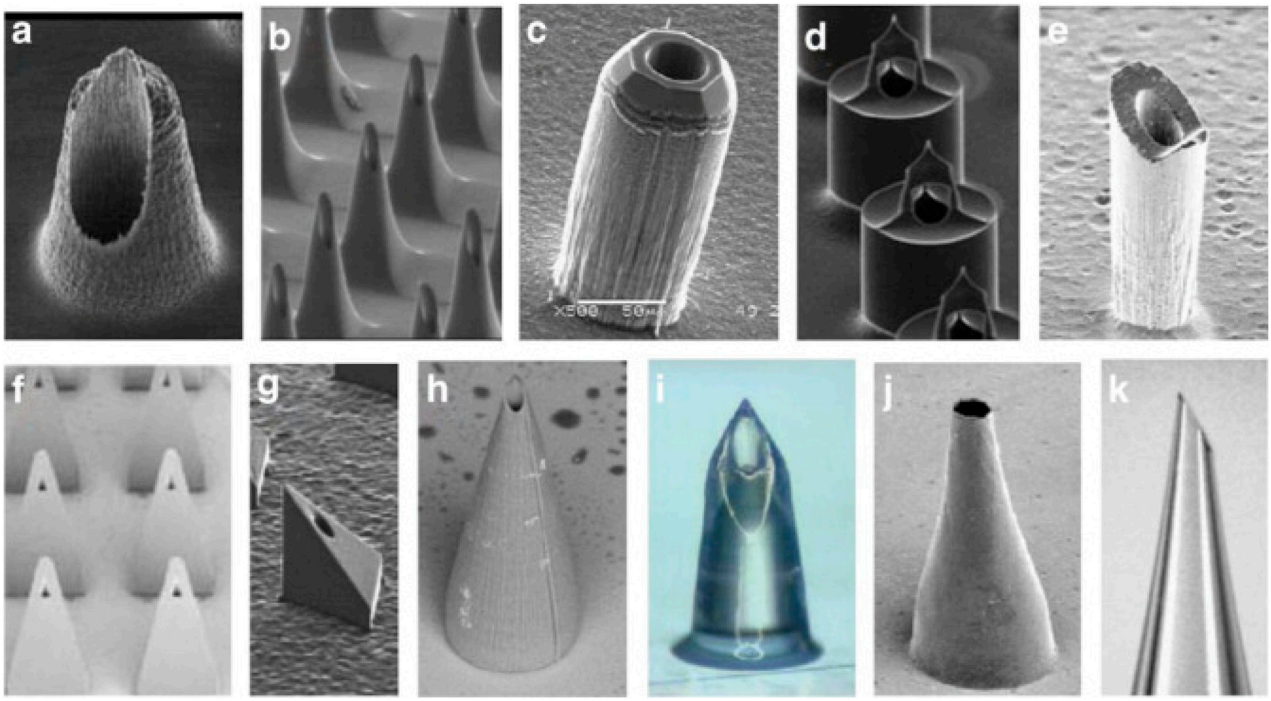

FIGURE 8
Hollow microneedles created from silicon and polymers. **(A, B)** Hollow microneedles with a tapered shape. Mukerjee et al. (2015), Wilke et al. (2005) **(C)** Hollow silicon microneedles with sharp tips Ma et al. (2006). **(D)** cylindrical microneedles with a side-opening orifice Zhang et al. (2009) **(E)** Hollow silicon microneedles with sharp tips Baron et al. (2008) **(F)** Hollow microneedles by exposing X-ray through a mask onto PolyMethylMetaAcrylic. Moon et al. (2005) **(G)** A micro-gear pump Amirouche et al. (2009) **(H)** Microneedles with on-board fluid pumps Lin and Pisano (1999) **(I)** Flow of liquid through glass hollow microneedles controlled by CO2 gas pressure Martanto et al. (2006) **(J)** An electrical microneedle applicator Verbaan et al. (2008) **(K)** Flow of liquid through hollow microneedles controlled by a syringe pump Gupta et al. (2009). Reproduced with permission from Kim et al. (2012).

et al., 2022). A significant limitation of conventional dressings, including gauze and hydrogels, is their singular functionality, which fails to adequately address the diverse challenges associated with diabetic wounds (Venkatesan and Rangasamy, 2023; Zhang et al., 2023a). These traditional dressings often lack the incorporation of bioactive agents that could facilitate healing, and their capacity to prevent bacterial proliferation is insufficient, leading to a heightened risk of infection (Zhou et al., 2024a). Furthermore, issues with adherence and retention of these dressings can necessitate frequent changes, which may disrupt the healing process and inflict additional pain and discomfort on patients (Jiang et al., 2023).

Moreover, the healing duration associated with conventional dressings can be extended, raising concerns for diabetic individuals who are predisposed to complications such as foot ulcers and potential amputations (Andrews et al., 2015; Sahu et al., 2018). The absence of advanced features in these dressings means they do not support critical physiological processes, such as angiogenesis and collagen deposition, which are essential for effective wound repair (Zhang et al., 2024). Consequently, there exists a pressing need for the formulation of more effective wound care solutions that integrate bioactive materials along with multifunctional attributes to enhance the healing of diabetic wounds (Cai F. et al., 2023). Various types of dressings, including conventional, bioactive, and interactive dressings, as well as skin substitutes, are being employed to treat wounds (Alven et al., 2020) (Figure 10).

In conclusion, while traditional dressings have played a crucial role in wound management, their inadequacies in addressing diabetic wounds underscore the necessity for a transition towards more innovative treatment strategies that can effectively tackle the distinct challenges they present. The diabetes patients can benefit significantly from the incorporation of sophisticated biomaterials and innovative technologies, which may prove instrumental in addressing existing challenges and enhancing patient outcomes in the management of diabetic wounds (refer to Table 3).

4.2 The utilization of innovative wound dressings in diabetic wound healing

Recent innovations in wound dressing technologies have culminated in the creation of multifunctional dressings that incorporate biocompatible materials along with bioactive agents (Figure 11). According to a systematic review conducted by Vargas et al., bioactive glass (BG)-based materials show promise in expediting all phases of diabetic wound healing and improving the overall quality of wound recovery (Vargas et al., 2024). For example, electrospun nanofibers and hydrogels are employed to fabricate dressings that not only provide a protective barrier but also deliver therapeutic agents directly to the wound site (Fahimirad and Ajalloueian, 2019; Hong et al., 2023; Yang and Xu, 2023). Furthermore, the integration of electrical stimulation within

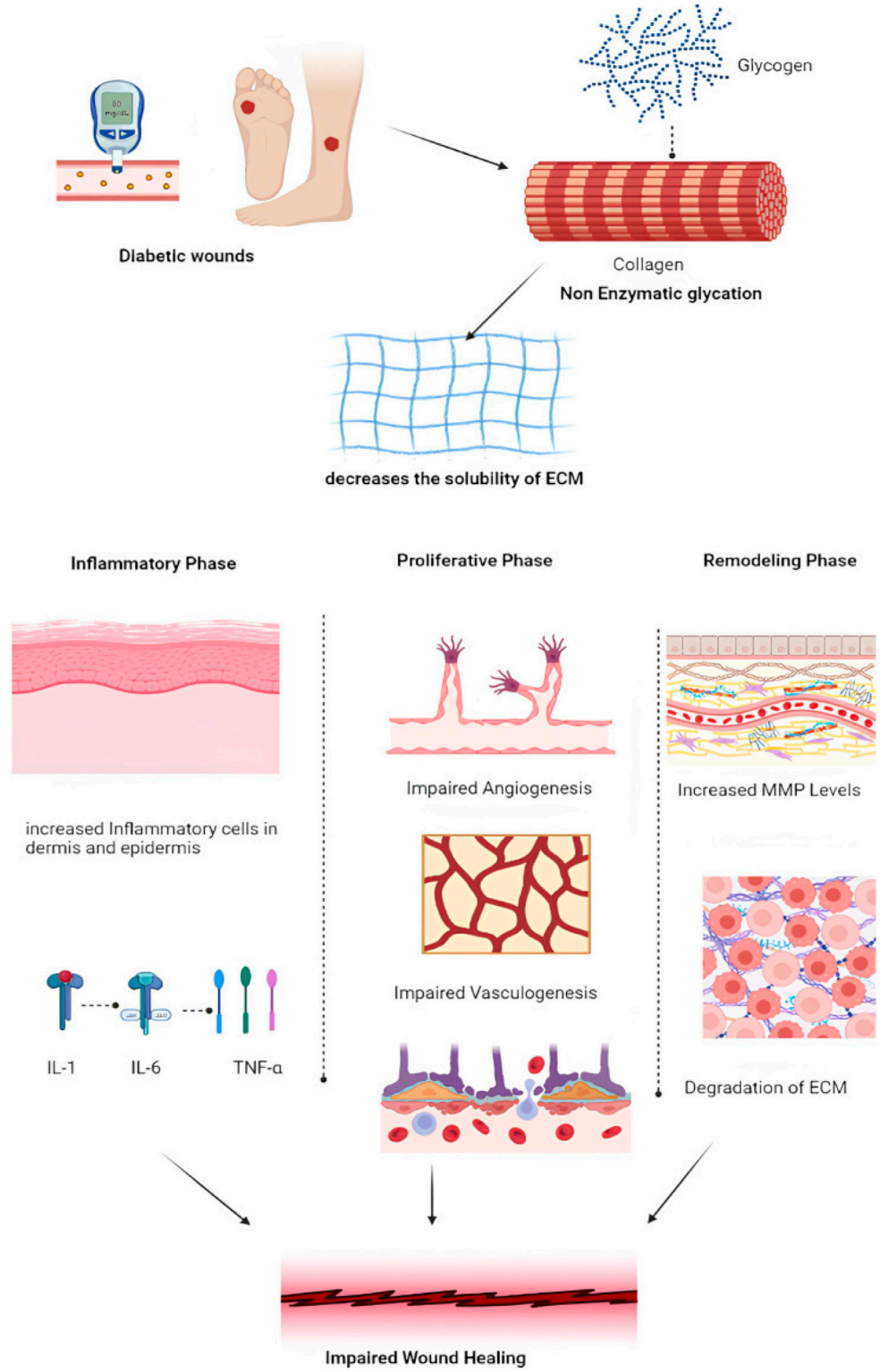

FIGURE 9
Schematic diagram of diabetic wound repair. Reproduced with permission from Aldahish et al. (2024).

wound dressings has revealed potential for enhancing healing rates by fostering cellular activities and optimizing blood circulation to the affected regions (Asadi and Torkaman, 2014; Fan et al., 2024; Hu Y. W. et al., 2024). Additionally, the incorporation of antimicrobial additives into wound dressings is increasingly gaining traction, providing an additional layer of defense against infections, which are a common complication in diabetic wounds (Chen et al., 2024d; Firoozbahr et al., 2023; Li et al., 2024; Rozman et al., 2020). In

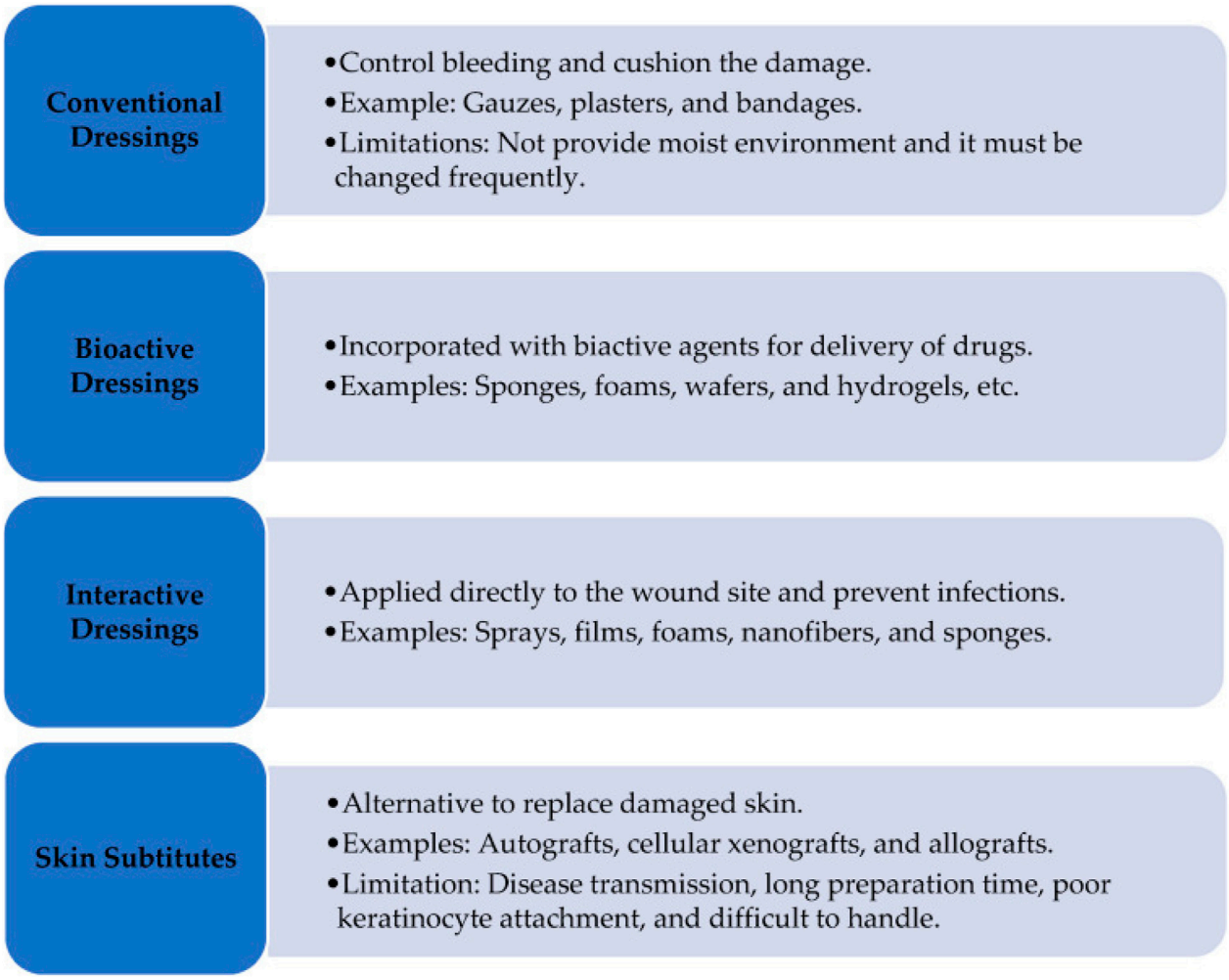

FIGURE 10
Classification of wound dressings. Reproduced with permission from Alven et al. (2020).

summary, advancements in wound dressing technologies signify a considerable leap forward in the effective management of diabetic wounds, offering tailored solutions.

4.2.1 Biocompatible materials

The biocompatibility of materials is a crucial factor in the development of biomaterials for biomedical applications, particularly in the context of diabetic wound healing (Nandhakumar et al., 2022; Ren et al., 2022; Xu et al., 2023). These materials are specifically designed to interact positively with biological systems, thereby reducing adverse reactions while facilitating healing processes (Chan et al., 2023; Naahidi et al., 2017). Recent studies have underscored the promising potential of various biocompatible materials, such as chitosan, alginate, and hyaluronic acid, which have shown encouraging outcomes in promoting the healing of diabetic wounds (Peng et al., 2022). Although clinical trials remain limited, chitosan has emerged as a highly effective alternative for modulating local inflammatory responses and promoting wound healing, especially in patients with comorbid conditions that hinder typical skin healing processes, such as diabetes and vascular insufficiency (Maita et al., 2022). Chitosan-based biomaterials have gained recognition for their efficacy in wound healing, characterized by their antibacterial properties and ability to enhance cellular proliferation, rendering them suitable candidates for applications in wound care (Cai and Li, 2020; Rajinikanth et al., 2024). Systematic reviews and meta-analyses have established that, relative to the standard of care (SOC), patients receiving placenta-derived biomaterial treatments demonstrate a superior rate of complete wound healing in cases of diabetic foot ulcers (DFUs) (Ruiz-Munoz et al., 2024). Chen et al. corroborated that placenta-based tissue products exhibited the highest likelihood of wound healing (p-score = 0.90), followed by living cell skin substitutes (p-score = 0.70), acellular skin substitutes (p-score = 0.56), and advanced topical dressings (p-score = 0.34) when measured against standard DFU care (Chen L. et al., 2024).

Angiogenesis and cellular migration are fundamental processes in wound healing, which are frequently disrupted in diabetic wounds (Yang et al., 2024). Consequently, an optimal biomaterial should facilitate the development of new blood vessels to enhance blood flow and oxygen supply at the wound site. Achieving these characteristics necessitates the engineering of physico-chemical properties at both chemical and molecular levels, ensuring

TABLE 3 A selection of biomaterial products for clinical management of diabetic wounds.

Product name	Main features	Clinical application status	Treatment Stage	References
Codfish Skin (After Decellularization and Freeze-drying Treatment)	1.Excellent biocompatibility 2.Abundant in collagen and growth factors 3.Natural antibacterial properties 4.Economical and readily available	In the Odinn Phase III clinical trial	Diabetic foot ulcer complication stage, especially suitable for deep diabetic foot ulcers (UT grade 2 or 3), that is, ulcers penetrating to the tendon or joint capsule (UT grade 2) or deep into the bone or joint (UT grade 3)	Esmaeili et al. (2023), Pei et al. (2023)
"Subiyi®" Xianglei Diabetic Foot Ointment	1.Modulates macrophage activity 2.Enhances inflammation resolution and promotes tissue repair 3.Reconfigures the wound microenvironment	Utilized in Taiwan (China), Singapore, Malaysia, etc.,; has received Fast Track Certification from the US FDA	Diabetic foot ulcer complication stage, applicable to patients with Wagner grade 1 diabetic foot ulcers and wound cross-sectional area less than 25 cm^2	(Chinese Society of Endocrinology, 2024)
Chitosan Pressure Ulcer and Diabetic Foot Dressing	1.Forms an artificial skin for protection and enhancement of wound healing 2.Free from antibiotics, analgesics, or anesthetics 3.No delayed hypersensitivity reactions or irritation to skin and mucous membranes	Aids in alleviating edema, pain, ulceration, and other complications associated with Stage I, II, and III pressure ulcers and diabetic foot ulcers	Diabetic foot ulcer complication stage, can be used to relieve complications such as stage I, II, and III pressure ulcers and diabetic foot ulcers	(Huang et al., 2023; Mirbagheri et al., 2023; Ren et al., 2022)
Mandabang Diabetic Foot Wound Cleaning Liquid Dressing	1.Highly efficient sterilization with a safety profile 2.Broad antibacterial spectrum 3.Acts within 15–30 s, achieving a 99.9999% kill rate 4.Exhibits antibacterial properties even at minimal concentrations	Applicable for wound care and debridement across various departments	Diabetic foot ulcer complication stage	From the internet (http://www.chinamsr.com/2021/0108/116520.shtml)
Recombinant Lysozyme-Antibacterial Peptide Fusion Protein	1.Secrete growth factors to achieve self-repair 2.Accelerate the formation of micro vessels 3.Exhibits low toxicity and minimal irritation 4.no inflammatory exudation	Under research	Diabetic complication stage	Chen et al. (2018)
Hairun Biology Anti-Infection Dressings	1.Exhibits anti-infection capabilities 2.Reduces dressing change frequency	Widely implemented in the clinical management of diabetic foot ulcers and other wound surfaces	Diabetic foot ulcer complication stage	From the internet (https://ylqx.qgyyzs.net/user/web7105/)
Recombinant Growth Factor Gel	1.Promotes wound healing 2.Aids in expediting the repair of diabetic foot ulcers	Extensively employed in the adjunctive treatment of wound surface repairs, including diabetic foot ulcers	Diabetic foot ulcer complication stage	Das et al. (2023)
PDA@Ag/SerMA microneedles	1.safe, effective, painless and minimally invasive medication administration through the skin 2.promote cell mitosis 3.accelerate wound healing 4. The wound healing rate of mice reached 95% within 12 days 5.approximately 100% antimicrobial efficacy against *Staphylococcus aureus* and *Escherichia coli* under 808 nm near-infrared irradiation	Only in mice	Diabetic foot ulcer complication stage	Chen et al. (2024d)

alignment with the required bioactivity for wound healing in diabetic conditions (Sharma and Kishen, 2024) (Figure 12). This necessity highlights the importance of comprehending the structure–function relationship within biopolymers.

Moreover, integrating natural compounds into these materials can enhance their biocompatibility and therapeutic efficacy, as demonstrated by the incorporation of honey and plant extracts in wound dressings (Prasathkumar and Sadhasivam, 2021; Yasin et al., 2023). The advancement of nanomaterials also presents novel opportunities for improving biocompatibility and functionality (Barhoum et al., 2022). Research has shown that these materials can enhance cellular responses and tissue integration (Bai et al., 2020). Overall, the creation of biocompatible materials is crucial for developing effective treatments for diabetic wounds, ensuring that they not only promote healing but also seamlessly integrate with the body's biological systems.

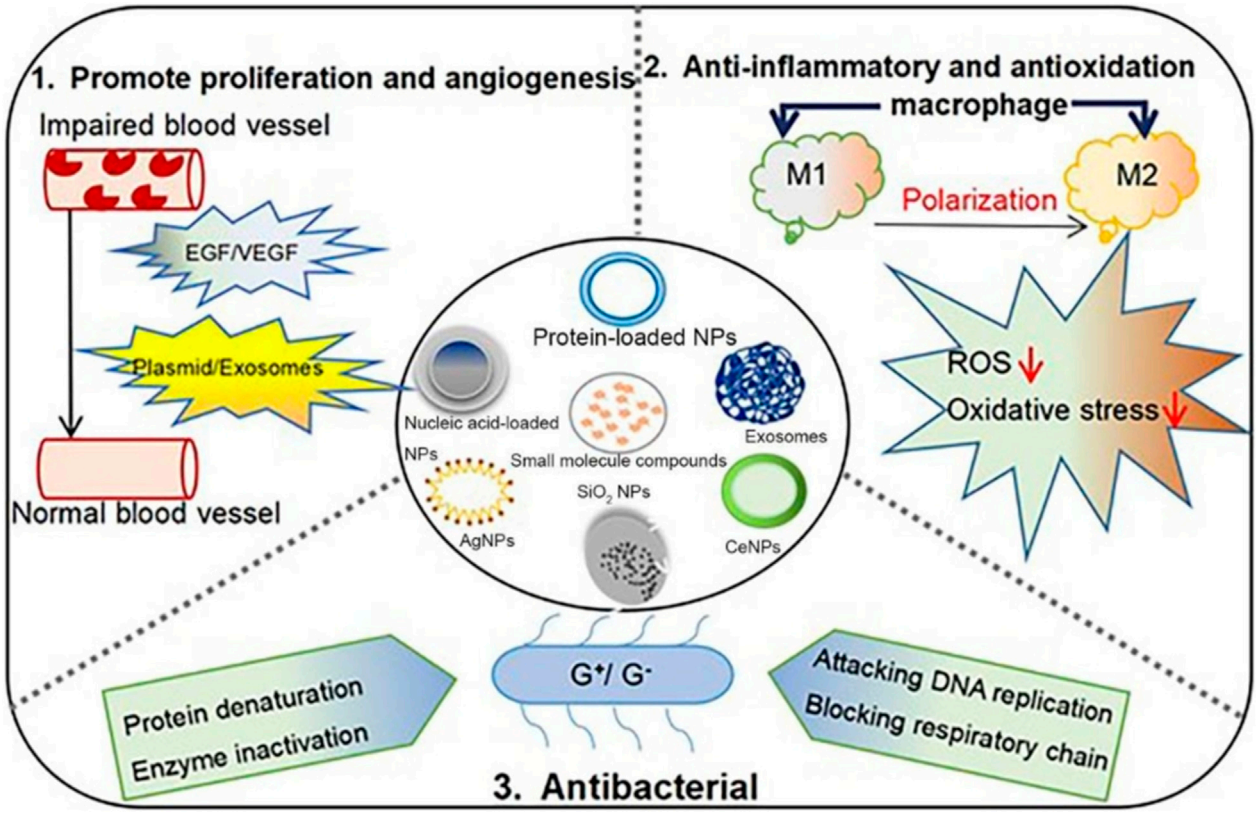

FIGURE 11
Presents a diagrammatic representation illustrating the various classifications and therapeutic mechanisms associated with biomaterials utilized in the management of diabetic wounds. This illustration is reproduced with permission from Qin et al. (2022).

4.2.2 Bioactive molecules

Bioactive molecules play a critical role in the wound healing process, especially for individuals with diabetes, where natural healing mechanisms are often hindered (Moses et al., 2023; Oprita et al., 2023; Sultana et al., 2024). These molecules can be integrated into biomaterials to bolster their therapeutic effects. For instance, growth factors, cytokines, and antimicrobial peptides are currently being studied for their capacity to stimulate essential cellular activities, including migration, proliferation, and angiogenesis (Takahashi et al., 2021; Umehara et al., 2022; Yue et al., 2022). Recent research indicates that the incorporation of bioactive molecules into hydrogels and scaffolds can markedly improve healing outcomes for chronic wounds (Chen et al., 2024b; Rathna and Kulandhaivel, 2024; Yusuf and Adeleke, 2023). Figure 13 provides a schematic representation of various biomaterial dressings. Additionally, studies have highlighted the potential of metal nanoparticles as bioactive agents in diabetic wound therapy, offering antimicrobial properties while facilitating tissue regeneration (Zheng et al., 2024). The development of intelligent biomaterials capable of controlling the release of these bioactive molecules represents a promising research area, enabling targeted delivery and enhanced therapeutic effectiveness (Huang et al., 2023). Therefore, the strategic incorporation of bioactive molecules alongside biomaterials marks a significant advancement in diabetic wound treatment, fostering a more effective healing process.

5 Challenges and future directions

The utilization of biomaterials in diabetes management represents a promising Frontier with significant potential, particularly in the domains of diabetes treatment and wound healing. Nonetheless, the deployment of biomaterials for diabetes management, especially in the context of wound healing, embodies a dual-edged sword characterized by both benefits and drawbacks.

From a positive perspective, biomaterials such as hydrogels, nanoparticles, and scaffolds present enhanced characteristics that can markedly improve outcomes in wound healing (Fadilah et al., 2022; Leng et al., 2022; Zhang Z. et al., 2024). These biomaterials can be meticulously engineered to facilitate controlled drug release, encourage angiogenesis, and amplify cellular responses, effectively addressing the complex, multifactorial nature of diabetic wounds. The integration of bioactive agents, including growth factors and exosomes derived from stem cells, into these materials has the potential to further stimulate tissue regeneration and enhance healing rates (Jing et al., 2023). Furthermore, biomaterials can be customized to exhibit antibacterial properties, thereby diminishing the risk of infection, a frequent complication associated with diabetic wounds (Zheng et al., 2024).

Conversely, the application of biomaterials is not devoid of challenges. A notable concern is the risk of immune rejection or adverse reactions, particularly in relation to synthetic materials (Tripathi et al., 2023). The biocompatibility of these materials is

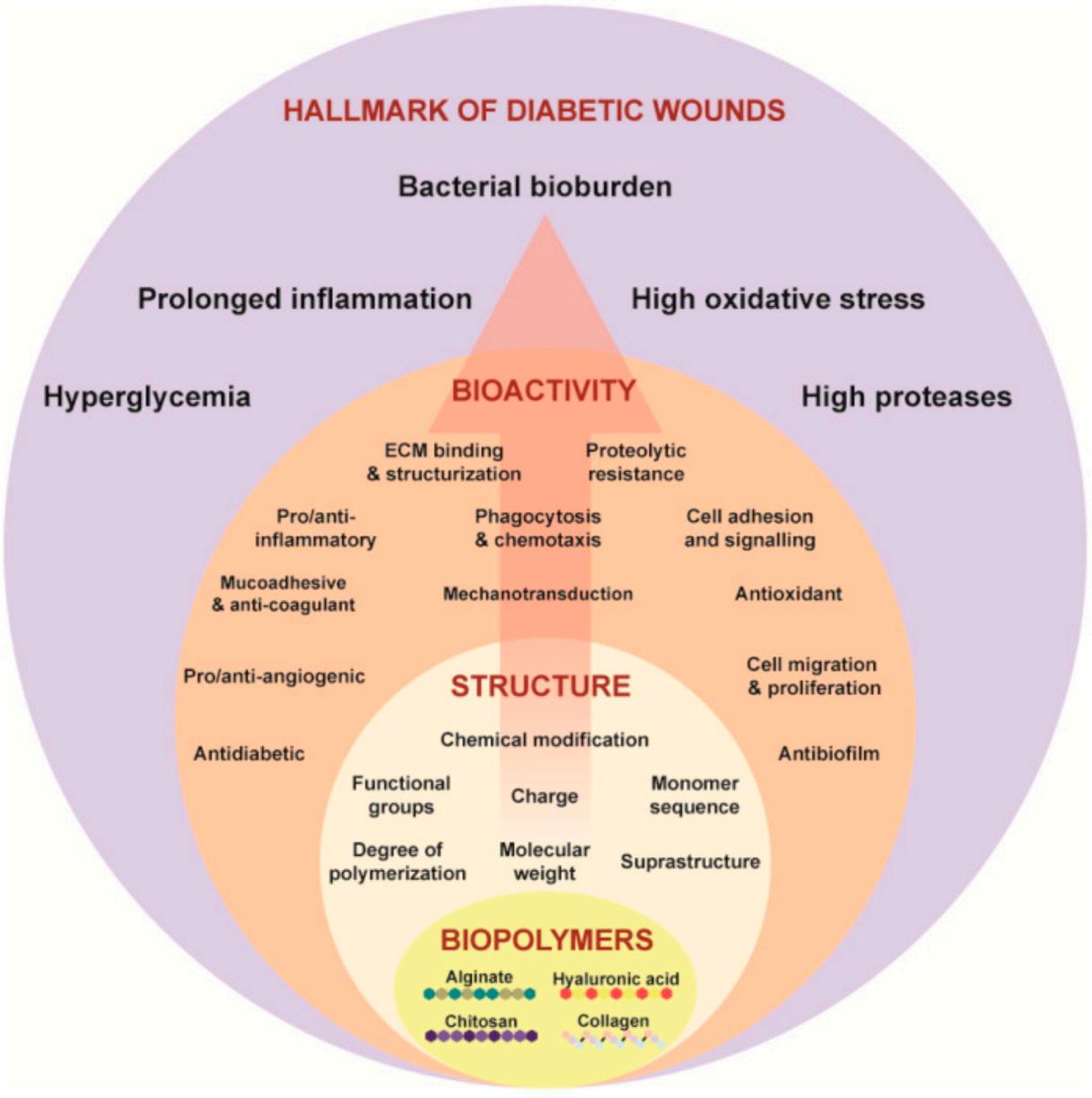

FIGURE 12
Illustrates the structure–function paradigm as represented in Equation concerning biopolymers such as alginate, chitosan, hyaluronic acid, and collagen, which target the critical features of chronic wounds. Reproduced with permission from Sharma and Kishen (2024).

a critical aspect that necessitates thorough evaluation to prevent complications that could impede rather than promote healing (Zhao et al., 2023). Additionally, the intricate environment of diabetic wounds may hinder the effective performance of biomaterials. Elevated levels of reactive oxygen species (ROS) within diabetic wounds can undermine the efficacy of specific biomaterials, highlighting the need for the development of advanced formulations capable of alleviating oxidative stress (Cai et al., 2023a; He et al., 2023; Yao et al., 2019). Moreover, the cost and accessibility of sophisticated biomaterials may present an obstacle to their wide-scale adoption in clinical settings (Ansari and Darvishi, 2024; Chen and Liu, 2016). While these materials exhibit considerable promise, their incorporation into standard diabetes management requires a meticulous assessment of their long-term effects, potential complications, and overall cost-effectiveness.

In summary, although biomaterials present exciting prospects for improving diabetes management and wound healing, it remains imperative to weigh their benefits against potential drawbacks. Critical factors regarding biocompatibility, safety profiles, and long-term efficacy of biomaterials necessitate further exploration to guarantee their safe integration into clinical practice. Ongoing research and clinical trials will play a vital role in identifying the most effective and safe applications of biomaterials in this context, ultimately striving to enhance patient outcomes in diabetes care.

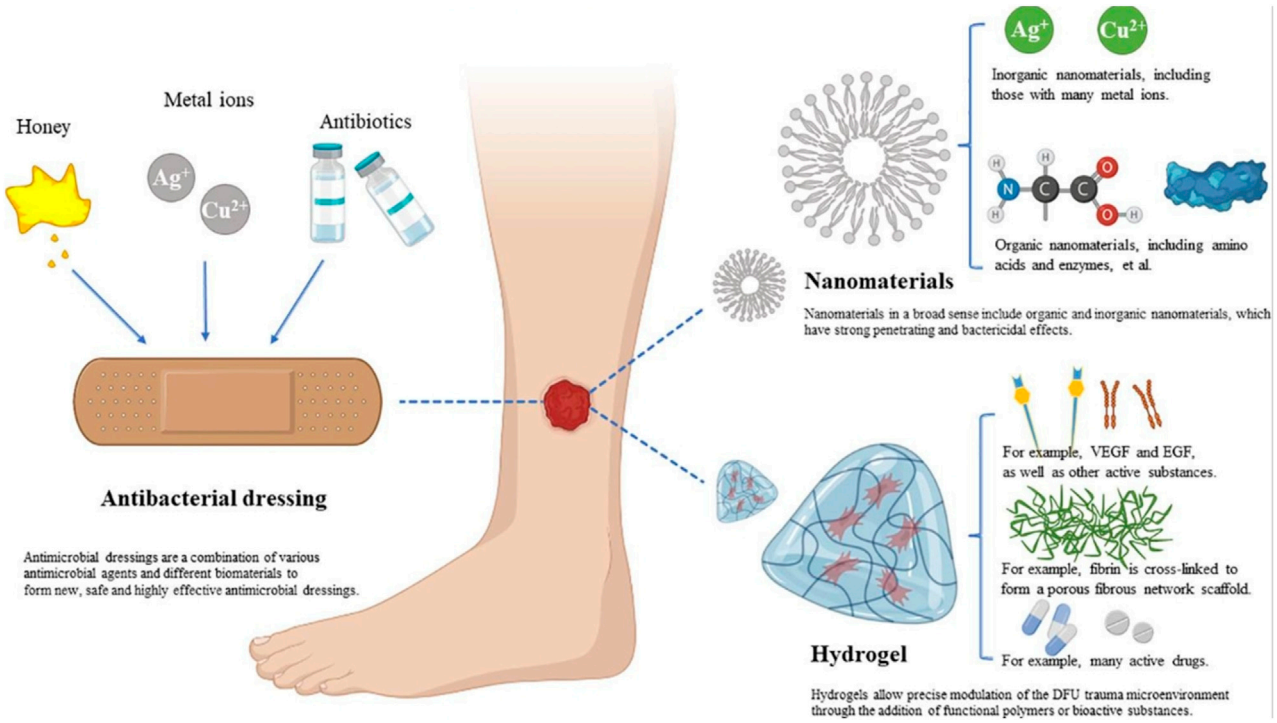

FIGURE 13
A visual representation illustrating antibacterial dressings, nanodressings, and hydrogel dressings. Reproduced with permission from Jiang et al. (2023).

5.1 Safety and efficacy of biomaterials

The safety and efficacy of biomaterials are of paramount concern as their use in clinical applications continues to expand (Kantak and Bharate, 2022). These materials must engage positively with biological systems, facilitating healing while minimizing adverse reactions (Knopf-Marques et al., 2016). The challenge lies in ensuring that these biomaterials do not provoke toxic responses or incite chronic inflammation, which could compromise their intended function. Advances in the understanding of the interaction between biomaterials and the immune system have paved the way for the design of materials capable of favorably modulating immune responses, thereby enhancing their therapeutic potential (Salthouse et al., 2023). Furthermore, the advancement of nanotoxicity evaluations is essential, as nanoparticles employed in biomaterials may pose risks distinct from their bulk forms (Akcan et al., 2020). As this discipline progresses, it is imperative for researchers to prioritize the creation of standardized protocols for assessing the safety of biomaterials to streamline regulatory approval processes and enhance clinical translation (Josyula et al., 2021).

In the last decade, a significant concentration of clinical research on biomaterials has emerged, closely linked to advances in fundamental research. Nonetheless, the findings derived from basic research may not necessarily translate directly to human applications (Socci et al., 2023). As previously noted in this manuscript, the biocompatibility and efficacy of certain established biodegradable biomaterials have been validated through clinical trials (Arrizabalaga and Nollert, 2018). The academic community broadly recognizes the potential for biomaterials to be integrated with agents such as stem cells and bioactive factors (Wilems et al., 2019). However, challenges such as ethical considerations and the variability in source materials hinder seamless clinical translation. Moreover, most animal models utilized in fundamental research are rodents, which, while advantageous due to their availability and established modeling techniques, present a significant limitation: their wound-healing mechanisms differ from those in humans (Nuutila et al., 2016). Several clinical trials have yet to achieve the anticipated outcomes in human subjects, causing stagnation in clinical translation efforts (Shamshad et al., 2023).

Consequently, it is crucial for basic research teams to foster close collaboration with clinical departments. By aligning with genuine clinical needs, they should conduct focused basic research aimed at facilitating clinical translation, thereby identifying safer and more effective biomaterials for application in clinical settings.

5.2 Possibility of personalized treatments

The capacity for real-time monitoring and data analysis marks a significant evolution in the domain of biosensors. With the progression of data analytics and machine learning, the interpretation of biosensor data has become increasingly sophisticated, enabling predictive insights and tailored healthcare solutions (Childs et al., 2024; Zhang et al., 2021; Schackart and Yoon, 2021). Real-time health monitoring systems can amalgamate data from various biosensors, offering a holistic view of a patient's health status (Paganelli et al., 2022; Wu et al., 2023; Li et al., 2021). This integration allows for timely interventions and enhanced

TABLE 4 Summarized some diabetes management systems that have obtained clinical approval.

Official title	Conditions	Intervention/Treatment	ClinicalTrials.gov ID	Study completion
A Randomized Cross-over Trial Evaluating Automated Insulin Delivery Technologies on Hypoglycemia and Quality of Life in Elderly Adults With Type 1 Diabetes	T1DM	• Device: Tandemt: slim X2 with HCL or PLGS	NCT04016662	2024–01
Use of the Guardian™ Connect System With Smart Connected Devices	T1DM	• Device: Guardian™ Connect system, InPen™ Basal smart cap, smart insulin pens, and InPen™ Diabetes Management app	NCT04809285	2023–09
Individualized Planned Eating Patterns to Improve Glycemic Management in Adolescents With Type 1 Diabetes: A Pilot Clinical Trial	T1DM	• Behavioral: "MyPlan" -Individualized Planned Eating Pattern	NCT05147324	2023–04
Randomized Controlled Trial To Assess the Benefits of Dexcom Continuous Glucose Monitoring With Glucose Telemetry System for the Management of Diabetes in Long-term Care Setting: The CGM-GTS in Long-term Care	T2DM	• Device: Dexcom G6 CGM with GTS • Diagnostic Test: POC Blood Glucose Test + Blinded CGM	NCT04818242	2022–10
ABC [Afrezza With Basal Combination]: A Phase 4 Study of Mealtime Control With Afrezza in Adult Subjects With Type 1 Diabetes Mellitus in Combination With an Automated Insulin Pump or Insulin Degludec	T1DM	• Biological: Afrezza (insulin human) Inhalation Powder • Biological: insulin degludec • Device: Continuous Subcutaneous Insulin Infusion (CSII) pump with Automatic Insulin Delivery (AID)	NCT05243628	2022–10
Hybrid Closed Loop Therapy and Verapamil for Beta Cell Preservation in New Onset Type 1 Diabetes (CLVer)	T1DM	• Device: HCL • Drug: verapamil 120 mg tablet • Device: non-HCL • Drug: placebo	NCT04233034	2022–09
Automated Insulin Delivery for INpatients With DysGlycemia (AIDING) Feasibility Study	DM	• Device: The Omnipod 5/Horizon HCL system	NCT04714216	2022–08
Feasibility of Outpatient Automated Blood Glucose Control With the iLet Bionic Pancreas for Treatment of Cystic Fibrosis Related Diabetes	Cystic Fibrosis-related Diabetes	• Device: Bionic Pancreas • Other: Usual Care	NCT03258853	2022–06
Demonstration Study of the Interest of the MEDTRUM A7+ TouchCare Insulin Patch Pump Versus INSULET Omnipod® Patch Pump	DM	• Device: Medtrum A7+ insulin Pump • Biological: Lab A1C	NCT04223973	2021–06
QBSAfe: A Novel Approach to Diabetes Management Focused on Quality of Life, Burden of Treatment, Social Integration and Avoidance of Future Events	DM	• Other: QBSAfe Toolkit	NCT04514523	2020–09
Assessment of a Novel Sensing Catheter During Automated Insulin Delivery in Patients with Type 1 Diabetes	T1DM	• Device: Artificial Pancreas Control system (APC) • Device: Pacific Diabetes Technologies CGM Insulin Infusion system	NCT03528174	2018–07
ACCU-CHEK Connect Personal Diabetes Management Study (PDM)	T1DM	• Device: ACCU-CHEK	NCT02600845	2017–02
A Multicenter Study of Outpatient Automated Blood Glucose Control With a Bihormonal Bionic Pancreas	T1DM	• Device: Bionic Pancreas • Device: Insulin pump with or without CGM	NCT02092220	2016–12
The Mobile Insulin Titration Intervention (MITI) Study: Innovative Chronic Disease Management of Diabetes	DM	• Other: Mobile Insulin Titration Intervention	NCT01879579	2015–06
Diabetes Remote Care Management System	DM	• Device: DRMS	NCT01354015	2014–09
Sensor and Software Use for Improved Glucose Control in MDI Managed Diabetes	DM	• Device: FreeStyle Navigator • Device: Standard SMBG	NCT01713348	2013–07

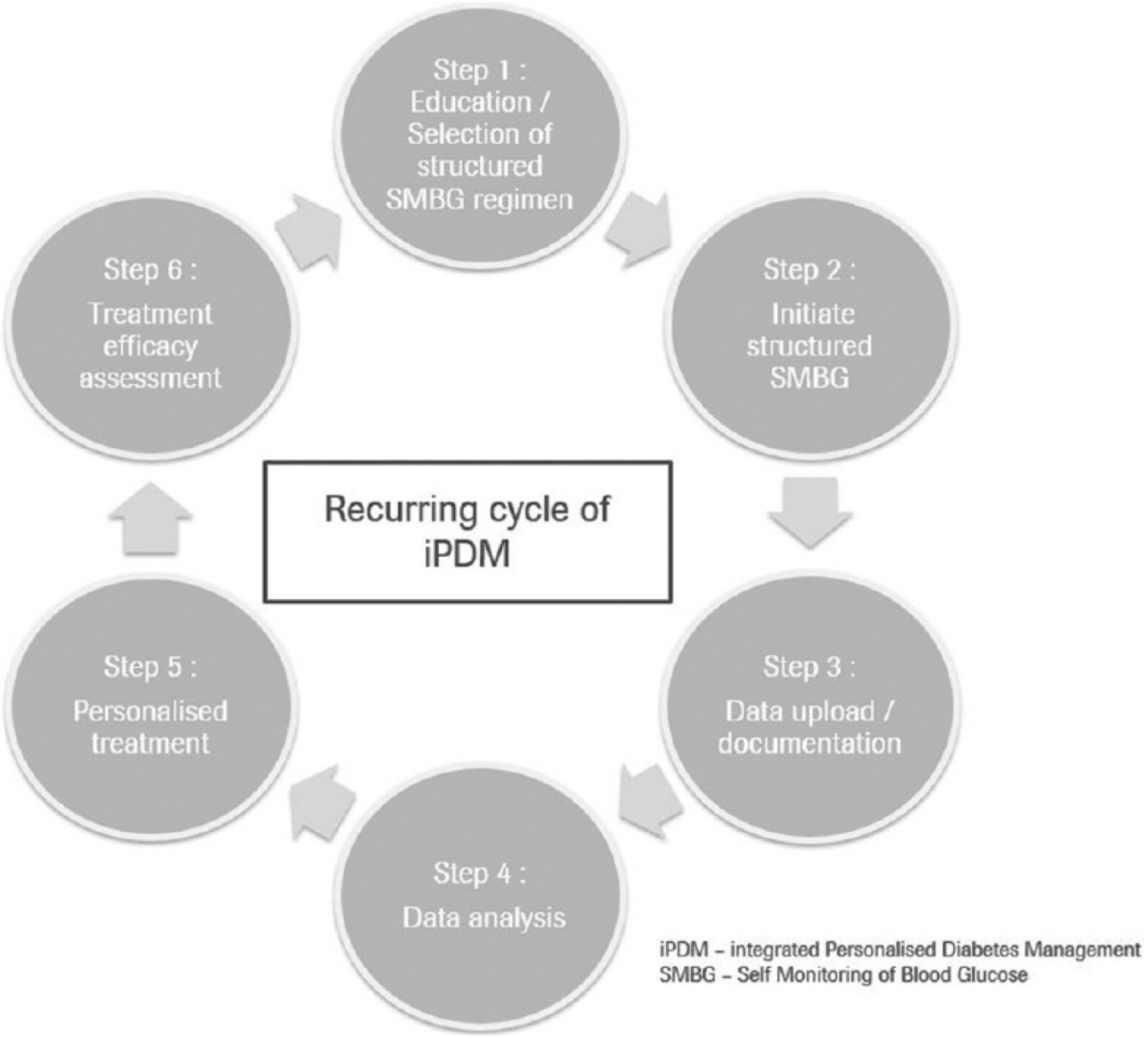

FIGURE 14
Depicts the Cycle of Integrated Personalized Diabetes Management, which comprises six iterative steps and forms a continuous revolving circle, applicable to each patient over differing timeframes. Reproduced with permission from Kalra et al. (2022).

management of chronic ailments, including diabetes and cardiovascular conditions. Additionally, the emergence of mobile applications that connect with biosensors empowers patients to conveniently monitor their health metrics, thus promoting greater involvement in their own care (Gecili et al., 2020). The future of biosensors is poised to enhance patient outcomes and healthcare efficiency through the provision of actionable insights derived from real-time data analysis.

The shift towards personalized medicine signifies a groundbreaking approach within healthcare, particularly regarding biomaterials. Individual patients exhibit variability in their financial resources and a range of personal factors. A systematic analysis conducted by Maria et al. revealed no statistically significant differences in HbA1c values among patients with type 1, type 2, or gestational diabetes when utilizing different diabetes monitoring systems (DMS). Future endeavors in personalized medicine will necessitate more extensive research to assess the effectiveness, cost-effectiveness, and comparative efficacy of DMS, allowing for stratification into the most suitable subgroups of diabetic patients (Kamusheva et al., 2021). Table 4 lists some diabetes management systems that have obtained clinical approval. By customizing treatments to individual patient profiles, which include genetic, environmental, and lifestyle factors, healthcare providers can enhance therapeutic outcomes and reduce adverse effects (Kalra et al., 2022). This concept is illustrated in Figure 14. The incorporation of artificial intelligence and machine learning into the analysis of patient data can substantially improve the accuracy of personalized treatment strategies (Clinton and Cross, 2023).

Nevertheless, challenges still exist in terms of the accessibility of personalized therapies and the need for solid clinical evidence to support their efficacy across diverse populations (Varela-Moreno et al., 2021). Future research must concentrate on developing scalable models for personalized interventions that can be effectively implemented in clinical practice, ensuring that all patients can benefit from these advancements (Chen et al., 2024c; Huckvale et al., 2019; Lydiard and Nemeroff, 2019).

5.3 Importance of multidisciplinary collaboration

Multidisciplinary collaboration is essential for tackling the intricate challenges associated with the development and execution of biomaterials and personalized treatments. By uniting expertise from various fields, including engineering, biology, medicine, and data science, researchers can foster innovation and accelerate the application of scientific breakthroughs in clinical settings. Effective collaboration not only enhances research quality but also addresses the complex dimensions of health issues, leading to more holistic solutions (Errecaborde et al., 2019). For instance, collaborative initiatives in bioimage analysis have demonstrated the potential to enhance diagnostic precision and treatment planning (Schlaeppi et al., 2022). Furthermore, establishing standards for interprofessional collaboration can improve communication and cooperation among healthcare providers, ultimately leading to better patient outcomes (Bowman et al., 2021). As the healthcare landscape evolves, nurturing a culture of collaboration will be critical in overcoming obstacles and advancing the disciplines of biomaterials and personalized medicine.

6 Conclusion

The prevalence of diabetes, a prevalent metabolic disorder, is escalating globally. Conventional treatment modalities, such as pharmacological interventions and lifestyle modifications, often fall short of achieving optimal glycemic control due to issues like poor patient adherence and complex treatment protocols. There is an urgent need for innovative approaches.

The integration of multidisciplinary strategies will be vital for advancing biomedical research in the future. By merging perspectives from materials science, biomedical engineering, and clinical medicine, researchers can devise innovative solutions to tackle the multifaceted challenges posed by diabetes. Biomaterials encounter hurdles such as immune rejection, biocompatibility, and high costs in diabetes management applications. It is imperative to synthesize these findings through systematic reviews and meta-analyses, which can elucidate which materials and delivery systems are most likely to yield favorable outcomes for patients. This collaborative effort can facilitate the design of biomaterials that not only enhance insulin delivery and foster tissue regeneration but also prioritize patient safety and comfort.

In the future, it is necessary to strengthen research on the safety and effectiveness of biomaterials and establish standardized evaluation protocols; promote personalized treatment and formulate precise treatment plans according to individual differences of patients; strengthen multidisciplinary cooperation and promote the transformation of biomaterials from laboratory to clinic to improve the treatment effect and quality of life of diabetic patients.

Author contributions

WG: Writing–original draft. LZ: Writing–review and editing.

Funding

The author(s) declare that no financial support was received for the research, authorship, and/or publication of this article.

Conflict of interest

The authors declare that the research was conducted in the absence of any commercial or financial relationships that could be construed as a potential conflict of interest.

Generative AI statement

The author(s) declare that no Generative AI was used in the creation of this manuscript.

Publisher's note

All claims expressed in this article are solely those of the authors and do not necessarily represent those of their affiliated organizations, or those of the publisher, the editors and the reviewers. Any product that may be evaluated in this article, or claim that may be made by its manufacturer, is not guaranteed or endorsed by the publisher.

References

Abozaid, O., El-Sonbaty, S. M., Hamam, N., Farrag, M. A., and Kodous, A. S. (2023). Chitosan-encapsulated nano-selenium targeting TCF7L2, PPARγ, and CAPN10 genes in diabetic rats. *Biol. Trace Elem. Res.* 201, 306–323. doi:10.1007/s12011-022-03140-7

Amirouche, F., Zhou, Y., and Johnson, T. (2009). Current micropump technologies and their biomedical applications. *Micro. Techno.* 15, 647–666. doi:10.1007/s00542-009-0804-7

Abdollahi, A., Aghayan, H.R., Mousivand, Z., Motasadizadeh, H., Maghsoudian, S., Abdorashidi, M., et al. (2024b). Chitosan based extruded nanofibrous bioscaffold for local delivery of mesenchymal stem cells to improve diabetic wound healing. *Stem Cell. Res. Ther.* 15, 262. doi:10.1186/s13287-024-03772-7

Ahmadian, N., Manickavasagan, A., and Ali, A. (2023). Comparative assessment of blood glucose monitoring techniques: a review. *J. Med. Eng. Technol.* 47, 121–130. doi:10.1080/03091902.2022.2100496

Akcan, R., Aydogan, H. C., Yildirim, M. S., Tastekin, B., and Saglam, N. (2020). Nanotoxicity: a challenge for future medicine. *Turk J. Med. Sci.* 50, 1180–1196. doi:10.3906/sag-1912-209

Aldahish, A., Shanmugasundaram, N., Vasudevan, R., Alqahtani, T., Alqahtani, S., Mohammad, A. A., et al. (2024). Silk fibroin nanofibers: advancements in bioactive dressings through electrospinning technology for diabetic wound healing. *Pharm. (Basel)* 17, 1305. doi:10.3390/ph17101305

Ali, A., Nouseen, S., Saroj, S., Shegane, M., Majumder, P., Puri, A., et al. (2022). Repurposing pinacol esters of boronic acids for tuning viscoelastic properties of glucose-responsive polymer hydrogels: effects on insulin release kinetics. *J. Mater Chem. B* 10, 7591–7599. doi:10.1039/d2tb00603k

Ali, A., Saroj, S., Saha, S., Gupta, S. K., Rakshit, T., and Pal, S. (2023). Glucose-responsive chitosan nanoparticle/poly (vinyl alcohol) hydrogels for sustained insulin release *in vivo*. *Acs Appl. Mater Interfaces* 15, 32240–32250. doi:10.1021/acsami.3c05031

Ali, H. S., York, P., and Blagden, N. (2009). Preparation of hydrocortisone nanosuspension through a bottom-up nanoprecipitation technique using microfluidic reactors. *Int. J. Pharm.* 375, 107–113. doi:10.1016/j.ijpharm.2009.03.029

Ali, Y., and Lehmussaari, K. (2006). Industrial perspective in ocular drug delivery. *Adv. Drug Deliv. Rev.* 58, 1258–1268. doi:10.1016/j.addr.2006.07.022

Al-Qerem, W., Jarab, A. S., Badinjki, M., Hammad, A., Ling, J., and Alasmari, F. (2022). Factors associated with glycemic control among patients with type 2 diabetes: a cross-sectional study. *Eur. Rev. Med. Pharmacol. Sci.* 26, 2415–2421. doi:10.26355/eurrev_202204_28475

Alven, S., Nqoro, X., and Aderibigbe, B. A. (2020). Polymer-based materials loaded with curcumin for wound healing applications. *Polym. (Basel)* 12, 2286. doi:10.3390/polym12102286

American Diabetes Association (2014). Diagnosis and classification of diabetes mellitus. *Diabetes Care* 37 (Suppl. 1), S81–S90. doi:10.2337/dc14-S081

Andrews, K. L., Houdek, M. T., and Kiemele, L. J. (2015). Wound management of chronic diabetic foot ulcers: from the basics to regenerative medicine. *Prosthet. Orthot. Int.* 39, 29–39. doi:10.1177/0309364614534296

Annicchiarico, A., Barile, B., Buccoliero, C., Nicchia, G. P., and Brunetti, G. (2024). Alternative therapeutic strategies in diabetes management. *World J. Diabetes* 15, 1142–1161. doi:10.4239/wjd.v15.i6.1142

Ansari, H. R., Kordrostami, Z., Mirzaei, A., and Kraft, M. (2024). Deep-learning-based blood glucose detection device using acetone exhaled breath sensing features of α-Fe_2O_3-MWCNT nanocomposites. *Acs Appl. Mater Interfaces* 16, 47973–47987. doi:10.1021/acsami.4c06855

Ansari, M., and Darvishi, A. (2024). A review of the current state of natural biomaterials in wound healing applications. *Front. Bioeng. Biotechnol.* 12, 1309541. doi:10.3389/fbioe.2024.1309541

Arrizabalaga, J. H., and Nollert, M. U. (2018). Human amniotic membrane: a versatile scaffold for tissue engineering. *Acs Biomater. Sci. Eng.* 4, 2226–2236. doi:10.1021/acsbiomaterials.8b00015

Arun, S., Sykes, E. R., and Tanbeer, S. (2024). Remotehealthconnect: innovating patient monitoring with wearable technology and custom visualization. *Digit. Health* 10, 20552076241300748. doi:10.1177/20552076241300748

Asadi, M. R., and Torkaman, G. (2014). Bacterial inhibition by electrical stimulation. *Adv. Wound Care (New Rochelle)* 3, 91–97. doi:10.1089/wound.2012.0410

Azad, A., Altunbas, H. A., and Manguoglu, A. E. (2024). From islet transplantation to beta-cell regeneration: an update on beta-cell-based therapeutic approaches in type 1 diabetes. *Expert Rev. Endocrinol. Metab.* 19, 217–227. doi:10.1080/17446651.2024.2347263

Baek, J. S., So, J. W., Shin, S. C., and Cho, C. W. (2012). Solid lipid nanoparticles of paclitaxel strengthened by hydroxypropyl-β-cyclodextrin as an oral delivery system. *Int. J. Mol. Med.* 30, 953–959. doi:10.3892/ijmm.2012.1086

Baron, N., Passave, J., Guichardaz, B., and Cabodevila, G. (2008). Investigations of development process of high hollow beveled microneedles using a combination of icp rie and dicing saw. *Micro. Techno.* 14, 1475–1480. doi:10.1007/s00542-008-0596-1

Bagheri, B., Zarrintaj, P., Samadi, A., Zarrintaj, R., Ganjali, M. R., Saeb, M. R., et al. (2020). Tissue engineering with electrospun electro-responsive chitosan-aniline oligomer/polyvinyl alcohol. *Int. J. Biol. Macromol.* 147, 160–169. doi:10.1016/j.ijbiomac.2019.12.264

Bai, Q., Han, K., Dong, K., Zheng, C., Zhang, Y., Long, Q., et al. (2020). Potential applications of nanomaterials and technology for diabetic wound healing. *Int. J. Nanomedicine* 15, 9717–9743. doi:10.2147/IJN.S276001

Barhoum, A., Garcia-Betancourt, M. L., Jeevanandam, J., Hussien, E. A., Mekkawy, S. A., Mostafa, M., et al. (2022). Review on natural, incidental, bioinspired, and engineered nanomaterials: history, definitions, classifications, synthesis, properties, market, toxicities, risks, and regulations. *Nanomater. (Basel)* 12, 177. doi:10.3390/nano12020177

Bent, B., Wang, K., Grzesiak, E., Jiang, C., Qi, Y., Jiang, Y., et al. (2020). The digital biomarker discovery pipeline: an open-source software platform for the development of digital biomarkers using mhealth and wearables data. *J. Clin. Transl. Sci.* 5, e19. doi:10.1017/cts.2020.511

Bhatti, P. K., Ghay, R., Singh, N. G., Thaman, V., and Narang, S. (2024). Estimation of hba1c levels in transfusion-dependent thalassemia patients in comparison with normal healthy individuals. *Cureus* 16, e73236. doi:10.7759/cureus.73236

Bigham, A., Zarepour, A., Khosravi, A., Iravani, S., and Zarrabi, A. (2025). Microneedle patches: a new vantage point for diabetic wound treatments. *Biomater. Sci.* 13, 379–407. doi:10.1039/d4bm01229a

Blagden, N., de Matas, M., Gavan, P. T., and York, P. (2007). Crystal engineering of active pharmaceutical ingredients to improve solubility and dissolution rates. *Adv. Drug Deliv. Rev.* 59, 617–630. doi:10.1016/j.addr.2007.05.011

Boucheta, H., Zouaoui, E., Ferkous, H., Madaci, A., Yadav, K. K., and Benguerba, Y. (2024). Advancing diabetes management: the future of enzyme-less nanoparticle-based glucose sensors-a review. *J. Diabetes Sci. Technol.* 570845427, 19322968241236211. doi:10.1177/19322968241236211

Boushra, M., Tous, S., Fetih, G., Xue, H. Y., Tran, N. T., and Wong, H. L. (2016). Methocel-lipid hybrid nanocarrier for efficient oral insulin delivery. *J. Pharm. Sci.* 105, 1733–1740. doi:10.1016/j.xphs.2016.02.018

Bowman, K. S., Suarez, V. D., and Weiss, M. J. (2021). Standards for interprofessional collaboration in the treatment of individuals with autism. *Behav. Anal. Pract.* 14, 1191–1208. doi:10.1007/s40617-021-00560-0

Burge, M. R. (2001). Lack of compliance with home blood glucose monitoring predicts hospitalization in diabetes. *Diabetes Care* 24, 1502–1503. doi:10.2337/diacare.24.8.1502

Cai, F., Chen, W., Zhao, R., and Liu, Y. (2023a). Mechanisms of Nrf2 and NF-κB pathways in diabetic wound and potential treatment strategies. *Mol. Biol. Rep.* 50, 5355–5367. doi:10.1007/s11033-023-08392-7

Cai, H., and Li, G. (2020). Efficacy of alginate-and chitosan-based scaffolds on the healing of diabetic skin wounds in animal experimental models and cell studies: a systematic review. *Wound Repair Regen.* 28, 751–771. doi:10.1111/wrr.12857

Cai, Y., Xu, X., Wu, M., Liu, J., Feng, J., and Zhang, J. (2023b). Multifunctional zwitterionic microneedle dressings for accelerated healing of chronic infected wounds in diabetic rat models. *Biomater. Sci.* 11, 2750–2758. doi:10.1039/d2bm02101c

Cano-Ibanez, N., and Bueno-Cavanillas, A. (2024). Lifestyle interventions in an aged population: challenges and opportunities from a public health perspective. *Nutrients* 16, 173. doi:10.3390/nu16010173

Carvalho, A. M., Nunes, R., and Sarmento, B. (2022). From pluripotent stem cells to bioengineered islets: a challenging journey to diabetes treatment. *Eur. J. Pharm. Sci.* 172, 106148. doi:10.1016/j.ejps.2022.106148

Chakraborty, C., Bhattacharya, M., and Lee, S. S. (2023). Currentstatus of microneedle array technology for therapeutic delivery: from bench to clinic. *Mol. Biotechnol.* 66, 3415–3437. doi:10.1007/s12033-023-00961-2

Chan, D., Maikawa, C. L., D'Aquino, A. I., Raghavan, S. S., Troxell, M. L., and Appel, E. A. (2023). Polyacrylamide-based hydrogel coatings improve biocompatibility of implanted pump devices. *J. Biomed. Mater Res. A* 111, 910–920. doi:10.1002/jbm.a.37521

Chaudhury, A., Duvoor, C., Reddy, D. V., Kraleti, S., Chada, A., Ravilla, R., et al. (2017). Clinical review of antidiabetic drugs: implications for type 2 diabetes mellitus management. *Front. Endocrinol. (Lausanne)* 8, 6. doi:10.3389/fendo.2017.00006

Chen, A. C., Lu, Y., Hsieh, C. Y., Chen, Y. S., Chang, K. C., and Chang, D. H. (2024a). Advanced biomaterials and topical medications for treating diabetic foot ulcers: a systematic review and network meta-analysis. *Adv. Wound Care (New Rochelle)* 13, 97–113. doi:10.1089/wound.2023.0024

Ciatti, C., Maniscalco, P., Bosio, S., Puma, P.C., Bianchi, G., and Quattrini, F. (2024). Pseudotumor from ceramic-on-ceramic total hip arthroplasty. *Int. J. Surg. Case. Rep.* 116, 109374. doi:10.1016/j.ijscr.2024.109374

Chen, X., Li, X., Xiao, X., Long, R., Chen, B., Lin, Y., et al. (2024d). Photothermal and antibacterial pda@ag/serma microneedles for promoting diabetic wound repair. *Acs. Appl. Bio. Mater.* 7, 6603–6616. doi:10.1021/acsabm.4c00793

Chen, F., Wu, P., Zhang, H., and Sun, G. (2024b). Signaling pathways triggering therapeutic hydrogels in promoting chronic wound healing. *Macromol. Biosci.* 24, e2300217. doi:10.1002/mabi.202300217

Chen, F. M., and Liu, X. (2016). Advancing biomaterials of human origin for tissue engineering. *Prog. Polym. Sci.* 53, 86–168. doi:10.1016/j.progpolymsci.2015.02.004

Chen, L., Sleeman, K. E., Bradshaw, A., Sakharang, W., Mo, Y., and Ellis-Smith, C. (2024c). The use of person-centered outcome measures to support integrated palliative care for older people: a systematic review. *J. Am. Med. Dir. Assoc.* 25, 105036. doi:10.1016/j.jamda.2024.105036

Chen, Q., Bao, K., Wang, X., and Chen, J. (2018). Recombinant fusion protein of lysozyme-antibacterial peptide for diabetic hand:clinical experience in one case. *Chin. General Pract.* 5, 620–622. doi:10.3969/j.issn.1007-9572.2017.00.211

Chen, S., Matsumoto, H., Moro-Oka, Y., Tanaka, M., Miyahara, Y., Suganami, T., et al. (2019). Smart microneedle fabricated with silk fibroin combined semi-interpenetrating network hydrogel for glucose-responsive insulin delivery. *Acs Biomater. Sci. Eng.* 5, 5781–5789. doi:10.1021/acsbiomaterials.9b00532

Chen, X., Li, X., Xiao, X., Long, R., Chen, B., Lin, Y., et al. (2024d). Photothermal and antibacterial pda@ag/serma microneedles for promoting diabetic wound repair. *Acs Appl. Bio Mater* 7, 6603–6616. doi:10.1021/acsabm.4c00793

Chen, X., Shen, J., Liu, C., Shi, X., Feng, W., Sun, H., et al. (2024e). Applications of data characteristic ai-assisted Raman spectroscopy in pathological classification. *Anal. Chem.* 96, 6158–6169. doi:10.1021/acs.analchem.3c04930

Chen, Y., Xie, T., Ye, M., Lai, Q., Wang, Y., Xu, Y., et al. (2021). Combination of pathological and spectroscopic characterization to promote diagnosis of retinal pigment epithelium-bruch's membrane complex in a diabetic rat model. *Biomed. Opt. Express* 12, 2221–2235. doi:10.1364/BOE.419716

Cheng, H., Guo, S., Cui, Z., Zhang, X., Huo, Y., Guan, J., et al. (2021). Design of folic acid decorated virus-mimicking nanoparticles for enhanced oral insulin delivery. *Int. J. Pharm.* 596, 120297. doi:10.1016/j.ijpharm.2021.120297

Chinese Society of Endocrinology, China Endocrinology and Metabolism Specialist Alliance (2024). Expert consensus on wound treatment of diabetic foot ulcer. *Chin. J. Endocrinol. Metabolism* 7, 565–569. doi:10.3760/cma.j.cn311282-20240625-00281

Chu, J., Shi, P., Yan, W., Fu, J., Yang, Z., He, C., et al. (2018). Pegylated graphene oxide-mediated quercetin-modified collagen hybrid scaffold for enhancement of mscs differentiation potential and diabetic wound healing. *Nanoscale* 10, 9547–9560. doi:10.1039/c8nr02538j

Childs, A., Mayol, B., Lasalde-Ramirez, J.A., Song, Y., Sempionatto, J.R., and Gao, W. (2024). Diving into sweat: advances, challenges, and future directions in wearable sweat sensing. *Acs. Nano.* 18, 24605–24616. doi:10.1021/acsnano.4c10344

Clinton, J. W., and Cross, R. K. (2023). Personalized treatment for crohn's disease: current approaches and future directions. *Clin. Exp. Gastroenterol.* 16, 249–276. doi:10.2147/CEG.S360248

Condren, M., Sabet, S., Chalmers, L. J., Saley, T., and Hopwood, J. (2019). Technology for augmenting type 1 diabetes mellitus management. *J. Pediatr. Pharmacol. Ther.* 24, 99–106. doi:10.5863/1551-6776-24.2.99

Dariya, B., Chalikonda, G., Srivani, G., Alam, A., and Nagaraju, G. P. (2019). Pathophysiology, etiology, epidemiology of type 1 diabetes and computational approaches for immune targets and therapy. *Crit. Rev. Immunol.* 39, 239–265. doi:10.1615/CritRevImmunol.2019033126

Das, P., Manna, S., Roy, S., Nandi, S. K., and Basak, P. (2023). Polymeric biomaterials-based tissue engineering for wound healing: a systemic review. *Burns Trauma* 11, tkac058. doi:10.1093/burnst/tkac058

Defronzo, R. A. (2009). From the triumvirate to the ominous octet: a new paradigm for the treatment of type 2 diabetes mellitus. *Diabetes* 58, 773–795. doi:10.2337/db09-9028

Deng, Z., Davis, J., Muniz-Rodriguez, F., and Richardson, F. (2018). Successful management of poorly controlled type 2 diabetes with multidisciplinary neurobehavioral rehabilitation: a case report and review. *Diabetes Ther.* 9, 1713–1718. doi:10.1007/s13300-018-0448-7

Deng, X., Gould, M., and Ali, M. A. (2022). A review of current advancements for wound healing: biomaterial applications and medical devices. *J Biomed Mater Res B Appl Biomater* 110, 2542–2573. doi:10.1002/jbm.b.35086

Dervisevic, M., Alba, M., Esser, L., Tabassum, N., Prieto-Simon, B., and Voelcker, N. H. (2022). Silicon micropillar array-based wearable sweat glucose sensor. *Acs Appl. Mater Interfaces* 14, 2401–2410. doi:10.1021/acsami.1c22383

Desai, A., Tankasala, D., Ng, G. P., Thakkar, P., Hoilett, O. S., Mather, K. J., et al. (2025). Selective collection of exhaled breath condensate for noninvasive screening of breath glucose. *J. Diabetes Sci. Technol.* 19, 161–164. doi:10.1177/19322968231179728

Du, Y., Zhang, X., Liu, P., Yu, D. G., and Ge, R. (2022). Electrospun nanofiber-based glucose sensors for glucose detection. *Front. Chem.* 10, 944428. doi:10.3389/fchem.2022.944428

Dua, A., Debnath, A., Kumar, K., Mazumder, R., Mazumder, A., Singh, R., et al. (2024). Advancements of glucose monitoring biosensor: current state, generations of technological progress, and innovation dynamics. *Curr. Pharm. Biotechnol.* 25. doi:10.2174/0113892010305386240625072535

Emad, N. A., Zai, I., Ahmad, S., Pandit, J., Khan, M. A., and Sultana, Y. (2024). Role of polyphenols, their nano-formulations, and biomaterials in diabetic wound healing. *Endocr. Metab. Immune Disord. Drug Targets* 24, 626–641. doi:10.2174/0118715303242310230927104709

Ernst, A.U., Wang, L.H., and Ma, M. (2019). Interconnected toroidal hydrogels for islet encapsulation. *Adv Healthc Mater* 8, e1900423. doi:10.1002/adhm.201900423

Errecaborde, K. M., Rist, C., Travis, D. A., Ragan, V., Potter, T., Pekol, A., et al. (2019). Evaluating one health: the role of team science in multisectoral collaboration. *Rev. Sci. Tech.* 38, 279–289. doi:10.20506/rst.38.1.2960

Esmaeili, A., Biazar, E., Ebrahimi, M., Heidari, K. S., Kheilnezhad, B., and Saeedi, L. F. (2023). Acellular fish skin for wound healing. *Int. Wound J.* 20, 2924–2941. doi:10.1111/iwj.14158

Esteves, C., Palma, S., Costa, H., Alves, C., Santos, G., Ramou, E., et al. (2022). Tackling humidity with designer ionic liquid-based gas sensing soft materials. *Adv. Mater* 34, e2107205. doi:10.1002/adma.202107205

Fadilah, N., Isa, I., Zaman, W., Tabata, Y., and Fauzi, M. B. (2022). The effect of nanoparticle-incorporated natural-based biomaterials towards cells on activated pathways: a systematic review. *Polym. (Basel)* 14, 476. doi:10.3390/polym14030476

Fahimirad, S., and Ajalloueian, F. (2019). Naturally-derived electrospun wound dressings for target delivery of bio-active agents. *Int. J. Pharm.* 566, 307–328. doi:10.1016/j.ijpharm.2019.05.053

Fan, W., Yang, X., Hu, X., Huang, R., Shi, H., and Liu, G. (2024). A novel conductive microtubule hydrogel for electrical stimulation of chronic wounds based on biological electrical wires. *J. Nanobiotechnology* 22, 258. doi:10.1186/s12951-024-02524-2

Firoozbahr, M., Kingshott, P., Palombo, E. A., and Zaferanloo, B. (2023). Recent advances in using natural antibacterial additives in bioactive wound dressings. *Pharmaceutics* 15, 644. doi:10.3390/pharmaceutics15020644

Flores-Guerrero, J. L., Munoz-Morales, A., Narea-Jimenez, F., Perez-Fuentes, R., Torres-Rasgado, E., Ruiz-Vivanco, G., et al. (2020). Novel assessment of urinary albumin excretion in type 2 diabetes patients by Raman spectroscopy. *Diagn. (Basel)* 10, 141. doi:10.3390/diagnostics10030141

Gupta, J., Felner, E. I., and Prausnitz, M. R. (2009). Minimally invasive insulin delivery in subjects with type 1 diabetes using hollow microneedles. *Diabetes Technol Ther* 11, 329–337. doi:10.1089/dia.2008.0103

Gecili, E., Huang, R., Khoury, J.C., King, E., Altaye, M., Bowers, K., et al. (2020). Functional data analysis and prediction tools for continuous glucose-monitoring studies. *J. Clin. Transl. Sci.* 5, e51. doi:10.1017/cts.2020.545

Galassetti, P. R., Novak, B., Nemet, D., Rose-Gottron, C., Cooper, D. M., Meinardi, S., et al. (2005). Breath ethanol and acetone as indicators of serum glucose levels: an initial report. *Diabetes Technol. Ther.* 7, 115–123. doi:10.1089/dia.2005.7.115

Ghasemi, A., and Norouzirad, R. (2019). Type 2 diabetes: an updated overview. *Crit. Rev. Oncog.* 24, 213–222. doi:10.1615/CritRevOncog.2019030976

Guo, L., Guan, N., Miao, W., Zhao, W., and Li, Q. (2022b). An electrospun scaffold loaded with an enteromorpha polysaccharide for accelerated wound healing in diabetic mice. *Mar. Drugs.* 20, 95. doi:10.3390/md20020095

Goonoo, N. (2022). Tunable biomaterials for myocardial tissue regeneration: promising new strategies for advanced biointerface control and improved therapeutic outcomes. *Biomater. Sci.* 10, 1626–1646. doi:10.1039/d1bm01641e

Govindaraj, M., Srivastava, A., Muthukumaran, M. K., Tsai, P. C., Lin, Y. C., Raja, B. K., et al. (2023). Current advancements and prospects of enzymatic and non-enzymatic electrochemical glucose sensors. *Int. J. Biol. Macromol.* 253, 126680. doi:10.1016/j.ijbiomac.2023.126680

Guan, Y., Li, X., Yang, H., Yang, Y., Du, Z., Hua, Z., et al. (2025). Pore-edge high active sites of 2d wo (3) nanosheets enhancing acetone sensing performance. *Talanta* 282, 127003. doi:10.1016/j.talanta.2024.127003

Han, H. H., Kim, S. K., Kim, S. J., Choi, I., Mok, J. W., Joo, C. K., et al. (2023). Long-term stable wireless smart contact lens for robust digital diabetes diagnosis. *Biomaterials* 302, 122315. doi:10.1016/j.biomaterials.2023.122315

Hao, L., Khajouei, F., Rodriguez, J., Kim, S., and Lee, E. (2024a). Unlocking the promise of decellularized pancreatic tissue: a novel approach to support angiogenesis in engineered tissue. *Bioeng. (Basel)* 11, 183. doi:10.3390/bioengineering11020183

Hao, X., Yu, T., Meng, X., Wei, C., Wang, Y., Sun, S., et al. (2024b). Efficient mixed-potential acetone sensor with yttria-stabilized zirconia and porous co (3)o(4) nanofoam sensing electrode for hazardous gas monitoring and breath analysis. *J. Hazard Mater* 478, 135462. doi:10.1016/j.jhazmat.2024.135462

He, Y., Liu, K., Guo, S., Chang, R., Zhang, C., Guan, F., et al. (2023). Multifunctional hydrogel with reactive oxygen species scavenging and photothermal antibacterial activity accelerates infected diabetic wound healing. *Acta Biomater.* 155, 199–217. doi:10.1016/j.actbio.2022.11.023

Hina, A., and Saadeh, W. (2020). A noninvasive glucose monitoring soc based on single wavelength photoplethysmography. *Ieee Trans. Biomed. Circuits Syst.* 14, 504–515. doi:10.1109/TBCAS.2020.2979514

Heidari, F., Yari, A., Teimourian, S., Joulai, V.S., and Nobakht, M. (2023). Effects of hair follicle stem cells coupled with polycaprolactone scaffold on cutaneous wound healing in diabetic male rats. *J. Surg. Res.* 281, 200–213. doi:10.1016/j.jss.2022.08.008

Hong, C., Chung, H., Lee, G., Kim, C., Kim, D., Oh, S. J., et al. (2023). Hydrogel/nanofiber composite wound dressing optimized for skin layer regeneration through the mechanotransduction-based microcellular environment. *Acs Appl. Bio Mater* 6, 1774–1786. doi:10.1021/acsabm.3c00014

Hong, Y., Yu, H., Wang, L., Chen, X., Huang, Y., Yang, J., et al. (2022). Transdermal insulin delivery and microneedles-based minimally invasive delivery systems. *Curr. Pharm. Des.* 28, 3175–3193. doi:10.2174/1381612828666220608130056

Hu, T., Fang, J., Shen, Y., Li, M., Wang, B., Xu, Z., et al. (2024a). Advances of naturally derived biomedical polymers in tissue engineering. *Front. Chem.* 12, 1469183. doi:10.3389/fchem.2024.1469183

Hu, Y., Xiong, Y., Tao, R., Xue, H., Chen, L., Lin, Z., et al. (2022). Advances and perspective on animal models and hydrogel biomaterials for diabetic wound healing. *Biomater. Transl.* 3, 188–200. doi:10.12336/biomatertransl.2022.03.003

Hu, Y. W., Wang, Y. H., Yang, F., Liu, D. X., Lu, G. H., Li, S. T., et al. (2024b). Flexible organic photovoltaic-powered hydrogel bioelectronic dressing with biomimetic electrical stimulation for healing infected diabetic wounds. *Adv. Sci. (Weinh)* 11, e2307746. doi:10.1002/advs.202307746

Huang, C., Yuan, W., Chen, J., Wu, L. P., and You, T. (2023). Construction of smart biomaterials for promoting diabetic wound healing. *Molecules* 28, 1110. doi:10.3390/molecules28031110

Huckvale, K., Venkatesh, S., and Christensen, H. (2019). Toward clinical digital phenotyping: a timely opportunity to consider purpose, quality, and safety. *Npj Digit. Med.* 2, 88. doi:10.1038/s41746-019-0166-1

Hwang, S. I., Chen, H. Y., Fenk, C., Rothfuss, M. A., Bocan, K. N., Franconi, N. G., et al. (2021). Breath acetone sensing based on single-walled carbon nanotube-titanium dioxide hybrids enabled by a custom-built dehumidifier. *Acs Sens.* 6, 871–880. doi:10.1021/acssensors.0c01973

Iitani, K., Ishizuki, N., Matsuhashi, Y., Yokota, K., Ichikawa, K., Toma, K., et al. (2024). Biofluorometric acetone gas sensor of sub-ppbv level sensitivity. *Anal. Chem.* 96, 20197–20203. doi:10.1021/acs.analchem.4c03816

Iqbal, S., Sohail, M., Fang, S., Ding, J., Shen, L., Chen, M., et al. (2023). Biomaterials evolution: from inert to instructive. *Biomater. Sci.* 11, 6109–6115. doi:10.1039/d3bm00322a

Jagannathan, M., Dhinasekaran, D., Rajendran, A. R., and Cho, S. (2023). A review of electroactive nanomaterials in the detection of nitrogen-containing organic compounds and future applications. *Biosens. (Basel)* 13, 989. doi:10.3390/bios13110989

Jarosinski, M. A., Dhayalan, B., Rege, N., Chatterjee, D., and Weiss, M. A. (2021). 'smart' insulin-delivery technologies and intrinsic glucose-responsive insulin analogues. *Diabetologia* 64, 1016–1029. doi:10.1007/s00125-021-05422-6

Jeong, G. J., Khan, S., Tabassum, N., Khan, F., and Kim, Y. M. (2022). Marine-bioinspired nanoparticles as potential drugs for multiple biological roles. *Mar. Drugs* 20, 527. doi:10.3390/md20080527

Jiang, L., Shen, Y., Liu, Y., Zhang, L., and Jiang, W. (2022). Making human pancreatic islet organoids: progresses on the cell origins, biomaterials and three-dimensional technologies. *Theranostics* 12, 1537–1556. doi:10.7150/thno.66670

Jiang, L., Wang, C., Fan, T., Lv, S., Pan, S., Sun, P., et al. (2024). Mixed potential type acetone sensor with ultralow detection limit for diabetic ketosis breath analysis. *Acs Sens.* 9, 464–473. doi:10.1021/acssensors.3c02253

Jiang, P., Li, Q., Luo, Y., Luo, F., Che, Q., Lu, Z., et al. (2023). Currentstatus and progress in research on dressing management for diabetic foot ulcer. *Front. Endocrinol. (Lausanne)* 14, 1221705. doi:10.3389/fendo.2023.1221705

Jin, X., Zhu, D. D., Chen, B. Z., Ashfaq, M., and Guo, X. D. (2018). Insulin delivery systems combined with microneedle technology. *Adv. Drug Deliv. Rev.* 127, 119–137. doi:10.1016/j.addr.2018.03.011

Jing, S., Li, H., and Xu, H. (2023). Mesenchymal stem cell derived exosomes therapy in diabetic wound repair. *Int. J. Nanomedicine* 18, 2707–2720. doi:10.2147/IJN.S411562

Josyula, A., Parikh, K. S., Pitha, I., and Ensign, L. M. (2021). Engineering biomaterials to prevent post-operative infection and fibrosis. *Drug Deliv. Transl. Res.* 11, 1675–1688. doi:10.1007/s13346-021-00955-0

K, S. K., Jothimani, D., Manoharan, M., Rela, M., Selvaraj, R., Seshadri, S., et al. (2025). Quartz-enhanced photoacoustic spectroscopy-based acetone and ammonia measurements from human breath near 8 μm wavelength band. *Acs. Sens.* doi:10.1021/acssensors.4c02336

Kalidoss, R., and Umapathy, S. (2019). An overview on the exponential growth of non-invasive diagnosis of diabetes mellitus from exhaled breath by nanostructured metal oxide chemi-resistive gas sensors and mu-preconcentrator. *Biomed. Microdevices* 22, 2. doi:10.1007/s10544-019-0448-z

Kalra, S., Bantwal, G., Sahay, R. K., Bhattacharya, S., Baruah, M. P., Sheikh, S., et al. (2022). Incorporating integrated personalised diabetes management (ipdm) in treatment strategy: a pragmatic approach. *Indian J. Endocrinol. Metab.* 26, 106–110. doi:10.4103/ijem.ijem_478_21

Kzhyshkowska, J., Gudima, A., Riabov, V., Dollinger, C., Lavalle, P., and Vrana, N.E. (2015). Macrophage responses to implants: prospects for personalized medicine. *J. Leukoc. Biol.* 98, 953–962. doi:10.1189/jlb.5VMR0415-166R

Kamusheva, M., Tachkov, K., Dimitrova, M., Mitkova, Z., Garcia-Saez, G., Hernando, M. E., et al. (2021). A systematic review of collective evidences investigating the effect of diabetes monitoring systems and their application in health care. *Front. Endocrinol. (Lausanne)* 12, 636959. doi:10.3389/fendo.2021.636959

Kantak, M. N., and Bharate, S. S. (2022). Analysis of clinical trials on biomaterial and therapeutic applications of chitosan: a review. *Carbohydr. Polym.* 278, 118999. doi:10.1016/j.carbpol.2021.118999

Karimi, M., Eslami, M., Sahandi-Zangabad, P., Mirab, F., Farajisafiloo, N., Shafaei, Z., et al. (2016). Ph-sensitive stimulus-responsive nanocarriers for targeted delivery of therapeutic agents. *Wiley Interdiscip. Rev. Nanomed Nanobiotechnol* 8, 696–716. doi:10.1002/wnan.1389

Kasputis, T., Clough, D., Noto, F., Rychel, K., Dye, B., and Shea, L. D. (2018). Microporous polymer scaffolds for the transplantation of embryonic stem cell derived pancreatic progenitors to a clinically translatable site for the treatment of type i diabetes. *Acs Biomater. Sci. Eng.* 4, 1770–1778. doi:10.1021/acsbiomaterials.7b00912

Kassem, M., Ali, A., Assal, M., and Badrawy, A. (2017). Formulation, characterization and *in vivo* application of oral insulin nanotechnology using different biodegradable polymers: advanced drug delivery system. *Int. J. Adv. Res. (Indore)* 5, 1028–1044. doi:10.21474/IJAR01/5863

Kaviani, M., and Azarpira, N. (2016). Insight into microenvironment remodeling in pancreatic endocrine tissue engineering: biological and biomaterial approaches. *Tissue Eng. Regen. Med.* 13, 475–484. doi:10.1007/s13770-016-0014-1

Khaiz, Y., Al, I. N., Bakkali, M., and Ahid, S. (2025). Association of the immunity genes with type 1 diabetes mellitus. *Curr. Diabetes Rev.* 21, 38–46. doi:10.2174/0115733998275617231218101116

Kim, J., Campbell, A. S., de Avila, B. E., and Wang, J. (2019). Wearable biosensors for healthcare monitoring. *Nat. Biotechnol.* 37, 389–406. doi:10.1038/s41587-019-0045-y

Kim, Y. C., Park, J. H., and Prausnitz, M. R. (2012). Microneedles for drug and vaccine delivery. *Adv. Drug Deliv. Rev.* 64, 1547–1568. doi:10.1016/j.addr.2012.04.005

Klangjareonchai, T., Eguchi, N., Tantisattamo, E., Ferrey, A. J., Reddy, U., Dafoe, D. C., et al. (2021). Current pharmacological intervention and medical management for diabetic kidney transplant recipients. *Pharmaceutics* 13, 413. doi:10.3390/pharmaceutics13030413

Knopf-Marques, H., Pravda, M., Wolfova, L., Velebny, V., Schaaf, P., Vrana, N. E., et al. (2016). Hyaluronic acid and its derivatives in coating and delivery systems: applications in tissue engineering, regenerative medicine and immunomodulation. *Adv. Healthc. Mater* 5, 2841–2855. doi:10.1002/adhm.201600316

Koh, W. L., Foster, T., Mooranian, A., and Al-Salami, H. (2022). Applications of bile acids as biomaterials-based modulators, in biomedical science and microfluidics. *Ther. Deliv.* 13, 591–604. doi:10.4155/tde-2022-0044

Kong, C., Guo, Z., Teng, T., Yao, Q., Yu, J., Wang, M., et al. (2024). Electroactive nanomaterials for the prevention and treatment of heart failure: from materials and mechanisms to applications. *Small* 20, e2406206. doi:10.1002/smll.202406206

Krauland, A. H., and Alonso, M. J. (2007). Chitosan/cyclodextrin nanoparticles as macromolecular drug delivery system. *Int. J. Pharm.* 340, 134–142. doi:10.1016/j.ijpharm.2007.03.005

Larijani, G., Parivar, K., Hayati, R. N., Yaghmaei, P., and Amini, N. (2024). Fortified electrospun collagen utilizing biocompatible poly glycerol sebacate prepolymer (pgsp) and zink oxide nanoparticles (zno nps) for diabetics wound healing: physical, biological and animal studies. *Regen. Ther.* 26, 102–113. doi:10.1016/j.reth.2024.05.009

Latham, J. (2019). The artificial pancreas: what school nurses need to know. *Nasn Sch. Nurse* 34, 86–89. doi:10.1177/1942602X18804491

Leng, T., Wang, Y., Cheng, W., Wang, W., Qu, X., and Lei, B. (2022). Bioactive anti-inflammatory antibacterial metformin-contained hydrogel dressing accelerating wound healing. *Biomater. Adv.* 135, 212737. doi:10.1016/j.bioadv.2022.212737

Li, Z., Hu, J., Yang, L., Zhang, X., Liu, X., Wang, Z., and Li, Y. (2020). Integrated poss-dendrimer nanohybrid materials: current status and future perspective. *Nanoscale* 12, 11395–11415. doi:10.1039/d0nr02394a

Li, R., Wei, X., Xu, J., Chen, J., Li, B., Wu, Z., and Wang, Z. L. (2021). Smart wearable sensors based on triboelectric nanogenerator for personal healthcare monitoring. *Micromachines (Basel)* 12. doi:10.3390/mi12040352

Li, Y., Yang, L., Hou, Y., Zhang, Z., Chen, M., Wang, M., et al. (2022). Polydopamine-mediated graphene oxide and nanohydroxyapatite-incorporated conductive scaffold with an immunomodulatory ability accelerates periodontal bone regeneration in diabetes. *Bioact Mater* 18, 213–217. doi:10.1016/j.bioactmat.2022.03.021

Li, S., Li, H., Lu, Y., Zhou, M., Jiang, S., Du, X., et al. (2023). Advanced textile-based wearable biosensors for healthcare monitoring. *Biosens. (Basel)* 13, 909. doi:10.3390/bios13100909

Li, W., Liu, Y., Lu, X., Huang, Y., Liu, Y., Cheng, S., et al. (2015). A cross-sectional study of breath acetone based on diabetic metabolic disorders. *J. Breath. Res.* 9, 016005. doi:10.1088/1752-7155/9/1/016005

Li, X., Jiang, X., Gao, F., Zhou, L., Wang, G., Li, B., et al. (2024). Study and evaluation of a gelatin-silver oxide nanoparticles releasing nitric oxide production of wound healing dressing for diabetic ulcer. *Plos One* 19, e0298124. doi:10.1371/journal.pone.0298124

Lim, J., Goh, L., Otake, K. I., Goh, S. S., Loh, X. J., and Kitagawa, S. (2023). Biomedically-relevant metal organic framework-hydrogel composites. *Biomater Sci.* 11, 2661–2677. doi:10.1039/d2bm01906j

Lin, H., Liu, J., Hou, Y., Yu, Z., Hong, J., Yu, J., et al. (2025a). Microneedle patch with pure drug tips for delivery of liraglutide: pharmacokinetics in rats and minipigs. *Drug Deliv. Transl. Res.* 15, 216–230. doi:10.1007/s13346-024-01582-1

Lin, L., and Pisano, A. P. (1999). Silicon-processed microneedles. *J. Microelectromech. Syst* 8, 78–84. doi:10.1109/84.749406

Lin, Y., Wu, J., Zhuang, Z., Gong, X., Jin, Z., Lin, X., et al. (2025b). A ph-responsive microneedle patch for the transdermal delivery of biomineralized insulin nanoparticles to diabetes treatment. *Int. J. Biol. Macromol.* 284, 137955. doi:10.1016/j.ijbiomac.2024.137955

Litra, D., Chiriac, M., Ababii, N., and Lupan, O. (2024). Acetone sensors based on al-coated and ni-doped copper oxide nanocrystalline thin films. *Sensors (Basel)* 24, 6550. doi:10.3390/s24206550

Loretelli, C., Assi, E., Seelam, A. J., Ben, N. M., and Fiorina, P. (2020). Cell therapy for type 1 diabetes. *Expert Opin. Biol. Ther.* 20, 887–897. doi:10.1080/14712598.2020.1748596

Luo, X., Yu, Q., Yang, L., and Cui, Y. (2023). Wearable, sensing-controlled, ultrasound-based microneedle smart system for diabetes management. *Acs Sens.* 8, 1710–1722. doi:10.1021/acssensors.2c02863

Lupascu, F. G., Sava, A., Tatarusanu, S. M., Iacob, A. T., Dascalu, A., Profire, B. S., et al. (2024). New chitosan-based co-delivery nanosystem for diabetes mellitus therapy. *Polym. (Basel)* 16, 1825. doi:10.3390/polym16131825

Lv, S., Zhang, S., Zuo, J., Liang, S., Yang, J., Wang, J., et al. (2023). Progress in preparation and properties of chitosan-based hydrogels. *Int. J. Biol. Macromol.* 242, 124915. doi:10.1016/j.ijbiomac.2023.124915

Lydiard, J., and Nemeroff, C. B. (2019). Biomarker-guided tailored therapy. *Adv. Exp. Med. Biol.* 1192, 199–224. doi:10.1007/978-981-32-9721-0_10

Maita, K. C., Avila, F. R., Torres-Guzman, R. A., Garcia, J. P., Eldaly, A. S., Palmieri, L., et al. (2022). Local anti-inflammatory effect and immunomodulatory activity of chitosan-based dressing in skin wound healing: a systematic review. *J. Clin. Transl. Res.* 8, 488–498.

Martanto, W., Moore, J. S., Kashlan, O., Kamath, R., Wang, P. M., and O'Neal, J. M. (2006). Microinfusion using hollow microneedles. *Pharm Res* 23, 104–113. doi:10.1007/s11095-005-8498-8

Mei, S., Yang, Y., and Wang, J. (2023). Synthesis of decellularized cartilage extracellular matrix hydrogels. *J. Vis. Exp.* doi:10.3791/64797

Memon, B., Elsayed, A. K., Bettahi, I., Suleiman, N., Younis, I., Wehedy, E., et al. (2022). Ipscs derived from insulin resistant offspring of type 2 diabetic patients show increased oxidative stress and lactate secretion. *Stem Cell Res. Ther.* 13, 428. doi:10.1186/s13287-022-03123-4

Mirbagheri, M. S., Akhavan-Mahdavi, S., Hasan, A., Kharazmi, M. S., and Jafari, S. M. (2023). Chitosan-based electrospun nanofibers for diabetic foot ulcer management; Recent advances. *Carbohydr. Polym.* 313, 120512. doi:10.1016/j.carbpol.2022.120512

Mohamed, A. A., Khater, S. I., Hamed, A. A., Metwally, M., Mostafa-Hedeab, G., and El-Shetry, E. S. (2021). Chitosan-stabilized selenium nanoparticles alleviate cardio-hepatic damage in type 2 diabetes mellitus model via regulation of caspase, bax/bcl-2, and fas/fasl-pathway. *Gene* 768, 145288. doi:10.1016/j.gene.2020.145288

Mohammad, K. A. (2024). Principles and biomedical applications of self-assembled peptides: potential treatment of type 2 diabetes mellitus. *Pharmaceutics* 16, 1442. doi:10.3390/pharmaceutics16111442

Morcol, T., Nagappan, P., Nerenbaum, L., Mitchell, A., and Bell, S. J. (2004). Calcium phosphate-peg-insulin-casein (capic) particles as oral delivery systems for insulin. *Int. J. Pharm.* 277, 91–97. doi:10.1016/j.ijpharm.2003.07.015

Moser, O., Zaharieva, D. P., Adolfsson, P., Battelino, T., Bracken, R. M., Buckingham, B. A., et al. (2025). The use of automated insulin delivery around physical activity and exercise in type 1 diabetes: a position statement of the european association for the study of diabetes (easd) and the international society for pediatric and adolescent diabetes (ispad). *Diabetologia* 68, 255–280. doi:10.1007/s00125-024-06308-z

Moses, R. L., Prescott, T., Mas-Claret, E., Steadman, R., Moseley, R., and Sloan, A. J. (2023). Evidence for natural products as alternative wound-healing therapies. *Biomolecules* 13, 444. doi:10.3390/biom13030444

Moon, S. J., Lee, S. S., Lee, H. S., and Kwon, T. H. (2005). Fabrication of microneedle array using liga and hot embossing process. *Micro. Techn.* 11, 311–318. doi:10.1007/s00542-004-0446-8

Metwally, W.M., El-Habashy, S.E., El-Hosseiny, L.S., Essawy, M.M., Eltaher, H.M., El-Khordagui, L.K., et al. (2023). Bioinspired 3d-printed scaffold embedding ddab-nano zno/nanofibrous microspheres for regenerative diabetic wound healing. *Biofabrication* 16, 015001. doi:10.1088/1758-5090/acfd60

Mukerjee, E.V., Collins, S.D., Isseroff, R.R., and Smith, R.L. (2015). Microneedle array for transdermal biological fluid extraction and in situ analysis. *Sensors & Actua. Phy.* 114, 267–275. doi:10.1016/j.sna.2003.11.008

Ma, B., Liu, S., Gan, Z., Liu, G., Cai, X., Zhang, H., et al. (2006). A pzt insulin pump integrated with a silicon microneedle array for transdermal drug delivery. *Microf. Nanoflu.* 2, 417–423. doi:10.1007/s10404-006-0083-x

Mousavi, S. M., Behbudi, G., Gholami, A., Hashemi, S. A., Nejad, Z. M., Bahrani, S., et al. (2022). Shape-controlled synthesis of zinc nanostructures mediating macromolecules for biomedical applications. *Biomater. Res.* 26, 4. doi:10.1186/s40824-022-00252-y

Na, E., Tao, S., Wang, W., Li, J., Guo, Y., Gao, R., et al. (2024). Ultrasensitive acetone gas sensor based on a k/sn-co (3)o(4) porous microsphere for noninvasive diabetes diagnosis. *Acs Sens.* 9, 6148–6156. doi:10.1021/acssensors.4c02009

Naahidi, S., Jafari, M., Logan, M., Wang, Y., Yuan, Y., Bae, H., et al. (2017). Biocompatibility of hydrogel-based scaffolds for tissue engineering applications. *Biotechnol. Adv.* 35, 530–544. doi:10.1016/j.biotechadv.2017.05.006

Nandhakumar, M., Gosala, R., and Subramanian, B. (2022). Invigorating chronic wound healing by nanocomposites composed with bioactive materials: a comprehensive review. *Biotechnol. Lett.* 44, 1243–1261. doi:10.1007/s10529-022-03303-5

Naranda, J., Bracic, M., Vogrin, M., and Maver, U. (2021). Recent advancements in 3d printing of polysaccharide hydrogels in cartilage tissue engineering. *Mater. (Basel)* 14, 3977. doi:10.3390/ma14143977

Nemati, M., Ebrahimi, Z., Karbalaei, N., Dastghaib, S., Khakshournia, S., and Sargazi, M. (2023). *In vitro* and *in vivo* improvement of islet quality and transplantation successes following islet treatment with biomaterials in diabetic rats. *J. Diabetes Res.* 2023, 1–14. doi:10.1155/2023/1399917

Ni, T., Dong, Z., Xi, K., Lu, Y., Chang, K., Ge, C., et al. (2024). Nitrogen-doped carbon quantum dots activated dandelion-like hierarchical wo (3) for highly sensitive and selective mems sensors in diabetes detection. *Acs Sens.* doi:10.1021/acssensors.4c01840

Nirenjen, S., Narayanan, J., Tamilanban, T., Subramaniyan, V., Chitra, V., Fuloria, N. K., et al. (2023). Exploring the contribution of pro-inflammatory cytokines to impaired wound healing in diabetes. *Front. Immunol.* 14, 1216321. doi:10.3389/fimmu.2023.1216321

Nisar, S., Dastgeer, G., Shazad, Z. M., Zulfiqar, M. W., Rasheed, A., Iqbal, M. Z., et al. (2024). 2d materials in advanced electronic biosensors for point-of-care devices. *Adv. Sci. (Weinh)* 11, e2401386. doi:10.1002/advs.202401386

Nuutila, K., Singh, M., Kruse, C., Philip, J., Caterson, E. J., and Eriksson, E. (2016). Titanium wound chambers for wound healing research. *Wound Repair Regen.* 24, 1097–1102. doi:10.1111/wrr.12472

Nyaga, D. M., Vickers, M. H., Jefferies, C., Perry, J. K., and O'Sullivan, J. M. (2018a). The genetic architecture of type 1 diabetes mellitus. *Mol. Cell Endocrinol.* 477, 70–80. doi:10.1016/j.mce.2018.06.002

Nyaga, D. M., Vickers, M. H., Jefferies, C., Perry, J. K., and O'Sullivan, J. M. (2018b). Type 1 diabetes mellitus-associated genetic variants contribute to overlapping immune regulatory networks. *Front. Genet.* 9, 535. doi:10.3389/fgene.2018.00535

Oliveira, M. J., Dalot, A., Fortunato, E., Martins, R., Byrne, H. J., Franco, R., et al. (2022). Microfluidic sers devices: brightening the future of bioanalysis. *Discov. Mater* 2, 12. doi:10.1007/s43939-022-00033-3

Oprita, E. I., Iosageanu, A., and Craciunescu, O. (2023). Natural polymeric hydrogels encapsulating small molecules for diabetic wound healing. *Gels* 9, 867. doi:10.3390/gels9110867

Otero, F., and Magner, E. (2020). Biosensors-recent advances and future challenges in electrode materials. *Sensors (Basel)* 20, 3561. doi:10.3390/s20123561

Pagliuca, F. W., Millman, J. R., Gurtler, M., Segel, M., Van Dervort, A., Ryu, J. H., et al. (2014). Generation of functional human pancreatic β cells In Vitro. *Cell* 159, 428–439. doi:10.1016/j.cell.2014.09.040

Pei, J., Palanisamy, C. P., Alugoju, P., Anthikapalli, N., Natarajan, P. M., Umapathy, V. R., et al. (2023). A comprehensive review on bio-based materials for chronic diabetic wounds. *Molecules* 28, 604. doi:10.3390/molecules28020604

Peng, W., Li, D., Dai, K., Wang, Y., Song, P., Li, H., et al. (2022). Recent progress of collagen, chitosan, alginate and other hydrogels in skin repair and wound dressing applications. *Int. J. Biol. Macromol.* 208, 400–408. doi:10.1016/j.ijbiomac.2022.03.002

Paganelli, A.I., Mondejar, A.G., Da, S.A., Silva-Calpa, G., Teixeira, M.F., Carvalho, F., et al. (2022). Real-time data analysis in health monitoring systems: a comprehensive systematic literature review. *J. Biomed. Inform.* 127, 104009. doi:10.1016/j.jbi.2022.104009

Prasathkumar, M., and Sadhasivam, S. (2021). Chitosan/hyaluronic acid/alginate and an assorted polymers loaded with honey, plant, and marine compounds for progressive wound healing-know-how. *Int. J. Biol. Macromol.* 186, 656–685. doi:10.1016/j.ijbiomac.2021.07.067

Putzbach, W., and Ronkainen, N. J. (2013). Immobilization techniques in the fabrication of nanomaterial-based electrochemical biosensors: a review. *Sensors (Basel)* 13, 4811–4840. doi:10.3390/s130404811

Qin, W., Wu, Y., Liu, J., Yuan, X., and Gao, J. (2022). A comprehensive review of the application of nanoparticles in diabetic wound healing: therapeutic potential and future perspectives. *Int. J. Nanomedicine* 17, 6007–6029. doi:10.2147/IJN.S386585

Qiu, H., Zhang, L., Wang, D., and Miao, H. (2022). Silver nanoparticles improve the biocompatibility and reduce the immunogenicity of xenogeneic scaffolds derived from decellularized pancreas. *Cell Reprogr.* 24, 38–47. doi:10.1089/cell.2021.0071

Queiroz, M., Shanmugam, S., Santos, L., Campos, C. A., Santos, A. M., Batista, M. S., et al. (2020). Microneedles as an alternative technology for transdermal drug delivery systems: a patent review. *Expert Opin. Ther. Pat.* 30, 433–452. doi:10.1080/13543776.2020.1742324

Renuka, R.R., Julius, A., Yoganandham, S.T., Umapathy, D., Ramadoss, R., Samrot, A.V., et al. (2022). Diverse nanocomposites as a potential dressing for diabetic wound healing. *Front. Endocrinol. (Lausanne)* 13, 1074568. doi:10.3389/fendo.2022.1074568

Rajinikanth, B. S., Rajkumar, D., K, K., and Vijayaragavan, V. (2024). Chitosan-based biomaterial in wound healing: a review. *Cureus* 16, e55193. doi:10.7759/cureus.55193

Rajput, A., Kulkarni, M., Deshmukh, P., Pingale, P., Garkal, A., Gandhi, S., et al. (2021). A key role by polymers in microneedle technology: a new era. *Drug Dev. Ind. Pharm.* 47, 1713–1732. doi:10.1080/03639045.2022.2058531

Ramesh, A., Chhabra, P., and Brayman, K. L. (2013). Pancreatic islet transplantation in type 1 diabetes mellitus: an update on recent developments. *Curr. Diabetes Rev.* 9, 294–311. doi:10.2174/15733998113099990063

Rathna, R. P., and Kulandhaivel, M. (2024). Advancements in wound healing: integrating biomolecules, drug delivery carriers, and targeted therapeutics for enhanced tissue repair. *Arch. Microbiol.* 206, 199. doi:10.1007/s00203-024-03910-y

Ravoor, J., Thangavel, M., and Elsen, S. R. (2021). Comprehensive review on design and manufacturing of bio-scaffolds for bone reconstruction. *Acs Appl. Bio Mater* 4, 8129–8158. doi:10.1021/acsabm.1c00949

Razzaghi, M., Ninan, J. A., Azimzadeh, M., Askari, E., Najafabadi, A. H., Khademhosseini, A., et al. (2024). Remote-controlled sensing and drug delivery via 3d-printed hollow microneedles. *Adv. Healthc. Mater* 13, e2400881. doi:10.1002/adhm.202400881

Ren, C., Zhong, D., Qi, Y., Liu, C., Liu, X., Chen, S., et al. (2023). Bioinspired ph-responsive microalgal hydrogels for oral insulin delivery with both hypoglycemic and insulin sensitizing effects. *Acs Nano* 17, 14161–14175. doi:10.1021/acsnano.3c04897

Ren, S., Guo, S., Yang, L., and Wang, C. (2022). Effect of composite biodegradable biomaterials on wound healing in diabetes. *Front. Bioeng. Biotechnol.* 10, 1060026. doi:10.3389/fbioe.2022.1060026

Renard, E. (2023). Automated insulin delivery systems: from early research to routine care of type 1 diabetes. *Acta Diabetol.* 60, 151–161. doi:10.1007/s00592-022-01929-5

Renzu, M., Hubers, C., Conway, K., Gibatova, V., Mehta, V., and Taha, W. (2024). Emerging technologies in endocrine drug delivery: innovations for improved patient care. *Cureus* 16, e62324. doi:10.7759/cureus.62324

Righettoni, M., Schmid, A., Amann, A., and Pratsinis, S. E. (2013). Correlations between blood glucose and breath components from portable gas sensors and ptr-tof-ms. *J. Breath. Res.* 7, 037110. doi:10.1088/1752-7155/7/3/037110

Rodriguez-Rodriguez, N., Martinez-Jimenez, I., Garcia-Ojalvo, A., Mendoza-Mari, Y., Guillen-Nieto, G., Armstrong, D. G., et al. (2022). Wound chronicity, impaired immunity and infection in diabetic patients. *Medicc Rev.* 24, 44–58. doi:10.37757/MR2021.V23.N3.8

Rozman, N., Tong, W. Y., Leong, C. R., Anuar, M. R., Karim, S., Ong, S. K., et al. (2020). Homalomena pineodora essential oil nanoparticle inhibits diabetic wound pathogens. *Sci. Rep.* 10, 3307. doi:10.1038/s41598-020-60364-0

Ruiz-Munoz, M., Martinez-Barrios, F. J., and Lopezosa-Reca, E. (2024). Placenta-derived biomaterials vs. Standard care in chronic diabetic foot ulcer healing: a systematic review and meta-analysis. *Diabetes Metab. Syndr.* 19, 103170. doi:10.1016/j.dsx.2024.103170

Saco, M., Howe, N., Nathoo, R., and Cherpelis, B. (2016). Comparing the efficacies of alginate, foam, hydrocolloid, hydrofiber, and hydrogel dressings in the management of diabetic foot ulcers and venous leg ulcers: a systematic review and meta-analysis examining how to dress for success. *Dermatol Online J.* 22. doi:10.5070/d3228032089

Sahu, B., Prusty, A., and Tudu, B. (2018). Total contact casting versus traditional dressing in diabetic foot ulcers. *J. Orthop. Surg. Hong. Kong* 26, 2309499018802486. doi:10.1177/2309499018802486

Salthouse, D., Novakovic, K., Hilkens, C., and Ferreira, A. M. (2023). Interplay between biomaterials and the immune system: challenges and opportunities in regenerative medicine. *Acta Biomater.* 155, 1–18. doi:10.1016/j.actbio.2022.11.003

Sarkar, S., Ekbal, K. M., Kalita, J., and Manna, P. (2023). Mesoporous silica nanoparticles: drug delivery vehicles for antidiabetic molecules. *Chembiochem* 24, e202200672. doi:10.1002/cbic.202200672

Sarkhel, S., Shuvo, S. M., Ansari, M. A., Mondal, S., Kapat, P., Ghosh, A., et al. (2024). Nanotechnology-based approaches for the management of diabetes mellitus: an innovative solution to long-lasting challenges in antidiabetic drug delivery. *Pharmaceutics* 16, 1572. doi:10.3390/pharmaceutics16121572

Scandurra, A., Iacono, V., Boscarino, S., Scalese, S., Grimaldi, M. G., and Ruffino, F. (2023). Model of chronoamperometric response towards glucose sensing by arrays of gold nanostructures obtained by laser, thermal and wet processes. *Nanomater. (Basel)* 13, 1163. doi:10.3390/nano13071163

Schlaeppi, A., Adams, W., Haase, R., Huisken, J., MacDonald, R. B., Eliceiri, K. W., et al. (2022). Meeting in the middle: towards successful multidisciplinary bioimage analysis collaboration. *Front. Bioinform* 2, 889755. doi:10.3389/fbinf.2022.889755

Schackart, K.R., and Yoon, J.Y. (2021). Machine learning enhances the performance of bioreceptor-free biosensors. *Sensors (Basel)* 21, 5519. doi:10.3390/s21165519

Shamshad, A., Kang, C., Jenny, L. A., Persad-Paisley, E. M., and Tsang, S. H. (2023). Translatability barriers between preclinical and clinical trials of aav gene therapy in inherited retinal diseases. *Vis. Res.* 210, 108258. doi:10.1016/j.visres.2023.108258

Sharma, S., and Kishen, A. (2024). Bioarchitectural design of bioactive biopolymers: structure-function paradigm for diabetic wound healing. *Biomimetics (Basel)* 9, 275. doi:10.3390/biomimetics9050275

Sharmah, B., Afzal, N. U., Loying, R., Roy, A., Kalita, J., Das, J., et al. (2024). Glucose-responsive insulin delivery via surface-functionalized titanium dioxide nanoparticles: a promising theragnostic against diabetes mellitus. *Acs Appl. Bio Mater* 8, 475–487. doi:10.1021/acsabm.4c01426

Socci, M. C., Rodriguez, G., Oliva, E., Fushimi, S., Takabatake, K., Nagatsuka, H., et al. (2023). Polymeric materials, advances and applications in tissue engineering: a review. *Bioeng. (Basel)* 10, 218. doi:10.3390/bioengineering10020218

Soetedjo, A., Lee, J. M., Lau, H. H., Goh, G. L., An, J., Koh, Y., et al. (2021). Tissue engineering and 3d printing of bioartificial pancreas for regenerative medicine in diabetes. *Trends Endocrinol. Metab.* 32, 609–622. doi:10.1016/j.tem.2021.05.007

Sonmezer, D., Latifoglu, F., Toprak, G., and Baran, M. (2023). A native extracellular matrix material for tissue engineering applications: characterization of pericardial fluid. *J. Biomed. Mater Res. B Appl. Biomater.* 111, 1629–1639. doi:10.1002/jbm.b.35260

Starlin, C. M., Mahmood, S., Mohamed, S. Z., Wan, H. C., Sundarapandian, R., Ahamed, H. N., et al. (2024). Biodegradable polymeric insulin microneedles - a design and materials perspective review. *Drug Deliv.* 31, 2296350. doi:10.1080/10717544.2023.2296350

Sultana, A., Borgohain, R., Rayaji, A., Saha, D., and Kumar, D. B. (2024). Promising phytoconstituents in diabetes-related wounds: mechanistic insights and implications. *Curr. Diabetes Rev.* 21, e270224227477. doi:10.2174/0115733998279112240129074457

Summers-Gibson, L. (2021). The relationships between diabetes self-care, diabetes time management, and diabetes distress in women with type 2 diabetes mellitus. *Sci. Diabetes Self Manag. Care* 47, 245–254. doi:10.1177/26350106211014438

Takahashi, M., Umehara, Y., Yue, H., Trujillo-Paez, J. V., Peng, G., Nguyen, H., et al. (2021). The antimicrobial peptide human β-defensin-3 accelerates wound healing by promoting angiogenesis, cell migration, and proliferation through the FGFR/JAK2/STAT3 signaling pathway. *Front. Immunol.* 12, 712781. doi:10.3389/fimmu.2021.712781

Tallapaneni, V., Kalaivani, C., Pamu, D., Mude, L., Singh, S. K., and Karri, V. (2021). Acellular scaffolds as innovative biomaterial platforms for the management of diabetic wounds. *Tissue Eng. Regen. Med.* 18, 713–734. doi:10.1007/s13770-021-00344-1

Tanda, N., Hinokio, Y., Washio, J., Takahashi, N., and Koseki, T. (2014). Analysis of ketone bodies in exhaled breath and blood of ten healthy Japanese at ogtt using a portable gas chromatograph. *J. Breath. Res.* 8, 046008. doi:10.1088/1752-7155/8/4/046008

Tankasala, D., and Linnes, J. C. (2019). Noninvasive glucose detection in exhaled breath condensate. *Transl. Res.* 213, 1–22. doi:10.1016/j.trsl.2019.05.006

Teymourian, H., Barfidokht, A., and Wang, J. (2020). Electrochemical glucose sensors in diabetes management: an updated review (2010-2020). *Chem. Soc. Rev.* 49, 7671–7709. doi:10.1039/d0cs00304b

Tripathi, A. S., Zaki, M., Al-Hussain, S. A., Dubey, B. K., Singh, P., Rind, L., et al. (2023). Material matters: exploring the interplay between natural biomaterials and host immune system. *Front. Immunol.* 14, 1269960. doi:10.3389/fimmu.2023.1269960

Tutty, M. A., Vella, G., and Prina-Mello, A. (2022). Pre-clinical 2d and 3d toxicity response to a panel of nanomaterials; Comparative assessment of nbm-induced liver toxicity. *Drug Deliv. Transl. Res.* 12, 2157–2177. doi:10.1007/s13346-022-01170-1

Umehara, Y., Takahashi, M., Yue, H., Trujillo-Paez, J. V., Peng, G., Nguyen, H., et al. (2022). The antimicrobial peptides human β-defensins induce the secretion of angiogenin in human dermal fibroblasts. *Int. J. Mol. Sci.* 23, 8800. doi:10.3390/ijms23158800

Vajhadin, F., Mazloum-Ardakani, M., and Amini, A. (2021). Metal oxide-based gas sensors for the detection of exhaled breath markers. *Med. Devices Sens.* 4, e10161. doi:10.1002/mds3.10161

Varela-Moreno, E., Carreira, S. M., Guzman-Parra, J., Jodar-Sanchez, F., Mayoral-Cleries, F., and Anarte-Ortiz, M. T. (2021). Effectiveness of ehealth-based psychological interventions for depression treatment in patients with type 1 or type 2 diabetes mellitus: a systematic review. *Front. Psychol.* 12, 746217. doi:10.3389/fpsyg.2021.746217

Vargas, G. M., Aendekerk, F., de Boer, C., Geurts, J., Lucchesi, J., and Arts, J. (2024). Bioactive-glass-based materials with possible application in diabetic wound healing: a systematic review. *Int. J. Mol. Sci.* 25, 1152. doi:10.3390/ijms25021152

Verbaan, F. J., Bal, S. M., van den Berg, D. J., Dijksman, J. A., van Hecke, M., Verpoorten, H., et al. (2008). Improved piercing of microneedle arrays in dermatomed human skin by an impact insertion method. *J. Control. Release.* 128, 80–88. doi:10.1016/j.jconrel.2008.02.009

Venkatesan, V., and Rangasamy, J. (2023). Diabetic pedal osteomyelitis and its treatment. *Chonnam Med. J.* 59, 109–114. doi:10.4068/cmj.2023.59.2.109

Volpatti, L. R., Facklam, A. L., Cortinas, A. B., Lu, Y. C., Matranga, M. A., MacIsaac, C., et al. (2021). Microgel encapsulated nanoparticles for glucose-responsive insulin delivery. *Biomaterials* 267, 120458. doi:10.1016/j.biomaterials.2020.120458

Wang, J., and Jin, X. (2024). Strategies for decellularization, re-cellularization and crosslinking in liver bioengineering. *Int J Artif Organs* 47, 129–139. doi:10.1177/03913988231218566

Wang, J., Duan, X., Zhong, D., Zhang, M., Li, J., Hu, Z., et al. (2024). Pharmaceutical applications of chitosan in skin regeneration: a review. *Int. J. Biol. Macromol.* 261, 129064. doi:10.1016/j.ijbiomac.2023.129064

Wang, X., Yang, Y., Zhao, W., Zhu, Z., and Pei, X. (2024). Recent advances of hydrogels as smart dressings for diabetic wounds. *J. Mater Chem. B* 12, 1126–1148. doi:10.1039/d3tb02355a

Wang, Y., Wang, H., Zhu, X. X., Guan, Y., and Zhang, Y. (2020). Smart microneedle patches for rapid, and painless transdermal insulin delivery. *J. Mater Chem. B* 8, 9335–9342. doi:10.1039/d0tb01822h

Wilems, T., Vardhan, S., Wu, S., and Sakiyama-Elbert, S. (2019). The influence of microenvironment and extracellular matrix molecules in driving neural stem cell fate within biomaterials. *Brain Res. Bull.* 148, 25–33. doi:10.1016/j.brainresbull.2019.03.004

Woo, S. H., Choi, J. H., Mo, Y. J., Lee, Y. I., Jeon, W. B., and Lee, Y. S. (2023). Engineered elastin-like polypeptide improves the efficiency of adipose-derived stem cell-mediated cutaneous wound healing in type ii diabetes mellitus. *Heliyon* 9, e20201. doi:10.1016/j.heliyon.2023.e20201

Wilke, N., Hibert, C., Brien, J.O., and Morrissey, A. (2005). Silicon microneedle electrode array with temperature monitoring for electroporation. *Sensors & Actuators a Physical* 123, 319–325. doi:10.1016/j.sna.2005.05.017

Wu, X., Liu, C., Wang, L., and Bilal, M. (2023). Internet of things-enabled real-time health monitoring system using deep learning. *Neural. Comput. Appl.* 35, 14565–14576. doi:10.1007/s00521-021-06440-6

Xie, B., Wang, K., Li, B., Huang, R., Xu, Z., and Li, X. (2023). Biomaterial-mediated strategies for accurate and convenient diagnosis, and effective treatment of diabetes: advantages, current progress and future perspectives. *J. Mater Chem. B* 11, 3766–3786. doi:10.1039/d3tb00034f

Xie, Z., Ramakrishnam, R. M., Stewart, A. C., Nantz, M. H., and Fu, X. A. (2018). Imparting sensitivity and selectivity to a gold nanoparticle chemiresistor through thiol monolayer functionalization for sensing acetone. *Rsc Adv.* 8, 35618–35624. doi:10.1039/c8ra06137h

Xing, C., Luo, M., Sheng, Q., Zhu, Z., Yu, D., Huang, J., et al. (2024). Silk fabric functionalized by nanosilver enabling the wearable sensing for biomechanics and biomolecules. *Acs Appl. Mater Interfaces* 16, 51669–51678. doi:10.1021/acsami.4c10253

Xu, B., Liu, H., Yang, G., Zhang, S., Zhou, Z., and Gao, Y. (2024). Novel double-layered plga microparticles-dissolving microneedle (mps-dmn) system for peptide drugs sustained release by transdermal delivery. *Int. J. Pharm.* 670, 125128. doi:10.1016/j.ijpharm.2024.125128

Xu, G., Zhang, W., Du, J., Yuan, X., Zhang, W., Yan, W., et al. (2022). Biomass-derived porous carbon with high drug adsorption capacity undergoes enzymatic and chemical degradation. *J. Colloid Interface Sci.* 622, 87–96. doi:10.1016/j.jcis.2022.04.064

Xu, R., Fang, Y., Zhang, Z., Cao, Y., Yan, Y., Gan, L., et al. (2023). Recent advances in biodegradable and biocompatible synthetic polymers used in skin wound healing. *Mater. (Basel)* 16, 5459. doi:10.3390/ma16155459

Yang, J., and Xu, L. (2023). Electrospun nanofiber membranes with various structures for wound dressing. *Mater. (Basel)* 16, 6021. doi:10.3390/ma16176021

Yang, P., Li, S., Zhang, H., Ding, X., and Tan, Q. (2024). LRG1 accelerates wound healing in diabetic rats by promoting angiogenesis via the wnt/β-catenin signaling pathway. *Int. J. Low. Extrem Wounds* 23, 568–576. doi:10.1177/15347346221081610

Yao, Y., Zhang, H., Wang, Z., Ding, J., Wang, S., Huang, B., et al. (2019). Reactive oxygen species (ros)-responsive biomaterials mediate tissue microenvironments and tissue regeneration. *J. Mater Chem. B* 7, 5019–5037. doi:10.1039/c9tb00847k

Yasin, S., Said, Z., Halib, N., Rahman, Z. A., and Mokhzani, N. I. (2023). Polymer-based hydrogel loaded with honey in drug delivery system for wound healing applications. *Polym. (Basel)* 15, 3085. doi:10.3390/polym15143085

Yoon, J., Cho, H. Y., Shin, M., Choi, H. K., Lee, T., and Choi, J. W. (2020). Flexible electrochemical biosensors for healthcare monitoring. *J. Mater Chem. B* 8, 7303–7318. doi:10.1039/d0tb01325k

Young, K. G., McGovern, A. P., Barroso, I., Hattersley, A. T., Jones, A. G., Shields, B. M., et al. (2023). The impact of population-level hba(1c) screening on reducing diabetes diagnostic delay in middle-aged adults: a UK biobank analysis. *Diabetologia* 66, 300–309. doi:10.1007/s00125-022-05824-0

Yue, H., Song, P., Sutthammikorn, N., Umehara, Y., Trujillo-Paez, J. V., Nguyen, H., et al. (2022). Antimicrobial peptide derived from insulin-like growth factor-binding protein 5 improves diabetic wound healing. *Wound Repair Regen.* 30, 232–244. doi:10.1111/wrr.12997

Yunos, M., Manczak, R., Guines, C., Mansor, A., Mak, W. C., Khan, S., et al. (2021). Rf remote blood glucose sensor and a microfluidic vascular phantom for sensor validation. *Biosens. (Basel)* 11, 494. doi:10.3390/bios11120494

Yusuf, A. A., and Adeleke, O. A. (2023). Nanofibrous scaffolds for diabetic wound healing. *Pharmaceutics* 15, 986. doi:10.3390/pharmaceutics15030986

Zafar, H., Channa, A., Jeoti, V., and Stojanovic, G. M. (2022). Comprehensive review on wearable sweat-glucose sensors for continuous glucose monitoring. *Sensors (Basel)* 22, 638. doi:10.3390/s22020638

Zaric, B. L., Obradovic, M., Sudar-Milovanovic, E., Nedeljkovic, J., Lazic, V., and Isenovic, E. R. (2019). Drug delivery systems for diabetes treatment. *Curr. Pharm. Des.* 25, 166–173. doi:10.2174/1381612825666190306153838

Zhang, F., Pei, X., Peng, X., Gou, D., Fan, X., Zheng, X., et al. (2022). Dual crosslinking of folic acid-modified pectin nanoparticles for enhanced oral insulin delivery. *Biomater. Adv.* 135, 212746. doi:10.1016/j.bioadv.2022.212746

Zhang, G., Ichikawa, K., Iitani, K., Iwasaki, Y., and Mitsubayashi, K. (2025a). A handheld biofluorometric system for acetone detection in exhaled breath condensates. *Analyst* 150, 505–512. doi:10.1039/d4an01281j

Zhang, K., Zhang, C., Zhou, H., Yang, Y., Wen, Y., Jiao, X., et al. (2024a). Elastic nanofibrous dressings with mesenchymal stem cell-recruiting and protecting characteristics for promoting diabetic wound healing. *Acs Appl. Mater Interfaces* 16, 41869–41880. doi:10.1021/acsami.4c07369

Zhang, P., Dalton, C., and Jullien, G.A. (2009). Design and fabrication of mems-based microneedle arrays for medical applications. *Micro. Techno.* 15, 1073–1082. doi:10.1007/s00542-009-0883-5

Zhang, S., Ge, G., Qin, Y., Li, W., Dong, J., Mei, J., et al. (2023a). Recent advances in responsive hydrogels for diabetic wound healing. *Mater Today Bio* 18, 100508. doi:10.1016/j.mtbio.2022.100508

Zhang, S., Zhao, W., Zeng, J., He, Z., Wang, X., Zhu, Z., et al. (2023b). Wearable non-invasive glucose sensors based on metallic nanomaterials. *Mater Today Bio* 20, 100638. doi:10.1016/j.mtbio.2023.100638

Zhang, T., Wu, H., Qiu, C., Wang, M., Wang, H., Zhu, S., et al. (2024b). Ultrasensitive hierarchical aunrs@sio(2)@ag sers probes for enrichment and detection of insulin and c-peptide in serum. *Int. J. Nanomedicine* 19, 6281–6293. doi:10.2147/IJN.S462601

Zhang, X., Zhang, Y., Zheng, H., Yang, X., Zou, S., and Chen, J. (2025b). Design, fabrication, and evaluation of antimicrobial sponge microneedles for the transdermal delivery of insulin. *Eur. J. Pharm. Biopharm.* 206, 114586. doi:10.1016/j.ejpb.2024.114586

Zhang, Y., Sun, J., Liu, L., and Qiao, H. (2021). A review of biosensor technology and algorithms for glucose monitoring. *J Diabetes Complications* 35, 107929. doi:10.1016/j.jdiacomp.2021.107929

Zhang, Z., Xue, H., Xiong, Y., Geng, Y., Panayi, A. C., Knoedler, S., et al. (2024c). Copper incorporated biomaterial-based technologies for multifunctional wound repair. *Theranostics* 14, 547–570. doi:10.7150/thno.87193

Zhao, H., Li, J., She, X., Chen, Y., Wang, M., Wang, Y., et al. (2024a). Oxygen vacancy-rich bimetallic au@pt core-shell nanosphere-functionalized electrospun znfe(2)o(4) nanofibers for chemiresistive breath acetone detection. *Acs Sens.* 9, 2183–2193. doi:10.1021/acssensors.4c00382

Zhao, H., Li, Z., Wang, Y., Zhou, K., Li, H., Bi, S., et al. (2023). Bioengineered msc-derived exosomes in skin wound repair and regeneration. *Front. Cell Dev. Biol.* 11, 1029671. doi:10.3389/fcell.2023.1029671

Zhao, S., Lu, Z., Cai, R., Wang, H., Gao, S., Yang, C., et al. (2024b). A wearable osmotic microneedle patch provides high-capacity sustained drug delivery in animal models. *Sci. Transl. Med.* 16, eadp3611. doi:10.1126/scitranslmed.adp3611

Zheng, Q., Chen, C., Liu, Y., Gao, J., Li, L., Yin, C., et al. (2024). Metal nanoparticles: advanced and promising technology in diabetic wound therapy. *Int. J. Nanomedicine* 19, 965–992. doi:10.2147/IJN.S434693

Zheng, Y., Ma, Y., He, P., Yan, L., Cao, H., and Shao, F. (2025). Phycocyanin/hyaluronic acid microneedle patches loaded with celastrol nanoparticles for synergistic treatment of diabetic nephropathy. *Acs Biomater. Sci. Eng.* 11, 371–382. doi:10.1021/acsbiomaterials.4c01787

Zhong, Y., Song, B., He, D., Xia, Z., Wang, P., Wu, J., et al. (2020). Galactose-based polymer-containing phenylboronic acid as carriers for insulin delivery. *Nanotechnology* 31, 395601. doi:10.1088/1361-6528/ab9e26

Zhou, D., Zhang, S., Khan, A. U., Chen, L., and Ge, G. (2023). A wearable aunp enhanced metal-organic gel (au@mog) sensor for sweat glucose detection with ultrahigh sensitivity. *Nanoscale* 16, 163–170. doi:10.1039/d3nr05179j

Zhou, Y. Y., Chen, J. P., Gan, L., Xu, W., Liu, Y., Zhao, Y. G., et al. (2022). A non-invasive method for the detection of glucose in human exhaled breath by condensation collection coupled with ion chromatography. *J. Chromatogr.* 1685, 463564. doi:10.1016/j.chroma.2022.463564

Zhou, Y., Huang, H., Chen, G., Yuan, Q., Ren, J., Wu, J., et al. (2024a). Promoting the healing of diabetic wounds with an antimicrobial gel containing agnps with anti-infective and anti-inflammatory properties. *J. Biomater. Sci. Polym.* 35, 1236–1257. doi:10.1080/09205063.2024.2324494

Zhou, Y., Li, L., Tong, J., Chen, X., Deng, W., Chen, Z., et al. (2024b). Advanced nanomaterials for electrochemical sensors: application in wearable tear glucose sensing technology. *J. Mater Chem. B* 12, 6774–6804. doi:10.1039/d4tb00790e

Zhu, X., Cao, P., Li, P., Yu, Y., Guo, R., Li, Y., et al. (2024). Bimetallic ptau-decorated sno (2) nanospheres exhibiting enhanced gas sensitivity for ppb-level acetone detection. *Nanomater. (Basel)* 14, 1097. doi:10.3390/nano14131097

Zong, Q., Guo, R., Dong, N., Ling, G., and Zhang, P. (2022). Design and development of insulin microneedles for diabetes treatment. *Drug Deliv. Transl. Res.* 12, 973–980. doi:10.1007/s13346-021-00981-y

frontiers | Frontiers in Bioengineering and Biotechnology

TYPE Original Research
PUBLISHED 20 March 2025
DOI 10.3389/fbioe.2025.1566946

OPEN ACCESS

EDITED BY
Xianzhi Zhang,
Yale University, United States

REVIEWED BY
Fei Chang,
University of Shanghai for Science and Technology, China
Yaxiong Tian,
Guilin University of Technology, China

*CORRESPONDENCE
Ye-Fu Liu,
hy8151@163.com

RECEIVED 26 January 2025
ACCEPTED 05 March 2025
PUBLISHED 20 March 2025

CITATION
Liu F-Y, Wang X and Liu Y-F (2025) Preparation of $La_2(WO_4)_3/CuWO_4$ composite nanomaterials with enhanced sonodynamic anti-glioma activity.
Front. Bioeng. Biotechnol. 13:1566946.
doi: 10.3389/fbioe.2025.1566946

Preparation of $La_2(WO_4)_3/CuWO_4$ composite nanomaterials with enhanced sonodynamic anti-glioma activity

Fang-Yu Liu[1], Xin Wang[2] and Ye-Fu Liu[3]*

[1]The First Clinical College, Liaoning University of Traditional Chinese Medicine, Shenyang, China, [2]Shenyang Key Laboratory for Causes and Drug Discovery of Chronic Diesases, Liaoning University, Shenyang, China, [3]Liaoning Cancer Hospital and Institute, Shenyang, China

Introduction: Sonodynamic therapy (SDT) is an innovative way to treat tumors by activating sonosensitizers via ultrasound (US). The development of sonosensitizers with high sonodynamic activity is the key to promote the clinical application of SDT.

Methods: In this study, a novel sonosensitizer, $La_2(WO_4)_3/CuWO_4$ composite LC-10, was prepared by two-step hydrothermal method and characterized. In addition, the sonodynamic antitumor activity of $La_2(WO_4)_3/CuWO_4$ composite LC-10 was investigated using u251 glioma cells as a model.

Results and Discussion: The results showed that compared with $La_2(WO_4)_3$ and $CuWO_4$, $La_2(WO_4)_3/CuWO_4$ composite had better sonodynamic antitumor activity, and LC-10 had good biosafety at concentrations below 50 μg/mL. After $La_2(WO_4)_3$ and $CuWO_4$ formed $La_2(WO_4)_3/CuWO_4$ composite, the recombination of electron-hole ($e^- - h^+$) pairs were effectively inhibited, and more strongly oxidizing ROS was produced, inducing apoptosis of u251 glioma cells. In which, singlet oxygen ($^1O_2$) and hydroxyl radical (·OH), especially the production of ·OH, played an important role in the $La_2(WO_4)_3/CuWO_4$ composite mediated SDT antitumor process. The results of this study would offer a foundation for the design of $CuWO_4$ base nano-sonosensitizers and its further clinical application in SDT antitumor. In addition, it also provided a new strategy for the design and development of novel nano-sonosensitizers with excellent sonodynamic activity.

KEYWORDS

$La_2(WO_4)_3/CuWO_4$ composite, nano-sonosensitizer, sonodynamic therapy (SDT), sonodynamic antitumor activity, reactive oxygen species (ROS)

1 Introduction

Sonodynamic therapy (SDT) is an emerging non-invasive cancer treatment derived from photodynamic therapy (PDT) (Canavese et al., 2018). SDT uses the focusing of ultrasound (US) and strong penetration of biological tissues to enrich tumor sites of sonosensitizers with certain frequency and intensity of US, and activates the sonosensitizers to produce cytotoxicity, thus producing antitumor effects (Rosenthal et al., 2004). In 1993, Umemura et al. (Umemura et al., 1993) named this method of combining sonosensitizer with US for tumor treatment as SDT according to the name of PDT. This method not only gets rid of the disadvantage of PDT's poor tissue permeability (Hachimine et al., 2007a), but

also shows unique advantages in the non-invasive treatment of deep tumors due to its local cytotoxic effect, which can minimize the damage of normal tissues around the tumor site (Yang et al., 2021). Therefore, SDT has attracted wide attention since it was proposed (Han et al., 2018; Wu et al., 2022).

According to the action mechanisms of SDT, the performance of sonosensitizers plays a crucial role in the SDT process. The traditional organic sonosensitizers used in early studies mainly include hematoporphyrin (Hp) (Umemura et al., 1989) and its derivatives such as ATX-70 (Sasaki et al., 1998), DCPH-P-Na(I) (Hachimine et al., 2007b), haematoporphyrin monomethyl ether (HMME) (Li et al., 2008) and protoporphyrin IX (PPIX) (Liu et al., 2006). In addition, some antitumor drugs and small molecule drugs such as curcumin (Jiang et al., 2020), acridine orange (Xing et al., 2021), methylene blue (He et al., 2015a), promethazine hydrochloride (He et al., 2011a), dioxypromethazine hydrochloride (He et al., 2011b), eosin B (He et al., 2015b), brilliant cresyl blue (Wang et al., 2018), toluidine blue and azure A (Qian et al., 2024) have also been proved to have good sonodynamic activity. The advantages of these organic sonosensitizers are that they all have clear chemical structures and excellent biodegradation rates. However, most of them have disadvantages such as greater hydrophobicity and phototoxicity, as well as lower tissue selectivity and stability when applied *in vivo* (Wu et al., 2022; Xing et al., 2021).

In recent decades, the research of inorganic nanoparticle based sonosensitizers such as titanium dioxide (TiO_2) has made great progress (Yang et al., 2021). Compared with organic small molecule drugs, inorganic nanomaterials have the advantages of excellent physical and chemical properties, easy manufacturing, low phototoxicity, good biocompatibility and stability (Yang et al., 2021; Li et al., 2023). At the same time, various inorganic nanomaterials such as $TiH_{1.924}$ (Gong et al., 2020), $BaTiO_3$ (Zhu et al., 2020) and Bi_2MoO_6 (Dong et al., 2021) were proved to have good sonodynamic activity. These inorganic nano-sonosensitizers absorb the energy generated by the US cavitation effect (thermal and sonoluminescence) and excite the sonosensitizers to produce electron-hole (e^-–h^+) separation. The separated e^- and h^+ migrate to the surface of the sonosensitizer to produce corresponding reduction and oxidation reactions, resulting in a large number of reactive oxygen species (ROS) generation and antitumor effects (Li et al., 2023). However, due to the rapid recombination of e^- and h^+ in the band structure, the efficiency of ROS generation of single-component sonosensitizer is relatively low, which affects the effect of SDT (Li et al., 2023; Ping et al., 2023). Therefore, the researchers overcome the recombination of carriers by forming oxygen defect layers on the surface of sonosensitizer (Zhou et al., 2022; Wang Y. et al., 2023), deposition of precious metals (Zhang et al., 2021), ion doping (Cheng et al., 2024), construction of heterojunction (Chen et al., 2022; Kang et al., 2022) and a combination of these strategies (Zhang et al., 2023a; Song et al., 2022), thus further improving the efficiency of SDT.

Because of the effective conversion of light energy into thermal and chemical energy, tungstate nanomaterials are often used as photoresponsive materials in the field of photocatalytic degradation of organic pollutants (Kumar et al., 2022), photothermal therapy (Xiao et al., 2016), PDT and radiotherapy (Zhang et al., 2018). $CuWO_4$ is an important semiconductor material with a band gap of about 2.60 eV (Liu et al., 2023). Compared with other tungstate structures, $CuWO_4$ exhibits stronger absorption in the near infrared region, indicating that $CuWO_4$ is a good candidate for PDT. For example, Cui et al. (2021) prepared a single original nanostructured $CuWO_4$ nanodots, and introduced the nanodots into tumor tissue to generate ROS to generate PDT under 808 nm light irradiation, and released copper ions into the acidic tumor microenvironment to promote Fenton-like reaction and generate chemodynamic therapy, which can effectively inhibit tumor tissue growth. Since most sonosensitizers are derived from photosensitizers, $CuWO_4$ nanomaterials may be a candidate sonosensitizer for SDT applications.

The construction of heterojunction can effectively inhibit the e^-–h^+ pairs recombination, promote the generation of ROS, and significantly improve the effect of SDT (Ping et al., 2023; Chen et al., 2022; Kang et al., 2022). Therefore, in this paper, $La_2(WO_4)_3$/$CuWO_4$ composites were prepared by two-step hydrothermal method, and the microstructure, morphology and elemental composition of $La_2(WO_4)_3$/$CuWO_4$ composites were analyzed by X-ray diffraction (XRD), scanning electron microscope (SEM), energy dispersive X-ray spectroscopy (EDX) and X-ray photoelectron spectroscopy (XPS). Using u251 glioma cells as model, the sonodynamic anti-glioma activity of $La_2(WO_4)_3$/$CuWO_4$ composites was investigated by MTT method. Finally, the sonodynamic antitumor mechanism of $La_2(WO_4)_3$/$CuWO_4$ composites was discussed based on the optical properties and electrochemical characteristics of $La_2(WO_4)_3$/$CuWO_4$ composites and ROS probe experimental results. It is expected that the results of this study will provide the research basis for the further development and application of $CuWO_4$ based sonosensitizers in SDT antitumor.

2 Experimental sections

2.1 Materials and reagents

$NaWO_4{\cdot}2H_2O$ (AR), 1, 3-diphenylisobenzofuran (DPBF, AR) and terephthalic acid (TA, AR) were purchased from Tianjin Hengxing Chemical reagent manufacturing Co., LTD., (China). NaOH (AR) was purchased from Tianjin Yongda Chemical reagent Co., LTD., (China). Anhydrous ethanol (AR), $Cu(NO_3)_2{\cdot}3H_2O$ and $La(NO_3)_3{\cdot}6H_2O$ were purchased from Tianjin Damao chemical reagent factory (China). Phosphate buffer (PBS, BR), thiazole blue (AR), RPMI Medium 1640 (BR), superior fetal bovine serum (BR), 0.25% trypsin/EDTA digestion solution (BR), serum-free cryopreservation (BR), dimethyl sulfoxide (DMSO, BR), 3-(4,5-dimethylthiazol-2-yl)-2,5 diphenyl-tetrazolium bromide (MTT, BR) and AO/EB Kit (LR) were purchased from Beijing Solarbio Technology Co., LTD., (China). Human glioma u251 cells were purchased from Cell Resource Center, Institute of Basic Medicine, Chinese Academy of Medical Sciences.

2.2 Preparation of $La_2(WO_4)_3$/$CuWO_4$ composite

1.0872 g $Cu(NO_3)_2{\cdot}3H_2O$ and 0.2165 g $La(NO_3)_3{\cdot}6H_2O$ were dissolved together in 40 mL deionized water. 2.3090 g

$Na_2WO_4{\cdot}_2H_2O$ was weight and dissolved in 20 mL deionized water. Then, under the condition of magnetic stirring, the Na_2WO_4 solution was added to the mixed solution of $Cu(NO_3)_2$ and $La(NO_3)_3$ drop by drop, and continued to stir for 30 min. Then the mixed solution was transferred to the polytetrafluoroethylene inner tank of 100 mL stainless steel reactor and reacted in a constant temperature drying oven at 180°C for 24 h. The reaction products were washed with deionized water and anhydrous ethanol three times respectively, and dried at 60°C for 8 h to obtain $La_2(WO4)_3$/$CuWO_4$ composite (LC-10) sample. According to the above experimental methods, $CuWO_4$ sample was prepared without adding $La(NO_3)_3{\cdot}6H_2O$ in the process of synthesis. Similarly, $La_2(WO_4)_3$ sample was prepared under the above experimental conditions without adding $Cu(NO_3)_2{\cdot}3H_2O$ in the process of synthesis. Detailed information on the various instruments used in the paper could be found in Supplementary Material.

2.3 Cytotoxicity assay

The cytotoxicity of nano-sonosensitizers and nano-sonosensitizers-mediated sonodynamic action on u251 glioma cells was tested by the typical MTT assay. The u251 glioma cells were plated in 96-well microplates (6×10^3 cells per well) and incubated at 37°C for 24 h. After removing the culture medium, 50 μL of base medium containing various concentrations of $La_2(WO_4)_3$, $CuWO_4$ and LC-10 samples (10, 20, 50, 100 and 200 μg/mL) were added. After incubation at 37°C for 24 h, 20 μL of medium containing MTT (0.5 mg/mL diluted with medium) was added to each well and continued incubation at 37°C for 4 h. Then, the supernatant in the well was discarded, 150 μL of DMSO was added to each well, and the optical density (OD) was measured at 490 nm using a microplate reader instrument. The cell viability was calculated by Graphpad Pism software. In the experiment on sonodynamic damage to u251 glioma cells, various concentrations of $La_2(WO_4)_3$, $CuWO_4$ and LC-10 samples (0, 10, 20, 30, 40 and 50 μg/mL) were added. After incubation at 37°C for 24 h, the cells were irradiated with a 1.0 MHz US probe for 1 min, and incubated at 37°C for 24 h. MTT assay was used to detect cell viability.

2.4 Detection of ROS

In order to detect the formation of singlet oxygen ($^1O_2$) in the SDT process, DPBF was used as a probe, which could react with $^1O_2$ to decompose DPBF into 1, 2-diphenyl-benzene, resulting in a decrease in the absorption intensity of its characteristic absorption peak at 410 nm (Zhou et al., 2024; Zhang et al., 2023b). The specific experimental method was as follows: 8 mL of 75% ethanol solution containing DPBF (8 mg/L) and sonosensitizer (20 μg/mL) were taken and placed in the US device for 5 min. Then centrifuged at 15,000 rpm for 10 min to remove the sonosensitizer. The absorption spectra of the solution near 410 nm were measured with an ultraviolet-visible (UV-Vis) spectrophotometer.

In order to detect the formation of hydroxyl radical (·OH) in the SDT process, TA was used as a probe, which could react with ·OH to produce 2-hydroxyterephthalic acid, resulting in a characteristic fluorescence emission peak generated around 430 nm (Pan et al., 2018). Typically, 8 mL 0.5 mmol/L TA solution containing 20 μg/mL of sonosensitizer was taken, then the solution was placed in US bath for US irradiation for 5 min, and centrifugated at 15,000 rpm for 10 min to remove the sonosensitizer. The emission spectrum of the supernatant near 425 nm was measured by a fluorescence spectrophotometer with excitation wavelength of 315 nm.

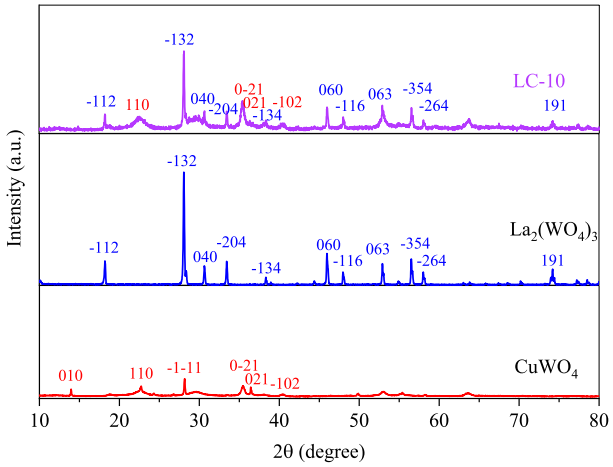

FIGURE 1
XRD patterns of the prepared $La_2(WO_4)_3$, $CuWO_4$ and LC-10 composite.

2.5 Statistical analysis

All data were expressed as mean ± SD, and one-way ANOVA was performed by Graphpad Pism software. When *P* was less than 0.05, it was statistically significant.

3 Results and discussions

3.1 Characterization of $La_2(WO_4)_3$/$CuWO_4$ composite

The XRD patterns of the prepared $La_2(WO_4)_3$, $CuWO_4$ and LC-10 composite were shown in Figure 1. As shown in Figure 1, the XRD patterns of $CuWO_4$ showed that the diffraction peaks were at 13.96°, 22.73°, 28.17°, 35.46°, 36.43° and 40.52°, which belonged to the (010), (110), (−1−11), (0−21), (021) and (−102) planes of $CuWO_4$, respectively. For $La_2(WO_4)_3$, the diffraction peaks at 18.20°, 28.08°, 30.64°, 33.44°, 38.34°, 45.98°, 47.98°, 52.92°, 56.52°, 58.02° and 74.20° were related to the planes (−112), (−132), (040), (−204), (−134), (060), (−116), (063), (−354), (−264) and (191) of $La_2(WO_4)_3$. For LC-10 composite, a series of characteristic peaks of $CuWO_4$ and $La_2(WO_4)_3$ appeared. The XRD diffraction peaks at 22.52°, 35.40°, 36.32° and 40.50° were attributed to the (110), (0-21), (021) and (−102) crystal planes of $CuWO_4$. The XRD diffraction peaks at 18.22°, 28.10°, 30.68°, 33.44°, 38.32°, 45.98°, 47.98°, 52.90°, 56.54°, 58.02° and 74.20° were attributed to the (−112), (−132), (040),

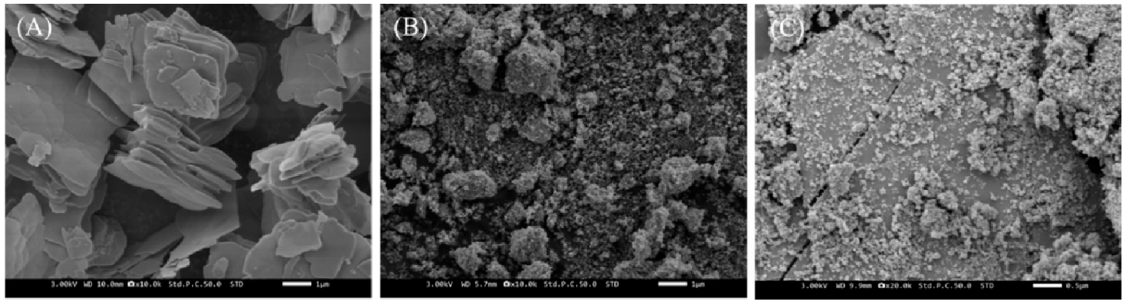

FIGURE 2
SEM images of synthesized $La_2(WO_4)_3$ **(A)**, $CuWO_4$ **(B)** and LC-10 **(C)** samples.

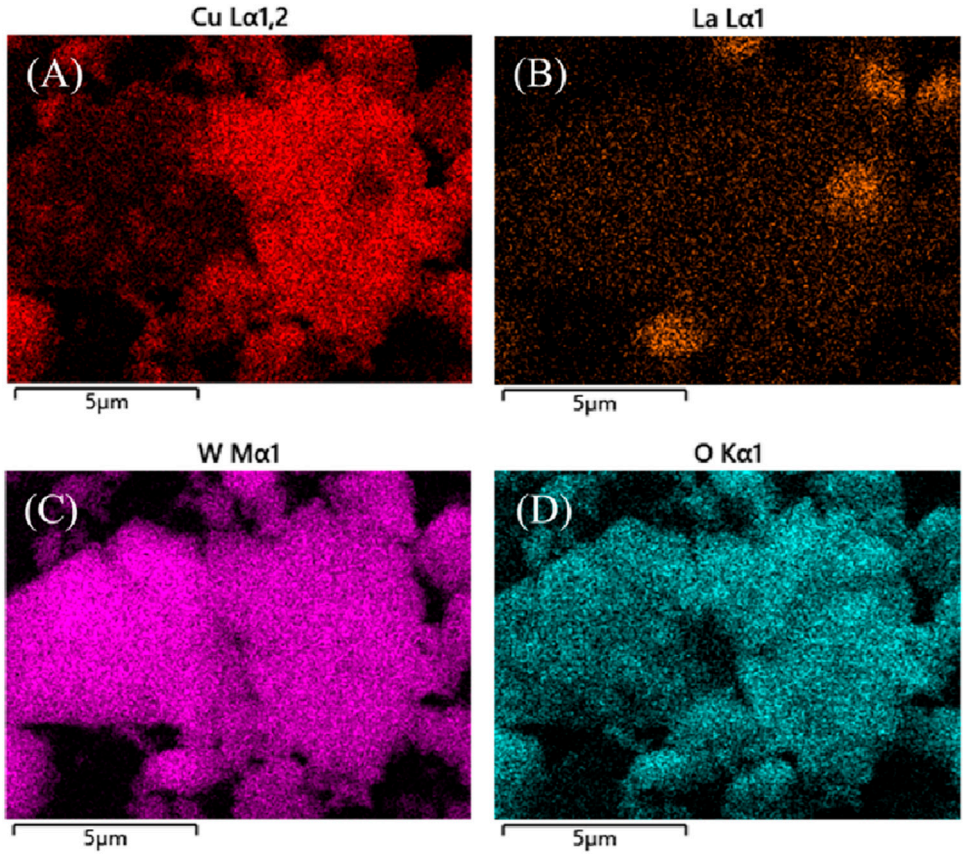

FIGURE 3
EDX diagrams of **(A)** Cu, **(B)** La, **(C)** W and **(D)** O elements in the synthesized LC-10 sample.

(−204), (−134), (060), (−116), (063), (−354), (−264) and (191) crystal planes of $La_2(WO_4)_3$. The above results confirmed the successful preparation of $La_2(WO_4)_3/CuWO_4$ composite.

The morphologies of the prepared $La_2(WO_4)_3$, $CuWO_4$ and LC-10 samples were analyzed by SEM, and the results were shown in Figure 2. It could be seen that the prepared $La_2(WO_4)_3$ sample had an irregular lamellar structure (Figure 2A), and the prepared $CuWO_4$ sample had a nanoparticle shape (Figure 2B). It could be seen from the SEM image of the prepared LC-10 sample (Figure 2C) that $CuWO_4$ nanoparticles were evenly distributed on the lamellar structure of $La_2(WO_4)_3$, which proved the successful composite of $La_2(WO_4)_3$ and $CuWO_4$. The EDX diagrams of Cu, La, W and O elements in the synthesized LC-10 sample were shown in Figure 3. It could be seen that Cu, La, W and O elements were evenly distributed on the surface of the synthesized LC-10 sample.

The elemental compositions and chemical valence states of synthesized $La_2(WO_4)_3$, $CuWO_4$ and LC-10 samples were analyzed by XPS measurement. As shown in Figure 4A, the three peaks of $La_2(WO_4)_3$ sample at 832.2, 32.6 and 527.7 eV were attributed to La 3*d*, W 4*f* and O 1*s*, respectively. As shown in

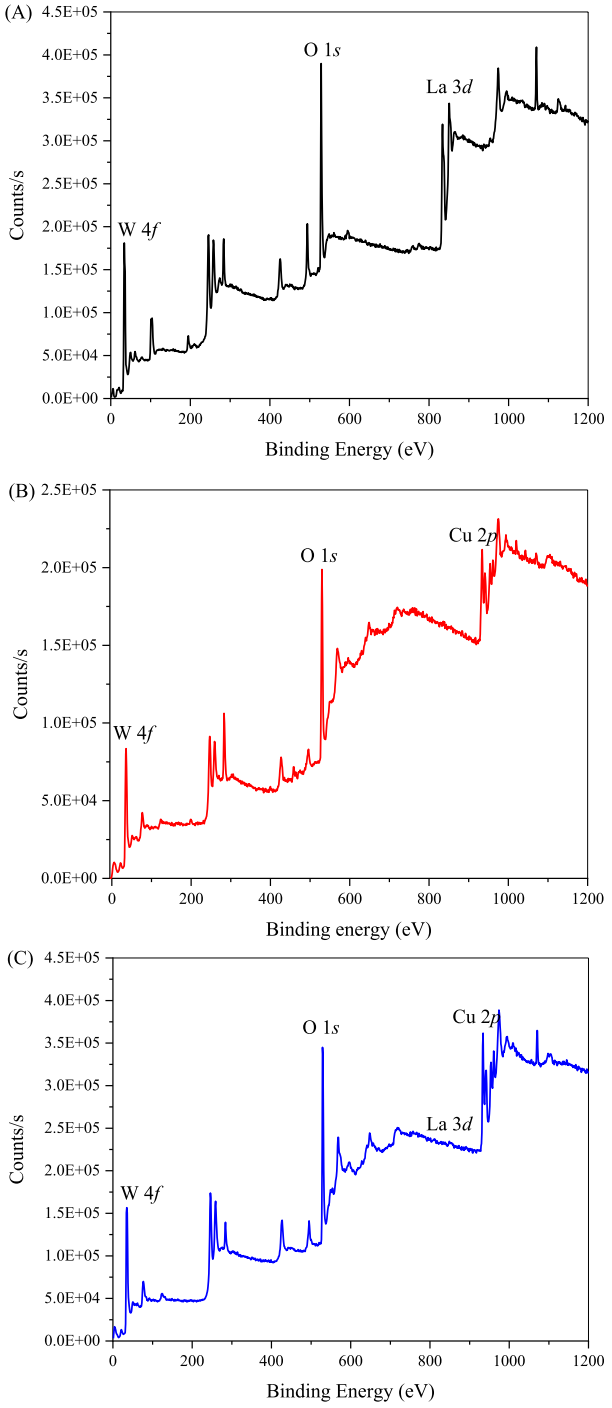

FIGURE 4
XPS spectra of synthesized $La_2(WO_4)_3$ **(A)**, $CuWO_4$ **(B)** and LC-10 **(C)** samples.

Figure 4B, the three peaks of the $CuWO_4$ sample at 932.2, 31.1 and 528.1 eV were attributed to Cu 2*p*, W 4*f* and O 1*s*, respectively. As shown in Figure 4C, the four peaks of LC-10 composite at 833.3, 932.5, 33.7 and 528.1 eV were attributed to La 3*d*, Cu 2*p*, W 4*f* and O 1*s*, respectively.

The high-resolution XPS spectra of Cu 2*p*, W 4*f*, O 1*s* and La 3*d* in the synthesized $CuWO_4$, $La_2(WO_4)_3$ and LC-10 samples were shown in Figure 5. The two peaks with binding energies of 933.12 and 952.90 eV in the spectrum of Cu 2*p* of $CuWO_4$ (Figure 5A) belonged to Cu $2p_{3/2}$ and Cu $2p_{2/1}$, respectively, which suggested that the presence of Cu^{2+} and the capture of photogenerated electrons by Cu^{2+} may cause the valence state change from Cu(II) to Cu(I) (Wang X. et al., 2023; Wan et al., 2013). Compared with $CuWO_4$, the two fitted peaks of Cu 2*p* of LC-10 composite sample shifted slightly to the higher energy, located at 933.57 and 953.36 eV, respectively. In the high resolution XPS spectrum of W 4*f* of $CuWO_4$ (Figure 5B), the two peaks at the binding energies of 33.83 and 35.97 eV belonged to W $4f_{7/2}$ and W $4f_{5/2}$, respectively, suggesting the existence of W^{6+} in the synthesized sample (Wang et al., 2021; Xu et al., 2023). The two fitted peaks of W 4*f* of $La_2(WO_4)_3$ were located at 33.73 and 35.89 eV, respectively. Compared with $CuWO_4$ and $La_2(WO_4)_3$, the two fitted peaks of W 4*f* of LC-10 composite sample shifted slightly to the higher energy, located at 34.07 and 36.18 eV, respectively. The high-resolution XPS spectra of O 1*s* of $CuWO_4$ shown in Figure 5C displayed two fitted peaks at 528.73 and 529.83 eV, respectively, indicating the presence of the lattice oxygen and O-H bonds absorbed on surface of the synthesized sample (He et al., 2024; Wei et al., 2023). The two fitted peaks of O 1*s* of $La_2(WO_4)_3$ were located at 528.85 and 531.16 eV, respectively. Compared with $CuWO_4$ and $La_2(WO_4)_3$, the two fitted peaks of O 1*s* of LC-10 composite sample shifted slightly to the higher energy or lower energy, located at 529.01 and 530.29 eV, respectively. The high-resolution XPS spectrum of La 3*d* of $La_2(WO_4)_3$ shown in Figure 5D displayed the spin–orbit splitting: La $3d_{5/2}$ (833.51 and 836.97 eV) and La $3d_{3/2}$ (850.28 and 854.00 eV), which were in accordance with the standard XPS peaks of La^{3+} (Baby et al., 2024). Compared with $La_2(WO_4)_3$, the fitted peaks of La 3*d* of LC-10 composite sample also shifted slightly. The above results indicated that the two substances, $CuWO_4$ and $La_2(WO_4)_3$ interacted with each other, and the heterojunction of $La_2(WO_4)_3/CuWO_4$ formed.

The UV-Vis diffuse reflectance spectra (DRS) of $CuWO_4$, $La_2(WO_4)_3$ and LC-10 were measured using a UV-Vis spectrophotometer in the wavelength range of 200–800 nm, and the results were shown in Figure 6. It could be seen that $CuWO_4$ had a strong light absorption capacity in the entire 200–800 nm range, indicating that $CuWO_4$ had a good light response ability to both UV and Vis light. $La_2(WO_4)_3$ had an obvious absorption boundary near 340 nm, which indicated that $La_2(WO_4)_3$ had a strong absorption capacity for UV light. It could be seen from the DRS of LC-10 that $La_2(WO_4)_3/CuWO_4$ composite had a good light response to both UV and Vis light. Based on the above DRS results, the band gap energy (E_g) of $CuWO_4$ and $La_2(WO_4)_3$ could be obtained by the Kubelka-Munk formula (Wang et al., 2021). The correlation curves of $(Ahv)^2$ vs. hv of $CuWO_4$ and $La_2(WO_4)_3$ were shown in Figures 7A, B, the *Eg* of $CuWO_4$ and $La_2(WO_4)_3$ were obtained as 2.99 and 2.54 eV, respectively.

3.2 Sonodynamic anti-glioma activity of $La_2(WO_4)_3/CuWO_4$ composite

First, the cytotoxicity of prepared $CuWO_4$, $La_2(WO_4)_3$ and LC-10 samples to u251 cells was investigated. In the presence of different concentrations (10, 20, 50, 100 and 200 μg/mL) prepared $CuWO_4$, $La_2(WO_4)_3$ and LC-10 samples, the cell viability of u251 cells during

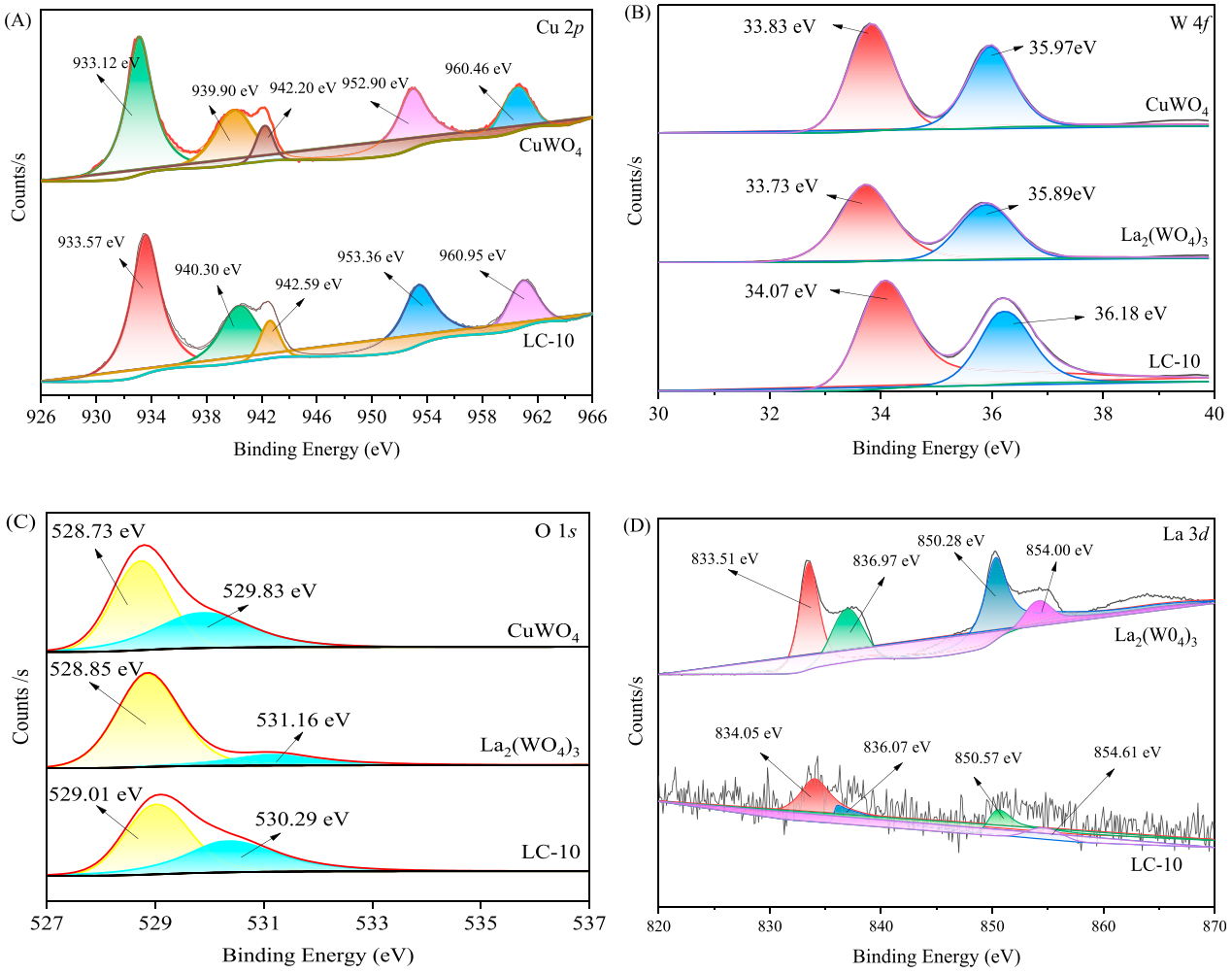

FIGURE 5
High-resolution XPS spectra of Cu 2*p* **(A)**, W 4*f* **(B)**, O 1*s* **(C)** and La 3*d* **(D)** in synthesized $CuWO_4$, $La_2(WO_4)_3$ and LC-10 samples.

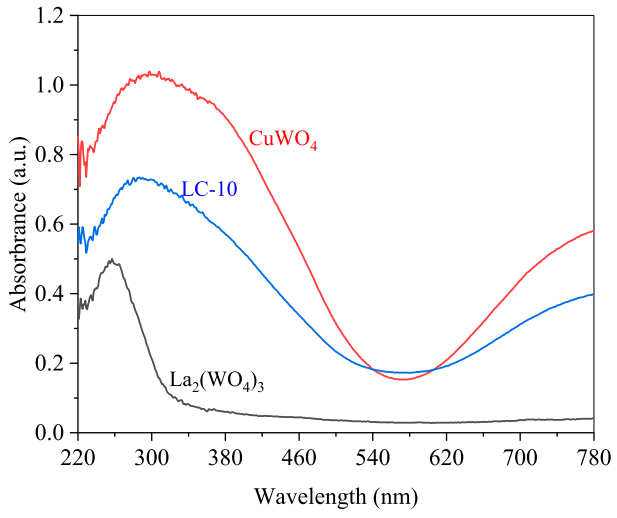

FIGURE 6
DRS spectra of $CuWO_4$, $La_2(WO_4)_3$ and LC-10 samples.

logarithmic growth was measured by MTT method. Figure 8A displayed the cytotoxicity test results of $CuWO_4$. When $CuWO_4$ concentration was 10, 20, 50, 100 and 200 μg/mL, the cell viability was 105.45% ± 5.05%, 103.01% ± 2.57%, 96.31% ± 3.71%, 93.50% ± 6.46% and 86.65% ± 8.08%, respectively. Figure 8B showed the cytotoxicity test results of $La_2(WO_4)_3$. When the concentration of $La_2(WO_4)_3$ was 10, 20, 50, 100 and 200 μg/mL, the cell viability was 97.72% ± 4.54%, 93.66% ± 4.80%, 90.84% ± 2.78%, 89.88% ± 4.15% and 85.65% ± 6.49%, respectively. The results showed that $CuWO_4$ and $La_2(WO_4)_3$ did not cause obvious cytotoxicity to u251 cells when the concentrations of $CuWO_4$ and $La_2(WO_4)_3$ were below 200 μg/mL. Figure 8C showed the cytotoxicity test results of LC-10 sample. When the concentration of LC-10 was 10, 20, 50, 100 and 200 μg/mL, the cell viability was 95.17% ± 4.35%, 94.40% ± 6.70%, 84.11% ± 5.31%, 79.26% ± 4.38% and 71.05% ± 6.12%, respectively. These results showed that with the increase of LC-10 concentration, the cell survival rate decreased gradually. When the concentration of LC-10 was higher than 50 μg/mL, it had a certain toxic effect on cells.

Next, u251 cells were treated differently to evaluate the sonodynamic therapeutic effect of $La_2(WO_4)_3/CuWO_4$ composite on tumor cells. It could be seen from Figure 9A that the cell viability

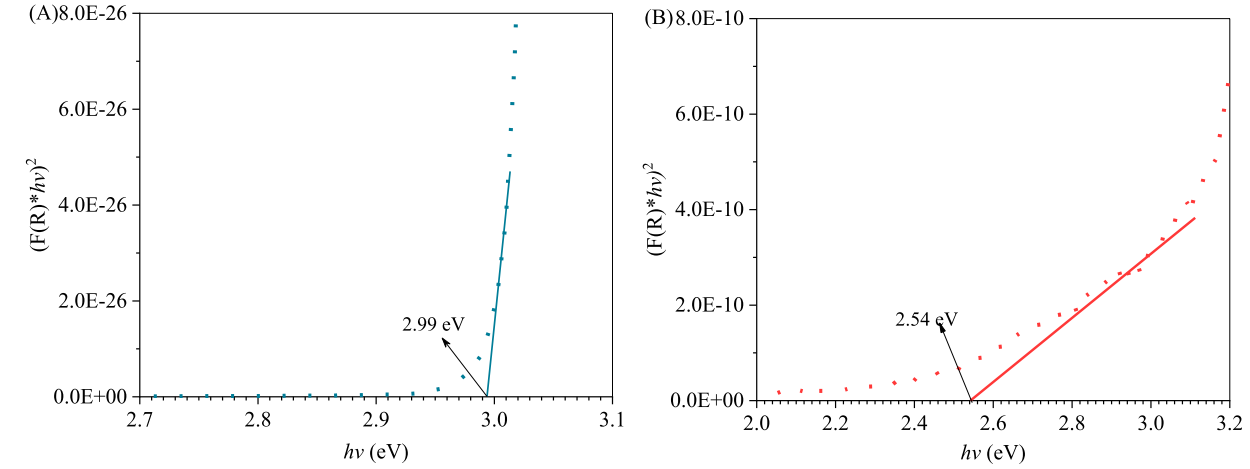

FIGURE 7
Correlation curves of $(Ah\nu)^2$ vs. $h\nu$ of $CuWO_4$ **(A)** and $La_2(WO_4)_3$ **(B)**.

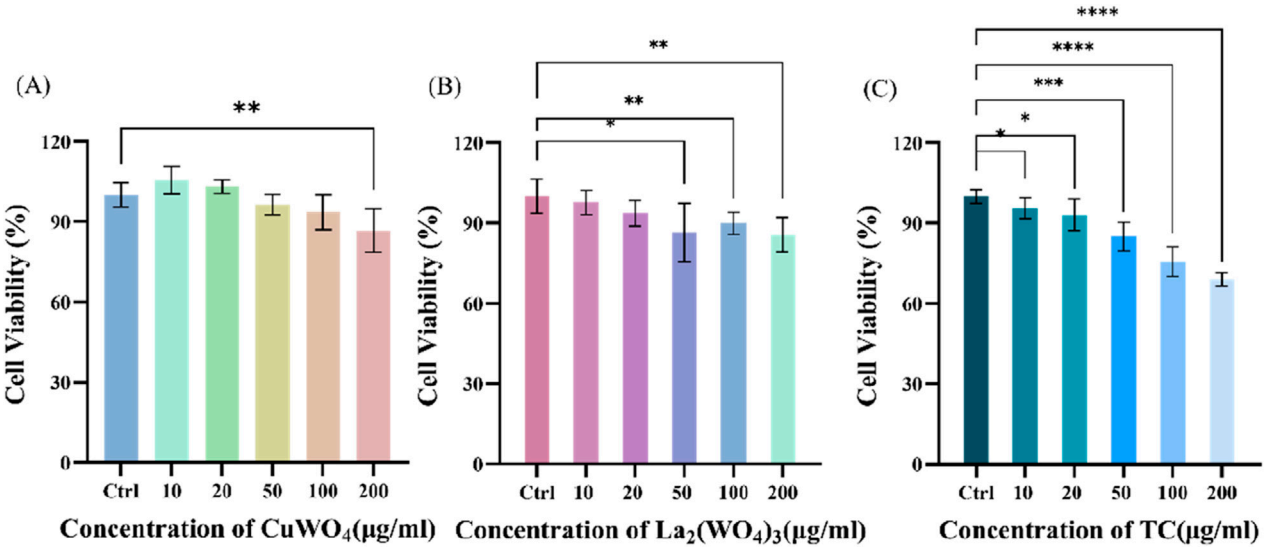

FIGURE 8
Cytotoxicity of $CuWO_4$ **(A)**, $La_2(WO_4)_3$ **(B)** and LC-10 **(C)** to u251 cells (*p < 0.05,**p < 0.01,***p < 0.001,****p < 0.0001).

decreased slightly under US irradiation alone. This was because the energy generated by the cavitation effect of US could lead to the cracking of water molecules, resulting in a strong oxidizing ·OH. The effects of different concentrations of LC-10 on the cell viability of u251 cells under US irradiation were shown in Supplementary Figures S1–S5. It could be clearly observed that the cell viability of u251 cells treated with SDT in the presence of LC-10 was significantly lower than that treated with LC-10 alone and US alone at any concentration of LC-10. These results suggested that $La_2(WO_4)_3/CuWO_4$ composite had excellent sonodynamic antitumor performance. The cell inhibition rate of u251 cells after SDT in the presence of different concentrations of $CuWO_4$, $La_2(WO_4)_3$ and LC-10 were shown in Figure 9B. It could be seen that the cell inhibition rate of u251 cells after SDT in the presence of LC-10 at any concentration was significantly higher than that in the presence of $CuWO_4$ and $La_2(WO_4)_3$ at same concentration. These results indicated that $La_2(WO_4)_3/CuWO_4$ composite had higher sonodynamic antitumor performance. In addition, it was also shown that the construction of heterojunction was an effective means to improve the sonodynamic antitumor performance of nano-sonosensitizers.

Subsequently, sonodynamic-induced cancer cell apoptosis was further evaluated using AO/EB staining. As shown in Figure 10, under the same experimental conditions, cells were divided into control group (A), US group (B), LC-10 group (C), and LC-10+US group (D). In the control group (Figure 10A), the quantity and intensity of green fluorescence were high, while the orange fluorescence was negligible, indicating good growth of cells. As shown in Figures 10B, C, the US group and the LC-10 group showed weak orange fluorescence, and most of the cells showed

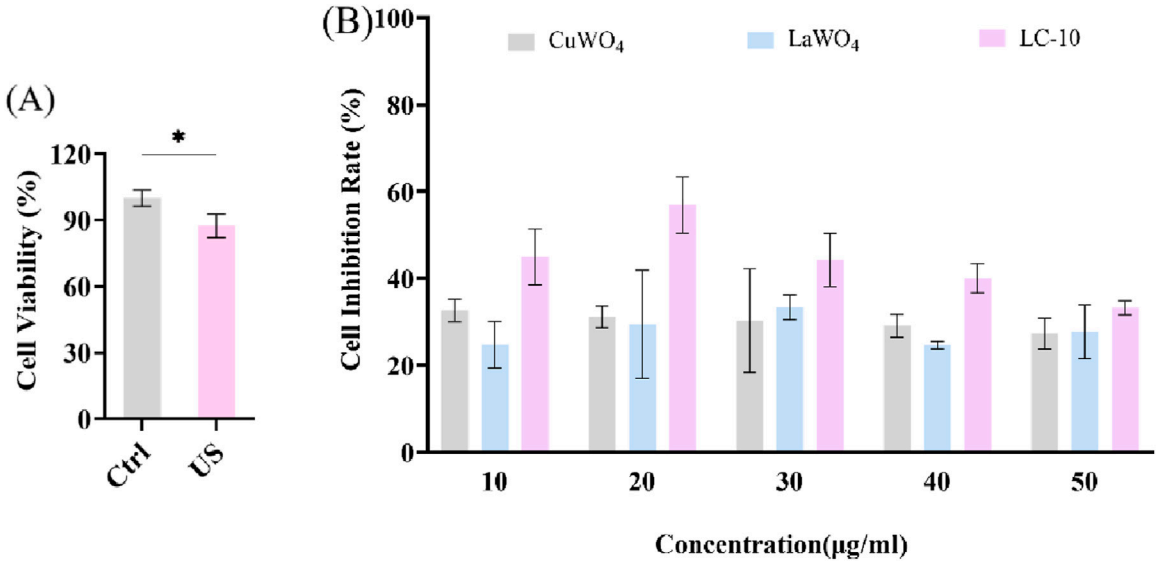

FIGURE 9
Cell viability of u251 cells under US irradiation **(A)** and cell inhibition rate of u251 cells after SDT in the presence of different concentrations of $CuWO_4$, $La_2(WO_4)_3$ and LC-10 **(B)** (*$p < 0.05$).

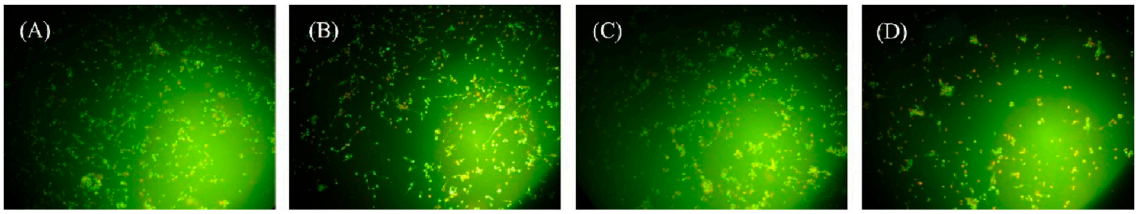

FIGURE 10
Confocal laser scanning microscopy images of u251 cells stained with AO/EB after various treatments. **(A)** control group, **(B)** US group, **(C)** LC-10 group, and **(D)** LC-10+US group.

green fluorescence, indicating that most of the cells had good viability. Figure 10D showed a large amount of orange fluorescence in the LC-10+US group, indicating that LC-10 produced a large number of ROS inducing apoptosis under US irradiation, and the experimental results were consistent with the above MTT results.

3.3 Sonodynamic antitumor mechanism of $La_2(WO_4)_3/CuWO_4$ composite

It could be clearly seen from the above results that the combined use of US and sonosensiizer LC-10 had a much higher inhibitory effect on the growth of u251 glioma cells than that of US alone and LC-10 alone. The combined use of US and sonosensiizer LC-10 also significantly inhibited the growth of u251 glioma cells compared with the combined effect of US and $La_2(WO_4)_3$ and the combined effect of US and $CuWO_4$, indicating that LC-10 had better sonodynamic antitumor activity. The essence of the good sonodynamic activity of the nano-sonosensitizer was that it could become a ROS generator under US irradiation (Duan et al., 2023). In order to study the ability of $La_2(WO_4)_3/CuWO_4$ composite as a sonosensitizer to produce ROS and the corresponding sonodynamic mechanism, specific ROS probes were used to verify the types of ROS produced during SDT process. The $^1O_2$ yields of $La_2(WO_4)_3/CuWO_4$ composite produced under US irradiation were evaluated using DPBF as a probe. It could be seen from Figure 11A, under US irradiation, the absorption peak of DPBF at 410 nm decreased in the presence of LC-10 compared with the control group of water, suggesting the generation of $^1O_2$ in the system. Similarly, the capture of ·OH was tracked by TA. It could be seen from Figure 11B, the combined use of US and LC-10 remarkably increased the fluorescence intensity of the solution around 430 nm. The results showed that $La_2(WO_4)_3/CuWO_4$ composite had good ·OH production ability under US irradiation.

The photoluminescence spectra of $CuWO_4$ and $La_2(WO_4)_3/CuWO_4$ composite LC-10 were measured with a fluorescence spectrophotometer in the wavelength range of 200–600 nm, and the results were shown in Figure 12. It could be seen that under the excitation condition of 269 nm wavelength, $CuWO_4$ had an obvious

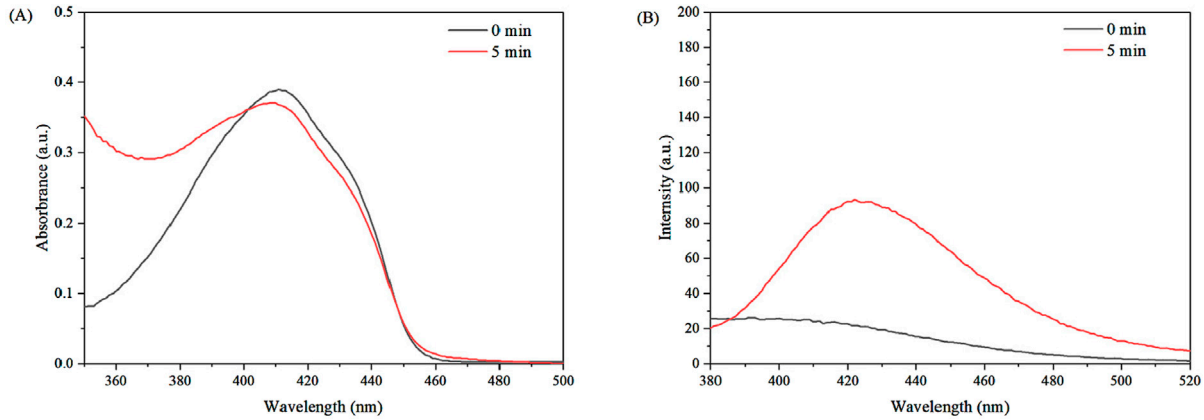

FIGURE 11
Detection of $^1O_2$ **(A)** and ·OH **(B)** in the combined use of US and LC-10 system.

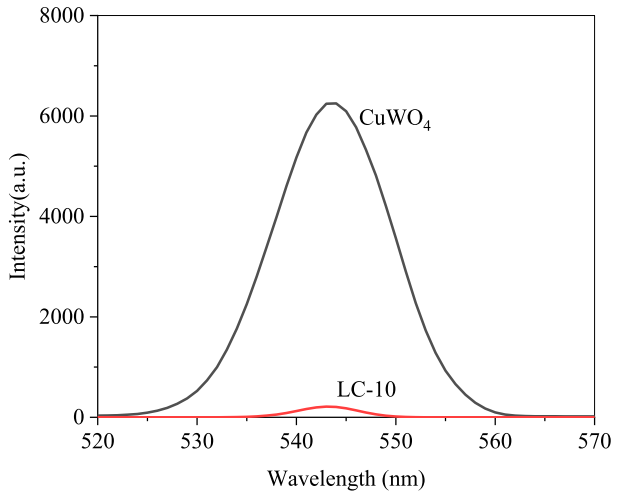

FIGURE 12
Photoluminescence spectra of $CuWO_4$ and LC-10.

emission peak near 520 nm. Similarly, the maximum emission wavelength of the emission peak of LC-10 was also around 520 nm, but its fluorescence intensity was significantly lower than that of $CuWO_4$, indicating that after $La_2(WO_4)_3$ and $CuWO_4$ formed a composite, carrier separation could be effectively realized in the catalyst, and the recombination rate of e^--h^+ pairs was significantly reduced (Liu et al., 2024). The production of ROS of the catalyst under US irradiation was improved significantly, thus displayed excellent sonodynamic antitumor performance.

The type of semiconductor material could be determined by whether the slope of the tangent in the Mott-Schottky curves was positive or negative. A positive slope indicated an n-type semiconductor and a negative slope indicated a p-type semiconductor (Chang et al., 2023; Chang et al., 2024). As seen in Figure 13, The slopes of tangent lines of the Mott-Schottky curves of $La_2(WO_4)_3$ and $CuWO_4$ were both positive. The results showed that all the prepared $La_2(WO_4)_3$ and $CuWO_4$ samples had n-type semiconductor characteristics. Additionally, the flat band potential (E_f) values of the prepared $La_2(WO_4)_3$ and $CuWO_4$ samples could be obtained from the intercept of the tangent with the X-axis (Huang et al., 2024a; Chang et al., 2025). Therefore, the E_f values of $La_2(WO_4)_3$ and $CuWO_4$ samples were determined to be −0.55 V and −0.30 V vs saturated calomel electrode (SCE), respectively. Accordingly, the E_f values of $La_2(WO_4)_3$ and $CuWO_4$ samples could be calculated as −0.31 V and −0.06 V vs standard hydrogen electrode (NHE), considering the correction value between SCE and NHE was 0.24 V (Lu et al., 2025; Huang et al., 2024b). It was known that for most n-type semiconductors, the minimum potential of the conduction band (E_{CB}) was about 0.1–0.3 V lower than the E_f value, and the middle value of 0.2 V was used here (Huang et al., 2024c; Chen et al., 2024). Therefore, the E_{CB} values of $La_2(WO_4)_3$ and $CuWO_4$ samples were calculated as −0.51 V and −0.26 V vs. NHE, respectively. According to the E_g values of $La_2(WO_4)_3$ and $CuWO_4$ samples were 2.54 and 2.99 eV, respectively, and the relationship between the maximum potential of valence band (E_{VB}), E_{CB} and E_g ($E_{VB} = E_{CB} + E_g$) (Han et al., 2025), E_{VB} values of $La_2(WO_4)_3$ and $CuWO_4$ samples relative to NHE could be calculated as 2.03 V and 2.73 V, respectively. Based on the above calculation, the schematic diagram of the band structure corresponding to $La_2(WO_4)_3/CuWO_4$ composite was shown in Figure 14. It could be seen that there are obvious differences in the band and energy level structure between $La_2(WO_4)_3$ and $CuWO_4$ in $La_2(WO_4)_3/CuWO_4$ composite, and a hypothesis that $La_2(WO_4)_3/CuWO_4$ n–n heterojunction formed was proposed.

Combined with the results of the above study and related literature reports, the main mechanism of LC-10-mediated SDT antitumor was proposed (as shown in Figure 14). Firstly, in the process of US irradiation, the tiny bubbles in the liquid were activated by US, resulting in a series of dynamic processes such as expansion, contraction, expansion and collapse, that was, the cavitation effect (Rosenthal et al., 2004; Teng et al., 2024). The cavitation effect (transient cavitation) generated by US could form local hot spots of high temperature and pressure, and its energy could cause water molecules to crack and produced ·OH (Rosenthal et al., 2004), which would cause damage to tumor cells. Secondly, the addition of $La_2(WO_4)_3/CuWO_4$ composite nanoparticles could

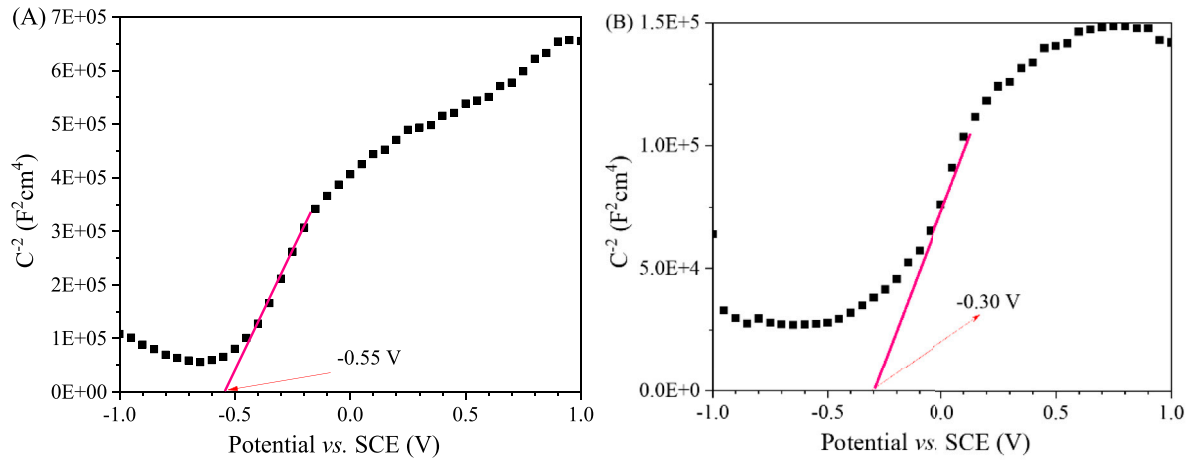

FIGURE 13
Mott-Schottky plots of $La_2(WO_4)_3$ **(A)** and $CuWO_4$ **(B)**.

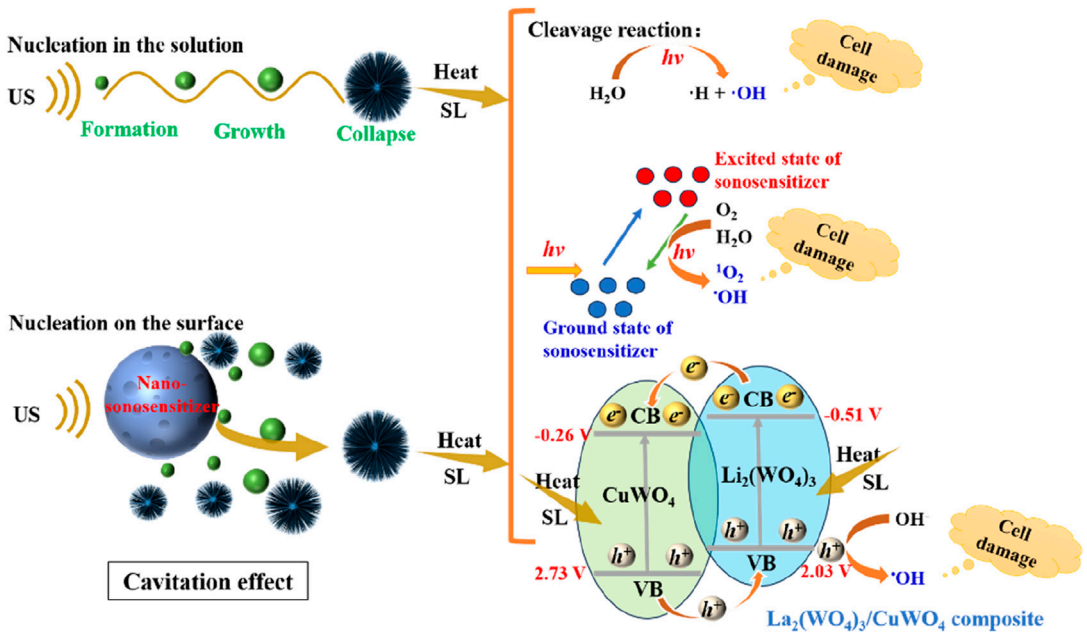

FIGURE 14
$La_2(WO_4)_3/CuWO_4$ composite mediated SDT antitumor mechanism diagram.

provide more active sites for the nucleation process and the formation of cavitation microbubbles (Qiu et al., 2018), which could generate more active free radicals, and then caused more serious damage to tumor cells. Thirdly, in the process of US irradiation, the cavitation effect of US would lead to sonoluminescence (Xu et al., 2025). The light energy generated by sonoluminescence and the heat energy from local hot spots could activate the sonosensitizer molecule to transition from the ground state to the excited state (Qian et al., 2024). In the process of the sonosensitizer molecule returning from the excited state to the ground state, the released energy was transferred to the water and oxygen molecules in the medium. ROS with strong oxidizing properties such as $^1O_2$ and ·OH were produced (Qian et al., 2024), thus causing damage to tumor cells. Finally, the $La_2(WO_4)_3/CuWO_4$ composite formed by $La_2(WO_4)_3$ and $CuWO_4$ was stimulated by the light generated by sonoluminescence and heat from local hot spots. When the light energy and the heat energy were equal to or exceeded the E_g of $La_2(WO_4)_3$ and $CuWO_4$ semiconductor, the photothermal generated e^- would produce on the VB of $La_2(WO_4)_3$ and $CuWO_4$, and then transferred to the CB, forming h^+ on the VB of $La_2(WO_4)_3$ and $CuWO_4$, respectively (Xu et al., 2025). Due to

obvious differences in the band and energy level structure between $La_2(WO_4)_3$ and $CuWO_4$ in $La_2(WO_4)_3/CuWO_4$ composite, the photothermal generated e^- on the CB of $La_2(WO_4)_3$ would transfer to the CB of $CuWO_4$, and photothermal generated h^+ on the VB of $CuWO_4$ would transfer to the VB of $La_2(WO_4)_3$. This could effectively inhibit the photothermal-generated e^-–h^+ pairs recombination in $La_2(WO_4)_3/CuWO_4$ composite. Because the E_{VB} oxidation potential (2.03 V) of $La_2(WO_4)_3$ was higher than that of ·OH/OH^- (1.99 V) (He et al., 2025; Sun et al., 2025), h^+ on VB could oxidize OH^- to ·OH, leading to oxidative damage of tumor cells. In addition, the CB reduction potential (−0.26 V) of $CuWO_4$ was not negative than that of $O_2/\cdot O_2^-$ (−0.33 V) (Wang et al., 2024; Sun et al., 2024), which suggested that the e^- on the CB of $CuWO_4$ could not reduce O_2 to superoxide anion radical ($\cdot O_2^-$). In summary, the production of ROS such as $^1O_2$ and ·OH, especially the production of ·OH, played an important role in the $La_2(WO_4)_3/CuWO_4$ composite mediated SDT antitumor process, which was consistent with the results of previous ROS probe experiments.

4 Conclusion

In summary, $La_2(WO_4)_3/CuWO_4$ composites were prepared by two-step hydrothermal method and characterized by XRD, SEM, XPS, EDX and DRS. On this basis, using u251 glioma cells as model, the sonodynamic antitumor activity of $La_2(WO_4)_3/CuWO_4$ composite LC-10 was investigated by MTT method and AO/EB staining. The results showed that compared with $La_2(WO_4)_3$ and $CuWO_4$, $La_2(WO_4)_3/CuWO_4$ composite had better sonodynamic antitumor activity, and LC-10 had good biosafety at concentrations below 50 $\mu g \cdot mL^{-1}$. After $La_2(WO_4)_3$ and $CuWO_4$ formed $La_2(WO_4)_3/CuWO_4$ composite, the photo-thermal generated e^- on the CB of $La_2(WO_4)_3$ would be transferred to the CB of $CuWO_4$, and the generated h^+ on the VB of $CuWO_4$ would be transferred to the VB of $La_2(WO_4)_3$ during SDT. The recombination of e^-–h^+ pairs was effectively inhibited, and more strongly oxidizing ROS was produced, inducing apoptosis of u251 glioma cells. In which, $^1O_2$ and ·OH, especially the production of ·OH, played an important role in the $La_2(WO_4)_3/CuWO_4$ composite mediated SDT antitumor process. In general, the results of this study would lay a foundation for the design of $CuWO_4$ base nano-sonosensitizer and its further clinical application in the study of sonodynamic antitumor. At the same time, it also provided a new strategy for the design and development of novel nano-sonosensitizers with excellent sonodynamic activity.

Data availability statement

The original contributions presented in the study are included in the article/Supplementary Material, further inquiries can be directed to the corresponding author.

Ethics statement

Ethical approval was not required for the studies on humans in accordance with the local legislation and institutional requirements because only commercially available established cell lines were used.

Author contributions

F-YL: Data curation, Investigation, Writing–original draft. XW: Conceptualization, Methodology, Project administration, Writing–review and editing. Y-FL: Funding acquisition, Project administration, Writing–review and editing.

Funding

The author(s) declare that financial support was received for the research, authorship, and/or publication of this article. This work was financially supported by the Medical and Industrial Cross Joint Fund of Liaoning Cancer Hospital and Institute and Dalian University of Technology (LD202212).

Conflict of interest

The authors declare that the research was conducted in the absence of any commercial or financial relationships that could be construed as a potential conflict of interest.

Generative AI statement

The author(s) declare that no Generative AI was used in the creation of this manuscript.

Publisher's note

All claims expressed in this article are solely those of the authors and do not necessarily represent those of their affiliated organizations, or those of the publisher, the editors and the reviewers. Any product that may be evaluated in this article, or claim that may be made by its manufacturer, is not guaranteed or endorsed by the publisher.

Supplementary material

The Supplementary Material for this article can be found online at: https://www.frontiersin.org/articles/10.3389/fbioe.2025.1566946/full#supplementary-material

References

Baby, B., Thomas, S., Jose, J., Thomas, K., Punathil, P., Unnikrishnan, N. V., et al. (2024). Luminescence studies and Judd Ofelt parameterization of Dy^{3+} activated $La_2(WO_4)_3$ yellow phosphor. *Inorg. Chem. Commun.* 165, 112550. doi:10.1016/j.inoche.2024.112550

Canavese, G., Ancona, A., Racca, L., Canta, M., Dumontel, B., Barbaresco, F., et al. (2018). Nanoparticle-assisted ultrasound: a special focus on sonodynamic therapy against cancer. *Chem. Eng. J.* 340, 155–172. doi:10.1016/j.cej.2018.01.060

Chang, F., Bao, W., Li, K., Bai, W., Shi, Z., Liu, D.-g., et al. (2024). Augmented photocatalytic NO removal by the S-scheme $Bi_7O_9I_3/Bi_2S_3$ heterojunctions with surface oxygen vacancies: experimental analyses and theoretical calculations. *J. Environ. Manag.* 370, 122390. doi:10.1016/j.jenvman.2024.122390

Chang, F., Lei, Y., Li, J., Li, S., Liu, D.-g., and Kong, Y. (2023). Externally modified $Bi_{12}SiO_{20}$ with BiOI: n-p heterojunctions for effectually photocatalytic degradation of bisphenol A. *Sep. Purif. Technol.* 323, 124516. doi:10.1016/j.seppur.2023.124516

Chang, F., Li, J., Kou, Y., Bao, W., Shi, Z., Zhu, G., et al. (2025). The intense charge migration and efficient photocatalytic NO removal of the S-scheme heterojunction composites $Bi_7O_9I_3$-BiOBr. *Sep. Purif. Technol.* 353, 128402. doi:10.1016/j.seppur.2024.128402

Chen, H., Sun, M., Zhao, J., Huang, X., Teng, H., Gao, Y., et al. (2024). *In-situ* assembling novel N-Ti_3C_2/$BiOCl_xBr_{1-x}$ composites with enhanced photocatalytic degradation and nitrogen reduction activity. *Spectrochimica Acta Part A Mol. Biomol. Spectrosc.* 316, 124331. doi:10.1016/j.saa.2024.124331

Chen, L., Mao, Z., Wang, Y., Kang, Y., Wang, Y., Mei, L., et al. (2022). Edge modification facilitated heterogenization and exfoliation of two-dimensional nanomaterials for cancer catalytic therapy. *Sci. Adv.* 8, eabo7372. doi:10.1126/sciadv.abo7372

Cheng, M., Liu, Y., You, Q., Lei, Z., Ji, J., Zhang, F., et al. (2024). Metal-doping strategy for carbon-based sonosensitizer in sonodynamic therapy of glioblastoma. *Adv. Sci.* 11, 2404230. doi:10.1002/advs.202404230

Cui, Y., Chen, X., Cheng, Y., Lu, X., Meng, J., Chen, Z., et al. (2021). $CuWO_4$ Nanodots for NIR-induced photodynamic and chemodynamic synergistic therapy. *ACS Appl. Mater. and Interfaces* 13, 22150–22158. doi:10.1021/acsami.1c00970

Dong, Y., Dong, S., Liu, B., Yu, C., Liu, J., Yang, D., et al. (2021). 2D piezoelectric Bi_2MoO_6 nanoribbons for GSH-enhanced sonodynamic therapy. *Adv. Mater.* 33, 2106838. doi:10.1002/adma.202106838

Duan, Y., Yu, Y., Liu, P., Gao, Y., Dai, X., Zhang, L., et al. (2023). Reticular chemistry-enabled sonodynamic activity of covalent organic frameworks for nanodynamic cancer therapy. *Angew. Chem. Int. Ed.* 62, e202302146. doi:10.1002/anie.202302146

Gong, F., Cheng, L., Yang, N., Gong, Y., Ni, Y., Bai, S., et al. (2020). Preparation of $TiH_{1.924}$ nanodots by liquid-phase exfoliation for enhanced sonodynamic cancer therapy. *Nat. Commun.* 11, 3712. doi:10.1038/s41467-020-17485-x

Hachimine, K., Shibaguchi, H., Kuroki, M., Yamada, H., Kinugasa, T., Nakae, Y., et al. (2007a). Sonodynamic therapy of cancer using a novel porphyrin derivative, DCPH-P-Na(I), which is devoid of photosensitivity. *Cancer Sci.* 98, 916–920. doi:10.1111/j.1349-7006.2007.00468.x

Hachimine, K., Shibaguchi, H., Kuroki, M., Yamada, H., Kinugasa, T., Nakae, Y., et al. (2007b). Sonodynamic therapy of cancer using a novel porphyrin derivative, DCPH-P-Na(I), which is devoid of photosensitivity. *Cancer Sci.* 98, 916–920. doi:10.1111/j.1349-7006.2007.00468.x

Han, X., Huang, J., Jing, X., Yang, D., Lin, H., Wang, Z., et al. (2018). Oxygen-deficient black titania for synergistic/enhanced sonodynamic and photoinduced cancer therapy at near infrared-II biowindow. *ACS Nano* 12, 4545–4555. doi:10.1021/acsnano.8b00899

Han, Y., Qi, X.-X., Liu, Y.-C., Wang, Y., Xiang, Z., and Wang, X. (2025). Preparation of $CuWO_4/Bi_2WO_6$ composite and its sonocatalytic removal of tetracycline by combined persulfate. *J. Alloys Compd.* 1010, 177505. doi:10.1016/j.jallcom.2024.177505

He, L.-L., Li, S., Qi, S., Wang, N., Sun, M.-T., Su, C., et al. (2024). Synthesis of three-dimensional flower-like $BiFeO_3$ with enhanced sonocatalytic performance for the removal of methylene blue. *Inorg. Chem. Commun.* 166, 112649. doi:10.1016/j.inoche.2024.112649

He, L.-L., Wang, N., Qi, S., Sun, M.-T., Kou, X.-W., Su, C., et al. (2025). Preparation of $CuWO_4/CaWO_4$ n–n heterojunction with enhanced sonocatalytic performance: characterization, sonocatalytic mechanism and degradation pathways of organic pollutant. *Inorg. Chem. Commun.* 171, 113564. doi:10.1016/j.inoche.2024.113564

He, L.-L., Wang, X., Liu, B., Wang, J., Sun, Y.-G., and Xu, S.-K. (2011a). Study on the sonodynamic activity and mechanism of promethazine hydrochloride by multi-spectroscopic techniques. *Spectrochimica Acta Part A Mol. Biomol. Spectrosc.* 81, 698–705. doi:10.1016/j.saa.2011.07.006

He, L.-L., Wang, X., Liu, B., Wang, J., Sun, Y.-G., and Xu, S.-K. (2011b). Spectroscopic investigation on the synergistic effects of ultrasound and dioxopromethazine hydrochloride on protein. *J. Fluoresc.* 21, 1847–1856. doi:10.1007/s10895-011-0879-2

He, L.-L., Wang, X., Wu, X.-X., Wang, Y.-X., Kong, Y.-M., Wang, X., et al. (2015a). Protein damage and reactive oxygen species generation induced by the synergistic effects of ultrasound and methylene blue. *Spectrochimica Acta Part A Mol. Biomol. Spectrosc.* 134, 361–366. doi:10.1016/j.saa.2014.06.121

He, L.-L., Wu, X.-X., Wang, Y.-X., Liu, X.-P., Song, Y.-L., Yang, Y.-J., et al. (2015b). Spectroscopic investigation on the sonodynamic damage to protein in the presence of eosine B. *Ultrason. Sonochemistry* 26, 93–98. doi:10.1016/j.ultsonch.2015.02.002

Huang, X., Chen, H., Sun, M., Zhao, J., Teng, H., Gao, Y., et al. (2024c). N-graphyne surrounded Bi_2S_3/BiOBr composites: in-situ ultrasound-assisted synthesis and superior photocatalytic activity. *Fuel* 375, 132613. doi:10.1016/j.fuel.2024.132613

Huang, X., Sun, M., Humayun, M., Li, S., Zhao, J., Chen, H., et al. (2024b). *In-situ* synthesis of efficient N-graphyne/Bi/BiOBr photocatalysts for contaminants removal and nitrogen fixation. *J. Alloys Compd.* 976, 173025. doi:10.1016/j.jallcom.2023.173025

Huang, X., Sun, M., Sun, W., Li, Z., Chen, H., and Zhao, J. (2024a). One-step hydrothermal formation of porous N-graphyne decorated TiO_2/Ti_3C_2 composites with enhanced photocatalytic activity. *Int. J. Hydrogen Energy* 55, 581–591. doi:10.1016/j.ijhydene.2023.11.203

Jiang, L., Wang, J., Jiang, J., Zhang, C., Zhao, M., Chen, Z., et al. (2020). Sonodynamic therapy in atherosclerosis by curcumin nanosuspensions: preparation design, efficacy evaluation, and mechanisms analysis. *Eur. J. Pharm. Biopharm.* 146, 101–110. doi:10.1016/j.ejpb.2019.12.005

Kang, Y., Mao, Z., Wang, Y., Pan, C., Ou, M., Zhang, H., et al. (2022). Design of a two-dimensional interplanar heterojunction for catalytic cancer therapy. *Nat. Commun.* 13, 2425. doi:10.1038/s41467-022-30166-1

Kumar, G., Kumar, J., Bag, M., and Kumar Dutta, R. (2022). Solar light induced photocatalytic process for reduction of hexavalent chromium and degradation of tetracycline and methylene blue by heterostructures made of SnS_2 nanoplates surface modified by $ZnWO_4$ nanorods. *Sep. Purif. Technol.* 292, 121040. doi:10.1016/j.seppur.2022.121040

Li, J.-H., Song, D.-Y., Xu, Y.-G., Huang, Z., and Yue, W. (2008). *In vitro* study of haematoporphyrin monomethyl ether-mediated sonodynamic effects on C6 glioma cells. *Neurol. Sci.* 29, 229–235. doi:10.1007/s10072-008-0972-8

Li, R., Wang, X., Shi, J., Kang, Y., and Ji, X. (2023). Sonocatalytic cancer therapy: theories, advanced catalysts and system design. *Nanoscale* 15, 19407–19422. doi:10.1039/d3nr04505f

Liu, Q., Wang, X., Wang, P., Qi, H., Zhang, K., and Xiao, L. (2006). Sonodynamic effects of protoporphyrin IX disodium salt on isolated sarcoma 180 cells. *Ultrasonics* 45, 56–60. doi:10.1016/j.ultras.2006.06.063

Liu, Y.-C., Ge, Y.-D., An, H.-L., Ju, W.-T., Zhou, X.-Y., Xing, M.-Y., et al. (2024). Synthesis of a novel double Z-scheme $BiVO_4/Cu_2O$/g-C_3N_4 sonocatalyst and research on sonocatalytic degradation of tetracycline. *J. Environ. Chem. Eng.* 12, 113668. doi:10.1016/j.jece.2024.113668

Liu, Y.-C., Liu, X., Wang, X., Li, Z.-H., Chen, C.-L., and Xiang, Z. (2023). Hybrid persulfate/sonocatalysis for degradation of acid orange 7 in the presence of Ag_2O/$CuWO_4$ composite: operating parameters and sonocatalytic mechanism. *J. Clean. Prod.* 394, 136287. doi:10.1016/j.jclepro.2023.136287

Lu, X., Li, J., and Chang, F. (2025). Sonocatalytic evaluation of binary composites $Bi_{12}GeO_{20}$/GO in degradation of tetracycline hydrochloride. *Mater. Sci. Semicond. Process.* 185, 108964. doi:10.1016/j.mssp.2024.108964

Pan, X., Bai, L., Wang, H., Wu, Q., Wang, H., Liu, S., et al. (2018). Metal–organic-framework-derived carbon nanostructure augmented sonodynamic cancer therapy. *Adv. Mater.* 30, 1800180. doi:10.1002/adma.201800180

Ping, J., Du, J., Ouyang, R., Miao, Y., and Li, Y. (2023). Recent advances in stimuli-responsive nano-heterojunctions for tumor therapy. *Colloids Surfaces B Biointerfaces* 226, 113303. doi:10.1016/j.colsurfb.2023.113303

Qian, M.-Q., Xiang, Z., and Wang, X. (2024). Sonodynamic inactivation of gram-negative and gram-positive bacteria in the presence of phenothiazine compounds toluidine blue and azurin A. *Biochimica Biophysica Acta (BBA) - General Subj.* 1868, 130711. doi:10.1016/j.bbagen.2024.130711

Qiu, P., Park, B., Choi, J., Thokchom, B., Pandit, A. B., and Khim, J. (2018). A review on heterogeneous sonocatalyst for treatment of organic pollutants in aqueous phase based on catalytic mechanism. *Ultrason. Sonochemistry* 45, 29–49. doi:10.1016/j.ultsonch.2018.03.003

Rosenthal, I., Sostaric, J. Z., and Riesz, P. (2004). Sonodynamic therapy––a review of the synergistic effects of drugs and ultrasound. *Ultrason. Sonochemistry* 11, 349–363. doi:10.1016/j.ultsonch.2004.03.004

Sasaki, K., Yumita, N., Nishigaki, R., and Umemura, S. (1998). Antitumor effect sonodynamically induced by focused ultrasound in combination with Ga-porphyrin complex. *Jpn. J. Cancer Res.* 89, 452–456. doi:10.1111/j.1349-7006.1998.tb00584.x

Song, K., Du, J., Wang, X., Zheng, L., Ouyang, R., Li, Y., et al. (2022). Biodegradable bismuth-based nano-heterojunction for enhanced sonodynamic oncotherapy through charge separation engineering. *Adv. Healthc. Mater.* 11, 2102503. doi:10.1002/adhm.202102503

Sun, L., He, X., Liu, B., Zhang, S., Xiang, Z., Wang, X., et al. (2025). Synergistic adsorption-photocatalytic degradation of tetracycline by S-scheme $InVO_4/ZnIn_2S_4$ heterojunction: mechanism, toxicity assessment, and potential applications. *Sep. Purif. Technol.* 353, 128515. doi:10.1016/j.seppur.2024.128515

Sun, M.-T., Qi, Q., Wang, X., and He, L.-L. (2024). Synthesis of $Ag_2O/CaMoO_4$ S-type heterojunction with enhanced sonocatalytic performance to remove crystal violet in dye wastewater. *Inorg. Chem. Commun.* 167, 112778. doi:10.1016/j.inoche.2024.112778

Teng, J., Xiong, S., Li, F., Wang, S., and Li, T. (2024). Sonocatalytic performance of Bi_2WO_6 nanoparticles for degradation of tetracycline antibiotics. *Appl. Catal. O Open* 191, 206957. doi:10.1016/j.apcato.2024.206957

Umemura, S., Yumita, N., Nishigaki, R., and Umemura, K. (1989). "Sonochemical activation of hematoporphyrin: a potential modality for cancer treatment," in *Ultrasonics symposium, proceedings* (IEEE), 955–960.

Umemura, S.-i., Yumita, N., and Nishigaki, R. (1993). Enhancement of ultrasonically induced cell damage by a gallium-porphyrin complex, ATX-70. *Jpn. J. Cancer Res.* 84, 582–588. doi:10.1111/j.1349-7006.1993.tb00179.x

Wan, L., Sheng, J., Chen, H., and Xu, Y. (2013). Different recycle behavior of Cu^{2+} and Fe^{3+} ions for phenol photodegradation over TiO_2 and WO_3. *J. Hazard. Mater.* 262, 114–120. doi:10.1016/j.jhazmat.2013.08.002

Wang, X., He, L.-L., Liu, B., Wang, X.-F., Xu, L., and Sun, T. (2018). Reactive oxygen species generation and human serum albumin damage induced by the combined effects of ultrasonic irradiation and brilliant cresyl blue. *Int. J. Biol. Macromol.* 120, 1865–1871. doi:10.1016/j.ijbiomac.2018.10.002

Wang, X., He, X.-S., Li, C.-Y., Liu, S.-L., Lu, W., Xiang, Z., et al. (2023b). Sonocatalytic removal of tetracycline in the presence of S-scheme $Cu_2O/BiFeO_3$ heterojunction: operating parameters, mechanisms, degradation pathways and toxicological evaluation. *J. Water Process Eng.* 51, 103345. doi:10.1016/j.jwpe.2022.103345

Wang, X., Yu, S., Li, Z.-H., He, L.-L., Liu, Q.-L., Hu, M.-Y., et al. (2021). Fabrication Z-scheme heterojunction of $Ag_2O/ZnWO_4$ with enhanced sonocatalytic performances for meloxicam decomposition: increasing adsorption and generation of reactive species. *Chem. Eng. J.* 405, 126922. doi:10.1016/j.cej.2020.126922

Wang, Y., Gong, F., Han, Z., Lei, H., Zhou, Y., Cheng, S., et al. (2023a). Oxygen-deficient molybdenum oxide nanosensitizers for ultrasound-enhanced cancer metalloimmunotherapy. *Angew. Chem. Int. Ed.* 62, e202215467. doi:10.1002/anie.202215467

Wang, Y., Li, F., and Li, T. (2024). Facile synthesis of $BiOI/BaNbO_3$ composite for rapid sonocatalytic degradation of tetracycline hydrochloride. *J. Solid State Chem.* 333, 124644. doi:10.1016/j.jssc.2024.124644

Wei, J., Li, T., and Li, F. (2023). Synthesis and sonocatalytic performance of $Dy_2Sn_2O_7$/Sepiolite nanocomposite. *J. Solid State Chem.* 328, 124368. doi:10.1016/j.jssc.2023.124368

Wu, N., Fan, C.-H., and Yeh, C.-K. (2022). Ultrasound-activated nanomaterials for sonodynamic cancer theranostics. *Drug Discov. Today* 27, 1590–1603. doi:10.1016/j.drudis.2022.02.025

Xiao, Z., Peng, C., Jiang, X., Peng, Y., Huang, X., Guan, G., et al. (2016). Polypyrrole-encapsulated iron tungstate nanocomposites: a versatile platform for multimodal tumor imaging and photothermal therapy. *Nanoscale* 8, 12917–12928. doi:10.1039/c6nr03336a

Xing, X., Zhao, S., Xu, T., Huang, L., Zhang, Y., Lan, M., et al. (2021). Advances and perspectives in organic sonosensitizers for sonodynamic therapy. *Coord. Chem. Rev.* 445, 214087. doi:10.1016/j.ccr.2021.214087

Xu, L., Ge, Y.-D., Zhou, X.-Y., Xing, M.-Y., Wu, X.-Q., Wang, Y., et al. (2025). Study on the sonocatalytic removal of tetracycline by an type-II heterojunction $CuS/FeWO_4$. *J. Alloys Compd.* 1015, 178826. doi:10.1016/j.jallcom.2025.178826

Xu, L., Wu, X.-Q., Li, C.-Y., Liu, N.-P., An, H.-L., Ju, W.-T., et al. (2023). Sonocatalytic degradation of tetracycline by $BiOBr/FeWO_4$ nanomaterials and enhancement of sonocatalytic effect. *J. Clean. Prod.* 394, 136275. doi:10.1016/j.jclepro.2023.136275

Yang, Y., Wang, X., Qian, H., and Cheng, L. (2021). Titanium-based sonosensitizers for sonodynamic cancer therapy. *Appl. Mater. Today* 25, 101215. doi:10.1016/j.apmt.2021.101215

Zhang, M., Cui, Z., Song, R., Lv, B., Tang, Z., Meng, X., et al. (2018). $SnWO_4$-based nanohybrids with full energy transfer for largely enhanced photodynamic therapy and radiotherapy. *Biomaterials* 155, 135–144. doi:10.1016/j.biomaterials.2017.11.013

Zhang, S., Xia, S., Chen, L., Chen, Y., and Zhou, J. (2023b). Covalent organic framework nanobowls as activatable nanosensitizers for tumor-specific and ferroptosis-augmented sonodynamic therapy. *Adv. Sci.* 10, 2206009. doi:10.1002/advs.202206009

Zhang, S., Zhang, L., Hu, J., He, X., Geng, B., Pan, D., et al. (2023a). Trienzyme-like $Co_3O_4@TiO_{2-x}$ nanozymes for heterojunction-enhanced nanocatalytic-sonodynamic tumor therapy. *Chem. Eng. J.* 458, 141485. doi:10.1016/j.cej.2023.141485

Zhang, T., Zheng, Q., Fu, Y., Xie, C., Fan, G., Wang, Y., et al. (2021). α-Fe_2O_3@Pt heterostructure particles to enable sonodynamic therapy with self-supplied O_2 and imaging-guidance. *J. Nanobiotechnology* 19, 358. doi:10.1186/s12951-021-01105-x

Zhou, Y., Cao, Z., Jiang, L., Chen, Y., Cui, X., Wu, J., et al. (2024). Magnetically actuated sonodynamic nanorobot collectives for potentiated ovarian cancer therapy. *Front. Bioeng. Biotechnol.* 12, 1374423. doi:10.3389/fbioe.2024.1374423

Zhou, Y., Yang, N., Gong, F., Wang, Y., Yang, X., Dai, Y., et al. (2022). Oxygen-deficient tungsten oxide (WO_x) nanobelts with pH-sensitive degradation for enhanced sonodynamic therapy of cancer. *ACS Nano* 16, 17242–17256. doi:10.1021/acsnano.2c07903

Zhu, P., Chen, Y., and Shi, J. (2020). Piezocatalytic tumor therapy by ultrasound-triggered and $BaTiO_3$-mediated piezoelectricity. *Adv. Mater.* 32, 2001976. doi:10.1002/adma.202001976

frontiers | Frontiers in Bioengineering and Biotechnology

TYPE Original Research
PUBLISHED 20 March 2025
DOI 10.3389/fbioe.2025.1557772

OPEN ACCESS

EDITED BY
Liqun Yang,
Shengjing Hospital of China Medical University, China

REVIEWED BY
Andrea Bianconi,
University of Genoa, Italy
Kaixiang Zhou,
Beijing Normal University, Zhuhai, China

*CORRESPONDENCE
Yuxin Han,
hanyuxin@hnpoly.com
Shuxu Yang,
3195019@zju.edu.cn

†These authors share first authorship

RECEIVED 09 January 2025
ACCEPTED 03 March 2025
PUBLISHED 20 March 2025

CITATION
Zhou X, Jiang K, Han Y and Yang S (2025) A preclinical study of a novel dual-modality contrast agent in rodent models.
Front. Bioeng. Biotechnol. 13:1557772.
doi: 10.3389/fbioe.2025.1557772

A preclinical study of a novel dual-modality contrast agent in rodent models

Xuelai Zhou[1†], Kangli Jiang[1†], Yuxin Han[1*] and Shuxu Yang[2*]

[1]Zhejiang Poly Pharm. Co., Ltd., Hangzhou, China, [2]Department of Neurosurgery, Sir Run Run Shaw Hospital, College of Medicine, Zhejiang University, Hangzhou, China

Introduction: Glioblastoma (GBM) represents the most aggressive and prevalent form of primary malignant brain tumor in adults, with surgical intervention being the primary treatment modality. To enhance surgical outcomes and extend patient survival, we have engineered a dual-modality MRI/FI contrast agent known as PL002 to aid in the surgical management of GBM.

Methods: In this study, an orthotopic glioma model was established in mice via intracranial injection of U-87 MG cells. Subsequently, the model animals were intravenously injected with PL002 and placed in a 7.0T magnetic resonance imaging (MRI) device to evaluate the imaging effects. After the MRI scan, fluorescence imaging techniques were employed to observe the distribution of PL002 at both the brain tissue and cellular levels. Moreover, healthy rat models were utilized to investigate the pharmacokinetic characteristics, tissue distribution, and safety profile of PL002.

Results: The molecular structure of PL002 contains both gadolinium (Gd^{3+}) and indocyanine green (ICG), demonstrating optimal imaging effects within the dosage range of 10-50 mg/kg, with a half-life of 2.51 to 4.87 hours. Even at relatively low concentrations in the brain, PL002 can provide stable and sustained support for MRI and fluorescence imaging for up to 72 hours. No abnormalities were observed in rats at a dosage of 100 mg/kg.

Discussion: Compared to Gadavist® and ICG, PL002 provided sustained support for MRI and FI of GBM for 72 h, with a broad therapeutic window. This dual-modality contrast agent holds significant potential and promise for applications in preoperative assessment of resection margins, real-time intraoperative guidance, and postoperative verification of the extent of resection.

KEYWORDS

gadolinium contrast agent, ICG, magnetic resonance imaging, fluorescence imaging, glioblastoma, intraoperative navigation

1 Introduction

Glioblastoma (GBM) is the most aggressive malignant brain tumor in adults, constituting approximately 50.9% of all malignant brain tumors according to the 2016–2020 CBTRUS Statistical Report (Wirtz et al., 2000; Qi et al., 2024). Compared to other malignancies, GBM is characterized by a poor prognosis and a short median survival time (Ostrom et al., 2023). Until to now, surgery remains the standard approach for GBM management. The extent of tumor resection is positively correlated with progression-free survival and quality of life. To achieve the maximum safe resection, neurosurgeons often

utilize additional tools such as neuronavigation, intraoperative magnetic resonance imaging (iMRI), and intraoperative fluorescence navigation (Wirtz et al., 2000; Staartjes et al., 2021; Schupper et al., 2021).

Neuronavigation relies on preoperative MRI to accurately pinpoint the lesion, select the optimal surgical approach, and reduce postoperative complications. However, it lacks the capability to offer real-time evaluation of tumor margins throughout the surgical procedure, with the exception of iMRI (Krivosheya et al., 2021; Li et al., 2017). But iMRI is time-consuming, costly, and does not significantly impact prognosis (Bonosi et al., 2023; Mosteiro et al., 2022). Intraoperative fluorescence navigation enhances the visualization of brain tumor tissue through selective fluorescence in tumor cells (Schupper et al., 2022), such as with 5-aminolevulinic acid (5-ALA) fluorescence-guided surgery, which has been shown to improve 6-month progression-free survival rates in randomized trials. However, the cost of 5-ALA and the need for specialized equipment limit its widespread use. Indocyanine green (ICG) is another compound used in intraoperative fluorescence navigation and can also be used for direct glioblastoma imaging, potentially improving the extent of resection (Acerbi et al., 2018). Clinically, each intraoperative imaging technology has its advantages and disadvantages, and no single imaging technology can address all pre- and post-surgical detection and diagnostic needs. The combination of multiple imaging modalities for intraoperative tumor recognition is gaining attention among neurosurgeons due to the limitations of single imaging modes. Studies (Eyüpoglu et al., 2012; Tsugu et al., 2011) have shown that the combination of intraoperative MRI and fluorescence guidance has a synergistic effect in glioma surgery, with the combination approach significantly improving the extent of tumor resection compared to fluorescence-guided surgery alone.

Given the clinical benefits of multimodal imaging, there is a need for contrast agents capable of both MRI and fluorescence enhancement. Our group has developed a compound that incorporates Gd^{3+} and ICG molecules, aiming to provide dual MRI and fluorescence imaging capabilities. This dual-modality agent is expected to offer complementary bioimaging information for GBM surgery, improving surgical outcomes and extending postoperative patient survival.

2 Materials and methods

2.1 Material

tert-butyl (10-aminodecy)carbamate (Nanjing Weichuangyuan Medical Technology Co., LTD.), Indocyanine green (Dandong medical innovation Pharmaceutical Co., LTD., 21081512), Gadavist®(Bayer, KT04KPK), PL002 (Zhejiang Poly Pharmaceutical Co., LTD., 00-003958-25-01), Cell Counting Kit-8(Beyotime Biotechnology). Other chemical reagents all came from Sahn Chemical Technology (Shanghai) Co., LTD.

L-O2(BOHUI Biotechnology (GUANGZHOU) Co., LTD., BH-C073), HEK293(National Collection of Authenticated Cell Culture, SCSP-5209), U-87 MG (Zhejiang Meisen Cell Technology Co., LTD., CTCC-001-0023), Culture medium and fetal bovine serum were purchased from Gibco Laboratories (Grand Island, NY), BALB/c nude mice (Zhejiang Weitong Lihua Experimental Animal Technology Co., LTD.), Sprague-Dawley rat (Beijing Vitonglihua Experimental Animal Technology Co., LTD.). All animal experiments were conducted with the approval of the Experimental Animal Welfare and Ethics Committee of Zhejiang Longchuan Biomedical Technology Co., LTD.

2.2 Synthesis

2.2.1 PL002-SMA

N, N-dimethylformamide, cyclotenine, and sodium acetate were mixed in a reaction flask, then tert-butyl bromoacetate and more N, N-dimethylformamide were added. The reaction was maintained at 25°C for 17 h with pH between 7 and 8, yielding SMA-1 as a white solid after filtration. In a new vessel, potassium carbonate, acetonitrile, methyl bromoacetate, and SMA-1 were stirred at 25°C for 6 h, resulting in SMA-2 as a yellow oil after filtration and concentration. Tetrahydrofuran, SMA-2, sodium hydroxide, and water were mixed and stirred at 30°C for 4 h, then the pH was adjusted to 6 with hydrochloric acid. After partitioning and drying, PL002-SMA was obtained as a white solid.

2.2.2 PL002-SMC

1,1,2-trimethyl-1H-benzo [e]indole, 1,4-butanolide, and toluene were mixed and refluxed at 110°C for 20–21 h to yield SMC-1 as a light blue solid after cooling and drying. In a new vessel, N, N-dimethylformamide was mixed with phosphorus oxychloride at 0°C–5°C, then cyclohexanone was added at 15°C–20°C, resulting in SMC-2 as an orange solid after filtration and drying. Toluene, SMC-1, SMC-2, and sulfolane were mixed, refluxed at 116°C–118°C for 5–6 h, and SMC-3 was obtained as a reddish-brown solid. Acetonitrile and p-hydroxyphenylpropionic acid were mixed with sodium hydroxide solution at 0°C–5°C, reacted at 25°C–30°C for 1 h, and SMC-4 was obtained as a gray solid. In another flask, DMSO and SMC-3 were mixed at 22°C, then SMC-4 was added, and after stirring, PL002-SMC was obtained as a dark green solid.

2.2.3 PL002

N, N-dimethylformamide, N, N-diisopropylethylamine, PL002-SMA, and PL002-SMB were combined in a reaction flask. PyBOP and more N, N-dimethylformamide were added and the mixture reacted for 4–6 h, then filtered to get PL001-01 filtrate. Hydrobromoacetic acid and triethylsilane were added to the filtrate at 0°C, mixed, and reacted at 20°C for 5 h to yield PL002-02 solid. PL002-02 was dissolved in water, gadolinium oxide was added, and the mixture was reacted at 100°C for 1 h. The pH was adjusted with sodium hydroxide solution, and the salt was removed by nanofiltration. PL002-03 was obtained by freeze-drying. In a new vessel, dimethyl sulfoxide, N, N-dimethylformamide, and N,N-diisopropylethylamine were added, followed by PL002-SMC, 1H-benzotriazole-1-hydroxy-tripyrroalkyl hexafluorphosphate, and PL002-03 at 15°C, and reacted for 2 h. After filtration and drying, PL002-05 was obtained. The liquid was purified using a DAC400 system, and PL002 was obtained by lyophilization. It was

then packaged in double-layer pharmaceutical low-density polyethylene bags and aluminum foil. The synthesis was completed using ChemDraw 21.

2.3 *In vitro* relaxivity

PL002 was prepared in six different concentrations (0.2, 0.5, 1.0, 1.5, 2.0, and 2.5 μg/mL) using ultrapure water and sequentially tested in the MZsoMR23-60H-I nuclear magnetic resonance (NMR) analyzer. The T1 acquisition was performed using an inversion recovery (IR) sequence with the following intrinsic parameters: SF = 12 MHz, O1 = 557,454.41 Hz, P1 = 5.8 μs, P2 = 9.6 μs. The adjustable parameters were set as follows: SW = 100 kHz, TW = 32,000 ms, RFD = 0.08 ms, RG1 = 20, NS = 4, DR = 1, PRG = 0, TE = 1 ms.

2.4 Cell proliferation assay

L-O2, HEK293, and U-87 MG cells were seeded in a 96-well plate at 2×10^5 cells/well and incubated overnight before being treated with various concentrations of PL002. After 24 h, cell proliferation was assessed using the CCK-8 assay. The culture medium was replaced with 100 μL of CCK-8 solution (10% reagent, 90% medium) per well, and the plate was incubated for 45 min at 37°C. Absorbance at 450 nm was measured using a SpectraMax_iD5 ELISA reader.

2.5 Animal modal

Human glioblastoma U87-MG cells were cultured in flasks with a 75 cm^2 base area, using standard methods and DMEM medium with 10% FBS and 1% P/S, under 37°C and 5% CO2. Anesthetized animals were placed on a stereotaxic frame, and a scalp incision was made. A burr hole was drilled in the skull without penetrating the dura mater. A 10 μL cell suspension with 1×10^6 cells was injected to a depth of 3 mm, then slowly infused over 5 min. The needle was left for 5 more minutes before withdrawal, and the hole was sealed with bone wax. The incision was closed and animals were monitored daily for health, including behavior, appetite, activity, and weight, after recovery on a heating pad.

2.6 MR imaging and fluorescent imaging *in vivo*

For *in vivo* MR and fluorescent imaging, 24 male BALB/c nude mice weighing about 20 g were divided into five groups: PL002 groups with doses of 5, 10, 50 mg/kg, a Gadavist® group with 18.14 mg/kg, and an ICG group with 5 mg/kg. Except for the high-dose PL002 and Gadavist® groups with 3 mice each, other groups had 6 mice. Mice were anesthetized and positioned for pre-injection MR imaging and at various post-injection time points using the BRUKER 7.0T MRI Biospoin GmbH nuclear magnetic resonance imaging system. T1-weighted imaging was conducted at several time points, excluding the high-dose groups from the 24-h scan. Scan parameters included: slice thickness (SL) = 0.700 mm, repetition time (TR) = 1,100.00 ms, echo time (TE) = 0.00 ms, filed of view (FOV) = 20 × 20 cm^2, image size = 192 × 192, bandwidth (BW) = 372.02 Hz, flip angle (FA) = 180.00. Mice from the 6 and 24-h MR Imaging groups were euthanized, and 2 from each group were selected for *ex vivo* fluorescence imaging at 745 nm excitation and 800 nm emission. The remaining mice's brains were fixed, embedded, sectioned, and stained with Hematoxylin and Eosin for histological examination. The same procedure was applied to the ICG group post-administration at 6 and 24 h.

All the animals were housed in a specific pathogen-free (SPF) animal facility and were removed from the facility on the day of imaging for the experiments.

2.7 Image analysis

After acquiring the MRI imaging data, manually trace the regions of interest (ROIs) for the tumor and normal tissues using ParaVision 360 software, and measure the signal intensity within these ROIs. Calculate the contrast-to-noise ratio (CNR) with the following formulas:

$$CNR = \frac{(S_1 - S_2)}{SD}$$

where S_1 is the signal intensity of the lesion, and S_2 is the signal intensity of the normal tissue. Signal acquisition in the tumor region involves first manually identifying the tumor contour based on the image, followed by delineating the signal measurement area using software and recording the average signal intensity within this region. Signal acquisition in the normal tissue region is performed by selecting an area outside the tumor contour, delineating the measurement area using software, and recording the average signal intensity within this region. Signal acquisition in the background region involves selecting an area outside the brain tissue, delineating the measurement area using software, and recording the average signal intensity within this region.

Following the completion of fluorescence imaging, manually delineate the tumor region of interest (ROI) using the IVIS Spectrum software on the captured images, and measure the signal intensity. Calculate the mean fluorescence intensity contrast (CAR) with the following formula:

$$CAR = \frac{F_1}{F_2}$$

where F_1 is the mean fluorescence intensity of the tumor, and F_2 is the mean fluorescence intensity of the normal tissue. For fluorescence acquisition in the tumor region, the tumor contour was first manually identified by integrating the fluorescence image with the original photograph. Subsequently, the signal measurement area was delineated using software, and the average signal intensity within this region was recorded. For signal acquisition in the normal tissue region, an area outside the tumor contour was selected. The measurement area was then delineated using software, and the average signal intensity within this region was recorded.

2.8 HE staining

After fixation in a 4% paraformaldehyde solution, mouse brains are embedded in paraffin with a HistoStar machine (Thermo) and sectioned to about 3 μm thickness using an HM 340E slicer (Thermo). The sections are deparaffinized with xylene and stained with hematoxylin and eosin. Post-staining, they are dehydrated through ethanol solutions, cleared with xylene, and mounted with neutral balsam. Light microscopy is used to observe tumor cell necrosis, number, density, and morphological changes.

2.9 *In vivo* pharmacokinetics, tissue distribution and safety tests

In the pharmacokinetic study, Sprague-Dawley rats (n = 18, 3/sex/group) were administered the test article PL002 via intravenous infusion at doses of 3, 10, and 30 mg/kg, with an infusion duration of approximately 4 min. Blood samples were collected from all animals at various time points: pre-dose, 4 min (immediately after infusion), 10, 15, 30, and 45 min, and 1, 2, 4, 6, 10, 24, and 48 h post-administration. Heparin sodium was utilized as an anticoagulant in this study. After blood sample collection, the samples were transferred to centrifuge tubes and manually mixed. Centrifugation was completed within 2 h. The centrifugation conditions were as follows: 3,000 g, at 2°C–8°C, for 10 min. After centrifugation, the plasma was collected into new centrifuge tubes and stored at below −60°C until analysis. LC-MS/MS (Applied Biosystems, 6500QTRAP) condition: The liquid chromatography (LC) system consists of a binary pump, an online degassing unit, an autosampler, and a column oven. The mass spectrometry (MS) system includes an electrospray ionization (ESI) source and a triple-quadrupole mass spectrometer, which are used for LC and MS data acquisition as well as for chromatographic analysis. Chromatographic separation was performed at an injection temperature of 4°C using an ACE3 C4 analytical column (50 mm × 2.1 mm, 3 μm, ACE). The retention times for PL002 and glimepiride (internal standard) were 2.6 min and 2.5 min, respectively. The mobile phase consisted of A (0.1% formic acid in water) and B (0.1% formic acid in acetonitrile). Sample preparation: Take 50 μL of plasma sample, then add 150 μL of internal standard solution (20 ng/mL) and vortex mix. Centrifuge for 15 min at 4°C and 3,200 g. Take 100 μL of the supernatant, add 100 μL of acetonitrile, vortex mix, and then inject for analysis.

In the tissue distribution study, Sprague-Dawley rats (n = 24, 3/sex/group) were given PL002 at a dose of 10 mg/kg via intravenous infusion for about 4 min. Blood and tissue samples were harvested from the animals at 2, 6, 24, and 72 h after dosing. The tissues sampled included the heart, liver, spleen, lung, kidney, stomach, small intestine, large intestine (colon), gonads (epididymis/testis/ovary), brain, fat, muscle, and skin. Heparin sodium was used as an anticoagulant for blood samples. Blood samples were processed in the same manner as in the pharmacokinetic study after collection. Tissue samples were weighed, homogenized, and the homogenates were stored at −60°C or below. The analytical method for PL002 in blood is the same as that in the pharmacokinetic study. The analytical method for PL002 in tissues has been adjusted as follows: Chromatographic separation is performed with retention times of 2.4 min for PL002 and 2.5 min for glimepiride (internal standard). The mobile phase consists of A (0.2% formic acid in water) and B (0.2% formic acid in acetonitrile). Preprocessing of tissue homogenate samples: Take 50 μL of tissue homogenate sample, then add 150 μL of internal standard working solution (20 ng/mL, glimepiride), and vortex mix. Centrifuge for 15 min at 2°C–8°C and 3,200 g. Take 20 μL of the supernatant, add 180 μL of diluent (acetonitrile:water = 90:10, v/v), vortex mix, and then analyze by LC-MS/MS. The gadolinium content of plasma and tissue was measured by ICP-MS (Agilent, 7900 ICP-MS). The ICP-MS was operated in the standard instrument mode. Instrument control, data acquisition, and analysis were performed using Plasma Lab software. The instrument and operating conditions were optimized using a tuning solution. During the detection process, rhodium (Rh) was used as an internal standard for monitoring. Plasma Preprocessing Method: Take 50 μL of plasma sample, then add 10 μL of internal standard working solution (2 μg/mL, rhodium element) and vortex mix. Add 1 mL of diluent (65% nitric acid and Triton X-100, both with a volume fraction of 0.1%) to the above sample and vortex mix. Take 0.25 mL of the solution, add 4.0 mL of diluent, vortex mix, and then analyze by ICP-MS. Tissue Homogenate Preprocessing Method:** Take 100 μL of tissue homogenate sample, then add 10 μL of internal standard working solution (200 ng/mL, rhodium element) and vortex mix. Add 500 μL of digestion solution (65% nitric acid) to the above sample and vortex mix. Digest in a water bath (75°C) for 2 h. Take 400 μL of the digested solution, add 2.0 mL of diluent (65% nitric acid and Triton X-100, both with a volume fraction of 0.1%), vortex mix, and then analyze by ICP-MS.

In the toxicity study, Sprague-Dawley rats (n = 40, 5/sex/group) were treated with either vehicle control (5% Glucose Injection) or PL002 at doses of 100, 300, and 1,000 mg/kg via intravenous infusion, with a volume of 20 mL/kg and an infusion rate of 5 mL/kg/min. Throughout the study, mortality and morbidity, clinical signs, body weights, and food consumption were monitored. Gross observations were conducted on deceased animals and those euthanized on Day 15. The brains, hearts, livers, spleens, lungs, and kidneys of deceased animals, as well as tissues with gross lesions from all animals, were processed using standard histological techniques: paraffin embedding, sectioning, mounting on glass slides, and staining with hematoxylin and eosin (H&E). All slides were examined microscopically. The non-compartmental analysis (NCA) method with WinNonlin 8.0 software was employed to calculate the pharmacokinetic parameters of the administered group.

All the animals were housed in a specific pathogen-free (SPF) animal facility.

2.10 Data analysis and image processing

Statistical data are showed as mean ± standard deviation (SD). The CNR data from *in vivo* MRI at 6 h and the safety experiment data (analyzed separately for males and females) were analyzed using SPSS 22.0. Levene's test was employed to assess the homogeneity of variance among groups. If the result of Levene's test showed no significant difference ($p \geq 0.01$), one-way analysis of variance (ANOVA) was used for variance (mean square error)

analysis, and Dunnett's test was applied for comparisons between the treatment groups and the control group. If Levene's test showed a significant difference ($p < 0.01$), Welch's test followed by Bonferroni correction was used for comparisons between the treatment groups and the control group. A two-tailed test was used with a confidence interval of 95%. $P > 0.05$ (NS) denotes there is no statistically significant. $P < 0.05$, $p < 0.01$, $p < 0.001$, were defined as statistically significant.

All data were processed and presented as images using GraphPad Prism 7 and Inkscape 1.4.

3 Results

3.1 Synthesis and characterization of PL002

PL002 was synthesized utilizing PL002-SMA and PL002-SMB as the initial reactants, which underwent a condensation reaction (①), an elimination reaction, a coordination reaction, and a subsequent condensation reaction (②) with the starting material PL002-SMC to yield the final PL002 product. The synthetic route of PL002 is shown in Figure 1.

The UV spectrum indicates that the absorption band attributed to the benzene ring appears at the maximum wavelength λmax = 216.5 nm, while the absorption band due to Gd^{3+} is observed at the maximum wavelength λmax = 805.0 nm. These characteristics are in alignment with the structural formula of PL002. In the IR spectrum, the C-H stretching vibration absorption peak is detected at 2,922.86 cm^{-1}, the C=O stretching vibration absorption peak for amide and carboxylic acid is found at 1,620.75 cm^{-1}, and the peaks at 1,357.47 cm^{-1} and 1,115.75 cm^{-1} correspond to the SO2 stretching vibration absorption of the sulfonic acid group. The absorption peak at 1,039.05 cm^{-1} is associated with the C-N stretching vibration, all of which are consistent with the structural formula of PL002. High-resolution mass spectrometry (HRMS) captured the excimer ion peaks at m/z 1,652.6564 $[M + H]^+$ and 826.8281 $[M+2H]^{2+}$. The exact molecular weight measured was in close agreement with the theoretical calculation of 1,652.6460 for the predicted molecular formula $C_{81}H_{106}N_8O_{15}S_2Gd$ $[M + H]^+$, with a difference (Diff) of

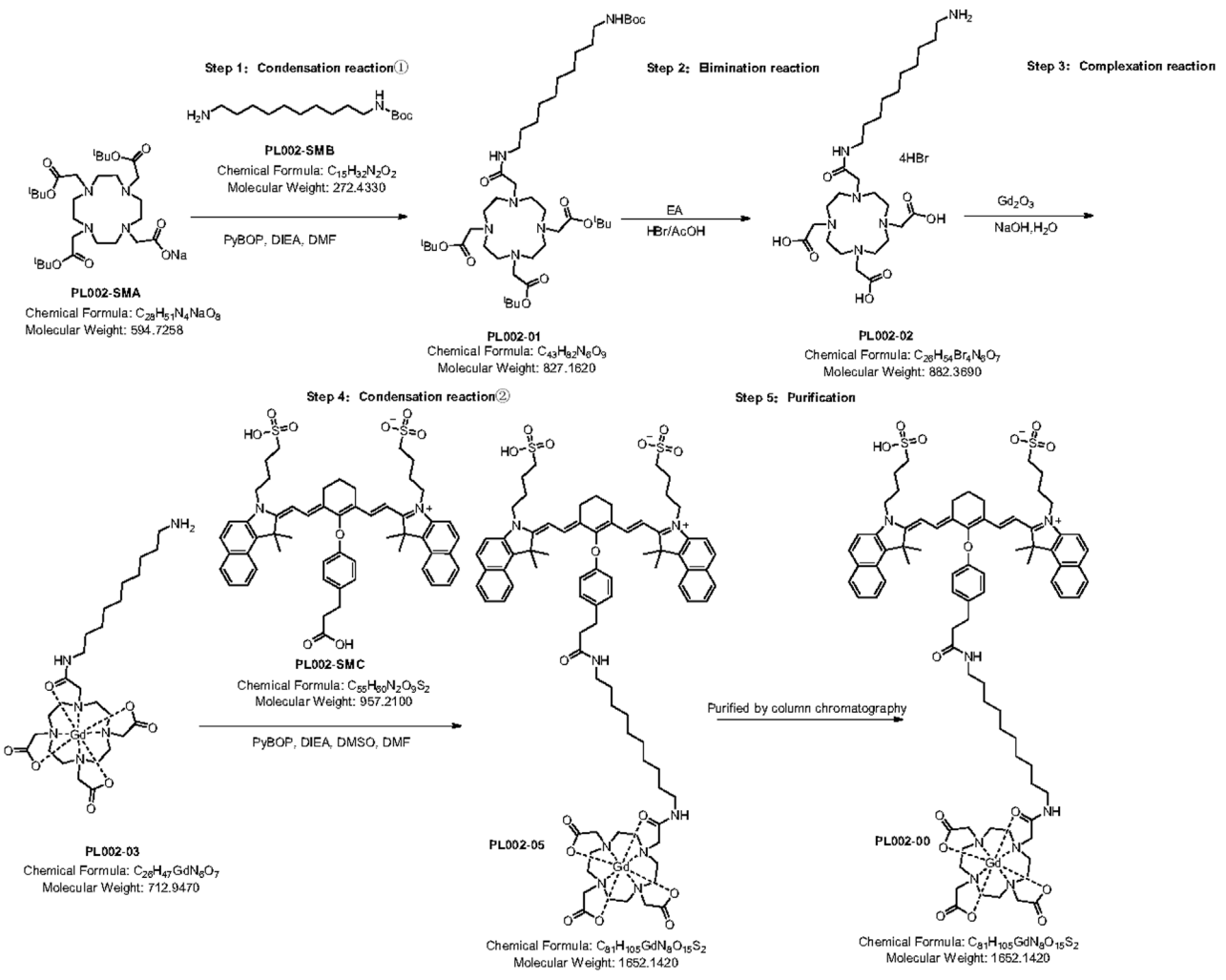

FIGURE 1
Synthetic route to PL002.

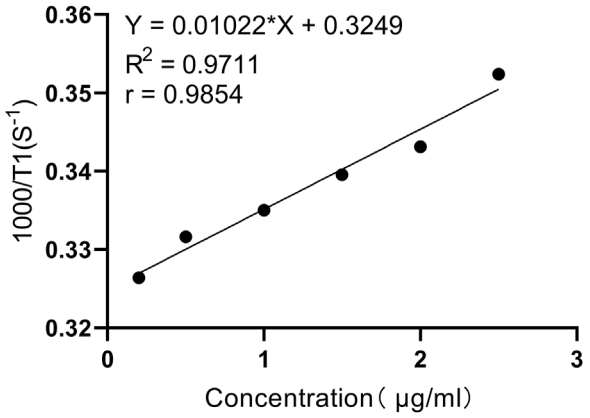

FIGURE 2
In vitro relaxation test curve (T1 sampling sequence: Intrinsic parameters SF = 12MHz, O1 = 557454.41Hz, P1 = 5.8us; Adjusted parameters SW = 1000KHz, TW = 32000 ms, RFD = 0.08 ms, RG1 = 20, DRG1 = 3, NS = 4, DR = 1, PRG = 0, TE = 1 ms.).

6.3 PPM, confirming the structural formula of PL002. Additionally, the relaxation rate test curve indicates that within the concentration range of 0–2.5ug/mL (0–1.5 μM in aqueous solution), as the concentration increases, the T1 relaxation time shortens and the relaxation rate enhances, suggesting that PL002 can serve as a T1-enhancing contrast agent for MRI (Figure 2).

3.2 MR imaging and fluorescent imaging *in vivo*

Before conducting *in vivo* imaging, the potential toxicity of PL002 on U-87 MG, L-O2, and HEK293 cell lines was assessed using the CCK-8 assay. They are used to assess the compound's potential toxicity *in vitro*, serving as a reference for its use in glioblastoma multiforme (GBM) surgery. The cells were treated with PL002 at various concentrations (ranging from 0 to 1250 μM) for a period of 24 h, followed by a 45-min incubation with a 10% CCK-8 solution to assess the compound's impact on cell growth. Figure 3 illustrates that PL002 does not exhibit cytotoxicity to U-87 MG, L-O2, and HEK293 cells at the tested concentrations (up to 1250 μM). These findings suggest that PL002 is biocompatible and has a low level of toxicity.

In comparative imaging experiments using a glioblastoma model, Gadavist® was used as a positive control against PL002. As illustrated in Figure 3, T1-weighted turbo spin echo (TSE) enhanced scans revealed that tumors in the models appeared as circular or quasi-circular masses. In larger tumors, signs of necrosis and bleeding could be observed. The mass effect was evident as a shift of midline structures to the opposite side and compression, expansion, and displacement of the ipsilateral ventricle. After intravenous administration via the tail vein, clear images of brain tumor tissue were obtained. On T1-weighted MRI (T1WI), the lesion site appeared as a high-signal mass, with brain parenchymal signals lower than those in the tumor region. The tumor imaging effect was determined by comparing the CNR of the different treatment groups.

Post-administration, the CNR in the PL002 group increased, with the signal remaining relatively stable at 0.5 h. After 0.5 h, the CNR in the PL002 group showed a trend of increasing with higher doses. At 6 h, the high-dose PL002 group demonstrated superior imaging performance compared to other groups. Meanwhile, the low and medium dose groups of PL002 maintained a steady signal over 24 h. Additionally, the CNR of the Gadavist® group increased rapidly post-administration, achieving optimal imaging effects at 5 min, and then gradually decreased. At 6 h, the signal of the Gadavist® group was significantly lower than that of the PL002 groups (p-values for comparison with high-, medium-, and low-dose PL002 groups were 0.317, 0.009, and 0.033, respectively).

After completion of MRI imaging, brain tissues were extracted from the PL002 and ICG groups at 6 h and 24 h post-administration, respectively. Fluorescence measurements were subsequently performed, with the results depicted in Figures 4, 5. ICG, serving as a fluorescent surgical marker, is capable of penetrating the blood-brain barrier and concentrating at tumor sites to facilitate targeted tumor imaging. However, fluorescence imaging revealed negligible fluorescence signals in the ICG group at both 6 and 24 h. In contrast, the PL002 group exhibited intense fluorescence within the tumor sites, with well-defined tumor margins and significantly higher mean fluorescence intensity compared to the ICG group. Moreover, comparison of tissue fluorescence and fluorescence intensity across different time points showed that, at 6 h, both normal tissues and blood vessels exhibited higher background fluorescence. In contrast, at 24 h, background fluorescence in normal tissues and blood vessels was reduced, resulting in more distinct tumor fluorescence margins and slightly higher mean fluorescence intensity compared to that at 6 h. Additionally, fluorescence microscopic sections revealed that only red fluorescence penetrated into the interior of the tumor without overlapping with the blue fluorescence of cell nuclei, with more red fluorescence aggregating at the tumor margins and in microvessels. These findings indicate that PL002 retains the passive targeting properties of ICG to pathological tissues, effectively crossing the blood-brain barrier, distributing around the tumor, and penetrating into the tumor interior along tumor vessels, thereby accumulating at the tumor site for an extended period.

3.3 Pharmacokinetics studies

Sprague-Dawley (SD) rats were used to evaluate the pharmacokinetic profile and tissue distribution of PL002. After a single intravenous injection of PL002 at dosages of 3 mg/kg, 10 mg/kg, and 30 mg/kg, the plasma concentration of PL002 peaked immediately following the infusion (at 4 min). Subsequently, it rapidly transitioned into the elimination phase, with an average terminal half-life of elimination ranging from 2.51 to 4.87 h (Figure 6).

Following the intravenous administration of PL002 at a dose of 10 mg/kg to SD rats, the compound demonstrated a degree of exposure across all tissues, indicating a widespread distribution. The findings revealed that PL002 was predominantly accumulated in tissues with abundant blood supply, such as the liver, kidneys, spleen, and lungs, as well as in the ovaries, small intestine, and testes. The distribution pattern of gadolinium within PL002 mirrored that of

10.3389/fbioe.2025.1557772

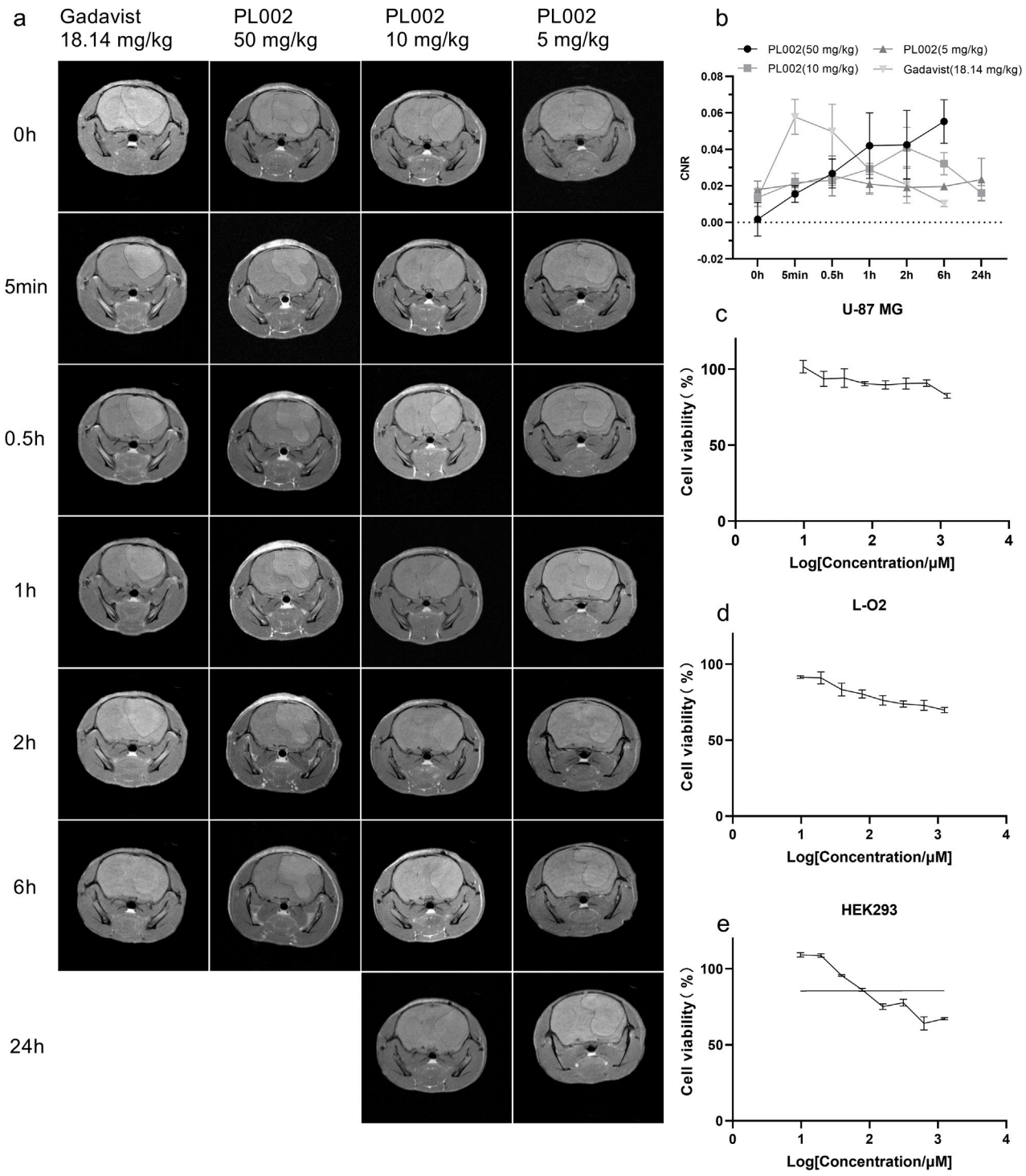

FIGURE 3
MR Imaging *in vivo*. **(a)** MR Imaging of PL002 and Gadavist® groups (PL002: ① 50 mg/kg, 30 uM Gd3+&ICG/kg; ② 10 mg/kg, 6 uM Gd3+&ICG/kg; ③ 5 mg/kg, 3 uM Gd3+&ICG/kg; GadavistR: ④ 18.14 mg/kg, 30 uM Gd3+/kg). **(b)** Contrast result of MR Imaging. **(c–e)** represent the proliferation activity results of PL002 evaluated by the CCK-8 method in U-87 MG, L-O2, and HEK293 cells, respectively.

the compound itself, with a significant concentration observed in the liver, kidneys, spleen, lungs, ovaries, large intestine, and small intestine (Figure 6). This suggests that, post intravenous infusion, the dual-modality contrast agent predominantly exists in tissues and plasma in the form of the parent drug.

3.4 Safety study *in vivo*

Drawing from the pharmacokinetic studies mentioned, PL002 is characterized by a slower metabolic rate and prolonged retention in the body, which could potentially

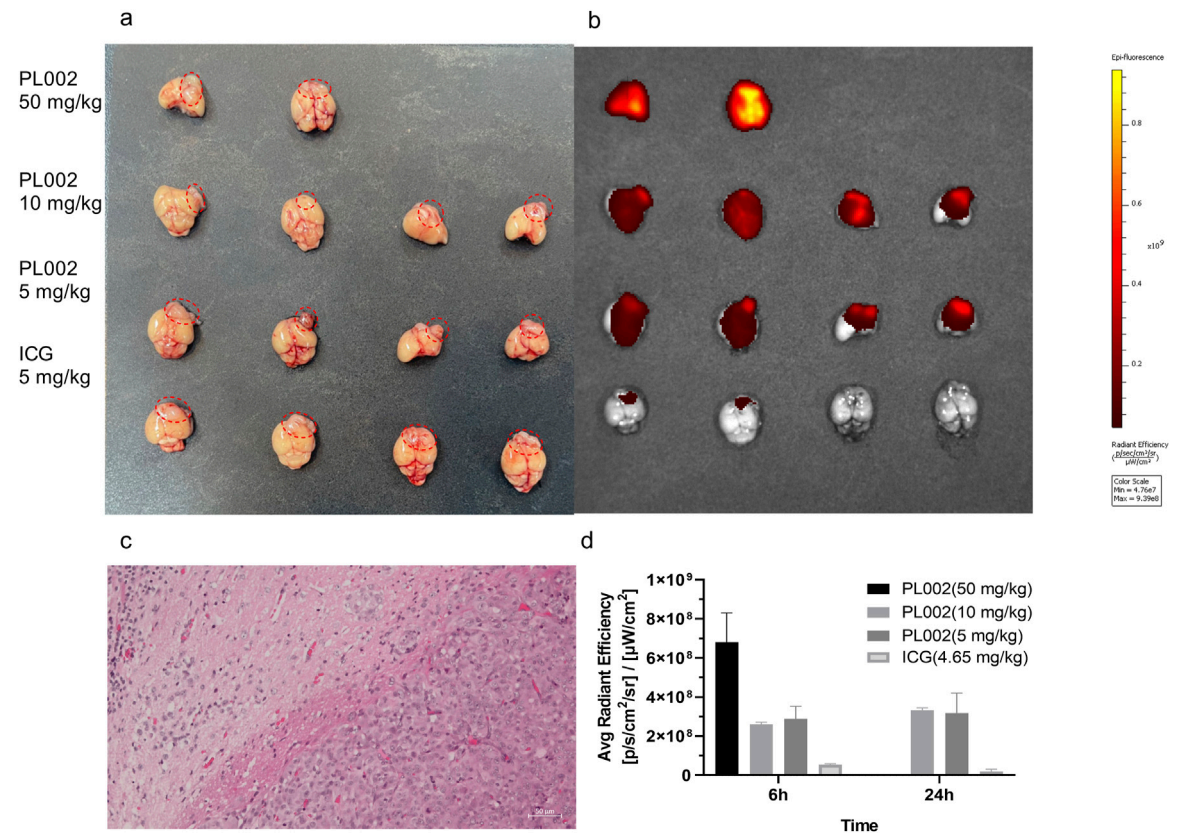

FIGURE 4
Fluorescent Imaging *in vivo*. **(a)** The brains in Fluorescent Imaging. **(b)** Fluorescent imaging result of PL002 and ICG groups. **(c)** HE staining figure. **(d)** Contrast result of Fluorescent Imaging (Due to the small sample size of only 2, no statistical analysis was performed.).

impose a significant physiological burden on subjects. To assess the safety of PL002, acute toxicity studies were conducted using SD rats following a single intravenous dose. The control group was administered a 5% glucose solution, whereas the experimental groups received PL002 at dosages of 100, 300, and 1,000 mg/kg. No adverse reactions were observed in the low-dose group rats; in the medium-dose group, 3 rats died within 30 min to 1 day after administration, and in the high-dose group, 10 rats died, suspected to be due to acute renal failure caused by PL002. Except for the low-dose group, animals exhibited reduced spontaneous activity, weight loss, and decreased appetite after administration, with more severe symptoms in the high-dose group. However, these conditions were reversible, and by the end of the 2-week observation period, the surviving rats had returned to normal, with body weight and food intake comparable to the control group. Gross anatomical observations revealed that the skin, adrenal glands, kidneys, testes, epididymis, ovaries and fallopian tubes, uterus, pancreas, lymph nodes (mesenteric and mandibular), and lungs appeared green in color. Histopathological examination showed varying degrees of cortical tubular necrosis in the kidneys, and minor injuries were also detected in the liver, heart, spleen, and lungs; the remaining discolored organs showed no abnormal findings under the microscope.

In summary, the acute toxicity of the test product led to significant mortality and adverse effects in the high-dose group. Conversely, the low-dose group did not show any unusual reactions. This indicates that while PL002 carries potential safety hazards at higher doses, it is deemed safe when administered at doses below 100 mg/kg.

4 Discussion

According to the 2022 Brain Glioma Diagnosis and Treatment Guidelines, the primary treatment for GBM involves surgical resection, complemented by radiotherapy and chemotherapy. The surgical objective is to safely remove the tumor to the greatest extent possible, with magnetic resonance imaging (MRI) playing a pivotal role throughout the procedure. Gadavist® is a novel and potent MRI contrast agent approved for enhancing the visibility of various body parts, including the brain, spinal cord, blood vessels, liver, and kidneys (Szomolanyi et al., 2019; Knobloch et al., 2020; Accessdata, 2020). According to the guidelines, the optimal imaging results with Gadavist® of MRI can be observed approximately 5 min post-injection, with tissue enhancement typically lasting until 45 min post-injection, which is suitable for preoperative imaging. Considering that glioblastoma surgery often lasts 4–5 h, if the surgeon needs to confirm the extent of resection during or after surgery, the patient would require another injection, imposing a significant physiological burden. Years of clinical research and post-marketing surveillance data have shown that Gadavist® has a

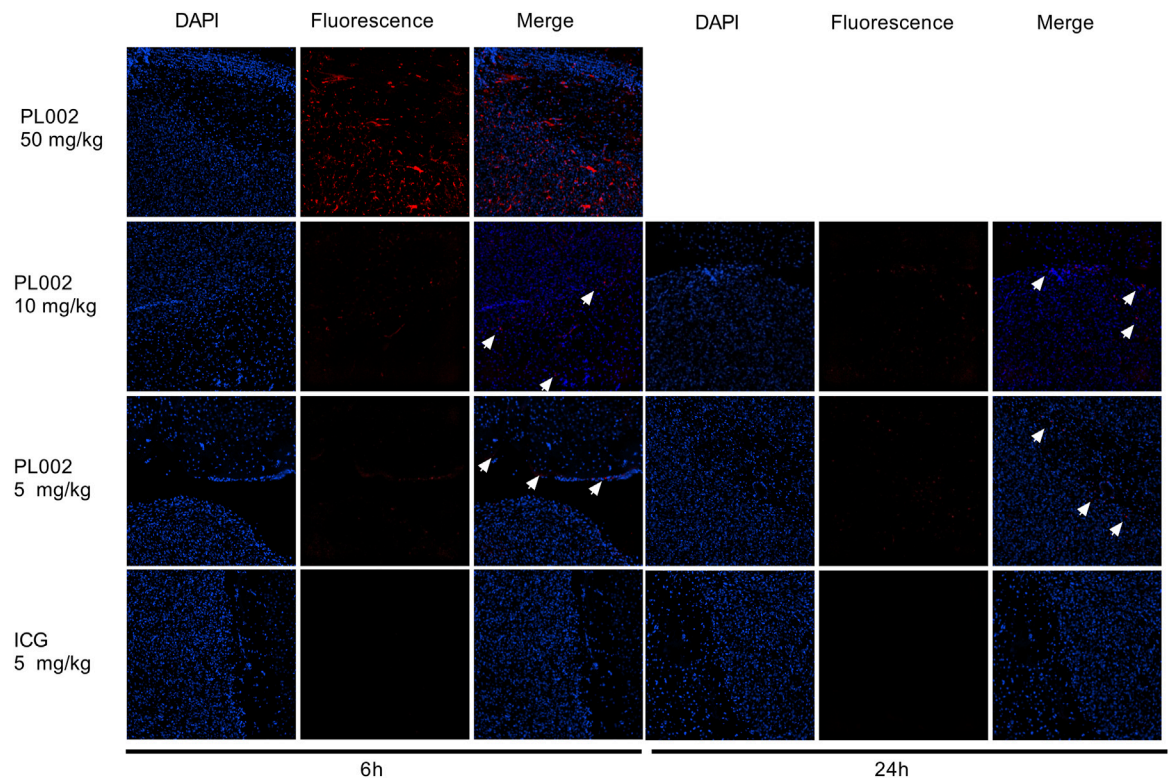

FIGURE 5
Fluorescence imaging of tumor microsections of PL002 and ICG groups in 6h and 24 h (200X; The white arrow indicates the location of the fluorescence).

relatively high safety profile (Forsting and Palkowitsch, 2010; Endrikat et al., 2024), but there is still a low probability of mild to moderate adverse reactions occurring after administration, such as headache, nausea, injection site reactions, taste disturbances, and a sensation of warmth. Severe adverse reactions include cardiac arrest, respiratory arrest, and anaphylactic shock, which may be related to the distribution of gadolinium ions or the stability of the drug itself.

PL002 can immediately enhance MRI imaging after injection at a relatively low dose, with the imaging effect gradually increasing within 6 h post-injection, and the tumor imaging boundaries remaining clear. Combined with its pharmacokinetic profile, PL002 has a half-life exceeding 2 h and prolonged *in vivo* circulation time, ensuring stable brain levels for up to 72 h. This stability fully supports pre-, intra-, and postoperative MRI needs for GBM surgery. In comparison, Gadavist® shows a signal decline starting at 5 min post-injection, with significantly lower MRI signals in tumor regions at 6 h post-injection compared to PL002. The tumor boundaries become blurred, and a single dose may not meet the imaging needs for the entire surgical procedure. Moreover, glioblastoma originates from glial cells and is characterized by rapidly proliferating tumor cells that infiltrate diffusely along white matter fibers and perivascular spaces. This leads to ill-defined tumor margins and incomplete resection. Glioblastoma is often accompanied by cerebral edema, which not only increases intracranial pressure but also obscures the actual tumor boundaries, complicating diagnosis and treatment. Gadavist® may have limitations in distinguishing tumor tissue from cerebral edema/infiltrative margins, as its short imaging window and mild enhancement signals in both cerebral edema and infiltrative margins reduce contrast and affect the accuracy of clinical diagnosis. However, PL002s prolonged retention and stable imaging within the tumor, coupled with the gradual decrease in drug concentration in normal tissues and edematous regions outside the tumor, enhance the sensitivity and specificity of PL002 in MRI diagnosis.

In addition to MRI, PL002 contains an ICG fluorescent moiety that provides fluorescence-guided technology. Fluorescence-guided techniques are also recommended as an adjunct in glioblastoma surgery. ICG is one of the commonly used clinical fluorophores, but its application in low-grade gliomas is limited. The accumulation of ICG in GBM and the delineation of brain boundaries are primarily attributed to the disrupted blood-brain barrier (BBB) and preferential accumulation in areas with enhanced vascular permeability due to defective vascular architecture, impaired lymphatic drainage, and increased permeability mediators (Ergin et al., 2012; Maeda et al., 2000). Clinical research results show that among four cases of brain gliomas assisted by ICG-guided surgery, the fluorescence positivity rate was 50%. In the two failed cases, ICG was administered 24 h before surgery (Bianconi et al., 2023). The long time interval between drug administration and surgery may have led to the clearance of the drug retained in the tumor. Moreover, ICG itself has a rapid metabolism, and the relatively less disrupted BBB in patients with low-grade gliomas results in insufficient accumulation of ICG in brain tumors (Watson et al., 2018). Coupled with the extracellular accumulation and uneven

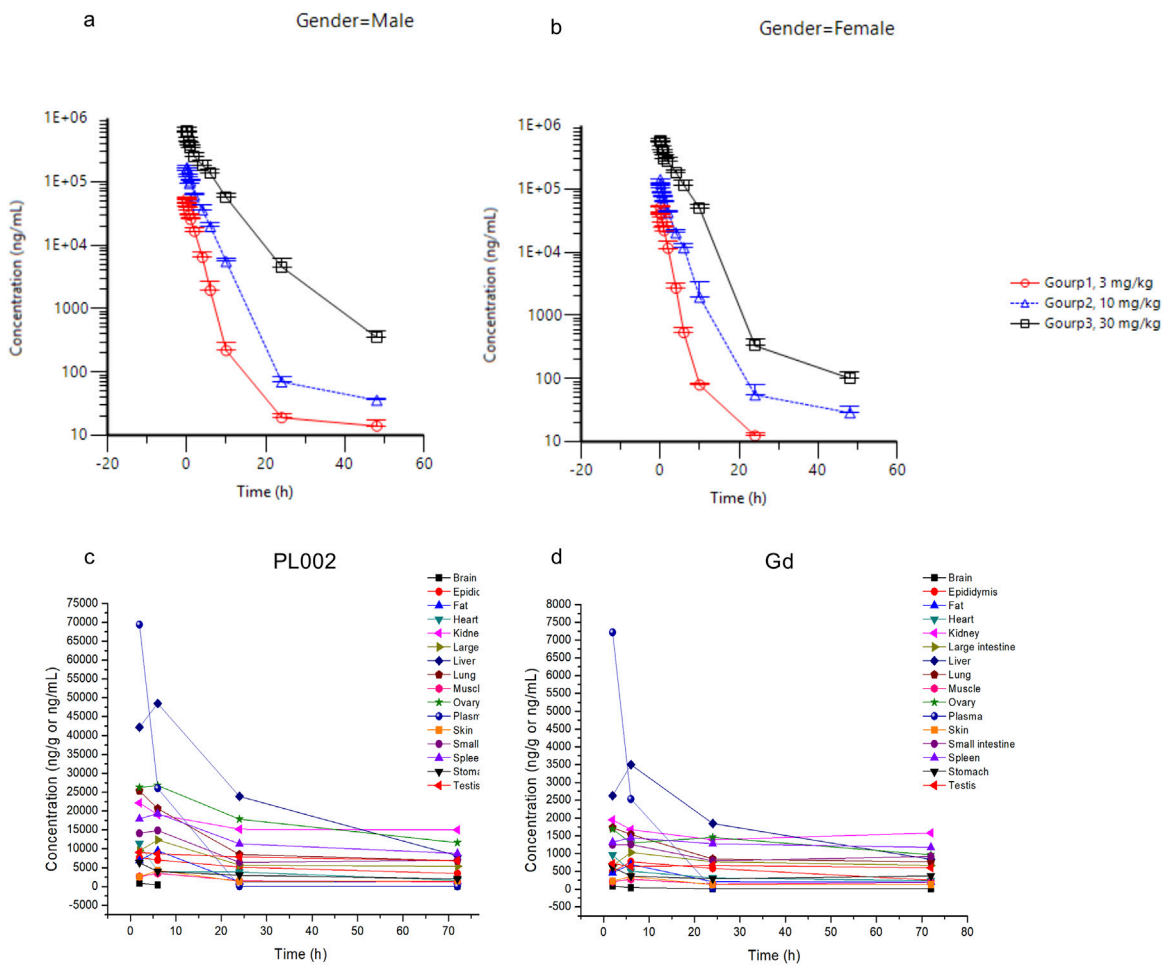

FIGURE 6
The pharmacokinetic profile and tissue distribution of PL002 *in vivo*. **(a)** The average plasma concentration in male animals of each dosage group; **(b)** The average plasma concentration in female animals of each dosage group; **(c)** Concentration of PL002 in plasma and major tissues; **(d)** Concentration of gadolinium in plasma and major tissues [In Figures **(a, b)**, plasma sampling time points are: pre-dose, 4 min, 10, 15, 30, and 45 min, and 1, 2, 4, 6, 10, 24, and 48 h post-administration; in Figures **(c, d)**, tissue sampling time points are: 2, 6, 24, and 72 h after dosing.].

distribution of ICG within tumor tissues, it may not accurately delineate tumor boundaries (Onda et al., 2016). This was also demonstrated in the fluorescence imaging at 6 and 24 h post-administration of ICG in this study. In contrast, PL002 crosses the blood-brain barrier in a manner similar to ICG and retains the advantage of passive accumulation in the tumor region. At 6 and 24 h post-injection, the fluorescent boundaries of the tumor region in the PL002 group remained stable and clearly delineated the tumor area. The slower metabolism of PL002 resulted in brighter and clearer fluorescent boundaries in the tumor region at 24 h, with higher average fluorescence intensity in the tumor area.

Finally, safety is an inevitable consideration in clinical applications. In imaging and pharmacokinetic studies, PL002 has been found to be highly stable, with its tissue distribution closely matching that of gadolinium ions. This indicates that PL002 primarily exists in its original form within the body after administration. Combined with acute toxicity studies, intravenous administration of PL002 at doses up to 100 mg/kg revealed no abnormalities, suggesting that there are likely no safety concerns in the short term. Moreover, compared to Gadavist®, PL002 has a longer half-life. According to tissue distribution data, after the same half-life period, the residual amount of gadolinium in tissues from PL002 may be lower than that from Gadavist®. The drug clearance from the body may be more extensive for PL002, which is advantageous for its long-term safety. Additionally, PL002 demonstrates good magnetic resonance imaging (MRI) and excellent fluorescence imaging at dosages of 10–50 mg/kg (0.006–0.03 mmol Gd/kg). The content of gadolinium in PL002 is less than 10%, which means that PL002 can be used at relatively lower doses in clinical applications, with correspondingly lower doses of gadolinium. To some extent, this can mitigate the safety concerns related to gadolinium deposition.

5 Conclusion

In summary, PL002 combines the advantages of MRI and fluorescence imaging while retaining the passive tumor targeting and strong imaging signal of ICG. Its extended half-life addresses the short imaging window issues associated with GBCAs and ICG, offering high tissue resolution, strong penetration, and high sensitivity. This ensures effective imaging while also having a broad therapeutic dose range. All

of these features suggest that PL002 has promising application values and development prospects in the evaluation of resection margins before surgery, real-time intraoperative navigation, and postoperative confirmation of the extent of resection.

Data availability statement

The original contributions presented in the study are included in the article/Supplementary Material, further inquiries can be directed to the corresponding authors.

Ethics statement

Ethical approval was not required for the studies on humans in accordance with the local legislation and institutional requirements because only commercially available established cell lines were used. The animal study was approved by Institutional Animal Care and Use Committee (IACUC) at JOINN Laboratories (Beijing) and the animal experiments in this study were conducted at the JOINN Laboratories (Beijing) and Zhejiang Longchuan Biotechnology Co., Ltd., in accordance with the regulations of their respective ethics committees. Zhejiang Longchuan Biopharmaceutical Technology Co., Ltd. Experimental Animal Welfare and Ethics Committee. The study was conducted in accordance with the local legislation and institutional requirements.

Author contributions

XZ: Project administration, Resources, Validation, Writing–review and editing. KJ: Data curation, Formal Analysis, Investigation, Visualization, Writing–original draft. YH: Conceptualization, Investigation, Project administration, Resources, Supervision, Writing–review and editing. SY: Conceptualization, Investigation, Methodology, Project administration, Supervision, Writing–review and editing.

Funding

The author(s) declare financial support was received for the research, authorship, and/or publication of this article. The authors express their gratitude to The Zhejiang Province Leading Geese Plan (Grant No. 2025C02063) for its financial support.

Acknowledgments

We would like to thank WuXi AppTec (Tianjin) Co., Ltd., JOINN LABORATORIES (CHINA) Co., Ltd., and Zhejiang Longchuan Biopharmaceutical Technology Co., Ltd. for their platform and technical support. We also appreciate the technical and methodological assistance provided by Zhu Xinglong, Jin Lei, Jia Mengjiao, Hu Rong, and Tao Qingfeng.

Conflict of interest

Authors XZ, KJ, and YH were employed by Zhejiang Poly Pharm. Co., Ltd.

The remaining authors declare that the research was conducted in the absence of any commercial or financial relationships that could be construed as a potential conflict of interest.

Generative AI statement

The author(s) declare that no Generative AI was used in the creation of this manuscript.

Publisher's note

Supplementary material

The Supplementary Material for this article can be found online at: https://www.frontiersin.org/articles/10.3389/fbioe.2025.1557772/full#supplementary-material

References

Accessdata (2020). Gadavist product label. Available online at: https://www.accessdata.fda.gov/drugsatfda_docs/label/2011/201277s000lbl.pdf (Accessed october 6, 2020).

Acerbi, F., Vetrano, I. G., Sattin, T., de Laurentis, C., Bosio, L., Rossini, Z., et al. (2018). The role of indocyanine green videoangiography with FLOW 800 analysis for the surgical management of central nervous system tumors: an update. *Neurosurg. Focus* 44 (6), E6. PMID: 29852759. doi:10.3171/2018.3.FOCUS1862

Bianconi, A., Bonada, M., Zeppa, P., Colonna, S., Tartara, F., Melcarne, A., et al. (2023). How reliable is fluorescence-guided surgery in low-grade gliomas? A systematic review concerning different fluorophores. *Cancers (Basel)* 15 (16), 4130. PMID: 37627158; PMCID: PMC10452554. doi:10.3390/cancers15164130

Bonosi, L., Marrone, S., Benigno, U. E., Buscemi, F., Musso, S., Porzio, M., et al. (2023). Maximal safe resection in glioblastoma surgery: a systematic review of advanced intraoperative image-guided techniques. *Brain Sci.* 13 (2), 216. PMID: 36831759; PMCID: PMC9954589. doi:10.3390/brainsci13020216

Endrikat, J., Gutberlet, M., Hoffmann, K. T., Schöckel, L., Bhatti, A., Harz, C., et al. (2024). Clinical safety of gadobutrol: review of over 25 Years of use exceeding 100 million administrations. *Invest. Radiol.* 59 (9), 605–613. Epub 2024 Mar 1. PMID: 38426761. doi:10.1097/RLI.0000000000001072

Ergin, A., Wang, M., Zhang, J. Y., Bruce, J. N., Fine, R. L., Bigio, I. J., et al. (2012). The feasibility of real-time *in vivo* optical detection of blood-brain barrier disruption with indocyanine green. *J. Neurooncol* 106 (3), 551–560. Epub 2011 Oct 1. PMID: 21964696. doi:10.1007/s11060-011-0711-5

Eyüpoglu, I. Y., Hore, N., Savaskan, N. E., Grummich, P., Roessler, K., Buchfelder, M., et al. (2012). Improving the extent of malignant glioma resection by dual intraoperative

visualization approach. *PLoS One* 7 (9), e44885. Epub 2012 Sep 26. PMID: 23049761; PMCID: PMC3458892. doi:10.1371/journal.pone.0044885

Forsting, M., and Palkowitsch, P. (2010). Prevalence of acute adverse reactions to gadobutrol--a highly concentrated macrocyclic gadolinium chelate: review of 14,299 patients from observational trials. *Eur. J. Radiol.* 74 (3), e186–e192. Epub 2009 Jul 2. PMID: 19574008. doi:10.1016/j.ejrad.2009.06.005

Knobloch, G., Frenzel, T., Pietsch, H., and Jost, G. (2020). Signal enhancement and enhancement kinetics of gadobutrol, gadoteridol, and gadoterate meglumine in various body regions: a comparative animal study. *Invest. Radiol.* 55 (6), 367–373. PMID: 31985602. doi:10.1097/RLI.0000000000000645

Krivosheya, D., Rao, G., Tummala, S., Kumar, V., Suki, D., Bastos, D. C. A., et al. (2021). Impact of multi-modality monitoring using direct electrical stimulation to determine corticospinal tract shift and integrity in tumors using the intraoperative MRI. *J. Neurol. Surg. A Cent. Eur. Neurosurg.* 82 (4), 375–380. Epub 2019 Oct 28. PMID: 31659724. doi:10.1055/s-0039-1698383

Li, P., Qian, R., Niu, C., and Fu, X. (2017). Impact of intraoperative MRI-guided resection on resection and survival in patient with gliomas: a meta-analysis. *Curr. Med. Res. Opin.* 33 (4), 621–630. Epub 2017 Feb 2. PMID: 28008781. doi:10.1080/03007995.2016.1275935

Maeda, H., Wu, J., Sawa, T., Matsumura, Y., and Hori, K. (2000). Tumor vascular permeability and the EPR effect in macromolecular therapeutics: a review. *J. Control Release* 65 (1-2), 271–284. PMID: 10699287. doi:10.1016/s0168-3659(99)00248-5

Mosteiro, A., Di Somma, A., Ramos, P. R., Ferrés, A., De Rosa, A., González-Ortiz, S., et al. (2022). Is intraoperative ultrasound more efficient than magnetic resonance in neurosurgical oncology? An exploratory cost-effectiveness analysis. *Front. Oncol.* 12, 1016264. PMID: 36387079; PMCID: PMC9650059. doi:10.3389/fonc.2022.1016264

Onda, N., Kimura, M., Yoshida, T., and Shibutani, M. (2016). Preferential tumor cellular uptake and retention of indocyanine green for *in vivo* tumor imaging. *Int. J. Cancer* 139 (3), 673–682. Epub 2016 Apr 4. PMID: 27006261. doi:10.1002/ijc.30102

Ostrom, Q. T., Price, M., Neff, C., Cioffi, G., Waite, K. A., Kruchko, C., et al. (2023). CBTRUS statistical Report: primary brain and other central nervous system tumors diagnosed in the United States in 2016—2020. *Neuro-Oncology* 25 (Suppl. ment_4), iv1–iv99. doi:10.1093/neuonc/noad149

Qi, Z., Yu, H., Chen, L., Qu, Y., Zhang, M., Qi, G., et al. (2024). Analysis and prediction of central nervous system tumor burden in China during 1990-2030. *PLoS One* 19 (4), e0300390. PMID: 38630737; PMCID: PMC11023588. doi:10.1371/journal.pone.0300390

Schupper, A. J., Rao, M., Mohammadi, N., Baron, R., Lee, J. Y. K., Acerbi, F., et al. (2021). Fluorescence-guided surgery: a review on timing and use in brain tumor surgery. *Front. Neurol.* 12, 682151. PMID: 34220688; PMCID: PMC8245059. doi:10.3389/fneur.2021.682151

Schupper, A. J., Roa, J. A., and Hadjipanayis, C. G. (2022). Contemporary intraoperative visualization for GBM with use of exoscope, 5-ALA fluorescence-guided surgery and tractography. *Neurosurg. Focus Video* 6, V5. doi:10.3171/2021.10.focvid21174

Staartjes, V. E., Togni-Pogliorini, A., Stumpo, V., Serra, C., and Regli, L. (2021). Impact of intraoperative magnetic resonance imaging on gross total resection, extent of resection, and residual tumor volume in pituitary surgery: systematic review and meta-analysis. *Pituitary* 24 (4), 644–656. Epub 2021 May 4. PMID: 33945115; PMCID: PMC8270798. doi:10.1007/s11102-021-01147-2

Szomolanyi, P., Rohrer, M., Frenzel, T., Noebauer-Huhmann, I. M., Jost, G., Endrikat, J., et al. (2019). Comparison of the relaxivities of macrocyclic gadolinium-based contrast agents in human plasma at 1.5, 3, and 7 T, and blood at 3 T. *Invest. Radiol.* 54 (9), 559–564. PMID: 31124800; PMCID: PMC6738537. doi:10.1097/RLI.0000000000000577

Tsugu, A., Ishizaka, H., Mizokami, Y., Osada, T., Baba, T., Yoshiyama, M., et al. (2011). Impact of the combination of 5-aminolevulinic acid-induced fluorescence with intraoperative magnetic resonance imaging-guided surgery for glioma. *World Neurosurg.* 76 (1-2), 120–127. PMID: 21839963. doi:10.1016/j.wneu.2011.02.005

Watson, J. R., Martirosyan, N., Lemole, G. M., Trouard, T. P., and Romanowski, M. (2018). Intraoperative brain tumor resection with indocyanine green using augmented microscopy. *J. Biomed. Opt.* 23(9):1–4. doi:10.1117/1.jbo.23.9.090501

Wirtz, C. R., Albert, F. K., Schwaderer, M., Heuer, C., Staubert, A., Tronnier, V. M., et al. (2000). The benefit of neuronavigation for neurosurgery analyzed by its impact on glioblastoma surgery. *Neurol. Res.* 22 (4), 354–360. PMID: 10874684. doi:10.1080/01616412.2000.11740684

Frontiers in
Bioengineering and Biotechnology

Accelerates the development of therapies, devices, and technologies to improve our lives

A multidisciplinary journal that accelerates the development of biological therapies, devices, processes and technologies to improve our lives by bridging the gap between discoveries and their application.

Discover the latest Research Topics

See more →

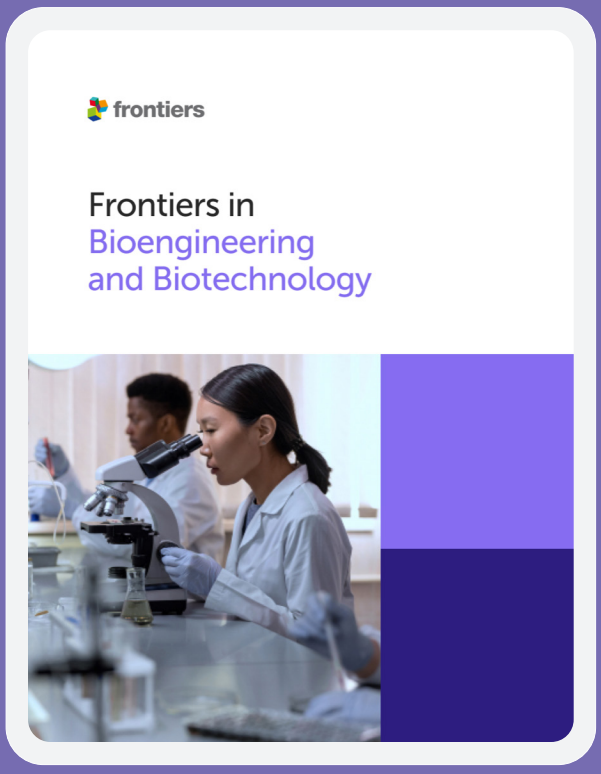

Frontiers

Avenue du Tribunal-Fédéral 34
1005 Lausanne, Switzerland
frontiersin.org

Contact us

+41 (0)21 510 17 00
frontiersin.org/about/contact